ALONG-TRENCH SEGMENTATION AND DOWN-DIP LIMIT OF THE SEISMOGENIC ZONE AT THE EASTERN ALASKA-ALEUTIAN SUBDUCTION ZONE

by

Harold Kuehn

Submitted in partial fulfillment of the requirements
for the degree of Doctor of Philosophy

at

Dalhousie University
Halifax, Nova Scotia
January 2019

Contents

List of Tables

List of Figures

Abstract

The largest and most destructive earthquakes nucleate on the seismogenic parts of megathrust faults along subduction zones. Understanding the controls of rupture propagation in along-trench and dip direction is a key factor to estimate size and location of future megathrust earthquakes. Various geologic features and subduction-related processes have been proposed to affect megathrust segmentation along the plate boundary zone, however, inaccessibility due to its deep location makes a detailed investigation challenging. The ALEUT project aims to overcome these difficulties by acquisition of state-of-the-art deep penetrating multichannel seismic reflection data combined with coinciding ocean bottom seismometer refraction data for a large section of the eastern Alaska-Aleutian subduction zone (AASZ). This thesis discusses results based on the ALEUT dataset and provides unique insights into possible morphological controls on along-strike rupture organization of the subduction thrust and new constraints on its seismogenic down-dip limit. Plate interface reflections recorded throughout the survey area were used to construct a 3D model of the interplate interface, on which two major crest-like have been identified. The spatial coincidence of these geometrical highs, interpreted to represent subducted seamounts chains, with boundaries of the region's great earthquake ruptures indicates that the megathrust geometry is the primary factor controlling the segmentation of the eastern AASZ. Furthermore, the plate interface reflection signatures appear to increase significantly with depth and have been correlated to 1) seismogenic, 2) conditionally stable and, 3) aseismic slip behavior. The results confirm the spatial extent of rupture areas derived from existing information, such as aftershock locations, inverse tsunami waveform modelling and the intersection of a serpentinized mantle wedge. However, contrary to recent geodetic dislocation models that suggest a widely free slipping segment along the ASSZ (Shumagin Gap), the results suggest a seismogenic plate interface for this area that extents from the trench up to 100 km landward. A partially seismogenic Shumagin Gap area could become part of a great future megathrust event as shallow rupture is propagating into this area and exposing it to strong ground shaking and large tsunami waves, as it might have happened in the 18^{th} and 19^{th} century.

List of Abbreviations Used

AASZ	Alaska-Aleutian subduction zone
ALEUT	Alaska Langseth Experiment to Understand the Megathrust
AVO	Amplitude variation with offset
BP	Band pass
CDP	Common depth point
EDM	Electronic distance measurements
ETS	Episodic tremor and slip
GPS	Global positioning system
HP	High pass
ISC-GEM	International Seismological Centre - Global earthquake model
LDEO	Lamont-Doherty Earth Observatory
LFE	Low frequency earthquake
LIFT	Leading Intelligent Filter Technology
LP	Low pass
MCS	Multichannel seismic
NMO	Normal move out
OBS	Ocean bottom seismomenter
PIM	Plate interface model
RMS	Root mean square
SRME	Surface related multiple elimination
SSE	Slow slip event
TWTT	Two way travel time
USGS	United States Geological Survey

Acknowledgements

There are numerous individuals who have greatly contributed to the completion of this thesis and I would not be at this point without their support, encouragement and guidance. Although, I could name many more people who helped me in various ways and during different episodes in the last seven years, I limit the number of persons to those I worked closest and most consistently with.

First and foremost, I would like to thank my advisor Mladen Nedimović. Mladen's guidance and support throughout the entire course of my studies has transformed me from being a novice graduate student with no major seismic background knowledge to becoming a controlled-source seismologist. I would like to thank him for this opportunity and the vast amount of time an effort he invested in me to slowly build up confidence and the courage to aim for higher goals. He also encouraged and supported me to apply for grants to travel to multiple international science conferences and workshops. This allowed me to visit many places in North America and Europe and to meet new and interesting people in the science community. All of these combined left a lasting impression on me that reaches far beyond the academic or professional work space and I am very grateful for that.

I want to thank Donna Shillington, Keith Louden and Matthias Delescluse for being part of my PhD committee. At any point, throughout the entire time of my studies, it felt so easy to approach them when I needed help or advice. This made my life so much easier. Thank you also for the time and effort it took to carefully read the thesis manuscript and providing me with your comments, which improved this thesis to a great deal.

Anne Bécel, Jiyao Li and Donna became close work colleagues and good friends since our cruise offshore Alaska in 2011. I am truly grateful to have met these wonderful people, who were always helpful and encouraging towards me, when I took my first steps into the science world. The generosity you showed in sharing results is admiring and I hope I can pass it on some day.

Thank you Louise Watremez and Paul Mattern for basically teaching me how to script and how to code Matlab. I do not remember how often you helped me out by finding bugs in my scripts or showing me new tricks to handle and format my data.

I do not want to imagine where I would be today without you.

To my lab mates and good friends Ana Corbalán, Masoud Aali, Helen Lau and Han Chao: Thank you for being in the lab. You guys made life bearable during times of frustration and stress. It is good to have you around. Thank you John Thibodeau for solving literally every technically problem I have encountered during the entire time.

Finally, I want to give my deepest gratitude to my dear parents Ludwig and Hsuey-Ying Kühn. Their unconditional support, encouragement and love throughout my entire life is the fundament for everything I have accomplished.

Chapter 1

Introduction

1.1 Historic view on subduction zones

The occurrence of very deep earthquakes (up to ∼660 km depth) along inclined planes near oceanic trenches has been known long before the establishment of the theory of plate tectonics and the concept of subduction zones [*Wadati*, 1935]. Hugo Benioff was first to relate these thin zones of seismicity to boundaries between oceanic and continental material [*Benioff*, 1949]. Soon after, the work of Harry Hess and Robert Dietz on oceanic crust led to the concept of seafloor spreading and provided a base for the development and final breakthrough of the theory of plate tectonics [*Dietz*, 1961; *Hess*, 1955] that was independently confirmed through observations by *Vine and Matthews* [1963] and *Morley* [1991].

The continuous formation of new crust at elongated mid-ocean ridges, as put forward in the plate tectonic theory, needs an opposite process (or counterpart) where crust is destroyed or consumed if the size of the earth is to remain the same (otherwise expanding earth). André Amschutz described observations in the Alps where geosynclines and adherent crustal material seem to be pulled below the foreland by descending convection currents and related them with dipping zones of seismicity found earlier by Wadati and Benioff (so called Wadati-Benioff zones). He also regarded subsequent gravity sliding into depression or trenches as indirect or auxiliary result of this *subduction* process, a term he introduced first in 1951 [*Amstutz*, 1951, 1957, 1962]. His ideas of descending rock masses are in remarkable accord with the modern theory of plate tectonics. But the first concept of subduction goes even further back. In 1911 Otto Ampferer published a study on thermally driven down-welling mantle convection currents causing orogenic faulting and shearing in areas he called *Verschluckungszonen* (lit. "*swallow-up zones*", see Fig. 1.1.1) [*Ampferer and Hammer*, 1911].

Today the concept of subduction zones is not debated. However, the mechanisms involved are still not fully understood and are scrutinized in view of recent

catastrophic disasters at subduction zones, such as tsunami-triggering great earthquakes in Indonesia (2004), Chile (2010) and Japan (2011), in which hundreds of thousands of people lost their lives and billions of dollars worth of property and infrastructure was destroyed.

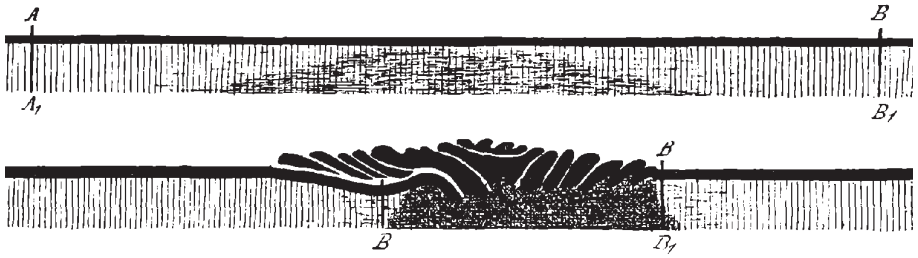

Figure 1.1.1: First schematic sketch of a subduction zone (or "*Verschluckungszone*") [*Ampferer and Hammer*, 1911].

1.2 Subduction zones

Subduction zones are three-dimensional manifestations of down-welling movements of tectonic plates. The deep-sea trenches and the volcanic arcs that parallel them are surficial features characterizing these convergent plate boundaries. The classical subduction zone model involves incoming oceanic crust and an overriding plate of continental crust (e.g. Aleutians, Andes, Cascades, Indonesia, Japan). Other types of subduction configurations occur when two oceanic plates converge (e.g. Izu-Bonin, Mariana, Tonga) or two continents collide (e.g. Himalaya) (Fig. 1.2.1). Combined, convergent margins have a total cumulative length of more than 55,000 km [*Lallemand*, 1999], almost equal in length to mid-ocean ridges with cumulative length of ca. 60,000 km [*Kearey et al.*, 2013] (Fig. 1.2.1).

Because the converging plates rub against each other, subduction zones are the source of the largest earthquakes on Planet Earth and are attracting significant attention from the general public on a continuous basis. Further raising public interest in subduction zones are geohazards related to arc volcanoes. Increasing pressure and temperature trigger dehydration reactions of the downgoing sedimentary, crustal, and serpentinized uppermost oceanic mantle material and the upward escape of water in turn leads to partial melting of continental mantle rocks. The generated magma rises vertically to the surface and forms volcanic arcs, which act as nurseries for new continental crust [*Stern*, 2002] (Fig. 1.2.2). But these zones

of plate convergence have received additional public attention in recent years due to their role in the global carbon cycle, which is controlled chiefly by plate subduction and volcanic outgassing with far reaching effects on the terrestrial climate [*Dasgupta and Hirschmann*, 2010].

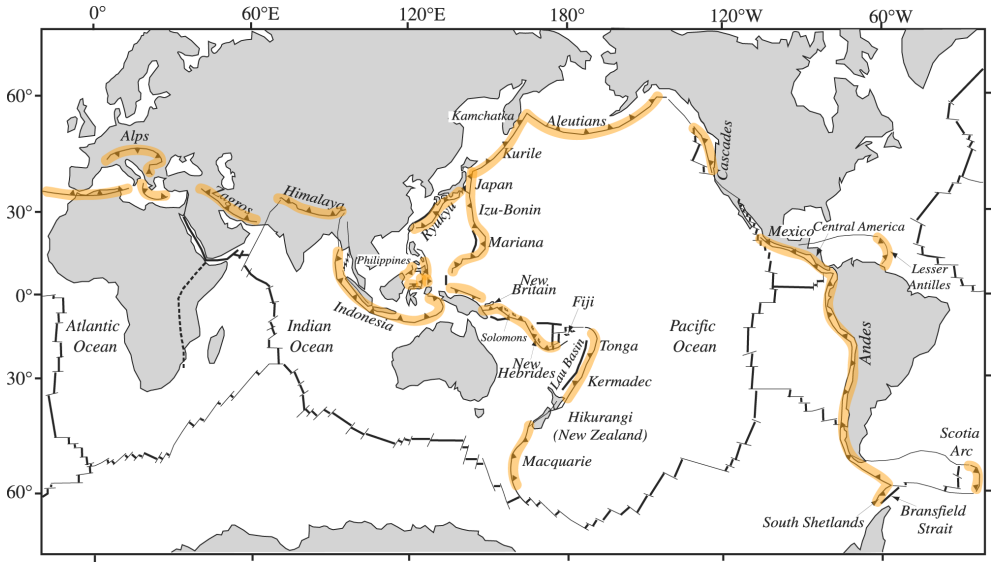

Figure 1.2.1: Plate tectonic boundaries [modified after *Lallemand* [1999]. Thick orange lines mark the location of subduction zones worldwide. Mid-ocean ridges are shown as thick solid black lines offset by thin solid black lines, which are fracture zones. Dashed black lines are developing continental rifts.

In the Earth's geodynamic system, subduction zones are believed to be large recycling machines where lithospheric mantle, crust, sediments and seawater enter the Earth's mantle. Despite this key common commonality, subduction zones worldwide exhibit a wide variety of characteristics that differentiate them. For example, there are large differences in subduction geometry, seismicity, structural framework, continental growth or loss, and net movement within a stationary reference frame. Some major controls on these parameters are slab temperature and sediment volume of the incoming plate, and plate convergence velocity. Subduction zones where the incoming plate is young, thin, hot and buoyant usually exhibit a shallow trench, shallow dipping interplate interface, limited and shallow intraslab seismicity, and a back-arc region showing compressional deformation [e.g., *Stern*, 2002]. Subduction zones where older, thicker, cooler and denser oceanic plates subduct show a much steeper dipping interplate interface, and wide-spread intraslab seismicity that can reach great depths of up to ~660 km. Cold subduction zones are characterized by the deepest trenches in the world and can exhibit extensional back-arc regions [e.g., *Deschamps and Fujiwara*, 2003; *Uyeda and Kanamori*, 1979].

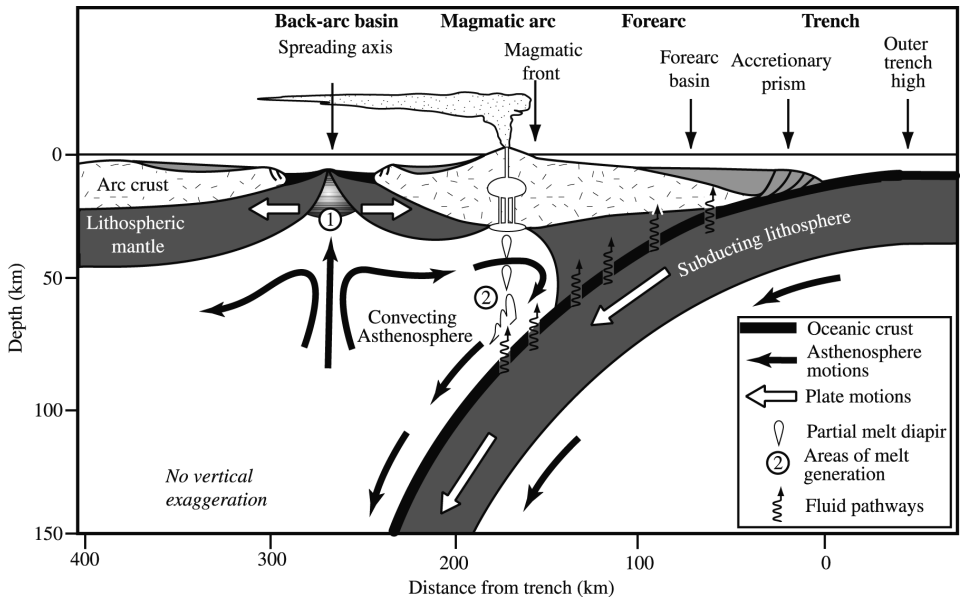

Figure 1.2.2: Schematic cross-section of a subduction zone [modified after *Stern* [2002]. Incoming oceanic lithosphere subducts beneath an overriding plate carrying fluids into the Earth's mantle where they trigger partial melting of continental mantle rock, which rises vertically upward and forms magmatic arcs. Back-arc spreading is presently concentrated in the western Pacific Ocean (e.g. Izu-Bonin, Mariana) where the back-arc crust is under extensional stress due to slab roll-back [e.g., *Deschamps and Fujiwara*, 2003].

The plate convergence rate and volume of sediment input appear to be main factors that control the long-term mass balance at convergent margins and classify them as accretionary when the balance is positive and erosional when negative [*Clift and Vannucchi*, 2004]. Accretion occurs by material transfer from the subducting plate to the overriding plate, either by off-scraping material at the trench axis and adding it to the frontal wedge or by underplating of subducted sediment, i.e. adding it to the base of the overriding plate at greater depth. Erosional margins are characterized by material removal from the upper plate at the frontal wedge or the underside of the overriding plate with the eroded material transported into the mantle. Both mechanisms contribute to the net growth or loss of the fore-arc prism, which is often manifested in landward or seaward motion of the fore-arc wedge over long periods of time.

Strong and destructive earthquakes are typical for subduction zones and nucleate at the contact zone between the down-going (underthrusted) plate and the overriding plate where plates are sufficiently coupled to accumulate elastic strain [*Pacheco et al.*, 1993; *Scholz*, 1998] (Fig. 1.2.3). Observations show that this so-called seismogenic zone or main thrust zone extends roughly from ca. 5 - 15 km depth at

the seaward end [*Hyndman et al.*, 1997] to a maximum depth at 40 - 60 km at the landward end [*Boyd et al.*, 1995] of the subduction zone. The focal mechanisms of these earthquakes indicate thrust faulting. Although the seismogenic zone generates most of the earthquake moment magnitude, the co-seismic slip or displacement between the two converging plates can propagate further through partially coupled zones of conditional stable slip and extend all the way up to the trench. This has been recently demonstrated during the M_W 9.0 Tohoku earthquake in 2011 [e.g., *Ito et al.*, 2011; *Pollitz et al.*, 2011]. Physical properties of the contact zone between the two plates, often called the interplate interface (or fault plane, rupture plane), are the key parameters that control the coupling degree and hence stress build-up and extent of co-seismic slip area between plates, which result in the so-called megathrust or subduction earthquakes. Even though these earthquakes occur on only up to 2 - 5% of the entire length of Wadati-Benioff zones, which is outlined by the location of the deeper, smaller in size, normal fault mechanism intraslab earthquakes, they contribute to more than 90% of all the energy ever recorded by modern seismic instruments worldwide [*Kanamori*, 1977; *Pacheco et al.*, 1993].

Since the slip along the subduction thrust that generates great earthquakes lies mostly at shallower depths and is located offshore, slip mechanics promote an upward movement of the seafloor on the overriding plate so megathrust earthquakes have a large potential for tsunami generation. Therefore, the controls on size and location of the megathrust earthquake seismogenic areas, including their potential to generate tsunamis, are important factors for seismic hazard evaluation and many studies are targeted to understand along-strike and up- and down-dip extent of possible rupture zones [e.g., *Oleskevich et al.*, 1999; *Song and Simons*, 2003; *Wells et al.*, 2003].

1.3 Megathrust seismogenic zones and tectonic segmentation at subduction zones

The occurrence and magnitude of earthquakes is dependent on stick-slip behavior at the interface (or fault) between two rock masses and is determined by friction laws [*Scholz*, 1998]. Scholz classifies the fault surface into three different frictional regimes: stable sliding (aseismic), unstable "stick-slip" behavior (seismogenic) and conditionally stable sliding (transitional) (Fig. 1.2.3). Earthquakes nucleate in unstable regions and may propagate also into conditionally stable regions. However,

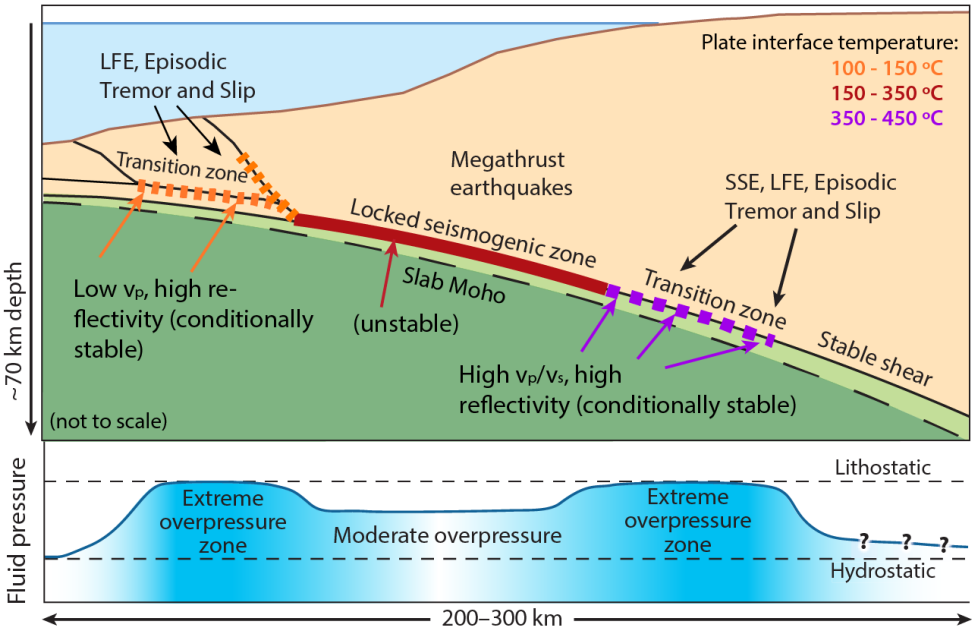

Figure 1.2.3: Schematic cross-section of the shallow (< ca. 70 km depth) plate interface of a subduction zone (modified after *Saffer and Tobin* [2011]). The locked (seismic unstable) part of the plate interface is located between transition zones of conditional stable sliding up- and down-dip of the rupture fault. Different temperature regimes correspond roughly to the locked seismogenic zone (thick red line) and transitional zone up- and down-dip of it (thick dashed orange and purple lines) [e.g., *Hyndman and Wang*, 1993]. Transitional zones to stable sliding are characterized by low v_p values, high v_p/v_s ratios and high amplitude seismic reflection signals with reversed polarities, induced by areas of elevated pore-fluid pressure. They also appear to correlate with the occurrence of Slow Slip Events (SSE), Low Frequency Earthquakes (LFE) and Episodic Tremor and Slip (ETS) [e.g., *Audet et al.*, 2009; *Ito and Obara*, 2006; *Kodaira et al.*, 2004].

rupture propagation will come to a stop when entering a zone of frictionally stable condition, such as are, for example, those of an unconsolidated granular material at shallow depth close to the trench (up-dip) or ductile deformation at large depth with the onset of higher temperatures (down-dip). The unstable and conditionally stable areas are in between these stable zones and define the extent of seismogenic zones, which are the areas that co-seismically slip during subduction earthquake ruptures. Frictional properties along the fault interface are related to temperature, rheology, rock type, sediment composition and roughness of the interface [e.g., *Bilek et al.*, 2003; *Oleskevich et al.*, 1999; *Ruff and Kanamori*, 1983; *Saffer and Marone*, 2003], all of which are difficult to directly assess. Frictional behavior in down-dip direction can be estimated from, for example, thermal modeling, past earthquake locations, geodetic observations on locking stages or gravity lows [e.g., *Fournier and Freymueller*, 2007; *Kanamori*, 1986; *Oleskevich et al.*, 1999; *Scholz*, 1998; *Song and Simons*, 2003]. An understanding of the controls of along-strike extents of slipping

areas is essential to determine rupture length and maximum magnitude expected during slip of tectonic segments. The dramatic lateral changes in seismogenic behavior that are observed in trench-parallel direction can be related to various causes, including variations in subducting plate fabric orientation and with it, different amounts of water intake [*Shillington et al.*, 2015], sediment input from the subducting oceanic plate [*Li et al.*, 2018; *Morgan and Ask*, 2004] or structural geologic anomalies at the interplate interface, such as are subducted seamount chains or high-relief fracture zones and ridges [*Bilek et al.*, 2003; *Das and Watts*, 2009; *Kodaira et al.*, 2000; *Watts et al.*, 2010]. Those morphologic features on the subducting interface can act as both, barriers to rupture and location of rupture nucleation.

Several data types and methods have been used so far and/or better determine the up-dip and down-dip extent of megathrust rupture, and trench-parallel segmentation on the subduction interface. These can be summarized as follows:

The outline of the great earthquake rupture area extent is often estimated based on the locations of aftershocks [e.g., *Davies et al.*, 1981; *Sykes*, 1971]. Aftershock earthquakes are usually of smaller magnitude than the main high-magnitude event and occur during the months that follow the main shock. With recurrence time periods (also called seismic cycles) of several decades to centuries for megathrust earthquakes, quantitative seismological data only available since roughly the beginning of the 20^{th} century, and a worldwide network of modern broadband recording stations monitoring seismic activity globally (World-Wide Standardized Seismograph Network - WSSNS) starting only in the 1960's, most seismological catalogues only cover one, if at all, seismic cycle. These catalogues are therefore, despite being highly useful, insufficient for making reliable predictions for future earthquakes regarding the repetitive nature of megathrust slip area failures.

One, but not the only factor controlling the up-dip and down-dip limit of seismogenic behavior in subduction zones might be critical temperatures at the interplate interface [*Oleskevich et al.*, 1999]. Empirical and laboratory studies suggest temperatures between 150 °C and 350 °C at the plate interface for the nucleation of megathrust ruptures and temperatures greater than 450 °C for the onset of plastic flow [*Harris and Wang*, 2002; *Hyndman and Wang*, 1993; *Tse and Rice*, 1986]. The transition zone with temperatures between 350 - 450 °C is considered as a region of conditional stable sliding (Fig. 1.2.3) [*Scholz*, 1998]. These

are, however, general estimates for all subduction zones that provide only limited constraints for the width of the seismogenic zone. Interplate interface temperature is determined based on heat flow measurements on the seafloor and from drill holes, where available, and/or numerical modeling with additional parameters based on various assumptions and simplifications, such as rock compositions or fluid-filled porosity [e.g., *Hyndman and Wang*, 1995; *Oleskevich et al.*, 1999]. The results are applicable only at a regional scale, especially in the Alaska-Aleutian region, where heat flow data measurements are sparse [*Pollack et al.*, 1993].

Geodetic measurements using high-precision Global Positioning System (GPS) data became an irreplaceable and routine tool for tectonic studies in the early 1990's [*Dixon*, 1991; *Hager et al.*, 1991]. These measurements provide horizontal relative velocities against a fixed reference frame with an uncertainty of ca. 2 - 5 millimeter per year [*Fletcher et al.*, 2001]. Monitoring these very slow movements of the crust requires continuous observation for at least a few years or repeated measurements at intervals of a few years before significant confidence in the results is attained. The vertical component is less well determined and needs even longer observation time. Therefore, an immediate evaluation of the tectonic setting in the study area is not possible with this method. The method also only allows to draw conclusions of the current or most recent state of crustal deformation in the investigated area which, although of great importance, can experience significant changes over the period of a single earthquake cycle that can last from tens to hundreds of years. Most importantly, geodetic measurements are confined to GPS stations located on land but seismically locked fore-arc areas of subduction zones that accumulate and release elastic strain energy are generally located offshore. Dislocation models for typical subduction zones to determine slip distribution, locking stage and coupling degree at subduction zones are therefore often only accurate at regional scale [*Fournier and Freymueller*, 2007].

Measurements of free air gravity anomalies along the strike of the deep-sea trenches were used by *Song and Simons* [2003] to predict variations of seismogenic behavior along subduction zones. Strong negative gravity values are interpreted as areas with high shear traction at the interplate interface that induces a decrease in vertical compressive stress thereby depressing fore-arc topography and gravity, as these depressions are filled with relatively low density sediments. Positive anomalies along the subduction zone are associated with relatively low shear traction and lesser seismogenic potential. Even though the gravity anomalies correspond with

variations in interplate interface coupling degree derived from geodetic observations, the link is not unambiguous. Free air gravity anomalies can also be caused by other factors, such as bathymetric highs, deep sediment basins formed by other causes or lithospheric flexure. Combined with the low resolution of satellite-based data, this technique is not suitable for detailed analysis of seismogenic properties but may provide a quick complementary insight into the basic tectonic features of subduction zones.

Devastating tsunamis triggered by great earthquakes can affect shorelines thousands of kilometers away from their origin. Gauge data at shoreline stations and/or locations offshore are used to estimate the location and extent of the tsunami source and slip distribution at the plate interface through inverse tsunami waveform modelling [e.g., *Fujii and Satake*, 2007]. The tsunami propagation is backtracked to a limited number of predetermined fault locations near the epicenter, from where its slip area is calculated. The method gives a good estimate of slip amount and distribution but the poor resolution prevents detailed conclusions about rupture segmentation or down-dip limits of the seismogenic zone.

Great megathrust earthquakes are often linked to sudden subsidence of shorelines to accommodate release of strain previously stored during the inter-seismic period of the earthquake cycle. Areas which fall below sea level during the earthquake experience deposition of suspended sediment and become marshland following the earthquake until the stress and elastic strain build up again to bring this land above sea level. The same area again subsides below sea level after the next great megathrust earthquake and so forth. Each tsunami flooding, often related to megathrust rupture, deposits a layer of coarse sediment in the low-lying coastlands. Identifying and dating these layered deposits formed by successive megathrust ruptures can extend the knowledge of historic occurrence of these events to thousands of years back [e.g., *Cisternas et al.*, 2005; *Nelson et al.*, 2015]. When a significant number of suitable data locations are found (often in estuaries), this method (paleo-seismology) can provide estimates on recurrence interval and the extent of great megathrust ruptures. However, large uncertainty is inherently associated with application of this method due to several factors, including the lack of knowledge on the origin of the tsunami source.

Historical written records and narratives can, to a certain degree, fill up data gaps caused by the short period of quantitative geophysical observation, under the

premise that local people left written transcripts of great earthquakes or tsunami events. For largely unpopulated areas like the Aleutian arc and Alaska, those records are very sparse.

1.4 Controlled source seismology

Earthquake, deformation, thermal, gravity, paleo-seismic and tsunami data and their interpretations, as well as written documents and narratives, have been instrumental in advancing knowledge of megathrust earthquake rupture areas, recurrence rates, subduction fault segmentation, strain accumulation, and three-dimensional spatial distribution of interplate coupling. Despite the great advances made, current estimates about the extent and location of the locked zones on the subduction thrusts are only regionally accurate. Better constraints can be obtained by, for example, repeat measurements of megathrust rupture areas based on earthquake and deformation studies. However, this requires an extremely long period of observations spanning multiple current global average life expectancies at birth to record a few seismic cycles of a megathrust rupture with intervals of many decades or hundreds of years. A new method for the future could be deep-sea geodesy, a technology still in the experimental stage despite the two decades or so of development [e.g., *Spiess et al.*, 1998]. Because the geo-hazards humanity is facing from great earthquakes are major, such as severe regional ground shaking followed by subsidence, liquefaction and other ground failure, as well as land inundation by tsunamis, alternative data and approaches are needed to obtain new information complementary to that provided by the methods discussed so far. One such possibility considered, because of its high resolving power and ability to apply at will, is to use controlled source seismology. This possibility has so far not been explored to its full potential likely because of its perceived high cost despite it being in general negligible relative to the material loses resulting from great earthquakes. Therefore, additional investment in using controlled source seismology to better understand the subduction zone structure and the great earthquake cycle may be worth the effort.

1.4.1 Development

Investigation of the subsurface structures with controlled seismic sources was first introduced at the beginning of the 20^{th} century with the development of a portable

seismograph by Emil Wiechert in Göttingen in 1906 and the use of large chemical explosions as "artificial earthquakes" in 1923 [*Angenheister*, 1927, 1928]. Large international co-operations started after the Second World War with increasingly better and more affordable technology to systematically investigate the structure of the Earth's crust, often in search for exploitable hydrocarbon sedimentary traps. Further technical developments improved capability of this method dramatically since its early days. The development of "air-gun" instruments (highly compressed air gets released from a submerged metal cylinder) as marine seismic sources in the 1970's allowed identical and repeating "shots" much more rapidly than it was possible with chemical explosives, which were used previously. Around the same time, self-containing recording units, "ocean-bottom" instruments were introduced. These devices, today called ocean bottom seismometers (OBS), are equipped with hydrophones and/or seismometers, sink to the seafloor, record seismic signals, and rise back to the surface after a ballast weight is discarded by an acoustic release command.

Another controlled source method for marine seismic investigations was conceived in parallel to air-gun and OBS development. It consists of towing behind the ship a string of hydrophones packed in a streamer or floating cable to record near-vertical incidence reflections of signals emitted by a seismic source, also towed behind the ship. This method quickly became a standard tool for commercial and scientific marine exploration. The hydrophone streamer consists of multiple groups of receivers acting as small receiver arrays, and is towed at shallow depth (e.g. from a few to 20 m). This multichannel seismic (MCS) method increased in capability with time by use of longer cables with a larger number of channels.

Compared to seismic land surveys, marine operations became relatively inexpensive and large amount of data could be collected efficiently at great speed. These technological advances offered much higher resolution of the recorded data and allowed interpretations with increasing detail. With the onset of digital recording and huge increases in computational power and data storing abilities at the beginning of the 1990's, major advances in processing and interpretation methodology also took place. Calculation of the full wave field or inversion of travel-time in laterally heterogeneous media became possible with new computing abilities [e.g., *Hole*, 1992; *Mechie et al.*, 1994; *Zelt and Smith*, 1992], although some of the theoretical background for these methods were formulated already in the 1970's [e.g., *Kelly et al.*, 1976]. Travel-time tomography is, for example, now widely

applied as a first approach to model large data sets and check the validity of the calculated model [e.g., *Zelt*, 1998, 1999; *Zelt and Barton*, 1998].

All these technological advances led to numerous scientific projects over the past half a century, first mostly along continental shelves and adjacent oceans [*Prodehl and Mooney*, 2012] to improve our understanding of shallow sedimentary structures and of the crystalline oceanic crust as this information is important for, for example, interpretations concerning sediment subduction, subduction erosion and growth of continental crust [*Huene and Scholl*, 1991]. However, imaging even the deep crustal structures was not off limits anymore.

1.4.2 Application to subduction zones

From a margin-normal perspective the zones of unstable (seismogenic), conditionally stable (transitional), and stable (aseismic) slip occur at different depths, temperatures and pressures down-dip along the interplate interface as seen in Figure 1.2.3. The shallowest part of that interface from the trench to roughly 5 - 15 km depth, is referred to as the shallow aseismic zone and is characterized by a hydrated sedimentary layer that is being pushed beneath a fore-arc wedge. The frontal part of the overriding plate above is built of either by accreted older and more compact sediments or an eroded basement of igneous or metamorphic origin. Increased pressure and temperature with greater depth induce consolidation within the subducting hydrated sediment layer, which triggers reduction in porosity and release of pore fluids [e.g., *Kimura et al.*, 1997], clay metamorphism [e.g., *Vrolijk*, 1990] and at greater depth dehydration of chemically bound water [*Bostock et al.*, 2002; *Peacock and Hyndman*, 1999].

It has been proposed that the onset of seismogenic slip is located where the plate interface reaches a temperature of ca. 150 °C [e.g., *Hyndman and Wang*, 1993; *Oleskevich et al.*, 1999]. That temperature coincides well with the temperature range in which the transformation of stable-sliding clays, such as smectite, into non-expandable clays, such as illite, that tend to exhibit stick-slip behavior, is completed [*Pytte and Reynolds*, 1988]. The apparent relationship was interpreted as an important mechanism to explain the increase in coupling and seismogenic fault behavior [*Byrne et al.*, 1988; *Vrolijk*, 1990]. However, laboratory investigations on frictional behavior of clays did not sustain that hypothesis [*Brown et al.*, 2003; *Saffer and Marone*, 2003]. So, instead, it was proposed that pore-fluids under

elevated pressure within the subduction channel may control the effective normal stresses and therefore seismogenic behavior on the fault [*Scholz*, 1998]. As temperature and pressure increase with increasing depth, metamorphic dehydration reactions alter subducting sediments and pore fluids are progressively released. In combination with sealed fluid pathways within the overlying crust, fluid overpressure is generated reaching its peak (near lithostatic level) at the up- and down-dip transition zones, thus enclosing the seismogenic zone of unstable slip, which is characterized by only moderate fluid overpressure (Fig. 1.2.3) [e.g., *Audet et al.*, 2009; *Kato et al.*, 2010; *Tobin and Saffer*, 2009]. Areas of elevated pore pressure have been identified in seismic data in form of unusually low seismic velocities and high v_p/v_s ratios [*Kato et al.*, 2010; *Kodaira et al.*, 2004] as well as high-amplitude, negative-polarity plate interface reflections [*Moore*, 1993]. Additional correlation with recently discovered seismological phenomena, such as Slow Slip Events (SSE), Episodic Tremor and Slip (ETS), and Low Frequency Earthquakes (LFE) provide further indications for linkages between over-pressured fluids along the slip interface and rupture behavior down-dip from the locked zone [*Audet et al.*, 2009; *Ito and Obara*, 2006; *Liu and Rice*, 2007; *Obana and Kodaira*, 2009], although causation, quantification and detailed mechanism are still not fully understood.

The shallow plate interface and inferred seismogenic up-dip limit have been characterized with controlled source reflection seismic in subduction zones worldwide [e.g., *Bangs et al.*, 2004; *Bell et al.*, 2010; *Ranero et al.*, 2008]. *Li et al.* [2018] show that thick packages of subducting sediment seem to induce increased fluid release and pore-pressure within the subduction channel and might explain the observed pattern of seismicity and locking stage for the shallow plate interface. However, controlled source studies characterizing the down-dip limit of the seismogenic zone (or transitional zone) have been conducted to a much lesser extent. A major obstacle is that the deep transitional zones from seismogenic to stable aseismic slip at megathrust faults are usually located near coastal areas. Illuminating this section of the megathrust with controlled source seismics would require expensive joint marine and land surveys. Even then, much of the marine coastal area would remain inaccessible for data acquisition with long streamers resulting in significant gaps between the two survey types at the most critical part of the interplate interface, and dense MCS on land can only be carried out on available roads. Combined, this makes it logistically and financially difficult to conduct effective land-marine surveys.

Within the seismogenic (or seismically coupled) zone spanning roughly from ∼10 to up to ∼60 km depth [*Boyd et al.*, 1995; *Hyndman et al.*, 1997], seismic slip is associated with brittle failure (Fig. 1.2.3). The aseismic slip further down dip is believed to be linked to fluids but, in addition to the discussed overpressures, this slip could be related to plastic deformation and ductile behavior. The onset of plastic deformation is thought to occur when the interface reaches a temperature of ∼450 °C [*Hyndman and Wang*, 1993]. Controlling factors for that temperature are thickness of insulating sediments on the incoming oceanic plate, plate age and thus heat flow, convergence rate and the dip angle of the subducting plate [e.g., *Hyndman and Wang*, 1993]. Another possible limit for the landward or down-dip extent of the seismogenic zone might be the contact of the plate interface with the fore-arc mantle beneath the overriding continental plate [*Ruff and Tichelaar*, 1996]. In these areas mantle olivine is hydrated by water carried down with the oceanic crust and sediments and is transformed by heat and pressure into stable-sliding serpentinite [*Anderson et al.*, 1976; *Fyfe*, 1986; *Peacock*, 1993]. At continental margins, the mantle wedge is commonly found some 100 km landward from the trench at a depth of ∼40 km.

At the northern Cascadia subduction zone, *Nedimović et al.* [2003] hypothesized that sharp thin ($<$ 2 km) seismic reflections signals from the interplate interface delineate the unstable seismogenic part of the plate interface, while the thick ($>$ 4 km) bands of multiple reflections mark the stable sliding aseismic portion of the deep subducting megathrust fault (Fig. 1.4.1). The major down-dip change in the reflection character from thin reflections to a broad reflection band was interpreted as the transition zone from seismogenic to aseismic slip region. This broadening of the sharp reflection zone into a several kilometer-thick reflection band can, at the Cascadia subduction zone, be explained by ductile shearing of sediments or quartz-rich crystalline rocks supported by fluids released from dehydration reactions of the subducting oceanic plate [*Hyndman*, 1988; *Nedimović et al.*, 2003].

If the megathrust reflection character hypothesis proposed for the northern Cascadia subduction zone [*Nedimović et al.*, 2003] is valid at other subduction zones, then there is a new quantitative tool at disposal to apply at any time and any place globally to delineate the down-dip limit of megathrust rupture zones. But the Cascadia subduction zone is unusual because the oceanic lithosphere generated at the Juan de Fuca Ridge and subducting beneath the North American continental plate is very young (6 - 9 Ma; [*Rogers*, 1988]) and warm in comparison to other

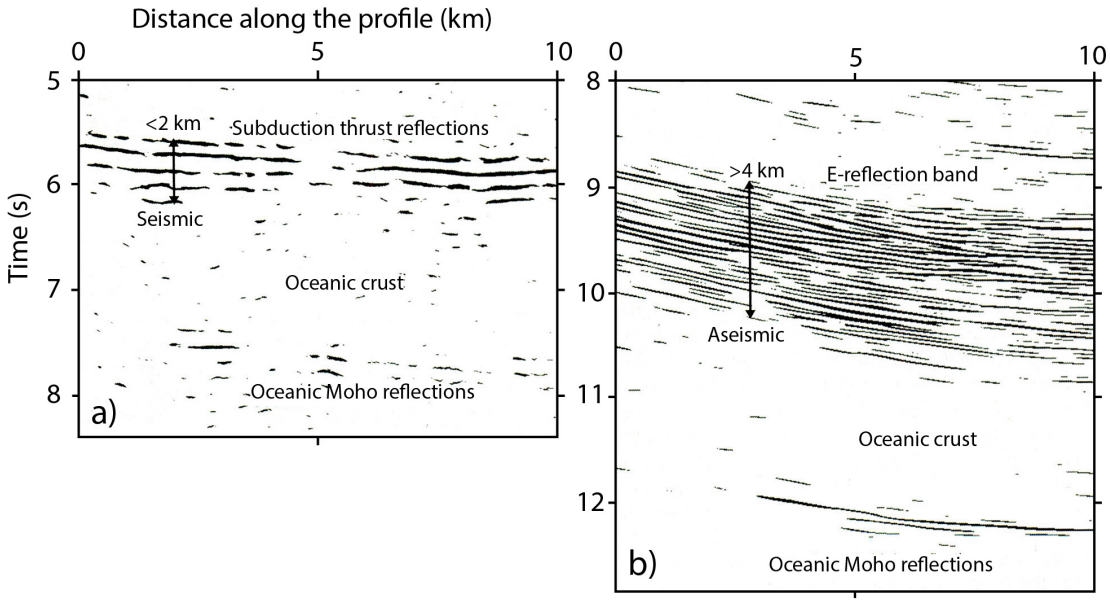

Figure 1.4.1: Variation of seismic reflection signature at the subduction thrust fault beneath the northern Cascadia subduction zone [after *Nedimović et al.*, 2003]. a) Thin reflection zone at shallow depth is associated with unstable seismogenic slip behavior, whereas b) a broader band of reflections at greater depth is thought to represent a stable aseismic part of the subduction thrust fault. The thick reflection band in (b) was originally named E-reflection band (or E-layer) by *Clowes et al.* [1987] for its enhanced electrical conductivity.

subduction zones (e.g. oceanic crust of 48 - 56 Ma at the eastern Alaska-Aleutian subduction zone [*Lonsdale*, 1988]). Because of its young age and high temperature, the Juan de Fuca plate is more flexible, dips shallower beneath the overriding plate, and presumably dewaters differently than most other, cold subducting plates bringing to question possible broad applicability of the proposed reflection method. Therefore, further testing of the proposed hypothesis at other subduction zones is needed. Nevertheless, sparse deep reflection images from Alaska [*Fisher et al.*, 1989; *Moore et al.*, 1991], Chile [*Buske et al.*, 2002; *Groß et al.*, 2008] and SW Japan [*Kodaira et al.*, 2002, 2005] show a megathrust signature much like the one observed at northern Cascadia, suggesting that reflectivity patterns similar to those in Cascadia may be widespread and that systematic new testing is warranted.

A number of the prominent subduction zones worldwide have been investigated in extended projects with this methods in the recent past. Parts of the LITHOPROBE project on Vancouver Island, for example, was conducted to study large-scale structure of several accreted terranes exposed on the island and to determine the geometry and structural characteristics of the subducting Juan de Fuca plate [e.g., *Hammer et al.*, 2011]. The ANCORP working group focussed their efforts on

seismic imaging the Nazca plate underneath South America by using a combined near-vertical, wide-angle reflection/refraction seismic investigation. The results were interpreted alongside seismological findings to explain petrological processes like dehydration and metamorphism in the downgoing slab and their possible relation to the active volcanism [e.g., *Group et al.*, 1999; *Oncken et al.*, 2003]. The Japanese subduction zone is probably the most investigated subduction zone worldwide. A large number of long-streamer seismic reflection studies has been conducted to image the geometry and structural characteristics of this subduction zone and to understand its seismogenic behavior [e.g., *Bangs et al.*, 2004; *Miura et al.*, 2005; *Nakanishi et al.*, 2008; *Park et al.*, 2010].

1.5 Aim, scope and structure of this thesis

Reliable information about the up-dip and down-dip limit as well as the lateral extent of seismogenic slip areas in subduction zones is essential to estimate maximum rupture area and hence maximum release of seismic moment during future earthquakes. These rupture parameters of great earthquakes, but especially its maximum landward extend, have direct implications for seismic risk assessments for coastal communities along subduction zones.

The aim with this thesis work is to test the hypotheses that seismic reflection imaging can be used to determine (1) the down-dip extent of megathrust rupture areas and (2) their lateral segmentation. The focus lies in imaging the interplate interface (or contact zone) between the subducting oceanic plate and overriding continental plate. The geometry of that interface can be used to determine the nature of the imaged structures, which may give indications about rupture area segmentation along-strike. For example, presence of seamounts or transform faults, which can act as boundaries separating megathrust regions, may impede rupture propagation during great megathrust events. Similarly, variations in the reflective nature of interplate reflections can be related to changes of seismogenic properties along the megathrust contact fault in down-dip direction and used to map the extent of variable coupled zones. Advantages of the MCS method over other methods are that high-resolution signals reflecting at the interplate interface allow precise location and mapping seismic response character at the top of the subducting slab. Furthermore, no long observation periods are needed to acquire controlled source seismic data, unlike methods using seismological or geodetic data.

Regional wide-angle seismic refraction data ideally complement the MCS data, especially when the profiles are coincident as they allow for development of crustal scale velocity models, information not possible to obtain from the MCS profiles because of insufficient length of source-receiver offsets.

The most appealing region worldwide to test the hypotheses put forward is a section of the eastern Alaska-Aleutian subduction zone (AASZ) that extends roughly 500 km from the south-west of Kodiak Island across the Semidi Segment to the west of the Shumagin Islands (Fig. 1.5.1). Here, the continental shelf area is wider than at other subduction zones and therefore accessible for relatively inexpensive marine MCS profiling. Mapping of the entire interplate interface from unstable locked zone to transitional zone, slow-slip events and stable shear further down-dip is therefore possible (see Fig. 1.2.3). The area highlighted in Figure 1.5.1 covers segments of the plate interface which have failed in the past during great megathrust events in 1938 (M_W 8.3) that ruptured the Semidi Segment and in 1964 (M_W 9.2) that ruptured Kodiak Asperity [*McCann et al.*, 1980; *Sykes*, 1971]. The Shumagin Gap is located adjacent to the Semidi Segment and is believed to be weakly coupled and slip freely [*Li and Freymueller*, 2017], and thus might not have the potential to generate great $M_W > 8$ megathrust earthquakes. An open question is if the dramatic change in seismogenic behavior over a very short distance of just tens of kilometers might also be manifested in form of variations in seismic reflection character of the plate interface. At this section of the AASZ offshore the Alaska Peninsula, the Pacific Plate is subducting with a plate motion velocity of around 63 mm/yr in north-west direction beneath the North-American continental plate [*Sella et al.*, 2002]. Convergence velocity as well as age of the down-going plate (50 - 55 Ma) is intermediate at the global scale and the almost margin-normal direction of subduction is expected to result in a thermally uniform regime along-strike the plate interface which makes it simpler to relate characteristics of along-strike variations in reflectivity with changes of seismogenic behavior.

To test the presented hypotheses, we collected state-of-the-art MCS and OBS datasets during the ALEUT (Alaska Langseth Experiment to Understand the megaThrust) program. The data were acquired in summer 2011 with the R/V *Marcus Langseth* and included six ca. 300 km-long trench-normal MCS lines, one ca. 300 km-long trench-parallel profile across the shelf, and several shorter connecting lines (Fig. 1.5.1). The MCS streamers used were 8 km long and the recording time was set to 22.5 s to ensure imaging to depth of more than 70 km

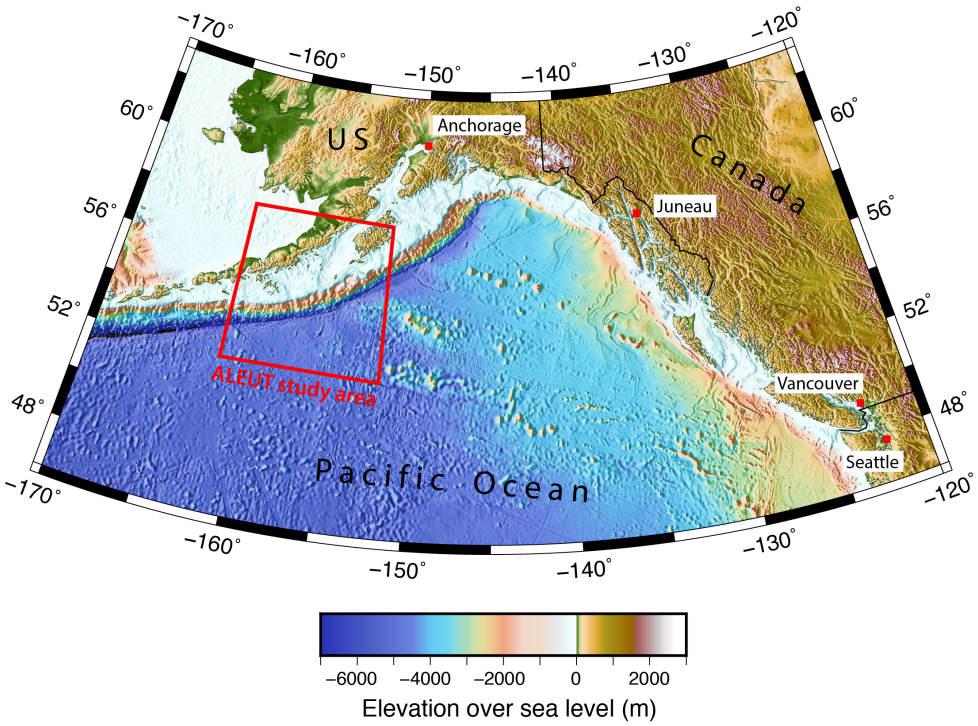

Figure 1.5.1: Topographic map of the north-western Pacific Ocean seafloor including southern Alaska, western Canada and the most north-western tip of the Continental United States of America. Red rectangular area outlines the ALEUT survey coverage, which includes a wide continental shelf area not commonly found at subduction zones.

beneath the continental shelf. The wide-angle data were acquired on two OBS profiles with 21instruments provided from Scripps Institution of Oceanography.

ALEUT data have been used to extent the understanding of a broad range of phenomena and subsurface structures at the eastern AASZ beyond this thesis work. A stark contrast in the observed seismicity pattern between the area of the highly coupled Semidi Segment and weakly coupled Shumagin Gap has been linked to changes in the crustal fabric orientation and hence slab hydration of the incoming subducting Pacific Plate [*Shillington et al.*, 2015]. A fossil triple junction marks the change in fabric orientation just offshore the segment boundary between Semidi Segment and the Shumagin Gap. It, however, also marks a change from intermediate (north-east) to fast-spreading (south-west) oceanic crust, where dipping structures within the lower crust were imaged that might have arose from shear zones that form near spreading centers [*Bécel et al.*, 2015]. Tsunamigenic structures in form of an active crustal-scale normal fault have been identified within the overriding crust in the Shumagin Gap [*Bécel et al.*, 2017]. This fault system resemble that involved in the 2011 Tohoku-oki earthquake in Japan and should be

considered in hazard assesments in this region. Downdip variations in the seismic reflection charachter of the plate interface on ALEUT MCS Line 4 has been linked to changes in the fault structure and its seismogenic behavior [*Li et al.*, 2015]. Synthetic waveform modelling suggests that the shallow thin reflection band is best explained by a single ca. 100 - 250 m thick low velocity zone, whereas the thicker band of reflections requires a 3 - 5 km thick zone of thin layers. Along-trench variations in pore-fluid pressure and sediment thickness appear to correlate with changes in seismicity, locking, and earthquake history [*Li et al.*, 2018].

This thesis comprises 5 chapters and 3 appendices which are organized as follows:

Chapter 1: Introduction
A short history of subduction zone research and its importance for understanding megathrust earthquakes and hazards is given first. This is followed by an overview of methods used for subduction zone research, including their limitations. Controlled source seismology is then introduced as a method that can in a timely manner provide accurate and complementary information much needed to efficiently determine key properties of seismogenic zones. The chapter ends with the main objectives of this thesis expressed through testable hypotheses, and the study area and data chosen for this task.

Chapter 2: ALEUT seismic survey and data analysis
Description is given for acquisition of 3700 km of MCS profiles and two OBS profiles coincident with MCS lines 3 and 5. This is followed by a description of MCS processing steps carried out with Paradigm software and OBS first arrival tomography inversion using Jive3d software from *Hobro et al.* [2003]. The effect of MCS processing steps is visualized on data examples before and after the procedure is applied, with the difference given where useful. Basic processing steps for OBS refraction data and first arrival picks are also presented to illustrate validity of the inverted velocity model for Line 3. This model is, in combination with the inversion model for Line 5 provided by our collaborators from Columbia University, used for generating velocity models tailored for time-depth conversions of the MCS reflection images.

Chapter 3: Interplate interface geometry and segmentation along the Alaska-Aleutian subduction zone from -161° E to -152° E
This chapter is written in article form and focuses on creation of a detailed 3D plate interface model for the study area which is done by identifying and picking the

contact zone between the Pacific and North America plates in all post-stack time migrated and depth converted MCS reflection sections. The constructed model is subtracted from an existing smooth low resolution interface model slab1.0 formed using regional seismicity data [*Hayes et al.*, 2012]. To find potential barriers to earthquake propagation, the differences in the plate interface location between the two models are then compared with the extent of the past megathrust ruptures. Location of the geometric anomalies identified on the plate interface is also compared with the location of various features on the incoming oceanic crust, such as are seamount chains, fracture zones, crustal fabric, sediment thickness and faulting.

Chapter 4: Variations in reflection signature and slip behavior of the subduction interface offshore Alaska Peninsula from -161° E to -152° E
The plate interface reflection signature has been characterized and mapped throughout the ALEUT survey area. The thickness of the reflective zone increases from a narrow band of reflections of less than 2 km thickness at the shallow plate interface ($<$ 30 km depth), to more than 5 km broad bands at greater depths ($>$ 40 km). The seismic appearance of the plate interface is can be related to structural changes along the plate boundary deformational zone, which is interpreted to reflect variations in seismic slip behavior. This allows us to estimate the seismogenic extent and the rupture down-dip limit for this area. Contrary to recent geodetic dislocation models that suggest a widely free slipping Shumagin Gap, our results show a seismogenic plate interface for this area that extents from the trench up to $\sim$100 km landward. This chapter is also written in article form to facilitate publication at a later stage.

Chapter 5: Conclusions
The final chapter describes the most important outcomes of the works carried out and provides an outlook for possible future.

Appendix A, B, C
A: Fully processed and post-stack time migrated ALEUT MCS reflection sections (1) with and (2) without superimposed velocity model and interplate interface interpretation, 3D plate interface models for the ALEUT survey area (ALEUT PIM, Slab1.0, Difference between the two) with seismicity (1900 - 2018) for $M_W < 6.9$ earthquakes, 2D gradient map of the difference between ALEUT PIM and Slab1.0, Slab2 plate interface model [*Hayes et al.*, 2018], Difference between ALEUT PIM

and Slab2 model, smoothed plate interface background model.
B: Fully processed and post-stack time migrated ALEUT MCS reflection sections with interpretation of plate interface reflection signature and continental Moho reflections. Alternative interpretation of plate interface thickness distribution assuming 1) thin plate interface for reflections < 1 km and thick plate interface reflections for > 3 km, 2) thin plate interface reflections for < 2 km and thick plate interface reflections for > 4 km thickness.
C: OBS seismograms including first arrival picks, pick uncertainty and calculated (synthetic) arrival times and Jive3d first arrival tomography model of OBS Line 3 and 5 including ray coverage.

Chapter 2

Data Analysis

2.1 Multichannel seismic (MCS) reflection data acquisition and processing

2.1.1 Data acquisition and survey geometry

A total length of ca. 3700 km 2D multichannel seismic (MCS) reflection data and two $>$ 300 km long profiles of wide angle refraction ocean bottom seismometer (OBS) data were collected with the R/V *Marcus Langseth* during the ALEUT project between July 11th and August 5th 2011 (Fig. 2.1.1). The data were acquired using two 8-km-long hydrophone cables (streamers), each consisting of 636 groups of hydrophones with a group spacing of 12.5 m. The two streamers are towed at different depth's (9 m and 12 m) to remedy losing signal frequencies by destructive interference of the signal when reflecting off the sea surface ("ghost notch") (Fig. 2.1.2). Depending on the tow depth of the streamer and the seismic source, the direct wave and reflected ghost are exactly 180° out of phase and canceling each other out for specific frequencies. Data recorded by these two streamers towed at different depth's are intended to ensure optimal recording coverage for high as well as low frequency signals. The nominal parallel separation distance between the two streamers was 225 m during most of the survey except for MCS Line 4, 45 and 5, where it was 450 m (Fig. 2.1.2). Recording time was for most of the profiles 22528 ms except for Line 12c, 7a and 7b where it was reduced to 18430 ms. This is because the ship needs to maintain a minimum speed through the water when towing streamers but when tail currents are present, the speed over ground can be too fast so that the time between two shots is too short for a specific recording length. The sampling interval for the data is 2 ms. A tuned airgun array consisting of 36 individual airguns with a total volume of 6600 cu in (ca. 108 l) and 2000 psi (ca. 1.4 * 10^6 kg/m^2) was used throughout the entire survey for both seismic reflection and wide angle refraction data acquisition. Shot distance was set to 62.5 m for MCS shooting resulting in a nominal common depth point (CDP) fold of 64,

and 310 m for OBS wide-angle refraction survey. To ensure safety for the abundant marine wildlife by respecting the Marine Mammal Protection Act, the full capacity of the seismic source was drastically reduced to a single airgun of 40 cu in (0.66 l) or shooting was even completely stopped when marine mammals were observed within a safety radius around the source. Due to technical problem only one streamer was used to acquire data for Lines 12e, 12f, 7a, 7b, 56, 6, 67a, 67b. The tow depth for the streamer was set to 12 m to capture the full low frequency bandwidth that is excepted to image deep crustal reflections.

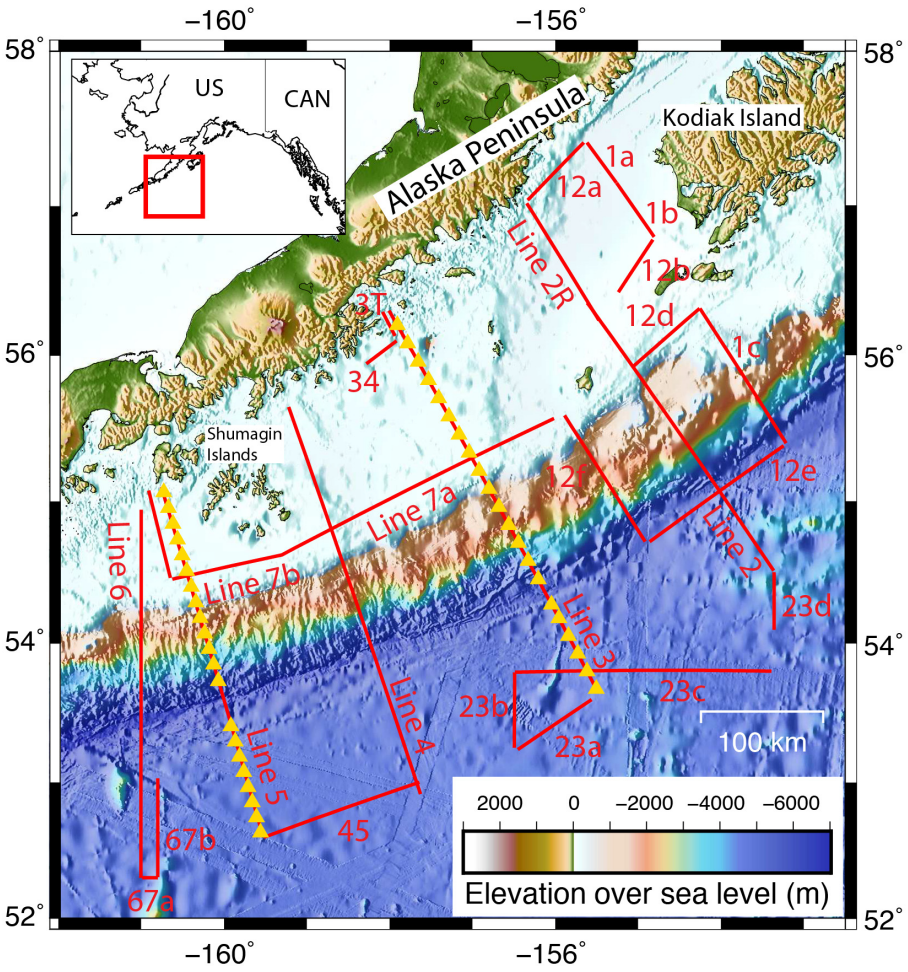

Figure 2.1.1: ALEUT project survey area with MCS profiles (red lines) and OBS locations (yellow triangles). The two OBS profiles coincide with MCS Lines 3 and 5 and consist of 21 OBS's each.

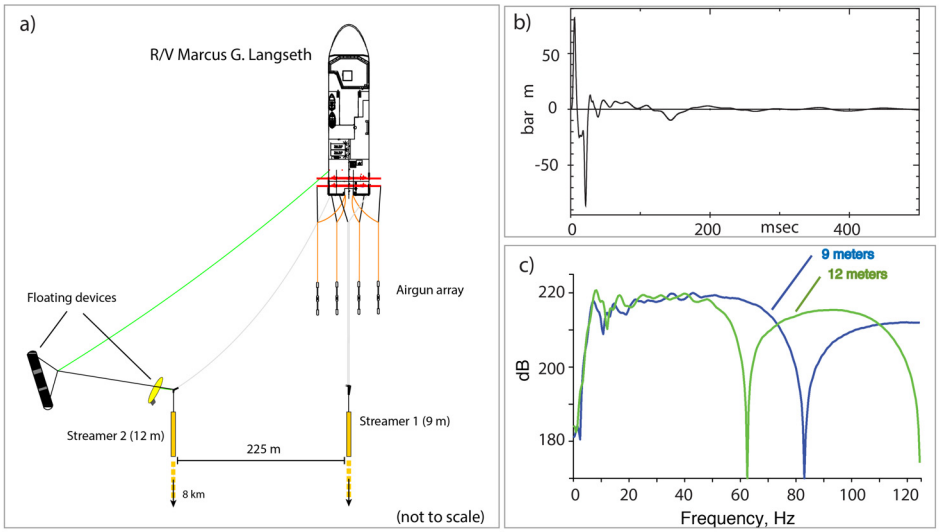

Figure 2.1.2: a) Acquisition configuration for most parts of the MCS survey. Nominal offset (parallel distance) between streamer 1 and 2 is 225 m but was set to 450 m for Line 4, 45 and 5. Tow depth for streamer 1 was 9 m below sea surface and 12 m for streamer 2. Total length of each streamer is 8 km. b) Seismic wavelet generated from R/V *Marcus Langseth's* tuned seismic source array consisting of 36 individual airguns with a total volume of 6600 cu in (∼108 l) at a source depth of 12 m below sea surface. c) Seismic source signature (modelled). Blue line represents the modelled source signature for the hydrophone strings (streamers) deployed at 9 m depth below the sea surface, green line when it is deployed at 12 m depth.

2.1.2 MCS data processing

Seismic trace header information and sorting The raw seismic data is stored in SEGD data format containing information from the two streamers sorted in shot gathers format with 636 traces per streamer and shot. Additional information about shot number, time of the shot, seafloor depth, corresponding vessel and position of the airgun array and other information are stored as seismic headers before the seismic data for each shot. To determine accurate geographical position of each hydrophone receiver group differential GPS from the ship and streamer tail buoys were used in combination with acoustic pods and compasses attached to the streamer. This information is compiled for each shot into a P190 format navigation file that was created for every MCS profile separately. After checking for acquisition errors in the navigation files (e.g., shot is fired but no file was written, bad headers information, undefined location, double use of the same shot number etc.), the seismic information in the SEGD file and navigational information in the P190 file are merged. This is a crucial processing step that enables sorting of each seismic trace to common depth point (CDP) gathers. The streamer position is usually not in perfect alignment with the ship's sailing direction because of crossing water

currents that cause the 8-km-long floating cables to deviate (cable feathering) from its intentional position, resulting in a spread out distribution of source-receiver midpoints. To gather all source-receiver pairs sharing the same CDP, rectangular areas (or bins) with spatial dimensions of 6.25 m long and 5 km wide (relative to the ship's travel direction) are defined. All source-receiver pairs that fall within one bin are assigned to a CDP number, which is stored in the header information of each seismic trace.

All processing steps were conducted using industry grade seismic processing software Paradigm Echos for generating 2D seismic images of the subsurface. The data was processed for each streamer separately and merged to a single seismic section at one of the final stages in the processing workflow. The complete processing workflow is shown in a schematic form in Figure 2.1.3. The effects of the following processing steps are demonstrated with data examples from ALEUT MCS Lines. A single shot gather at shallow water depth is used in most examples that show pre-stack processing.

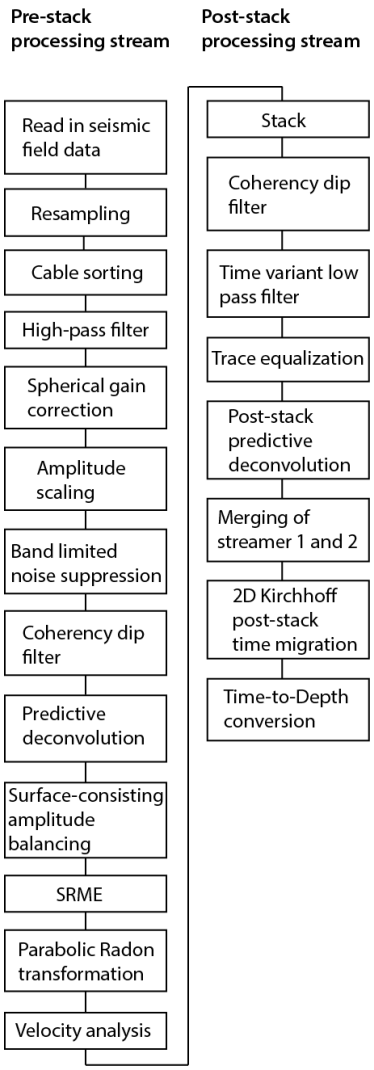

Figure 2.1.3: MCS data processing workflow. Individual processing steps are explained with the help of examples in section 2.1.2.

2.1.2.1 Resampling

The first basic processing step was to increase the sampling rate of the seismic data from 2 ms to 4 ms with Echos module RESAMP to reduce the data size by half. According to the Nyquist criterion, this increase reduces the successfully recoverable maximum signal frequency, from 250 Hz to 125Hz [e.g., *Yilmaz*, 1987].

$$f_{\mathrm{Nyq}} = \frac{1}{2\Delta t}$$

Although, we do observe minor deterioration in the vertical resolution as higher

frequencies above 125 Hz are filtered out (Fig. 2.1.4 and Fig. 2.1.5). This effect is negligible as the energy of signals with very high frequencies get absorbed quickly at shallow depth [*Telford et al.*, 1990] and do not reach deeper parts of the crust, where the main target for the ALEUT survey, the interplate interface, is located. The amplitude spectrum before and after resampling is shown in Figure 2.1.5 to emphasize the consistency in the frequency spectrum below 100 Hz. Resampling of the data set reduced the overall file size by the factor 2 and is thereby greatly simplifies data management and shortens processing times.

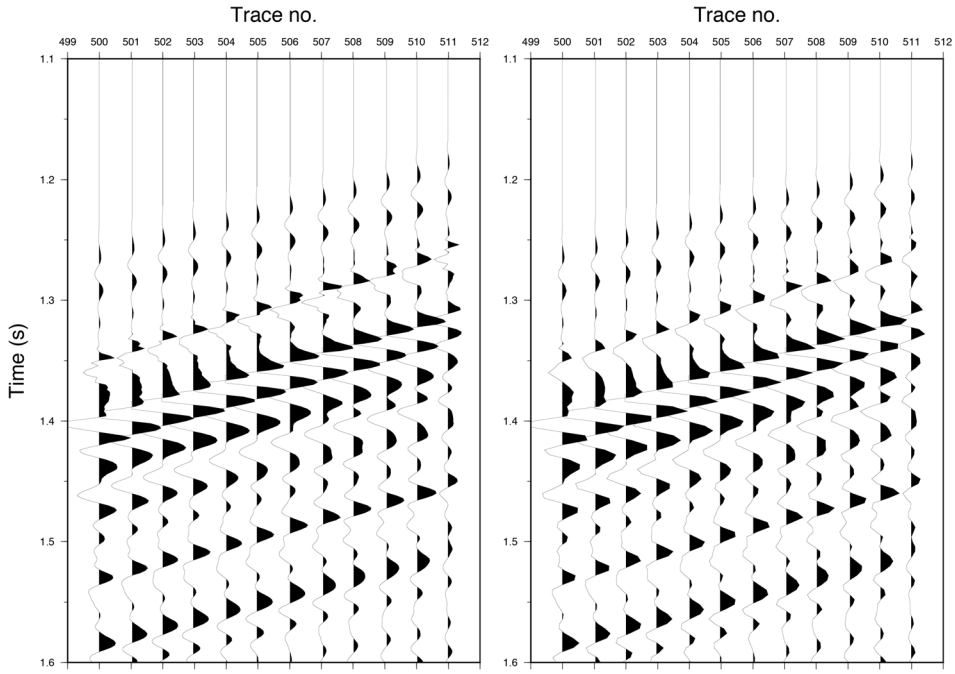

Figure 2.1.4: Comparison between traces with 2 ms sampling rate (left) and 4 ms sampling rate (right). Note the high frequency component in the left image, for example at trace 501 at ca. 1.35 s, which is absent in the right image.

2.1.2.2 Spherical divergence correction

Seismic energy is emitted by the acoustic source and diverges on a spherical wavefront as it propagates through the subsurface. The energy density at the wavefront decays proportionally with $1/r^2$ in a homogenous medium, where r is the radius of the wavefront. The wavefront amplitude is proportional to the square root of the energy density and decays with $1/r$. To compensate for the amplitude loss a spherical divergence correction is applied to the seismic data in form of a function of offset and traveltime (Fig. 2.1.6). In practice, the subsurface is not a homogeneous

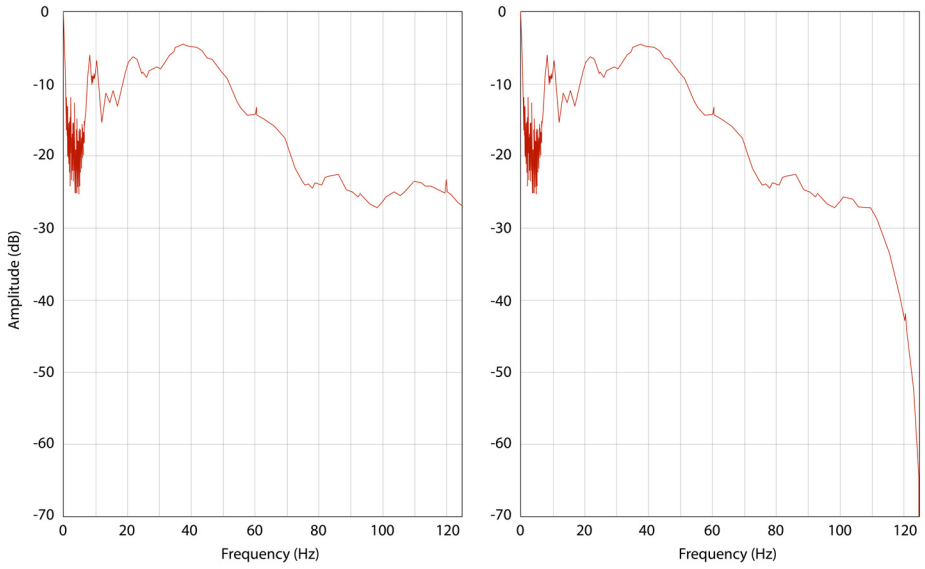

Figure 2.1.5: Amplitude spectra of an unprocessed shot gather (shot number 1400) from Line 1c. The amplitude spectrum in the left image is from a shot gather with 2 ms sampling rate and the right image from a shot gather with 4 ms sampling rate. All signals in the shot gather with 4 ms sampling rate have frequencies lower than 125 Hz.

medium and seismic velocities usually increase with depth, which causes further divergence. In this early stage of processing, however, we do not have more accurate subsurface velocity information and applied a standard exponential, offset-dependent function to recover amplitude decay (Echos module GAIN).

2.1.2.3 Noise removal

Noise removal is an essential step in data processing as unwanted noise signals can superimpose reflection signals from geological structures and impede their interpretation. Generally, there are two categories of noise: random noise and coherent noise. If not removed properly, noise can become a source of artificially introduced artefacts at later processing stages, for example during migration processes. Four separate techniques were applied to the seismic data to remove or attenuate unwanted noise signals and to increase the signal-to-noise (s/n) ratio: 1) Dominant very low frequency cable noise was filtered out by a trapezoid high pass (HP) filter with corner frequencies of 1-2-0-0 Hz (Echos module FILTER) (Fig. 2.1.7), 2) High amplitude noise artefacts that are caused, for example, by cable clashes or air blasts, are identified by the median root mean square (RMS) amplitudes in overlapping spatial and temporal windows (window length 200 ms).

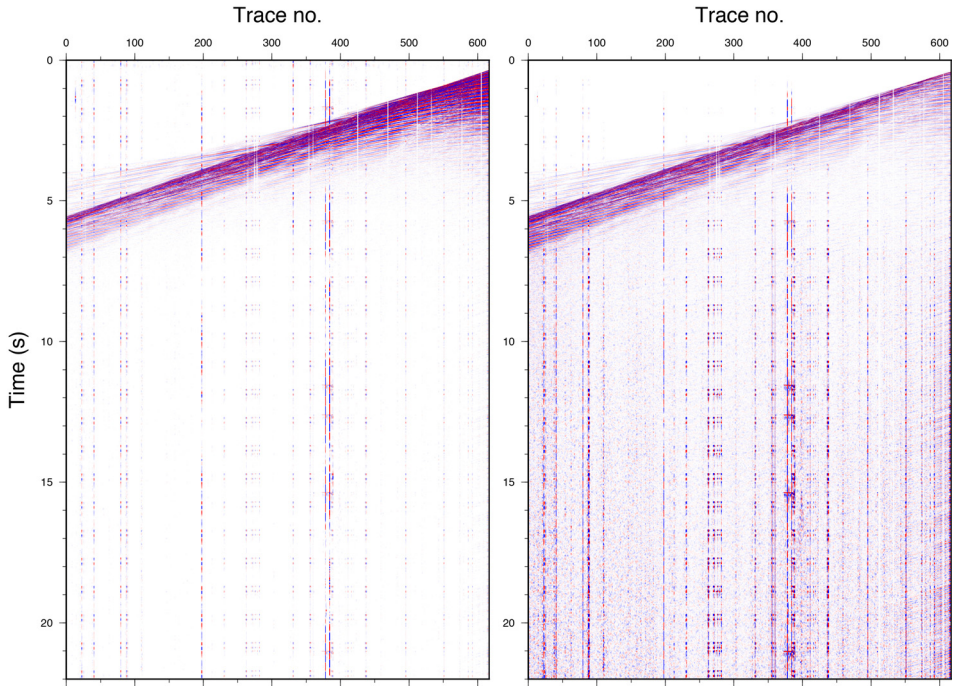

Figure 2.1.6: Comparison of shot gathers with no gain correction applied (left image) and offset dependent spherical divergence correction applied (right image). Shotgather 1400, Line 1c.

By comparing the window RMS amplitude with neighboring traces, anomalously high trace amplitudes (twice the median amplitude than on neighboring traces) are scaled down (AMPSCALE) (Fig. 2.1.8), 3) Noise with a specific frequency range from 0 - 4 Hz (e.g. swell noise, ground roll) is targeted by band-limited noise suppression. The seismic trace is decomposed into signal and noise components and envelopes for both signal and noise are calculated and compared. Where noise envelopes exceed signal envelopes along the trace, the noise will be scaled down to match the level of the signal envelope (SUPPRESS) (Fig. 2.1.9), 4) In some shot gathers at shallow water depths, near offset linear dipping events are observed, possibly caused by intensive cable pulling related to strong cross water currents. These linear dipping events have been attenuated by a coherency filter that removes any coherent dip signals between -6° and -9°. To prevent removal of any genuine reflection signals in this dip range at shallow depth, the coherency filter was applied only at recording times $>$ 3000 ms (COHERE) (Fig. 2.1.10).

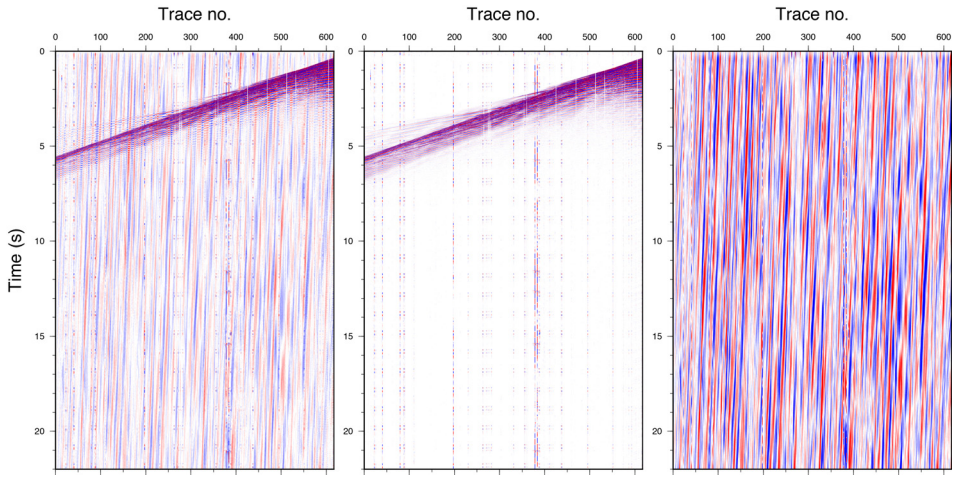

Figure 2.1.7: High pass (HP) frequency filter with corner frequencies of 1-2-0-0 Hz is applied to a shot gather (Echos module FILTER). Shot gather before HP filter (left), after filter (middle) and difference between the two (right). Shotgather 1400, Line 1c.

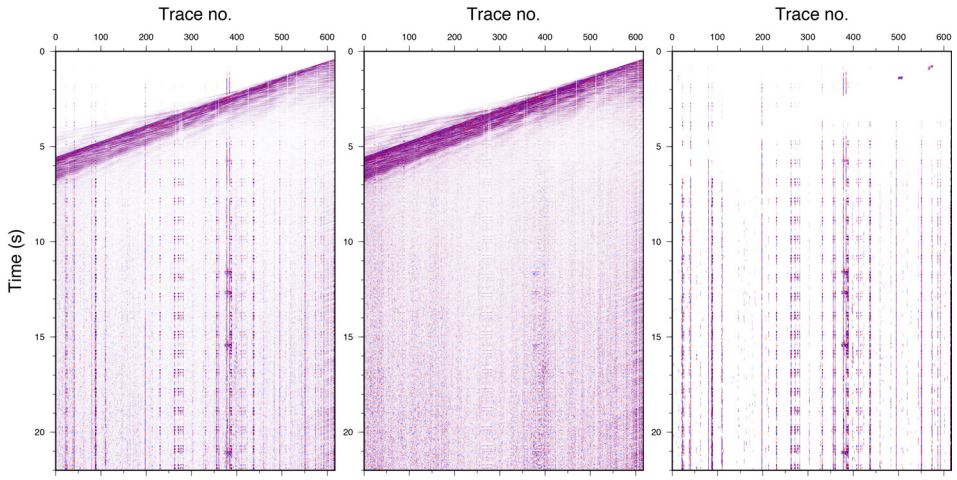

Figure 2.1.8: HP filtered shot gather before (left) and after (middle) an amplitude scaling module is applied to scale down anomalous high amplitudes (Echos module AMPSCALE). Right image shows the difference between the two. Shotgather 1400, Line 1c.

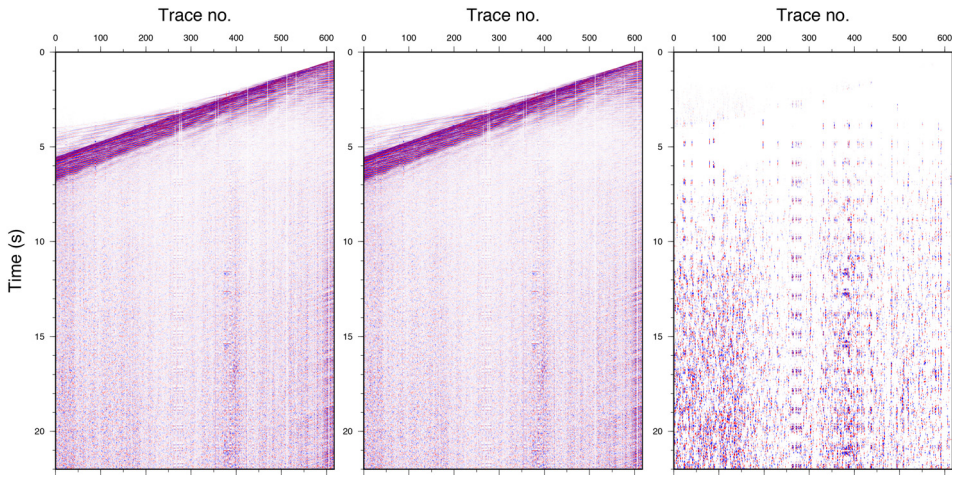

Figure 2.1.9: HP filtered shot with scaled down amplitudes before (left) and after (middle) a band-limited noise suppression module is applied (Echos module SUPPRESS). Right image shows the difference between the two. Shotgather 1400, Line 1c.

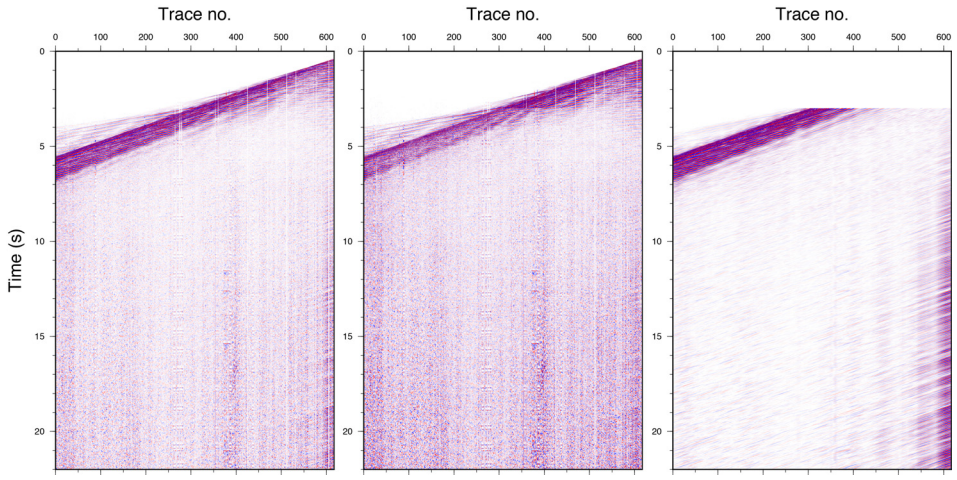

Figure 2.1.10: HP filtered shot with amplitude scaled down and band limited noise suppressed before (left) and after (middle) a coherency dip filter was applied (Echos module COHERE). The filter was only applied later than 3 s, so that steep dipping shallow reflection signals are not accidently removed. Right image shows the difference between the two. Shotgather 1400, Line 1c.

2.1.2.4 Deconvolution

Deconvolution is an inverse filtering process that aims to increase the temporal resolution and remove repeating signals (e.g. reverberations) from a seismic trace. To remove, or at least attenuate shallow water bottom reverberations that appear in data collected on the relatively flat continental shelf, predictive deconvolution was applied. A filter operator was defined (filter length 360 ms and lag length 32 ms) that identified and removed the predictable part of a seismic trace (short-period multiples), leaving only the non-predictable part (signal) in the data (Fig. 2.1.11). Predictive deconvolution was applied successfully twice in the processing stream: a first time on pre-stack data in shot gather format and a second time on the post-stack seismic section (MCDECON).

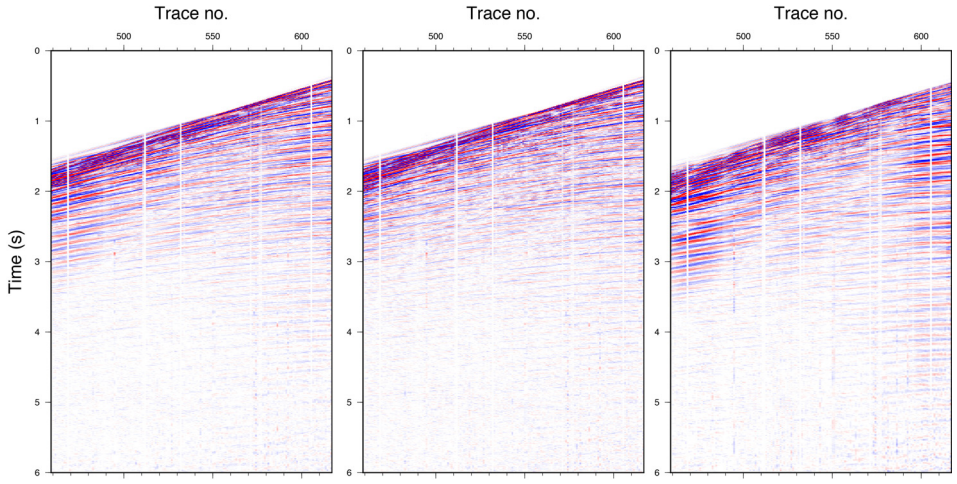

Figure 2.1.11: Shot gather before (left) and after (middle) predictive deconvolution filter was applied to increase temporal resolution and remove water reverberations (Echos module MCDECON). Right image shows the difference between the two. Shotgather 1400, Line 1c.

2.1.2.5 Surface-consistent amplitude balancing

This method aims to compensate trace amplitudes for changing near surface recording conditions, such as variations in receiver coupling or shot strength. The seismic data is decomposed into shot, channel and CDP components. Near surface variations that are reflected in the amplitudes are removed in the shot and channel components but variations in the CDP component are preserved as they represent geological effects. This processing step is more common in land seismic surface, where near-surface conditions exhibit greater variability or AVO analysis where

accurate amplitude information is a key factor. The differences we observe after applying surface-consistent amplitude balancing are minor but we applied the process nevertheless to achieve a more uniform appearance of seismic traces.

2.1.2.6 Multiple removal

The seismic profiles of the ALEUT survey cross parts of the continental shelf, slope and the deep sea (Fig. 2.1.1). The water depth on most trench-normal profiles changes substantially from ca. 100 m on the shelf to up to 5500 - 6000 m in the deep sea trench and to 4000 - 5000 m seaward of it. While short-period seafloor multiples and water reverberations are mainly encountered in the shelf-area (and are addressed by the application of predictive deconvolution), seafloor multiples increase their periods with increasing water depth and superimpose genuine structural reflections beneath the continental slope. These multiples are highly undesirable, as they can coincide with arrival times of the targeted reflections of the plate interface in this area and impede their interpretation. We applied surface related multiple elimination (SRME) [*Verschuur et al.*, 1992] to remove these multiples, followed by parabolic radon transform to remove multiple residuals.

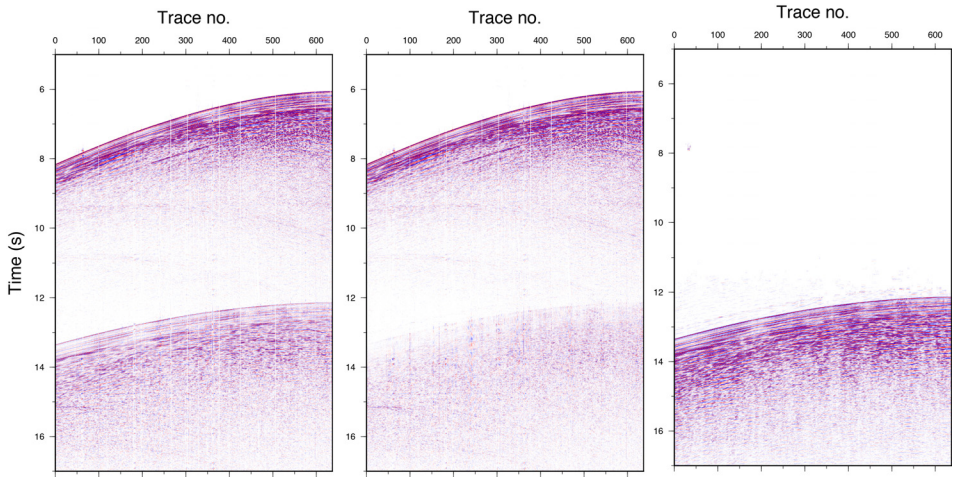

Figure 2.1.12: Shot gather before (left) and after (middle) the application of SRME to remove multiple noise. Right image shows the difference between the two. Multiple noise is significantly attenuated but residual remains. Shotgather 6288, Line 3.

2.1.2.7 Surface related multiple elimination (SRME)

SRME is an algorithm that aims to predict surface multiples without the help of any subsurface information and can also be applied in complex subsurface geometries such as greatly changing water depths on continental slopes. Once the multiple arrival times are predicted (SMACTRM), the multiple reflections can be removed from the data by a matching filter (SMACMS). Figure 2.1.12 shows an example of a shot gather before and after SRME and the difference between the two. However, this technique requires dense and regular acquisition geometry such as the same shot and receiver spacing. We interpolated 4 additional shots between two existing shot points (original shot spacing was 62.5 m), to generate an interpolated shot spacing of 12.5 m, which is equal to the receiver spacing (REGLO). The dominant frequencies of crustal reflections are lower than ca. 15 Hz. To avoid the risk of accidentally taking out any true reflection signal by SRME, the input data was divided into a low and high frequency band and only on the later has SRME been performed. A low pass frequency filter with corner frequencies of 0-0-14-18 Hz was used to divide the data set into two frequency ranges, which were put back together once the multiples had been attenuated in the higher frequency part. Residual multiples were addresses with the Radon transformation approach to further decrease their strength.

2.1.2.8 Radon transformation

The Radon transform is a mathematical technique that is widely used in seismic data processing to attenuate multiple noise. Various forms of the Radon transform exist, e.g. slant-stack or τ-p transform (also known as linear Radon transformation), hyperbolic Radon transform and parabolic transform. We applied a parabolic Radon transform (RADNPAR), which is specifically designed to attenuate multiple energy. The basic idea behind this technique is to transform seismic data from time and space domain (x-t) (e.g. CDP gather) to the Radon domain or "τ-p" domain, where tau is the intercept time and p is a ray parameter [*Yilmaz*, 1987]. Multiple events, for example, differ from their primaries in their normal-move-out (NMO) times, especially at large offset, and can be more easily distinguished and processed in the transformed Radon domain. After the events are filtered out and removed, the data is transformed back to x-t domain, with multiple reflection ideally also removed. An example for the effect of the Radon transformation is given in Figure

2.1.13. A relatively strong and almost horizontal reflection at ca. 3.5 s is masked by multiple noise but becomes recognizable after the Radon transformation is applied.

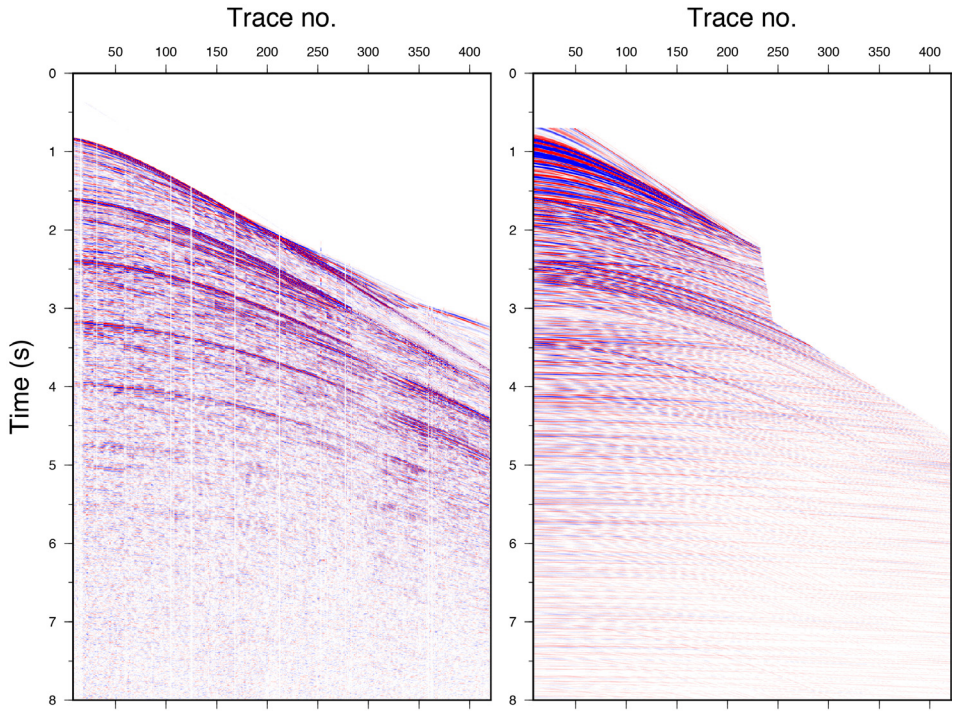

Figure 2.1.13: Multiple attenuation on a super-CDP gather before (left) and after (right) Radon transformation was applied. Note the nearly horizontal reflection hyperbola at ca. 3.5 s after Radon transformation, which was masked by strong multiple noise previously. Super CDP gather 1001, Line 3.

2.1.2.9 Velocity Analysis and Stacking

Seismic velocity analysis is used to determine CDP stacking velocities along each seismic line. The derived velocity models are used in various processing stages but primarily for NMO correction, that enables trace stacking and the generation of geologically interpretable seismic sections. To obtain more coherent and higher resolved velocity spectra that facilitates the determination of velocity functions, the seismic data is gathered into ensembles of 10 adjacent CDP gathers (so-called super-CDP's or super gathers), rather than one single CDP. The trace number per gather is thereby increased from ca. 64 to ca. 640 traces (Fig. 2.1.14). Velocity functions were determined for every 50^{th} super-CDP (every ca. 3 km) along the profile, except on the slope, where large lateral changes in seismic velocities are present due to the rapid changing water depth. Here, the interval was decreased to 25 super-CDP (every ca. 1.5 km). Velocity analysis on the slope was challenging

because of large lateral changes in water depth and highly irregular slope topography that resulted in disturbed reflection hyperbolas in the super-CDP gathers. Velocity spectra analysis is a common practice to determine seismic velocity functions for CDP gathers. The velocity spectrum displays how well a given hyperbolic event matches real data on the Super-CDP and calculates a coherency value (or semblance) for a range of trial hyperbolas. Coherent reflections result in a high semblance value in the velocity spectrum and are manually picked at the given CDP interval along the profile. The theoretical hyperbolas are calculated for a velocity range of 1350 to 3000 m/s with 20 m/s interval every 60 ms. Multiple events can be easily identified in the velocity spectrum as they exhibit high coherency value at unrealistically low velocities (Fig. 2.1.15). Deep crustal reflections are usually more challenging to identify in the velocity spectrum because of their low signal strength. If no reflections, and therefore no velocity constraints, are observed below the acoustic basement, a velocity layer of ca. 6000 km/s is assumed from the last picked reflection (usually the acoustic basement) until the end of the recording time. The absence of clear continuous reflectors that could be traced from the shallow part of the slope to the deep sea prevented a clear imaged acoustic basement reflection and other geological structures in the slope area of the final seismic section. The stacking quality is observed after application of NMO (Fig. 2.1.16).

A mute function in the super-CDP gathers is defined that removed low-frequency stretch-mute artefacts that occur at larger offsets after NMO corrections (green line in Fig. 2.1.6). The velocity functions are interpolated in between the given super-CDP interval, resulting in a velocity model that is used for NMO correction for all CDP gathers for a given MCS Line, followed by trace summation (stacking), which results in a seismic section (Fig. 2.1.18).

2.1.2.10 Post-stack signal enhancement and deconvolution

Deep plate interface reflections are clearly seen in the seismic sections. To further enhance these low frequency signals after the stacking process, the following filters and methods have been applied: 1) A coherency filter for dips between -3° and +3° was applied to enhance sub-horizontal reflections (COHERE with filter length: 60 ms, filter width: ca. 400 m (or 63 traces)), 2) After a static shift was applied to correct for the changing water depth, a time variant LP filter was used to remove high frequency noise in the deeper part of the sections. Below 3 s from the seafloor,

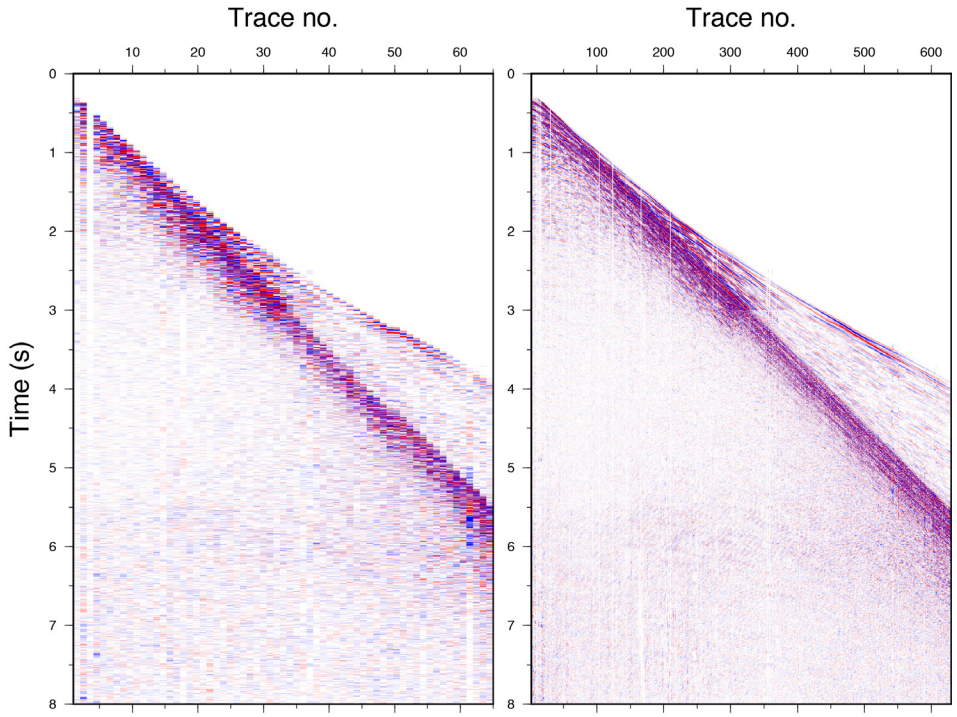

Figure 2.1.14: Comparison of a single CDP gather (left) consisting of maximal 64 seismic traces and super-CDP gather consisting of 10 adjacent CDP's and ca. 640 seismic traces (right).

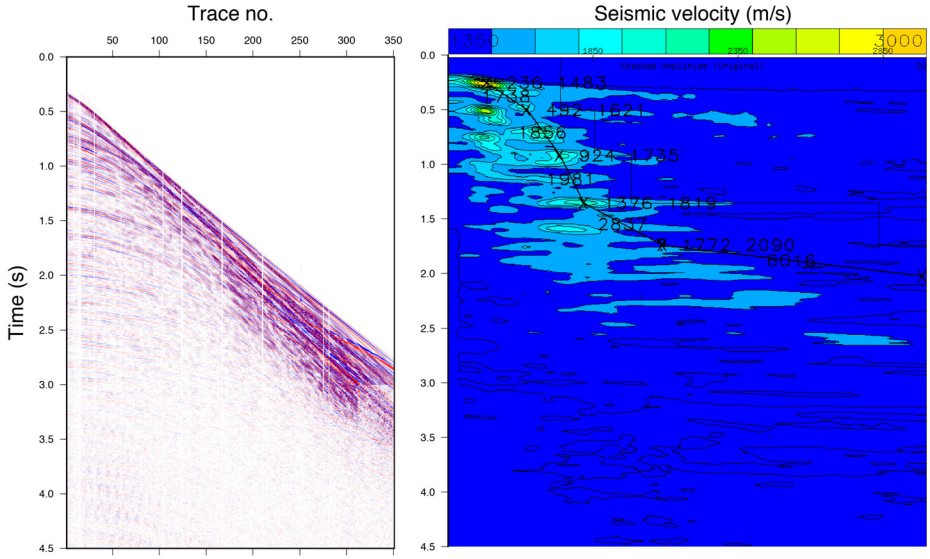

Figure 2.1.15: Seismogram of a super-CDP gather and its velocity spectrum. High coherency (semblance) between calculated trial hyperbolas and reflection events in the real data is displayed by warmer colors in the velocity spectrum.

only low frequency signals remained (FILTER with LP corner frequencies 0-0-10-16 Hz), 3) Amplitude balancing was applied to improve the appearance of the plotted

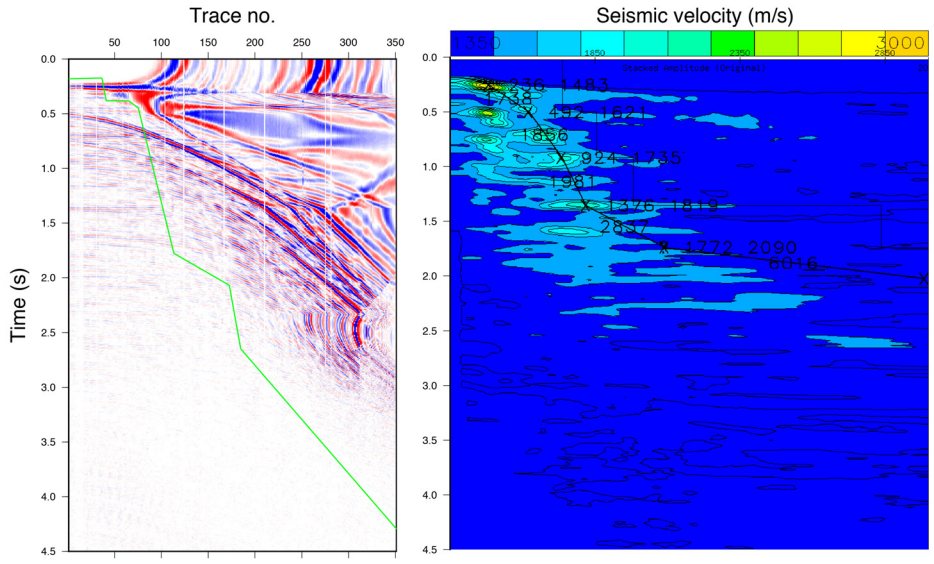

Figure 2.1.16: Super-CDP gather from Figure 2.1.14 with NMO corrections (left). NMO times are derived from picked velocities in the velocity spectrum (right). Low frequency NMO-stretch noise is clearly visible in the NMO corrected super-CDP gather and will be muted at the green line for larger offsets later in the stacking process.

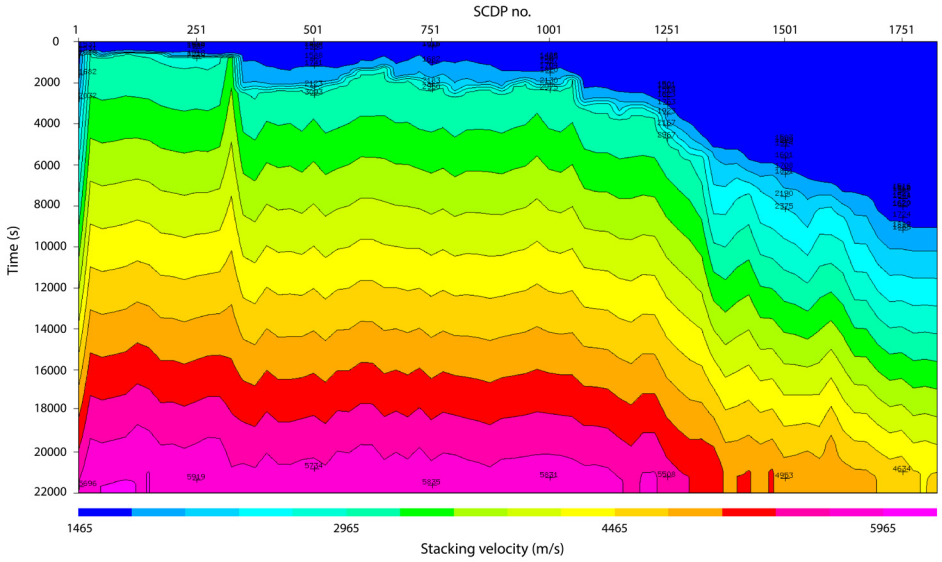

Figure 2.1.17: Stacking velocity model for Line 1c.

seismic data. Areas of the weakest trace amplitudes are strengthened relative to areas of the strongest (BALANCE), 4) Post-stack predictive deconvolution (MCDECON) was applied using the same parameters as in the pre-stack predictive deconvolution, which significantly removed water reverberation (Fig. 2.1.19, 2.1.20).

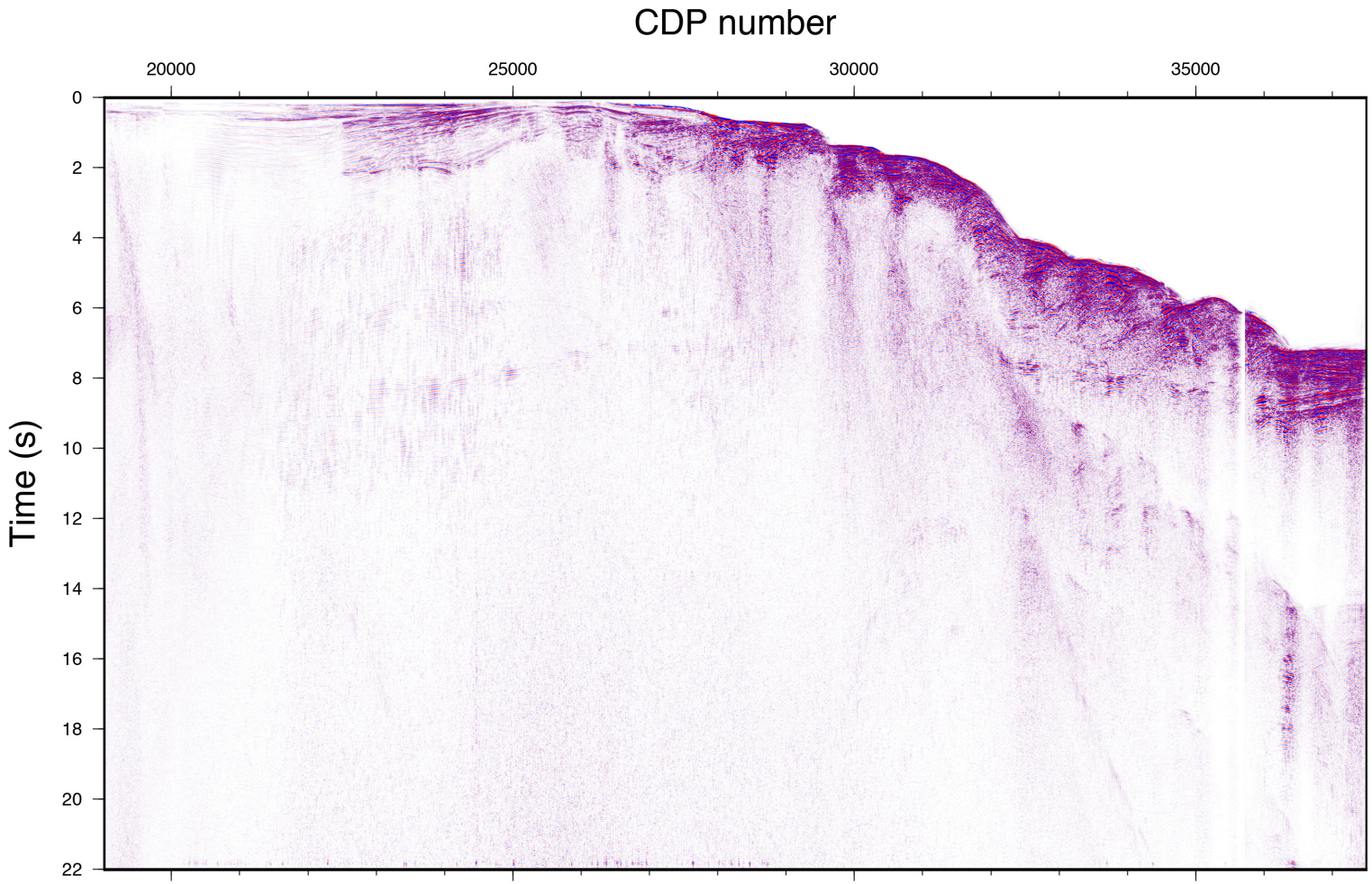

Figure 2.1.18: Seismic section of Line 1c after noise removal, spherical divergence correction, multiple removal, NMO correction and CDP stacking.

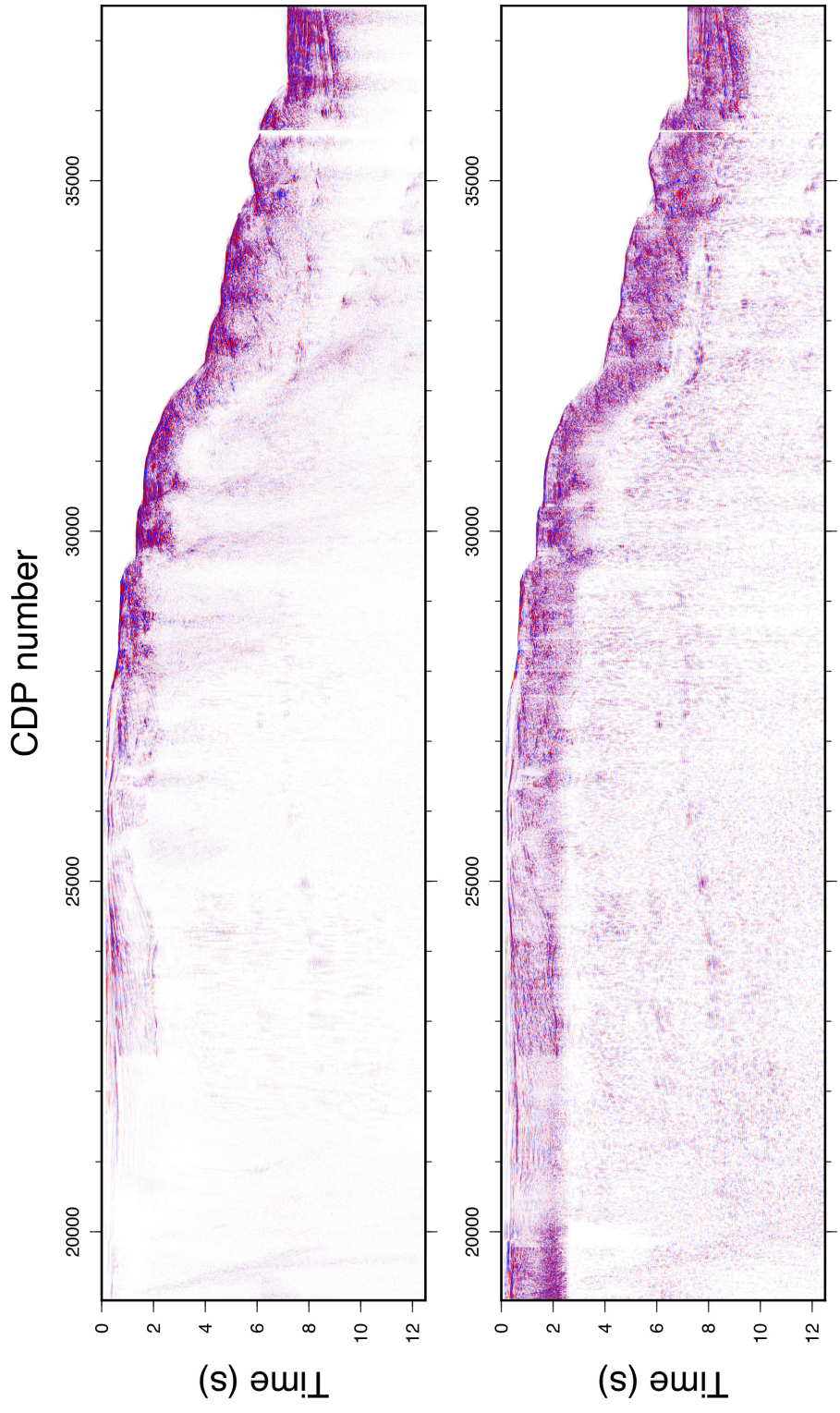

Figure 2.1.19: Seismic section before (above) and after (below) post-stack noise removal and signal enhancement.

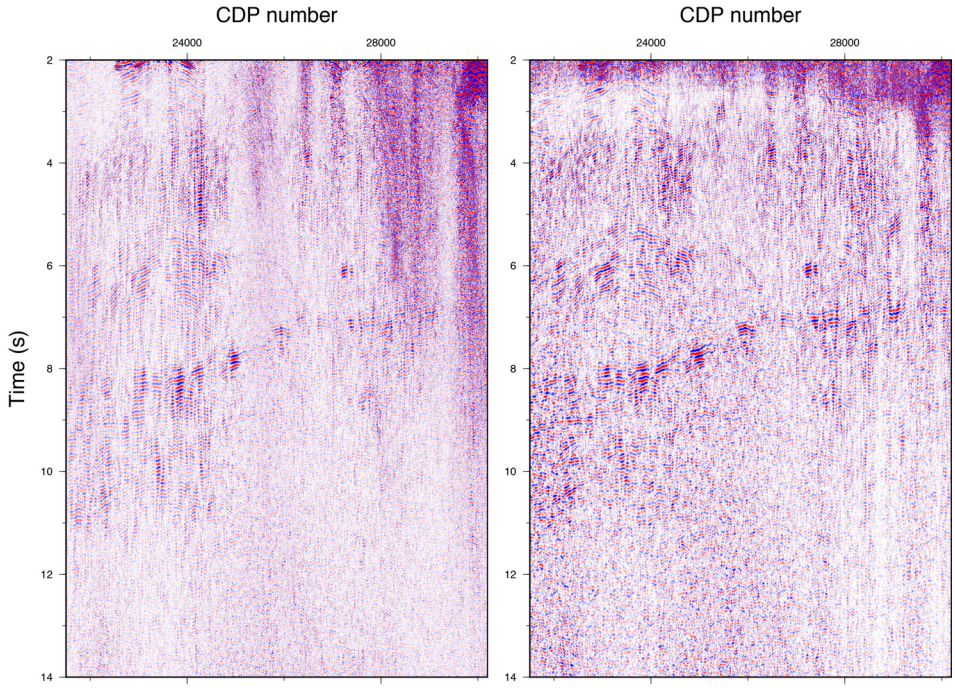

Figure 2.1.20: Zoomed in areas from seismic section Line 1c as seen in Figure 2.1.17 before (above) and after (below) post-stack noise removal and signal enhancement. Water reverberation has significantly decreased and deep crustal reflections are clearer after the post-stack noise removal and signal enhancement.

2.1.2.11 Merging

The processing workflow to increase the signal-to-noise ratio and to sharpen the signal has been applied to both streamers separately. The parameters used during data processing were identical but the velocities analysis had to be conducted for each streamer individually. SRME and Radon transformation to remove multiple noise has been tested, but was not applied to streamer 1, since only the shallow sedimentary part above the acoustic basement was used in the final section, where no long period seafloor multiples are present. Acquisition parameters for streamer 1 aimed to image upper sedimentary structures, whereas streamer 2 was designed to focus on lower frequency deep crustal reflections (see 2.1). Accordingly, both seismic sections were divided along the acoustic basement (basement reflection has been identified and were muted above or below by a 1-s-tapered mute function to avoid an abrupt cut), and were merged together afterwards by using the top section of streamer 1 and the bottom section of streamer 2 (Fig. 2.1.21).

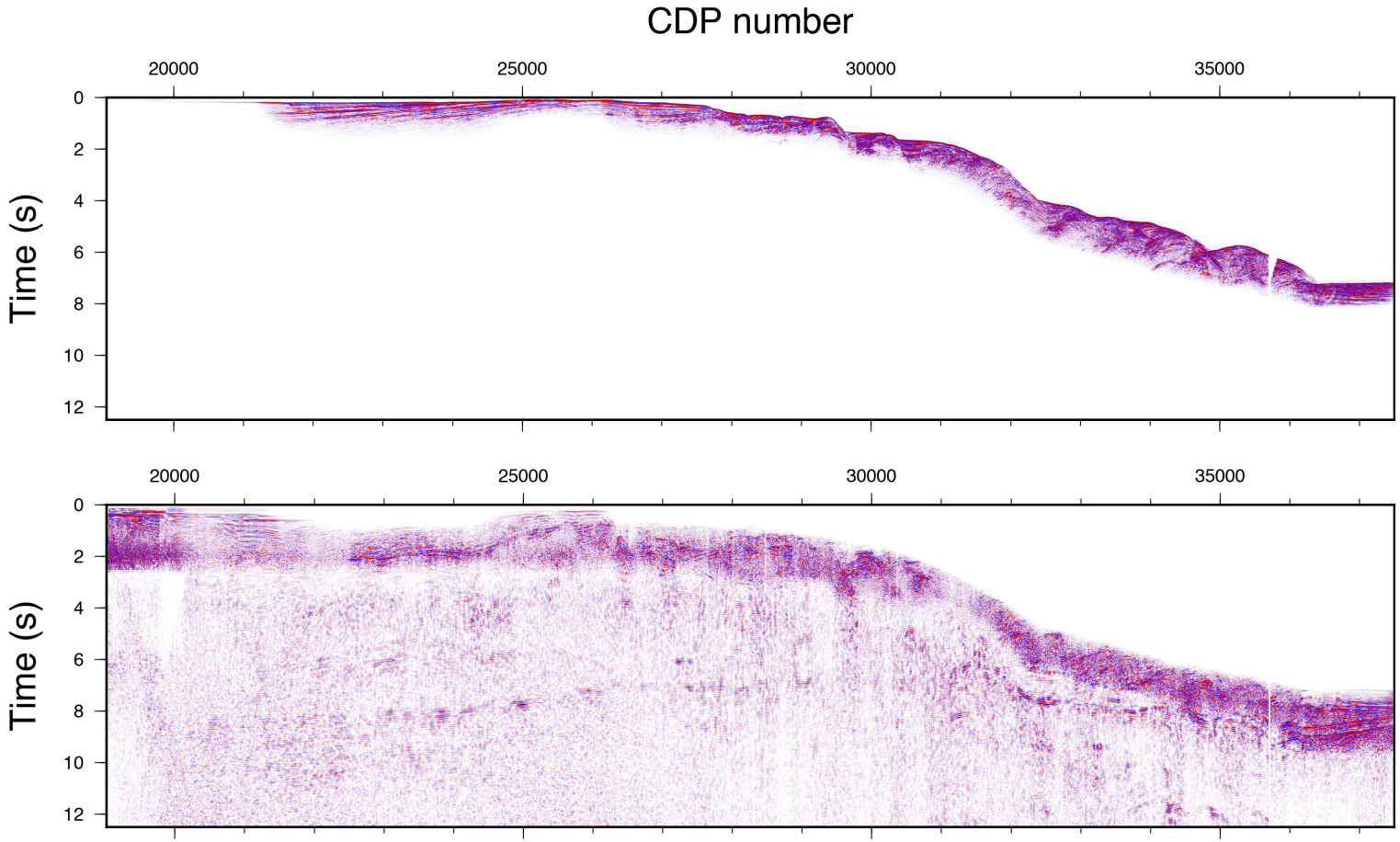

Figure 2.1.21: Seismic section in the upper image shows the sedimentary part above the acoustic basement acquired with streamer 1, which was towed at 9 m depth below the sea surface. Seismic section below shows crustal material below the acoustic basement acquired with streamer 2, which was towed at 12 m depth. The data of the two streamers is merged into one seismic section in the next processing step.

2.1.2.12 2D post-stack Kirchhoff time migration

Migration is an essential step in seismic data processing that attempts to reposition reflections in the seismic data into their true geological position in the subsurface. The Kirchhoff migration is one migration technique among many and tries to sum up the amplitudes along a hyperbolic diffraction curve and place the summed amplitude at its apex. Dipping reflective events consist of the superposition of many diffraction hyperbolas (following Huygen's principle), and are steepened and moved to their correct position by migration (Fig. 2.1.22). The quality of the diffraction summations or diffraction stacks, and eventually of the migration process itself, is controlled by the provided velocity model. If the migration velocities are incorrect migration artefacts can occur (e.g., so-called migration smiles). Time-Space 2D Kirchhoff migration module (MIGTX) was applied to the post-stack seismic data with surface distance between the CDP's of 6.25 m, a maximum dip to migrate of 20° and smoothed velocity model built from MCS stacking velocity functions, tomographic inversion results (see section 2.2) and deep crustal velocities from the literature. A detailed description of the velocity models and how they were built is given in Chapter 3.

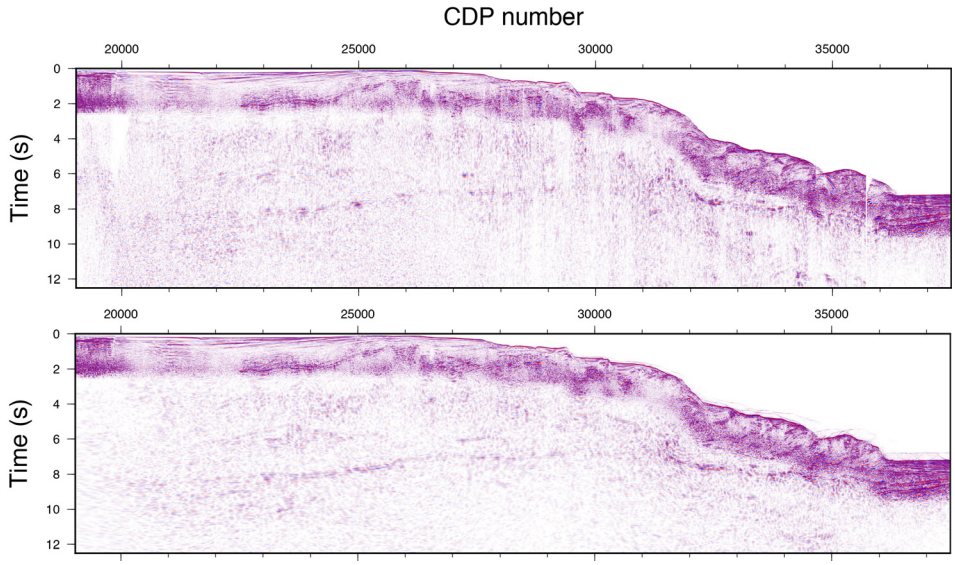

Figure 2.1.22: Merged seismic section before (above) and after (below) 2D Kirchhoff post-stack time migration.

2.1.2.13 Time to Depth conversion

To convert the seismic sections into interpretable geological images of the subsurface, they had to be converted from time domain (Fig. 2.1.23) into depth domain (Fig. 2.1.24). Velocity information needed to perform the time to depth conversion are provided in by the same velocity models used in the migration process. The final depth-converted seismic sections for all ALEUT Lines (except profiles located solely in the deep sea part) are shown in Appendix A (Fig. A.2 - A.29).

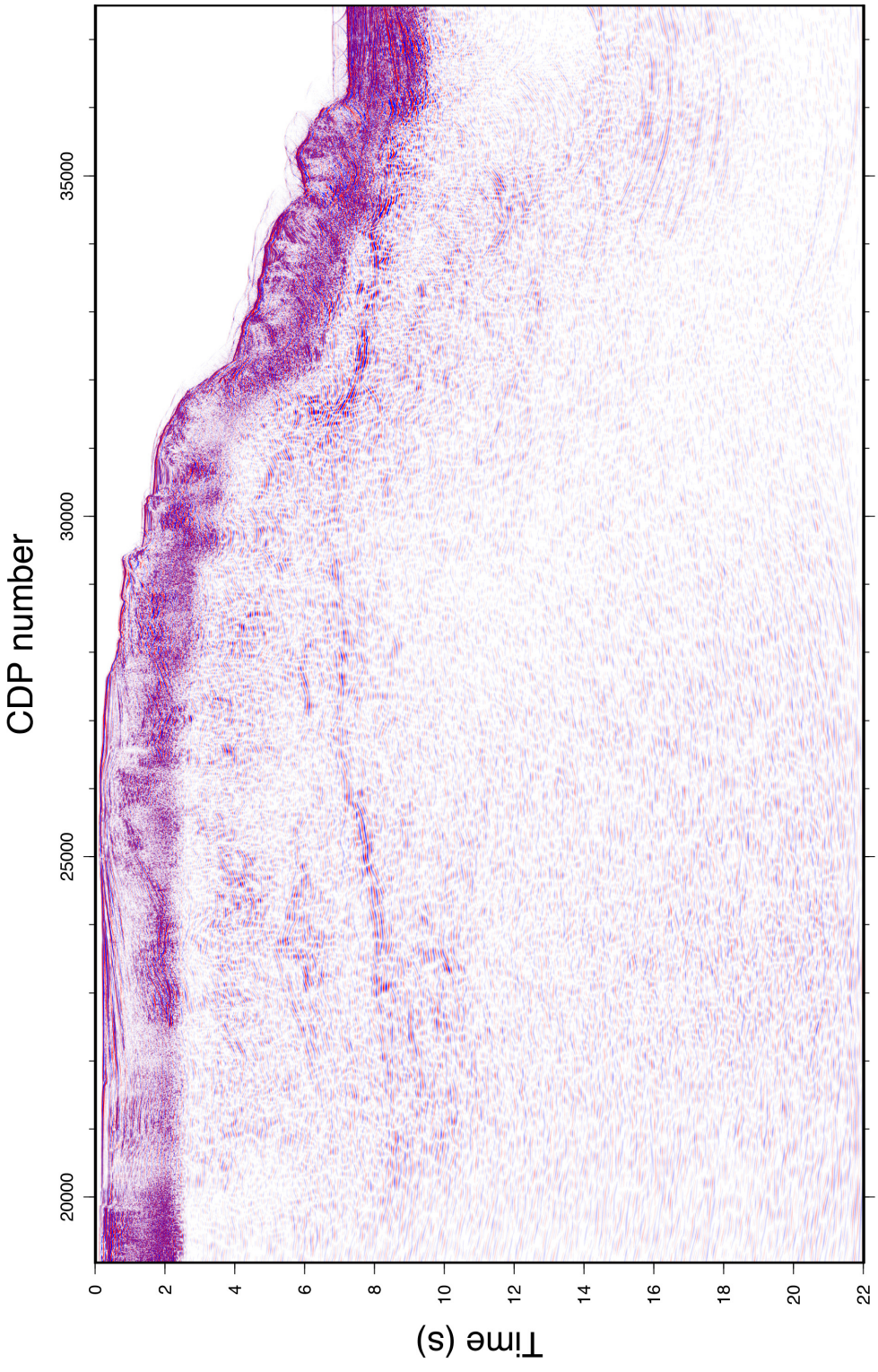

Figure 2.1.23: Final seismic stack section of MCS Line 1c in time domain.

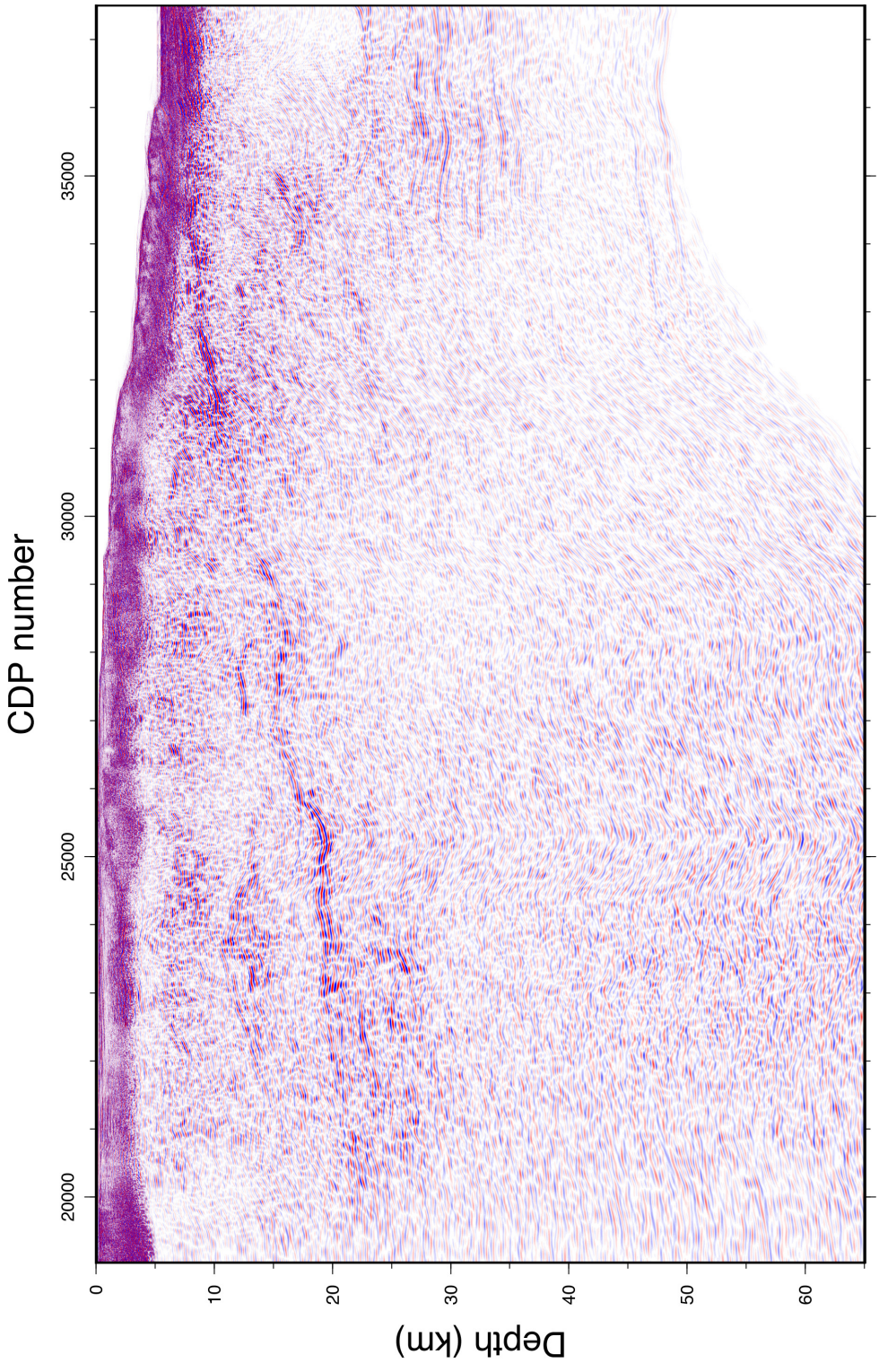

Figure 2.1.24: Final seismic stack section of MCS Line 1c in depth domain.

2.1.3 Resolution

Seismic resolution of reflections within a seismogram relates to the minimum spatial or temporal distance between two close, but separate, features so they can be distinguished and defined as two rather than as one feature. There are two types of seismic resolutions considered - vertical (temporal) and horizontal (spatial). Whereas the vertical resolution is controlled by the signal wavelength, which is dependent on the frequency and velocity, the horizontal resolution is additionally controlled by the reflectors depth or its two-way-traveltime (TWTT). The seismic wavelength (λ) is a fundamental property of a seismic signal and defined by the equation $\lambda = \frac{v}{f}$, where v is the seismic velocity and f the frequency. Smaller wavelengths (and higher frequencies) provide better resolution, whereas seismic signals with wavelengths too large compared to the dimensions of a subsurface feature, fail to detect it. In general, seismic resolution deteriorates with increasing depth as higher frequencies are being attenuated and seismic velocities increase. However, vertical resolution can be enhanced during data processing by deconvolution, which compresses the seismic wavelet by increasing the effective bandwidth. A quarter of the dominant wavelength ($\frac{\lambda}{4}$) is generally considered an acceptable threshold for vertical resolution [*Yilmaz*, 1987]. An estimate for the seismic resolution of the imaged deep plate interface reflection in the ALEUT dataset is given in the following paragraphs.

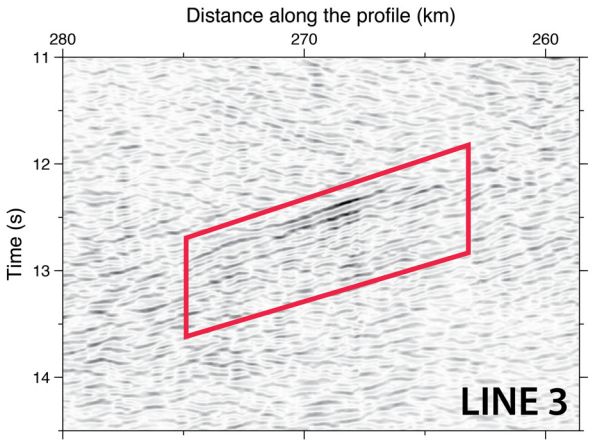

Figure 2.1.25: Plate interface reflection on Line 3. Red box shows signals used for the calculation of the frequency spectrum shown in Fig. 2.1.26.

The deep plate interface reflection signal consists of a dominant frequency of ∼5 - 15 Hz and an approximate seismic interval velocity of ∼7 km/s at ∼40 km depth

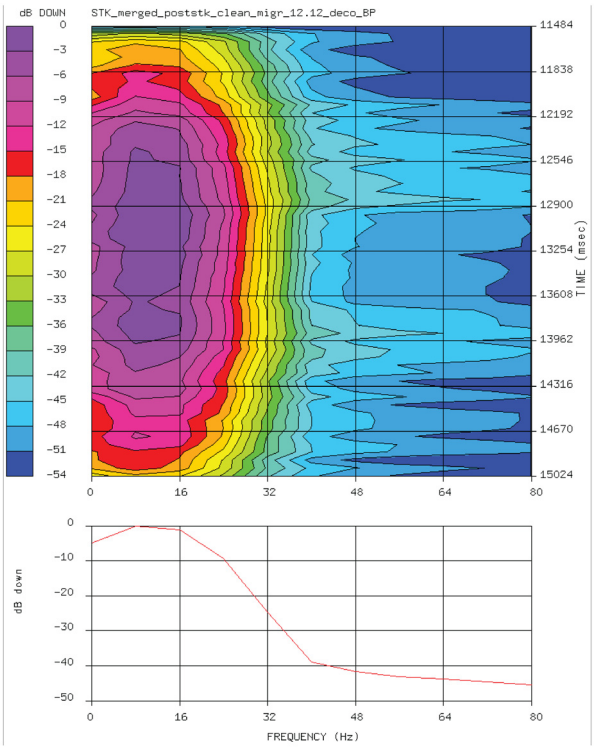

Figure 2.1.26: Frequency spectrum for part of seismic section of Line 3 (see Fig. 2.1.25). Highest amplitudes (purple area) are observed between ∼5 - 15 Hz.

(see Fig. 2.1.25, 2.1.26 or insert b) in Fig. 3.7.1) a dominant wavelength λ of ∼467 - 1400 m is calculated and results in a vertical resolution ($\frac{\lambda}{4}$) of ∼117 - 350 m. The horizontal resolution (for unmigrated seismic data) is defined by the width of the Fresnel zone [*Hilterman*, 1982], which is a theroretical (round) area with the radius r (or $\overline{OA'}$ in Fig. 2.1.27). The radius of the Fresnel zone is given by

$$r = \sqrt{\frac{z_0 \lambda}{2}}$$

or

$$r = \frac{v_{\mathrm{RMS}}}{2} \sqrt{\frac{t_0}{f}}$$

Seismic reflection points within that area are generally considered indistinguishable as observed from the earth's perspective. Thus, the smaller the Fresnel zone is, the higher is the horizontal resolution in the seismic data. However, at great depth (∼40 km or ∼12.5 s TWTT) and high velocities (v_{RMS} = ∼3500 m/s) the Fresnel zone becomes very large (∼3200 - 5400 m). Migration techniques are used to increase the horizontal resolution significantly and it has been demonstarted to

constrain the limit of horizontal resolution up to $\frac{\lambda}{4}$ [*Nanda*, 2016], similarly to the vertical resolution. Since both resolutions depend on seismic velocity, it must be stressed that vertical resolution depends on interval velocity while horizontal resolution is dependent on overburden (or RMS) velocity [e.g., *Nanda*, 2016].

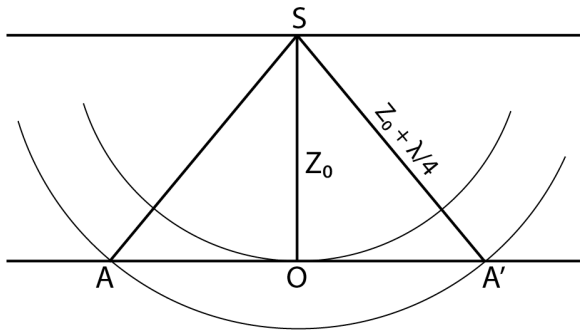

Figure 2.1.27: Definition of the Fresnel zone $\overline{AA'}$. Spherical wavefronts are sent out at source/receiver position S and reach the reflector at O at a depth of Z_0. A subsequent wavefront reaches A and A' after a distance of $Z_0 + \frac{\lambda}{4}$. The distance $\overline{AA'}$ represents the width of the Fresnel zone (modified after *Yilmaz* [1987]).

2.2 Ocean bottom seismometer (OBS) data analysis

2.2.1 Data acquisition and survey geometry

Wide-angle refraction/reflection OBS data was acquired along two profiles coinciding with ALEUT MCS Lines 3 and 5 (Fig. 2.1.1, 2.2.1), subsequently called accordingly OBS Line 3 and 5. These locations were chosen to investigate deep crustal structure and composition along profiles crossing the center of the Semidi Segment and Shumagin Gap, i.e. two segments that have exhibit vast differences in seismological behavior in the past [e.g., *Estabrook et al.*, 1994; *Shillington et al.*, 2015; *Sykes*, 1971]. Furthermore, the velocity information obtained from this data will provide essential complementary information to build velocity models for migration and time-to-depth conversion of the ALEUT MCS reflection data. 21 OBS were deployed on both profiles each with an interval spacing of ca. 16 km (OBS Line 3) and ca. 13 km (OBS Line 5).

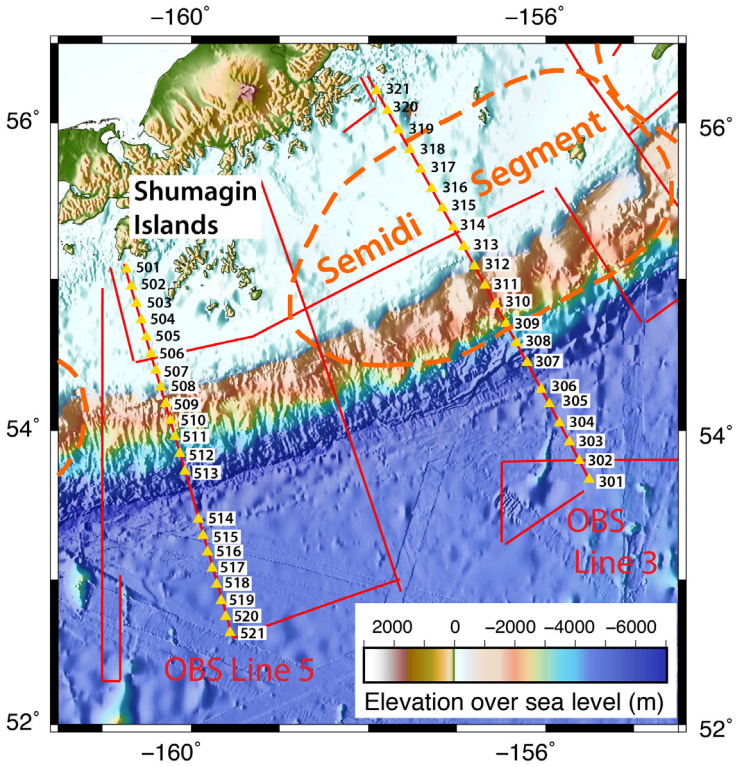

Figure 2.2.1: 21 OBS distributed are along OBS Line 3 and 5 (coincident with MCS Line 3 and 5) offshore the Alaska Peninsula. Yellow triangles show OBS (deployment) location and black numbers represent every 5th OBS name along the line. Red lines are MCS profiles as shown in Figure 2.1.1.

The seismic source is identical to the source used during the MCS reflection survey (section 2.1.1) but exhibits greater shot spacing of 310 m (or every ∼120 s) during all OBS shooting. This long shot interval is necessary to prevent the recording of previous shot noise (so-called wrap-around noise). All OBS instruments used during the survey were four-component OBS (LC4x4) from Scripps Institution of Oceanography in San Diego and recorded continuously during ca. 3-day deployment at a data sampling rate of 5 ms. The OBS instruments are equipped with a L28 gimbaled 3-component geophone, and a hydrophone. To reduce the risk of losing an instrument, no OBS was deployed in water depths greater than 5500 m, which left a ca. 40 km wide gap at the deepest part of the trench on OBS Line 5 between OBS 513 and OBS 514 (Fig. 2.2.1).

The task of processing of the OBS data was split between myself and our collaborators at Lamont-Doherty Earth Observatory (LDEO) at Columbia University in New York. OBS Line 3 was processed and interpreted here at Dalhousie University, while OBS Line 5 was processed and interpreted at the LDEO. However, close communication between Dalhousie and LDEO and free exchange of information ensured a similar processing standards on both OBS Lines.

2.2.2 Relocation of OBS instruments

The OBS instruments are deployed at predetermined locations at the sea surface and free fall through the water until they rest on the ocean floor. The OBS falls approximately 1-km every 10 min and can therefore drift large distances from its deployment position depending on water depth and underwater currents. Accuracy and resolution of travel time tomography requires knowledge of exact positions of both the receiver and shot. While the shot position is known from GPS measurements (extrapolated from the ships navigational point to the center of the seismic source array towed behind the ship), the exact position of the OBS on the seafloor is unknown and must be determined. This new corrected OBS location can be calculated by an inverse approach to minimizing the difference between the measured direct signal travel time between shot and receiver and the estimated travel time based on position of shot and the (deployed) OBS location [e.g., *Creager and Dorman*, 1982]. This process is called relocation and has been conducted during the cruise as part of onboard processing. A set of new SEGY files with updated receiver positions and source-receiver offsets has been generated and were

passed on for further processing and analysis.

2.2.3 OBS data processing

Arrival times in wide-angle seismic refraction and reflection data should be picked on non-processed data whenever it is possible to avoid unintentionally picking arrival times of an altered or shifted signal. At longer source-receiver offsets (and secondary signal arrivals) the signal-to-noise (s/n) ratio might get too large and simple processing steps are necessary to identify the refracted (or reflected) signal. Data processing is much less extensive than for MCS data as mostly non-coherent or random noise is attenuated to increase the s/n ratio. It should also be applied with caution to preserve as much of the original signal as possible to avoid phase shifts that would alter the signal arrival time. The focus in wide-angle first arrival OBS data analysis lies in the arrival times of refracted signals, which are recorded along large offsets (source-receiver distances) that can extent up to more than 100 kilometers. To display refraction arrivals at these large offsets in a convenient and more distinguishable way, the arrival times T are subtracted depending on their offset by x/v, where x is the offset and v the apparent velocity. Refracted signals with the apparent velocity appear horizontal in these so-called reduced traveltime plots, which makes them easier to trace and identify. It also facilitates picking of weak and secondary arrivals. The raw OBS data (Fig. 2.2.2) is processed with Paradigms Echos and the enhancement of the s/n ratio has been addressed in three ways: 1) Very low and high frequency noise has been removed by a trapezoidal bandpass filter with the corner frequencies 1-3-10-18 Hz. The filter is minimum phase and does not apply a phase shift as observed when using a zero-phase filter (FILTER) (Fig. 2.2.3), 2) DC bias is removed, i.e. the mean amplitude of a trace is calculated and subtracted from every sample along the trace (DEBIAS) (Fig. 2.2.4), 3) Coherent signals are enhanced by a two-dimensional dip filter across three traces and a dip range of -35° to +35° (COHERE) (Fig. 2.2.5).

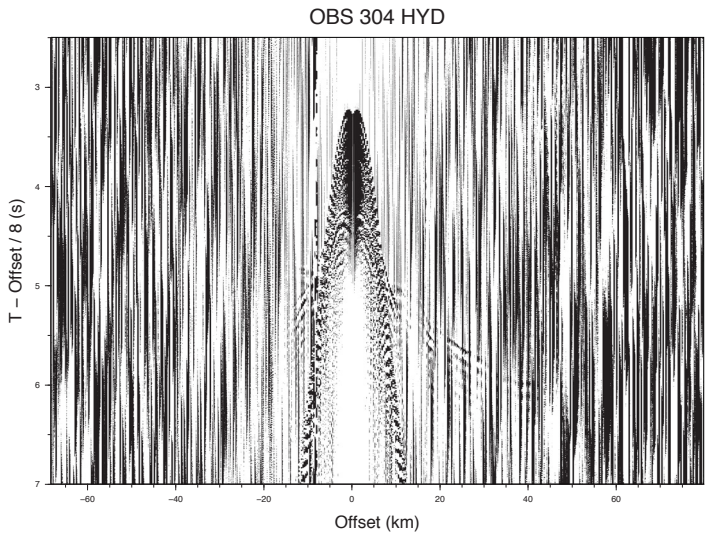

Figure 2.2.2: Seismogram of OBS 304's hydrophone channel. Unprocessed data with a reduced velocity of 8 km/s.

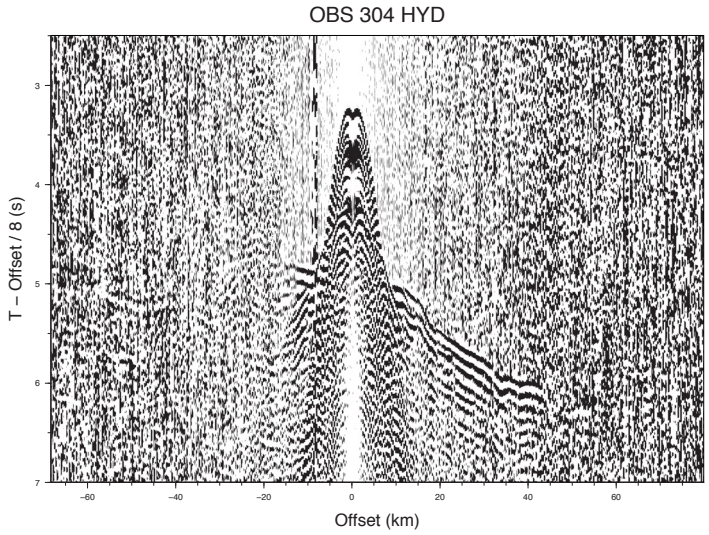

Figure 2.2.3: Seismogram of OBS 304's hydrophone channel with reduced velocity of 8 km/s and processed with bandpass filter (1-3-10-18 Hz).

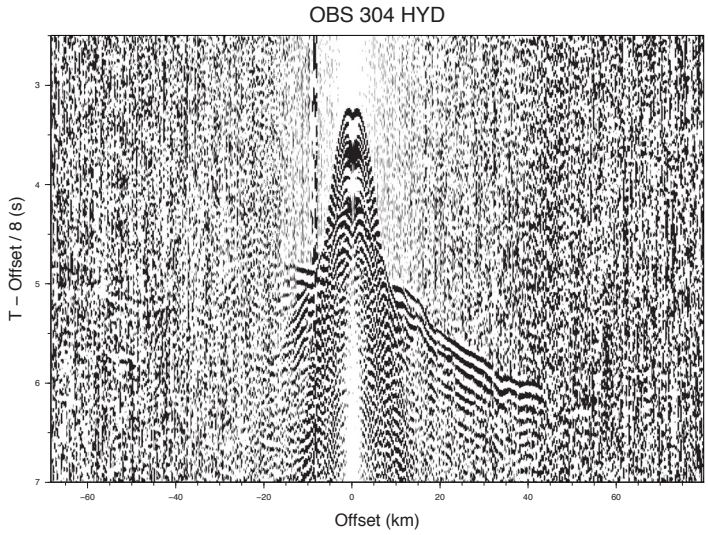

Figure 2.2.4: Seismogram of OBS 304's hydrophone channel with reduced velocity of 8 km/s and processed with bandpass filter (1-3-10-18 Hz) and DC bias removed.

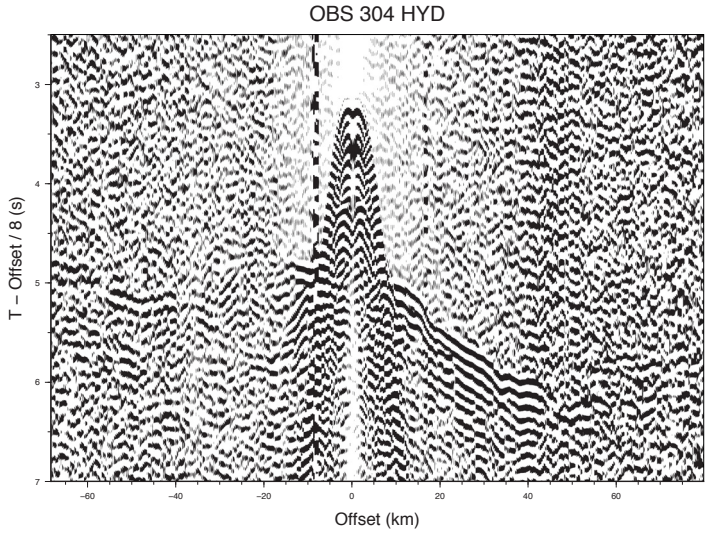

Figure 2.2.5: Fully processed seismogram of OBS 304's hydrophone channel with reduced velocity of 8 km/s and processed with bandpass filter (1-3-10-18 Hz), DC bias removed and enhancement of coherent refraction signals.

The seismic data set was recorded on four channels: two horizontal (X, Y), one vertical (Z) geophone component and one hydrophone channel (HYD). However, all processing and data analysis was conducted only the hydrophone channel because is yielded the clearest arrival signals and the most consistent signal quality. The OBS Z-component seismograms displayed signal quality in various qualities, sometimes first arrival signals seem to be recorded even clearer than on the hydrophone channel but sometimes they are less clear. Furthermore, 3 out of 21 OBS recorded no data on the Z-component. Thus, for consistency reasons, I only used first arrival travel times picked on the hydrophone channel. A data example to compare the data quality for all four channels of OBS 304 is given in Figure 2.2.6 - 2.2.8. OBS instrument 314 had timing errors and was not used during the tomographic inversion.

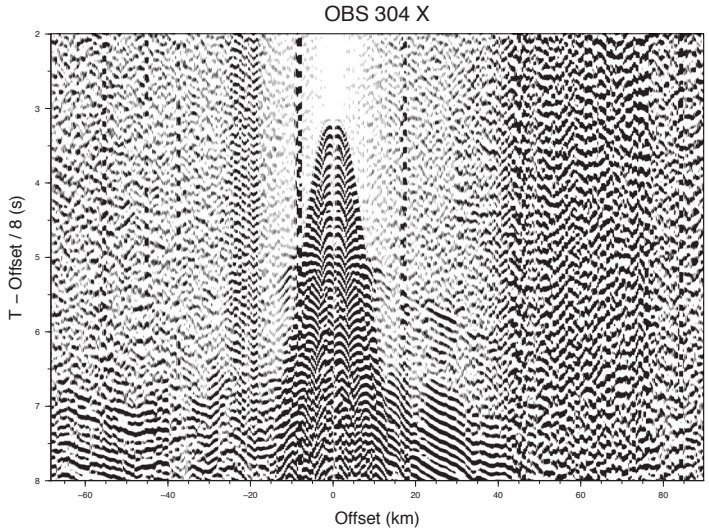

Figure 2.2.6: Seismogram of OBS 304's geophone horizontal channel X. The seismic data was processed in the same way than the hydrophone channel in Figure 2.2.4.

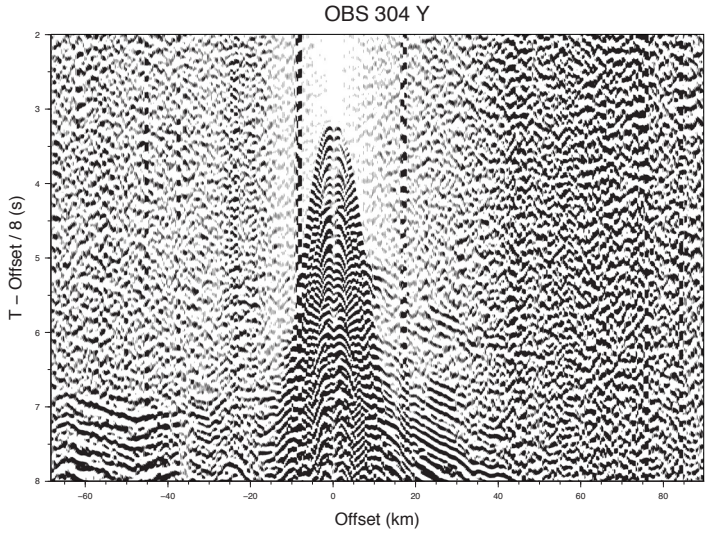

Figure 2.2.7: Seismogram of OBS 304's geophone horizontal channel Y. The seismic data was processed in the same way than the hydrophone channel in Figure 2.2.4.

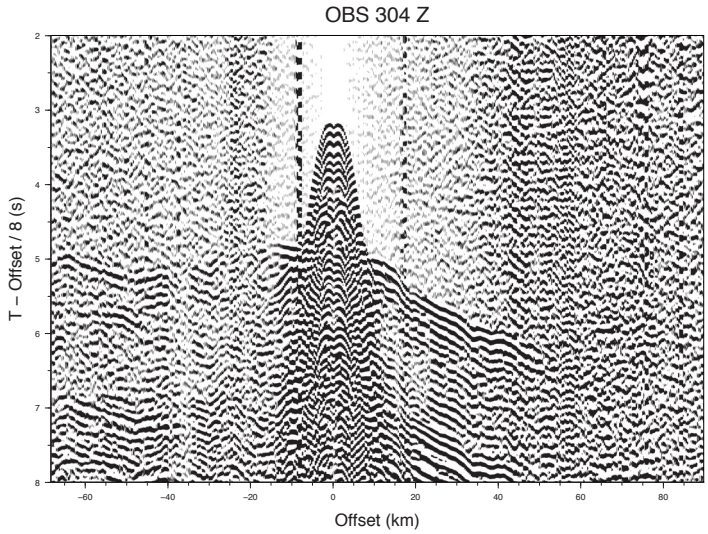

Figure 2.2.8: Seismogram of OBS 304's geophone vertical channel Z. The seismic data was processed in the same way than the hydrophone channel in Figure 2.2.4.

2.2.4 Arrival time picking and uncertainties

For this thesis, only first arrivals of the refracted waves have been picked and were used in the inversion to obtain a two-layer tomographic velocity model. The model consists of a water layer with constant velocity and the computed smooth sub-sea-bottom velocity distribution. Both layers are separated by a discrete boundary representing the sea bottom, that was derived from bathymetric data. The most robust inversion results were achieved by a conservative style of arrival time picking, i.e. only the clearest arrivals (usually at short or moderately far distances) were used. An example of first arrival picking is shown in Figure 2.2.9. One of six different uncertainty values are assigned visually to each travel time pick according to its signal clarity. The uncertainty values are, ranging from clearest to most uncertain pick: 40 ms, 70 ms, 100 ms, 150 ms, 200 ms and 250 ms. A collection of all OBS seismograms including their first arrival picks, associated uncertainties and conparison with calculated (synthetic) arrival times can be found in Appendix C (Fig. C.2 - C.61). Picking the seafloor multiple in support of first arrival identification has not been conducted because in most instruments the multiple signal was not much clearer than the primary signal. Furthermore, inversion test runs with extended offsets picks appeared to result in unstable models or a bad fit with the observed data. However, for future processing and second arrival picking, this technique might be beneficial.

2.2.5 Seismic tomographic inversion using Jive3d software [*Hobro et al.*, 2003]

The Jive3d program is used to produce seismic velocity models to fit a given set of travel time data. These data may contain near and far offset arrivals from reflected and refracted seismic rays acquired during 2D wide-angle surveys. The generated velocity models are described as a stack of layers separated by discrete interfaces. Velocity distribution within these layers and the geometry of the interfaces can be fixed during the inversion, or it may vary to accommodate and fit the observed travel times. The Jive3d algorithm is designed to produce the simplest model possible (minimum-structure model) that explains the observed travel time data to the required accuracy [*Hobro et al.*, 2003].

The inversion method uses a linearized iterative inversion approach. In other words,

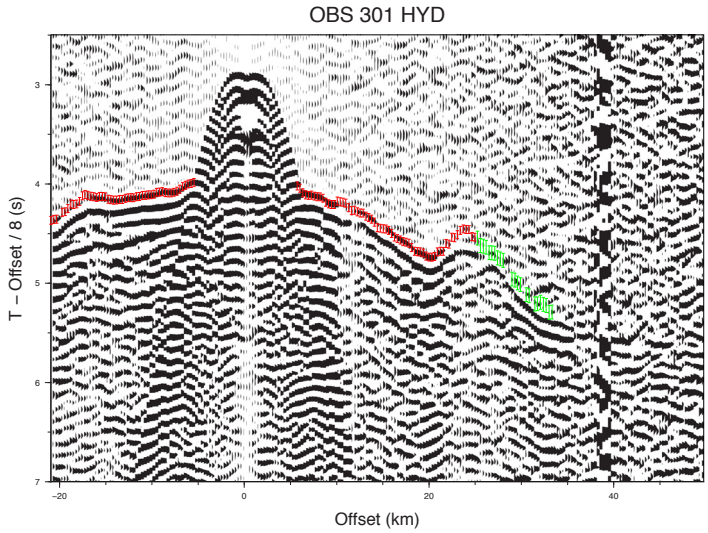

Figure 2.2.9: Example of travel time picks (first arrivals) of OBS 301 (hydrophone channel). Red error bars represent first-arrival time including an uncertainty of 40 ms. Green error bars represent a picking time uncertainty of 70 ms.

it applies a series of small refinements to a starting model to improve its fit with the provided travel time data including their uncertainties. To identify an improved (better fitting) model, a set of synthetic travel time is calculated and compared with the observed travel times and the difference between these two is optimized. The perturbations in the model must be small enough that the resulting changes in the synthetic travel times may be approximated by a linear equation. If the inversion proceeds successfully, a final velocity model will eventually be generated that provides a satisfactory fit with the observed travel time data.

The inversion process can be highly subjective as the final model depends on the starting model and model parameters used during the inversion. A starting model is first refined with strong constraints. In this early inversion stage, bulk characteristics and large-scale structure within the data is modelled. The strength of the smoothing constraints is reduced step by step as the inversion proceeds, allowing greater details to emerge in the model. The inversion process is stopped so that the final model contains the minimum degree of structure required to provide a satisfactory fit with the data without modelling noise [*Hobro et al.*, 2003]. In experimental science, a common measure for the "goodness of the fit" between modelled and observed data is the criterion of least-squares, in which chi-square (χ^2) is aimed to be minimized as a function of the model m:

$$\chi^2 = \frac{1}{N_\mathrm{d}} \sum_{i=1}^{N_\mathrm{d}} \left(\frac{d^{\mathrm{synt}}{}_\mathrm{i} - d^{\mathrm{obs}}{}_\mathrm{i}}{\sigma_\mathrm{i}}\right)^2$$

Where N_d is the number of sample points (number of travel time picks), d is the travel time (observed and calculated) and σ is the assigned uncertainty. If the modelled data fit the observed data within the given uncertainty range, a χ^2 value around "1" is expected and regarded as a good fit. However, as χ^2 in the equation (see above) is largely depended on the sigma, the uncertainty value should be chosen adequately and must not be too large to avoid having a good fit solely because of large uncertainties instead of strong constraints on the subsurface structure.

Running the seismic inversion program Jive3d from *Hobro et al.* [2003] requires four input files that specify: 1) a starting model, including model geometry for the entire inversion, 2) the geometry of the seismic experiment, and ray-tracing parameters to simulate the experiment, 3) a set of travel time data with estimated uncertainties, and 4) parameters required for the inversion process. While the starting model and survey geometry were kept fixed, numerous variations in inversion parameters and travel times picks including their uncertainties were tested to find an acceptable subsurface velocity model.

2.2.6 Inversion results for OBS Line 3

A total of 360 inversions with various parameters, travel time picks and uncertainties have been run and compared. A model that contained a minimum degree of structure required to provide a satisfactory fit to the data without modelling noise has been chosen for the final model. The starting model for the inversion process is built from a simple 1-D-velocity function (linear increase over 20 km depth from 1.5 km/s to 8 km/s) that is hung from the seafloor (Fig. 2.2.10). After 26 from 30 inversion steps a smooth minimum structure velocity model is generated with a good fit to the observed travel time data represented by a χ^2 value of 1.02 (Fig. 2.2.11). Although the model extends to 40 km depth, the areas with sufficient ray coverage is much shallower (Fig. 2.2.12). The profile edges and the subsurface of more than ca. 10 km below the seafloor is not constrained by first arrival travel time data and is therefore not considered in the data interpretation and further processing as described in Chapter 3.

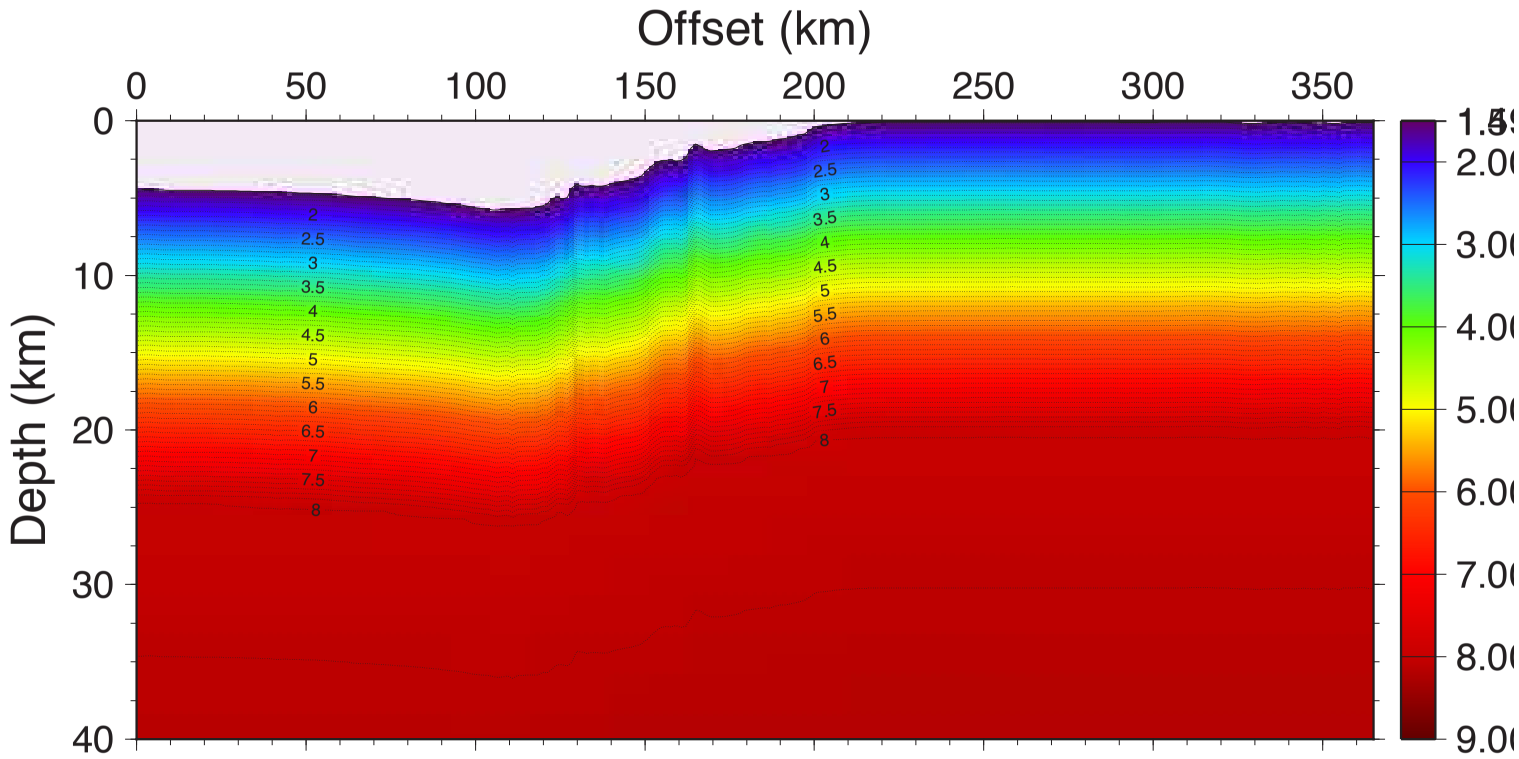

Figure 2.2.10: Jive 3D starting model for Line 3 with linear velocity function hang from the seafloor.

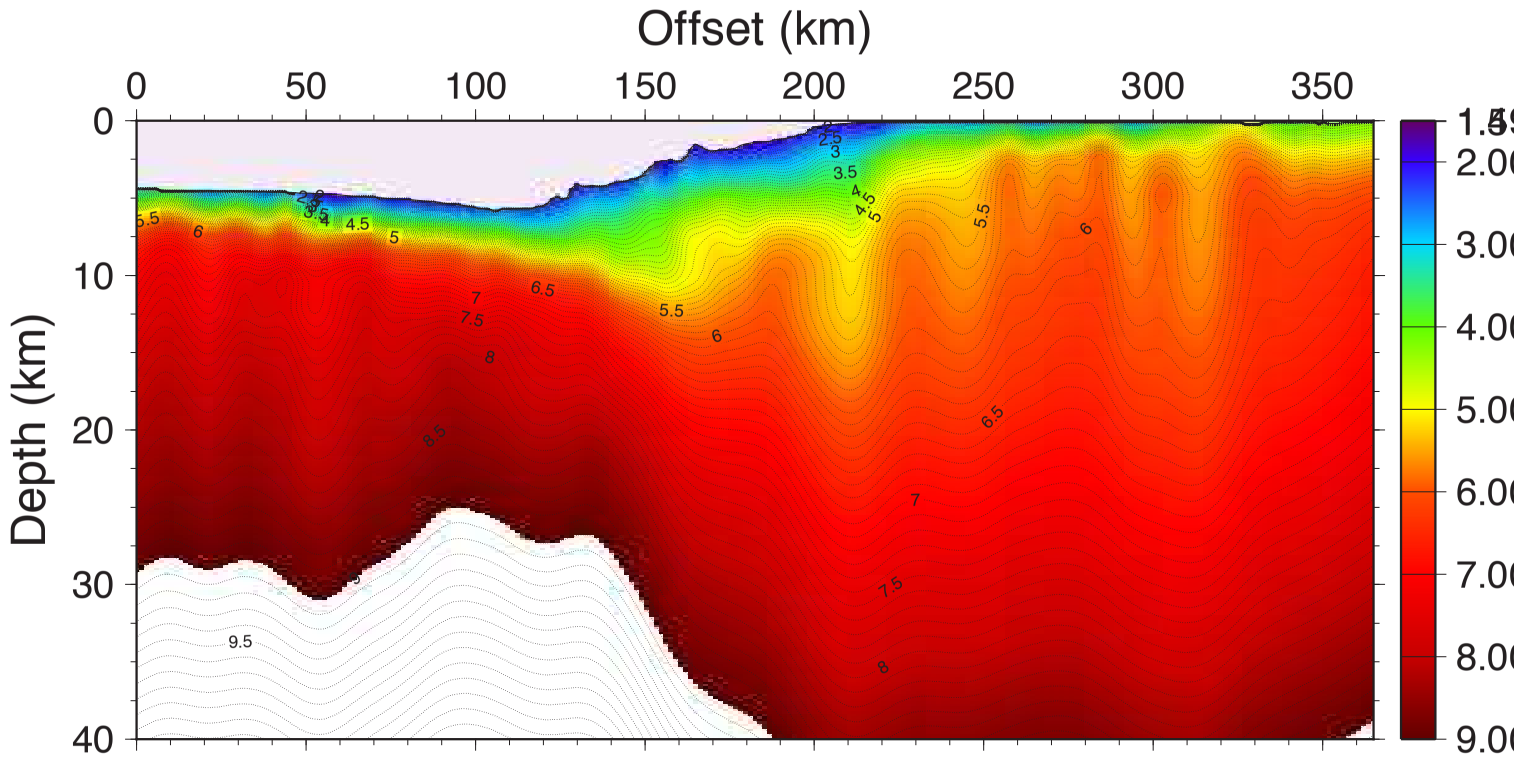

Figure 2.2.11: Final seismic tomography model for OBS Line 3.

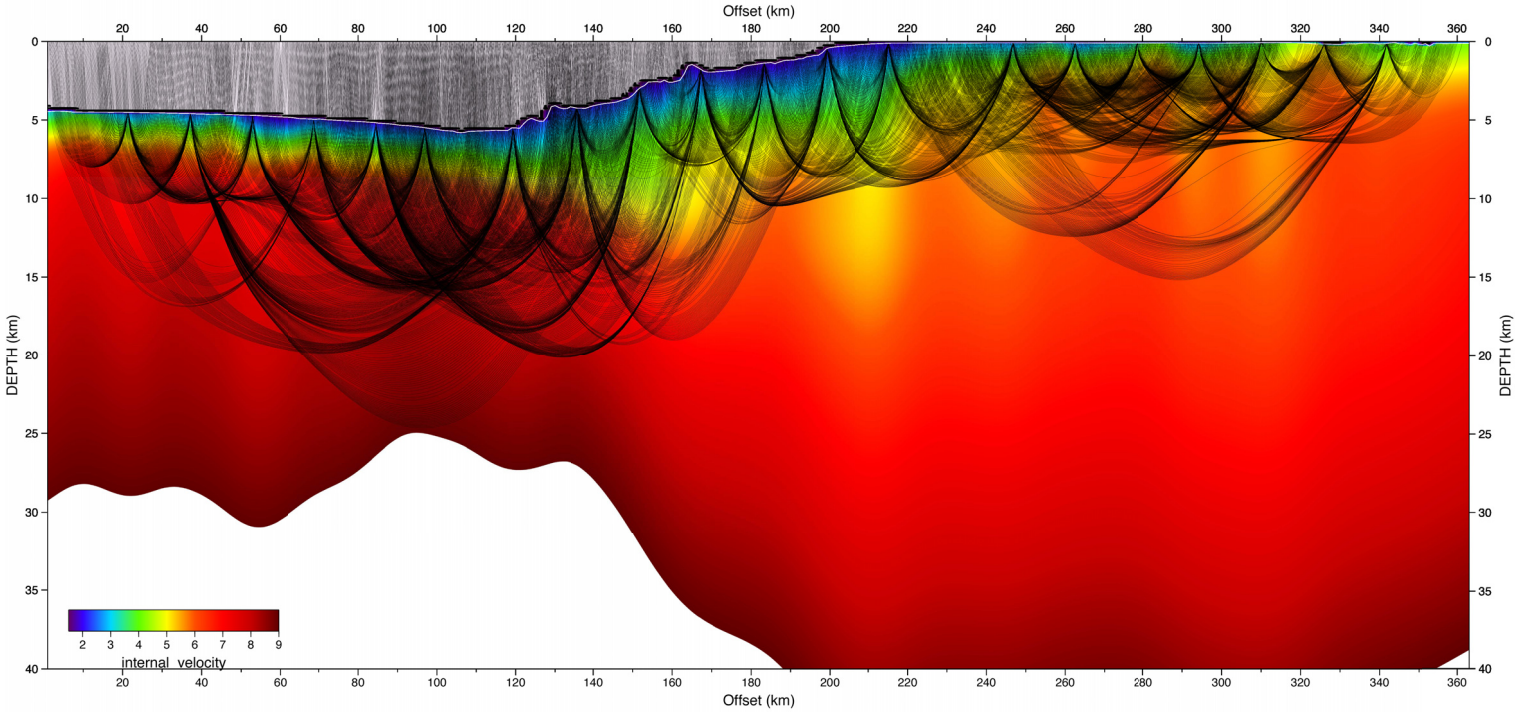

Figure 2.2.12: Final seismic tomography model for OBS Line 3.

Chapter 3

Interplate interface geometry and segmentation along the Alaska-Aleutian subduction zone from -161° E to -152° E

3.1 Abstract

Earthquake magnitude and therefore its destructive power are proportional to rupture area, yet it remains unknown if future megathrust events, the largest earthquakes on Earth, stick to the same pattern of ruptures, propagate into adjacent segments to produce even larger magnitudes, or break entirely different segments. Lateral variations in geologic features and subduction-related processes (e.g. sediments, seamounts, crustal fabric, faulting, serpentinization, dewatering) have been proposed to affect megathrust segmentation. However, while all of these factors are likely important, they seem to vary gradually or are too subtle and cannot account for segment boundaries determined from seismicity, dislocation modeling, tsunamis, paleoseismology, and gravity. We use deep-penetration seismic reflection data from the ALEUT project to construct a 3D model of the interplate interface along the eastern Alaska-Aleutian subduction zone (AASZ). Megathrust reflections are traced nearly continuously from the trench to a record depth of > 65 km, providing unique insight into possible morphological controls on along-strike rupture organization of the subduction thrust. We identify two major crest-like structures on the interplate interface that coincide with the boundaries of the region's great earthquake ruptures and the extrapolated trajectories of the two offshore seamount chains. The spatial coincidence of these geometrical highs, interpreted to represent subducted seamount chains, with the edges of the 1938 Semidi and 1964 Prince William ruptures indicates that the megathrust geometry is the primary factor controlling the segmentation of the eastern AASZ. Moreover, this suggests that the rupture pattern likely persists over many earthquake cycles, until current major morphological features on the seismogenic part of the megathrust subduct.

(260 words)

3.2 Introduction

Nearly the entire Alaska-Aleutian subduction zone (AASZ) has ruptured in a series of great $M_W > 8$ megathrust earthquakes in the mid 20^{th} century: 1938 M_W 8.2 Kodiak Island, 1946 M_W 8.6 Unimak Island (Aleutian "tsunami" earthquake), 1957 M_W 8.6 Andreanof Islands, 1964 M_W 9.2 Prince William Sound (Good Friday earthquake), and 1965 M_W 8.7 Rat Island (Fig. 3.2.1) [*Davies et al.*, 1981; *López and Okal*, 2006; *Nishenko and Jacob*, 1990; *Sykes*, 1971]. Each hypocenter of these great earthquakes has been the origin point of rupture of large interplate interface segments with along-trench dimensions of up to hundreds of kilometers (an exception is, for example, the M_W 9.2 Good Friday earthquake, which has ruptured two large segments: Prince William Sound Segment and Kodiak Asperity). Locations of aftershock earthquakes related to each of the main events have been used to estimate the extent of the rupture areas and to determine seismogenic interplate interface segmentation of the AASZ [*Davies et al.*, 1981; *López and Okal*, 2006; *Nishenko and Jacob*, 1990; *Sykes*, 1971]. The first pre-instrumental record of an intense earthquake event followed by tsunami flooding only goes back to 1788 [*Soloviev*, 1990]. These records, based on individual experiences and isolated observations of tsunami run-up heights, are insufficient for reliable constraints on epicenter locations but give indications for a possible rupture propagation from the Semidi Islands region into the Shumagin Islands area [*Davies et al.*, 1981]. This relatively short record of seismic activity of roughly 200 years likely does not contain a complete subduction zone seismic cycle for large rupture areas with potential for giant earthquakes [*McCaffrey*, 2008]. Moreover, modern broadband seismometer network data first became available in the mid 1980s, allowing earthquakes to be evaluated not only for their epicentral location and magnitude but also for hypocenter depth, seismic moment release and breaking mechanism. Hence, data for detailed analyses of earthquake source parameters are only available for approximately the last 30 years. Prehistoric records of great earthquakes and subsequent tsunamis in form of sediment layers that record land level changes and inundation patterns at estuaries and lagoons are scarce at the eastern AASZ between Kodiak Island and the Shumagin Islands. There are, however, indication of multiple great earthquake cycles that might have had varying rupture dimensions [Briggs et al., 2014]. Whether future megathrust events stick to the same pattern of

ruptures, whether they propagate into adjacent segments and produce even larger earthquake magnitudes as might have happened with the Good Friday earthquake in 1964, or whether they break entirely different segments remains unknown.

Areas of the AASZ that did not rupture in great earthquakes in the past century are located between the 1938 and 1946 rupture zone near the Shumagin Islands and possibly a megathrust section landward of the eastern part of the 1957 rupture zone (Fig. 3.2.1) [*Davies et al.*, 1981; *Sykes*, 1971]. Although, recent simulations to model tsunami generation do indicate slip of the shallow eastern portion of the 1957 rupture zone [*Nicolsky et al.*, 2016], it is still debated if these "seismic gaps" are capable of producing great megathrust earthquakes or at least allow rupture propagation from nearby segments to enter them. Geodetic measurements constraining the deformation process and interplate coupling indeed show a weak locking degree for the northeastern portion of the Shumagin Gap and freely slipping behavior in the southwestern portion [*Fournier and Freymueller*, 2007; *Li and Freymueller*, 2018], but data point distribution is generally very sparse and confined to land, so the shallow part of the megathrust is particulary poorly constrained. Pre-instrumental eyewitness reports (see above), however, describe intense shaking and large tsunamis in this very area of the Shumagin Islands in 1788 [*Soloviev*, 1990].

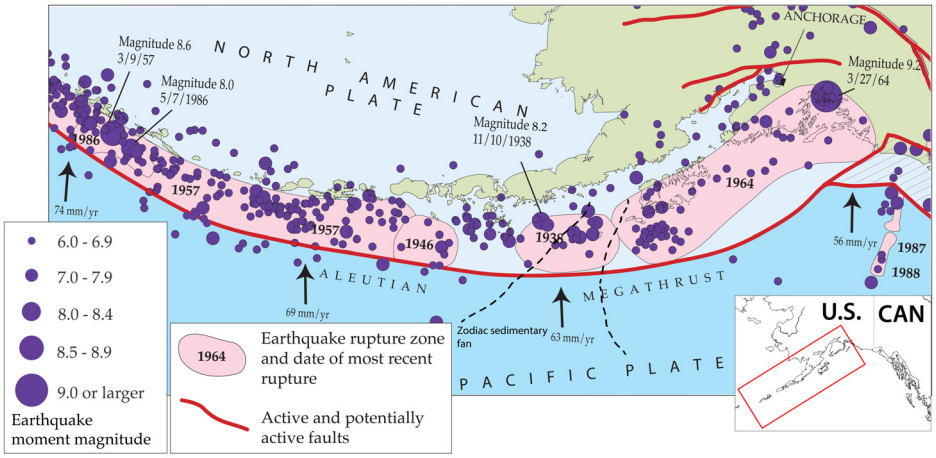

Figure 3.2.1: The eastern and central Alaska-Aleutian subduction zone with past megathrust rupture areas and earthquake epicenter from the Alaska Earthquake Information Center (AEIC) covering period from 1899 - 2003 [modified after *Eberhart-Phillips et al.* [2003]].

It has long been noted that for regions where seamount chains or other bathymetric highs intersect subduction trenches, large earthquakes occur less frequently and are generally of shorter rupture length than large megathrust events along adjacent

segments of the plate margin [*Kelleher and McCann*, 1976; *Kelleher et al.*, 1973]. The early observations have led to more detailed investigations on the effect of seamount subduction on seismic coupling and the generation of large megathrust earthquakes. As a result, seamounts, or other protruding elements on the subducting seafloor, have been proposed to act as strong asperities capable of producing large megathrust ruptures [*Cloos*, 1992; *Husen et al.*, 2002; *Scholz and Small*, 1997], geometrical barriers that stop propagation of large earthquakes [*Kodaira et al.*, 2000; *Watts et al.*, 2010], and sections of the megathrust that tend to creep [e.g., *Bell et al.*, 2010; *Mochizuki et al.*, 2008; *Ranero and von Huene*, 2000], as they might develop a fractural network along their paths that promotes strain energy release by numerous small earthquakes [*Wang and Bilek*, 2011]. The controls on this dissimilar behavior are presently unclear but crucial to understanding the tectonic segmentation of subduction zones.

Morphologic features and material on the oceanic plate approaching the eastern AASZ, the area investigated in this work, as well as the morphology of the plate interface to a depth of ca. 5 km below the seafloor, were investigated by *Von Huene et al.* [2012], including their possible effect on the lateral extent of past megathrust ruptures. The Kodiak-Bowie seamount ridge (also known as Pratt-Welker seamount chain) subducts beneath Kodiak Island and appears to correlate with local areas of high friction that form the Kodiak Asperity. In contrast, the inferred subduction path of both the Patton-Murray ridge (also known as Cobb-Eickelberg seamount chain) and the Aja Fracture zone seem to coincide with the aftershock limits of the 1938 and 1964 earthquakes south of Kodiak Island and are therefore interpreted as a barriers, which stopped rupture propagation. To support that theory, *Von Huene et al.* [2012] identified coinciding upper plate structures, such as embayments and uplift in the forearc, formed independently from the arrival of incoming seamounts, that might reinforce the effect on rupture organization by geologic structures.

Lateral variations in sedimentation may be linked to subduction zone segmentation. The area of the Semidi Segment coincides with the inferred head of the partially subducted Zodiac fan, which covers large parts of the seafloor in the western Gulf of Alaska (Fig. 3.2.1). The fan began entering the subduction trench between Kodiak Island and the Shumagin Islands around 3 Ma and is presently subducting over a down-dip distance of ca. 200 km, i.e. almost the entire width of the continental shelf, given an average plate convergence velocity of 65 mm/yr. The fan's strata comprise homogeneous fine grained sediments, compacted since the Eocene, that

built up the decollement at the top of the subduction channel, whereas younger pelagic sediments and trench fill sediments accrete to the frontal prism [*Marlow et al.*, 1973; *Stevenson et al.*, 1983; *Von Huene et al.*, 2012]. Analysis of ALEUT seismic reflection data show that along-strike changes in the thickness of subducting sediment and disruption of sediment by bending faulting result in very different properties along the plate boundary [*Bécel et al.*, 2017; *Li et al.*, 2018]. Such changes in properties are proposed to contribute to changes in seismicity and potentially plate coupling between Semidi and Shumagin segments [*Li et al.*, 2018; *Shillington et al.*, 2015; *Von Huene et al.*, 2012]. It also might explain the southwestern rupture extent of the Semidi Segment, since no physical barrier on the upper or lower plate is obvious that could have stopped the rupture, although *Von Huene et al.* [2012] suggest that a deeper than usual basement mass beneath the Shumagin Island could have acted as such barrier.

The inferred subduction trajectories of seamount chains beneath the fore-arc are based on the orientation of existing seamounts found seaward on the Pacific plate, and provide only a rough estimate of possible locations of major features on the interplate interface. How many seamounts currently on the megathrust, their size and down-dip location, and how this information correlates with current estimates of the megathrust coupling and segmentation is not known. Also lacking is any information about the possible consumption of the subducting seamounts by the overriding plate in the past. For the Alaska Langseth Experiment to Understand the megaThrust (ALEUT project), we use long streamer (8-km) 2D multichannel seismic (MCS) data in combination with wide-angle ocean bottom seismometer (OBS) profiling to image and resolve the interplate interface geometry, including possible subducted seamounts, up to a depth of almost 70 km below sea level at the eastern AASZ between -161° E to -152° E. This is globally the greatest depth to which megathrust reflections have been imaged, providing us with a unique insight into possible lower (or upper) plate controls, in form of geometrical irregularities, on along-strike rupture organization of this seismically segmented megathrust region.

3.3 Geologic history and present tectonic setting of the eastern Alaska-Aleutian subduction zone

The entire AASZ stretches ca. 3000 km, from the Kenai Peninsula in the Gulf of Alaska at the east end to Bering Island nearly to Kamchatka in the far west (Fig.

3.2.1). The AASZ is the result of a northwest movement of the Pacific Plate and west-southwest movement of the North American Plate, which leads to convergence between the two plates and subduction of the denser Pacific Plate beneath the more buoyant North American Plate. Near Unimak Pass, the compositional nature of the overriding plate changes dramatically from continental crust built up by accreted terranes of the Alaska Peninsula in the east to oceanic crust of the entrapped Kula plate, overlain by 3 - 12 km thick basin-filling sediments, in the west [*Lizarralde et al.*, 2002; *Scholl*, 2016; *Steven Holbrook et al.*, 1999]. The modern oceanic Aleutian arc west of this transition evolved around 56 Ma ago, when subduction of the old Kula Plate beneath the western Alaska margin ceased and jumped southward to its present position where it triggered subduction related volcanism resulting in its present-day legacies in form of the Aleutian Island chain (Fig. 3.3.1) [*Scholl et al.*, 1986; *Worrall*, 1991].

At the eastern part of the AAZS, approximately from the Kenai Peninsula to Sanak Island, the subducting Pacific Plate and the overriding North American Plate are converging orthogonally at a rate that ranges from 54 to 65 mm/yr [*DeMets et al.*, 2010]. The age of the subducting oceanic crust is 48 - 56 Ma [*Lonsdale*, 1988], but increases towards the west as the relative plate movements change gradually from almost perpendicular in the east to nearly parallel, strike-slip motion at the western end of the arc. However, plate age, thermal structure, convergence rate and obliquity remain relatively uniform between Kodiak Island and Sanak Island region west of the Shumagin Islands. In contrast, magnetic anomalies indicate a dramatic change in the direction and spreading rate of oceanic lithosphere caused by tectonic reorganization during the entrapment of the Kula plate around 56 Ma - 40 Ma ago (Fig. 3.3.1) [*Engebretson*, 1985; *Lonsdale*, 1988]. Incoming oceanic crust generated at the Kula-Farallon ridge formed at an intermediate spreading rate (half spreading rate $\sim$24 mm/yr) and is now highly oblique (up to 70°) relative to the trench near Semidi Segment, whereas oceanic crust entering the Shumagin Gap originates from the Kula-Pacific ridge, which had fast spreading rates (half rate $\sim$70 mm/yr), and is now orientated almost parallel (10° - 25°) to the trench near the Shumagin Islands [*Bécel et al.*, 2015; *Lonsdale*, 1988; *Shillington et al.*, 2015].

Sediment thickness on top of the incoming oceanic crust is approximately 500 m within our survey area, except on the seafloor that is in the depositional environment of the sedimentary Zodiac fan, where a significant increase in thickness to about 1000 - 1500 m on top of the basaltic basement is observed (see Appendix

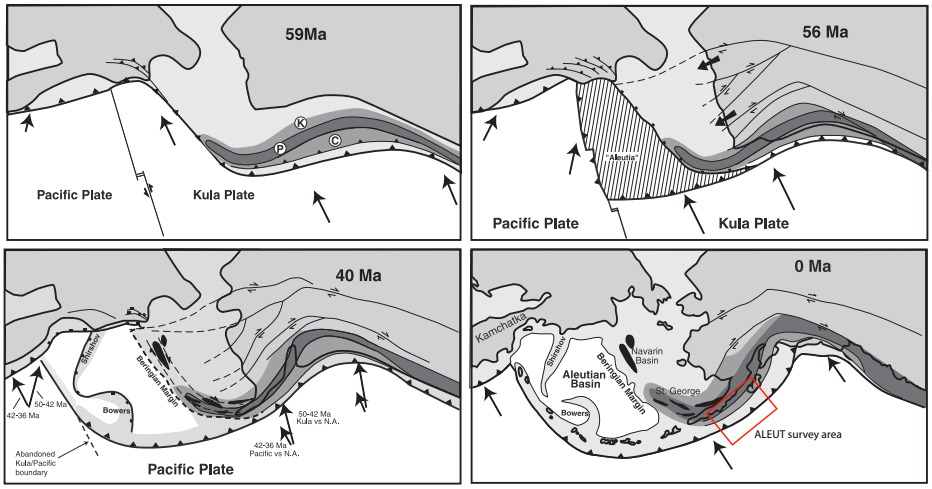

Figure 3.3.1: Tectonic history of the Alaska-Aleutian subduction zone based on the work of *Scholl et al.* [1986] and *Worrall* [1991] (figure modified after *Lizarralde et al.* [2002]). Around 59 Ma, three allochthonous terranes (Kahiltna - K, Peninsula - P, and Chugach - C) begin docking on the Alaskan mainland. By 56 Ma subduction at the western Alaska margin ceases and jumps southward to begin forming the Alaska-Aleutian magmatic arc. An old part of the Kula plate becomes the entrapped Aleutia micro plate. By around 40 Ma, continued clogging of Kamtchatka subduction causes the Aleutian subduction to migrate westward and form the modern shape of the present Alaska-Aleutian subduction zone. Red rectangle shows the ALEUT survey area.

A, Fig. A.4, A.5). The stratigraphic sequence of the Zodiac fan is traced and identified by deep sea drilling sites as early Tertiary turbidites below a carbonate-rich top, which are deposited in between an older and a younger pelagic sediment cover [*Reece et al.*, 2011; *Stevenson et al.*, 1983; *Von Huene et al.*, 2012]. The Zodiac fan sediments are topped by a carbonate-rich sediment sequence characterized by high-amplitude reflections that can be traced below the frontal prism and sometimes further down dip in seismic reflection sections [*Li et al.*, 2018; *Von Huene et al.*, 2012] and is thought to represent the contact layer of the down-going oceanic lithosphere and the overriding continental plate. The younger and weaker pelagic cover sediments on top are scrapped and are accreted to the frontal prism [*Li et al.*, 2018; *Von Huene et al.*, 2012]. In immediate adjacent areas, next to the Zodiac fan, the sediment cover sequences are of pelagic origin with generally a lower total thickness. However, the incoming plate offshore Kodiak Asperity and farther north are covered by thick sediments of the Surveyor fan [*Reece et al.*, 2011]. The overriding continental crust of the Alaska Peninsula is built up of terranes accreted against the Alaska mainland during the Mesozoic and Cenozoic (Fig. 3.3.1) [*Coney and Jones*, 1985; *Jones et al.*, 1977; *Ridgway et al.*, 2002]. This assemblage of rocks is one of the largest subduction-related accretionary complexes

in the world. It is composed of deep marine sediments intruded extensively by Tertiary granitoid plutons and overlain by basinal deposits of Late Cenozoic age [*Plafker and Berg*, 1994]. As a result, the Pacific Plate subducts beneath an unusually wide continental shelf, which is part of the Alaska Peninsula and measures ca. 150 - 200 km in width from the southeastern coastline to the shelf break.

3.4 Subduction interface coupling and earthquakes along the eastern AASZ

3.4.1 Historical seismicity

The eastern part of the AASZ, where oceanic lithosphere subducts beneath continental lithosphere, has ruptured in three large segments in the past (Fig. 3.2.1). The extents of these segments are estimated by aftershock locations of great earthquakes in 1938 (M_W 8.2), 1946 (M_W 8.6) and 1964 (M_W 9.2). Our study area (Fig. 3.4.1) covers the whole 1938 rupture, central and eastern sections of the Shumagin Gap, and the Kodiak Asperity rupture area for the 1964 event. During the Good Friday earthquake in 1964, an area 200 km wide with an extent of roughly 950-km along trench direction, slipped from the Prince William Sound to the southwestern end of Kodiak Island.

It was the result of a combined rupture of two separate tectonic segments: Prince William Segment in the northeast and Kodiak Asperity (or Kodiak Segment) in the southwest [*Christensen and Beck*, 1994]. Paleo-seismology records in the Prince William Sound area indicate a recurrence time for such an enormous event of 333 - 875 years [*Carver and Plafker*, 2008]. Immediately to the southwest, the Semidi Segment has ruptured during the 1938 earthquake in an area that extends from the southwest end of the Kodiak Asperity to the Shumagin Islands [*Davies et al.*, 1981; *Estabrook et al.*, 1994]. The ∼200-km-wide area found between the 1938 and 1946 ruptures and centered on the Shumagin Islands has not slipped in a great earthquake (> 8 M_W) since the beginning of seismological recording that started in the early 20^{th} century and is, therefore, known as the "Shumagin Gap". The largest earthquake recorded in this segment, however, reached a surface Magnitude (M_S) of 7.9 in 1917, but probably did not rupture large segments of the plate interface [*Estabrook et al.*, 1994]. Geodetic measurements indicate very weak coupling between the down-going and overriding plate in this area [*Fournier and*

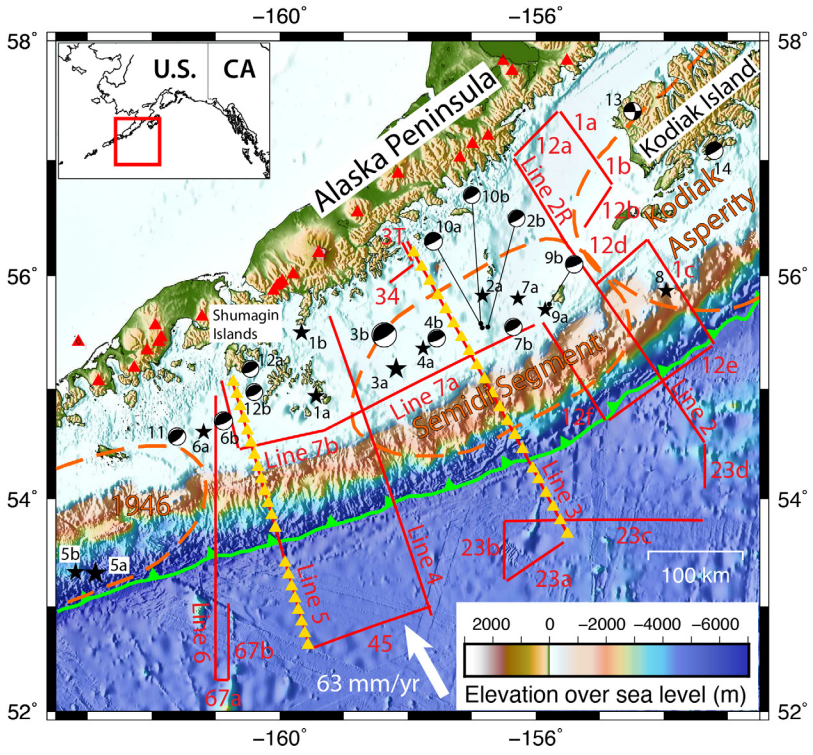

Figure 3.4.1: ALEUT project survey area. Thick red lines mark positions of collected MCS profiles and yellow triangles show the locations of OBSs used during the survey. Dashed orange lines show the rupture extent of tectonic segments derived by *Sykes* [1971] and *Benz et al.* [2011] with the name of the segment or the year of the rupture. Black stars show epicenter locations of all recorded $>$ M_W 6.9 earthquakes with size according to their magnitude. When available, focal mechanisms are shown instead. A list of all shown earthquake events is given in Table 2.1. Green line shows the position of the trench, while red triangles show the location of active volcanoes along the arc (from the website of the Alaska Volcano Observatory: www.avo.alaska.edu/volcanoes/latlong.php (last modified on December 2, 2016 10:12)).

Freymueller, 2007; *Li and Freymueller*, 2018], and it is believed that the megathrust is freely slipping. However, it is still not clear if great earthquakes can nucleate within the Shumagin Gap or, whether or not tectonic ruptures originating in adjacent segments can propagate into this area. Pre-instrumental records of earthquakes and tsunamis from Russian settlers exist since the late 18th century but can give only weak constraints on the along-strike extent of past ruptures. Nevertheless, it has been reported that one big earthquake might have occurred near Chirikof Island in the eastern part of Semidi Segment in 1880 and two great events in 1788 and 1847, that are thought to have occurred between the Shumagin Islands and Kodiak Island, based on historical records, and might have ruptured the Shumagin Gap and Semidi Segment combined [*Davies et al.*, 1981; *Soloviev*, 1990]. Relying on both the instrumental and historic records, *Davies et al.* [1981]

estimated a 50- to 75-year great earthquake (> 8 M_W) seismic cycle in the Semidi Segment and Shumagin Gap region, which is central to this investigation.

3.4.2 Geodetic measurements of active deformation processes

Current relative plate movements and deformation rates for large parts of southern Alaska and the AASZ are based on data of repeated surveys of high-precision Global Positioning System (GPS) and Electronic Distance Measurements (EDM) taken during the last two decades or so [e.g., *Freymueller et al.*, 2008; *Li and Freymueller*, 2018]. The results indicate dramatic along-strike variability in the behavior of seismogenic zones and magnitude of slip deficit suggesting huge and sharp lateral changes in the degree of interplate interface coupling. The area between -161° E and -152° E encompasses three tectonic segments: 1) Kodiak Asperity, 2) Semidi Segment, and 3) Shumagin Gap. Based on the geodetic observations the southwestern part of Kodiak Asperity and the northeastern part of the Semidi Segment are nearly fully locked (90 %), with the remaining part of the Semidi Segment locked to a high degree (70 %). The eastern Shumagin Gap, however, exhibits a significantly smaller coupling degree (30 %), with almost no coupling determined for the southwestern Shumagin Gap [*Fournier and Freymueller*, 2007]. Hence, in comparison to the Semidi Segment and the Kodiak Asperity, the Shumagin Gap as a whole accumulates little to no strain at all. However, there are practically no data points near or at the slope region, where the highest deformation would be expected. Numerical dislocation models cannot rule out that at least parts of the shallow plate interface are locked and capable of producing M∼7 earthquakes [*Fournier and Freymueller*, 2007; *Freymueller and Beavan*, 1999].

3.4.3 Tsunami waveform inversion

One of the methods used to resolve earthquake source parameters, such as spatial rupture extent and slip distribution, is inverse tsunami waveform modelling [*Geist and Dmowska*, 1999; *Johnson et al.*, 1996; *Ortiz and Bilham*, 2003; *Piatanesi et al.*, 1996; *SATAKE*, 1987]. Tsunamis are often triggered by megathrust earthquakes and affect shorelines close to and thousands of kilometers away from the initial rupture location. Tide gauge data and information of run up heights collected at the affected shorelines are used to backtrack tsunami travel times and to estimate the

aforementioned tsunamigenic earthquake parameters. Johnson and Satake [1994] confirmed the spatial extent of the Semidi Segment, previously determined with seismological data by *Sykes* [1971] and *Davies et al.* [1981], but estimate the seismic moment release only to be about half of that determined from aftershock locations by *Estabrook et al.* [1994]. Although in spatial accordance with slip segments outlined by *Sykes* [1971] and *Davies et al.* [1981] the slip distance estimates for four predefined segments (all 100 km wide and 150 km in length) inhibit discrepancies ranging from 55 % to 540 % of the values presented by *Estabrook et al.* [1994], which suggests significant error bounds for all slip estimates for the 1938 earthquake.

3.4.4 Paleoseismology

Paleoseismic studies can help reconstruct the history of multiple cycles of strain accumulation and release on megathrust faults over hundreds to thousands of years. Coarse and fine layers of sediment close to the shoreline record alternating flooding events and subsequent marsh build-up during uplift due to strain accumulation during interseismic periods and subsidence after the release of accumulated energy during a megathrust rupture. The Prince William Sound Segment has ruptured simultaneously with the Kodiak Asperity in a 950-km-long rupture zone [*Carver and Plafker*, 2008] during the M_W 9.2 Good Friday earthquake in 1964 and has been studied thoroughly along shores and inlets of the Kenai Peninsula [e.g., *Carver and Plafker*, 2008; *Shennan et al.*, 2008, 2014]. Only a few paleoseismic studies targeted tsunami deposits on shorelines in the Kodiak Asperity [*Briggs et al.*, 2014; *Plafker and Kachadoorian*, 1966; *Shennan et al.*, 2014], and shorelines near the Semidi Segment have been investigated to an even lesser degree [*Nelson et al.*, 2015; *Witter et al.*, 2014]. The lack of data points in the Semidi region prevents a reliable location of earthquake sources or magnitudes based on tsunami-deposited beds. However, until more complete tsunami chronologies are available, *Nelson et al.* [2015] give an estimation of tsunami re-occurrence of every 180 - 270 yr for at least the past 3500 yr in the Semidi Segment region and *Briggs et al.* [2014] suggest a non-permanent rupture boundary between the Semidi Segment and Kodiak Asperity.

3.4.5 Gravity studies

Slope area free-air gravity anomalies that parallel the deep sea trenches might correspond to variations in seismogenic behavior as *Song and Simons* [2003]

suggested at the Alaska-Aleutian arc. Strong negative gravity values are interpreted as areas with high shear traction at the interplate interface that induces a decrease in vertical compressive stress thereby depressing fore-arc topography. This leads to sediment accumulation within the accommodation space and, consequently, lower gravity because sediments are less dense than the crystalline rocks. Positive anomalies along the subduction zone are associated with relatively low shear traction and lesser seismogenic potential [*Song and Simons*, 2003]. At a regional scale, gravity anomaly observations seem to conform to the geodetic measurements of strain accumulation [*Fournier and Freymueller*, 2007] and the megathrust rupture extent for the Semidi Segment, Kodiak Asperity and Prince William Sound Segment [*Ruff and Kanamori*, 1983; *Sykes*, 1971]. However, the link between gravity anomalies and seismic behavior is not unambitious and the low resolution of satellite-based data, while providing a quick overview, prevents a detailed and accurate evaluation of the megathrust coupling.

3.5 ALEUT survey area and data

The ALEUT survey area stretches for 500 km along the Alaska Peninsula continental margin, from southwest of Kodiak Island in the east to the west of the Shumagin Islands in the west (Fig. 3.4.1). This region exhibits high seismological activity with at least 14 earthquakes recorded with a magnitude of M_W 6.9 or higher since 1900 (Table 3.1) and two rupture areas that slipped during megathrust events in 1938 (Semidi Segment) and in 1964 (Kodiak Asperity). A total length of ca. 3700 km MCS profiles is spread between six $>$ 250-km-long trench-normal lines, one trench-parallel profile across the shelf (ca. 300 km long) as well as 20 shorter connecting lines, adding up to a total of 27 profiles (Fig. 3.4.1). The trench-normal profiles, which cross the shelf, slope and parts of the outer rise in the deep sea, provide full access to the seismogenic portion on the interplate interface, as well as its transitional zones to stable sliding (aseismic) parts found up and down dip of the seismogenic section. The investigated section of the eastern AASZ is globally unique as it comprises a wide-enough shelf to allow marine seismic data acquisition to image the complete spectrum of seismic coupling of the plate interface. This facilitates seismic imaging of the seismogenic down-dip limit, which is usually found at coastlines and is difficult to assess. Furthermore, the surveyed Semidi Segment and the Shumagin Gap are adjacent sections of the eastern AASZ but exhibit

completely different seismological behavior. This permits an investigation into possible lateral correlation between changes in the degree of coupling and the seismic reflection character of the plate interface. To that effect, MCS Lines 3 and 5 have an outstanding role, since they cross the central part of the seismically locked Semidi Segment (Line 3) and the assumed freely slipping to weakly coupled Shumagin Gap (Line 5) (Fig. 3.4.1). To complement MCS reflection surveys and provide detailed subsurface velocity information, OBS data on two profiles coincident to MCS Lines 3 and 5 were acquired as well.

The ALEUT seismic survey was conducted in summer 2011 with the R/V *Marcus Langseth* during research cruise MGL1110. For MCS data acquisition, two streamers were used with 636 receiver groups each spaced at 12.5 m yielding a maximum offset of 8 km. One of the streamers was towed at 12-m depth to enhance recording of low frequency signals reflecting from the megathrust interface and other deep targets, while the other streamer was towed at 9-m depth to enhance recording of higher frequency signals originating within the sediments and other shallow targets. The recording time for most of the profiles is 22.5 s but at places had to be reduced to 18.75 s when greater ship speeds were needed (e.g., caused by following currents). The acquisition sampling interval is 2 ms but was reduced to 4 ms for processing purposes and resulted in a usable signal frequency range of up to 125 Hz. Acoustic signals were generated by a tuned air gun array consisting of 36 individual guns with a combined total volume of 6600 cu. in. ($\sim$108 l). Shot spacing of 62.5 m and hydrophone group interval of 12.5 m resulted in a common mid-point (CMP) spacing of 6.25 m with a nominal fold of 64. To investigate subsurface properties like seismic velocity distribution, we acquired additional wide-angle refraction data on two OBS profiles coincident with MCS lines 3 and 5. Twenty-one 4-component OBSs from Scripps were used with a sampling rate of 5 ms and a continuous recording over the entirety of their deployment. OBS spacing was approximately 16 km on Line 3 and 13 km on Line 5, with a greater spacing at the trench to avoid deployment in $>$ 5500 m water depth and the risk of losing the instruments. The shot interval for both lines was 120 s or roughly every 310 m to avoid previous shot noise. The acoustic source was identical to the one used for the MCS survey.

Earthquakes above M_W 6.9					
#	Date (YYYY-MM-DD)	Magnitude (Mw)	Hypocenter Depth (km)	Focal Mechanism (Y)es (N)o	Located by
1a	1917-05-31	7.4	35.0	N	ISC-GEM*
1b	1917-05-31	M_S 7.9	n/a	N	Boyd and Lanert-Lam, 1988
2a	1923-05-04	7.0	25.0	N	ISC-GEM
2b	1923-05-04	7.0	27.0 ± 4	Y	Sykes et al., 1971
3a	1938a-11-10	8.3	35.0	N	ISC-GEM
3b	1938a-11-10	8.2	26.0	Y	Davies et al., 1981
4a	1938b-11-17	6.9	35.0	N	ISC-GEM
4b	1938b-11-17	7.0	27.0 ± 2	Y	Sykes, 1971
5a	1946a-04-01	8.6	n/a	N	Lopez and Okal, 2006
5b	1946b-04-01	M_S 7.4	n/a	N	Sykes, 1971
6a	1948-05-14	7.1	25.0	N	ISC-GEM
6b	1948-05-14	7.2	31.0 ± 2	Y	Sykes, 1971
7a	1951-02-13	6.9	20.0	N	ISC-GEM
7b	1951-02-13	7.0	25.0 ± 2	Y	Sykes, 1971
8	1957-04-10	7.0	15.0	N	ISC-GEM
9a	1964-02-06	6.9	20.0	N	ISC-GEM
9b	1964-02-06	7.0	24.0 ± 3	Y	Sykes, 1971
10a	1989-09-04	7.1	11.4	Y	ISC-GEM
10b	1989-09-04	6.9	26.0 ± 3	Y	Sykes, 1971
11	1991-05-30	7.0	28.4	Y	ISC-GEM
12a	1993-05-13	6.9	32.3	Y	ISC-GEM
12b	1993-05-13	6.9	36.0 ± 2	Y	Abers et al., 1995
13	1999-12-06	7.0	66.0	Y	ISC-GEM
14	2001-01-10	7.0	33.0	Y	ISC-GEM

Table 3.1: List of earthquake parameter for $M_W \geq 6.9$ earthqakes in the ALEUT survey area as shown in Figures 2.2 and 2.10. *International Seismological Centre - Global Earthquake Model [*On-line Bulletin, http://www.isc.ac.uk, Internatl. Seismol. Cent., Thatcham, United Kingdom*, 2018].

3.6 Data Analysis

3.6.1 MCS data processing

Data processing was carried out for each of the two streamers separately. Data from streamer 1 (towed at 9 m) data were used to image upper crustal structure and sediments up to the acoustic basement, and data from streamer 2 (towed at 12 m) data were used to image structures below the crystalline basement. Noise removal was identical for both streamers and included high pass frequency filtering to cut out very low frequency noise (< 2 Hz), amplitude downscaling for abnormal high amplitude peaks and frequency band limited noise suppression. An offset dependent spherical divergence correction and surface consistent amplitude correction were applied to counteract amplitude loss due to geometrical spreading and inconsistencies of RMS trace amplitudes, respectively. Due to the large change in water depth on the trench normal MCS profiles, water multiples and reflection signal from the interplate interface become superimposed in some areas across the slope. To reduce the amplitudes of multiple reflections, both Surface Related Multiple Elimination (SRME) and Radon transformation multiple removal were applied [*Verschuur et al.*, 1992]. Interpolation of shot gathers so that shot spacing equals receiver group spacing is necessary prior to using SRME. In order to preserve the interplate interface reflection signals, SRME was applied only on frequencies higher than 18 Hz. Radon transformation multiple removal weakens multiple signal further and enhances low frequency deep reflections. After CMP sort, NMO velocity analysis, stacking, and post-stack coherency filtering to further increase the signal to noise ratio, we combined the data from the two streamers into one seismic section. This is done by merging the part above the crystalline basement in the data from streamer 1 with the part below the crystalline basement in the data from streamer 2. To relocate dipping events and collapse diffraction hyperbolas in the seismic section, 2D Kirchhoff time migration was applied after stacking. Smoothed velocity models for the migration process are based on RMS velocities for the sedimentary areas and on OBS velocities for the crust. Predictive deconvolution was also applied before stacking and after migration to reduce signal reverberation. This process results in a more distinct signal with improved temporal resolution. All lines except for 4, 5, and 6 were processed as part of this thesis work. Lines 4, 5 and 6 were processed by a working group at the Lamont-Doherty Earth Observatory of Columbia University [*Bécel et al.*, 2015, 2017; *Li et al.*, 2015]. In addition to the processing steps in our

workflow, they added the LIFT method [*Choo et al.*, 2004] for noise attenuation and applied SRME with slightly different parameters. An amplitude balancing procedure was needed afterwards for Lines 4, 5 and 6 to equalize background noise and form uniform looking sections [*Li*, 2016; *Li et al.*, 2015].

3.6.2 Velocity model development and depth conversion

Because pre-stack depth migration of our data to full crustal depths is not possible due to the lack of continuous reflectors in the continental crust, needed to developed a sufficiently accurate migration velocity model, our MCS reflection processing was done in two-way traveltime and our final migrated sections are in time domain. Interpretation in time domain is challenging and can lead to wrong conclusions about subsurface structure and geometry. Some of the most common challenges encountered are pull-up structures, incorrect dipping angles, and a deceptive presentation of layer thicknesses. To remedy this situation and carry our quantitative geological interpretation, we built velocity models to convert our sections from the time into depth domain. Building the velocity models for the time-depth conversion consisted of combining the best available information about the seismic velocity distribution in the subsurface. Most of the input information was derived through analysis of ALEUT MCS data (see Section 3.6.1) to constrain sedimentary velocities and ALEUT OBS data to determine a representative function for continental upper crustal velocities.

Two crustal scale 2-D seismic velocity models were derived from the OBS wide-angle data, one for Line 3 (Fig. 3.6.1) and the other for Line 5 (Fig. 3.6.2). We used Jive3D [*Hobro et al.*, 2003] software for tomographic travel-time inversion with the main target to model the velocity structure of the continental crust. Only first arrivals were picked and used to produce smoothed 2-layer velocity models through a series of linear inversion steps. A fixed seafloor interface separates the water layer from the subsurface layer. As the starting velocity model, we used a 1D velocity function extracted from a regional velocity profile constructed by *Lizarralde et al.* [2002] for the western Alaska Peninsula. OBS positions were relocated based on direct wave arrivals and a minimum-phase bandpass filter with corners at 1, 3, 10, and 18 Hz was applied to the data to improve signal to noise ratio before picking. Clarity of the signal onset was visually evaluated and graded with six possible uncertainties assigned ranging from 40 ms (very clear onset) to 250 ms (very poor

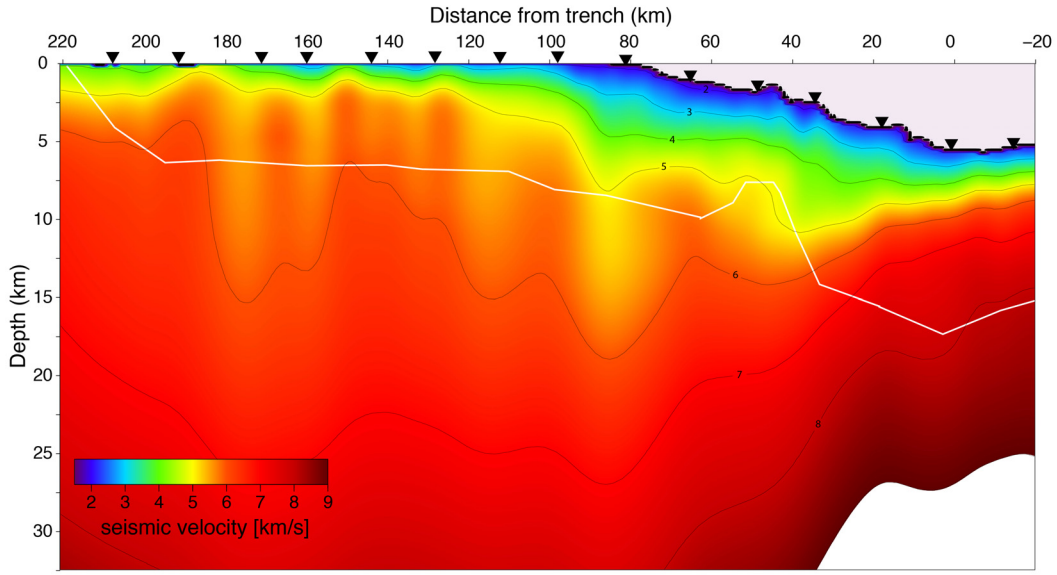

Figure 3.6.1: First arrival travel-time tomography model for OBS Line 3 formed using Jive3D [*Hobro et al.*, 2003]. White line represents the extent of dense ray coverage. Vertical exaggeration is 1:4, black triangles are OBS locations.

onset). Model grid dimensions were chosen to be one cell per km horizontally and two cells per km vertically resulting in a total grid size of 366 km x 40 km for Line 3 and 304 km x 40 km for Line 5. Different smoothing parameters were tested and the best compromise between feature roughness and a good data fit was chosen resulting in an overall data fit with χ^2 of 1.02 for Line 3 (Fig. 3.6.1) and χ^2 of 1.77 for Line 5 (Fig. 3.6.2).

The velocity models used for depth conversion were built for each MCS profile and have the same dimensions as the migrated stacks (i.e., same profile length (x-axis) and same two-way travel time (y-axis)). The constructed velocity models consist of four layers: 1) Water layer between the sea surface and the seafloor (set to constant velocity of 1.5 km/s).

2) Sediment layer from the seafloor to the top of the acoustic basement. Velocities in the sediments (including the accretionary prism) increase gradually following the average velocity function derived from normal-move-out (NMO) velocity analysis of the MCS data from the deep fore-arc sediment basins on Lines 2 and 3. 3) The velocity functions representing the continental crust were obtained by averaging the tomographic profiles of OBS Lines 3 (Fig. 3.6.1) and 5 (Fig. 3.6.2) between the top of the crystalline basement and an assumed continental Moho depth of 39 km [*Janiszewski et al.*, 2013]. One velocity function was derived for the shelf area and

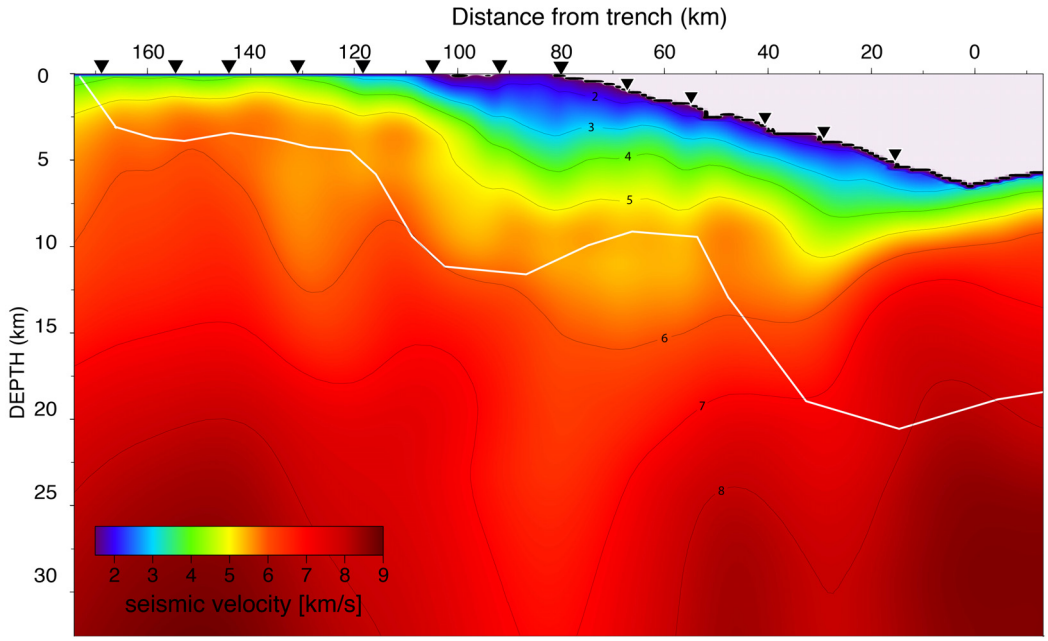

Figure 3.6.2: First arrival travel-time tomography model for OBS Line 5 formed using Jive3D [*Hobro et al.*, 2003]. White line represents the extent dense of ray coverage. Vertical exaggeration is 1:4, black triangles are OBS locations.

the other for the slope area. Because sufficiently dense ray coverage (constrained visually) for the OBS surveys of Lines 3 and 5 does not exceed ca. 7 km depth below the top of the crystalline basement (Fig. 3.4, 3.5 and Appendix C, Fig. C.42, C.43), average lower crustal velocities derived for continental arcs by *Christensen and Mooney* [1995] based on expected rock types and their high-pressure laboratory p-wave velocity (v_p) measurements for these depths, are combined with those derived through earthquake studies for the eastern Aleutian arc [*Abers*, 1994] and a mean of these functions was determined (dashed yellow line in Fig. 3.6.3). The composite 1-D velocity functions constructed for the shelf and slope area of the continental crust (Fig. 3.6.3) were then hung from the acoustic crust basement as interpreted in the reflection sections. Linear lateral blending was done along 50 km centered at the shelf break to smooth out the differences between the shelf and slope continental crust velocity functions. Upper mantle velocities below the continental Moho at 39 km depth [*Janiszewski et al.*, 2013] is set to a velocity of 7.95 km/s [*Christensen and Mooney*, 1995].

4) The velocity for the subducting oceanic crustal layer is, for simplicity, set to a constant of 6.5 km/s. This average velocity is based on igneous crustal velocities for a layered oceanic crust composed of basaltic pillow lavas and a sheeted dyke

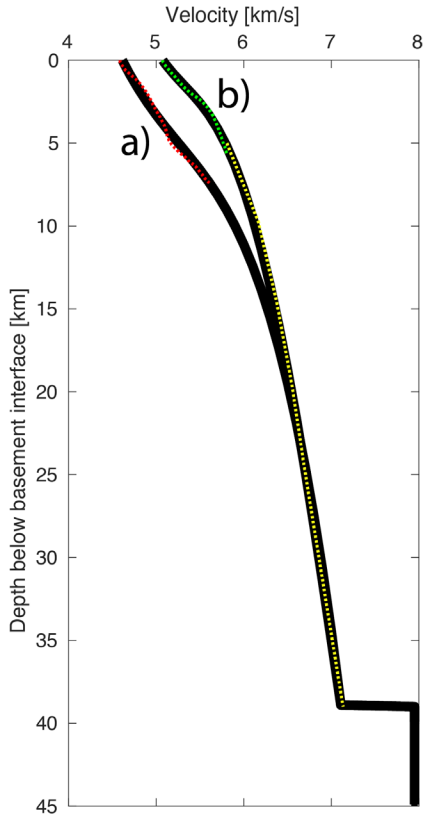

Figure 3.6.3: P-wave velocities (V_p) for upper continental crust from the top (0 km) to 45 km below the top of the crystalline basement (thick black lines) for (a) slope and (b) shelf area. Red dashed line shows averaged upper crustal V_p derived from Jive3D tomography model in the slope area of ALEUT OBS line 3 and 5. Green dashed line shows averaged V_p from the shelf area. Yellow dashed line shows the mean of high-pressure laboratory V_p values for upper crustal rocks [*Christensen and Mooney*, 1995] and V_p values from earthquake studies of the eastern Aleutian arc [*Abers*, 1994]. Continental Moho in this region was determined to be 39 km deep by *Janiszewski et al.* [2013]. Shallow crustal velocities in the slope area (a) are lower than for the shelf area (b) according to tomographic inversion results, but converge at a depth of about 15 km.

complex (layer 2a and 2b, respectively) of 5.04 - 5.19 km/s and a much thicker layer of intrusive gabbroic rocks (layer 3) of 6.69 - 6.81 km/s [*White et al.*, 1992]. Layer 1, which consists of deep sea sediments, is ignored for the subducted part of the oceanic crust from the trench landwards because it is relatively thin ($<$ 1 km [*Li et al.*, 2018]) and sometimes difficult to identify its top interface in the MCS sections. The overall thickness of the oceanic crustal slab is set to 6 km [*White et al.*, 1992] and oceanic mantle velocity is set to 7.95 km/s. An example of a velocity model constructed following the outlined procedure is shown in Figure 3.6.4.

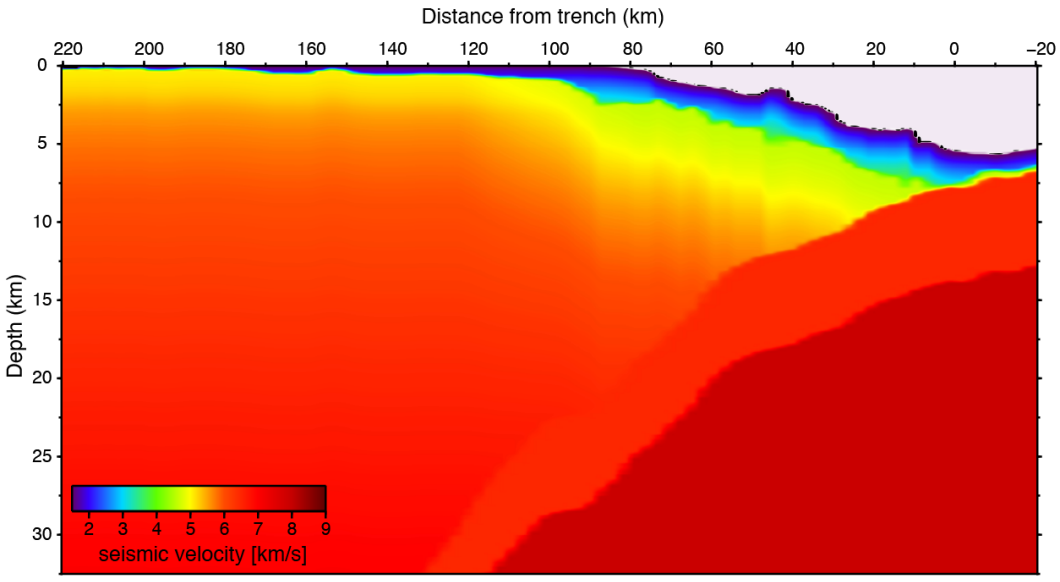

Figure 3.6.4: Velocity model constructed for depth conversion of MCS Line 3.

3.7 Results

3.7.1 Plate interface reflections

Landward dipping reflection signals interpreted to arise from the interface between the subducting Pacific plate and the overriding North America plate can be identified in all trench-normal ALEUT MCS profiles starting from a depth of 6 - 7 km at the trench and extending landward to maximum depth of ca. 65 km near the coastline (see Fig. 3.7.1 and Appendix A). Trench-parallel MCS profiles also contain these reflections and are used to provide additional constraints on the plate interface (Fig. 3.7.2 and Appendix A). Seismic reflections, interpreted to represent the oceanic Moho, are imaged in places and the interplate interface is inferred to be some 6 km above, thus serving as an additional constraint for its location. The characteristics of the interplate interface reflections change from clear distinct signals near the trench at shallow depth to a broad band of reflections several kilometers thick farther down dip at the landward end of the profiles (e.g. see inlets in Fig. 3.7.1 or Figs. A.2 - A.29 in Appendix A and *Li et al.* [2015]). As it becomes more difficult to identify a clear interface location with depth, the middle of this broad band of reflections is interpreted as the plate interface. The plate interface or the top of the subducting slab is represented by a dotted green line in the interpreted MCS sections shown in Figures 3.8, 3.9. Two dotted blue lines above

and below the plate interface represent uncertainties based on 5 % increase and decrease of sediment and crustal velocity in the models that were used for time-depth conversion of the migrated stacks. There are small sections of the interplate interface, especially at the deep landward end, where reflections have a low signal-to-noise ratio and are not well imaged. The resulting gaps in the interpreted location of the plate interface were closed by linear interpolation or, if at the end of the profile, extrapolation.

Strong reflections interpreted to arise from within the continental crust are observed at ca. 150 - 200 km distance landward from the trench at ca. 15 - 30 km depth, and they sometimes interfere with the plate interface reflections making interpretation of the megathrust location difficult. These intracrustal reflections tend to be horizontal or slightly dipping towards the coastline.

3.7.2 ALEUT Plate Interface Model

The traced interplate interface reflections are used to constrain the plate interface geometry for the study area. Using a triangular based linear interpolation algorithm, the plate interface is represented in the form of a fine-meshed (0.005° x 0.005°) three-dimensional (3D) grid model as shown in Figure 3.7.3. This model, herein after referred to as ALEUT Plate Interface Model (PIM), extends laterally between MCS Line 1a, 1b and 1c in the northeast to Line 6 in the southwest, and represents the complete plate interface beneath the shelf and slope area. A depth uncertainty of ±5 % is assigned to the plate interface depth location due to errors in the velocity models used for time-depth conversion (e.g. Figs. 3.7.1, 3.7.2). The depth values shown in Figure 3.7.3 are measured from the sea surface to the plate interface. The ALEUT PIM model starts at the trench at a minimum depth of ca. 5 - 7 km and extends to a maximum depth of ca. 65 km in the very north of the study area at the intersection of Line 1a and 12a, where the maximum landward distance to the trench is reached. For better comparison, ALEUT PIM depth values are specified for each trench-normal profile at 50 km distance intervals from the trench up to maximum distance of 250 km (see green lines and white circles in Fig. 3.7.3). USGS legacy profiles, acquired in the same area in the late 70s and early 80s (https://walrus.wr.usgs.gov/), were not used to constrain the ALEUT PIM model because the deep plate interface has not been imaged on these sections.

At 50 km distance landward from the trench, the interplate interface is found at

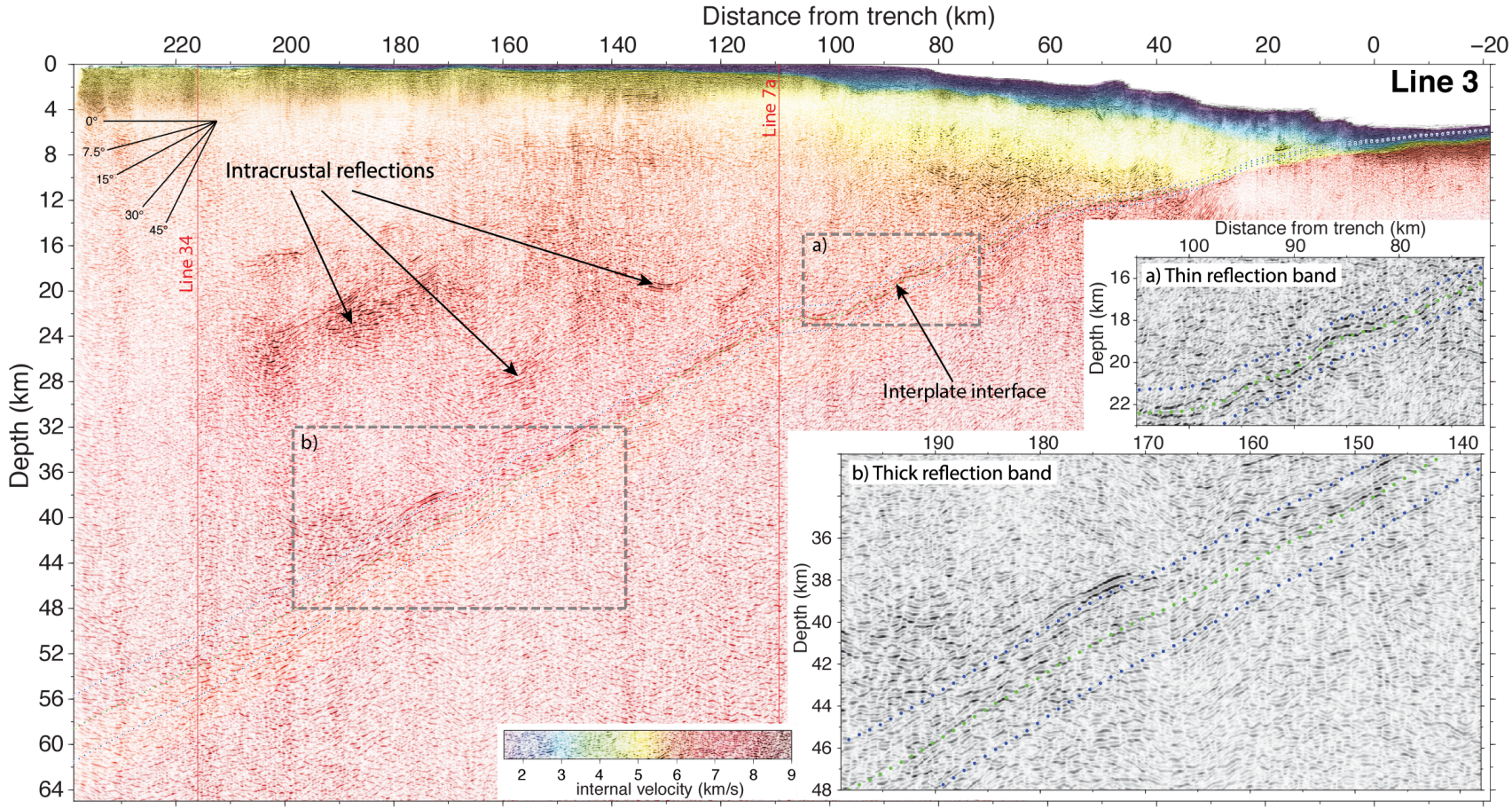

Figure 3.7.1: Trench-normal ALEUT MCS reflection profile 3 overlying the coincident colour velocity model (Fig. 3.6.4) used for depth conversion. The green dotted line represents the interpreted plate interface location with uncertainty estimates shown as blue dotted lines above and below, and based on a ±5 % variation in sediment and crustal velocity. Inserts are zooms on areas that show a) distinct plate interface reflections of small vertical extent thought to be associated with the seismogenic zone and b) broad band of reflections thought to possibly be caused by vertical thickening of the zone of plate interface deformation [e.g., *Li et al.*, 2015; *Nedimović et al.*, 2003]. To make the reflections easier to trace, no colour velocity overlay is given for the inserts. Red thin vertical lines show intersection points with other ALEUT MCS profiles (see Fig. 3.4.1).

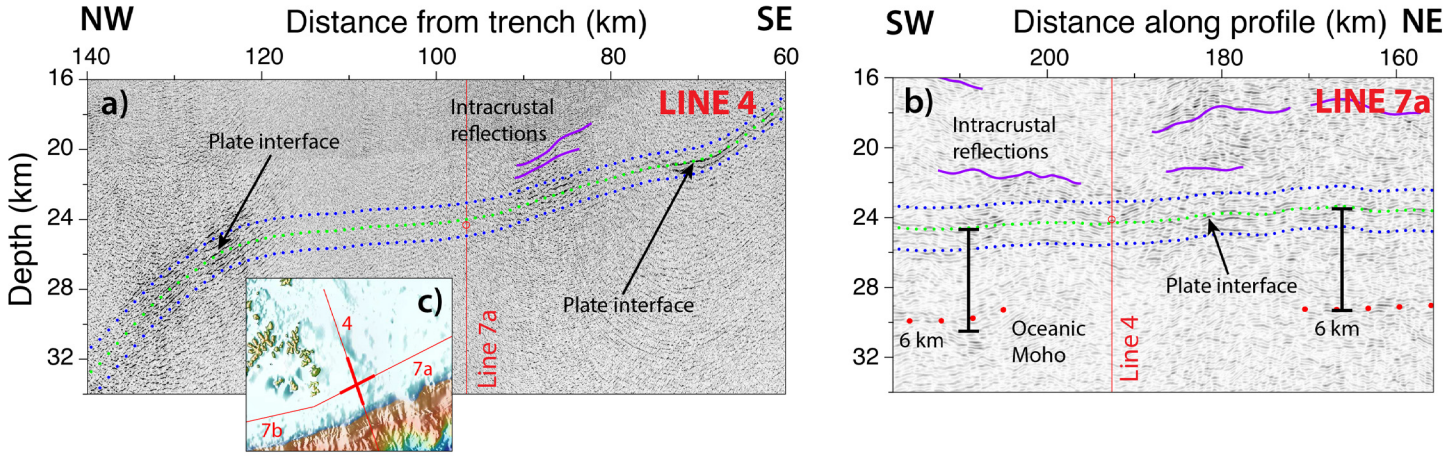

Figure 3.7.2: Trench-parallel ALEUT MCS reflection profiles 7a and 7b (see Fig. 3.7.2) overlying the coincident colour velocity models used to depth convert them. Small red circle shows plate interface depth locations at intersecting line for comparison. See Figure 3.7.1 caption for explanation of additional figure components.

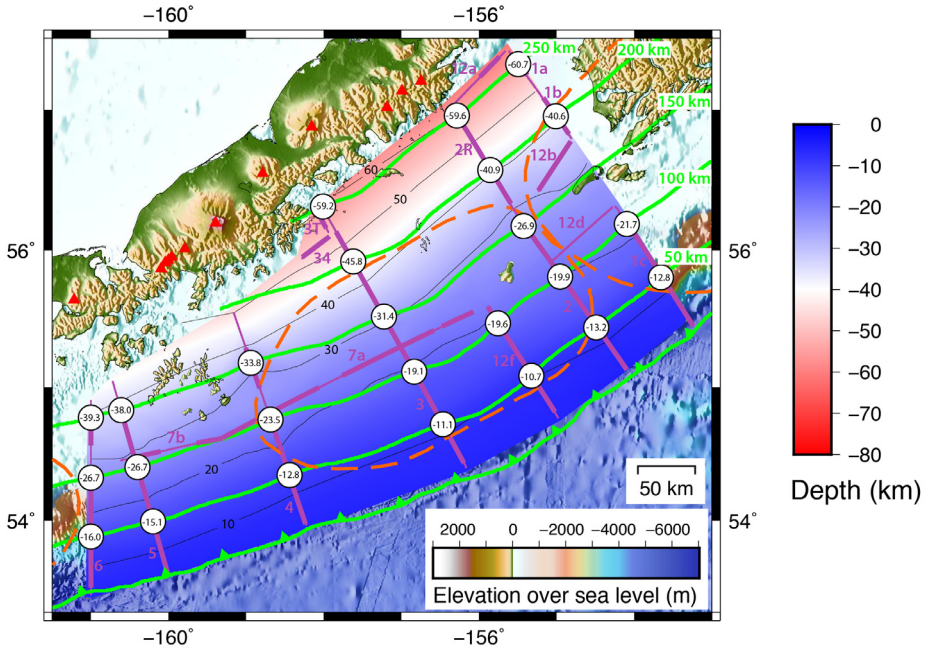

Figure 3.7.3: ALEUT Plate Interface Model based on interpolation of interpreted plate interface locations on ALEUT MCS reflection profiles. Thick purple lines are MCS profile locations where plate interface reflections were identified, thin purple lines are MCS line locations where no plate interface reflection could be observed. Thin black lines are depth contour lines for the interplate interface at 10-km intervals. Green lines connect equidistant points to the trench (green line with triangles) at 50-km interval. White circles are located at cross points between MCS profiles (red lines) and lines of equidistance from the trench, with specified slab interface depth values in km shown inside. Dashed orange lines show the extent of tectonic segments derived by *Sykes* [1971] and *Benz et al.* [2011] for the Kodiak Asperity in the northeast, Semidi Segment in the center and the 1946 earthquake rupture area in the southwest. Red triangles show the location of active volcanoes along the arc (from the website of the Alaska Volcano Observatory: www.avo.alaska.edu/volcanoes/latlong.php (last modified on December 2, 2016 10:12)).

depths from 10.7 to 16.0 km, and it appears to show a gentle convex shape across the Semidi Segment that flattens toward the Kodiak Asperity and steepens across the Shumagin Gap. A similar convex shape centered on the central Semidi Segment with southwest and northeast steepening trends is observed at a constant distance of 100 km from the trench and is located at depths from 19.1 to 26.7 km. At 150 km distance landward from the trench, the convex shape of the interface remains showing a similar (8 km) increase in plate interface depth from the central Semidi Segment (26.9 km depth) toward the western end of the Shumagin Gap (39.3 km depth). However, the apex has shifted eastward and is located at the boundary between the Semidi Segment and the Kodiak Asperity. At the farthest landward iso-distances of 200 and 250 km relative to the trench, the number of data points decreases as islands and the mainland were encountered in the southwest blocking

access by the research vessel. Nevertheless, available data from the central Semidi Segment toward northeast show that at 200 km the interplate interface appears to exhibit the same shape as at 150 km distance. It's flat across the Kodiak Asperity all the way to the boundary with the Semidi Segment (from 40.6 to 40.9 km depth), after which it starts to dip toward southwest where it reaches 45.8 km depth and, assuming minor data extrapolation, > 50 km at the boundary between the Semidi Segment and the Shumagin Gap. At 250 km, the interface appears to be mostly flat or mildly dipping from the Kodiak Asperity (60.7 km) to the central Semidi Segment (59.2 km), though the clarity of (the band of) interface reflection signals at this depth is reduced.

Most noticeable deviations in the plate interface geometry in the trench perpendicular direction from a smoothly bending slab interface are observed between ca. 20 - 30 km depth on MCS Line 2 and, even more pronounced, on Line 4 (see 20 and 30 km iso-depth lines in Fig. 3.7.3, and Fig. A.2 and A.6 in Appendix A). These profiles are positioned at the northeastern and southwestern edges of the Semidi Segment.

To demonstrate that the anomalous interface topography we derived from the MCS data is true and not caused by pick uncertainties or misinterpretations of the plate interface reflections, we show parts of intersecting seismic profiles as examples of plate interface pickings and other structural interpretations in enlarged cutouts of MCS Line 2 and 12b (Fig. 3.7.2), and 4 and 7a (Fig. 3.7.4).

Both Lines cross the inferred geometrical anomalies mentioned above. MCS Line 12b is located near the northeastern edge of Semidi Segment and is oriented almost perpendicular to Line 2. Line 12b does not, however, intersect with Line 2 as its southeastern end is located ca. 30 km before Line 2 (Fig. 3.7.4). Extending Line 12b farther southwest to intersect with Line 2 and extrapolating interpreted structures from Line 12b onto this intersection will give estimates of pick consistency in this area. Intracrustal reflections seem to be irregular and exhibit large changes in dip angles. We estimate their intersection with Line 2 at depth between 20 - 26 km. At Line 2 similar structures are observed at 22 - 24 km depth. Plate interface reflections at Line 12b are extrapolated to intersect with Line 2 at ca. 27 km depth, and are observed at Line 2 at ca. 29 km. We projected oceanic Moho reflections on Line 12b to intersect with Line 2 at around 32 km. On Line 2 the Moho reflections are observed at around 36 km depth. Plate interface reflections signals on Line 4 are discontinuos, leaving the plate interface unconstraint between ca. 90 - 120 km

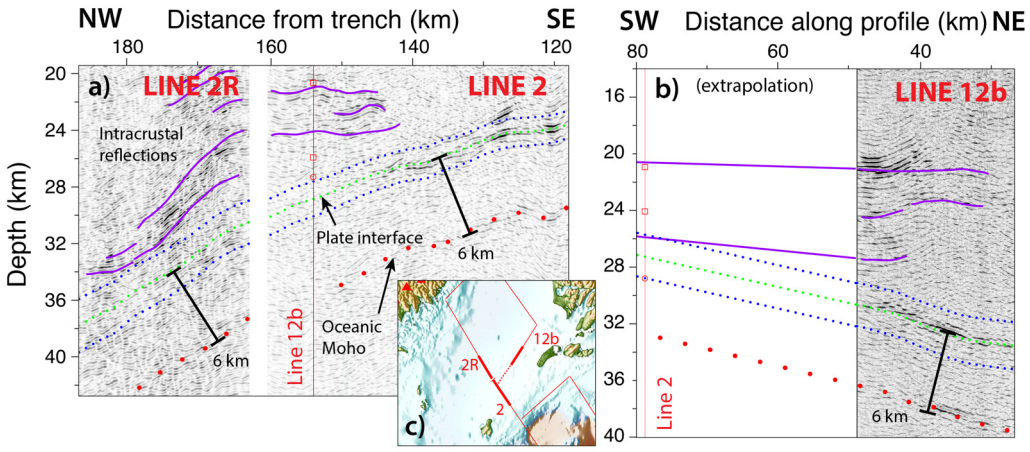

Figure 3.7.4: Cutout parts of ALEUT MCS sections from a) Line 2, 2R and b) Line 12b. Line 12b does not intersect with Line 2 but is extended approximately 30 km to the southwest to cross it. Structural interpretations, such as plate interface, oceanic Moho and intracrustal reflections are extrapolated onto Line 2 to estimate picking consistency between the two Lines. Thin red vertical lines in a) and b) represent intersection point of Line 2 and Line 12b. Oceanic Moho is located ca. 6 km below plate interface reflections. Inserts c) shows parts of the ALEUT survey area (entire survey area in Fig. 3.4.1) with location of ALEUT MCS Line 2, 2R and 12b (thin red lines) and parts along their profile, which are presented in a) and b) (thick red lines). Red dashed line extending Line 12b shows the distance over which structural observations on Line 12b are extrapolated to estimate intersectional depth on Line 2. Small red circle and red squares show depth locations for the plate interface and intracrustal reflection at intersecting line for comparison.

distance from the trench (Fig. 3.7.2). But strong bands of reflections at the deeper landward end (ca. 26 km depth) and distinctive narrow reflections at the shallow seaward end of the gap (ca. 22 - 24 km depth) constrain the plate interface location well and the plate interface in between is interpolated visually. Line 4 is intersected by Line 7a, which exhibits a relatively clear plate interface reflection zone of ca. 3 km thickness and distinct oceanic Moho reflections. This allows us to place the plate interface location 6 km above it, where it coincides with the center of the reflective broad band (Fig. 3.7.2). At the intersection of Line 4 and Line 7a, we observe the plate interface reflection on both lines at a depth of ca. 24 km. More intracrustal reflections can be observed on Line 7a in contrast to very few on Line 4.

3.8 Discussion

3.8.1 Plate interface morphology and its segmentation

To describe the plate interface dip in a simplified manner, we fit several straight-line, single-dip segments to different parts of the interface each dip profile

(Fig. 3.8.1). All trench-normal ALEUT MCS profiles show that the oceanic lithosphere and the overlying subducting sediments, within which the interplate interface is formed, enter the subduction zone along the deep sea trench at a low dip angle of 3° - 5°. This dip extends for approximately the first 20 km landward from the trench, after which it becomes steeper but variable in the along-strike direction. Lines 3, 5 and 6 show a landward increase in dip angle of the plate interface over the entire profile lengths whereas Lines 1, 2 and 4 show an interplate interface that is characterized by alternating shallowing and deepening sections, although there is an overall increase in plate interface dip angle in the landward direction. On Line 3, the plate interface dip increases to 10° from 20 - 120 km landward from the trench, after which it increases to 16° until the end of the profile (235 km). On Line 5, the dip also increases to 10° after the initial shallow part near the trench (0 - 20 km) but remains as such only until ca. 60 km distance, where it steepens to 14° and continuous this dip until the profile end at 170 km. An increase in dip to 12° is observed on the plate interface on Line 6 from 20 to 100 km, followed by slight steepening to 14° from 100 - 160 km, where the profile ends.

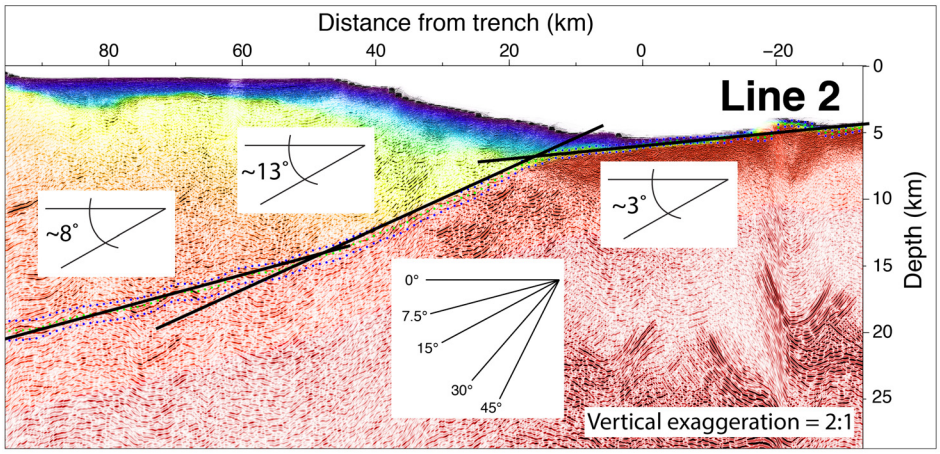

Figure 3.8.1: Cutout part of ALEUT MCS Line 2. Variations of dip angles along the thrust fault are approximated by three straight-line single dip segments (black thick lines) of ca. 3, 13° and 8°. Dip angles for 0°, 7.5°, 15°, 30° and 45° are given as reference.

Lines 1, 2 and 4 exhibit a more complex shape of the plate interface. After the first 20 km from the trench the shallow plate interface dip increases substantially to 14° on Line 1c, 13° on Line 2 (Fig. 3.8.1) and 16° on Line 4. These relatively steep dips continue until ca. 50 km landward from the trench where another change is observed for these three profiles. Here the plate interface flattens to 8° on Line 1c and it continues at this dip until 110 km, where Line 1c ends due to the Tugidak

and Sitkinat islands. This results in a 60-km data gap before the profile is restarted with Lines 1b and 1a, which show a steeply (25°) dipping interplate interface from 170 to 255 km distance from the trench. The plate interface on Line 2, also experiences a similar flattening to 8° from 50 - 160 km distance followed by a significant dip increase to 19° until the end of the profile (160 to 255 km). Line 4 shows the biggest changes in plate interface dip angle. At 50 km from the trench there is a large decrease from 16° to 6°. The 6° dip angle continues until ca. 120 km where it steepens significantly to 22° and stays that way until the end of the profile at ca.180 km. Line 12f is the shortest of all trench-normal profiles and extents only to ca. 100 km distance from the trench. It is positioned between Lines 2 and 3 and exhibits a transitional plate interface shape that seems to accommodate dip changes between these two lines. At around 20 - 70 km distance landward from the trench the plate interface dip jumps to 11° followed by a decrease to 8° at ca. 70 - 100 km. For better comparison and overview of plate interface dip angle between all trench-normal profiles, we plotted the plate interface depth versus distance from the trench in Figure 3.8.2.

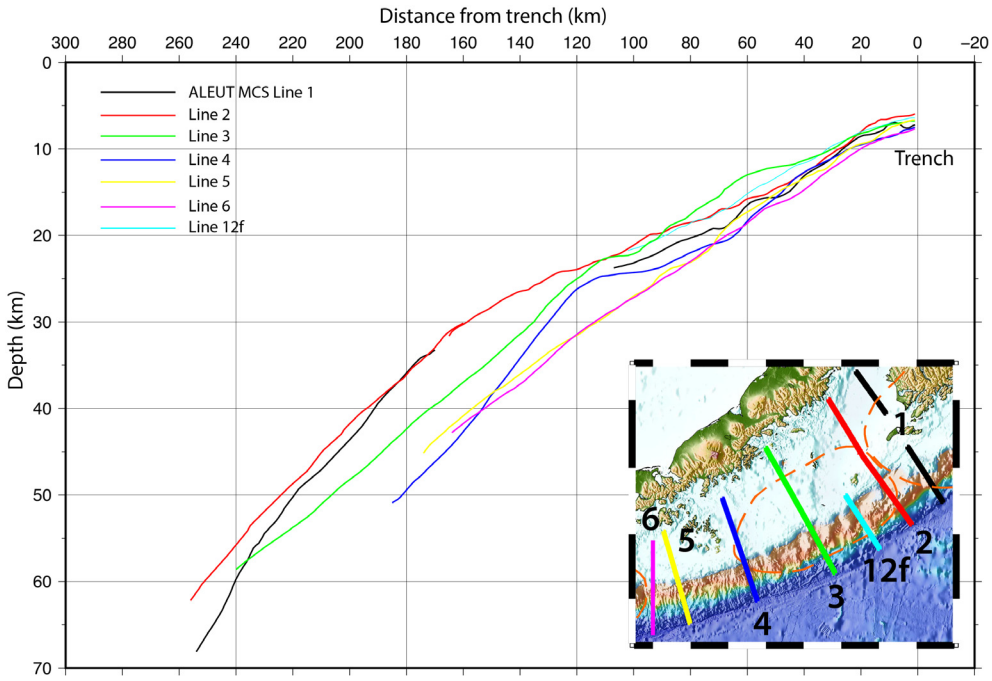

Figure 3.8.2: Plate interface depth versus distance from the trench for all ALEUT MCS trench-normal profiles. Inserts at the bottom right corner shows position of the displayed profiles (thick multi-colored lines) in the ALEUT survey area. Steepening of the plate interface is observed from the northeast (Line 1) towards the southwest (Line 6).

The described variations in the plate interface dip angle both downdip and along

strike are indicative of significant topography on the plate interface. These topographic features, especially the largest ones at 20 - 30 km depth and crossed by Lines 4 and 2, are easiest to observe on the black iso-depth contours in Figure 3.7.3 or by comparing their plate interface depth profiles in Figure 3.8.2. To better emphasize and understand the topography of the interplate interface in our model, we compare it with the Slab1.0 model of *Hayes et al.* [2012].

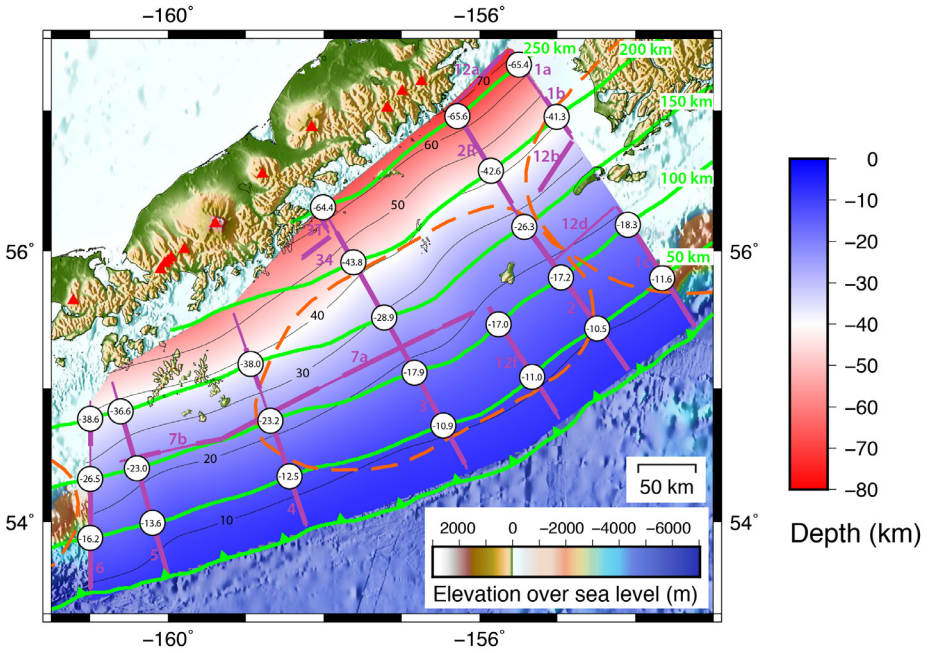

Figure 3.8.3: Slab1.0 interface model for ALEUT survey area based on *Hayes et al.* [2012]. Thick purple lines are MCS profile locations where plate interface reflections were identified, thin purple lines are MCS line locations where no plate interface reflection could be observed. Thin black lines are iso-depth contour lines of the interplate interface at 10-km intervals. Green lines show equidistance to trench location (green line with triangles) at 50-km interval. White circles are located at cross points between MCS profiles and equidistance from trench with Slab1.0 interface depth values in km shown inside. See Figure 3.7.3 caption for explanations of additional figure components.

Slab1.0 is a model covering ca. 85 % of all subduction zones worldwide, that gives an estimate of the top slab interface location and geometry from the trench to the intersection with the upper continental mantle, and farther downdip if information is available to constrain this part of interface at any given convergent margin. This model is unique in combining historic earthquake catalogues, centroid moment tensor solutions, global plate boundary data, bathymetry, sediment thickness and controlled source seismic reflection images and velocity models to locate the interplate interface in subduction zones in a consistent manner to build a global model. Major challenges in developing a model like this are aseismic (stable sliding)

areas, not capable of generating earthquakes, and data gaps in controlled source seismic survey coverage. At the eastern AASZ, for instance, only three seismic profiles were used for a ca. 2000-km-long section of the interplate interface with none of these three profiles inside the ALEUT study area. For Slab1.0 model this issue was addressed by averaging existing profiles along-strike, which resulted in minimal along-strike variability of the interplate interface depth, especially for the shallow region (ca. $<$ 5 km depth below seafloor) where no thrust seismicity is detected. The deeper part of the slab is modelled by probability density functions, for which a line of best fit is found through earthquake hypocenter locations, that is representing the estimated location of the subducting slab interface. For the seismogenic depth range, only well-constrained thrust earthquakes were considered and taken from historic earthquake catalogues. However, with sparse distribution of seismological stations found only on land and lack of an appropriate crustal velocity model, even these events exhibit large hypocenter depth uncertainty. Intermediate intraslab earthquakes were also considered but their hypocenter locations were shifted 10 km horizontally in a direction away from the trench to account for their occurrence within the slab rather than at its top interface. The 3D character of the Slab1.0 model was achieved by sampling the slab geometry in transverse direction, every 10 km along-strike and interpolating in between to generate a continuous slab surface. Figure 3.8.3 shows a part of the global Slab1.0 model that coincides with the spatial extent of the ALEUT PIM shown in Figure 3.7.3.

The Slab1.0 model, despite consisting of orders of magnitude less depth to the plate interface data points, appears to be similarly detailed as the ALEUT PIM. This is because the data points for the ALEUT PIM, while densely distributed, are only found along the seven trench-normal profiles (roughly spaced every 50 - 100 km) and a number of supporting along-strike profiles, so the final 3D model (Fig. 3.8.3) is obtained by lateral interpolation. Therefore, the strength of the ALEUT PIM lies in the accuracy and density of the depth points along the MCS profiles, which are well constrained by time-to-depth converted reflection sections produced with the area's new and most accurate seismic velocity model, while its weakness is in the significant interpolation required to obtain the final gridded 3D model. In contrast, the strength of the Slab1.0 model is a much more uniform distribution of the depth points but its weakness is that these points are sparse, have larger uncertainties, and there also is little or no data in shallow and deep areas of the interface where no thrust earthquakes are recorded. Because the Slab1.0 depth points are obtained by

averaging of individual depth information characterized by large scattering and uncertainties, it is best viewed as a smooth regionally accurate background model of the plate interface.

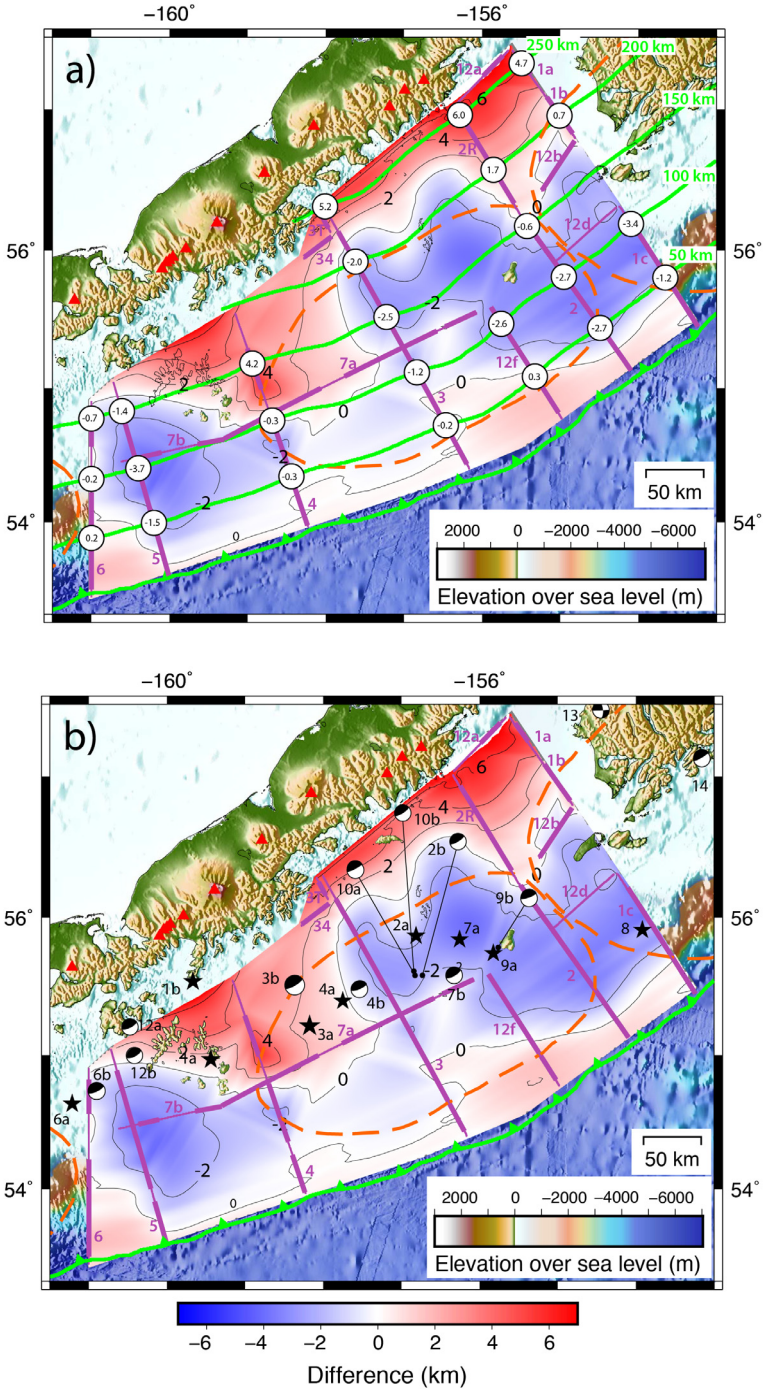

Figure 3.8.4: (Caption next page.)

Figure 3.8.4: (Previous page.) Difference map between the Slab1.0 model [*Hayes et al.*, 2012] and the ALEUT PIM. Red (positive) colour shows areas where the ALEUT model is shallower than the Slab1.0 model. Blue (negative) colour shows the opposite. Contour lines are shown in black and have a 2-km interval. Dashed orange lines outline the extent of rupture areas derived from aftershock locations for the 1938 Semidi Segment earthquake and 1964 Good Friday earthquake [*Benz et al.*, 2011; *Sykes*, 1971]. Green lines in show equidistance to trench location at 50-km interval. Red triangles show the location of active volcanoes along the arc. White circles in (a) are located at cross points between MCS profiles and equidistance from trench with specified slab interface depth-difference values in km shown inside. Black stars in (b) show epicenter locations of all recorded $>$ M_W 6.9 earthquakes with size according to their magnitude. When available, focal mechanisms are shown instead. The black star symbol (3a) represents the 1938 M_W 8.3 earthquake located by the Internation Seismological Center at a depth of 35.0 km. The identical earthquake is located by [*Davies et al.*, 1981] and is represented by a focal mechanism (3b) with a M_W of 8.2 and a depth of 26.0 km. A list of all shown earthquake events is given in Table 3.1.

We highlight the morphology of the plate interface by subtracting the Slab1.0 plate interface model from the ALEUT PIM. The result is a residual map (Fig. 3.8.4) where blue colors (negative values) show areas where ALEUT PIM is *deeper* than the Slab1.0 model and red colors (positive values) are areas where ALEUT PIM is *shallower* than the Slab1.0 model. White represents places where the depth to both models coincides. The ALEUT model shows only small deviations from the Slab 1.0 model (up to $\sim\pm2$ km) from the trench to the 50-km trench-parallel isoline, with the ALEUT model being slightly shallower especially closer to the trench. Greater differences between the two models of up to $\sim$6 km are found from the 50-km-trench-parallel isoline to the landward end of the model. However, with an exception of two places, the depth variation between the two models is $<\pm3$ - 4 km for all of this area. The two areas of the ALEUT model that exhibit significantly shallower plate interface than the Slab1.0 model coincide with the along-strike (lateral) boundaries of the deeper portion of the Semidi Segment, as defined by the M_W 8.2 1938 rupture aftershocks. The rest of the residual map (Fig. 3.8.4) not only shows much smaller depth to the plate interface difference but its lateral variation is much smoother.

The more pronounced of the two plate interface crests is the one located at the transition from the Semidi Segment to the Shumagin Gap. This morphological feature has one peak centered at ca. 100 - 150 km away from the trench and another broader top downdip at the landward end of the model. The area at the segment boundary between the Semidi Segment and the Kodiak Asperity likewise exhibits a plate interface bump starting at $\sim$150 km away from the trench and gradually increasing in magnitude down dip all the way toward the landward end of the model. The spatial coincidence of the two elevated highs with the edges of the 1938 Semidi Segment rupture and the southwestern edge of the 1964 Prince William rupture is most interesting because it invokes the simplest possible mechanism for explaining great earthquake rupture segmentation. These ruptures stop in areas characterized by greatest morphological and structural variation of the megathrust. Moreover, as discussed in more detail below, another implication of our observation is that the general megathrust rupture segmentation pattern could persist over many earthquake cycles, until current major morphological features on the subduction thrust are subducted and new ones develope.

An updated version of the global Slab1.0 subduction plate interface model was published during the writing of this thesis (Fig. A.34 in Appendix A). The updated

model, called Slab2 [*Hayes et al.*, 2018], differs significantly from Slab1.0, for example it exhibits more than 10 km difference to the ALEUT PIM in the eastern part of the survey area, while the western part shows no significant deviation (Fig. A.35 in Appendix A). Between the Semidi Segment and Shumagin Gap, however, a geometrical high of $>$ ca. 2 km is still present when Slab2 and ALEUT PIM are subtracted, while for the northeastern boundary between Semidi Segment and Kodiak Asperity only large negative values are observed, suggesting a major reduction of plate depth in this part of the survey area compared to the plate interface in the Slab1.0 model. We favor our plate interface interpretation represented by ALEUT PIM because of the well constrained velocity models used for time to depth conversion and distinct plate interface reflections that can be traced up to depth of more than 60 km. In contrast, we found no specific information that could explain the large change observed in the Slab2 model compared to Slab1.0 for the Alaska-Aleutian plate interface [*Hayes et al.*, 2018].

To demonstrate that the observed anomalies, located at the northeastern and southwestern edges of the Semidi Segment (Fig. 3.8.4), are indeed produced solely by the ALEUT PIM and not by small wavelength variations of the Slab1.0 model, we subtract a highly-smoothed background model from ALEUT PIM. Geometrical highs at the same locations, as seen in Figure 3.8.4, confirm that the anomalies are caused by the irregular shaped plate interface of ALEUT PIM (Fig. 3.8.5). This smoothed model is based on plate interface depth trend represented by quadratic functions that are fitted through the interpreted plate interface location on all trench-normal profiles (see Fig. A.36 in Appendix A). These smoothed plate interface profiles are then interpolated using continuous curvature splines function resulting a very smooth plate interface surface (see Fig. A.37 in Appendix A). The difference between this smoothed plate interface model and ALEUT PIM is shown in Figure 3.8.5, and similar features to the difference map between Slab1.0 model and ALEUT PIM (Fig. 3.8.4) are clearly observed, including a $>$ 4-km positive anomaly between Semidi Segment and Shumagin Gap and a $>$ 2-km high between Semidi Segment and Kodiak Asperity. It should be noted however, that the deep landward end shows significant differences to the Slab1.0 difference model, which suggests that the Slab1.0 model plate interface is located deeper and is more steeply dipping than the plate interface interpretations in the ALEUT MCS sections.

Furthermore, we tested a different interpolation algorithms (continous curvature spline function (surface) from General Mapping Tool (GMT)) to calculate the plate

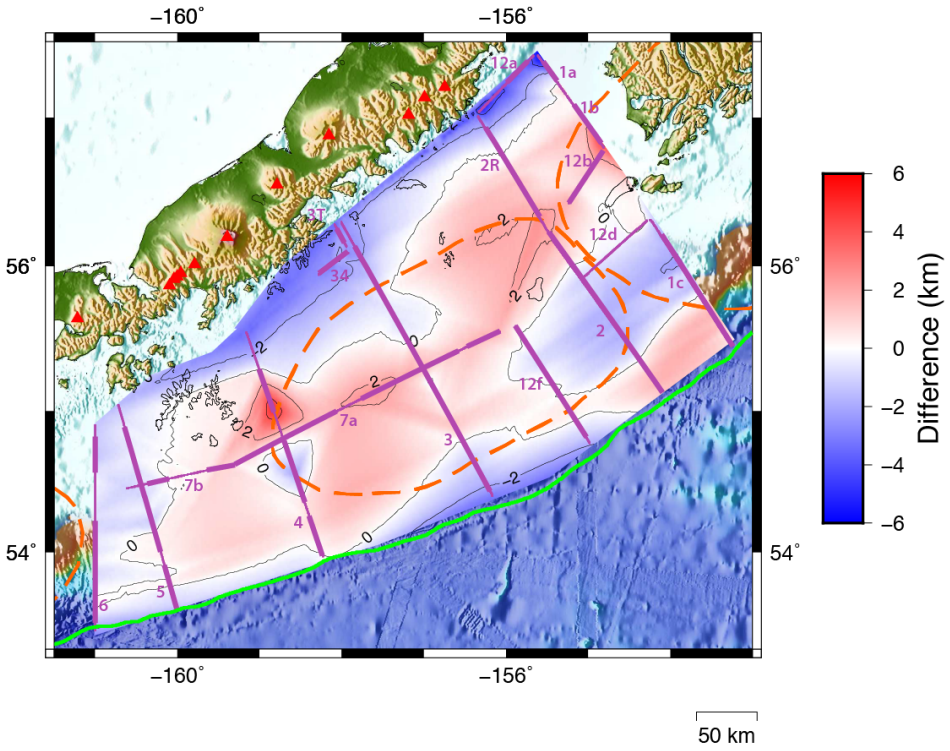

Figure 3.8.5: Difference between ALEUT PIM and a highly-smoothed plate interface model. Positive geometrical highs of the plate interface are located at the southwestern and northeastern edge of the Semidi Segment. The similarity to the Slab1.0 difference model (Fig. 3.8.4) suggest that the geometrical anomalies are caused by plate interface irregularities of ALEUT PIM.

interface in between profile locations for the ALEUT PIM (Fig. A.31 in Appendix A.). When subtracted from Slab1.0 model, the result (Fig. 3.8.6) looks very similar to the Difference model in Fig. 3.8.4. High negative difference values ($>$ 4 km) are observed (e.g. between Line 2 and 3 or on Line 5). However, the overall appearance shows little variations to Fig. 3.8.4 and the two distinct positive geometrical anomalies at the south-western end of 1938 rupture area (Semidi Segment) and its north-eastern border adjacent to the 1964 rupture area (Kodiak Asperity) are similarly pronounced. The result in Fig. 3.8.6 clearly indicates similar morphological features at the plate interface as seen with alternative interpolation algorithms.

3.8.2 Subducted seamounts at the eastern AASZ

Topography of the incoming oceanic plates at subduction zones is often examined for possible clues on subducted features that may cause great earthquake rupture segmentation [e.g., *Bilek*, 2010; *Das and Watts*, 2009; *Kelleher and McCann*, 1976].

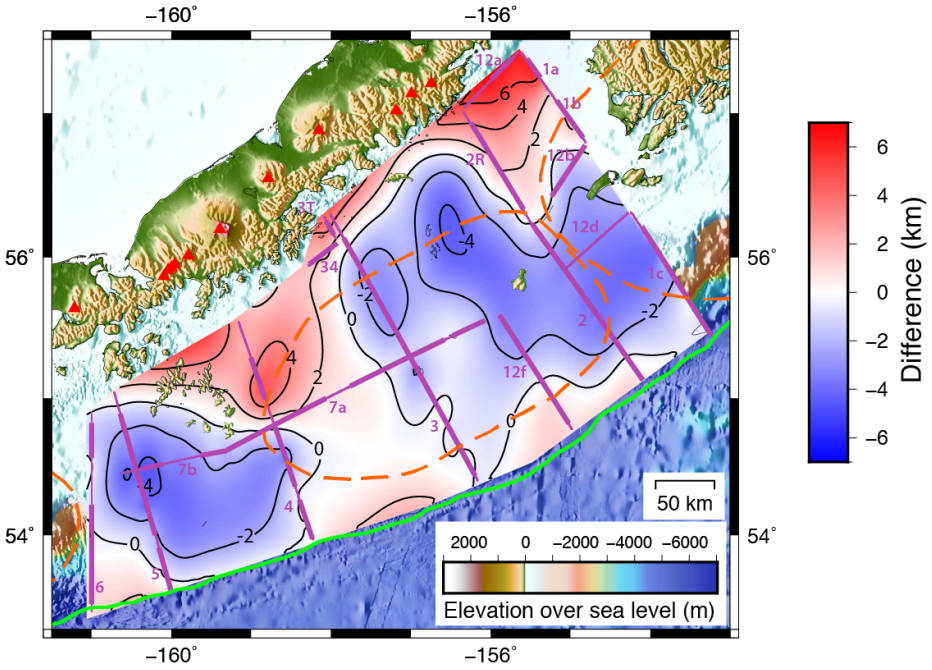

Figure 3.8.6: Difference between the Slab1.0 model and PIM, which was interpolated using a continous curvature spline function (from GMT). Overall appearance shows little variations to Fig. 3.8.4 and the two distinct positive geometrical anomalies at the south-western end of 1938 rupture area (Semidi Segment) and its north-eastern border adjacent to the 1964 rupture area (Kodiak Asperity), indicated by orange dashed lines, are similarly pronounced.

Our interpretation of the two imaged interplate interface crests as subducted seamounts requires the same for our study area. The oceanic plate offshore Alaska Peninsula shows at least two pronounced seamount chains (Fig. 3.8.7), the Kodiak-Bowie seamount ridge (also known as Pratt-Welker seamount chain) and the Patton-Murray ridge (also known as Cobb-Eickelberg seamount chain). To estimate the position where the Kodiak-Bowie and Patton-Murray seamount chains enter the AASZ, as well as their possible location within the AASZ, we fit straight-line trajectories using seamounts from both chains that are protruding the Pacific Plate seafloor (black dashed lines in Fig. 3.8.7). In doing this, we only use the seamount groups belonging to these chains that are closest to the trench (which will be subducted at the current plate convergence speed of 63 mm/yr in 6.5 - 8 Ma). This is because the convex northward shape of these chains, especially of the Kodiak-Bowie seamount ridge, and the lack of parallelism between them and with the Hawaiian chain, suggest that the melting spots that are generating them move both in the absolute reference frame and relative to each other (Fig. 3.8.8) [*Silver et al.*, 1974].

Based on our fits, the Kodiak-Bowie seamount chain enters the AASZ at ca. 56.5° N and Patton-Murray seamount chain enters at ca. 54.5° N (Fig. 3.8.7). The location of both of the crested structures imaged on the interplate interface at the boundary between the Semidi Segment and the Shumagin Gap, as well as between Semidi Segment and Kodiak Asperity appear to be located south of the projected seamount trajectories but still within the error bounds (grey dashed lines in Fig. 3.8.7). However, if the convex northward curving, which is clearly observed for this seamount chain offshore the trench region (Fig. 3.8.8) [*Silver et al.*, 1974], continues into the subduction zone, the fit to the features on the interface would be significantly improved. Maximum height of individual seamounts found seaward of the trench in both chains exceeds 3500 m above seafloor. While this is less than the maximum shallowing of the interplate interface of ∼4000 - 5000 m observed at both imaged crested structures (Fig. 3.8.4), it is large enough to suggest that it is highly likely that subducted seamounts of the Kodiak-Bowie and Patton-Murray seamount chains are the most probable underlying cause. This would also mean that these barriers to megathrust rupture are long-lived features.

The Gulf of Alaska encompasses an area extending from the Juan de Fuca Ridge offshore Washington and British Columbia to the deep sea trench at the Alaska-Aleutian arc. The seafloor topography in this region is dominated by the above-mentioned Kodiak-Bowie seamount chain in the north and the Patton-Murray seamount chain farther south, both stretching in southeast to northwest direction over the entire Gulf of Alaska and containing more than 100 distinct seamounts, each of them over 1000 m tall (Fig. 3.8.8) [*Chaytor et al.*, 2007]. It is generally assumed that seamounts chains are formed by underwater volcanic activity as the plate passes over a stationary focus of melting (e.g. sub-lithospheric hot spot or mantle plume) [e.g., *Wilson*, 1963]. Seamount chains are therefore expected to display age-progression away from their originating hot spot and alignment with the direction of plate motion. The Kodiak-Bowie chain is assumed to have been formed by the Bowie Hot Spot off Queen Charlotte Island [*Turner et al.*, 1973] and the Patton-Murray chain by the Cobb Hot Spot farther south on the Juan de Fuca ridge (Fig. 3.8.8) [*Desonie and Duncan*, 1990]. Both seamount chains exhibit large gaps in between individual seamounts, that appear to reflect long periods of volcanic inactivity. For example, at least three ca. 250 - 430 km wide gaps are observed between the Eickelberg seamounts and Murray seamount at the Patton-Murray chain (Fig. 3.8.8). Seamounts of the Pathfinder group, located

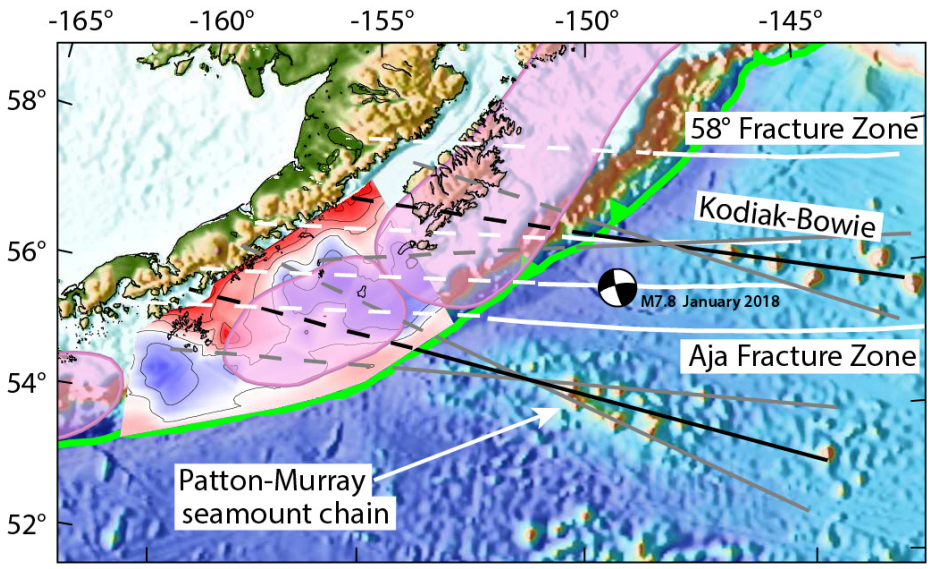

Figure 3.8.7: Gulf of Alaska and eastern AASZ seafloor topography in gnomonic map projection (great circles are straight lines) with residual map that emphasizes differences between ALEUT PIM and Slab1.0 model (see Fig. 3.8.4). Pink transparent areas are megathrust rupture zones of the great earthquakes in 1938, 1946 and 1964 defined by *Sykes* [1971] and *Benz et al.* [2011]. The inferred trajectories of Kodiak-Bowie and Patton-Murray seamount chains into the subduction system are displayed by black lines, with gray lines showing minimum and maximum fits as ±10° rotations of the best fit line. Solid white lines are transform faults (fracture zones) [*Atwater and Menard*, 1970] with their inferred subduction path shown as dashed white lines. Focal solution shows location and breaking mechanism of M_W 7.9 earthquake from January 2018. Green line shows trench location, i.e. surface trace of the plate boundary between Pacific Plate and North American plate.

farther south, are believed to not have been attributed to any active hot spot in the region [*Desonie and Duncan*, 1990]. The Kodiak-Bowie chain seems to be interrupted by at least two ca. 220 - 400 km wide stretches where no seamounts have formed (Fig. 3.8.8). Despite showing a general increase in age from the youngest seamounts in the southeast to the oldest (> 24 Ma) in the northwest [*Turner et al.*, 1973], some seamounts in the Gulf of Alaska also show out-of-sequence ages [*Dalrymple et al.*, 1987; *Silver et al.*, 1974], suggesting that not all seamounts within a chain have been formed over one hot spot. Furthermore, the geochemical composition of the seamounts is unusual in that they lack the distinctive radiogenic isotope signatures associated with most hot spots [e.g., Hegner and Tatsumoto, 1989; Desonie and Duncan, 1990; Keller et al., 1997][e.g., *Desonie and Duncan*, 1990; *Hegner and Tatsumoto*, 1989; *Keller et al.*, 1997]. These aspects have called into questions the validity of the hot spot mantle plume model for forming these seamounts [*Allen et al.*, 1993; *Dalrymple et al.*, 1987; *Smoot*, 1985]. Alternate plume models have been suggested that are thermally buoyant,

rather than compositionally buoyant, which could explain the discontinuous nature and anomalous isotopic composition of these seamount chains [*Desonie and Duncan*, 1990]; however, open questions regarding the out-of-sequence ages remain unanswered. The estimated gaps between the last known seamount on the Pacific Plate and the modelled plate interface anomalies on the subducted Pacific Plate are ca. 410 km for the Kodiak-Bowie chain and ca. 530 km for the Patton-Murray chain (Fig. 3.8.8). Given that the distance between the Eickelberg and Miller seamount can be more than 800 km, if the smaller isolated seamounts in the middle are disregarded, both distances fall inside the range of volcanic inactivity observed on the Pacific Plate. From these observations, we conclude, that it seems possible that the variable hot spot activity (or different volcanic seamount forming mechanism) can be extrapolated for greater plate ages, that have entered the Alaska-Aleutian subduction zone where they appear as geometrical anomalies at the plate interface and influence earthquake rupture propagation.

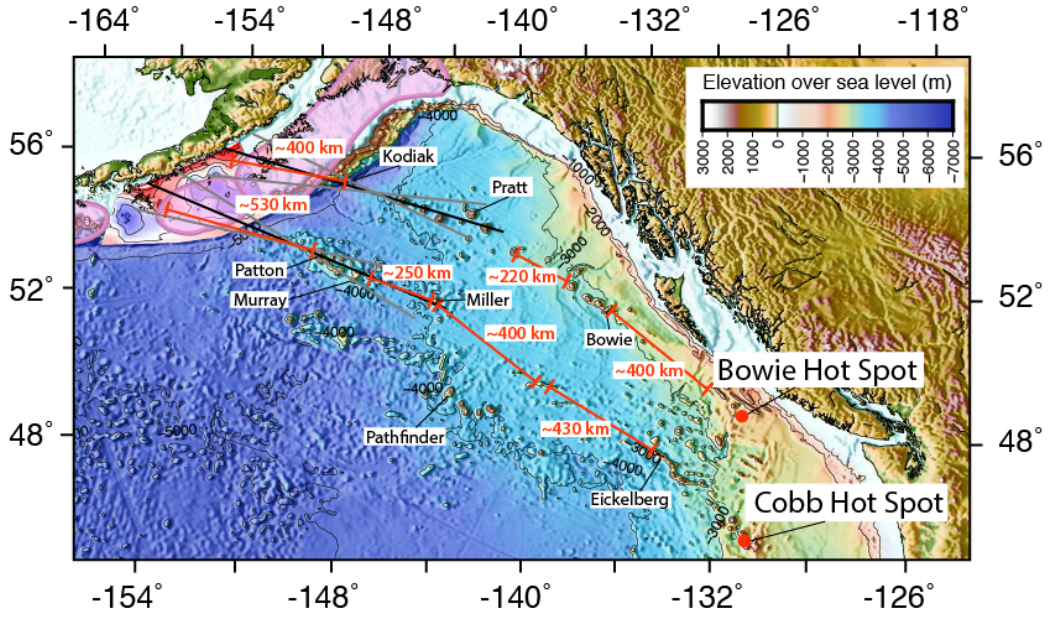

Figure 3.8.8: Bathymetric map of the Gulf of Alaska (in gnomonic projection) with selected seamounts and approximate hot spot locations (red dots) [*Chaytor et al.*, 2007]. Pink areas are rupture areas of past megathrust earthquakes [*Davies et al.*, 1981; *Sykes*, 1971] and residual map from Figure 3.8.4 shows location of the subducted plate interface anomalies in respect to extrapolated seamount chain trajectories (thick black lines with grey lines showing minimum and maximum fit as seen in Fig. 3.8.7). Red lines show distances along the Bowie-Kodiak and Patton-Murray seamount chains paths, where seamounts are absent, possibly due to hot spot inactivity for longer time periods. Extrapolation of these gaps into the Alaska-Aleutian subduction zone, from the last known seamount at the Pacific Plate to the modelled plate interface anomalies, show comparable ranges (ca. 400 km and ca. 530 km) than observed on the younger Pacific Plate in the southeast.

A global marine free air gravity data set with enhanced resolution and ∼2 mGal accuracy [*Sandwell et al.*, 2014] is filtered by a 75-km median filter to obtain a smooth gravity background model. This model is subtracted from the original data to produce a residual gravity map, where the regional background anomaly (long spatial wavelength associated with the Aleutian arc, trench and the outer gravity high), is removed in an attempt to emphasize shorter wavelength frequencies expected to be generated by seamounts (Fig. 3.8.10).

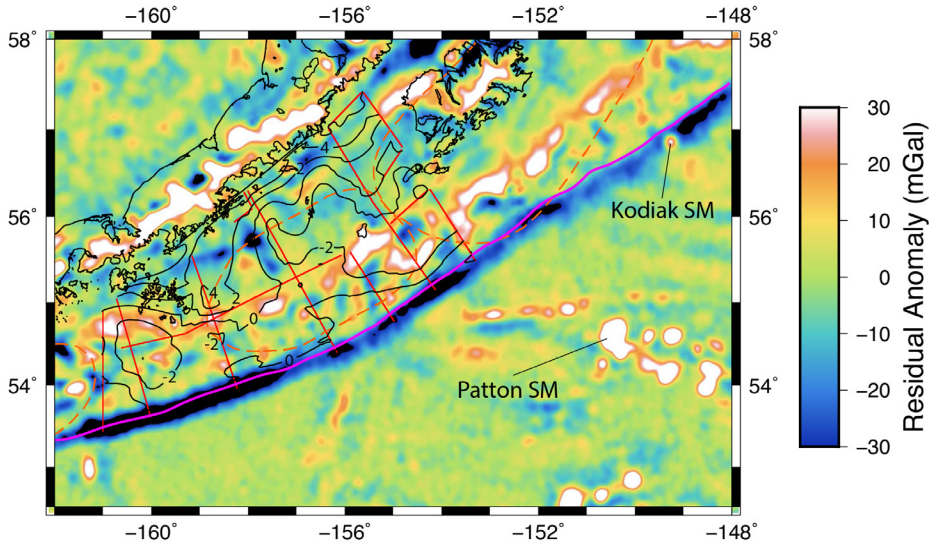

Figure 3.8.9: Residual gravity anomalies in the ALEUT survey area and adjacent incoming Pacific Plate after the removal of a smooth background gravity model to empathize shorter wavelength frequencies associated with, for example, subducted seamounts (gravity data from *Sandwell et al.* [2014]). Thin black lines are depth contour line (2-km interval) of plate interface residual model as seen in Figure 3.8.4. Dashed orange lines show the rupture extent of tectonic segments derived by *Sykes* [1971] and *Benz et al.* [2011] and pink line represents location of deep sea trench. Red lines are locations for ALEUT MCS profiles as seen as in Figure 3.3.

When comparing the residual gravity map with the location of the modelled plate interface anomalies, which we interpret as subducted seamounts, we expect an excess of higher density rocks and therefore positive gravity anomalies in the vicinity of plate interface highs. We observe such a positive gravity residual (ca. 30 mGal) at the southwestern edge of the Semidi Segment, although its peak is ca. 20 km south of the modelled plate interface anomaly. The peak coincides with intersection of MCS Line 4 and 7a. At the second geometrical plate interface high at northeastern landward edge of the Semidi Segment and the southwestern Kodiak Asperity no gravity anomaly is observed. It should be noted that the plate interface anomaly between Semidi Segment and Kodiak Asperity is less pronounced and is located much deeper than the anomaly on the southwestern edge of Semidi Segment

(Fig. 3.8.4). Both aspects might be the reason for the lack of an observable positive anomaly here. We also note that fracturing of the upper plate due to the subduction of the seamounts [*Wang and Bilek*, 2011] could produce regions of low density that counterbalance the positive density contrast expected for the seamounts itself. A magnetic anomaly map for this area shows good correlation of the plate interface anomalies at either lateral edge of Semidi Segment with the positive magnetic highs (Fig. 3.8.10). The magnetic anomalies, however, could also be the result of structural or compositional changes in form of, for example, plutonic intrusions in the upper and shallow crust, rather than from subducted seamounts in 30 - 40 km depth [*Plafker and Berg*, 1994].

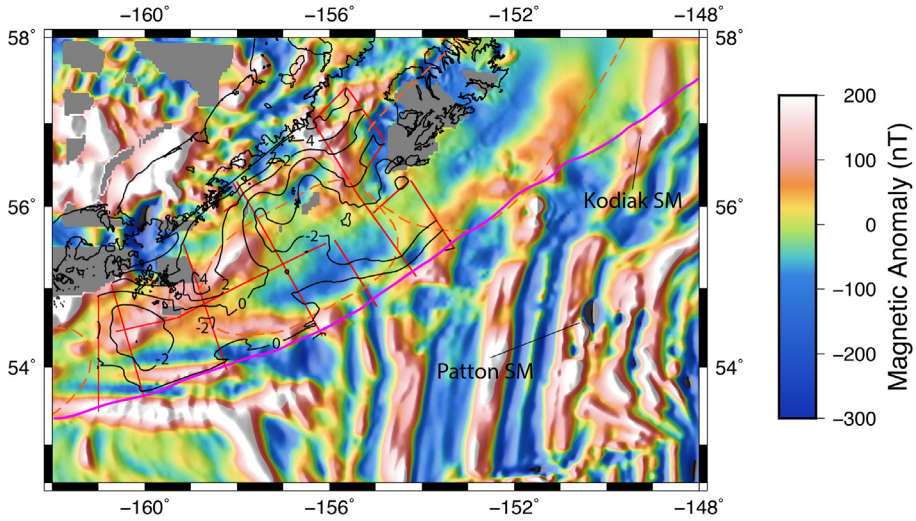

Figure 3.8.10: Geomagnetic anomalies in the ALEUT survey area and adjacent incoming Pacific Plate from EMAG2 dataset [*Meyer et al.*, 2017]. Thin black lines are depth contour line (2-km interval) of plate interface residual model as seen in Figure 3.8.4. Dashed orange lines show the rupture extent of tectonic segments derived by *Sykes* [1971] and *Benz et al.* [2011] and pink line represents location of deep sea trench. Red lines are locations for ALEUT MCS profiles as seen as in Figure 3.3.

A long-lived rupture barrier between the Kodiak Asperity and Semidi Segment has been previously proposed by *Wesson et al.* [2007] and *Von Huene et al.* [2012]. However, this possible rupture barrier was related to the subducting Patton-Murray seamount chain and aligned fracture zone. It is likely that the discrepancy between these earlier interpretations and our interpretation stems from use of different map projections and different seamount age ranges used for fitting. While the map projections used by *Wesson et al.* [2007] and *Von Huene et al.* [2012] are not known, they both appear to be Mercator. In Mercator projection, great circles lines are

curved except at the equator and meridians, resulting in inaccuracies for straight-line fits of features like seamount chains. In this work we use a gnomonic map projection, where great circles are straight lines. *Wesson et al.* [2007] and *Von Huene et al.* [2012] also seem to use all available Kodiak-Bowie and Patton-Murray seamounts for their fits, while we try to minimize the effect of their convex northward trajectory by only using the seamount groups found closest to the trench (up to 6.5 - 8.0 Ma away from the trench at current, 63 mm/yr convergence rate).

Abnormal geochemical signatures of arc lavas could theoretically be a strong indication for subducted seamounts if they are significantly different geochemically from their surroundings. Seamounts in the Gulf of Alaska are indeed isotopically distinctive and might be therefore distinguishable from Pb-rich volcanic arc rocks [personal communication with Yogodzinski, 2018]. The assumption that seamounts are subducting or have been subducted at the eastern AASZ could therefore be further strengthen if variations in the Pb isotope ratio between island-arc volcanic rocks and older seamounts could be found.

3.8.3 Effects of the incoming Pacific Plate on megathrust segmentation

3.8.3.1 Seamounts

The most plausible interpretation for the two discussed crested structures on the interplate interface is presence of subducted seamounts. While the effect of seamount subduction on the degree of friction on the interplate interface is debated, with some authors proposing increased coupling [e.g., *Cloos*, 1992; *Husen et al.*, 2002; *Kodaira et al.*, 2000; *Scholz and Small*, 1997; *Watts et al.*, 2010] and others decreased coupling [*Bell et al.*, 2010; *Mochizuki et al.*, 2008; *Ranero and von Huene*, 2000; *Wang and Bilek*, 2011], both indicate abnormal sections on the megathrust that generally act as barriers to rupture propagation. This is because seamount subduction leading to a creeping megathrust [*Bell et al.*, 2010; *Mochizuki et al.*, 2008; *Ranero and von Huene*, 2000; *Wang and Bilek*, 2011] prevents significant stress accumulation at the two imaged plate interface crests located at the transitions from the Semidi Segment to the Shumagin Gap and from the Semidi Segment to the Kodiak Asperity. If this scenario is correct, then these two crests will have too little strain energy stored to slip and/or promote further slip, and will

act as barriers to megathrust rupture propagation on a continuous basis until they are subducted to greater depths than the seismogenic zone. A similar scenario is expected if seamount subduction, on the other hand, leads to anomalously increased normal stress because of seamounts excess mass and buoyancy, and thus to locally anomalously high friction [*Cloos*, 1992; *Husen et al.*, 2002; *Kodaira et al.*, 2000; *Scholz and Small*, 1997; *Watts et al.*, 2010]. The two imaged plate interface crests will in most cases act as barriers to great earthquake rupture propagation due enhanced seismic coupling in these affected areas that might be too strong to break. However, as the stresses on the imaged interplate interface crests increase with megathrust ruptures in the region, there will be occurrences when these sections of the megathrust not only rupture but also generate more moment magnitude per unit area than the surrounding subduction thrust.

Our interpretation for the two imaged interplate interface crests being subducted seamounts that generally act as barriers to megathrust rupture propagation seems to fit well with what is known about the subduction zone earthquakes in the study area. The crested barrier between Semidi Segment and Shumagin Gap seems to have impeded along-strike rupture propagation of two moderate to large subduction earthquakes on either side of it. The epicenter of the M_S 7.9 1917 earthquake [*Boyd and Lerner-Lam*, 1988] is located west of the barrier in the Shumagin Gap and the M_W 8.2 1938 epicenter is located east of it within the Semidi Segment (Fig. 3.8.4). Both occurred at the deep end of the seismogenic zone more than 150 km away from the trench. Aftershock locations indicate that both events were unilateral (i.e. rupturing in only one trench-parallel direction; 3.8.11). While the 1917 earthquake rupture propagated to the southwest [*Boyd and Lerner-Lam*, 1988], the 1938 event ruptured toward the northeast (with minimum slip of 0.8 m at its origin and maximum slip of 3.3 m in the eastern part of the segment) where it may have been stopped at the crested barrier between the Kodiak Asperity and Semidi Segment [*Johnson and Satake*, 1994]. Both earthquakes appear to have been unable to propagate into their adjacent tectonic segments [*Nishenko and Jacob*, 1990] (Fig. 3.8.11). Similarly, the M_W 9.2 1964 Good Friday earthquake was generated in Prince William Sound and propagated unilaterally in the southwest direction and may not have been able to propagate through the crested barrier between the Kodiak Asperity and Semidi Segment (Fig. 3.8.11). Therefore, rupture propagation of all three of the most recent subduction earthquakes in our study area are consistent with the two crested interplate interface structures imaged with our

survey acting as barriers.

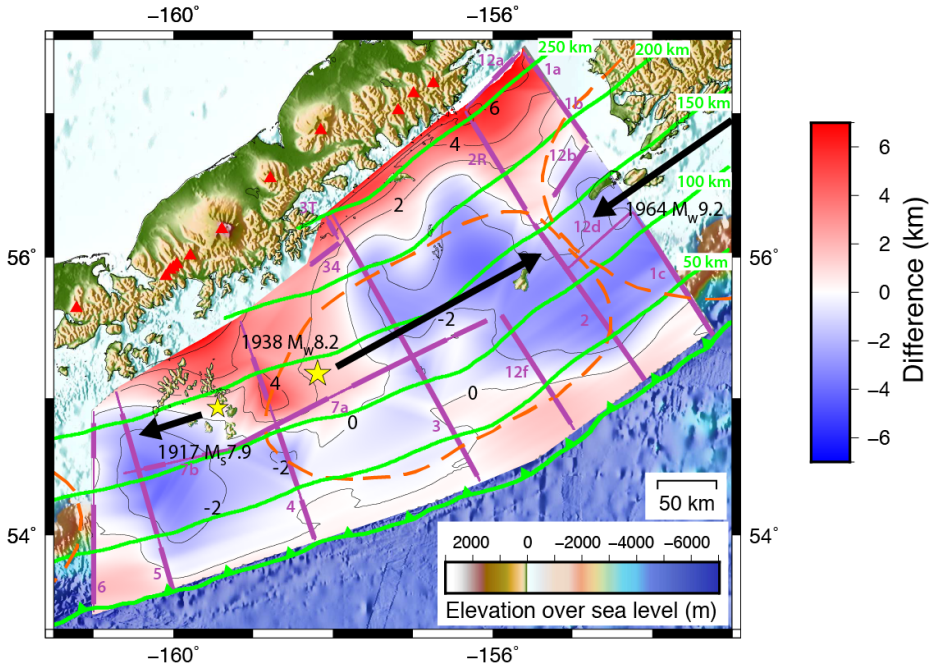

Figure 3.8.11: Residual map as presented in Fig. 3.8.4 but with added epicenters of the two largest earthquakes ever recorded in this area. Green lines show equidistance to trench location (green line with triangles) at 50-km interval. Dashed orange lines outline the extent of rupture areas derived from aftershock locations for the 1938 Semidi Segment earthquake and 1964 Good Friday earthquake [*Benz et al.*, 2011; *Sykes*, 1971]. Yellow stars show epicenter location of the 1938 M_W 8.2 event that ruptured Semidi Segment and 1917 M_S 7.9 earthquake within the Shumagin Gap. Black thick arrows show direction of rupture for 1917, 1938 and 1964 event, respectively. Rupture is moving away or stops at the crested shaped interplate interface features, shown as large positive anomalies located on Line 4 at a distance of 100 - 150 km, and on Line 2 at a distance of 150 - 250 km from trench [*Estabrook and Boyd*, 1992; *Johnson and Satake*, 1994].

It is not quite clear why the 1917 earthquake occurred in the Shumagin Gap. Using dislocation models to estimate both the width of locked zones and the degree of coupling, and then fitting them with geodetic measurements yields a freely slipping plate interface for the western part and weak interplate coupling for the eastern part of the Shumagin Gap [*Fournier and Freymueller*, 2007; *Freymueller and Beavan*, 1999]. Geodetic data points are, however, bound to land sites, which are naturally scarce or do not exist in the vicinity of trench and slope where the highest strain accumulation rate is expected. Because of this lack in data coverage, a small locked region some 55 km in width located near the trench cannot be ruled out [*Fournier and Freymueller*, 2007]. If locked, this area of the subduction thrust is itself large enough to generate a M∼7 earthquake, or it can at least rupture as part of a greater propagating slip event nucleated on other parts of the arc. Both great

pre-instrumental recorded earthquakes from 1788 and 1847 might have ruptured that shallow section of the plate interface near the Shumagin Islands and the Semidi Segment [*Davies et al.*, 1981]. It is unknown, however, if these historic earthquakes also propagated through the crested barrier located at interplate interface depths greater than 20 - 25 km.

Evidence for abrupt changes in the geometry of the subducting plate interface exists for Japan, off Miyagi in the central Japan Trench forearc region [*Fujie et al.*, 2006; *Ito et al.*, 2005], and for the northern Chile [*Contreras-Reyes et al.*, 2012] subduction zone at around 22° S latitude. In both cases, the sharp change in the dip is thought to affect up- and down-dip rupture propagation of megathrust earthquakes. At the Chile subduction zone, it appears that the location of the abrupt margin-normal change in plate interface dip also acted as along-strike barrier for at least two moderate earthquakes of M_W 7.4 (1967) and M_W 7.7 (2007). This barrier must have been overcome during a great M_W 8.8 earthquake that ruptured a much larger region, including this zone. However, this interpretation is based on only one seismic profile.

3.8.3.2 Fracture zones and oceanic crust fabric

Fracture zones, created along transform faults that separate sections of oceanic crust spreading in opposite directions from a mid-ocean ridge, are parallel to the direction of spreading and create topographic relief with height that is proportional to the amount of offset between the two neighboring ridge segments. As the oceanic crust ages and cools, this topographic relief diminishes but some fraction of it can be supported by buoyancy linked to chemical alteration into less dense serpentinized rocks induced by fracture and water penetration. This, in turn, can cause anomalous normal stresses as has been determined for elevated bathymetric features that are associated with buoyancy and, when subducted, might lead to formation of asperities and barriers and thus megathrust segmentation on the interplate interface [*Contreras-Reyes and Carrizo*, 2011].

The topographic expressions of the Aja and three other fracture zones in the study area (Fig. 3.8.8) are, unlike for the seamounts, challenging to observe in bathymetric data but a significant degree of hydration via serpentinization is expected in the 30 - 40 Ma old oceanic lithosphere beneath these features [*Contreras-Reyes et al.*, 2008]. Large earthquakes, such as the M_W 7.9 strike-slip

event in January 2018, are uncommon for intraplate earthquakes located distant to any plate boundary and possibly the result of intraplate stresses accommodated by rupturing of old fracture zones. Despite this, possible seismogenic effect of the four subducting fracture zones identified in the study area remains unclear. The subducting fracture zones impinge on the trench at an angle of about 45°, similar to the seamount chains. Their spacing is significantly smaller than the width of the known rupture segments (e.g., 1938 M_W 8.2 Semidi Segment rupture). As such, these fracture zones coincide with both centers of locked asperities and segment boundaries suggesting that their impact on the interface interplate coupling in the study area is both difficult to evaluate and secondary.

The eastern Aleutian arc between Kodiak Island and the Shumagin Islands exhibits very little along-strike variability in subduction related parameters. Oceanic crust formed 50 - 55 Ma ago is presently subducting at ca. 63 mm/yr orthogonally beneath continental crust [*Sella et al.*, 2002] resulting in relatively uniform temperature regime along strike. However, a T-shaped magnetic anomaly representing a fossil triple junction is found offshore the Shumagin Gap and Semidi Segment boundary (Fig. 3.8.11) [*Bécel et al.*, 2015; *Shillington et al.*, 2015]. Oceanic crust located northeast of that magnetic anomaly, subducting beneath Semidi Segment and Kodiak Asperity, has been formed at the Kula-Farallon intermediate spreading center (half spreading rate: ∼24 mm/yr) and has crustal fabric that is highly oblique (up to ∼70°) relative to the trench (Fig. 3.8.11). This geometry results in greater resistance to bend faulting and greater fault spacing thus possibly inhibiting serpentinization of the subducting plate. In contrast, incoming oceanic crust southwest of it was generated by the fast spreading Kula-Pacific ridge (half rate: ∼ 70 mm/yr) and has crustal fabric oriented at a lower angel 10° - 25° to the trench making it easier to reactivate this existing ridge-generated fabric [e.g., *Masson*, 1991], and therefore more thoroughly serpentinize the subducting plate. In agreement, vertical fault offsets caused by bend faulting are abundant and the fault displacements easily observed and measured at the outer rise offshore Shumagin Gap [*Shillington et al.*, 2015]. This is accompanied by a reduction in the oceanic uppermost mantle velocities. In contrast, weakly faulted sediments with small vertical offsets due to bending faulting are observed on top of the incoming plate offshore Semidi Segment northeast of the fossil triple junction with little variation in uppermost mantle velocity measured [*Shillington et al.*, 2015].

The heterogeneity of the plate boundary caused by a combination of limited

sediment thickness and bending faulting of the subducting oceanic plate between the Shumagin Gap and the Semidi Segment must contribute to lateral variation in megathrust behavior. However, the coincident MCS and OBS profiles 3 and 5 are almost 300 km apart (Fig. 3.4.1) and cannot themselves resolve if the change in the hydration pattern is gradual or sudden over this distance. Reflection MCS profile 4, located between lines 3 and 5, shows bend related faulting that is intermediate of that observed on lines 3 and 5. This suggests that the lateral change in hydration of the incoming oceanic plate is gradual. If this is true, then this change in bending faulting and differences in heterogeneity of the plate boundary cannot be the main cause for the existence of a narrow segment boundary just to the southwest of Line 4 (Fig. 3.8.4). The primary cause is the rough geometry of the interplate interface generated by the imaged subducted seamounts.

3.8.3.3 Sediments

An additional controlling factor in interplate coupling, earthquake behavior and thus tectonic segmentation is believed to be the amount of subducted sediment entering the subduction zone [*Contreras-Reyes et al.*, 2010; *Ruff*, 1989]. At the eastern AASZ, the incoming plate subducting beneath the Semidi Segment is covered by relatively thick sedimentary cover (∼1000 - 1200 m), which includes a ca. 800-m-thick layer of distal turbidites from terrigenous Zodiac fan deposited in the Eocene (Fig. 3.8.12), and an upper pelagic cover approximately 300 - 400 m thick [*Stevenson et al.*, 1983]. The complete lower sediment package of the Zodiac fan seems to enter the subduction channel, as clearly distinguishable by down-dip continuation of high seismic impedance contrast of the top layer [*Li et al.*, 2018]. This highly reflective sediment layer boundary is also observed on all other ALEUT deep sea lines, although layer thickness beneath it is decreasing significantly on adjacent profiles of Line 3 to the southwest and northeast, whereas the thickness of the top layer of pelagic sediments remains uniform. This observation is in accordance with the outlined extent of the Zodiac sedimentary fan with Line 3 crossing its central part and Line 4 the western edge of the fan (Fig. 3.8.12). At the Shumagin Gap, overall sediment thickness decreases significantly to ∼500 - 700 m and thickness of Zodiac fan sediments are reduced to 100 - 200 m on the incoming oceanic crust as observed on Lines 4 and 5. Irregular shaped igneous basement can also be inferred from the bathymetry due to the thin sediment cover on top. The

upper pelagic sediments are accreted onto the edge of the overriding continental plate alongside eroded continental shelf sediments that are deposited as trench infill and transported along the trench in margin-parallel direction from the northeast to the southwest [*Reece et al.*, 2011].

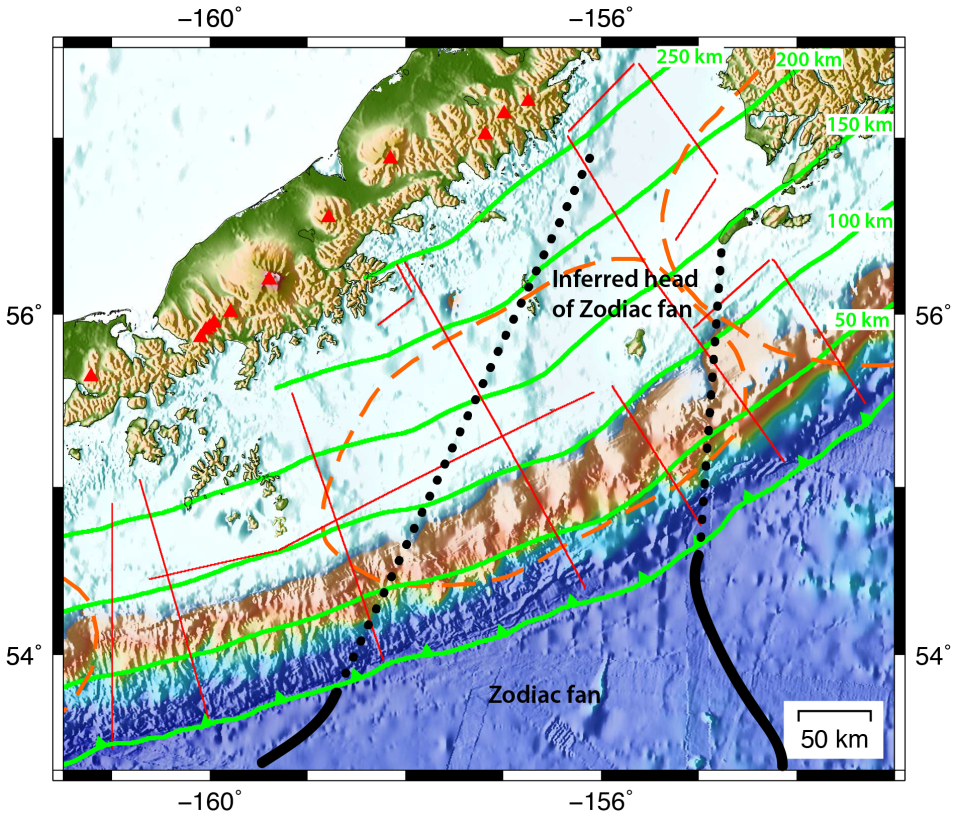

Figure 3.8.12: ALEUT survey area with inferred extent of subducted Zodiac sedimentary fan (modified from *Von Huene et al.* [2012]) shown with black dotted lines (solid black line where known seaward from the trench). Interplate interface beneath highly coupled Semidi Segment is mainly covered by thick sediments of the Zodiac fan. Green lines show equidistance to trench location (green line with triangles) at 50-km interval. Dashed orange lines outline the extent of rupture areas derived from aftershock locations for the 1938 Semidi Segment earthquake and 1964 Good Friday earthquake [*Benz et al.*, 2011; *Sykes*, 1971]. ALEUT MCS reflection profiles are red lines.

These systematic variations in incoming and subducted sediment thickness at the eastern AASZ correlate with along-strike changes in subducted sediment pore pressure, and result in changes in effective stress and fault roughness along the plate boundary that contribute to different styles of seismic behavior [*Li et al.*, 2018]. Offshore the Semidi Segment, where thicker, weakly faulted sediments subduct and smooth out irregular shaped basement topography, the shallow section is highly overpressured and may inhibit shallow seismic slip on the megathrust. After drainage and consolidation at greater depths, the same subducted sediments may

promote formation of a large and coherent asperity that exhibits low levels of seismicity but is locked and regularly facilitates long rupture propagation in great earthquakes. In contrast, where a thinner, faulted sedimentary section subducts, a heterogeneous plate boundary results that cannot accumulate large quantities of elastic strain energy and stress is released in abundant smaller earthquakes, creeping behavior, and less regular megathrust earthquakes [*Bécel et al.*, 2017; *Li et al.*, 2018].

Changes in sediment input and properties on the subducting oceanic plate along a subduction zone could therefore influence interplate coupling, seismicity, and therefore segmentation on the rupture fault. However, the Zodiac fan sediment distribution (Fig. 3.8.12) only partially fits with the existing observations of segmentation at the eastern AASZ thrust and the work of *Li et al.* [2018] on ALEUT profiles 3, 4 and 5 indicates a gradual along-strike change in megathrust coupling. This suggest that the more likely primary underlying cause for an abrupt boundary between the Semidi Segment and Shumagin Gap is the rough geometry of the megathrust caused by the subducting Patton-Murray seamounts.

In summary, along-strike changes in sediment thickness and bending faulting likely contribute to changes in megathrust behavior along strike, but are unlikely to define segmentation because they likely vary gradually along-strike.

3.8.4 Comparison with interplate coupling from GPS data

Significant effort has been invested in the past two decades to determine current megathrust coupling distribution along the eastern AASZ using dislocation modeling constrained by GPS data [e.g., *Freymueller and Beavan*, 1999]. The coupling model for the area most commonly referred to is that of *Fournier and Freymueller* [2007], which is based on GPS measurements taken between 1991 and 2005 at 27 permanent and campaign sites. This result has recently been refined by *Li and Freymueller* [2018] using a much enhanced and more accurate data set collected at 78 sites between 1992 and 2016. Here we compare how these two megathrust coupling models fit with the plate interface geometry derived in this work.

The *Fournier and Freymueller* [2007] and *Li and Freymueller* [2018] locking fraction models show similarities at the regional scale but differences at more local scales (Fig. 3.8.13). These large-scale similarities are not surprising because, though the more recent model is based on data from almost three times the number of GPS

sites, these sites cover similar sections of the study area with major offshore observation gaps remaining largely intact. Both models have the study area divided into four plate interface sections which show a clear decrease in the coupling degree laterally from northeast to southwest that ranges from strongly locked at the Kodiak Asperity and eastern Semidi Segment section to mostly creeping at the western Shumagin Gap section. The sharp along-strike changes in locking between these sections are the result of *a priori* definitions of segments that improve the model fit. However, the locations of the abrupt lateral changes in locking between these four plate interface sections in the two models differ by up to ∼50 km. Moreover, while in the earlier model of *Fournier and Freymueller* [2007], all four sections show constant locking fraction, the four sections in the model of *Li and Freymueller* [2018] show a varying degree of decreasing plate locking fraction in the down-dip direction. The steepest drop from ∼90 % locking to ∼40 % locking is modelled for the Kodiak Asperity and eastern Semidi Segment section at ∼100 to ∼150 km landward from the trench. The western Semidi Segment section also shows a drop in the locking fraction at ∼50 km landward form the trench but it is far less steep. The two plate interface sections farther west show only gradual decrease in coupling in the landward direction.

Li and Freymueller [2018] compare their locking model with the structure of the incoming oceanic plate and with the seismicity observed within the subduction zone to propose that the modeled sharp along-strike changes in seismic coupling correlate with both but mostly with the change in plate fabric orientation of the incoming oceanic plate. A less fractured oceanic crust, smoothed out by a thick sediment cover, will form a relatively uniform plate interface that would allow co-seismic slip at greater depth while thick sediment contribute to pore-fluid overpressure and stable sliding at shallow depths as observed at the Semidi Segment [*Li et al.*, 2018]. In contrast bending faulting offshore the Shumagin Gap, impacts the megathrust by making its fault surface more irregular and in combination with thin sediments cover results promotes heterogeneous stress distribution that promotes creep along the entire plate boundary [*Wang and Bilek*, 2011], accompanied by abundant smaller thrust earthquakes [*Li et al.*, 2018].

The along-strike change in sediment thickness and oceanic plate structure may happened over short distances of just tens of kilometer, however, it is likely too subtle to arrest rupture propagation and define segmentation. A pattern of a more gradual change is also observed in the seismicity patterns. These observations do

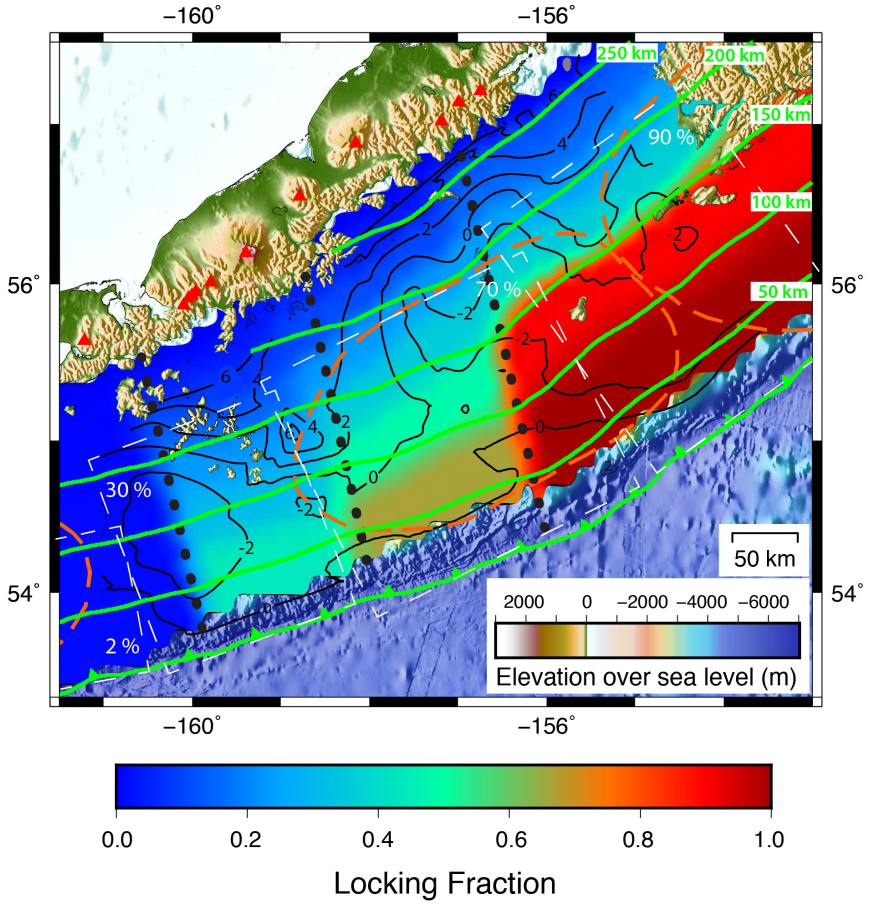

Figure 3.8.13: ALEUT survey area residual plate interface geometry from Figure 3.8.4 (thin black lines representing 2-km intervals) overlies the locking fraction distribution between the overriding North American Plate and subducting Pacific Plate as put forward by *Fournier and Freymueller* [2007] (dashed white rectangles) and *Li and Freymueller* [2018] (colour map). Black dotted lines mark sharp changes in lateral and down-dip locking for *Li and Freymueller* [2018] model. Dashed orange lines outline the extent of rupture areas derived from aftershock locations for the 1938 Semidi Segment earthquake and 1964 Good Friday earthquake [*Benz et al.*, 2011; *Sykes*, 1971]. Green lines connect equidistant points to the trench at 50-km intervals. Red triangles show the location of active volcanoes along the arc and green line with triangles shows the position of the trench.

not agree with sharp lateral changes in megathrust locking degree, despite immanent uncertainties for the coupling as well as rupture extent. The two other sharp lateral transitions in coupling occur in the middle of the Semidi Segment rupture and the middle of the Shumagin gap, and there is no transition in coupling at the boundary between the 1938 M_W 8.2 Semidi Segment and 1964 M_W 9.2 Good Friday earthquakes. These discrepancies could be comprehend by considering that the far offshore areas, where the coupling is the greatest, are poorly resolved due to the lack of geodetic data for the offshore areas, especially near the trench. This lack

of data coverage at critical areas combined with the lack of detailed definition of the megathrust geometry were probably the key factor for *Li and Freymueller* [2018] to rely only on fitting the horizontal velocities during the inversion process.

While the characteristics of the incoming oceanic fabric and sediment thickness are important factors to consider when evaluating lateral variations in megathrust coupling, the first order contributors to trench-parallel rupture propagation arrest seems to be related to the current structure of the megathrust and the characteristics of the subducted sections of the oceanic plate, as well as the overlying plate which, until now, have not been fully revealed in the study area even at a regional scale. With the newly constructed ALEUT PIM (Fig. 3.7.3) and the residual plate interface geometry (Fig. 3.8.4) obtained by subtracting the Slab1.0 interface model [*Hayes et al.*, 2012] (Fig. 3.8.3) from the ALEUT PIM, detailed comparison with the locking models can be made to gain new insights into the plate interface behavior. In the further text, we only consider the most recent plate-interface locking model of *Li and Freymueller* [2018]. The most notable correlations between two is marked by the coincidence of low coupling areas with the location of two crest-like structures on the residual plate interface geometry map denoted as high positive difference values found at the boundary between the Semidi Segment and both the Shumagin Gap and the Kodiak Asperity. These crest-like structures with amplitude of up to ∼4 km are interpreted to be subducted seamounts. It is interesting to note that the large down-dip drop in megathrust coupling within the Kodiak Asperity and the eastern Semidi Segment section occurs at ∼150 km landward from the trench, which is at the seaward end of the northeastern high positive peak in the residual plate interface geometry map. This also is the area where the highly-coupled megathrust within the Kodiak Asperity and the eastern Semidi Segment section is the narrowest in the down-dip direction, though only by ∼10 km or so.

The larger and the more seaward of the two high positive peaks in the residual plate interface geometry map, located at the southwestern end of the 1938 M_W 8.2 Semidi rupture area, approximately coincides with the abrupt lateral but also down-dip change in megathrust coupling between the western Semidi Segment and eastern Shumagin Gap model sections. The center of the main interpreted seamount is located some 15 - 20 km westward of this boundary between the two model sections, and the seaward limit (0 km on the residual plate interface geometry map) of the interpreted seamount anomaly is ∼100 km seaward from the trench and about

midway within the western Semidi Segment section of the coupling model. Overall, these observations seem to support the work by *Wang and Bilek* [2011], which proposes that the subducted seamounts decrease interplate coupling by fracturing and thus weakening the upper plate structure.

We do not observe structures on the residual plate interface geometry map that we can relate with the very weak to no coupling areas of the western Shumagin Gap section but this location is also at the southwestern end of our study area. However, the described largest high-elevation seafloor feature located at the southwestern end of the 1938 Semidi Segment rupture is likely the trailing end of the subducted section of the Patton-Murray seamount chain located offshore the eastern AASZ. If this is correct, the subduction path of this seamount chain had to cross the Shumagin Gap, possibly leaving behind damaged and reworked rocks and a network of fractures in the overriding crust that continue to provide a strongly heterogeneous underside of the upper crust plate interface long after the seamounts passed that region. That could lead to the impediment of strong coupling, especially in the observed absence of a thick sediment cover (Line 4 and 5) on the subducting oceanic plate that could smooth out geometrical irregularities on the interplate interface. This process resulting in a damaged overriding plate is well documented on exhumed ancient subduction zones that show pervasive upper plate fracturing caused by seamount subduction [e.g., *Vannucchi et al.*, 2006].

3.9 Conclusions

We analyze the ALEUT network's 3700 km of deep penetrating MCS profiles to image the subduction thrust and built a 3D PIM of the eastern AASZ spanning from the southwestern end of the Kodiak Island at ca. -152° E to west of the Shumagin Islands at ca. -161° E. Nearly continuous megathrust reflection signals are imaged from the trench up to ∼65 km depth near the Alaska Peninsula shoreline on all of the 27 regional profiles. This is the largest depth at which plate interface reflections from a controlled source seismic survey have been recorded. Migrated reflection profiles in time domain were converted to depth prior to interpretation using velocity models designed for each profile and based on MCS data (sediments), OBS profiles coincident with MCS lines 3 and 5 (top 7 km of the crystalline basement), and previously derived velocities from local earthquake studies [*Abers*, 1994] and laboratory measurements on rocks (lower crust and uppermost mangle

[*Christensen and Mooney*, 1995]). Interpolation between all MCS profiles yields a 3D model representing the geometry of the entire plate interface beneath the eastern AASZ, which provides us with a unique insight into possible controls, in form of geometrical irregularities, on along-strike rupture organization of this 500 km long seismically segmented megathrust region. Our key observations are as follows:

1. The ALEUT PIM has minimum depth of 5 - 7 km below the sea surface at the trench and maximum depth of ∼65 km at the northeastern landward corner of the study area. Viewed from offshore, the model shows a gentle convex shape that is centered at the middle of the Semidi Segment for distances 0 to 125 km landward from the trench. Further landward, from 125 to 225 km, the apex of the model is shifted to the eastern part of the study area. The megathrust flattens at the very landward end ($>$ 250 km) of the model.

2. From 0 - 20 km landward from the trench, the downgoing Pacific Plate subducts at a low dip angle of 3° - 5°. Farther landward, Lines 3, 5 and 6 show a landward increase in dip angle of the plate interface over their entire lengths reaching 14° - 16° at their ends. For Lines 1, 2 and 4, although there is an overall increase in plate interface dip angle in the landward direction, shallowing and deepening sections alternate with the most landward profile sections reaching dips of 19° - 25°. These variations in the dip angle both downdip and along strike are indicative of significant topography of the plate interface imprinted on its overall gently arching structure.

3. We highlight the morphology of the plate interface by subtracting the Slab1.0 plate interface model [*Hayes et al.*, 2012] from the ALEUT PIM. At 0 to 50 km from the trench, the residual topography map of the plate interface shows only small deviations between the two models of up to ±2 km. From 50 to $>$ 250 km the depth variation between the two models is moderate and smooth ($<$ ±3 - 4 km), with an exception of two places with greater (up to ∼6 km) and more abrupt differences. Based on their geometrical characteristics, and their alignment with the trajectories of incoming Kodiak-Bowie and Patton-Murray seamount chains, we interpret the two imaged plate interface crests as subducted seamounts.

4. The locations of the two elevated highs coincide with the segment boundaries in the study area as inferred from aftershocks [*Benz et al.*, 2011; *Davies et al.*, 1981; *Estabrook et al.*, 1994; *Nishenko and Jacob*, 1990; *Sykes*, 1971], indicating that the subducted seamounts generally act as barriers to megathrust rupture propagation. The crested barrier between Semidi Segment and Shumagin Gap seems to have

impeded along-strike rupture propagation of two earthquakes on either side of it. The epicenter of the M_S 7.9 1917 earthquake is located west of the barrier in the Shumagin Gap and the M_W 8.2 1938 epicenter is located east of it within the Semidi Segment. Both occurred at the deep end of the seismogenic zone $>$ 150 km away from the trench and both were unilateral with the 1917 earthquake rupture propagating to the southwest and the 1938 event rupturing toward the northeast where it was stopped at the crested barrier between the Kodiak Asperity and Semidi Segment. Similarly, the M_W 9.2 1964 Good Friday earthquake was generated in Prince William Sound and propagated unilaterally in the southwest direction until it could not propagate through the crested barrier between the Kodiak Asperity and Semidi Segment.

5. If the primary factor influencing megathrust partitioning is the plate interface morphology, as inferred here for the eastern AASZ, then the general pattern of megathrust rupture segmentation are likely to persist over many earthquake cycles, until current major morphological features on the subduction thrust move out of the way (subduct) and new ones develop. However, there may be occasions where earthquakes overcome these long-term barriers and propagate through into neighboring segments, as may have been the case with the 1788 and 1847 events [*Soloviev*, 1990] that may have ruptured shallow parts of the plate interface located seaward from the imaged barriers.

6. Geologic features and processes on the incoming Pacific Plate such as fracture zones, crustal fabric, sediments, faulting, serpentinization and dewatering are known to influence seismicity and plate coupling at the eastern AASZ [*Bécel et al.*, 2015; *Li et al.*, 2018; *Shillington et al.*, 2015]. However, their effect appears to vary gradually in the along-strike direction and thus they are unlikely to form barriers to rupture propagation that define segmentation.

7. The low coupling areas in the region's plate locking model [*Li and Freymueller*, 2018] coincide with the two imaged crest-like structures. This supports *Wang and Bilek* [2011] who proposed that the subducted seamounts decrease interplate coupling by fracturing and thus weakening the upper plate structure. No structures can be related to the weakly coupled western Shumagin Gap. However, the southwestern crest-like feature likely represents the trailing end of the subducted Patton-Murray seamounts which had to cross the Shumagin Gap, possibly leaving behind damaged and reworked rocks in the overriding crust and a weak plate

interface long after. Another possibility is given by *Bécel et al.* [2017] and *Li et al.* [2018] who suggest that heterogeneity from weakly sedimented and faulted promotes creeping movements of the Shumagin Gap. A hypothetical explanation for the modeled weak coupling in the Shumagin Gap by the existence of an old transform fault crossing the overriding crust was discarded when no spatial correlation between them was found. This transform fault was formed by convergence or strike-slip motion between the Kula and North American plate and marks a major change in the nature of the overriding plate from continental crust east of the fault to oceanic crust to its west. Rocks of the overriding crust along this major transform fault should be characterized by similar heterogeneity and result in weakening of the upper crust plate interface, similar to that caused by passing of subducted seamounts, but its impact to rupture propagation remains unclear.

The presented work may impact new regional seismic hazard assessments because it indicates that the future megathrust earthquakes in the eastern AASZ are in most cases likely to stick to the same pattern of ruptures over many impending earthquake cycles.

Chapter 4

Variations in reflection signature and slip behavior of the subduction interface offshore Alaska Peninsula from -161° E to -152° E

4.1 Abstract

Determining the spatial distribution of seismic slip behavior at subduction zones is a key factor for estimating the size and location of future megathrust earthquakes. Subduction interfaces prone to earthquake rupture generation and propagation can extend to great depths, which makes them difficult to investigate, resulting in a lack of detailed information about these plate interface zones. Here, we present deep penetrating multichannel seismic reflection data from the ALEUT project to characterize the plate interface up to depth of $>$ 65 km on a network of profiles covering an area of $\sim$130,000 km^2 area offshore the Alaska Peninsula, we correlate variations in their reflection signature to 1) seismogenic, 2) conditionally stable, and 3) aseismic slip behavior. Similar observations were made in several warm subduction zones worldwide. The eastern Alaska-Aleutian subduction zone (AASZ) is the first colder subduction zone, where the seismogenic behavior of the thrust fault plane is characterized based on its plate interface reflection signature. Our results confirm the spatial extent of rupture areas derived from existing information, such as aftershock locations, inverse tsunami waveform modelling and the intersection of a serpentinized mantle wedge. However, contrary to recent geodetic dislocation models that suggest a widely free slipping Shumagin Gap, our results show a seismogenic plate interface for this area that extents from the trench up to $\sim$100 km landward. A partially seismogenic Shumagin Gap area could become part of a great megathrust event, as rupture propagates into the area, as might have happened in the 18$^{\text{th}}$ and 19$^{\text{th}}$ century, and exposes it to strong ground shaking with the potential to create large tsunami waves.

(262 words)

4.2 Introduction

At subduction zones, lithospheric plates converge along a contact fault known as the megathrust, subduction thrust, or plate/interplate interface. Strong mechanical connection can develop between the two plates that form a megathrust, resulting in storage of great amounts of elastic strain energy. When this connection breaks, the two plates slip past each other in opposite direction releasing vast amounts of seismic energy in an event called megathrust, subduction, or great earthquake. These events are the largest and most destructive earthquakes on Earth reaching magnitudes of 8-9 and above.

During megathrust earthquakes, intense shaking can lead to tsunami generation offshore and strong ground movements onshore. While tsunamis often cause the greatest loss of life in such disasters, the intense ground movements, and in some cases liquefaction effects and ground failure, also endanger coastal populations and can cause extensive damage to buildings and infrastructure at nearby settlements and cities. The larger the megathrust earthquake magnitude, which is proportional to the plate interface rupture area, slip, and friction [*Scholz*, 2002] and the nearer the rupture is to the coast, the larger and longer the onshore ground movements will be [*Petersen et al.*, 2002]. Therefore, to better mitigate seismic hazards at coastal communities and urban centers close to subduction zones, it is crucial to reduce uncertainties in probabilistic seismic hazard maps by improving constraints on the maximum magnitude and the maximum landward extent of rupture along the megathrusts.

Various types of earthquake slip mechanisms are observed in subduction zone settings from 0 to $>$ 600 km depth, but the source of the megathrust earthquakes is confined to a narrow part of the entire subduction boundary fault where unstable stick-slip behavior is dominant, and thrust earthquakes can nucleate [*Scholz*, 2002]. This shallow part of the plate boundary fault that is capable of storing elastic strain energy is called the seismogenic zone, and it extends within the depth range of approximately 5 to 45 km [e.g., *Oleskevich et al.*, 1999; *Ruff and Kanamori*, 1983; *Saffer and Marone*, 2003; *Scholz*, 2002; *Tichelaar and Ruff*, 1993]. Earthquake thrust rupture, however, is not restricted to this part of the fault but can propagate into transitional zones of conditionally stable slip behavior to a limited extent up- and down-dip from the seismogenic zone. Parts of the fault where plate thrust motion is completely accommodated by ductile deformation or, where they slip

freely are considered aseismic. Rupture cannot propagate or nucleate in aseismic zones, which are usually located at the shallowest part of a megathrust fault, near the trench, and/or down-dip of the seismogenic and transitional zones. The seismogenic part of the fault is considered to be (at least partially) locked or coupled between the subducting and overriding plate and thus accumulating elastic strain energy supplied by converging plate motion over decades or even centuries before it breaks and the energy is released in form of an earthquake. Because the size of an earthquake is strongly linked to its slip area, estimating the maximum expected magnitude of a megathrust earthquake requires constraining the spatial limit of its seismogenic zone, as well as its conditionally stable zones in along-strike and up- and down-dip direction.

Two basic mechanisms have been proposed to explain the seismogenic up-dip limit: 1) a change in the frictional behaviour from stable to unstable slip within the fault zone; either due to thermally controlled transformation of clay minerals [e.g., *Hyndman et al.*, 1997; *Vrolijk*, 1990] or due to diagenesis the sedimentary rocks and the reduction of fluid pressure [*Moore and Saffer*, 2001], and 2) a change of the location of the plate boundary thrust fault from the aseismic décollement into the basement basalts due to lithification and hardening of the underthrust sediments [*Matsumura et al.*, 2003] or reactivation of a roof thrust, which is abandoned during underplating [*Kitamura et al.*, 2005]. The seismogenic down-dip limit may be defined 1) thermally, when a certain temperature is reached and the rocks start to deform plastically [e.g., *Hyndman and Wang*, 1993; *Savage et al.*, 1991; *Tichelaar and Ruff*, 1993], or 2) when the subduction thrust encounters the weak aseismic slipping overriding forearc mantle wedge [e.g., *Peacock and Hyndman*, 1999; *Ruff and Tichelaar*, 1996]. The seismogenic part in warm subduction zones, characterized by a subducting young, hot and buoyant oceanic plate, seemed to be controlled in downward direction by the temperature limit, whereas in colder subduction zones, with older and denser downgoing oceanic plates, it is probably defined by the intersection with the mantle forearc wedge.

From a geological perspective, the hanging wall and footwall of megathrust faults are composed of sheared upper and lower plate material, respectively, and subducted sediments that form some tens to thousands of meters thick deformation zones [*Angiboust et al.*, 2011; *Rowe et al.*, 2013]. This complex fault zone structure of variable width seems to develop geologic texture that is parallel to the slip direction and is known to be reflective [e.g., *Jones and Nur*, 1984], allowing for its

detailed imaging using controlled source seismic methods. Major variations in the seismic reflection nature of the plate interface have so far been observed at several subduction zones, including northern Cascadia [*Nedimović et al.*, 2003], Alaska [*Fisher et al.*, 1989; *Li et al.*, 2015; *Moore et al.*, 1991], south Chile [*Buske et al.*, 2002; *Groß et al.*, 2008] and southwest Japan [*Kodaira et al.*, 2002, 2005; *Kurashimo et al.*, 2013; *Sato et al.*, 2005]. These changes in the megathrust reflection character may provide means to map down-dip limits of the seismogenic zone at subduction thrusts at unprecedented spatial resolution because it is likely that the brittle (sudden and seismic) and the slow-slip (lasting and aseismic) deformation, being vastly different physical processes, embed a different fault zone structure into the surrounding rock mass with different reflection signatures.

At the northern Cascadia subduction zone, the location of the seismogenic down-dip limit of the megathrust fault was interpreted at the transition from a relatively shallow thin seismic reflection expression of the plate interface to a broader band of reflections found deeper. This transition in the plate interface reflection character correlates with the modeled slab temperature increase that is thought to induce changes in the rheological behavior from brittle to ductile [e.g., *Hyndman et al.*, 1997]. Moreover, the areal distribution of the thick reflection band correlates with the spatial extent of the episodic tremors and slip [*Nedimović et al.*, 2003]. The incoming oceanic slab temperature is a key parameter in subduction zones that appears to not only control seismic slip behavior [e.g., *Oleskevich et al.*, 1999] but also slab geometry (e.g. subduction dip angle) and metamorphism of the subducting slab and surrounding material. Therefore, a similar interpretation to that done for northern Cascadia should be applicable to south Chile and southwest Japan because these regions, like northern Cascadia, are warm subduction zones where very young and hot oceanic lithosphere subducts and, thus the change in the thermally controlled brittle to ductile deformation behavior occurs at a relatively shallow depth of less than 40 km [*Syracuse et al.*, 2010].

The oceanic lithosphere that subducts beneath the eastern Alaska-Aleutian subduction zone (AASZ), in contrast, is of intermediate age (ca. 50 Ma old) and relatively cool, thus the transition from brittle to ductile behavior occurs at a much greater depth of around 80 km [*Syracuse et al.*, 2010]. And yet, despite the large disparities between warm and cold subduction environments, similar thickening of the subducting plate interface reflections has been observed at the eastern AASZ [*Fisher et al.*, 1989; *Li et al.*, 2015; *Moore et al.*, 1991]. While these observations

come from three individual profiles 700 - 800 km apart and were collected by three different surveys, they raise major questions such as: (1) Is the down-dip variation in the megathrust reflection signature omnipresent in the AASZ? (2) Can this change in the megathrust reflection signature be used to infer the down-dip limit of interplate coupling at the AASZ? (3) What are the possible geological causes for the widening of the megathrust reflection band at cold subduction zones?

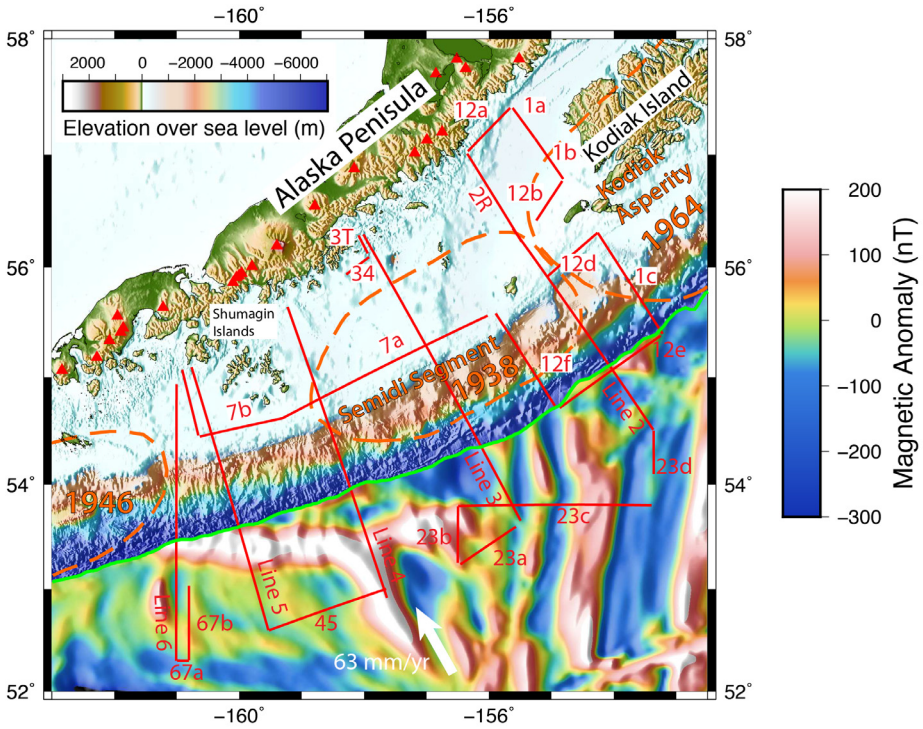

Figure 4.2.1: ALEUT survey area with red lines representing the location of MCS reflection profiles. Green line represents the location of the Aleutian deep sea trench. Magnetic anomalies of the incoming Pacific Plate are shown southward of the trench and topography of the overriding North American Plate north of it. Dashed orange lines show the rupture extent of tectonic segments derived by *Sykes* [1971] and *Benz et al.* [2011] with the name of the segment or the year of the rupture. The red triangles show the location of active volcanoes along the arc.

We use all 17 multichannel seismic (MCS) profiles, covering shelf, slope, trench and outer rise area, from the Alaska Langseth Experiment to Understand the megaThrust (ALEUT) (Fig. 4.2.1) in an attempt to answer these questions. The ALEUT regional MCS survey covers an area spanning ∼130,000 km^2, from south of Kodiak Island to the western Shumagin Islands. This large area is ideal for our investigation because it shows variable megathrust coupling in the down-dip direction, but also in the along-strike direction from almost fully locked at the Kodiak Asperity and eastern Semidi Segment to a nearly free slipping section

beneath the western Shumagin Gap [*Fournier and Freymueller*, 2007; *Li and Freymueller*, 2018]. Moreover, availability of other independent constraints on the megathrust coupling and the determination of the seismogenic down-dip limit in the study area from, for example, aftershock distribution, slab temperature modelling, dislocation modeling of geodetic data, and low frequency earthquake and associated tectonic tremor event distribution makes it possible to ground truth our interpretation based on the plate interface reflection signature.

4.3 Tectonic setting and megathrust seismicity in the ALEUT survey area

The overriding continental crust at the eastern AASZ is part of the Alaska mainland that has been formed through the accretion of three large terranes during the Paleocene [*Lizarralde et al.*, 2002; *Scholl et al.*, 1986; *Worrall*, 1991]. This rock complex builds up an unusually wide continental shelf (200 - 250 km wide) and is composed of deep marine sediments intruded extensively by Tertiary granitoid plutons and overlain by basinal deposits of Late Cenozoic age [*Plafker and Berg*, 1994].

The incoming oceanic plate subducts nearly orthogonally beneath the continental crust with a convergence velocity of ca. 63 mm/year [*Sella et al.*, 2002]. It consists of intermediate age crust that was formed ca. 50 - 55 Ma ago resulting in a uniform thermal regime at the down going subduction thrust fault. A change in oceanic plate fabric orientation is indicated by the magnetic signature of a fossil triple junction at ca. -158° E close to the trench (Fig. 4.2.1) [*Engebretson*, 1985; *Lonsdale*, 1988]. The plate fabric east of this point, produced by the Kula - Farallon ridge with intermediate spreading rates, is orientated at a highly oblique angle (up to 70°) relative to the trench near Semidi Segment. In contrast, oceanic crust west of the triple junction originated from the fast spreading Kula-Pacific ridge and its fabric forms a 10° - 25° angle with the trench at the Shumagin Gap [*Shillington et al.*, 2015]. The almost trench-parallel plate fabric orientation offshore Shumagin Gap appears to facilitate reactivation of preexisting crustal faults and results in enhanced bend-related faulting at the outer rise [*Masson*, 1991; *Shillington et al.*, 2015]. There, the fault offsets at the seafloor of up to 250 m form an oceanic basement topography that is heterogeneous landward of the outer rise leading to a rough subducting plate interface. In contrast, the highly oblique plate fabric

orientation offshore Semidi Segment results in reduced bend-related faulting which, combined with a thicker layer of sediments in this area, leads to a smoother (more homogeneous) subducting seafloor topography.

Sediments on top of the crystalline oceanic basement vary along-strike in composition and thickness. Whereas oceanic crust offshore Semidi Segment is covered by ca. 1-1.5 km thick deposits that originate from both pelagic sources and the terrigenous Zodiac sedimentary deep sea fan [*Stevenson and Embley*, 1987; *Stevenson et al.*, 1983], the ca. 0.5-km-thick sediment cover farther southwest and offshore Shumagin Gap is thought to consist only of pelagic sediments [*Creager et al.*, 1973]. The top of the earlier deposited Zodiac sediments is characterized by a high-amplitude reflection that can be traced below the frontal prism in seismic reflection sections [*Li et al.*, 2018; *Von Huene et al.*, 2012] with the upper pelagic sediments accreting to the overriding plate. The older Zodiac fan sediments, originally deposited on the incoming oceanic plate, are assumed to have entered the subduction zone ca. 3 Ma ago and since that time, assuming present day plate convergence velocities, traveled ∼200 km down-dip into the subduction zone.

Both features, topography of the oceanic basement and thickness of the sediment cover are thought to be key elements that affect interplate coupling and megathrust seismicity at the AASZ [*Bécel et al.*, 2017; *Li et al.*, 2018]. Slab temperatures are expected to be relatively cool for the eastern AASZ ($<$ 100 °C within 30 km landward of the trench [*Syracuse et al.*, 2010]) and therefore fluid release is expected to come from disequilibrium sediment compaction rather than dehydration reactions at the shallow part beneath the forearc crust. Thick sediment layers, such as observed offshore the Semidi Segment, are likely to exhibit relatively high pore fluid pressure once they subduct because 1) they can store more fluids, 2) the vertical drainage paths are longer and 3) a thicker sediment package results in lower porosity and thus lower permeability [*Saffer and Bekins*, 2006]. Short vertical drainage paths within thin sediment layers and abundant seafloor irregularities associated with bend-related faulting, as observed in the Shumagin Gap area, allow for enhanced lateral dewatering drainage and lead to lower pore-fluid pressure at the plate interface.

As the sediments within the subduction channel consolidate and dewater with greater depth they form a broad and relatively uniform plate interface that allows nucleation and seismic slip of large to great earthquakes [*Li et al.*, 2015; *Ruff*, 1989].

This is in agreement with the megathrust slip pattern observed at the Semidi Segment, which is overall characterized by infrequent seismicity and very few large M ∼7 to great M > 8 earthquakes. At the Shumagin Gap, in contrast, where creeping slip motion of the plate interface is assumed, abundant low-magnitude seismicity is observed, especially at depths > ∼25 km, but no large or great earthquakes have been instrumentally recorded [*Abers et al.*, 1995; *Davies et al.*, 1981].

4.4 ALEUT survey

The primary goal of the ALEUT project is to map the seismogenic down-dip extent of the megathrust in the eastern AASZ by means of the seismic reflection method. To achieve this goal nearly ca. 3700 km of near-incident 2D multichannel seismic (MCS) data and two ca. 350-km long wide-angle ocean bottom seismometer (OBS) profiles were acquired during a 5-week cruise with the R/V *Marcus Langseth* in summer 2011 (Fig. 4.2.1). The survey area is located between Kodiak Island (153° W) and the Shumagin Islands (161° W) offshore the Alaska Peninsula encompassing three tectonic segments along the AASZ: the Kodiak Asperity in the east that ruptured as part of the 1964 Good Friday earthquake, the Semidi Segment in the central part, which has last ruptured in 1938, and the Shumagin Gap in the west, which is believed to be weakly coupled to freely slipping and has not ruptured in a great > M 8 earthquake in at least the last 150 years [*Davies et al.*, 1981]. Of the long (100s of km) MCS profiles, six are trench-normal and extend from the Pacific Plate seaward of the trench to close to the Alaska Peninsula coast, and one is trench-parallel and extends across the continental shelf near the shelf break covering much of the study area. The OBS profiles are coincident with MCS Lines 3 and 5 that cross the highly coupled Semidi Segment and the weakly coupled to freely slipping Shumagin Gap, respectively.

4.5 Data Analysis

4.5.1 Processing of MCS data acquired in the eastern part of the ALEUT survey area

MCS data for profiles 1a, 1b, 1c, 12a, 12b, 12d, 12f, 2, 2R, 3, 3T, 34, 7a, 7b were processed at Dalhousie University. Processing steps included 1) enhancement of signal-to-noise ratio by removal of very low frequency signals ($<$ 2 Hz), amplitude downscaling of abnormally high amplitude peaks and frequency band limited noise suppression (2 - 4 Hz), 2) an offset dependent spherical divergence correction to counteract amplitude loss due to geometrical spreading and a surface consistent amplitude correction to remove inconsistencies caused by variations in shot strength and/or receiver sensitivity, 3) removal of seafloor multiples by both Surface Related Multiple Elimination (SRME) and Radon transformation, 4) velocity analyses, normal move out (NMO) removal and stacking, 5) pre- and poststack predictive deconvolution to reduce signal reverberations and 6) 2D Kirchhoff post-stack time migration to collapse diffraction hyperbolas and correct for misplaced dipping reflections. Furthermore, the MCS data were collected by two streamers, both towed at different depth (12 and 9 m) to enhance recording of both low and high frequency signal content to achieve highest resolution for sedimentary upper crustal structures as well as for deep reflections within the lower crust and upper mantle. Both processed seismic sections for each line were combined into one final section to benefit from enhanced high, as well as low, frequency content. The processing sequence was the same for all lines. The greatest challenge during data processing was the removal of seafloor multiples that overlap in two-way travel time with the plate interface reflections across the slope region. Despite successful multiple suppression, slope parts of the reflection sections remain a challenge to interpret because of residual multiple noise that in some cases is spread across the image by migration, thus complicating clear identification of plate interface reflections difficult. Nevertheless, it is still possible to identify the plate interface reflections even if the slope area and the character and amplitude of these reflections clearly changes down-dip. In general, the continuity of the plate interface reflection signal is only occasionally interrupted by a weaker signal-to-noise ratio at some places, especially along the slope and at great depth.

4.5.2 Processing of MCS data acquired in the western part of the ALEUT survey area

MCS data for profiles 4, 5, 6 were processed by our collaborators at the Lamont-Doherty Earth Observatory (LDEO) of Columbia University in New York City. The processing steps applied at LDEO are basically identical to the ones applied at Dalhousie University except that colleagues at LDEO added the LIFT method [*Choo et al.*, 2004] to further reduce noise, and used slightly different module parameters for SRME followed by an amplitude balancing procedure to equalize background noise [*Li*, 2016]. However, most processing steps were applied with the same module parameters at both institutions. Reduction of reverberations using predictive deconvolution of prestack and poststack data, for example, was applied to all of the data using identical parameters (filter length 360 ms and prediction lag length 32 ms). Therefore, the character of the plate interface reflection signal is comparable on all ALEUT profiles.

4.5.3 Time to Depth conversion of MCS sections

All processing steps described in 4.5.1 and 4.5.2 were applied to the seismic data in two-way travel time (seismic signals have return travel paths, first going from the seismic source to the reflector and then back to a receiver) resulting in fully processed and post-stack migrated seismic sections in time domain. Several geometrical artifacts are linked to seismic reflection sections in time domain, such as pull-up structures, incorrect dipping angles, and a deceptive presentation of layer thicknesses. To circumvent these problems and to extract quantitative and geologically meaningful information we built velocity models and used them to convert our reflection sections from time into depth domain. Individual velocity models for each ALEUT MCS reflection section used for the time-depth conversion are based on MCS stacking velocities for sedimentary structures, tomographic inversion of OBS first arrivals for the upper crust, and available information from the literature for the lower continental crust and uppermost mantle. For a more thorough description of the construction of these velocity models, please refer to Chapters 2 and 3 of this thesis.

4.6 Results

4.6.1 Imaged reflection structures and their possible geologic origin

Structures commonly imaged in subduction zone settings are also observed on the processed, time migrated and depth converted ALEUT profiles (e.g. Fig. 4.2.1, Appendix B). The shallow, upper ∼2 km below the seafloor of the seismic sections exhibit mostly continuous flat lying and sub-horizontal reflection events that are characteristically produced by sedimentary layering. From this, we infer that the continental shelf is in general covered by a thin sediment blanket with an average thickness of ca. 0.2 km and a maximum thickness of ca. 1 km below an average water depth of ca. 150 m. ALEUT Lines 2 and 5 are an exception as they each show an up to 5-km-thick sedimentary forearc basin located near the shelf break. The continental slope is 80 - 100 km wide on all trench-normal profiles and shows sedimentary deposits covering highly irregular basement structures. The top of the crystalline basement across the slope is challenging to image and so determining the sediment thickness in this area is difficult. We observe ∼0.5 - 0.7 km thick sediment cover on top of the oceanic basement of the incoming plate, with an exception of Line 3, which exhibits a sediment thickness of ∼1 - 1.5 km seaward of the trench.

The Pacific Plate enters the subduction zone at the deep-sea trench in a water depth of ca. 4 - 5.5 km. We observe a wide range of intracrustal continental, interplate, and oceanic and continental Moho reflections beneath the slope and shelf that jointly exhibit varying degrees of dip, signal strength and reflection character. Reflections thought to arise from the shallow plate interface allow for tracing the decollement continuously 20 - 30 km landward from the trench on all margin-normal profiles (Fig. B.2 - B.6, B.9, B.10). Farther down-dip, a mostly continuous landward dipping reflection band, thought to originate at the interplate interface, can be traced to a maximum depth of more than 60 km close to the coastline (Fig. 4.6.1, 4.6.2, B.3). At some places, we also image reflections parallel to but 6 km deeper than those inferred to arise at the plate interface (here interpreted to be located at the center of the reflection band), which we interpret as an oceanic Moho reflection (e.g., Fig. B.2, B.4 - B.7, B.12). Moreover, we observe ∼10 - 20-km-long and 2 - 4-km-thick bands of what seem to be continental Moho reflections at ca. 40 km depth that dip seaward and seem to intersect with the reflections arising at the subduction interface (Fig. B.2 - B.6, B.8, B.15). Various high-amplitude reflections

are located within the upper continental crust at ∼15 - 30 km depth at ∼150 - 200 km distance landward from the trench. However, these intracrustal reflections apparently do not seem to be related to any major tectonic boundary identified at the surface (Fig. B.2 - B.7).

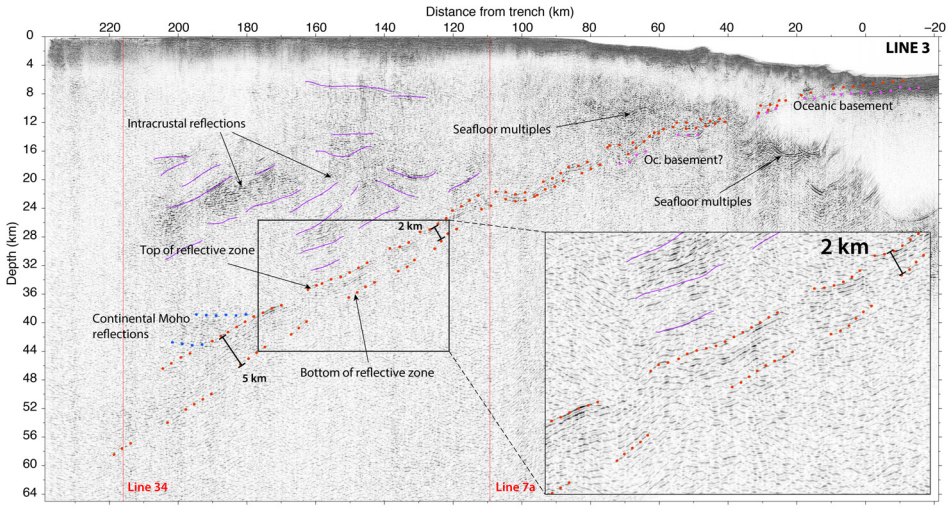

Figure 4.6.1: Trench-normal ALEUT MCS reflection profile of Line 3 and highlighted structural interpretation. The extent of the plate interface reflection band is shown by two red dotted lines, representing top and bottom of the deformational shear zone. Short blue dotted lines at the landward end of the profile encompass the reflection package from the continental forearc Moho. Magenta colored dots below the plate interface near the trench represent the top of the oceanic basement that is overlain by a thick layer of sediments. Thin purple lines highlight strong continental intracrustal reflectors. Red thin vertical lines show intersection points with other ALEUT profiles (see Fig. 4.2.1). Inserts is a detail of the area that shows the broadening of the plate interface reflection band from thin (< 2 km thick) to thick (> 5 km thick).

4.6.2 Plate interface reflections

Seismic reflection signals coming from the inferred subducting plate interface are identified on all processed and depth converted ALEUT MCS sections (see Appendix A, Fig. 3.2). The inferred zone of plate interface reflections is observed on trench-normal profiles starting from approximately 6 - 7 km depth, below the trench fill, until a maximum depth of ∼65 km near the coastline of the Alaska Peninsula (Fig. 4.2.1 or Appendix B). Additional constraints on the location and thickness of the inferred plate interface deformational zone are provided by trench-parallel ALEUT profiles, and reflection signals from the oceanic Moho, which we interpret to be approximately 6 km below the top of the subducting oceanic crystalline basement. However, these Moho reflection signals are often not continuous and

could not be imaged on every profile. The tops and bottoms of the plate interface reflection zones are picked on all profiles where observed, as shown in Figure 4.2.1.

The seismic signature of the plate interface changes from relatively concise reflection signals in the shallow parts to a broadening band of reflections that reaches several kilometers in thickness at greater depth. We interpret this plate interface reflection zone to represent the extent of the megathrust damage zone formed by the subduction process. We subdivide the plate interface based on this reflection appearance into three categories: 1) thin, with thickness of the plate interface reflection band of up to 2 km, 2) transitional, with thickness between 2 and 5 km, and 3) thick, with a broad band of reflections that exceeds a thickness of 5 km (Fig. 4.6.2). Although this subdivision is somewhat arbitrary, it reflects the observation of the three distinctive parts of the reflection signature of the plate boundary fault zone: 1) a thin but laterally extensive shallow section of the megathrust, 2) a relatively laterally restrictive section of large progressive increase in vertical thickness of the megathrust, and 3) a developed thick megathrust section characterized by less defined reflection events and, in some instances, minor further increase in thickness as a function of depth. This quantitative characterization of the plate interface reflection band based on its appearance (especially its thickness) is similar to the interpretation made in other subduction zones [*Groß et al.*, 2008; *Kurashimo et al.*, 2013; *Nedimović et al.*, 2003] and from previous qork on a subset of this dataset from Alaska [*Li et al.*, 2015].

To facilitate regional analysis, the spatial extents of the thin, transitional, and thick plate interface reflection zones, as inferred on all ALEUT profiles, are projected onto a map view and shown in Figure 4.6.3. The maximum landward extent of the thin plate interface reflection zone shows a gradual decrease in the southwest direction. Line 12b, located at the northeastern end of the ALEUT survey area, displays thin plate interface reflection character at the greatest distance (∼175 km) from the trench. The end of the thin plate interface reflection zone and the beginning of the transition zone for Line 2 is at ∼149 km from the trench, with further decrease to 135 km on Line 3. The extent of the thin plate interface reflection zone for Line 4 is unclear due to our inability to continuously image megathrust reflections, but it must be at least ∼92 km wide and at most ∼118 km wide. For Line 5, the end of this zone is just ∼102 km landward from the trench and for Line 6, due to discontinuous imaging of the megathrust reflections, only the minimum width of ∼83 km is possible to constrain accurately. However, imaging of the thick band of

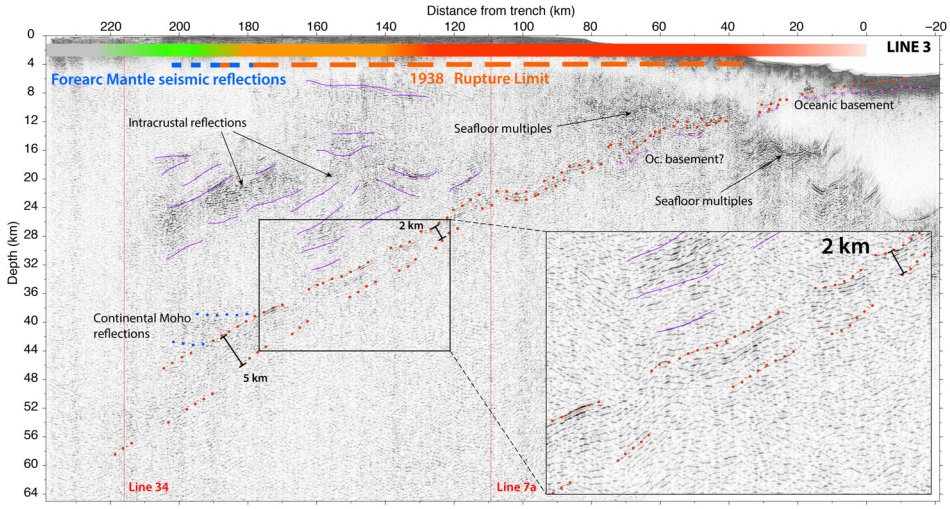

Figure 4.6.2: Line 3 reflection profile from Figure 4.2.1 with interpreted plate interface reflection character shown at the top of the section using a coloured horizontal bar: red represents thin (< 2 km), orange transitional (2 - 5 km), and green thick (> 5 km) band of reflections. Grey sections of the bar represent areas where no clear reflection signal from the plate interface could be identified. The spatial extent of past megathrust ruptures is represented by a thick horizontal dashed orange line. The thick horizontal dashed blue line shows the spatial extent of our interpreted continental Moho reflections. Red thin vertical lines show intersection points with other ALEUT profiles (see Fig. 4.2.1). Insert is a detailed zoom that shows the broadening of the reflection zone from thin (< 2 km thick) to thick (> 5 km thick) band of plate interface reflections.

reflections on this profile starting at ∼122 km landward of the trench does constrain the maximum landward extent of the thin reflection zone. Considering that the transitional zone has not been imaged on this profile but that where imaged on other profiles it is on average ca. 30 - 50 km wide, it is likely that the maximum extent of the thin plate interface reflection zone on Line 6 must also be < 100 km landward from the trench, similar to Line 5. Interestingly, despite the differences in the width of the thin plate interface reflection zone on various ALEUT profiles, the depth at which the thin zone ends is relatively constant on all profiles. It is ∼30 - 34 km for Line 12b and ∼28 km for Lines 2, 3 and 5. On Lines 4 and 6, the reflection signal diminishes at around 24 km depth so we cannot determine the exact depth for the end of the thin reflection zone.

4.6.3 Kodiak Asperity (Lines 1abc, 12abd)

Line 1 is the only trench-normal oriented profile that crosses the Kodiak Asperity, which is located at the southwestern end of the area that ruptured during the 1964 Great Alaska earthquake. The Trinity Islands, near the southern tip of Kodiak

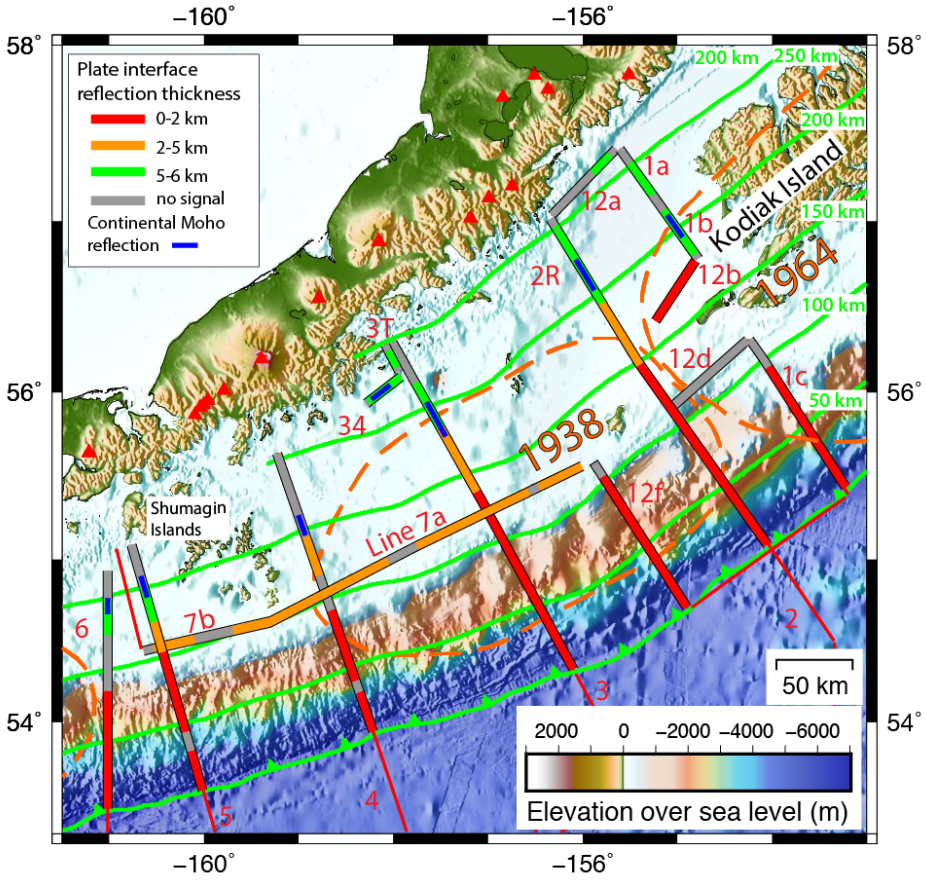

Figure 4.6.3: ALEUT survey area with plate interface reflection thickness presented in colour (see legend) for all MCS reflection profiles. The spatial extent of the thin (red), transitional (orange) and thick (green) plate interface interpretation for each profile is listed in Table B.1 in Appendix B. Green line with triangles is the trench location, green trench-parallel lines represent iso-distances to the trench at a 50-km-interval, and red triangles show the location of active volcanoes along the arc.

Island, are found along the path of Line 1 and had to be circumnavigated during marine data acquisition resulting in partitioning of this profile into three sections (1a, 1b, 1c) and a ca. 60-km wide gap in between Line 1b and 1c (Fig. 4.2.1). In the seismic reflection section of Line 1c, we observe a clear $<$ 2-km-thick signal arising at the plate interface from the trench to ∼93 km landward, where the signal to noise ratio becomes too weak to follow the interface for the remaining 20 km of the profile (Fig. B.9). Signal strength is low on Lines 1a and 1b, although clearly identifiable on Line 1b as a ca. 6-km-thick band of reflections between ∼178 - 214 km distance from trench and relatively weaker signals from ∼227 - 250 km on Line 1a.

Line 12a is located at the greatest distance from the trench ($>$ 250 km) of all the profiles, and it is oriented perpendicular to Line 1, and parallel to the coastline and

trench. It is directly connected to the northward end of Line 1a and exhibits the deepest signals interpreted to be reflected from the plate interface at ca. 65 km depth (Fig. B.11). This thick reflection band ($>$ 6 km), however, can be tracked over only $\sim$16 km. Line 12b, oriented almost perpendicular to Line 1 and connected to the southeastern end of Line 1b, is still within the Kodiak Asperity at ca. 160 - 170 km distance to the trench. We observe here the clearest signal from the plate interface for the entire ALEUT survey area imaged on the full extent of Line 12b in form of a 49-km long and ca. 1-km thick reflection signature that is located at 34 km depth but substantially shallowing to 30 km depth toward the west (Fig. B.12). Very strong and concise ca. 1-km thick reflections are also clearly observed 6 km below the inferred plate interface and are interpreted as the Moho reflection event. On Line 12d we observe no clear signals from the plate interface despite its relatively close distance to the trench (ca. 120 km distance) and expected shallow plate interface location. However, this does not come as a surprise because a drastic change in acquisition parameters has been applied on this line for much of the data acquisition as marine mammals have been encountered at close range to the research ship. As a protective measure, the energy released by the seismic source had to be significantly reduced by powering down to using only the mitigation gun, which had a very limited depth penetration power due to its small volume (40 cu. in. or more than two orders of magnitude less than the full airgun array used). The transition from thin to thick plate interface reflection at the Kodiak Asperity is not imaged but appears to be very narrow ($<$ 5 km) based on the megathrust reflection signal imaged on profiles 12b and 1b.

4.6.4 Semidi Segment (Lines 2, 2R, 12f, 3, 3T, 34, 4, 7a)

On the extended trench-normal ALEUT Lines crossing the locked Semidi Segment (Lines 2, 2R, 12f, 3, 4) we observe a gradual thickening of the plate interface reflection signal from around 1 - 2 km to 5 - 6 km thickness. On Lines 2 and 2R, at the northeastern end of the Semidi Segment, we image a distinct $<$ 2-km thick reflection for the first $\sim$149 km from the trench after which the reflections weaken for around 10 km before they strengthen again landward as a broader band of reflections $\sim$4 km thick, with increasing thickness in the down-dip direction (Fig. B.2). We interpret this section of the profile to exhibit a transition zone where plate interface thickness increases from $<$ 2 km to $>$ 5 km over a distance of $\sim$46 km.

The identification of the plate interface is impeded at around 150 - 180 km from the trench because of strong intracrustal reflections located near the inferred plate interface. However, strong oceanic Moho reflections can be traced some 6 km below and parallel to the inferred plate interface reflections providing additional constraints. A 5-to-6-km-thick plate interface reflective zone is observed from ∼195 - 249 km, but signal amplitudes are very weak. Between Lines 2 and 3 is a relatively short (∼120 km) Line 12f. A thin megathrust reflection package is imaged along the whole length of this profile (Fig. B.10). However, the eastern end of the margin-parallel Line 7a is located close to the landward end of Line 12f and also shows transitional megathrust reflection character (B.7). This suggests that the thickening of the plate interface reflection band likely occurs just landward of Line 12f.

Line 3 overall exhibits a strong and relatively continuous thin reflection package from the inferred plate interface from the trench to ∼135 km landward (Fig. B.3). Subsequently, a transitional zone is imaged from thin ($<$ 2 km thickness) to thick ($>$ 5 km) plate interface reflections between ∼135 and ∼184 km from the trench. Further landward the reflection band thickness gradually increases to ∼6 km at ca. 219 km from the trench, after which the signal from the plate interface is too weak to trace. However, only some 5 km west and parallel to the landward end of Line 3 is a very short (∼20 km) Line 3T, which shows that the thick reflection zone extends at least to almost 200 km landward from the trench (Fig. B.14). Lines 7a and 34 are positioned perpendicular to Line 3 and Line 7a crosses Line 3. These margin-parallel profiles provide additional information on the thickness of the plate interface reflections. Line 34 shows a thick reflection band similar to that observed on Line 3 (Fig. B.15). However, at the crossing of Lines 7a and 3, Line 7a shows a transitional ∼3-km-thick reflection band that is slightly thicker than the thin one ($<$ 2 km) imaged on Line 3 (Fig. B.7). The cause for this discrepancy is not known but it could be due to, for example, the uncertainty in interpretation of the images characterized by different signal to noise ratio or the anisotropic character of the reflection response from a thick and layered plate interface.

Line 4 shows a very distinct $<$ 2 km thick reflection signature of the plate interface from the trench up ∼92 km landward and a ∼5 km thick reflection band between ∼118 to 145 km landward from the trench. Between these profile sections are plate interface reflectivity gaps at ∼30 to 40 km and ∼92 to 118 km. No clear plate interface reflection signal could be imaged landward of the transitional zone at ∼145

km until the end of the profile. Thus, the transition zone from thin to thick plate interface reflection band is not constrained in both trenchward and landward directions. However, the intersection with Line 7a provides a constraint on the trenchward extent of the transitional zone in this area as a transitional reflection package is imaged on Line 7a just landward of the thin reflection package imaged on Line 4. Oceanic Moho reflections here also help to constrain the center of the plate interface band of reflections up to a depth of ∼28 km.

Line 7 (7a and 7b) is the only long profile in the ALEUT data set with trench-parallel orientation. Its total length is 325 km with Line 7a amounting for 235 km and Line 7b for 90 km. Line 7 is positioned some 100 km landward of the trench near the continental shelf break, where it crosses the central and western parts of the Semidi Segment (Line 7a) and changes its orientation slightly as it parallels the curvature of the trench and enters the central and eastern Shumagin Gap area (Line 7b). On Line 7a, we observe sub-horizontal reflections from the plate interface beginning at ca. 22 km depth in the east (0 km profile distance) and continuing westward with a slight increase in depth to ca. 24 km at the western end of the Semidi Segment at 200 km profile distance (Fig. B.7). The plate interface reflection signal character along this part of Line 7a is relatively uniform with a thickness of ∼3 km. Line 7a intersects trench-normal oriented Lines 3 and 4 within Semidi Segment. The imaged plate interface reflections at ca. 85 km profile distance are ∼ 3-km-thick and therefore slightly thicker than on the intersecting Line 3, which only has a ∼2 km thick reflection signature. On Line 7a at ca. 190 km profile distance, plate interface reflection band thickness is consistent at around ∼3 km, whereas the intersection point with Line 4 is located within a reflectivity gap between thin and transitional plate interface reflection bands. Oceanic Moho is imaged relatively consistently at its expected positioned ∼6 km below the plate interface and provides complementary information for delineating the plate interface location (Fig. B.4).

4.6.5 Shumagin Gap (Lines 5, 6, 7b)

The inferred plate interface on the two trench-normal oriented Lines 5 and 6 is imaged by a clear and distinct $<$ 2-km-thick reflection package almost continuously from the trench to ∼102 km on Line 5 and ∼83 km on Line 6 landward (Fig. B.5, B.6). On Line 5, the thin reflection package shows a narrow gap at ∼30 - 44 km

from the trench. Transitional zone on Line 5 is imaged from ∼102 - 125 km followed by ∼5-km-thick plate interface reflection package until ∼149 km from the trench. Landward from 149 km until the end of the Line at ca. 180 km from the trench the reflectivity of the plate interface is not captured by our survey. Interpretation of the plate interface is impeded at ca. 30 - 40 km depth, where the top of the transitional to thick plate interface reflective zone coincides with reflections from a splay fault system that intersects the plate interface and extends to the seafloor at ca. 80 km from the trench [*Bécel et al.*, 2017]. Oceanic Moho reflections ca. 6 km below the center of transitional reflection zone and reflections on the intersecting trench-parallel oriented Line 7b at ∼100 km distance from the trench provide some additional constraints to the plate interface location, although the signal strength on Line 7b is weak in this part of the profile (Fig. B.7). The section with the thin band of plate interface reflections on Line 6 is characterized relatively continuous reflections of the oceanic Moho some 6 km below. The reflection signal is lost from ∼83 - 122 km and reappears as a thick reflection band (∼5 km) with weak amplitudes from ∼122 - 148 km before the signal is lost until the end of the profile at ca. 170 km distance from the trench. Due to the lack of a transitional zone displaying gradual increase in the thickness of plate interface reflective zone from $<$ 2 km to $>$ 5 km, the end of a thin and the beginning of a thick reflective zone are not defined. The western part of Line 7a (∼200 - 235 km profile distance) and Line 7b (∼235 - 325 km profile distance) are oriented parallel at ca. 100 km distance to the trench, crossing the Shumagin Gap area from east to west (Fig. 4.2.1). Plate interface reflection characteristics remain consistent with those imaged across the Semidi Segment (eastern part of Line 7a) until ∼250 km profile distance. Westward of that distance, a slight increase in plate interface depth from ∼24 km to 28 km (at ∼310 km profile distance) is observed along-side thickening of the reflective zone to ∼4 km, a general decrease in signal strength, and discontinuous reflectivity.

4.6.6 Intracrustal reflections

Strong reflections within the upper continental crust are observed at approximately ∼100 - 200 km distance landward from the trench between ∼15 to 30 km depth. These intracrustal reflections tend to be horizontal or slightly dipping landward or even seem to be anticlinal at some places, for example on Line 2, 3, or 7 (Fig. B.2, B.3 and B.7). The depth range in which these reflections occur is at places close to

the location of the plate interface thus impeding clear identification of the megathrust location in these specific areas. The possibilities for improving recognition of these reflections include 1) using oceanic Moho to estimate where the top of the oceanic crystalline basement is, and therefore the approximate center of the plate interface reflection package (∼6 km above the oceanic Moho), 2) intersecting profiles that provide clearer distinction between plate interface and intracrustal reflections (e.g. Line 4 and Line 7a), or 3) interpolation/extrapolation of strong amplitude plate interface reflections up- or down-dip into areas where the imaging works less well.

Additionally, small reflection packages are observed at greater depth consistently in the entire survey area. On almost all ALEUT sections that sample deep crustal structures of the most landward part of the continental shelf, we observe short ∼10 - 20 km long reflection clusters seemingly intersecting the inferred plate interface at a depth range of ∼36 - 43 km (Fig. 4.6.4 and Fig. B.16 - B.22). The reflection clusters are, although covering a relatively short distance on the profiles, clearly identifiable as they exhibit a slight seaward dip, which contradicts the plate interface landward dipping angle, and encompass a ∼2 - 4 km thick package of reflections. Evaluation of these deep intracrustal reflections observed on Lines 1b, 2R, 3, 34, 4, 5, 6 (Table 4.1) shows a clear southwest to northeast thickening trend as the depth of the reflection package increases from ∼34 - 36 km on Lines 4, 5 and 6 in the southwest to ∼38 - 39 km depth on Lines 3, 34 and 2R in the northeast. Line 1b shows again reflections at a shallower depth of ∼34 km.

4.7 Discussion

4.7.1 Geologic meaning of thin and thick plate interface reflection bands and influence on their seismic slip behavior

The geological thickness of the plate interface at the eastern AASZ has been estimated by synthetic waveform modelling based on observations on MCS ALEUT Line 4 by *Li et al.* [2015]. Accordingly, thin plate interface reflections (reflection thickness of ca. < 2 km) are caused by a narrow low velocity zone (LVZ) of ca. 100 - 250 m thickness and thick plate interface reflections (up to 6 km thickness) by multiple LVZs with various thickness and spacing and a total thickness of ca. 3 - 5 km. During the numerical simulation of waveform modelling, the velocity within the

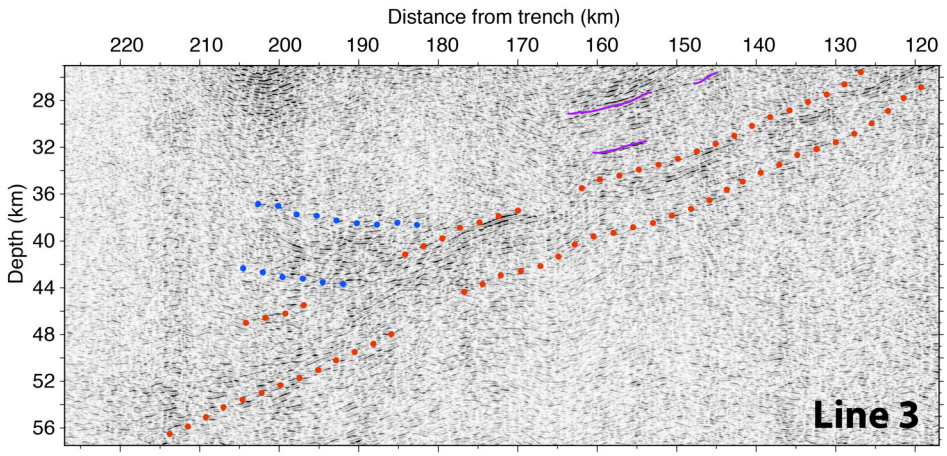

Figure 4.6.4: An example of continental Moho reflections near the subduction thrust fault. A zoomed part of MCS section from ALEUT Line 3 shows a clear, slightly seaward dipping reflection package (top and bottom encompassed by blue dots) that intersects with the landward dipping deformational zone (top and bottom encompassed by red dots) of the subducting plate interface. The top of the interpreted Moho reflections intersects the top of the plate interface reflection zone at ca. 39 km depth. Thin purple lines represent strong intracrustal reflections.

LVZ was set to 5 km/s and the background velocity to 6 km/s. ALEUT MCS data show a single and narrow reflection zone that mark the plate boundary in general between ca. 50 - 120 km distance from the trench up to a depth of approximately 30 km.

We relate changes in the structural appearance of the plate boundary fault and its seismic reflection band thickness, respectively, to its seismogenic behavior. Accordingly, the eastern AASZ is divided into different zones of inferred slip behavior (Fig. 4.7.1). This characterization is inspired by earlier proposed models of distinct radiation patterns for megathrust earthquakes nucleating at different depths, slab temperatures and distances from the coastline [e.g., *Lay et al.*, 2012; *Oleskevich et al.*, 1999]. *Nedimović et al.* [2003], provided a map of varying spatial seismogenic behavior for the warm Cascadian subduction zone. However, at the cold subduction zone at the eastern AASZ the controlling mechanism for the seismogenic behavior is likely different, despite a similar seismic appearance of the deformational zone of the plate interface.

4.7.1.1 Thin plate interface reflections

The thin reflection signal of less than 2 km thickness could be generated by a narrow, ca. 100 - 250 m thick zone of consolidated and highly sheared sediments

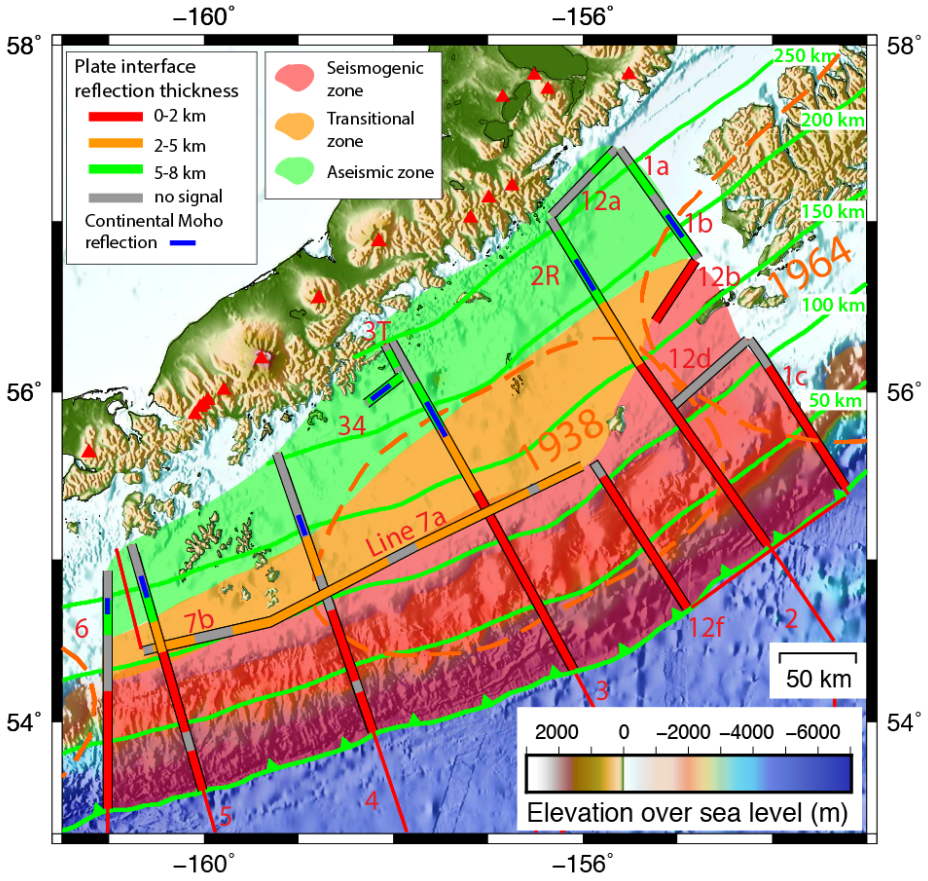

Figure 4.7.1: Seismic slip behavior in the ALEUT survey area based on plate interface reflection thicknesses. Green line with triangles is the trench location, green trench-parallel lines represent iso-distances to the trench in 50-km-intervals and red triangles show the location of active volcanoes along the arc. The seismogenic up-dip limit (red area) is not constrained by plate interface reflection thicknesses but is displayed here to extent all the way to the trench until better constraints are available.

[*Calahorrano et al.*, 2008; *Li et al.*, 2015]. The seismogenic behavior of this zone is strongly influenced by pore-fluid pressure emanating from compaction disequilibrium and low temperature clay dehydration reactions [e.g., *Moore and Vrolijk*, 1992; *Tobin and Saffer*, 2009] that vary considerably with depth [e.g., *Saffer and Tobin*, 2011]. The plate interface close to the trench at shallow depth consists of weakly consolidated sediments with low rigidity which are incapable of storing large amounts of elastic energy. These sediments experience rapid compaction with increasing depth that leads to the release of water and enhanced pore-fluid pressure, and low effective normal stress at this shallow part of the plate interface that, inhibit shallow seismicity [e.g., *Scholz*, 2002]. The thrust fault becomes seismogenic, as release of excess fluids tapers off with greater depth (e.g. 5 - 10 km depth or ca.

30 - 40 km distance from the trench) [e.g., *Bangs et al.*, 2004]. Thick sediment blankets form large asperities in the form of a homogeneous and coherent frictional unstable contact zone of reduced pore fluid pressure between the subducting and overriding plate, which extents to depths of 30 - 40 km and can rupture in great megathrust earthquakes.

The geologic nature of the shallow fault, exhibiting a thin seismic reflection zone, is thought to be a narrow concentrated zone of brittle deformation combined with highly sheared sediments in between the upper and lower plate [e.g., *Calahorrano et al.*, 2008; *Nedimović et al.*, 2003]. Support for this assumption comes from observations made on exhumed fossil plate interfaces that exhibit fault strands and ∼100 - 350 m thick deformation zone and is assumed to be of constant thickness until at least 15 km depth [*Angiboust et al.*, 2011; *Rowe et al.*, 2013]. Although the damaged and fractured zone might be several hundreds of meters thick the actual deformation during co-seismic slip is constrained to an individual narrow fault of just tens of centimeters thickness [*Rowe et al.*, 2013]. The thickness of the subducted sediment covering the oceanic crust might also contribute to size of the reflective zone that is associated with the plate boundary. At the eastern AASZ we observe relatively thin subducting sediment cover on top of the incoming oceanic plate with an exception of Line 3, where a maximum sediment layer of ∼500 m enters the subduction zone at the trench (Appendix A, Fig. A.5). Thickening of the plate boundary zone is observed down-dip of that zone in both, the seismic reflection images as well as on exhumed fossil plate boundaries, and are interpreted to be related to the change from seismic to aseismic behavior.

4.7.1.2 Thick plate interface reflections

Below ∼30 km depth gradual thickening begins where the reflection thickness increases from < 2 km to > 5 km. The length in trench-normal direction of this transitional zone is approximately 30 - 80 km wide and is observed on 4 out of 6 trench-normal profiles (Fig. 4.7.1). Discontinuities or weak reflection signals impede imaging efforts of this part on the remaining profiles. Because the incoming subducting oceanic lithosphere is relatively cold, the increase in reflection zone thickness is most likely not related to temperature induced ductile banding and dehydration reactions as suggested by *Nedimović et al.* [2003], who investigated the warm Cascadia subduction zone with an incoming young and hot oceanic plate.

Still, the appearance of seismic reflectivity of the inferred plate interface zone at the eastern AASZ has similarities, but also differences, to that imaged at Cascadia, south Chile or southwest Japan [*Groß et al.*, 2008; *Kurashimo et al.*, 2013; *Nedimović et al.*, 2003].

All of the above-mentioned subduction zones exhibit plate interfaces represented by thin $<$ 2 - 3 km and thick $>$ 5 - 8 km-thick reflection bands with the transition zones located at approximately 20 - 30 km depth [*Groß et al.*, 2008; *Kurashimo et al.*, 2013; *Nedimović et al.*, 2003]. However, the seismic reflectivity seems to be much higher at warm subduction zones and can easily be imaged up to more than 40 km depth despite inferior seismic acquisition equipment. The reflective zone at the eastern AASZ, in contrast, is characterized by weak reflections, especially at greater depth that makes it sometimes challenging to continuously trace top and bottom of the reflective zone to greater depth. At the Cascadia subduction zone, a broad (5 - 8-km-thick) highly reflective layer (so called "E-layer") is interpreted to be located just above the top of the subducting oceanic basement crust and acting as a current zone of aseismic slow slip and active deformation plate boundary [*Nedimović et al.*, 2003]. Similarly, the plate interface reflective zones at south Chile and southwest Japan are also interpreted to be located above the top of the subducting oceanic plate. But seismic reflection data from the eastern AASZ suggest that the reflective zone associated with the plate interface might include deformed material from both, the oceanic crust as well as the upper overriding crust as presented by Model B in *Bostock* [2013] (Fig. 4.7.2). Support for this interpretation comes from oceanic Moho reflections located some 6 km below the center of the plate interface reflective zone. If the reflective zone would be entirely above the oceanic crust, as observed in Cascadia or Chile, the oceanic Moho reflection would be located 2 - 3 km deeper, given a constant oceanic crust thickness of $\sim$6 km [*White et al.*, 1992]. Nevertheless, a clear and consistent trend to thickening of the plate interface is observed at around 30 km depth on all elongated trench-normal MCS ALEUT profiles.

The observed thickening of the deformational zone associated with the interplate boundary in cold subduction zones could be explained by: 1) Subduction erosion of material from the forearc crust that has been transported downwards, underplating subducted sediments and fragments of the oceanic plate to the overriding plate [e.g., *Calvert et al.*, 2006]; 2) Interlayering of different lithologies by fault branching and tectonic mixing as observed on exhumed fossil plate interfaces [e.g., *Angiboust et al.*, 2011]; 3) Increase in dip angle of the subducting plate that promotes stress and

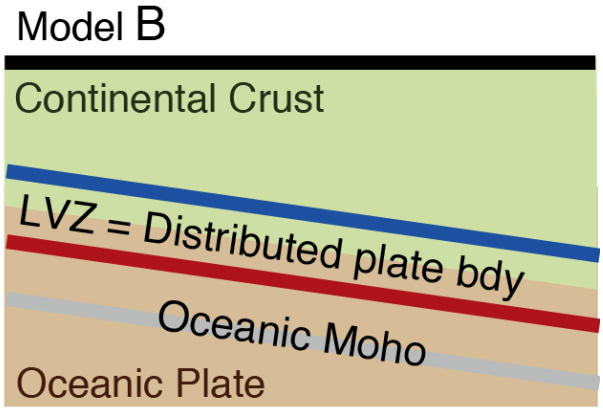

Figure 4.7.2: Schematic model of the plate boundary deformation zone (represented by a low velocity zone (LVZ)) after Figure 7 in *Bostock* [2013]. This model appears to best explain best our observations of the plate boundary reflective zone in the ALEUT MCS profiles (see Appendix B).

deformation on the upper overriding crust and on the subducting oceanic crust; 4) Dehydration processes and fluid release that increase the impedance contrast and result in enhanced seismic reflectivity in fractured, interlayered and/or underplated rocks [e.g., *Saffer and Tobin*, 2011].

1) Underplating of subducted material is a common process in subduction zones [e.g., *Matzel et al.*, 2004] and it has also been observed in the northeastern part of the AASZ [*Moore et al.*, 1991; *Sample and Moore*, 1987]. Although it has been suggested that this process could cause thick bands of reflections at several subduction zones [*Calvert et al.*, 2006], we do not think that this is the primary reason for the plate interface reflection thickening with depth. On exhumed fossil subduction thrust faults observations indicate underplating at discrete locations with varying degree of thickness and formation of the underplated material [e.g., *Bergh et al.*, 2012; *Konstantinovskaya and Malavieille*, 2011]. It seems therefore unlikely that the uniform and regional consistent thickening of the plate interface, that is observed at the eastern AASZ, is solely caused by tectonic underplating. Furthermore, an increase in plate reflection thickening with depth has been observed at several other subduction, thus it appears unlikely that underplating would occur on all of these consistently despite large variations in sediment input, plate convergence speed and other parameters.

2) Geologic evidence for a widening of the deformational zone that is associated with the interplate boundary has been found in an exhumed fossil subduction zone at the transition zone region between seismogenic and aseismic slip behavior at

approximately 30 - 40 km paleodepth [*Angiboust et al.*, 2011]. Field observations suggest that this zone exhibits highly sheared sediments, fault branches that cause interlayering of sediments, upper crustal material and serpentinite. In combination with the results from synthetic waveform modeling [*Li et al.*, 2015] and seismic reflection imaging, it seems that these structures that consist of a network of parallel or intersecting shearing zones with varying seismic velocities cause the thick band of reflections that are characteristic of aseismic slipping parts of the subduction fault. However, paleo-slab-temperatures at the fossil subduction interface are estimated to be $>$ 500 °C, which is several hundred °C higher than expected for 30 - 40 km depth at a cold subduction zone [*Angiboust et al.*, 2011]. However, a lower temperature mechanism that would cause fault branching and interlayering of subducted sediments with upper and lower crustal material has not yet been proposed.

3) We suggest a possible relation between the steepening of the subducting plate dip angle, usually observed at depth of around 25 - 30 km depth, and the beginning of thickening of plate reflections (transitional zone) as observed on trench-normal MCS ALEUT Lines 2, 3, 4 and less prominent on Line 5 and 6 (Fig. A.2 - A.11 in Appendix A). The most pronounced example is observed on Line 4 at a depth of $\sim$28 km and about 130 km distance from the trench (Fig. A.6 in Appendix A). Here the dip angle increases drastically from ca. 6 ° to 22 ° over a short distance of $<$ 20 km. The plate interface bending point coincides with the occurrence of a distinct band of high reflectivity of more than 4 km thickness. Rock masses of the overriding plate and the subducting plate interface experience a massive increase in normal stress as the subducting plate is forced against the overriding plate as a result of the sudden change of its dip angle. This zone would be susceptible to possible damage and fracture and might facilitate fluid transfer from the hydrated narrow plate interface into the damaged lower continental crust, therefore decreasing fluid-pressure along the fault plane and possibly changing its seismogenic behavior to further structurally weaken the overriding crust. While changing pore-fluid pressure has been invoked for a wide range of seismological observations along the seismogenic rupture fault [e.g., *Scholz*, 2002], its influence on promoting or impeding a wide range of slip behavior (e.g. earthquakes, seismic tremor, slow slip events) is not fully understood [e.g., *Fagereng and Ellis*, 2009; *Ito and Obara*, 2006; *Park et al.*, 2002]. By deformation the upper and/or lower crust, hydro-fracturing might affect pore-fluid pressure along the fault and result in a high permeability plate interface down-dip of subducting plate bending point that could control

seismic slip behavior between the plates [e.g., *Audet et al.*, 2009; *Kato et al.*, 2010]. However, without detailed information about seismic velocities and vp/ps ratio in that area, our attempts to explain its slip behavior remain speculative.

4) As sediments and oceanic crust are transported to greater depth and experience increasing pressure and temperature (p-t) conditions they undergo structural and geochemical changes that are often accompanied by the release of water (either by compaction or mineralogical dehydration). Compaction of sediments and the related fluid release is generally largest at ca. 3 - 7 km from initial burial [*Bekins and Dreiss*, 1992; *Bray and Karig*, 1985]. At larger depth and increasing p-t conditions, clay dehydration reactions at temperatures at ca. 60 - 150 °C [e.g., *Bekins and Dreiss*, 1992; *Bethke*, 1986; *Spinelli and Saffer*, 2004] as well as transition from shale to chloritide schists at temperatures of 100 - 225 ° C [e.g., *Kerrick and Connolly*, 2001] become a significant source of fluids. For the eastern AASZ the estimated slab temperature of the seismogenic down-dip limit in ca. 30 - 40 km depth is approximately between 120 and 180 °C [*Syracuse et al.*, 2010]. The above mentioned dehydration reactions could, therefore, contribute to the release of fluids that are migrating into the crustal surroundings promoted by deformed zones and fractures in the upper plate, where they change the impedance contrast and cause enhanced seismic reflectivity as well as seismogenic slip behavior.

4.7.2 Megathrust reflection package character and slip behavior along the plate interface at the eastern AASZ

Correlation between megathrust slip behavior and various thicknesses of plate interface seismic reflection packages has been observed at several warm subduction zones worldwide [*Groß et al.*, 2008; *Kurashimo et al.*, 2013; *Nedimović et al.*, 2003]. It has been interpreted by seismic reflection imaging that a gradual increase in thickness of the plate interface reflection band from relatively narrow ∼2 - 3 km to around ∼4 - 6 km thickness coincides with a change from seismogenic to aseismic slip behavior. While surveying the cold subduction zone offshore the Alaska Peninsula during the ALEUT project, we observe similar thickening trends of the plate interface reflection packages with increasing depths and distances landward from the trench. According to observations made at several warm subduction zones, we correlate reflection packages of varying thicknesses with portions of the plate interface that are capable of rupturing during megathrust events or that are slipping

freely and determine the extent of seismogenic slip areas and their down-dip limit in the ALEUT survey area. However, it should be noted that, especially at greater depths, the amplitudes of the lower boundary of plate interface reflection package are often weak and indistinct. I aim to encompass all notable reflections when defining the upper and lower boundary limit, but it might be possible that the thickness of the reflection package exceeds its interpretational boundaries at larger depths.

The spatial extent of thin, transitional and thick plate interface reflection character and their slip behavior, respectively, is visually interpolated based on the plate interface interpretation, as seen in seismic sections in Appendix B (Fig. B.2 - B.15) and its projection to map view in Figure 4.6.3, to generate a map of plate interface reflection package thickness and varying slip behavior for the entire ALEUT survey area (Fig. 4.7.1). The seismogenic zone (red colored area in Fig. 4.7.1) is characterized by packages of plate interface reflections with a thickness of up to 2 km and is constrained in landward direction by the onset of a transitional zone (orange) of 2 - 5 km thickness that exhibit conditionally stable slip behavior [e.g., *Lay et al.*, 2012]. The seismogenic up-dip limit has not been determined in this study. Although it is displayed to extend up to the trench, it should be noted that this might not be correct, as the shallowest part of the subduction thrust fault is often assumed to behave aseismically due to weak upper and lower plate material (e.g. unconsolidated sediments) and high pore fluid pressure along the fault [e.g., *Bangs et al.*, 2004; *Saffer and Tobin*, 2011]. However, it is placed at the trench until better constraints on its seismogenic up-dip limits are available. The transitional zone exhibits conditional stable slip conditions, favorable for rupture propagation, and extents to the onset of thick plate interface reflections (with more than 5 km thickness). Furthermore, the change from transitional to thick packages of plate interface reflections nearly coincides with the intersection of the mantle forearc wedge, as identified by reflection signals of the continental Moho (see paragraph 4.6.3).

The generated map of seismic slip behavior in the ALEUT survey area (Fig. 4.7.1) shows the greatest maximum landward extent of the seismogenic zone in the northeastern part of the survey area (within the 1964 rupture segment), extending up to ca. ∼170 - 180 km distance from the trench. Its maximum landward extent decreases quickly in southwest direction to ∼150 km from the trench at the segment boundary to the 1938 rupture area and ∼120 - 130 km in the Semidi Segment. At

the Shumagin Islands area in the southwest its maximum landward extent is ∼100 km from the trench. A conditionally stable slipping zone between the seismogenic part and the aseismic slipping part is not observed in the most northeastern part of the survey area (between Line 1b and 12b) but it begins to emerge in the southwest direction and reaches a maximum of ∼80 km in trench-normal direction at the center of the Semidi Segment. However, the trench-normal extent of this zone gradually decreases towards the southwest and reaches ∼30 km distance at the southwestern end of the survey area. This transitional zone is constrained in the landward direction by the onset of an aseismic slipping plate interface represented by thick plate interface reflection packages, which is located relatively consistently at ∼190 km distance from the trench from the northeastern end of the survey area until Line 3 before shifting in the seaward direction towards the southwest to ∼125 km from the trench at the western Shumagin Islands.

As the result, the most southwestern part of the 1964 rupture segment (Kodiak Asperity) is largely seismogenic but exhibits a small aseismic slipping zone at its most landward extent from ∼180 km from the trench until the coastline. The 1938 rupture area (Semidi Segment) is partly divided along the trench-parallel Line 7, with a seaward seismogenic part and a conditionally stable slipping part landward of the profile. The onset of the aseismic behaving plate interface is almost coinciding with the maximum landward rupture extent derived from aftershock locations [*Sykes*, 1971]. The Shumagin Gap area exhibits, similar to the adjacent Semidi Segment, a seismogenic zone up to ∼100 km from the trench but a very narrow transitional zone of ∼30 - 40 km distance. The deeper landward part of the plate interface beneath the Shumagin Islands exhibit thick packages of plate interface reflections and is interpreted to accommodate tectonic plate movements aseismically.

4.7.3 Continental Moho reflections

We interpret the top of the deep intracrustal reflection package at ∼40 km depth (see 4.6.6, Fig. 4.6.4 and Fig. B.16 - B.22) as the continental crust-mantle boundary (or Moho). The Moho depth along the central Alaska-Aleutian subduction zone has been estimated by receiver functions complemented with active-source seismic refraction data to 27 - 41 km [*Janiszewski et al.*, 2013; *Shillington et al.*, 2004]. The eastern end of this study area is located at the Shumagin Islands and coincides with the western end of the ALEUT study area. The continental Moho depth in this area

is determined by receiver functions to 35 - 41 km (station SDPT in *Janiszewski et al.* [2013]). This is in agreement with the depth of the deep intracrustal reflection packages observed throughout the ALEUT survey area (Table 4.1). Based on active-source wide-angle refraction data of an trench-normal oriented profile (Line A3 from the Aleutian Seismic Experiment in 1994) at ∼165° W, it has been also suggested that the continental crust is thinning significantly in seaward direction resulting in a continental Moho intersecting the subduction thrust much shallower at around ∼15 km depth [*Li et al.*, 2015; *Lizarralde et al.*, 2002]. However, this interpretation is based on velocity modelling with very sparse ray coverage in the mantle forarc region. The model is thus poorly constrained in this particular area. While *Li et al.* [2015] is interpreting shallower intracrustal reflections (at ∼20 km depth) on ALEUT Line 4 as possible continental Moho reflections (in accordance to a thinning continental crust in *Lizarralde et al.* [2002] model), we suggest deeper intracrustal reflections at at ∼40 km depth that appear to intersect the plate interface. Although these reflections are relatively short and observed only over a trench-normal distance of 10 - 20 km, they are imaged consistently at ∼40 km depth seemingly intersecting the subduction thrust fault throughout the entire ALEUT survey area. The intersection of the weak and probably aseismic behaving hydrated forearc mantle wedge also coincides spatially with the landward limit of megathrust rupture areas as defined by aftershock locations [*Sykes*, 1971] (Fig. 4.7.1).

Interestingly, the reflection packages tend to exhibit a slight seaward dip (at least close to the intersecting subduction thrust interface) in contrast to other subduction zones where a thinning of the overriding crust (landward dipping continental Moho) is observed. However, since the imaged reflections are very short, this could exhibit a local phenomena and might have been evoked by local zone of lower seismic velocities above the reflection package, which was not accounted for in the velocity models used for time-to-depth conversion. This theory is supported by seismic images before time-to-depth conversion, that show much more horizontal reflections. The origin of a zone of reduced seismic velocities is not clear but might include damaged, fractured and hydrated upper plate rocks. However, wedge hydration might be limited in cool subduction zones, such as the eastern AASZ [*Abers et al.*, 2017].

Line	Continental Moho Depth	Distance from the trench
1b	34 km	193 - 210 km
2R	38 km	203 - 227 km
3	39 km	179 - 202 km
34*	38 km	0 - 26 km
4	36 km	147 - 160 km
5	36 km	144 - 158 km
6	34 km	138 - 150 km

Table 4.1: Continental Moho reflection depth and spatial extent as determined from Figure B.16 - B.22. Asterisk (*) denotes trench-parallel oriented profile and distance along the profile (in east to west direction).

4.7.4 Comparison of the rupture extent and slip behavior determined by other methods at the eastern AASZ

There have been several attempts to estimate the extent of the seismogenic zone at the eastern AASZ in trench-parallel, and in particular, in down-dip directions of the subducting plate. These approaches are based on (a) indirect measurements, such as aftershock locations, (b) numerical modelling (e.g. slab temperature, coupling distribution), (c) intersection with the aseismic sliding mantle forearc wedge or the location of low frequency earthquakes with associated tectonic tremor usually found down-dip of the seismogenic zone and (d) historic reports. These approaches will be presented in the following paragraphs and compared with the interpretation of the seismic plate interface reflection signature made in Figure 4.7.1.

4.7.4.1 Aftershock location and tsunami waveform modelling

It has long been known that increased earthquake activity following a big earthquake occurs on and around the main shock region [*Omori*, 1894]. These earthquakes are called aftershocks and have smaller magnitudes and often negligible seismic moment (of usually a few percent) compared to the main earthquake. They occur in regions where the stresses have increased because of the nucleation of the main shock. The frequency of these aftershocks dies off hyperbolically after the main event but can still last several months for very large earthquakes. A direct link between the aftershock distribution and the extent of rupture area was made first by *Gutenberg and Richter* [1955] and was since then wildly used to estimate the main rupture area of an earthquake. With improvement in determining earthquake

location by both numerous and higher quality seismograms and better knowledge of the Earth's structure, a clearer picture of aftershock distribution emerges. They tend to cluster at the edges or ends of the faults and usually, though not always, have the largest aftershocks there as well. But they also occur over the entire fault and off the main fault in a direction perpendicular to it [*Das and Henry*, 2003]. The slip mechanism is not limited to the specific tectonic setting and can include all types of slips (thrust, normal, strike-slip mechanisms). Modern high-quality data provided by broad band seismometers determine details of the slip history of earthquakes by a formal seismogram inversion [e.g., *Henry*, 2002; *Henry et al.*, 2000]. This is especially useful to analyze earthquakes in remote regions with sparse seismic station coverage, such as over most of the oceans. However, accurate seismological broad band data is only available since the mid 1990s, and thus cannot be used to determine detailed rupture segments at the eastern AASZ, which slipped in large earthquakes in 1964, 1938 and 1946. Moreover, a complete seismic cycle for great megathrust earthquakes can consist of many decades to hundreds of years [e.g., *Davies et al.*, 1981; *Nelson et al.*, 2015]. With seismological catalogues reaching only ca. 100 years back, a full sequence of the great rupture of large segments has to date not been recorded at the Alaska-Aleutian subduction zone. The aftershock distributions of these events are still the best estimates of the main shock area or rupture extent to this date [*Benz et al.*, 2011; *Estabrook et al.*, 1994; *López and Okal*, 2006; *Sykes*, 1971].

The interpretation of seismic unstable (seismogenic), conditionally stable and stable (aseismic) slip behavior (Fig. 4.7.1) is consistent with the spatial extent of the rupture area that was derived from past megathrust aftershock locations [*Sykes*, 1971] and inverse tsunami waveform modelling [*Johnson and Satake*, 1994] for the Semidi Segment and the western part of Kodiak Asperity. Slip estimates derived from tsunami waveform modelling based on the 1938 event show minor slip (0.34 m - 0.79 m) for the western and central Semidi Segment area but large slip (3.3 m) for the eastern Semidi Segment that coincides with the widened and landward extended seismogenic area between Line 2 and 12f (Fig. 4.7.1) [*Johnson and Satake*, 1994].

4.7.4.2 Numerical models of slab temperature and slip behavior

Megathrust earthquakes are restricted to a certain depth range along the plate interface thrust fault. This depth range is defined by a seismogenic up-dip and

down-dip limit. The shallowest region of the interplate interface, commonly overlain by an accretionary prism, is generally thought to accommodate relative plate movements mostly aseismically with unconsolidated sediments at the interplate interface undergoing anelastic deformation. The depth from where sediment compaction and dewatering has reached a certain level, so that plate motion is accommodated seismically (i.e. elastic strain energy is stored and released in an earthquake), is defined as the upper seismogenic limit on the fault plane and usually lies around 5 to 10 km depth [*Lay et al.*, 2012]. The succeeding seismogenic rupture plane extends until its down-dip limit, where it is believed that the deformation mechanism changes from seismic to aseismic behavior, after exceeding a temperature threshold of ca. 350 °C [e.g., *Oleskevich et al.*, 1999] or the encounter of a serpentinized mantle forearc wedge [e.g., *Ruff and Tichelaar*, 1996].

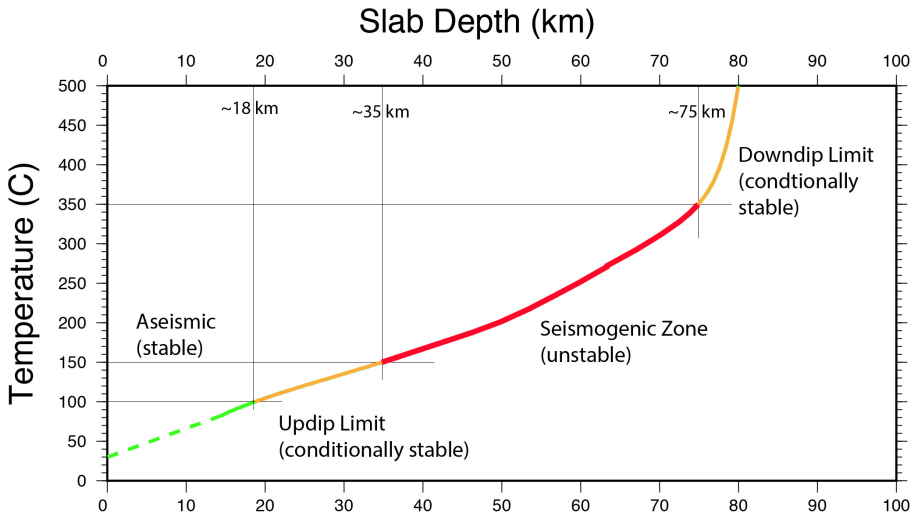

Figure 4.7.3: Slab temperature estimation with slab depth below seafloor for the eastern AASZ as modelled by *Syracuse et al.* [2010]. Temperature controlled frictional behavior of the plate interface [after *Vrolijk* [1990]; *Hyndman et al.* [1997]; *Tse and Rice* [1986]; *Oleskevich et al.* [1999]] with green line for shallow aseismic part of the thrust fault near the trench, orange lines are transitional zones, which are considered to be slipping under conditional stable conditions, where rupture can propagate through, and red line presenting the unstable sliding seismogenic part of the fault, where thrust earthquakes nucleate. The dashed green line is an extrapolation for slab temperatures for shallower depth. Thin black lines emphasize the specific depth of the modelled slab interface for critical temperatures (seismogenic up-dip limit: 100 - 150 °C) [e.g., *Hyndman et al.*, 1997; *Vrolijk*, 1990] and the onset of ductile sliding as quartzo-felspathic rocks change the rheological behavior 350 °C [e.g., *Oleskevich et al.*, 1999; *Tse and Rice*, 1986].

This temperature corresponds globally approximately with the maximum depth of continental earthquakes [e.g., *Hyndman and Wang*, 1993; *Tse and Rice*, 1986] and the change from velocity weakening (seismic) to velocity strengthening (stable

sliding) behavior that is observed in laboratory measurements on quartzo-feldspathic rocks [*Blanpied et al.*, 1991, 1995; *Tse and Rice*, 1986]. Rupture control in subduction settings at great depth is most likely controlled by a sandwich layer of subducted sediments and eroded material from the upper crust that is located in between the rigid upper and lower plate [*Cloos and Shreve*, 1988]. The composition of this decollement layer is believed to be roughly similar to the rocks used in the laboratory measurements [*Oleskevich et al.*, 1999] and the critical temperature of 350 °C is therefore understood as the thermal boundary where stable sliding begins. An abrupt termination in rupture mechanism is physically unrealistic and [*Tse and Rice*, 1986] observed a rapid increase of instantaneous shear stress in laboratory crustal rocks for temperatures above 450 °C and ductile flow for even higher temperatures. It is reasoned that 450 °C might be a second temperature limit, where rupture of large earthquakes, that have been initiated at temperatures less than 350 °C, might extend. The transitional zone in between 350 - 450 °C is considered a region of conditional stability, whereas ca. 450 °C marks the change from brittle to ductile behavior of the slip fault.

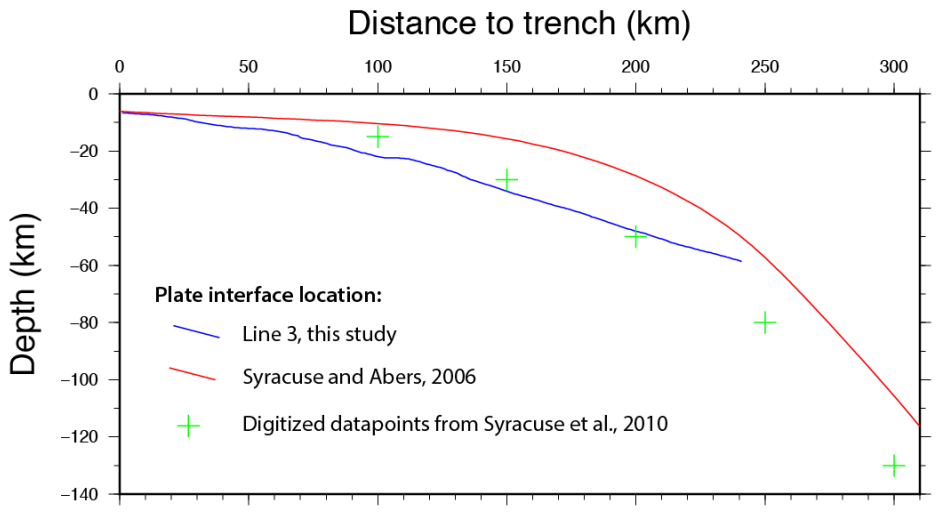

Figure 4.7.4: Comparison of the plate interface location in the eastern AASZ: 1) based on seismological data from the International Seismic Centre (red line) [*Syracuse and Abers*, 2006], 2) used for slab temperature modelling (green crosses, digitized from *Syracuse et al.* [2010]) and 3) drived from ALEUT MCS reflection data (blue line).

Temperature conditions at the subducting interface are modelled numerically based on plate age, convergence rate, incoming sediment thickness, plate dip angle and thrust temperature at the trench for oceanic plates, and rely as well on thermal conductivity and radioactive heat generation for the overriding continental rocks

[*Oleskevich et al.*, 1999; *Syracuse et al.*, 2010]. Heat flow measurements and slab temperature models at the eastern AASZ are scarce. The most recent thermal model for this region is presented by *Syracuse et al.* [2010] (Fig. 4.7.3). The slab geometry used to model temperatures along the plate interface in this study is based on 43 years of seismological data (1964 - 2007) of the International Seismic Centre catalog with improved hypocenter location [*Syracuse and Abers*, 2006]. Furthermore, this slab interface location in *Syracuse et al.* [2010] is corrected for bias in intermediate-depth earthquake locations that originate from using a 1D rather than a 3D global velocity model for earthquake location, as described in *Syracuse and Abers* [2009]. As a results, the slab interface location used for slab temperature modelling coincides relatively well with the plate interface location derived from the ALEUT MCS data (Fig. 4.7.4) and thus provides a reliable estimate of slab depth versus slab temperature relationship for the eastern AASZ [*Syracuse et al.*, 2010]. The critical slab temperature of 350 °C that is believed to mark the transition from brittle to ductile sliding, is predicted to be reached at a depth of ca. 75 km (Fig. 4.7.3), which is deeper that any plate interface imaged in the MCS ALEUT dataset. This characterizes the eastern AASZ as a relatively cold subduction zone compared, e.g. to Cascadia, southwest Japan or south Chile, where these temperatures are encountered at much shallower depth.

4.7.4.3 Interplate coupling distribution

Geodetic dislocation models that estimate interplate coupling distribution are based on GPS measurements that record even the smallest movements of the crust related to the subduction process and provide valuable insights into strain accumulation and frictional properties along fault planes in subduction zones. But geodetic surveying of ongoing crustal deformation caused by two converging plates have two shortcomings:

1) Accumulating elastic strain energy by converging plate motion is manifested in horizontal and vertical crustal movements of the overriding plate, with the highest rates of deformation expected in the forearc region close to the trench. This area is, however, often located offshore below sea level and thereby off limits for land based GPS measuring devices. For this reason, it is common that the distribution of data points on subduction zones is constrained mostly to coastal areas close to the arc. This is especially true for tectonic settings such as the eastern AASZ where an

unusual wide shelf area spans across the entire forearc region. The data point coverage is therefore often not optimal.

2) Interseismic periods in seismic cycles for great megathrust earthquakes can last many decades to hundreds of years [e.g., *Davies et al.*, 1981; *Nelson et al.*, 2015]. But the GPS data used to model the coupling distribution at the eastern AASZ only consists of around 20 years of observations [*Li and Freymueller*, 2018]. It is, however, unclear if crustal deformation during the interseismic phase occurs continuously or episodically. GPS observations over a short period of time (relative to the length of a seismic cycle), can therefore provide only information about the present state of deformation but are unable to infer the deformational state of the past or the near and distant future.

Dislocation models are based on geodetic measurements and are primarily used to explain slip deficits of the plate convergence rate along active tectonic fault systems. The locking fraction is defined as the ratio of the slip deficit rate to the long-term slip rate with a range from 0 to 1 (0% to 100%), where 0 means aseismic creep or 0% coupling and 1 means a fully locked plate interface or 100% coupling. The most recent interplate coupling model for the eastern AASZ is presented by *Li and Freymueller* [2018] (Fig. 4.7.5. I refer to Chapter 3.8.4 of this thesis for a more detailed description of this model.

The well-defined and highly-coupled plate interface in the northeastern part of the survey area, as modelled by *Li and Freymueller* [2018], shows remarkable correlation with the extent of the seismogenic zone derived from thin plate interface reflection bands in this area (Fig. 4.7.5). The highly-coupled zone of ∼80 - 100 % locking fraction is constrained in landward direction as well as in trench-parallel direction. It encompasses the almost entire northeastern half of the ALEUT survey area up to 150 km distance to the trench and laterally by a sharp change in coupling located at the center of the Semidi Segment (black dotted line in Fig. 4.7.5). At nearly the same extent we observe thin reflection packages ($<$ 2 km thickness) from the plate interface. The only location for thin bands of plate interface reflections that falls beyond the maximum landward extent of the highly-coupled zone is observed on Line 12b, which is located ca. 20 - 30 km down-dip of it. The most eastern part of Line 7 extends into the highly-coupled zones and exhibits plate interface reflection bands of intermediate thickness of $\sim$ 3 km. We do, however, also observe thin plate interface reflection bands on the remaining trench-normal lines in the western part

of the survey area with their maximum landward extent gradually shortening towards the southwest. The locations of these lines are outside of the highly-coupled area and the coupling degree of the shallow plate interface near the trench decreases in southwest direction from ∼70 % on Line 3 over 50 % on Line 4 to almost 0 % (free slipping) at the western Shumagin Gap. The plate coupling degree for more landward and deeper parts of the interplate boundary is modelled to be even less and decreases linearly in landward direction. No correlation between the maximum landward extent of the seismogenic area (thin bands of plate interface reflections) and high degree in plate coupling is observed in the Shumagin Island area. In earlier studies, the same area is considered to be weakly coupled or to slip freely [e.g., *Freymueller and Beavan*, 1999; *Li and Freymueller*, 2018]. Conditional stable sliding areas are located at ∼100 - 130 km from the trench in the western Shumagin Gap and ∼100 - 150 km in the eastern Shumagin Gap (Fig. 4.7.5). This is the first indication based on geophysical data that megathrust rupture can nucleate and propagate into the shallow plate interface area beneath the Shumagin Island area.

4.7.4.4 Hydrated (serpentinzed) mantle wedge

In cold subduction zones, such as the eastern AASZ, the entrance of the subduction thrust fault into the mantle is generally regarded as the maximum down-dip limit of the seismogenic and/or conditional stable sliding zone [e.g., *Hyndman et al.*, 1997; *Peacock and Hyndman*, 1999]. This alternative concept to a temperature controlled seismogenic limit was introduced by *Ruff and Tichelaar* [1996], who suggested that the intersection of the overriding plate's Moho with the top of the subducting slab determines the down-dip edge of the seismogenic zone. The theory of a rock-compositional control of the seismogenic down-dip limit is especially meaningful when the plate interface intersects with the forearc mantle wedge before the critical plate temperature of 350 °C is reached (e.g. for subduction beneath thin oceanic crust or beneath continental crust where temperatures are low because of an older, cool incoming oceanic crust with only thin sediment cover, such as in the eastern AASZ). Water carried downwards in free form between pore space or bound in hydrous minerals are released with increasing depth by compaction and dehydration reactions [e.g., *Peacock*, 1990; *Schmidt and Poli*, 1998]. Adding water to the dry forearc mantle, which is inferred to be composed of depleted ultramafic rocks, may generate a variety of hydrous minerals including serpentinite, talc and

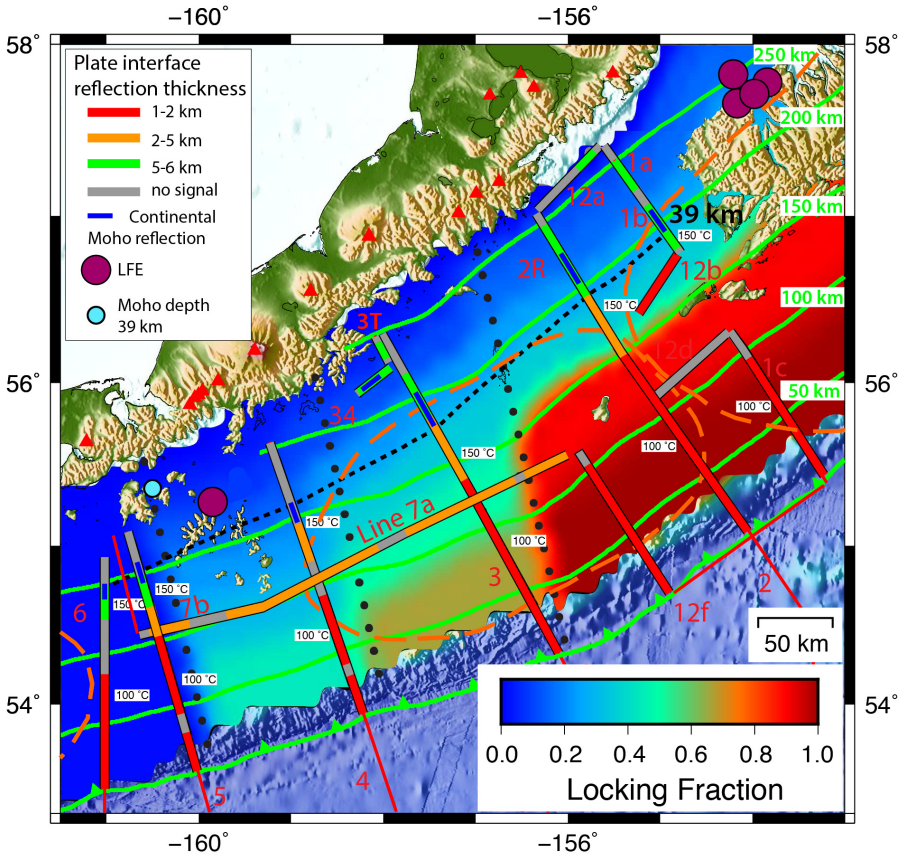

Figure 4.7.5: ALEUT survey area with thickness of seismic appearance of the plate interface along all ALEUT MCS profiles overlying the locking fraction distribution between the overriding North American Plate and subducting Pacific Plate as put forward by *Li and Freymueller* [2018] (colour map). Thick red lines indicate thin plate interface reflections ($<$ 2 km), green thick lines are broad bands of reflection ($>$ 4 km) and orange parts in between are transitional zones (2 - 5 km). Thick grey lines represent parts in the seismic sections where no plate interface signal could be identified. Thin red lines show the location of ALEUT MCS Lines with their specific Line numbers. Dashed orange lines outline the extent of rupture areas derived from aftershock locations for the 1938 Semidi Segment earthquake and 1964 Good Friday earthquake [*Benz et al.*, 2011; *Sykes*, 1971]. Black dotted lines mark sharp changes in lateral and down-dip locking for *Li and Freymueller* [2018] model. Black dashed line shows the location of mantle forearc intersection assuming a continental Moho depth of 39 km [*Janiszewski et al.*, 2013]. Thin and short blue lines show the extent of seismic reflection within the ALEUT MCS seismic sections associated with continental forearc Moho reflections. The purple dots show the location of VLF earthquake swarms by *Brown et al.* [2013]. Slab temperature is given along MCS profiles according to depth and trench distance information provided by *Syracuse et al.* [2010]. Black dotted lines mark sharp changes in lateral and down-dip locking for *Li and Freymueller* [2018] model. Green lines connect equidistant points to the trench at 50 km interval. Red triangles show the location of active volcanoes along the arc and green line with triangles shows the position of the trench.

brucite depending on temperature, pressure and bulk composition [*Evans*, 1977; *Manning and Decleer*, 1995]. The presence of these materials affects physical and mechanical properties of the forearc mantle substantially, such as causing a decrease

in seismic velocity, increase in Poisson ratio, generation of seismic reflectivity, increase in magnetization, reduction in density, increase in electrical conductivity, and reduction in mechanical strength [e.g., *Hyndman and Peacock*, 2003]. The later in combination with the generation of very weak layered rocks, such as serpentinite and talc, may be the primary factor that explains the aseismic behavior below the forearc Moho.

The degree of serpentinization of the forearc mantle wedge is commonly around 20 % but can reach up to 50 % locally [*Hyndman and Peacock*, 2003]. Serpentinization reduces the seismic velocity and Poisson ration in the mantle rocks so significantly that it can approximate the seismic characteristics of the overlying continental crust, thus impeding seismic reflection imaging of the crust-mantle boundary (or Moho) beneath the forearc. Remarkably, we could image consistent, clear but short reflection bands near the subducting thrust fault at the expected Moho depth of approximately 40 km throughout the entire ALEUT survey area. We interpret these reflections as part of the continental Moho, which is located right at the intersection with the subducting plate boundary deformational zone and extents for only ca. 10 - 20 km landward before the signal is lost (Appendix B, Fig. B.2 - B.6, B.8, B.15). This could be an indication for a changing degree of serpentinization and thus a changing impedance contrast that leads to higher reflectivity because of lesser (or higher) hydrated mantle rocks. A thorough analysis of seismic velocities in this area would be crucial to further understand the geologic origin of these reflections and explain the origin of tectonic tremors and slow slip events (SSE) that have been observed in this region [*Brown et al.*, 2013].

The best estimate for the Moho depth of overriding crust (oceanic and continental) along the central Aleutian Arc is based on receiver functions combined with controlled source seismic data and has been determined to be an average of 38.5 km with an uncertainty of +-3 km [*Janiszewski et al.*, 2013]. However, the ALEUT study area is farther to the east from the data points used in this study, and the easternmost data point in this study is located at the Shumagin Islands (with a Moho depth of 39 km +- 2.5 km). Thus, as a reference the Moho depth for the Shumagin Islands is assumed to be constant for the remaining ALEUT survey area to be 39 km (black dashed line in Fig. 4.7.5). Remarkably, this depth is in relatively good agreement with seismic continental Moho reflections as interpreted in the ALEUT survey areas (Table 1). Furthermore, we observe an increase in the Moho depth from 34 - 36 km depth to 38 - 39 km towards the northeast that coincides

with the beginning of thick ($>$ 5 km) reflection packages associated with the plate interface and the maximum landward extent of past megathrust rupture areas (Fig. 4.7.1).

4.7.4.5 Episodic Tremor and Slip (EPS), Low Frequency Earthquakes (LFE's) and Slow Slip Events (SSE's)

Over the last 60 years, evidence have been uncovered for a new type of earthquake [e.g., *Benioff and Press*, 1958; *Kanamori*, 1972; *Sacks et al.*, 1981]. The rupture process of these earthquake is unusually slow and can last hours, days or even weeks at a time, in contrast to the co-seismic slip of regular earthquakes that only lasts seconds [e.g., *Beroza and Ide*, 2011]. Seismic wave energy of these so called slow earthquakes is dominated by low frequencies (e.g. found in tremor signals) or do not radiate any seismic energy at all, due to its very slow rupture process. These events are most commonly to referred as SSE and EPS event and comprise spatially and temporarily coinciding periodic events of slow slip in correlation with tectonic tremor [*Obara et al.*, 2004; *Rogers and Dragert*, 2003]. These events have sparked great interest, as they are suspected to accommodate much of the plate motion at tectonic plate boundaries without generating great megathrust earthquakes [e.g., *Heki et al.*, 1997; *Schwartz and Rokosky*, 2007; *Wesson*, 1988]. Thus, they are expected to be located outside of the maximum extent of the seismogenic zone in subduction zones [e.g., *Brown et al.*, 2009]. Tectonic tremors are intrinsically difficult to study because of their low signal-to-noise ratio and lack of distinct impulsive signal arrivals, which make an exact location of events challenging. It appears however, that tremor signals comprise LFE swarms, which despite their low magnitude, could be located much more precisely with suitable cross-correlation and other techniques [*Shelly et al.*, 2006, 2007; *Waldhauser and Ellsworth*, 2000]. The occurrence of these LFE's could be constrained to the plate interface where they appear as shear slip events and could be correlated with SSE's [e.g., *Brown et al.*, 2009; *Obara et al.*, 2004; *Shelly et al.*, 2007]. ETS events or LFE swarms have been detected down-dip of locked rupture zones in multiple subduction zones worldwide [*Brown et al.*, 2009, 2013]. Two clusters of LFE's have been detected near the Shumagin Islands and northwest of Kodiak Islands (Fig. 4.7.5) [*Brown et al.*, 2013]. The Shumagin clusters is located down-dip of the maximum seismogenic extent as determined by plate interface reflection package thickness and continental Moho

reflections. The cluster near Kodiak Islands is located outside of the ALEUT survey area and landward of the maximum landward extent of the 1964 rupture area, thus probably also within an aseismic slipping zone.

4.7.4.6 Historic events

The historical record of large earthquakes in the Alaska-Aleutians area is generally poor and incomplete for the time prior to the begin of global instrumental seismological recordings in 1897. However, written transcripts of large shaking events or floodings exist, in form of letters and reports, since the late 18^{th} century when the first russian settlers arrived at the Alaska Peninsula, including Kodiak, Shumagin and Unalaska Islands [*Davies et al.*, 1981]. According to these reports, at least seven events have been reported between the late 18^{th} century and 1987, that fulfill at least two of the following criteria: extremly strong ground shaking ($>$ IX on the Mercalli scale) at two locations in considerable distance [*Kelleher*, 1972], strong ground motion over a duration of several minutes, permanent change in elevation, a large tsunami associated with the shock, numerous fissures and landslides, and reports of aftershocks lasting a period of weeks to months [*Davies et al.*, 1981]. These events have occurred in 1788, 1792, 1844, 1847, 1854, 1880, and possibly, in 1848 [*Davies et al.*, 1981]. The 1788 might have been the greatest event [*Davies et al.*, 1981; *Soloviev*, 1990], in which it has been proposed that it has ruptured at least a 600-km-long segment including the the entire 1938 rupture zone and parts of the Shumagin Gap. Thus, a permanently weak coupled Shumagin segment would be surprising since historic transcripts from russian settlers on both, the Shumagin Islands and Kodiak Island, report extremely strong ground shaking "[...] so strong that one could not stand on his feet." combined with large tsunami flooding in elevated areas of more that 30 m in 1788 [*Soloviev*, 1990]. We believe that rupture events of that scale cannot be explained by a weakly coupled or freely slipping segment at the Shumagin Islands and propose an, at least partially, seismogenic plate interface in this area.

4.8 Conclusion

The plate interface representing the subduction thrust fault has been imaged by controlled source MCS reflection data for the ALEUT survey area covering

$\sim$130,000 km^2 from southwest of Kodiak Island to the west of the Shumagin Islands. The seismic reflective zone associated with the plate boundary is mapped almost continuously on all but one ALEUT profiles. The plate interface reflective zone exhibits relatively constant thickness of less than 2 km for the shallow part up to a depth of $\sim$30 km, followed in down-dip direction by a transitional zone exhibiting a gradual increase from 2 to 5 km thickness and at $\sim$40 km depth a thick reflection zone of $\sim$5 - 6 km thickness. Nearly identical observations have been made at several warm subduction zones worldwide, where the plate interface reflection character was correlated with seismic slip behavior along the plate interface between the overriding and subducting plate. Both appearances are linked to structural weakened deformational zones that seem to control the seismic slip behavior in down-dip direction by gradually decreasing its seismogenic potential. Applying these relationship to the ALEUT dataset at the eastern AASZ indicate an extended seismogenic zone into the Shumagin Island region, an area that is assumed to be only weakly coupled or free slipping. Additionally, we imaged the continental Moho above the mantle forearc wedge and pinpoint the intersection with the subduction thrust fault. The eastern AASZ is the first cold subduction zone, where the seismogenic behavior of the thrust fault plane is similarly characterized based on plate interface reflection thickness. Our main conclusions are as follows:

1) Rupture extent of past megathrust events
Seismogenic and conditional stable slipping zones, as interpreted from the seismic reflection character of the plate interface, show a good correlation with the rupture extent derived from aftershock distributions of past megathrust earthquakes in the ALEUT survey area. The southwestern end of the 1964 rupture zone (Kodiak Asperity), extending into the survey area, exhibits a largely seismogenic plate interface and the 1938 rupture area (Semidi Segment) exhibits a seismogenic seaward part and a conditionally slipping landward part. Furthermore, a landward widening of the seismogenic area in the northeastern part of the Semidi Segment coincides with the largest slip estimate location based on inverse tsunami waveform modelling.

2) Seismogenic Shumagin Gap
Based on our results, the previously regarded freely slipping Shumagin Gap is interpreted to be partially seismogenic. The seismogenic zone is mapped by a distinct reflection band representing a thin plate interface reflection zone. It extends from the trench up to $\sim$100 km landward before it broadens up into a narrow

transitional zone and thick reflection bands at greater depth. Combined rupture of the partially seismogenic Shumagin Segment with its adjacent tectonic segments could result in great megathrust earthquakes as has been reported in the pre-instrumental era of the 18^{th} and 19^{th} century. This interpretation contradicts geodetic dislocation models that suggest very weak coupling for this region. However, these coupling models are based on GPS information without optimal data coverage and only provide information about the present state of crustal deformation, which might change over the extended time-period between great megathrust events and therefore might not reflect its long-term seismic behavior.

3) Plate interface broadening

The clearly observed broadening of the plate interface reflection zone with increasing depth exhibits similarities to observations made on warm subduction zones, such as depth of the onset of thickening and changes in plate interface reflection thickness from $>$ 2 km to $>$ 5 km. However, we observe weaker seismic reflectivity, possibly because of reduced dehydration reactions due to lower temperatures compared to warm subduction environments [e.g., *Saffer and Tobin*, 2011]. The mechanism that causes a widening of the seismic reflective plate boundary zone is not clear, but we suspect a correlation with sudden increases in the subduction dip angle at around 30 km depth that causes increased normal stress on the overriding plate and subducting plate which makes them susceptible to fractures and fluid migration, thus enhancing structural weaknesses and seismic reflectivity.

4) Seismogenic down-dip limit

A plate interface reflection thickness of ca. 5 km shows a good correlation with the seismogenic down-dip limit as estimated by previous other methods, such as earthquake aftershock studies [*Sykes*, 1971], location of the intersecting mantle wedge by receiver functions [*Janiszewski et al.*, 2013] and location of low frequency earthquakes that are identified within seismic tremor signals [*Brown et al.*, 2013]. Thick bands of plate interface reflections correlate consistently throughout the whole survey area with the predefined seismogenic down-dip limit. The thickness is also comparable with observations at other subduction zones at which changes in seismogenic slip behavior along the fault are determined [*Groß et al.*, 2008; *Kurashimo et al.*, 2013; *Nedimović et al.*, 2003].

5) Continental Moho reflections

Intracrustal reflections located at the crust mantle boundary above the mantle

wedge has been successfully imaged on all elongated trench-normal ALEUT MCS profiles. The Moho locations are interpreted to be at the top of the reflection package and are largely consistent with previous efforts to determine the seismogenic down-dip limit, including the begin of >5-km-thick plate interface reflection zones. Imaging the continental Moho at the mantle wedge is notable because of the expected high degree of mantle rock serpentinization that would reduce its seismic velocity und thus impedance contrast to the surrounding rocks. Strong reflections above the mantle wedge could indicate, therefore, a very high or very low degree of mantle rock serpentinization. Both possibilities would result in an enhanced impedance contrast. The imaged band of reflection is very short (10 - 20 km), which might be the result of changes in the seismic velocities farther down-dip that reduces the impedance contrast. This could be an indication for varying dehydration processes that might also influence seismic slip behavior and the generation of seismic tremor and slow slip events.

Chapter 5

Conclusions and Future work

5.1 Conclusions

The Alaska-Aleutian subduction zone (AASZ) is one of the seismically most active convergent margins on earth. Almost the entire arc has ruptured in hundreds of kilometers wide segments during several great earthquakes > M 8 in the last 80 years [*Davies et al.*, 1981]. Only a ∼250-km-wide segment near the Shumagin Islands has not experienced substantial rupture in at least 150 years. The plate interface between the overriding and subducting plate in this area seems to be, in contrast to its adjacent segments, weakly coupled [*Li and Freymueller*, 2018]. To study these dramatic variations in seismological behavior along the arc, geometry and seismic reflection signature of the plate interface beneath this so-called Shumagin Gap and two of its neighboring segments to the east have been mapped using the ALEUT network of deep penetrating MCS reflection profiles. This seismic reflection dataset is complemented by two coincident wide-angle OBS refraction profiles that cross both a highly and a weakly coupled segments.

On six trench-normal oriented ca. 200-km-long profiles, the interplate interface reflection could be traced nearly continuously from the trench to a maximum depth of ca. 65 km. This is deeper than in any other marine controlled source seismic reflection survey to date. One ca. 300-km-long and several shorter connecting profiles oriented in trench-parallel direction provide additional constrains on the plate interface location and its seismic reflection character. Whereas the travel times from migrated seismic reflection data yield a clear image of structural features in the subsurface, accurate depth information is obtained by conversion of the seismic sections from time to depth domain using hybrid velocity models constructed for each MCS reflection profile. The inputs for the constructed velocity models were interval velocities for the sediments as extracted from the MCS data, first arrival traveltime tomography velocities for the upper crust, and velocities from literature for the lower crust and uppermost mantle. Interpolations between all

MCS profiles yield 3D models representing the geometry and reflection character of the entire plate interface beneath the eastern AASZ, which provides us with a unique insight into possible controls on rupture organization and extent along this ∼500 km long tectonically segmented megathrust region.

The results are summarized in the following paragraphs and will demonstrate how trench-parallel tectonic segmentation is controlled at the eastern AASZ and how to estimate the seismogenic down-dip limit of megathrust faults in cold subduction zones. Furthermore, the obtained results indicate a locked and seismogenic part of the plate interface across the Shumagin Gap that was previously considered weakly coupled or even freely slipping.

5.1.1 Margin-parallel segmentation of the megathrust

Distinct and mostly continuous plate interface reflections traced on ALEUT MCS profiles were used as constraints to construct an interpolated 3D plate interface model spanning the AASZ from the southwestern end of Kodiak Island at ca. -153° E to west of the Shumagin Islands at ca. -161° E. To highlight the plate interface morphology, the model was subtracted from the smooth regional plate interface model Slab1.0 [*Hayes et al.*, 2012]. The residual topography map revealed mostly minor differences between the two models of up to ±2 km within 50 km distance from the trench and up to ±3 - 4 km from 50 - 250 km distance to the trench. However, two geometrical anomalies of greater magnitude ($>$ 4 km) can clearly be observed protruding and forming crest-shaped features, as they are shallower than the Slab1.0 model. Based on their geometrical characteristics, and their alignment with the trajectories of the incoming Kodiak-Bowie and Patton-Murray seamount chains, the two imaged plate interface crests are interpreted as subducted seamounts. The location of these elevated highs coincides precisely with segment boundaries inferred from aftershock locations and tsunami waveform inversion, and suggests that subducted seamounts could generally act as barriers to megathrust rupture propagation. These features persist over many earthquake cycles until they move away by subducting to greater depth and, therefore, likely define long-term tectonic segmentation along this part of the subduction zone.

5.1.2 Down-dip limit of the seismogenic zone

The imaged plate interface reflection signature shows significant variations as a function of depth and is classified into three categories: 1) thin, with a $<$ 2-km-thick reflection package found next to the trench and showing little variation spatially, 2) transitional, with 2 km thickness at the shallow end, 5 km thickness at the deep end, and showing gradual thickening in-between, and 3) thick, $>$ 5-km-thick reflection band found further down-dip and usually characterized by a slight increase in thickness with depth. The extents of the thin, transitional and thick megathrust reflection packages are defined for all ALEUT reflection profiles and interpolated to form a map. Following the hypothesis put forward by *Nedimović et al.* [2003] that correlates the thin reflection package with seismogenic stick-slip and thick reflection band with aseismic slip megathrust behavior, with the transitional region in-between, the produced map shows that: (1) The seismogenic zone extends to depth of 25 - 30 km, the transitional zone to 35 - 40 km, and the aseismic slip zone is found at greater depth and imaged to at least ∼65 km depth; (2) The seismogenic zone is observed throughout the survey area extending from the trench up to ∼170 km in landward direction in the northeast but narrows in along-strike direction towards the southwest to ∼100 km maximum landward extent. A transitional zone with conditionally stable slip behavior is not imaged at the very northeastern part of the survey area, but is imaged throughout the Semidi Segment, where it reaches its maximum trench-normal extent of ∼80 km but decreases to the southwest to ∼30 km at the western Shumagin Island area. Down-dip of this zone the aseismic zone begins at ∼190 km distance from the trench for the northeastern half of the survey area until Line 3 and gradually decreasing to ∼125 km at the southwestern end. The landward end of this zone is constrained by the landward limit of the ALEUT MCS profiles.

5.1.3 Seismogenic Shumagin Gap

The interpretation developed in this thesis suggests that, contrary to current predictions, the Shumagin Islands segment is characterized by a seismogenic zone capable of rupturing in a megathrust event. However, this zone is narrower than for the Semidi and Kodiak segments and therefore can store relatively less seismic energy. We base this hypothesis on the following rationale: 1) A 100-km-wide, distinct and thin ($<$ 2-km-thick) shallow plate interface reflection package

represents an image of long-term (many earthquake cycles) fault structure along the plate boundary, which appears identical to what is imaged on adjacent strongly coupled plate interface segments in the survey area and seismogenic megathrust faults in other subduction zones worldwide (e.g. Cascadia, south Chile, southwest Japan); 2) All geodetic data used in the dislocation study are collected at distances greater than 100 km landward from the trench, thus providing no constrains on the shallow part of the subduction zone ($<$ 100 km from the trench), which is expected to deform the most during elastic strain accumulation; 3) Geodetic measurements were taken during the last ca. 20 years and can only model the present state of deformation. Long-term deformation over decades or centuries might vary; 4) Historic reports from settlers of the Shumagin Islands clearly state very strong ground shaking and major flooding events in the past, indicating that this segment might have ruptured during megathrust events in the past [*Davies et al.*, 1981; *Soloviev*, 1990].

5.2 Future Work

5.2.1 Shallow seismogenic up-dip limit and slope structure

The research work presented in this thesis is focuses on characterizing and spatially constraining rupture segments laterally and in down-dip direction along the eastern AASZ. The results could support efforts in estimating the seismogenic risk for coastal communities and settlements in this region. However, possibly even greater risk to human lives and infrastructure is posed by both shallow sections of the megathrust that rupture during great earthquakes and splay faults that can suddenly lift-up the seafloor, displace large amount of water, and cause devastating tsunami waves. Therefore, the up-dip limit of the seismogenic portion along the plate interface boundary is an important parameter in tsunami genesis as it helps constrain the areas where the tsunamigenic earthquake ruptures are likely to occur. But besides rough estimation of rupture zone extent based on aftershock distributions [*Estabrook et al.*, 1994; *Sykes*, 1971] and the identification of a local tsunamigenic lower slope structure near the Shumagin Islands [*Bécel et al.*, 2017], no constraints or regional evaluations on the seismogenic up-dip limit has been made so far at the eastern AASZ.

The up-dip limit of seismic rupture is assumed to be controlled by the degree of

sediment consolidation and fluid pressure along the shallow part subduction zone located beneath the trench and slope region [e.g., *Saffer and Tobin*, 2011]. Despite its significant potential, there are only few attempts to directly map the seismogenic up-dip limit with high-resolution seismic reflection data in subduction zones [*Bangs et al.*, 2004]. Therefore, a possible future study target is the plate interface seismic reflection signature between the overriding accretionary wedge and the down going sediment package covering the oceanic crust for the initial ∼60 km down-dip from the trench. The top of the sediment package consists of highly reflective sediment strata that make this area an ideal place for this study [*Von Huene et al.*, 2012]. Variations in reflection amplitudes can be linked to fluid loss and decreasing fluid pressure down dip along the subduction thrust, which has the potential to constrain its slip behavior [*Bangs et al.*, 2004]. Furthermore, a detailed structural analysis of the overriding accreted sediments along the slope is possible to determine tsunami potential caused by splay faults or sediment slumps.

The aim would be to produce high-resolution pre-stack depth migrated seismic sections for seven trench-normal orientated MCS profiles. Approximately 40-km-long parts of ALEUT Lines 3, 4 and 5 have been pre-stack depth migrated by *Li and Freymueller* [2018] to determine detailed velocity information and derive pore-fluid pressure estimates. The length of these profiles would be extended and the remaining trench-normal lines would added to ensure a continuous along-strike coverage. To ensure capturing the seismogenic up-dip limit and possible splay fault structures, each profile would be ∼100 km long (starting from the trench) and would include parts of the seismogenic zone for Semidi Segment and Kodiak Asperity, as well as the shallow plate interface of the Shumagin Gap. The seven trench-normal profiles have an along-strike separation distance of 50 - 100 km and would provide a good regional coverage for evaluation of the shallow thrust interface over areas characterized by largely variable coupling and seismicity.

The results of this study would provide new constraints on the seismic up-dip limit at slope areas, which are usually out of reach of land-based GPS stations and thus only poorly constrained by geodetic data. Until new instruments to precisely record seafloor deformation become available, it is crucial to test alternative concepts to constrain seismogenic up-dip limits. The seismically extracted detailed information on the shallow megathrust would also help constrain dislocation models and from there improve our regional understanding of the megathrust coupling.

5.2.2 Development of structurally detailed RAYINVR models using OBS profiles crossing Semidi Segment and Shumagin Gap

Wide-angle seismic data were acquired on two profiles coincident with MCS Lines 3 and 5. Each profile consists of 21 OBS. The data were exploited to form 1) smooth, single layer, first arrival velocity models via traveltime tomography to support MCS processing (see Chapter 3), and 2) 3-layer velocity models for the outer rise and lower slope area that additionally employed secondary arrivals [*Shillington et al.*, 2015]. The 3-layer models contain interface boundaries in form of discrete velocity discontinuities between water and sediment layer, sediment layer and oceanic crust and oceanic crust and the upper mantle. In both cases the tomographic package Jive 3D [*Hobro et al.*, 2003] was used for the inversion process. The work conducted so far has contributed significantly to our knowledge of the AASZ but also shows that more structural detail can extracted along the whole length of both profiles using a layered modeling approach that relies on all pickable secondary arrivals in addition to first arrivals. A possibly fruitful approach for future work is to use the forward modelling software RAYINVR [*Zelt and Smith*, 1992] in combination with the design and structural geometry of the subsurface models guided by structural information provided by coincident migrated MCS sections (Line 3 and 5, Fig. A4 and A8 in Appendix A). The inclusion of MCS reflection constraints significantly reduces the problem of non-uniqueness of the wide-angle data modeling while allowing a much higher level of detail than possible with the tomographic inversion approach. The new RAYINVR models would provide complementary detailed velocity information that would allow conclusions about, for example, the degree of serpentinization of the forearc mantle wedge and upper mantle rocks. Comparison between the combined MCS and OBS data on Line 3 and 5 crossing the highly locked Semidi Segment and Shumagin Gap area, where the landward part is only weakly coupled might help to understand the drastically different seismological behavior which this region exhibited during at least 150 years.

5.2.3 Intracrustal reflections on the inner continental shelf

High amplitude intracrustal reflections have been imaged on almost all ALEUT MCS profiles at ca. 100 - 200 km distance landward from the trench and between ca. 15 - 30 km depth (Fig. 5.2.1). These reflections appear too shallow to be caused by the present plate interface or any other known major tectonic boundary in this

area. Similar reflections located at comparable depth and distance to the trench have been observed on the seismic reflection EDGE transect [*Moore et al.*, 1991; *Ye et al.*, 1997] and other early seismic reflection profiles beneath the inner continental shelf area north of Kodiak Island [*Fisher et al.*, 1983]. It has been proposed that these reflections are caused by underplating of detached pieces of the oceanic crust or submarine fan-deposits [*Byrne*, 1986; *Moore et al.*, 1991]. A continuation of these reflections from the north of Kodiak Islands into the ALEUT survey area could indicate that tectonic underplating at the eastern AASZ is not a local phenomenon, but extends to a regional scale of hundreds of kilometers in along-strike direction. Detailed analysis of these continental intracrustal structures, which is beyond the scope of this thesis work, is proposed to be carried out in the future using state-of-the-art deep penetrating ALEUT MCS reflection data, detailed subsurface velocity information from inversion and forward models of coincident OBS profiles, and MCS and other available information from the area northeast of the ALEUT survey.

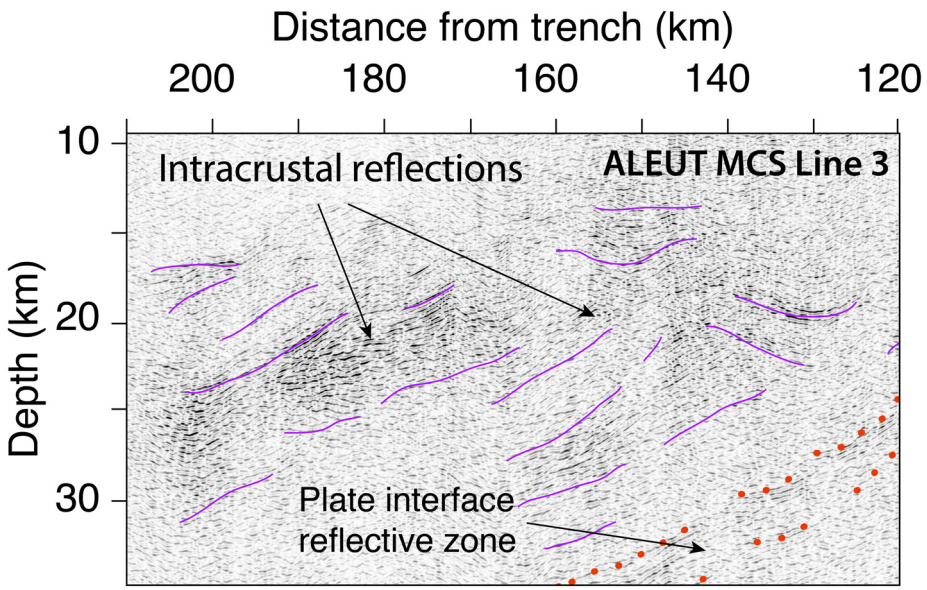

Figure 5.2.1: Part of ALEUT MCS seismic section (Line 3) showing continental intracrustal reflections (thin purple lines) above the plate interface reflection zone (top and bottom represented by red dotted lines).

5.2.4 Relationship between the subducting plate dip, overriding plate composition and seismic coupling

The dip of the plate interface steepens on a regional scale as the composition of the overriding plate changes from continental crustal composition to oceanic crustal composition (Fig. 5.2.2). At the same time, the age of the subducting oceanic crust increases towards the southwest. The ALEUT research area seems to be located at a transitional zone (red profiles in Fig. 5.2.2, 5.2.3) between shallow plate interface dip northeast of Kodiak Island (green profiles) and steep plate interface dip westward of the Shumagin Islands (blue profiles). Future studies on the compositional and structural along-strike variations in the overriding plate might reveal a relationship between the transition from continental to oceanic crustal composition in the overriding plate and its age with the steepening of the plate interface dip angle, and could give indications about reduced plate coupling in the Shumagin Island area. We plotted the plate interface depth based on Slab1.0 model [*Hayes et al.*, 2012] for 19 trench-normal profiles, including profiles coinciding with ALEUT MCS lines, from the Kenai Peninsula in the northeast until approximately Adak Island in the central Aleutians (Fig. 5.2.3). We observe a clear steepening along-strike from the northeast to the southwest. The relatively shallow plate

interface in the northeast might be influenced by the continental Yukatan microplate pushing against the Alaska mainland from the west. The ALEUT survey area appears to be in a transitional zone (represented by red profiles in Fig. 5.2.2 and Fig. 5.2.3) between the shallow plate interface in the northeast (green profiles) and the steep dipping plate in the southwest (blue profiles). This plate steepening might be caused by a major change in the subduction environment, as the overriding plate compositional structure changes from continental crust in the northeast to oceanic crust in the southwest. The beginning of steep plate interface coincides exactly where we suspect the ancient upper plate transform fault is located at the AASZ, which marks the begin of subduction beneath oceanic crust. This huge increase in the subduction dip angle in along-strike direction might reduce normal stresses in the Shumagin Gap area, as the plate interface experiences steep descent. But it is also not excluded that instead of a gradual steepening towards the southwest within the ALEUT survey area, the plate interface dip angle experiences an abrupt break and step like geometrical change from relatively shallow (northeastern part of ALEUT survey area) to relatively deep (southwestern part). This step would be, according to the plate interface depth profiles (grey profiles in Fig. 5.2.3), located right at ALEUT MCS Line 4, which also displays a large geometrical anomaly.

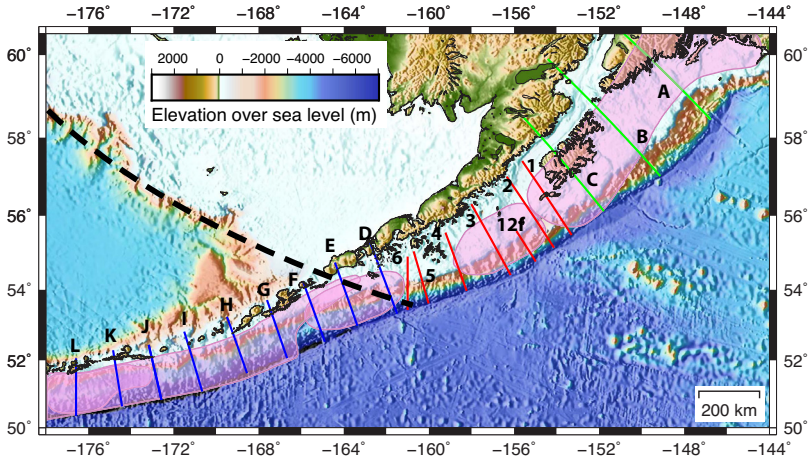

Figure 5.2.2: Eastern Alaska-Aleutian subduction zone with southeastern Bering Sea. Pink areas are rupture zones derived from aftershock locations of past megathrust earthquakes [*Davies et al.*, 1981; *López and Okal*, 2006; *Sykes*, 1971]. Dashed black line shows paleo-Berengian margin that extents to the shelf edge into the 1946 rupture zone. Plate interface depth according to Slab1.0 [*Hayes et al.*, 2012] is sampled in trench-normal profiles along the AASZ with green profiles (A-C) representing plate interface of pure oceanic-continental plate subduction, red profiles (1-6, 12f) are coinciding ALEUT MCS profile locations that represents a transitional zone, and blue lines (D-L) sample the subducting plate interface of an oceanic-oceanic plate subduction. Plate interface depth function for all profiles are shown in Figure 5.3.

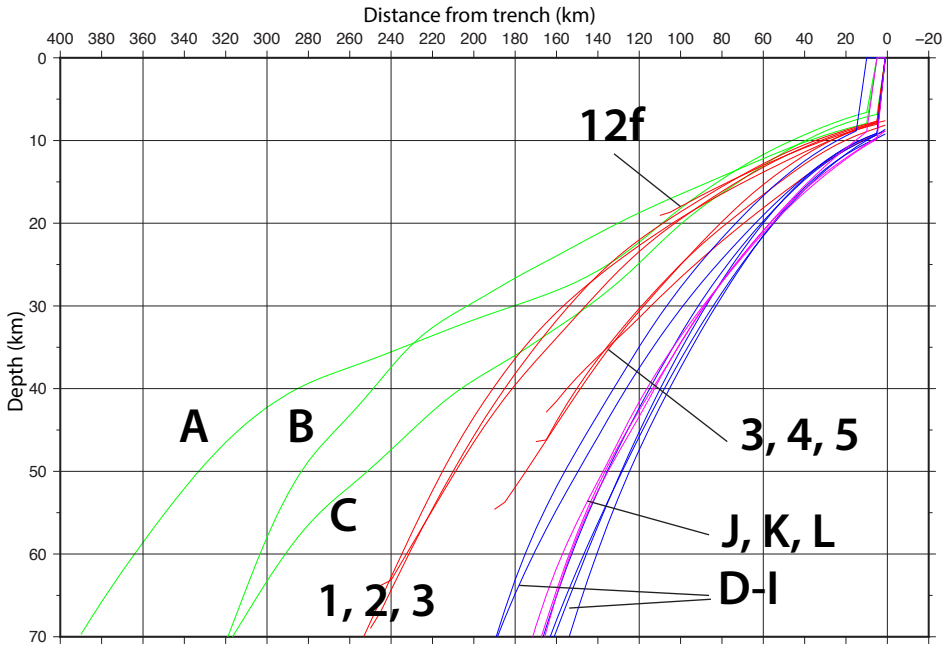

Figure 5.2.3: Plate interface depth functions based on Slab1.0 model [*Hayes et al.*, 2012] for trench-normal profiles along the AASZ as seen in Figure 5.2. Green curves (A-C) represent the plate interface at a pure continental-oceanic plate subduction at the northeastern edge of the AASZ, possibly influenced by subduction of the continental Yucatan block beneath southeast Alaska. Red curves (1-6, 12f) show depth functions at a transitional zone located at the ALEUT survey area with profile number and location coinciding with ALEUT MCS profiles. Blue curves (D-L) represent depth profiles at oceanic-oceanic plate subduction west of the Shumagin Gap. Light grey lines are plate interface depth functions according to the ALEUT PIM of trench-normal ALEUT MCS profiles. Clear steepening of the plate interface from the northeast (green lines) to the southwest (blue lines) is observed, with the ALEUT survey area located between in the transitional zone.

Bibliography

Abers, G., P. Van Keken, and B. Hacker (2017), The cold and relatively dry nature of mantle forearcs in subduction zones, *Nature Geoscience*, *10*(5), 333.

Abers, G. A. (1994), Three-dimensional inversion of regional p and s arrival times in the east aleutians and sources of subduction zone gravity highs, *Journal of Geophysical Research: Solid Earth*, *99*(B3), 4395–4412.

Abers, G. A., X. Hu, and L. R. Sykes (1995), Source scaling of earthquakes in the shumagin region, alaska: time-domain inversions of regional waveforms, *Geophysical Journal International*, *123*(1), 41–58.

Allen, M., B. Windley, and C. Zhang (1993), Palaeozoic collisional tectonics and magmatism of the chinese tien shan, central asia, *Tectonophysics*, *220*(1-4), 89–115.

Ampferer, O., and W. Hammer (1911), Geologischer querschnitt durch die ostalpen vom allgäu zum gardasee.

Amstutz, A. (1951), Sur l'évolution des structures alpines, *Arch. Sci*, *4*(5), 323–329.

Amstutz, A. (1957), Subductions et nappes simploniques, *Comptes rendus hebdomadaires des seances de l'Academie des Sciences*, *244*(20), 2531.

Amstutz, A. (1962), Notice pour une carte géologique de la vallée de cogne et de quelques autres espaces au sud d'aoste.

Anderson, R. N., S. Uyeda, and A. Miyashiro (1976), Geophysical and geochemical constraints at converging plate boundaries part i: Dehydration in the downgoing slab, *Geophysical Journal International*, *44*(2), 333–357.

Angenheister, G. (1927), Beobachtungen bei sprengungen, *Zeitschrift für Geophysik*, *3*, 28–33.

Angenheister, G. (1928), Seismik (erdbebenwellen), pp. 566–622.

Angiboust, S., P. Agard, H. Raimbourg, P. Yamato, and B. Huet (2011), Subduction interface processes recorded by eclogite-facies shear zones (monviso, w. alps), *Lithos*, *127*(1-2), 222–238.

Atwater, T., and H. Menard (1970), Magnetic lineations in the northeast pacific, *Earth and Planetary Science Letters*, *7*(5), 445–450.

Audet, P., M. G. Bostock, N. I. Christensen, and S. M. Peacock (2009), Seismic evidence for overpressured subducted oceanic crust and megathrust fault sealing, *Nature*, *457*(7225), 76–78.

Bangs, N. L., T. H. Shipley, S. P. Gulick, G. F. Moore, S. Kuromoto, and Y. Nakamura (2004), Evolution of the nankai trough décollement from the trench into the seismogenic zone: Inferences from three-dimensional seismic reflection imaging, *Geology*, *32*(4), 273–276.

Bécel, A., D. J. Shillington, M. R. Nedimović, S. C. Webb, and H. Kuehn (2015), Origin of dipping structures in fast-spreading oceanic lower crust offshore alaska imaged by multichannel seismic data, *Earth and Planetary Science Letters*, *424*, 26–37.

Bécel, A., D. J. Shillington, M. Delescluse, M. R. Nedimović, G. A. Abers, D. M. Saffer, S. C. Webb, K. M. Keranen, P.-H. Roche, J. Li, et al. (2017), Tsunamigenic structures in a creeping section of the alaska subduction zone, *Nature Geoscience*, *10*(8), 609.

Bekins, B. A., and S. J. Dreiss (1992), A simplified analysis of parameters controlling dewatering in accretionary prisms, *Earth and Planetary Science Letters*, *109*(3-4), 275–287.

Bell, R., R. Sutherland, D. H. Barker, S. Henrys, S. Bannister, L. Wallace, and J. Beavan (2010), Seismic reflection character of the hikurangi subduction interface, new zealand, in the region of repeated gisborne slow slip events, *Geophysical Journal International*, *180*(1), 34–48.

Benioff, H. (1949), Seismic evidence for the fault origin of oceanic deeps, *Geological Society of America Bulletin*, *60*(12), 1837–1856.

Benioff, H., and F. Press (1958), Progress report on long period seismographs, *Geophysical Journal of the Royal Astronomical Society*, *1*(3), 208–215.

Benz, H. M., M. Herman, A. C. Tarr, G. P. Hayes, K. P. Furlong, A. Villaseñor, R. L. Dart, and S. Rhea (2011), Seismicity of the earth 1900-2010 aleutian arc and vicinity, *Tech. rep.*, US Geological Survey.

Bergh, S. G., F. Corfu, P. I. Myhre, K. Kullerud, P. E. Armitage, K. B. Zwaan, E. K. Ravna, R. E. Holdsworth, and A. Chattopadhya (2012), Was the precambrian basement of western troms and lofoten-vesterålen in northern norway linked to the lewisian of scotland? a comparison of crustal components, tectonic evolution and amalgamation history, in *Tectonics-Recent Advances*, Intech.

Beroza, G. C., and S. Ide (2011), Slow earthquakes and nonvolcanic tremor, *Annual review of Earth and planetary sciences*, *39*, 271–296.

Bethke, C. M. (1986), Inverse hydrologic analysis of the distribution and origin of gulf coast-type geopressured zones, *Journal of Geophysical Research: Solid Earth*, *91*(B6), 6535–6545.

Bilek, S. L. (2010), Invited review paper: Seismicity along the south american subduction zone: Review of large earthquakes, tsunamis, and subduction zone complexity, *Tectonophysics*, *495*(1-2), 2–14.

Bilek, S. L., S. Y. Schwartz, and H. R. DeShon (2003), Control of seafloor roughness on earthquake rupture behavior, *Geology*, *31*(5), 455–458.

Blanpied, M., D. Lockner, and J. Byerlee (1991), Fault stability inferred from granite sliding experiments at hydrothermal conditions, *Geophysical Research Letters*, *18*(4), 609–612.

Blanpied, M. L., D. A. Lockner, and J. D. Byerlee (1995), Frictional slip of granite at hydrothermal conditions, *Journal of Geophysical Research: Solid Earth*, *100*(B7), 13,045–13,064.

Bostock, M. (2013), The moho in subduction zones, *Tectonophysics*, *609*, 547–557.

Bostock, M., R. Hyndman, S. Rondenay, and S. Peacock (2002), An inverted continental moho and serpentinization of the forearc mantle, *Nature*, *417*(6888), 536–538.

Boyd, T. M., and A. L. Lerner-Lam (1988), Spatial distribution of turn-of-the-century seismicity along the alaska-aleutian arc, *Bulletin of the Seismological Society of America*, *78*(2), 636–650.

Boyd, T. M., E. R. Engdahl, and W. Spence (1995), Seismic cycles along the aleutian arc: Analysis of seismicity from 1957 through 1991, *Journal of Geophysical Research: Solid Earth*, *100*(B1), 621–644.

Bray, C., and D. Karig (1985), Porosity of sediments in accretionary prisms and some implications for dewatering processes, *Journal of Geophysical Research: Solid Earth*, *90*(B1), 768–778.

Briggs, R. W., S. E. Engelhart, A. R. Nelson, T. Dura, A. C. Kemp, P. J. Haeussler, D. R. Corbett, S. J. Angster, and L.-A. Bradley (2014), Uplift and subsidence reveal a nonpersistent megathrust rupture boundary (sitkinak island, alaska), *Geophysical Research Letters*, *41*(7), 2289–2296.

Brown, J. R., G. C. Beroza, S. Ide, K. Ohta, D. R. Shelly, S. Y. Schwartz, W. Rabbel, M. Thorwart, and H. Kao (2009), Deep low-frequency earthquakes in tremor localize to the plate interface in multiple subduction zones, *Geophysical Research Letters*, *36*(19).

Brown, J. R., S. G. Prejean, G. C. Beroza, J. S. Gomberg, and P. J. Haeussler (2013), Deep low-frequency earthquakes in tectonic tremor along the alaska-aleutian subduction zone, *Journal of Geophysical Research: Solid Earth*, *118*(3), 1079–1090.

Brown, K., A. Kopf, M. Underwood, and J. Weinberger (2003), Compositional and fluid pressure controls on the state of stress on the nankai subduction thrust: A weak plate boundary, *Earth and Planetary Science Letters*, *214*(3), 589–603.

Buske, S., S. Lüth, H. Meyer, R. Patzig, C. Reichert, S. Shapiro, P. Wigger, and M. Yoon (2002), Broad depth range seismic imaging of the subducted nazca slab, north chile, *Tectonophysics*, *350*(4), 273–282.

Byrne, D. E., D. M. Davis, and L. R. Sykes (1988), Loci and maximum size of thrust earthquakes and the mechanics of the shallow region of subduction zones, *Tectonics*, *7*(4), 833–857.

Byrne, T. (1986), Eocene underplating along the kodiak shelf, alaska: implications and regional correlations, *Tectonics*, *5*(3), 403–421.

Calahorrano, A., V. Sallarès, J.-Y. Collot, F. Sage, and C. R. Ranero (2008), Nonlinear variations of the physical properties along the southern ecuador subduction channel: Results from depth-migrated seismic data, *Earth and Planetary Science Letters*, *267*(3-4), 453–467.

Calvert, A. J., K. Ramachandran, H. Kao, and M. A. Fisher (2006), Local thickening of the cascadia forearc crust and the origin of seismic reflectors in the uppermost mantle, *Tectonophysics*, *420*(1), 175–188.

Carver, G., and G. Plafker (2008), Paleoseismicity and neotectonics of the aleutian subduction zoneâĂŤan overview, *Active Tectonics and Seismic Potential of Alaska*, pp. 43–63.

Chaytor, J. D., R. A. Keller, R. A. Duncan, and R. P. Dziak (2007), Seamount morphology in the bowie and cobb hot spot trails, gulf of alaska, *Geochemistry, Geophysics, Geosystems*, *8*(9).

Choo, J., J. Downton, and J. Dewar (2004), Lift: A new and practical approach to noise and multiple attenuation, *First Break*, *22*(5), 39–44.

Christensen, D. H., and S. L. Beck (1994), The rupture process and tectonic implications of the great 1964 prince william sound earthquake, *Pure and Applied Geophysics*, *142*(1), 29–53.

Christensen, N. I., and W. D. Mooney (1995), Seismic velocity structure and composition of the continental crust: A global view, *Journal of Geophysical Research: Solid Earth*, *100*(B6), 9761–9788.

Cisternas, M., B. F. Atwater, F. Torrejón, Y. Sawai, G. Machuca, M. Lagos, A. Eipert, C. Youlton, I. Salgado, T. Kamataki, et al. (2005), Predecessors of the giant 1960 chile earthquake, *Nature*, *437*(7057), 404–407.

Clift, P., and P. Vannucchi (2004), Controls on tectonic accretion versus erosion in subduction zones: Implications for the origin and recycling of the continental crust, *Reviews of Geophysics*, *42*(2).

Cloos, M. (1992), Thrust-type subduction-zone earthquakes and seamount asperities: A physical model for seismic rupture, *Geology*, *20*(7), 601–604.

Cloos, M., and R. L. Shreve (1988), Subduction-channel model of prism accretion, melange formation, sediment subduction, and subduction erosion at convergent plate margins: 1. background and description, *Pure and Applied Geophysics*, *128*(3-4), 455–500.

Clowes, R., M. Brandon, A. Green, C. Yorath, A. S. Brown, E. Kanasewich, and C. Spencer (1987), LithoprobeâĂŤsouthern vancouver island: Cenozoic subduction complex imaged by deep seismic reflections, *Canadian Journal of Earth Sciences*, *24*(1), 31–51.

Coney, P., and D. Jones (1985), Accretion tectonics and crustal structure in alaska, *Tectonophysics*, *119*(1-4), 265–283.

Contreras-Reyes, E., and D. Carrizo (2011), Control of high oceanic features and subduction channel on earthquake ruptures along the chile–peru subduction zone, *Physics of the Earth and Planetary Interiors*, *186*(1-2), 49–58.

Contreras-Reyes, E., I. Grevemeyer, E. R. Flueh, and C. Reichert (2008), Upper lithospheric structure of the subduction zone offshore of southern arauco peninsula, chile, at 38 s, *Journal of Geophysical Research: Solid Earth*, *113*(B7).

Contreras-Reyes, E., E. R. Flueh, and I. Grevemeyer (2010), Tectonic control on sediment accretion and subduction off south central chile: Implications for coseismic rupture processes of the 1960 and 2010 megathrust earthquakes, *Tectonics*, *29*(6).

Contreras-Reyes, E., J. Jara, I. Grevemeyer, S. Ruiz, and D. Carrizo (2012), Abrupt change in the dip of the subducting plate beneath north chile, *Nature Geoscience*, *5*(5), 342.

Creager, J. S., D. W. Scholl, R. Boyce, H. J. L. Echols, H. Y. Ling, R. J. Stewart, P. R. Supko, and T. R. Worsley (1973), Deep sea drilling project initial report, leg 19: Initial reports of the deep sea drilling project, *Initial Reports of the Deep Sea Drilling Project*, *19*(-), –.

Creager, K. C., and L. M. Dorman (1982), Location of instruments on the seafloor by joint adjustment of instrument and ship positions, *Journal of Geophysical Research: Solid Earth*, *87*(B10), 8379–8388.

Dalrymple, G. B., D. A. Clague, T. L. Vallier, and H. W. Menard (1987), 40ar/39ar age, petrology, and tectonic significance of some seamounts in the gulf of alaska, *Seamounts, Islands, and Atolls*, *43*, 297–315.

Das, S., and C. Henry (2003), Spatial relation between main earthquake slip and its aftershock distribution, *Reviews of Geophysics*, *41*(3).

Das, S., and A. Watts (2009), Effect of subducting seafloor topography on the rupture characteristics of great subduction zone earthquakes, *Subduction Zone Geodynamics*, pp. 103–118.

Dasgupta, R., and M. M. Hirschmann (2010), The deep carbon cycle and melting in earth's interior, *Earth and Planetary Science Letters*, *298*(1-2), 1–13.

Davies, J., L. Sykes, L. House, and K. Jacob (1981), Shumagin seismic gap, alaska peninsula: History of great earthquakes, tectonic setting, and evidence for high seismic potential, *Journal of Geophysical Research: Solid Earth*, *86*(B5), 3821–3855.

DeMets, C., R. G. Gordon, and D. F. Argus (2010), Geologically current plate motions, *Geophysical Journal International*, *181*(1), 1–80.

Deschamps, A., and T. Fujiwara (2003), Asymmetric accretion along the slow-spreading mariana ridge, *Geochemistry, Geophysics, Geosystems*, *4*(10).

Desonie, D. L., and R. A. Duncan (1990), The cobb-eickelberg seamount chain: Hotspot volcanism with mid-ocean ridge basalt affinity, *Journal of Geophysical Research: Solid Earth*, *95*(B8), 12,697–12,711.

Dietz, R. S. (1961), Continent and ocean basin evolution by spreading of the sea floor, *Nature*, *190*(4779), 854–857.

Dixon, T. H. (1991), An introduction to the global positioning system and some geological applications, *Reviews of Geophysics*, *29*(2), 249–276.

Eberhart-Phillips, D., P. J. Haeussler, J. T. Freymueller, A. D. Frankel, C. M. Rubin, P. Craw, N. A. Ratchkovski, G. Anderson, G. A. Carver, A. J. Crone, et al. (2003), The 2002 denali fault earthquake, alaska: A large magnitude, slip-partitioned event, *Science*, *300*(5622), 1113–1118.

Engebretson, D. C. (1985), *Relative motions between oceanic and continental plates in the Pacific basin*, vol. 206, geological Society of America.

Estabrook, C. H., and T. M. Boyd (1992), The shumagin islands, alaska, earthquake of 31 may 1917, *Bulletin of the Seismological Society of America*, *82*(2), 755–773.

Estabrook, C. H., K. H. Jacob, and L. R. Sykes (1994), Body wave and surface wave analysis of large and great earthquakes along the eastern aleutian arc, 1923–1993: Implications for future events, *Journal of Geophysical Research: Solid Earth*, *99*(B6), 11,643–11,662.

Evans, B. W. (1977), Metamorphism of alpine peridotite and serpentinite, *Annual Review of Earth and Planetary Sciences*, *5*(1), 397–447.

Fagereng, A., and S. Ellis (2009), On factors controlling the depth of interseismic coupling on the hikurangi subduction interface, new zealand, *Earth and Planetary Science Letters*, *278*(1-2), 120–130.

Fisher, M. A., R. Huene, G. L. Smith, and T. R. Bruns (1983), Possible seismic reflections from the downgoing pacific plate, 275 kilometers arcward from the eastern aleutian trench, *Journal of Geophysical Research: Solid Earth*, *88*(B7), 5835–5849.

Fisher, M. A., T. M. Brocher, W. J. Nokleberg, G. Plafker, and G. L. Smith (1989), Seismic reflection images of the crust of the northern part of the chugach terrane, alaska: Results of a survey for the trans-alaska crustal transect (tact), *Journal of Geophysical Research: Solid Earth*, *94*(B4), 4424–4440.

Fletcher, H. J., J. Beavan, J. Freymueller, and L. Gilbert (2001), High interseismic coupling of the alaska subduction zone sw of kodiak island inferred from gps data, *Geophysical research letters*, *28*(3), 443–446.

Fournier, T. J., and J. T. Freymueller (2007), Transition from locked to creeping subduction in the shumagin region, alaska, *Geophysical Research Letters*, *34*(6).

Freymueller, J. T., and J. Beavan (1999), Absence of strain accumulation in the western shumagin segment of the alaska subduction zone, *Geophysical Research Letters*, *26*(21), 3233–3236.

Freymueller, J. T., H. Woodard, S. C. Cohen, R. Cross, J. Elliott, C. F. Larsen, S. Hreinsdottir, and C. Zweck (2008), Active deformation processes in alaska, based on 15 years of gps measurements, *Active tectonics and seismic potential of Alaska*, pp. 1–42.

Fujie, G., A. Ito, S. Kodaira, N. Takahashi, and Y. Kaneda (2006), Confirming sharp bending of the pacific plate in the northern japan trench subduction zone by applying a traveltime mapping method, *Physics of the Earth and Planetary Interiors*, *157*(1-2), 72–85.

Fujii, Y., and K. Satake (2007), Tsunami source of the 2004 sumatra–andaman earthquake inferred from tide gauge and satellite data, *Bulletin of the Seismological Society of America*, *97*(1A), S192–S207.

Fyfe, W. (1986), Fluids in deep continental crust, *Reflection Seismology: The Continental Crust*, pp. 33–39.

Geist, E. L., and R. Dmowska (1999), Local tsunamis and distributed slip at the source, in *Seismogenic and tsunamigenic processes in shallow subduction zones*, pp. 485–512, Springer.

Groß, K., U. Micksch, and S. T. TIPTEQ Research Group (2008), The reflection seismic survey of project tipteqâĂŤthe inventory of the chilean subduction zone at 38.2 s, *Geophysical Journal International*, *172*(2), 565–571.

Group, A. W., et al. (1999), Seismic reflection image revealing offset of andean subduction-zone earthquake locations into oceanic mantle, *Nature*, *397*(6717), 341.

Gutenberg, B., and C. Richter (1955), Magnitude and energy of earthquakes, *Nature*, *176*(4486), 795.

Hager, B. H., R. W. King, and M. H. Murray (1991), Measurement of crustal deformation using the global positioning system, *Annual review of earth and planetary sciences*, *19*(1), 351–382.

Hammer, P. T., R. M. Clowes, F. A. Cook, K. Vasudevan, and A. J. van der Velden (2011), The big picture: A lithospheric cross section of the north american continent, *GSA Today*, *21*(6), 4–10.

Harris, R. N., and K. Wang (2002), Thermal models of the middle america trench at the nicoya peninsula, costa rica, *Geophysical Research Letters*, *29*(21).

Hayes, G. P., D. J. Wald, and R. L. Johnson (2012), Slab1. 0: A three-dimensional model of global subduction zone geometries, *Journal of Geophysical Research: Solid Earth*, *117*(B1).

Hayes, G. P., G. L. Moore, D. E. Portner, M. Hearne, H. Flamme, M. Furtney, and G. M. Smoczyk (2018), Slab2, a comprehensive subduction zone geometry model, *Science*, *362*(6410), 58–61.

Hegner, E., and M. Tatsumoto (1989), Pb, sr, and nd isotopes in seamount basalts from the juan de fuca ridge and kodiak-bowie seamount chain, northeast pacific, *Journal of Geophysical Research: Solid Earth*, *94*(B12), 17,839–17,846.

Heki, K., S. Miyazaki, and H. Tsuji (1997), Silent fault slip following an interplate thrust earthquake at the japan trench, *Nature*, *386*(6625), 595.

Henry, C. (2002), Teleseismic studies of large submarine earthquakes, Ph.D. thesis, University of Oxford.

Henry, C., S. Das, and J. Woodhouse (2000), The great march 25, 1998, antarctic plate earthquake: Moment tensor and rupture history, *Journal of Geophysical Research: Solid Earth*, *105*(B7), 16,097–16,118.

Hess, H. H. (1955), The oceanic crust, *Journal of Marine Research*, *14*(4), 423–439.

Hilterman, F. J. (1982), Interpretative lessons from three-dimensional modeling, *Geophysics*, *47*(5), 784–808.

Hobro, J. W., S. C. Singh, and T. A. Minshull (2003), Three-dimensional tomographic inversion of combined reflection and refraction seismic traveltime data, *Geophysical Journal International*, *152*(1), 79–93.

Hole, J. (1992), Nonlinear high-resolution three-dimensional seismic travel time tomography, *Journal of Geophysical Research: Solid Earth*, *97*(B5), 6553–6562.

Huene, R., and D. W. Scholl (1991), Observations at convergent margins concerning sediment subduction, subduction erosion, and the growth of continental crust, *Reviews of Geophysics*, *29*(3), 279–316.

Husen, S., E. Kissling, and R. Quintero (2002), Tomographic evidence for a subducted seamount beneath the gulf of nicoya, costa rica: The cause of the 1990 mw= 7.0 gulf of nicoya earthquake, *Geophysical Research Letters*, *29*(8).

Hyndman, R. (1988), Dipping seismic reflectors, electrically conductive zones, and trapped water in the crust over a subducting plate, *Journal of Geophysical Research: Solid Earth*, *93*(B11), 13,391–13,405.

Hyndman, R., and K. Wang (1995), The rupture zone of cascadia great earthquakes from current deformation and the thermal regime, *Journal of Geophysical Research: Solid Earth*, *100*(B11), 22,133–22,154.

Hyndman, R. D., and S. M. Peacock (2003), Serpentinization of the forearc mantle, *Earth and Planetary Science Letters*, *212*(3-4), 417–432.

Hyndman, R. D., and K. Wang (1993), Thermal constraints on the zone of major thrust earthquake failure: The cascadia subduction zone, *Journal of Geophysical Research: Solid Earth*, *98*(B2), 2039–2060.

Hyndman, R. D., M. Yamano, and D. A. Oleskevich (1997), The seismogenic zone of subduction thrust faults, *Island Arc*, *6*(3), 244–260.

Ito, A., G. Fujie, S. Miura, S. Kodaira, Y. Kaneda, and R. Hino (2005), Bending of the subducting oceanic plate and its implication for rupture propagation of large interplate earthquakes off miyagi, japan, in the japan trench subduction zone, *Geophysical research letters*, *32*(5).

Ito, T., K. Ozawa, T. Watanabe, and T. Sagiya (2011), Slip distribution of the 2011 off the pacific coast of tohoku earthquake inferred from geodetic data, *Earth, planets and space*, *63*(7), 21.

Ito, Y., and K. Obara (2006), Very low frequency earthquakes within accretionary prisms are very low stress-drop earthquakes, *Geophysical Research Letters*, *33*(9).

Janiszewski, H. A., G. A. Abers, D. J. Shillington, and J. A. Calkins (2013), Crustal structure along the aleutian island arc: New insights from receiver functions constrained by active-source data, *Geochemistry, Geophysics, Geosystems*, *14*(8), 2977–2992.

Johnson, J. M., and K. Satake (1994), Rupture extent of the 1938 alaskan earthquake as inferred from tsunami waveforms, *Geophysical Research Letters*, *21*(8), 733–736.

Johnson, J. M., K. Satake, S. R. Holdahl, and J. Sauber (1996), The 1964 prince william sound earthquake: Joint inversion of tsunami and geodetic data, *Journal of Geophysical Research: Solid Earth*, *101*(B1), 523–532.

Jones, D. L., N. Silberling, and J. Hillhouse (1977), WrangelliaâĂŤa displaced terrane in northwestern north america, *Canadian Journal of Earth Sciences*, *14*(11), 2565–2577.

Jones, T. D., and A. Nur (1984), The nature of seismic reflections from deep crustal fault zones, *Journal of Geophysical Research: Solid Earth*, *89*(B5), 3153–3171.

Kanamori, H. (1972), Mechanism of tsunami earthquakes, *Physics of the earth and planetary interiors*, *6*(5), 346–359.

Kanamori, H. (1977), The energy release in great earthquakes, *Journal of geophysical research*, *82*(20), 2981–2987.

Kanamori, H. (1986), Rupture process of subduction-zone earthquakes, *Annual Review of Earth and Planetary Sciences*, *14*(1), 293–322.

Kato, A., T. Iidaka, R. Ikuta, Y. Yoshida, K. Katsumata, T. Iwasaki, S. Sakai, C. Thurber, N. Tsumura, K. Yamaoka, et al. (2010), Variations of fluid pressure within the subducting oceanic crust and slow earthquakes, *Geophysical research letters*, *37*(14).

Kearey, P., K. A. Klepeis, and F. J. Vine (2013), Global tectonics.

Kelleher, J., and W. McCann (1976), Buoyant zones, great earthquakes, and unstable boundaries of subduction, *Journal of Geophysical Research*, *81*(26), 4885–4896.

Kelleher, J., L. Sykes, and J. Oliver (1973), Possible criteria for predicting earthquake locations and their application to major plate boundaries of the pacific and the caribbean, *Journal of Geophysical Research*, *78*(14), 2547–2585.

Kelleher, J. A. (1972), Rupture zones of large south american earthquakes and some predictions, *Journal of Geophysical Research*, *77*(11), 2087–2103.

Keller, R. A., M. R. Fisk, R. A. Duncan, and W. M. White (1997), 16 my of hotspot and nonhotspot volcanism on the patton-murray seamount platform, gulf of alaska, *Geology*, *25*(6), 511–514.

Kelly, K., R. Ward, S. Treitel, and R. Alford (1976), Synthetic seismograms: A finite-difference approach, *Geophysics*, *41*(1), 2–27.

Kerrick, D., and J. Connolly (2001), Metamorphic devolatilization of subducted marine sediments and the transport of volatiles into the earth's mantle, *Nature*, *411*(6835), 293.

Kimura, G., E. Silver, P. Blum, , et al. (1997), Proceedings of the ocean drilling program, vol. 170, initial reports, costa rica accretionary wedge.

Kitamura, Y., K. Sato, E. Ikesawa, K. Ikehara-Ohmori, G. Kimura, H. Kondo, K. Ujiie, C. T. Onishi, K. Kawabata, Y. Hashimoto, et al. (2005), Mélange and its seismogenic roof décollement: A plate boundary fault rock in the subduction zoneâĂŤan example from the shimanto belt, japan, *Tectonics*, *24*(5).

Kodaira, S., N. Takahashi, A. Nakanishi, S. Miura, and Y. Kaneda (2000), Subducted seamount imaged in the rupture zone of the 1946 nankaido earthquake, *Science*, *289*(5476), 104–106.

Kodaira, S., E. Kurashimo, J.-O. Park, N. Takahashi, A. Nakanishi, S. Miura, T. Iwasaki, N. Hirata, K. Ito, and Y. Kaneda (2002), Structural factors controlling the rupture process of a megathrust earthquake at the nankai trough seismogenic zone, *Geophysical Journal International*, *149*(3), 815–835.

Kodaira, S., T. Iidaka, A. Kato, J.-O. Park, T. Iwasaki, and Y. Kaneda (2004), High pore fluid pressure may cause silent slip in the nankai trough, *Science*, *304*(5675), 1295–1298.

Kodaira, S., T. Iidaka, A. Nakanishi, J.-O. Park, T. Iwasaki, and Y. Kaneda (2005), Onshore-offshore seismic transect from the eastern nankai trough to central japan crossing a zone of the tokai slow slip event, *Earth, planets and space*, *57*(10), 943–959.

Konstantinovskaya, E., and J. Malavieille (2011), Thrust wedges with décollement levels and syntectonic erosion: A view from analog models, *Tectonophysics*, *502*(3-4), 336–350.

Kurashimo, E., T. Iwasaki, T. Iidaka, A. Kato, F. Yamazaki, K. Miyashita, T. Shibutani, K. Ito, T. Takeda, K. Obara, et al. (2013), Along-strike structural changes controlled by dehydration-related fluids within the philippine sea plate around the segment boundary of a megathrust earthquake beneath the kii peninsula, southwest japan, *Geophysical Research Letters*, *40*(18), 4839–4844.

Lallemand, S. (1999), La subduction océanique, *Pour la Science*, (259), 108.

Lay, T., H. Kanamori, C. J. Ammon, K. D. Koper, A. R. Hutko, L. Ye, H. Yue, and T. M. Rushing (2012), Depth-varying rupture properties of subduction zone megathrust faults, *Journal of Geophysical Research: Solid Earth*, *117*(B4).

Li, J. (2016), Seismicity and seismic imaging of the alaska megathrust, Ph.D. thesis, Columbia University New York.

Li, J., D. J. Shillington, A. Bécel, M. R. Nedimović, S. C. Webb, D. M. Saffer, K. M. Keranen, and H. Kuehn (2015), Downdip variations in seismic reflection character: Implications for fault structure and seismogenic behavior in the alaska subduction zone, *Journal of Geophysical Research: Solid Earth*, *120*(11), 7883–7904.

Li, J., D. J. Shillington, D. M. Saffer, A. Bécel, M. R. Nedimović, H. Kuehn, S. C. Webb, K. M. Keranen, and G. A. Abers (2018), Connections between subducted sediment, pore-fluid pressure, and earthquake behavior along the alaska megathrust, *Geology*, *46*(4), 299–302.

Li, S., and J. T. Freymueller (2017), Spatial variation of slip behavior beneath the alaska peninsula along alaska-aleutian subduction zone, *Geophysical Research Letters*.

Li, S., and J. T. Freymueller (2018), Spatial variation of slip behavior beneath the alaska peninsula along alaska-aleutian subduction zone, *Geophysical Research Letters*, *45*(8), 3453–3460.

Liu, Y., and J. R. Rice (2007), Spontaneous and triggered aseismic deformation transients in a subduction fault model, *Journal of Geophysical Research: Solid Earth*, *112*(B9).

Lizarralde, D., W. S. Holbrook, S. McGeary, N. L. Bangs, and J. B. Diebold (2002), Crustal construction of a volcanic arc, wide-angle seismic results from the western alaska peninsula, *Journal of Geophysical Research: Solid Earth*, *107*(B8).

Lonsdale, P. (1988), Paleogene history of the kula plate: Offshore evidence and onshore implications, *Geological Society of America Bulletin*, *100*(5), 733–754.

López, A. M., and E. A. Okal (2006), A seismological reassessment of the source of the 1946 aleutian âĂŸtsunamiâĂŹearthquake, *Geophysical Journal International*, *165*(3), 835–849.

Manning, D. A., and J. Decleer (1995), Introduction to industrial minerals.

Marlow, M. S., D. W. Scholl, E. C. Buffington, and T. RHO ALPHA (1973), Tectonic history of the central aleutian arc, *Geological Society of America Bulletin*, *84*(5), 1555–1574.

Masson, D. (1991), Fault patterns at outer trench walls, *Marine Geophysical Researches*, *13*(3), 209–225.

Matsumura, M., Y. Hashimoto, G. Kimura, K. Ohmori-Ikehara, M. Enjohji, and E. Ikesawa (2003), Depth of oceanic-crust underplating in a subduction zone: Inferences from fluid-inclusion analyses of crack-seal veins, *Geology*, *31*(11), 1005–1008.

Matzel, J. E., S. A. Bowring, and R. B. Miller (2004), Protolith age of the swakane gneiss, north cascades, washington: Evidence of rapid underthrusting of sediments beneath an arc, *Tectonics*, *23*(6).

McCaffrey, R. (2008), Global frequency of magnitude 9 earthquakes, *Geology*, *36*(3), 263–266.

McCann, W. R., O. J. Pérez, and L. R. Sykes (1980), Yakataga gap, alaska: Seismic history and earthquake potential, *Science*, pp. 1309–1314.

Mechie, J., G. R. Keller, C. Prodehl, S. Gaciri, L. Braile, W. Mooney, D. Gajewski, and K.-J. Sandmeier (1994), Crustal structure beneath the kenya rift from axial profile data, *Tectonophysics*, *236*(1-4), 179–200.

Meyer, B., A. Chulliat, and R. Saltus (2017), Derivation and error analysis of the earth magnetic anomaly grid at 2 arc min resolution version 3 (emag2v3), *Geochemistry, Geophysics, Geosystems*, *18*(12), 4522–4537.

Miura, S., N. Takahashi, A. Nakanishi, T. Tsuru, S. Kodaira, and Y. Kaneda (2005), Structural characteristics off miyagi forearc region, the japan trench seismogenic zone, deduced from a wide-angle reflection and refraction study, *Tectonophysics*, *407*(3-4), 165–188.

Mochizuki, K., T. Yamada, M. Shinohara, Y. Yamanaka, and T. Kanazawa (2008), Weak interplate coupling by seamounts and repeating m˜ 7 earthquakes, *Science*, *321*(5893), 1194–1197.

Moore, G. (1993), Character of the décollement in the leg 131 area, nankai trough, *131*, 73–82.

Moore, J. C., and D. Saffer (2001), Updip limit of the seismogenic zone beneath the accretionary prism of southwest japan: An effect of diagenetic to low-grade metamorphic processes and increasing effective stress, *Geology*, *29*(2), 183–186.

Moore, J. C., and P. Vrolijk (1992), Fluids in accretionary prisms, *Reviews of Geophysics*, *30*(2), 113–135.

Moore, J. C., J. Diebold, M. Fisher, J. Sample, T. Brocher, M. Talwani, J. Ewing, R. v. Huene, C. Rowe, D. Stone, et al. (1991), Edge deep seismic reflection transect of the eastern aleutian arc-trench layered lower crust reveals underplating and continental growth, *Geology*, *19*(5), 420–424.

Morgan, J. K., and M. V. Ask (2004), Consolidation state and strength of underthrust sediments and evolution of the decollement at the nankai accretionary margin: Results of uniaxial reconsolidation experiments, *Journal of Geophysical Research: Solid Earth*, *109*(B3).

Morley, L. W. (1991), The role of magnetic surveying in developing the concept of plate tectonics, *Tectonophysics*, *187*(1-3), 23–25.

Nakanishi, A., S. Kodaira, S. Miura, A. Ito, T. Sato, J.-O. Park, Y. Kido, and Y. Kaneda (2008), Detailed structural image around splay-fault branching in the nankai subduction seismogenic zone: Results from a high-density ocean bottom seismic survey, *Journal of Geophysical Research: Solid Earth*, *113*(B3).

Nanda, N. C. (2016), *Seismic data interpretation and evaluation for hydrocarbon exploration and production: A practitionerâĂŹs guide*, Springer.

Nedimović, M. R., R. D. Hyndman, K. Ramachandran, and G. D. Spence (2003), Reflection signature of seismic and aseismic slip on the northern cascadia subduction interface, *Nature*, *424*(6947), 416.

Nelson, A. R., R. W. Briggs, T. Dura, S. E. Engelhart, G. Gelfenbaum, L.-A. Bradley, S. L. Forman, C. H. Vane, and K. A. Kelley (2015), Tsunami recurrence in the eastern alaska-aleutian arc: A holocene stratigraphic record from chirikof island, alaska, *Geosphere*, *11*(4), 1172–1203.

Nicolsky, D., J. Freymueller, R. Witter, E. Suleimani, and R. Koehler (2016), Evidence for shallow megathrust slip across the unalaska seismic gap during the great 1957 andreanof islands earthquake, eastern aleutian islands, alaska, *Geophysical Research Letters*, *43*(19).

Nishenko, S., and K. Jacob (1990), Seismic potential of the queen charlotte-alaska-aleutian seismic zone, *Journal of Geophysical Research: Solid Earth*, *95*(B3), 2511–2532.

Obana, K., and S. Kodaira (2009), Low-frequency tremors associated with reverse faults in a shallow accretionary prism, *Earth and Planetary Science Letters*, *287*(1), 168–174.

Obara, K., H. Hirose, F. Yamamizu, and K. Kasahara (2004), Episodic slow slip events accompanied by non-volcanic tremors in southwest japan subduction zone, *Geophysical Research Letters*, *31*(23).

Oleskevich, D., R. Hyndman, and K. Wang (1999), The updip and downdip limits to great subduction earthquakes: Thermal and structural models of cascadia, south alaska, sw japan, and chile, *Journal of Geophysical Research: Solid Earth*, *104*(B7), 14,965–14,991.

Omori, F. (1894), *On the after-shocks of earthquakes*, vol. 7, The University.

Oncken, O., G. Asch, C. Haberland, J. Metchie, S. Sobolev, M. Stiller, X. Yuan, H. Brasse, S. Buske, P. Giese, et al. (2003), Seismic imaging of a convergent continental margin and plateau in the central andes (andean continental research project 1996 (ancorp'96)), *Journal of Geophysical Research: Solid Earth*, *108*(B7).

Ortiz, M., and R. Bilham (2003), Source area and rupture parameters of the 31 december 1881 mw= 7.9 car nicobar earthquake estimated from tsunamis recorded in the bay of bengal, *Journal of Geophysical Research: Solid Earth*, *108*(B4).

Pacheco, J. F., L. R. Sykes, and C. H. Scholz (1993), Nature of seismic coupling along simple plate boundaries of the subduction type, *Journal of Geophysical Research: Solid Earth*, *98*(B8), 14,133–14,159.

Park, J.-O., T. Tsuru, N. Takahashi, T. Hori, S. Kodaira, A. Nakanishi, S. Miura, and Y. Kaneda (2002), A deep strong reflector in the nankai accretionary wedge from multichannel seismic data: Implications for underplating and interseismic shear stress release, *Journal of Geophysical Research: Solid Earth*, *107*(B4).

Park, J.-O., G. Fujie, L. Wijerathne, T. Hori, S. Kodaira, Y. Fukao, G. F. Moore, N. L. Bangs, S. Kuramoto, and A. Taira (2010), A low-velocity zone with weak reflectivity along the nankai subduction zone, *Geology*, *38*(3), 283–286.

Peacock, S. M. (1990), Numerical simulation of metamorphic pressure-temperature-time paths and fluid production in subducting slabs, *Tectonics*, *9*(5), 1197–1211.

Peacock, S. M. (1993), Large-scale hydration of the lithosphere above subducting slabs, *Chemical Geology*, *108*(1), 49–59.

Peacock, S. M., and R. D. Hyndman (1999), Hydrous minerals in the mantle wedge and the maximum depth of subduction thrust earthquakes, *Geophysical Research Letters*, *26*(16), 2517–2520.

Petersen, M. D., C. H. Cramer, and A. D. Frankel (2002), Simulations of seismic hazard for the pacific northwest of the united states from earthquakes associated with the cascadia subduction zone, in *Earthquake Processes: Physical Modelling, Numerical Simulation and Data Analysis Part I*, pp. 2147–2168, Springer.

Piatanesi, A., S. Tinti, and I. Gavagni (1996), The slip distribution of the 1992 nicaragua earthquake from tsunami run-up data, *Geophysical research letters*, *23*(1), 37–40.

Plafker, G., and H. C. Berg (1994), Overview of the geology and tectonic evolution of alaska, *The Geological Society of America, Boulder, Co*, pp. 989–1021.

Plafker, G., and R. Kachadoorian (1966), *Geologic effects of the March 1964 earthquake and associated seismic sea waves on Kodiak and nearby islands, Alaska*, US Government Printing Office.

Pollack, H. N., S. J. Hurter, and J. R. Johnson (1993), Heat flow from the earth's interior: analysis of the global data set, *Reviews of Geophysics*, *31*(3), 267–280.

Pollitz, F. F., R. Bürgmann, and P. Banerjee (2011), Geodetic slip model of the 2011 m9. 0 tohoku earthquake, *Geophysical Research Letters*, *38*(7).

Prodehl, C., and W. D. Mooney (2012), Exploring the earth's crust: history and results of controlled-source seismology, *208*.

Pytte, A., and R. Reynolds (1988), The thermal transformation of smectite to illite. pp. 133ā140 in: Thermal history of sedimentary basins (nd naeser and th mcculloh, editors).

Ranero, C. R., and R. von Huene (2000), Subduction erosion along the middle america convergent margin, *Nature*, *404*(6779), 748.

Ranero, C. R., I. Grevemeyer, H. Sahling, U. Barckhausen, C. Hensen, K. Wallmann, W. Weinrebe, P. Vannucchi, R. von Huene, and K. McIntosh (2008), Hydrogeological system of erosional convergent margins and its influence on tectonics and interplate seismogenesis, *Geochemistry, Geophysics, Geosystems*, *9*(3).

Reece, R. S., S. P. Gulick, B. K. Horton, G. L. Christeson, and L. L. Worthington (2011), Tectonic and climatic influence on the evolution of the surveyor fan and channel system, gulf of alaska, *Geosphere*, *7*(4), 830–844.

Ridgway, K. D., J. M. Trop, W. J. Nokleberg, C. M. Davidson, and K. R. Eastham (2002), Mesozoic and cenozoic tectonics of the eastern and central alaska range: Progressive basin development and deformation in a suture zone, *Geological Society of America Bulletin*, *114*(12), 1480–1504.

Rogers, G., and H. Dragert (2003), Episodic tremor and slip on the cascadia subduction zone: The chatter of silent slip, *Science*, *300*(5627), 1942–1943.

Rogers, G. C. (1988), An assessment of the megathrust earthquake potential of the cascadia subduction zone, *Canadian Journal of Earth Sciences*, *25*(6), 844–852.

Rowe, C. D., J. C. Moore, F. Remitti, and I. E. T. Scientists (2013), The thickness of subduction plate boundary faults from the seafloor into the seismogenic zone, *Geology*, *41*(9), 991–994.

Ruff, L., and H. Kanamori (1983), Seismic coupling and uncoupling at subduction zones, *Tectonophysics*, *99*(2-4), 99–117.

Ruff, L. J. (1989), Do trench sediments affect great earthquake occurrence in subduction zones?, in *Subduction Zones Part II*, pp. 263–282, Springer.

Ruff, L. J., and B. W. Tichelaar (1996), What controls the seismogenic plate interface in subduction zones?, *Subduction: Top to bottom*, *96*, 105–111.

Sacks, I. S., A. T. Linde, J. A. Snoke, and S. Suyehiro (1981), A slow earthquake sequence following the izu-oshima earthquake of 1978, *Earthquake Prediction: An International Review*, *4*, 617–628.

Saffer, D. M., and B. A. Bekins (2006), An evaluation of factors influencing pore pressure in accretionary complexes: Implications for taper angle and wedge mechanics, *Journal of Geophysical Research: Solid Earth*, *111*(B4).

Saffer, D. M., and C. Marone (2003), Comparison of smectite-and illite-rich gouge frictional properties: application to the updip limit of the seismogenic zone along subduction megathrusts, *Earth and Planetary Science Letters*, *215*(1), 219–235.

Saffer, D. M., and H. J. Tobin (2011), Hydrogeology and mechanics of subduction zone forearcs: Fluid flow and pore pressure, *Annual Review of Earth and Planetary Sciences*, *39*, 157–186.

Sample, J. C., and J. C. Moore (1987), Structural style and kinematics of an underplated slate belt, kodiak and adjacent islands, alaska, *Geological Society of America Bulletin*, *99*(1), 7–20.

Sandwell, D. T., R. D. Müller, W. H. Smith, E. Garcia, and R. Francis (2014), New global marine gravity model from cryosat-2 and jason-1 reveals buried tectonic structure, *Science*, *346*(6205), 65–67.

SATAKE, K. (1987), Inversion of tsunami waveforms for the estimation of a fault heterogeneity: Method and numerical experiments, *Journal of Physics of the Earth*, *35*(3), 241–254.

Sato, H., N. Hirata, K. Koketsu, D. Okaya, S. Abe, R. Kobayashi, M. Matsubara, T. Iwasaki, T. Ito, T. Ikawa, et al. (2005), Earthquake source fault beneath tokyo, *Science*, *309*(5733), 462–464.

Savage, J., M. Lisowski, and W. Prescott (1991), Strain accumulation in western washington, *Journal of Geophysical Research: Solid Earth*, *96*(B9), 14,493–14,507.

Schmidt, M. W., and S. Poli (1998), Experimentally based water budgets for dehydrating slabs and consequences for arc magma generation, *Earth and Planetary Science Letters*, *163*(1-4), 361–379.

Scholl, D. (2016), The argument that the oceanic crust of the backarc aleutian basin (bering sea) is a terrane of pacific oceanic crust, possibly the kula plate, accreted to the north american plate at 50-55 ma, in *AGU Fall Meeting Abstracts*.

Scholl, D. W., T. L. Vallier, and A. J. Stevenson (1986), Terrane accretion, production, and continental growth: A perspective based on the origin and tectonic fate of the aleutian–bering sea region, *Geology*, *14*(1), 43–47.

Scholz, C. H. (1998), Earthquakes and friction laws, *Nature*, *391*(6662), 37–42.

Scholz, C. H. (2002), *The mechanics of earthquakes and faulting*, Cambridge university press.

Scholz, C. H., and C. Small (1997), The effect of seamount subduction on seismic coupling, *Geology*, *25*(6), 487–490.

Schwartz, S. Y., and J. M. Rokosky (2007), Slow slip events and seismic tremor at circum-pacific subduction zones, *Reviews of Geophysics*, *45*(3).

Sella, G. F., T. H. Dixon, and A. Mao (2002), Revel: A model for recent plate velocities from space geodesy, *Journal of Geophysical Research: Solid Earth*, *107*(B4).

Shelly, D. R., G. C. Beroza, S. Ide, and S. Nakamula (2006), Low-frequency earthquakes in shikoku, japan, and their relationship to episodic tremor and slip, *Nature*, *442*(7099), 188.

Shelly, D. R., G. C. Beroza, and S. Ide (2007), Complex evolution of transient slip derived from precise tremor locations in western shikoku, japan, *Geochemistry, Geophysics, Geosystems*, *8*(10).

Shennan, I., N. Barlow, and R. Combellick (2008), Paleoseismological records of multiple great earthquakes in southcentral alaska: A 4000-year record at girdwood, *Active Tectonics and Seismic Potential of Alaska*, pp. 185–199.

Shennan, I., N. Barlow, R. Combellick, K. Pierre, and O. STUART-TAYLOR (2014), Late holocene paleoseismology of a site in the region of maximum subsidence during the 1964 mw 9.2 alaska earthquake, *Journal of Quaternary Science*, *29*(4), 343–350.

Shillington, D. J., H. J. Van Avendonk, W. S. Holbrook, P. B. Kelemen, and M. J. Hornbach (2004), Composition and structure of the central aleutian island arc from arc-parallel wide-angle seismic data, *Geochemistry, Geophysics, Geosystems*, *5*(10).

Shillington, D. J., A. Bécel, M. R. Nedimović, H. Kuehn, S. C. Webb, G. A. Abers, K. M. Keranen, J. Li, M. Delescluse, and G. A. Mattei-Salicrup (2015), Link between plate fabric, hydration and subduction zone seismicity in alaska, *Nature Geoscience*, *8*(12), 961.

Silver, E. A., R. von Huene, and J. K. Crouch (1974), Tectonic significance of the kodiak-bowie seamount chain, northeastern pacific, *Geology*, *2*(3), 147–150.

Smoot, N. C. (1985), Observations on gulf of alaska seamount chains by multi-beam sonar, *Tectonophysics*, *115*(3-4), 235–246.

Soloviev, S. (1990), Sanak-kodiak tsunami of 1788, *Science of Tsunami Hazards*, *8*(1), 34–38.

Song, T.-R. A., and M. Simons (2003), Large trench-parallel gravity variations predict seismogenic behavior in subduction zones, *Science*, *301*(5633), 630–633.

Spiess, F. N., C. D. Chadwell, J. A. Hildebrand, L. E. Young, G. H. Purcell, and H. Dragert (1998), Precise gps/acoustic positioning of seafloor reference points for tectonic studies, *Physics of the Earth and Planetary Interiors*, *108*(2), 101–112.

Spinelli, G. A., and D. M. Saffer (2004), Along-strike variations in underthrust sediment dewatering on the nicoya margin, costa rica related to the updip limit of seismicity, *Geophysical Research Letters*, *31*(4).

Stern, R. J. (2002), Subduction zones, *Reviews of geophysics*, *40*(4).

Steven Holbrook, W., D. Lizarralde, S. McGeary, N. Bangs, and J. Diebold (1999), Structure and composition of the aleutian island arc and implications for continental crustal growth, *Geology*, *27*(1), 31–34.

Stevenson, A. J., and R. Embley (1987), Deep-sea fan bodies, terrigenous turbidite sedimentation, and petroleum geology, gulf of alaska.

Stevenson, A. J., D. W. Scholl, and T. L. Vallier (1983), Tectonic and geologic implications of the zodiac fan, aleutian abyssal plain, northeast pacific, *Geological Society of America Bulletin*, *94*(2), 259–273.

Sykes, L. R. (1971), Aftershock zones of great earthquakes, seismicity gaps, and earthquake prediction for alaska and the aleutians, *Journal of Geophysical Research*, *76*(32), 8021–8041.

Syracuse, E. M., and G. A. Abers (2006), Global compilation of variations in slab depth beneath arc volcanoes and implications, *Geochemistry, Geophysics, Geosystems*, *7*(5).

Syracuse, E. M., and G. A. Abers (2009), Systematic biases in subduction zone hypocenters, *Geophysical Research Letters*, *36*(10).

Syracuse, E. M., P. E. van Keken, and G. A. Abers (2010), The global range of subduction zone thermal models, *Physics of the Earth and Planetary Interiors*, *183*(1-2), 73–90.

Telford, W. M., W. Telford, L. Geldart, R. E. Sheriff, and R. E. Sheriff (1990), *Applied geophysics*, vol. 1, Cambridge university press.

Tichelaar, B. W., and L. J. Ruff (1993), Depth of seismic coupling along subduction zones, *Journal of Geophysical Research: Solid Earth*, *98*(B2), 2017–2037.

Tobin, H. J., and D. M. Saffer (2009), Elevated fluid pressure and extreme mechanical weakness of a plate boundary thrust, nankai trough subduction zone, *Geology*, *37*(8), 679–682.

Tse, S. T., and J. R. Rice (1986), Crustal earthquake instability in relation to the depth variation of frictional slip properties, *Journal of Geophysical Research: Solid Earth*, *91*(B9), 9452–9472.

Turner, D. L., R. B. Forbes, and C. W. Naeser (1973), Radiometric ages of kodiak seamount and giacomini guyot, gulf of alaska: implications for circum-pacific tectonics, *Science*, *182*(4112), 579–581.

Uyeda, S., and H. Kanamori (1979), Back-arc opening and the mode of subduction, *Journal of Geophysical Research: Solid Earth*, *84*(B3), 1049–1061.

Vannucchi, P., D. M. Fisher, S. Bier, and T. W. Gardner (2006), From seamount accretion to tectonic erosion: Formation of osa mélange and the effects of cocos ridge subduction in southern costa rica, *Tectonics*, *25*(2).

Verschuur, D. J., A. Berkhout, and C. Wapenaar (1992), Adaptive surface-related multiple elimination, *Geophysics*, *57*(9), 1166–1177.

Vine, F. J., and D. H. Matthews (1963), Magnetic anomalies over oceanic ridges, *Nature*, *199*(4897), 947–949.

Von Huene, R., J. J. Miller, and W. Weinrebe (2012), Subducting plate geology in three great earthquake ruptures of the western alaska margin, kodiak to unimak, *Geosphere*, *8*(3), 628–644.

Vrolijk, P. (1990), On the mechanical role of smectite in subduction zones, *Geology*, *18*(8), 703–707.

Wadati, K. (1935), On the activity of deep-focus earthquakes in the japan islands and neighbourhoods, *Geophys. Mag.*, *8*, 305–325.

Waldhauser, F., and W. L. Ellsworth (2000), A double-difference earthquake location algorithm: Method and application to the northern hayward fault, california, *Bulletin of the Seismological Society of America*, *90*(6), 1353–1368.

Wang, K., and S. L. Bilek (2011), Do subducting seamounts generate or stop large earthquakes?, *Geology*, *39*(9), 819–822.

Watts, A. B., A. A. Koppers, and D. P. Robinson (2010), Seamount subduction and earthquakes, *Oceanography*, *23*(1), 166–173.

Wells, R. E., R. J. Blakely, Y. Sugiyama, D. W. Scholl, and P. A. Dinterman (2003), Basin-centered asperities in great subduction zone earthquakes: A link between slip, subsidence, and subduction erosion?, *Journal of Geophysical Research: Solid Earth*, *108*(B10).

Wesson, R. L. (1988), Dynamics of fault creep, *Journal of Geophysical Research: Solid Earth*, *93*(B8), 8929–8951.

Wesson, R. L., O. S. Boyd, C. S. Mueller, C. G. Bufe, A. D. Frankel, and M. D. Petersen (2007), Revision of time-independent probabilistic seismic hazard maps for alaska, *Tech. rep.*, Geological Survey (US).

White, R. S., D. McKenzie, and R. K. O'Nions (1992), Oceanic crustal thickness from seismic measurements and rare earth element inversions, *Journal of Geophysical Research: Solid Earth*, *97*(B13), 19,683–19,715.

Wilson, J. T. (1963), A possible origin of the hawaiian islands, *Canadian Journal of Physics*, *41*(6), 863–870.

Witter, R. C., R. W. Briggs, S. E. Engelhart, G. Gelfenbaum, R. D. Koehler, and W. D. Barnhart (2014), Little late holocene strain accumulation and release on the aleutian megathrust below the shumagin islands, alaska, *Geophysical Research Letters*, *41*(7), 2359–2367.

Worrall, D. M. (1991), *Tectonic history of the Bering Sea and the evolution of Tertiary strike-slip basins of the Bering Shelf*, vol. 257, Geological Society of America.

Ye, S., E. Flueh, D. Klaeschen, and R. Von Huene (1997), Crustal structure along the edge transect beneath the kodiak shelf off alaska derived from obh seismic refraction data, *Geophysical Journal International*, *130*(2), 283–302.

Yilmaz, O. (1987), Seismic deta processing, *Investigation in geophysics*, *2*, 526.

Zelt, C., and R. Smith (1992), Seismic traveltime inversion for 2-d crustal velocity structure, *Geophysical journal international*, *108*(1), 16–34.

Zelt, C. A. (1998), Lateral velocity resolution from three-dimensional seismic refraction data, *Geophysical Journal International*, *135*(3), 1101–1112.

Zelt, C. A. (1999), Modelling strategies and model assessment for wide-angle seismic traveltime data, *Geophysical Journal International*, *139*(1), 183–204.

Zelt, C. A., and P. J. Barton (1998), Three-dimensional seismic refraction tomography: A comparison of two methods applied to data from the faeroe basin, *Journal of Geophysical Research: Solid Earth*, *103*(B4), 7187–7210.

Appendix A

ALEUT MCS reflection images with and without plate interface interpretation and superimposed corresponding velocity model

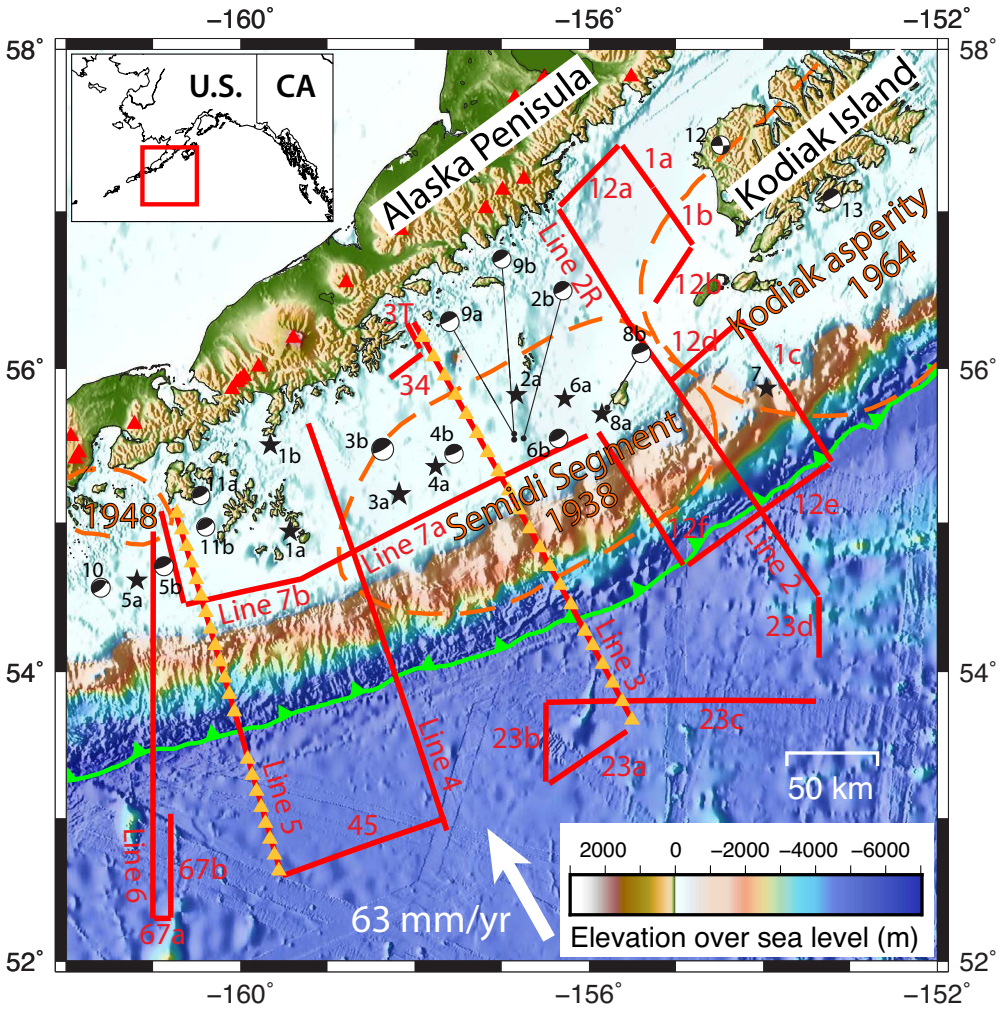

Figure A.1: (Caption next page.)

Figure A.1: (Previous page.) Survey area of the ALEUT project with the location of the collected seismic profiles. Thin solid red lines are MCS profiles with line numbers also in red. Blue triangles are OBS deployment positions that outline two wide-angle profiles coincident in location with MCS lines 3 and 5. Thick dashed lines (orange, black, mangenta) outline rupture areas derived from aftershock locations for the M_W 8.3 1938 earthquake at the Semidi Segment (orange), M_W 9.2 1964 Prince William Sound earthquake (black) and M_W 7.1 earthquake (mangenta) (after McCann et al., 1980). The Shumagin Gap area lies adjacent to the Semidi Segment to the west in the vicinity and around the Shumagin Islands. The epicenter for the 1938 earthquake is the black star with the orange edging located by USGS. Same symbol with an asterisk show alternate location by Sykes (1971). The epicenter for the 1948 rupture area is the black star with the mangenta edging, alternate location by Boyd and Larner-Lam (1988) is annoted by an asterisk. Note that there is a mismatch between epicenter locations and rupture area outline for the 1948 event. The epicenter for the 1964 earthquake falls outside the study area. Stars and focal mechanisms with colored edging show epicenters of all $\geq M_W$ 6.9 earthquakes since the beginning of instrumental seismic recording as catalogued in the latest version of the USGS database (https://earthquake.usgs.gov/earthquakes/). When available, focal mechanisms are shown. Symbols with the same color show alternate locations, where the asterisk represents a location source other than USGS. A detailed list for all events are given in table 1. Green line is the trench position, i.e. surface trace of the plate boundary between the overriding North America and the subducting Pacific Plates. Red triangles show the position of active volcanoes taken from the Alaska Volcano Observatorys web page (https://www.avo.alaska.edu/volcanoes/).

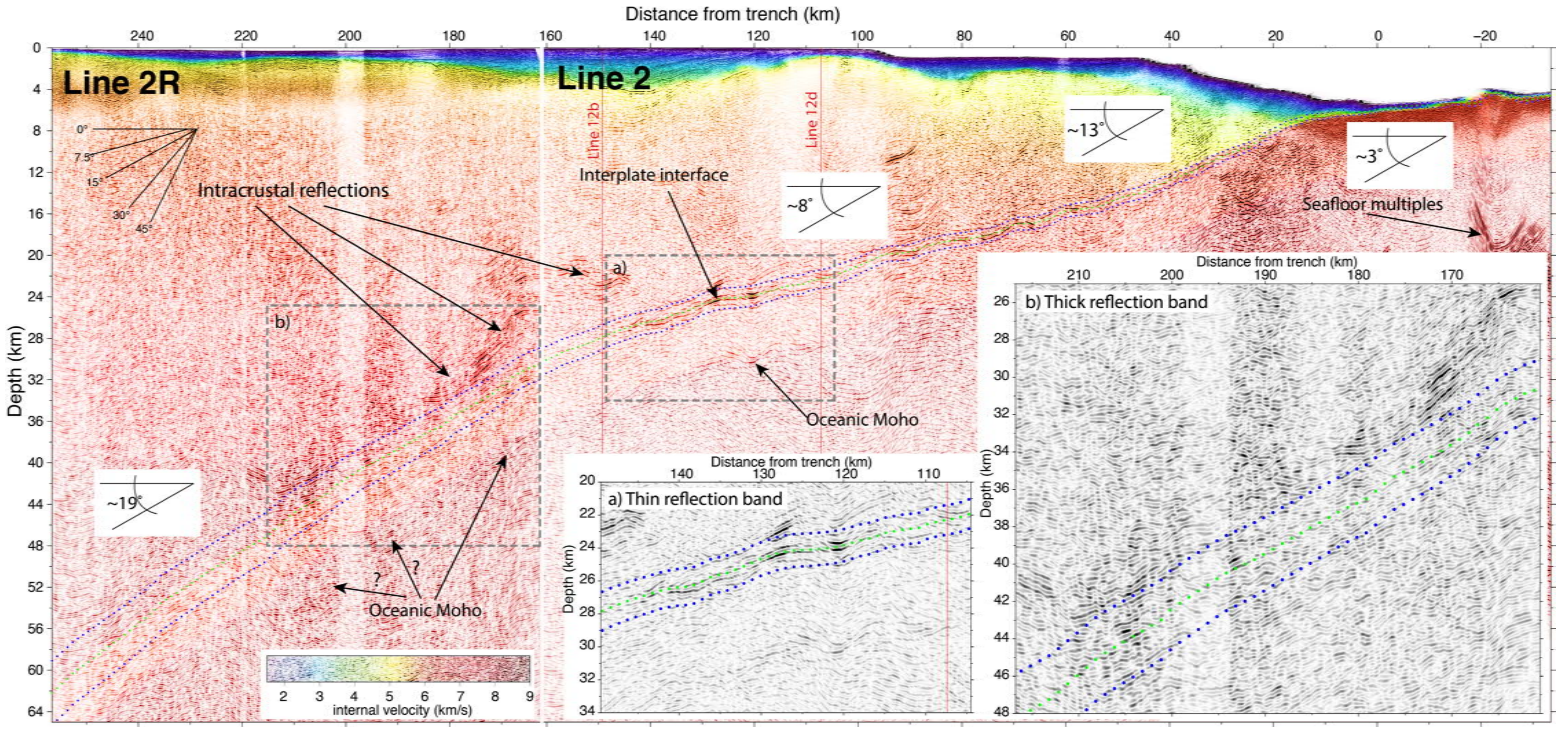

Figure A.2: Migrated and depth converted stack of MCS Lines 2 and 2R in gray scale with the corresponding color composite velocity model superimposed. The velocity model was developed using: a) average sediment interval velocities for the survey area derived from the MCS data; b) averaged upper crustal interval velocities for the continental crust based of OBS first arrival traveltime tomography; c) lower crustal interval velocities for the continental crust from Christensen and Mooney, 1995; d) upper mantle velocity from Christensen and Mooney, 1995; e) velocity of the oceanic crust was set to a constant velocity of 6.5 km/s. Green dotted line is the interpreted location of the interplate interface between North America and Pacific Plates. Blue dotted lines show the location of the interplate interface assuming uncertainty of 5% in the velocity model below the seafloor. Boxes with dashed outline are zoomed and shown as figure inlets to emphasize the interplate interface picks within the thin and thick reflection band areas. Thin vertical red lines are intersections with other ALEUT MCS profiles.

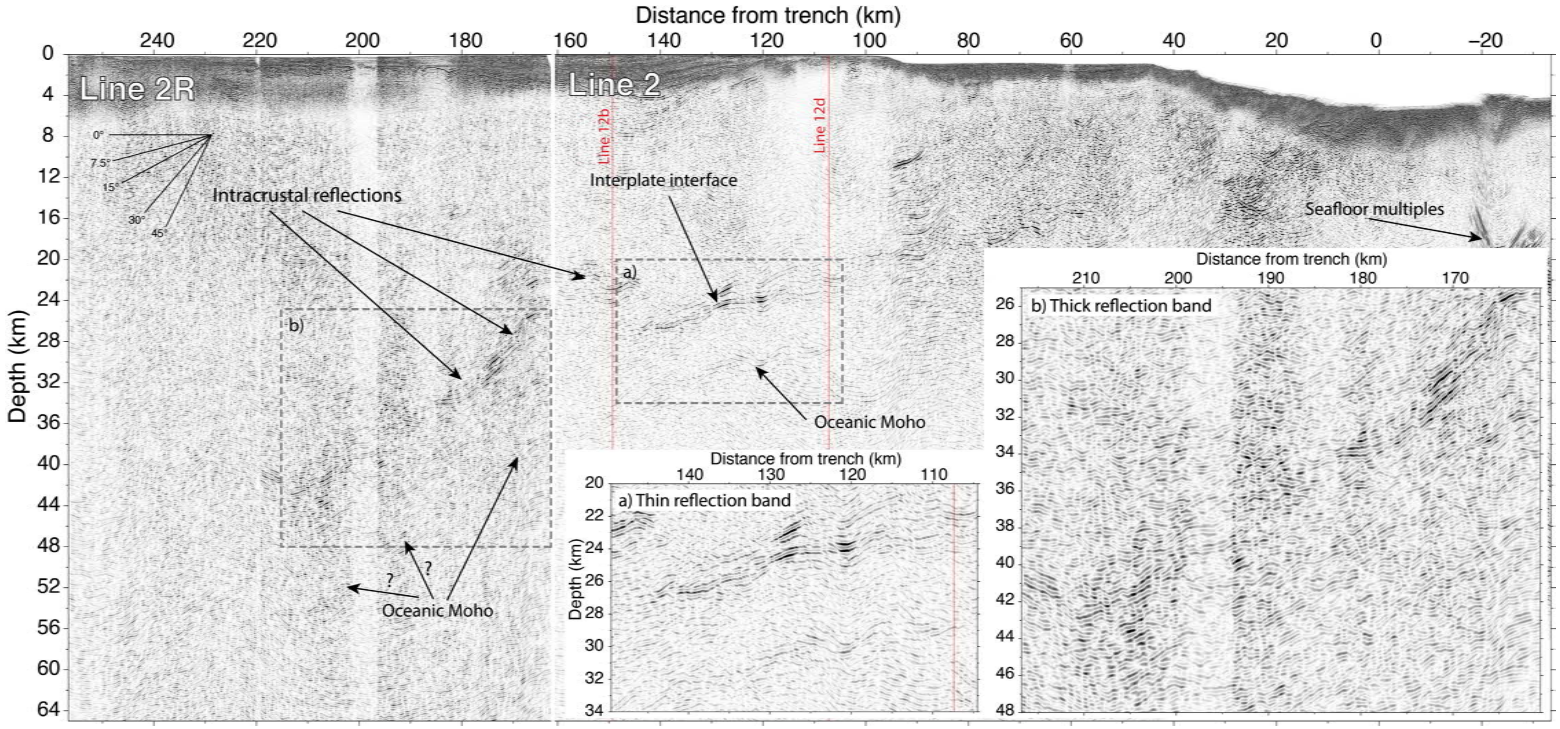

Figure A.3: Same as Figure A.2 but without the velocity model overlay and interplate interface interpretation.

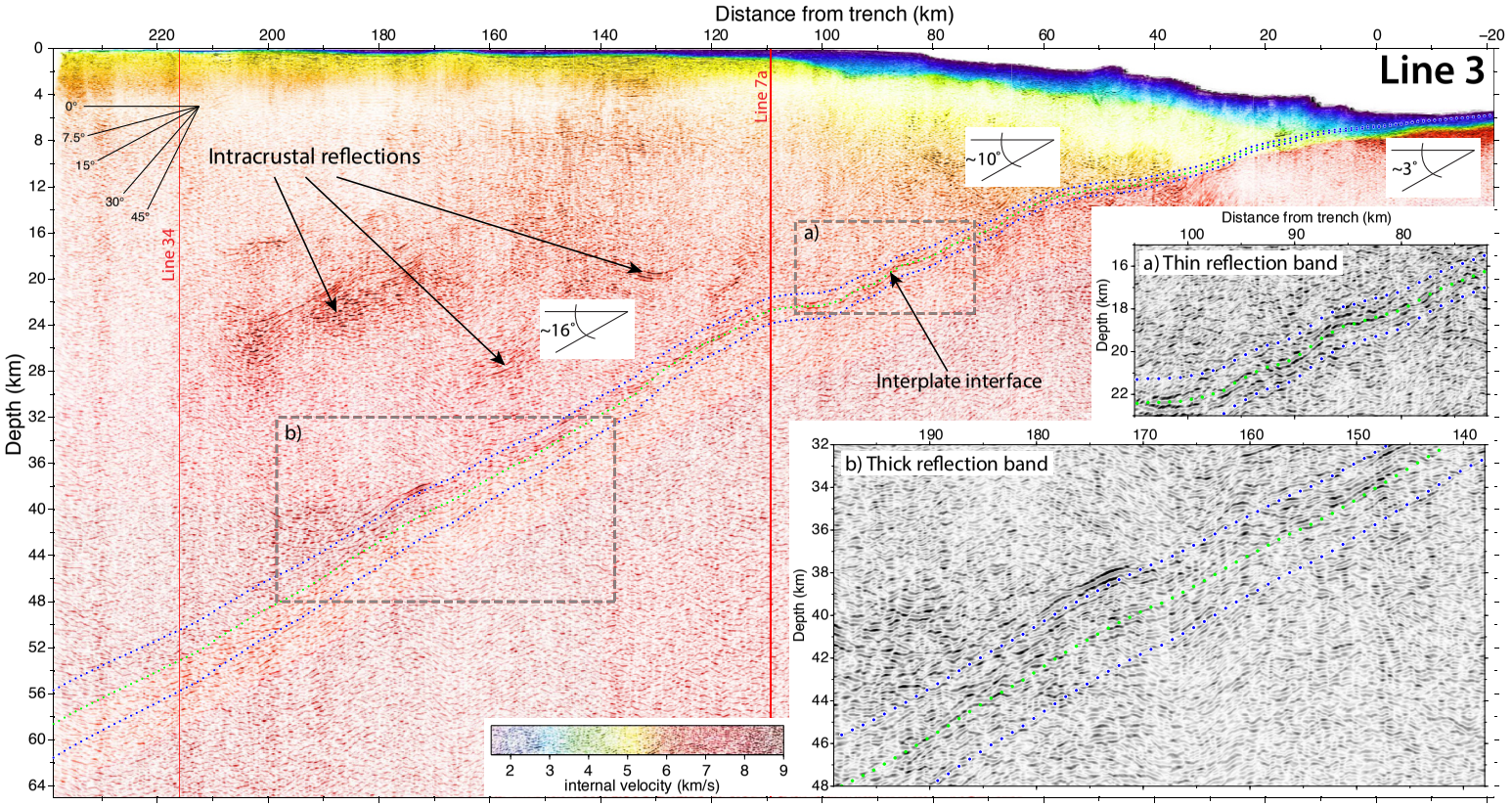

Figure A.4: Migrated and depth converted stack of MCS Line 3 in gray scale with the corresponding color composite velocity model superimposed. See Figure A.2 caption for explanations of additional figure components.

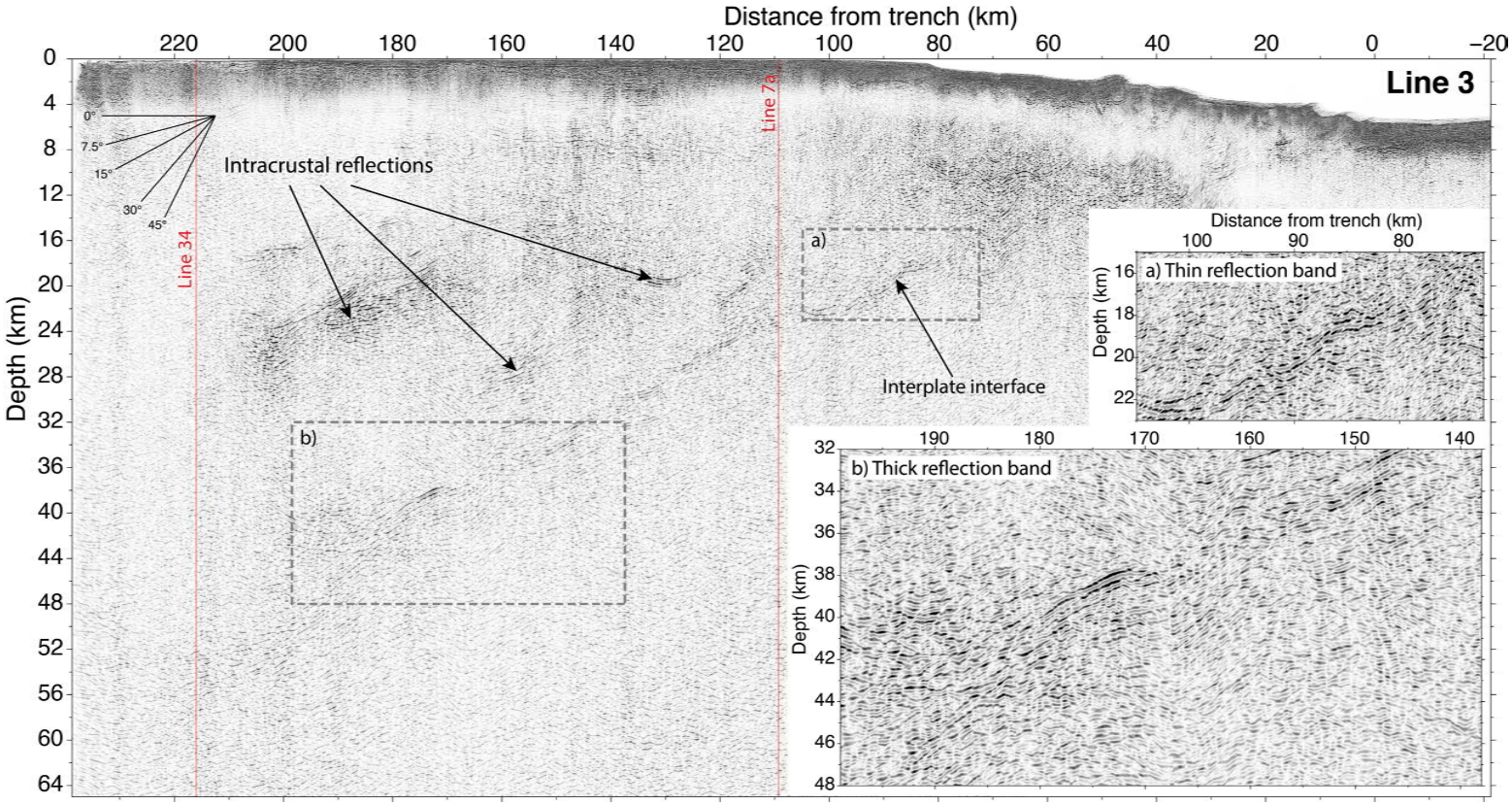

Figure A.5: Same as Figure A.4 but without the velocity model overlay and interplate interface interpretation.

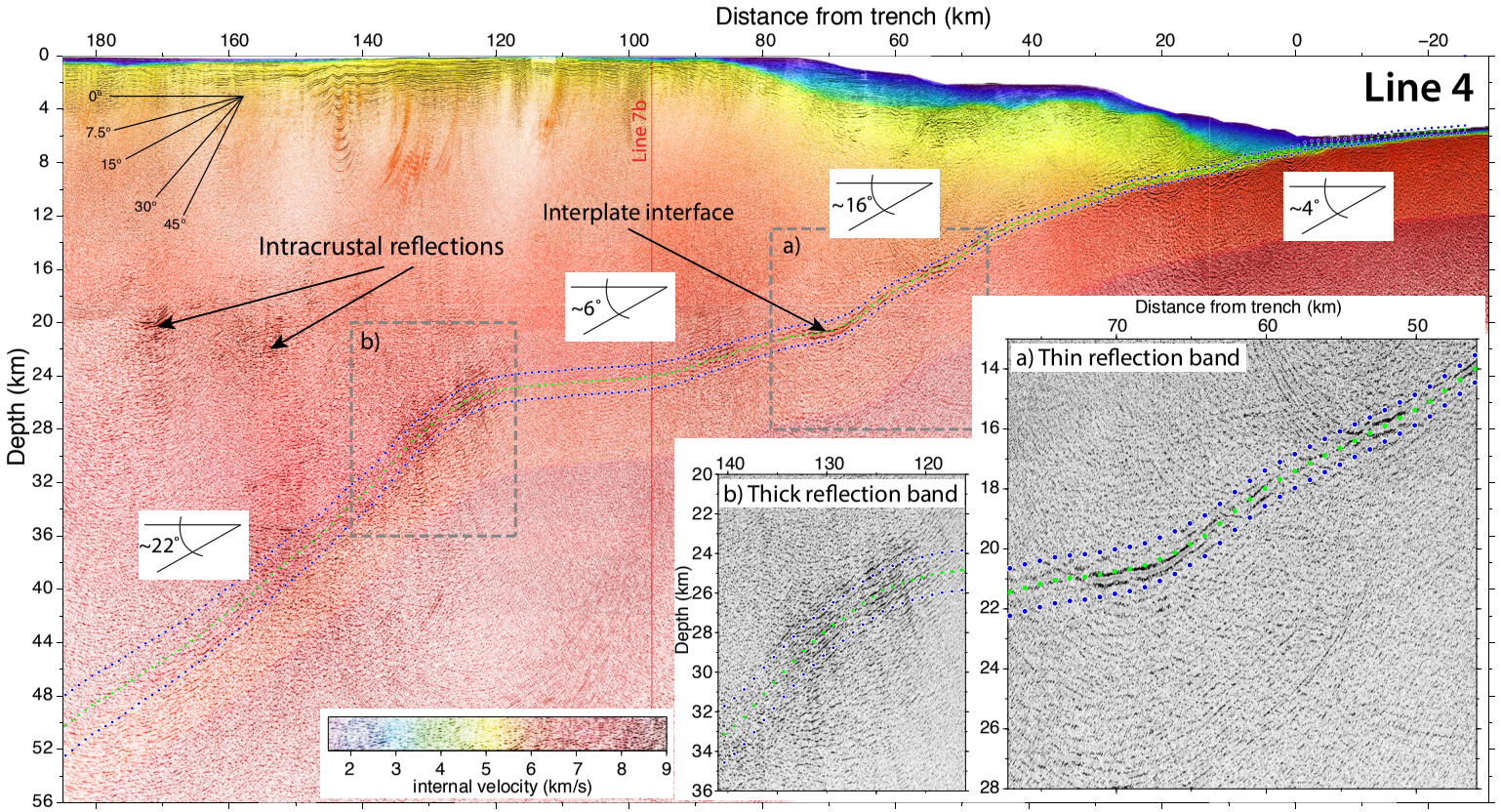

Figure A.6: Migrated and depth converted stack of MCS Line 4 in gray scale with the corresponding color composite velocity model superimposed. See Figure A.2 caption for explanations of additional figure components.

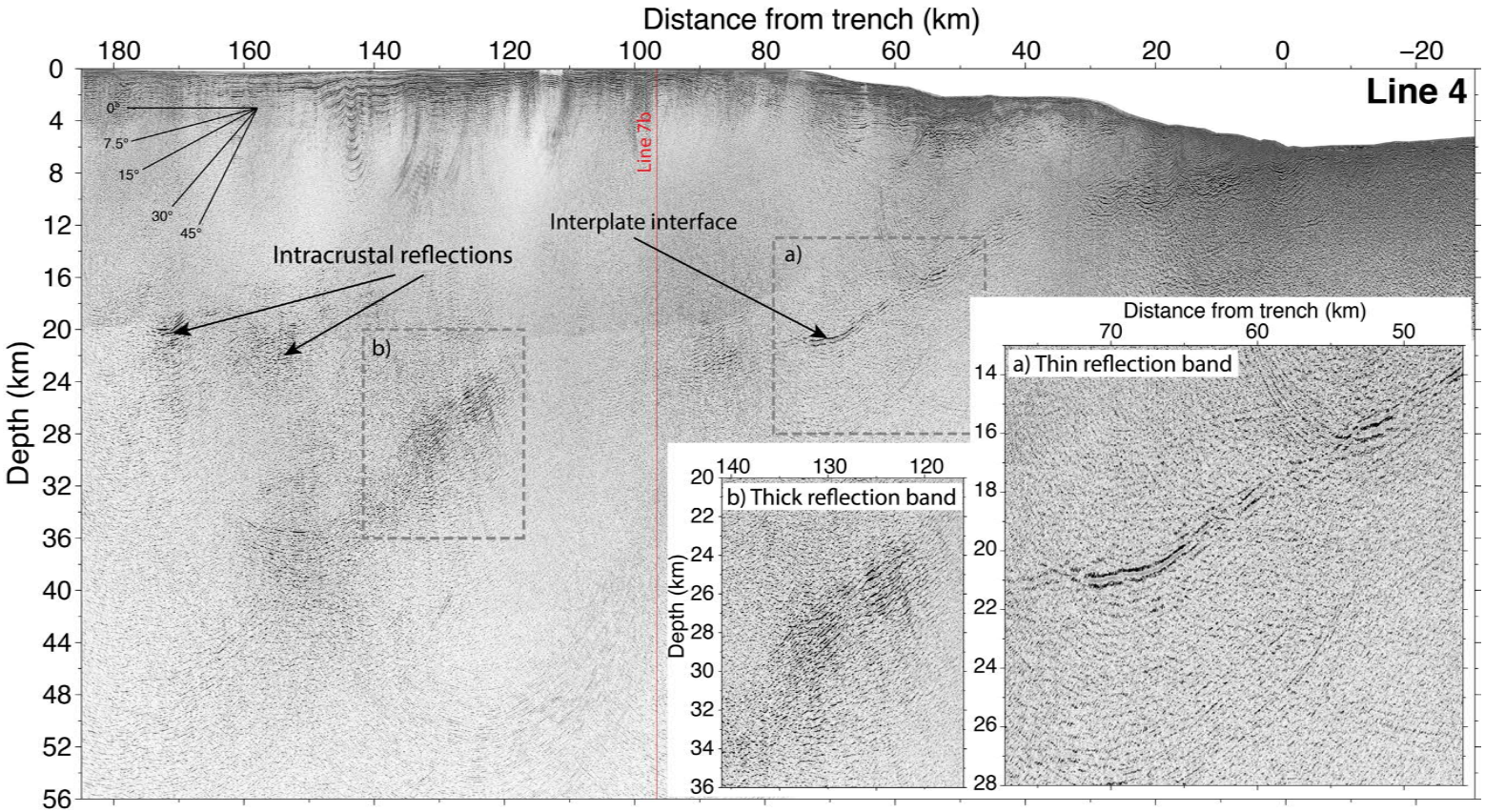

Figure A.7: Same as Figure A.6 but without the velocity model overlay.

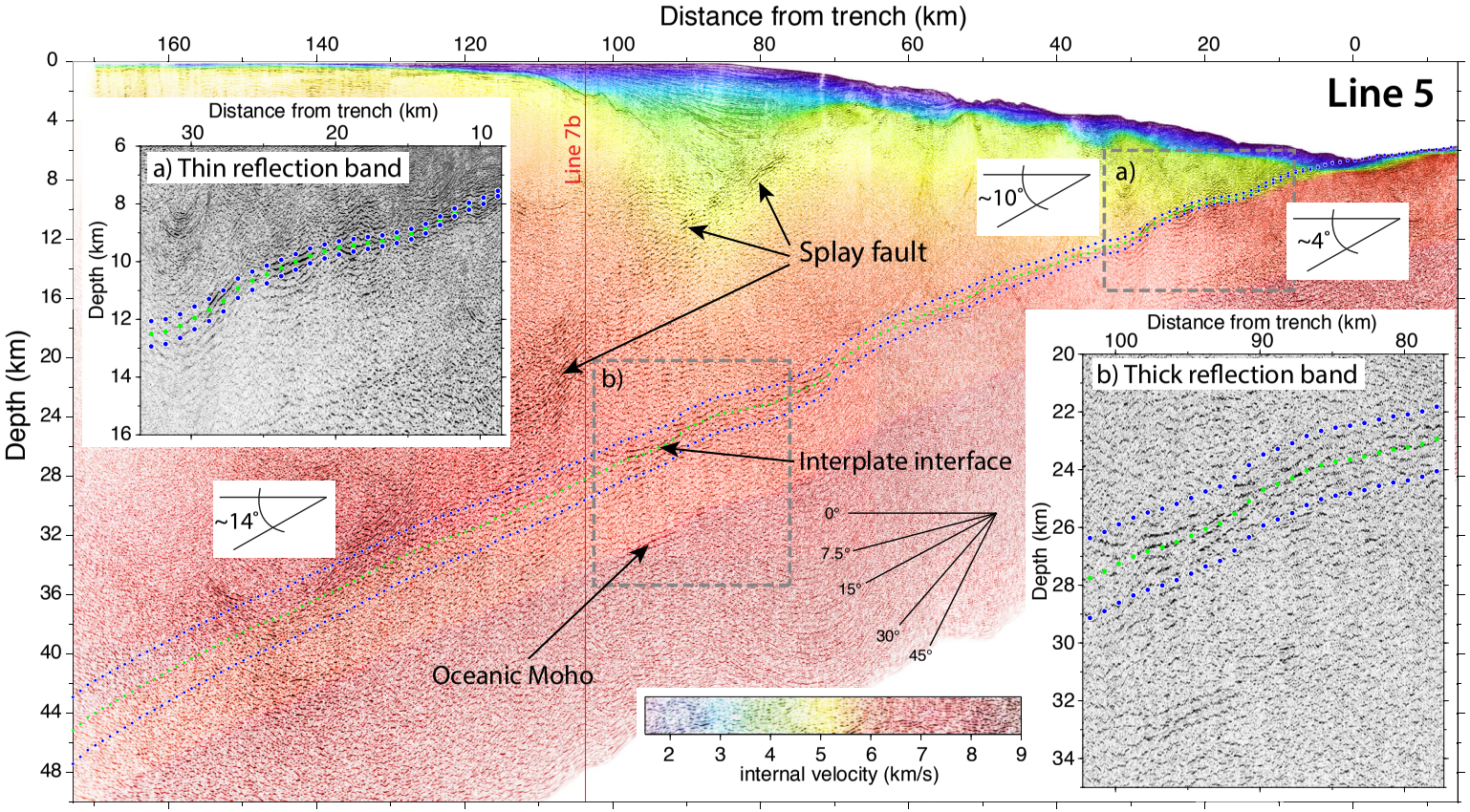

Figure A.8: Migrated and depth converted stack of MCS Line 5 in gray scale with the corresponding color composite velocity model superimposed. See Figure A.2 caption for explanations of additional figure components.

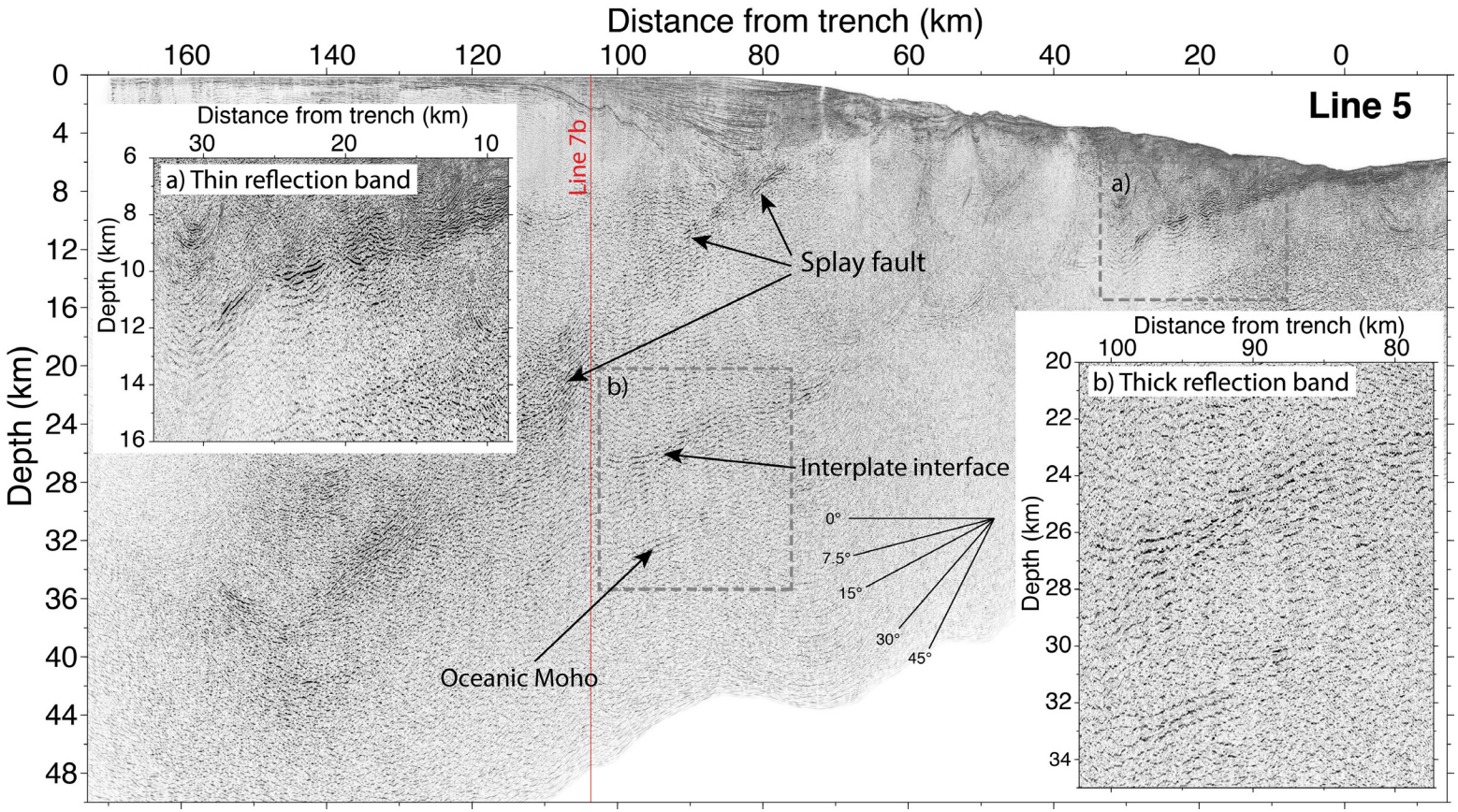

Figure A.9: Same as Figure A.8 but without the velocity model overlay and interplate interface interpretation.

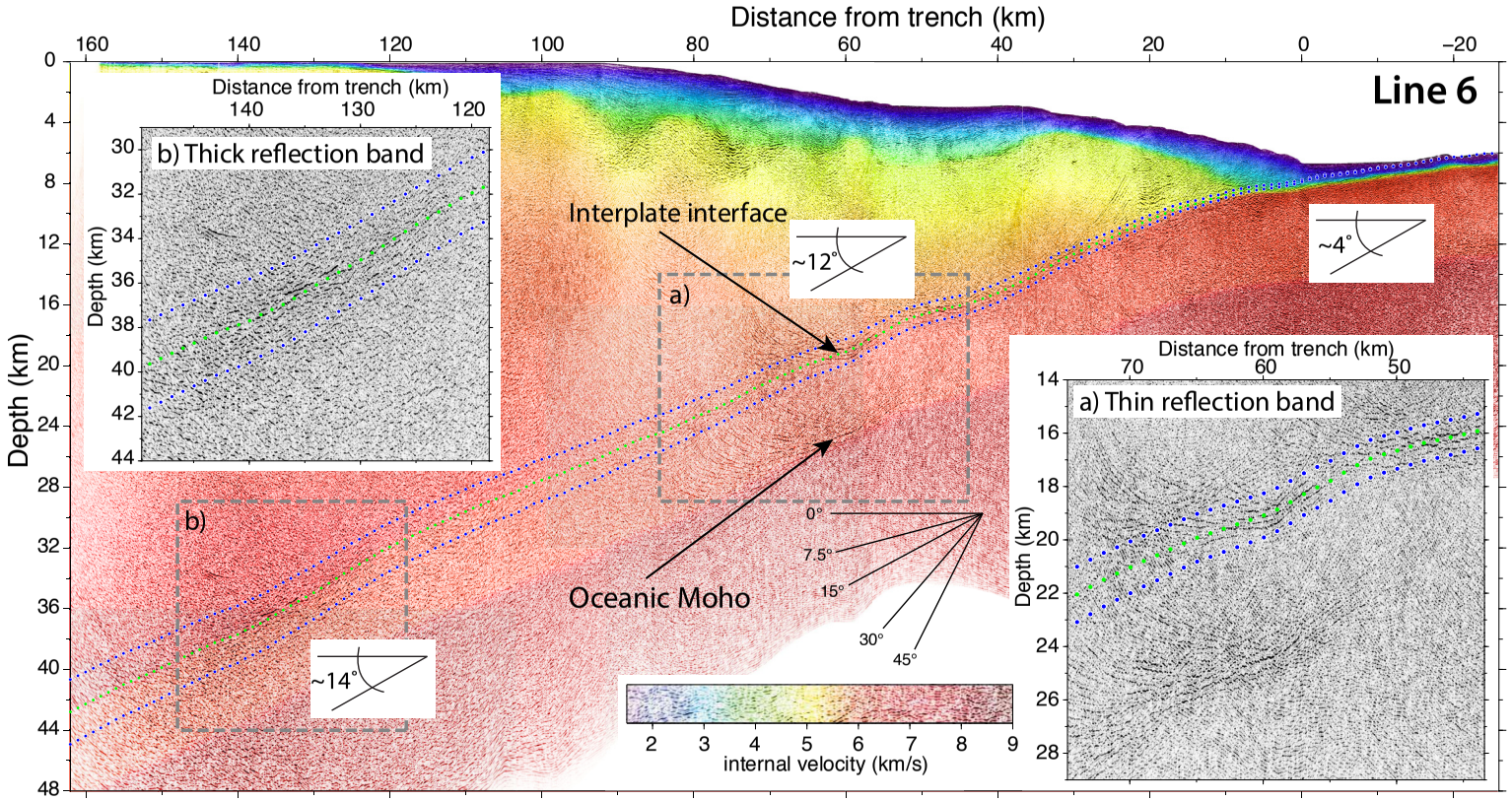

Figure A.10: Migrated and depth converted stack of MCS Line 6 in gray scale with the corresponding color composite velocity model superimposed. See Figure A.2 caption for explanations of additional figure components.

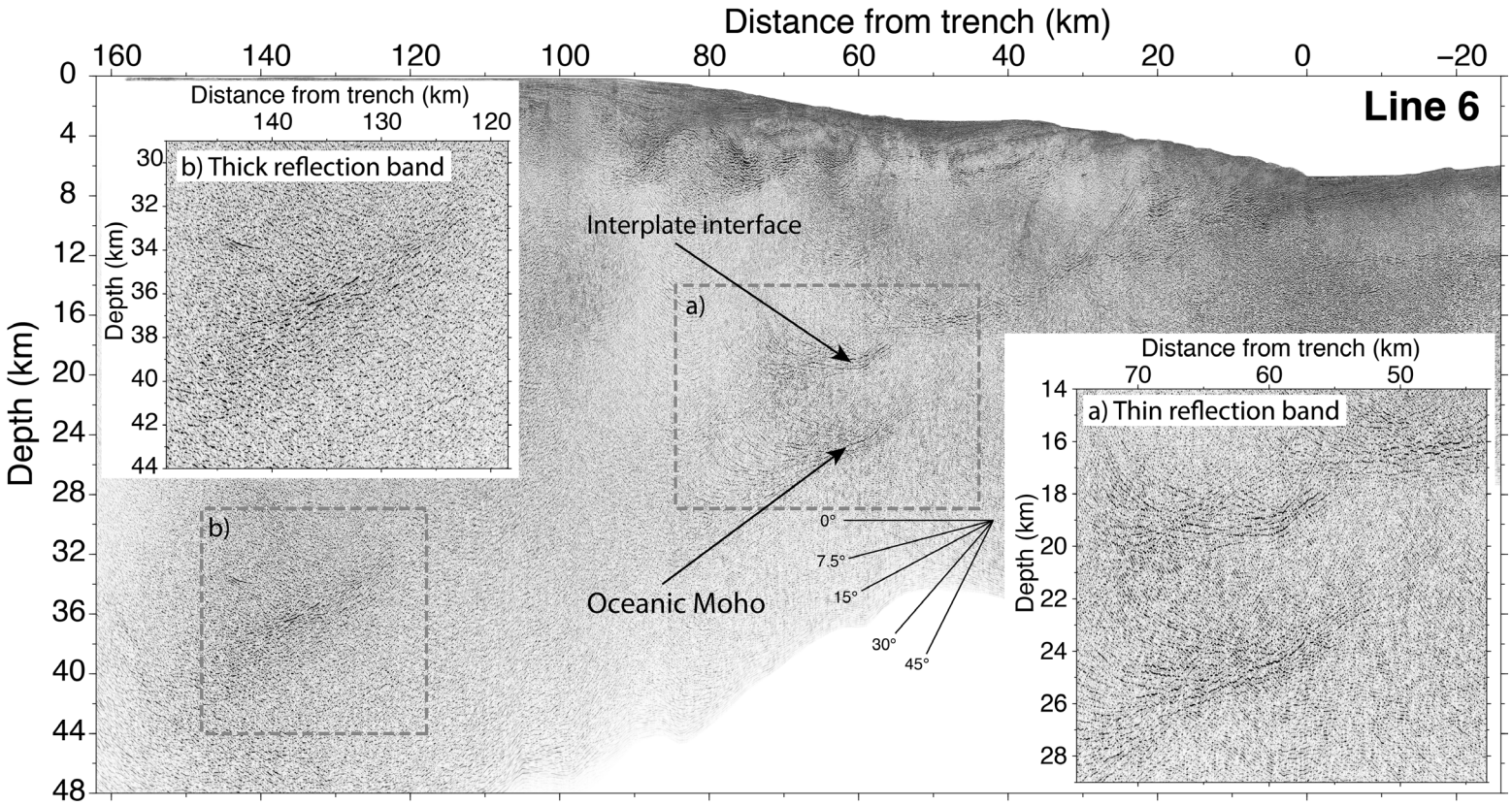

Figure A.11: Same as Figure A.10 but without the velocity model overlay and interplate interface interpretation.

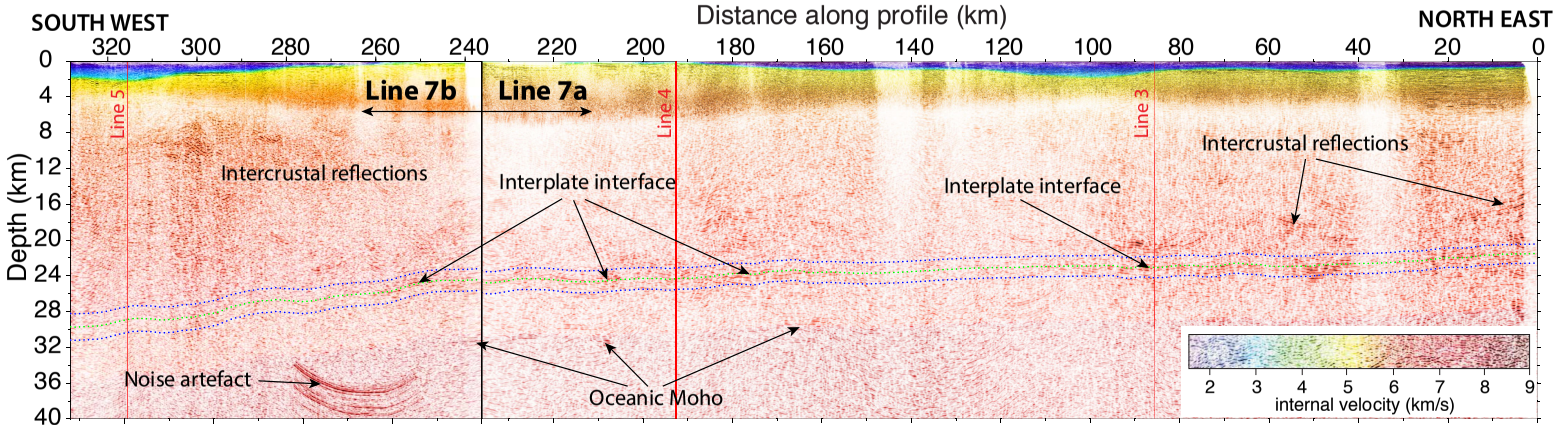

Figure A.12: Migrated and depth converted stack of MCS Lines 7a and 7b in gray scale with the corresponding color composite velocity model superimposed. See Figure A.2 caption for explanations of additional figure components.

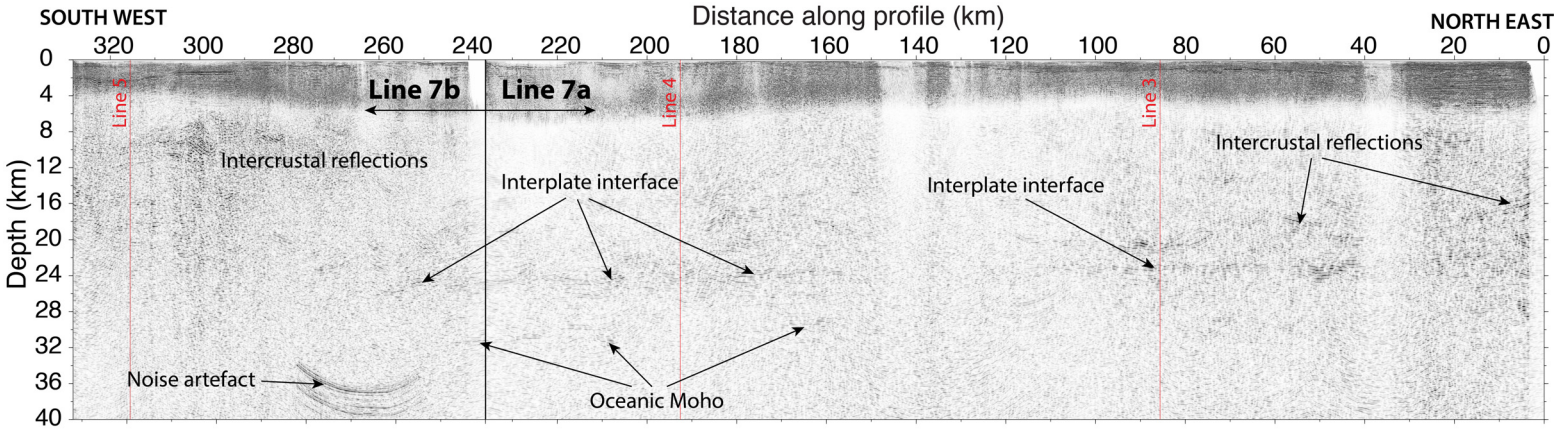

Figure A.13: Same as Figure A.12 but without the velocity model overlay and interplate interface interpretation.

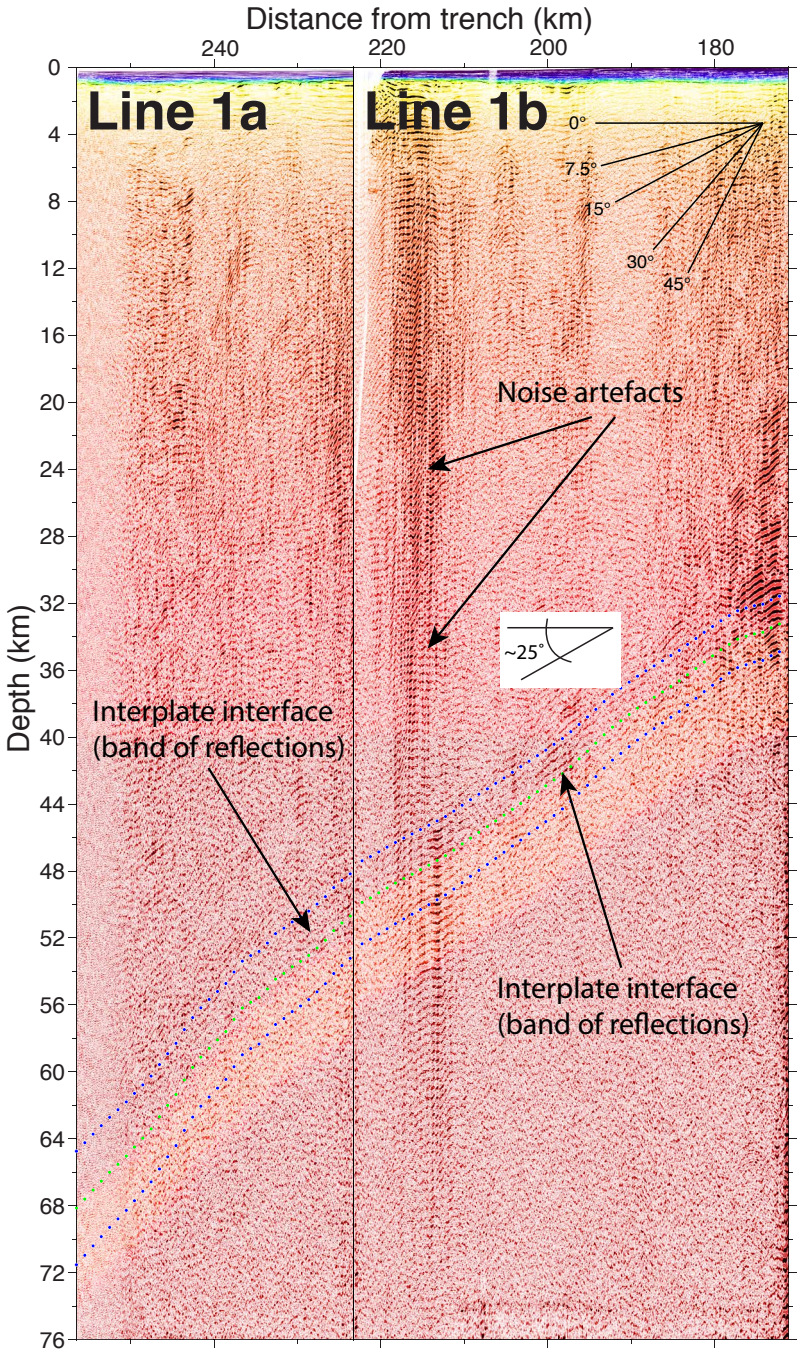

Figure A.14: igrated and depth converted stack of MCS Lines 1a and 1b in gray scale with the corresponding color composite velocity model superimposed. See Figure A.2 caption for explanations of additional figure components.

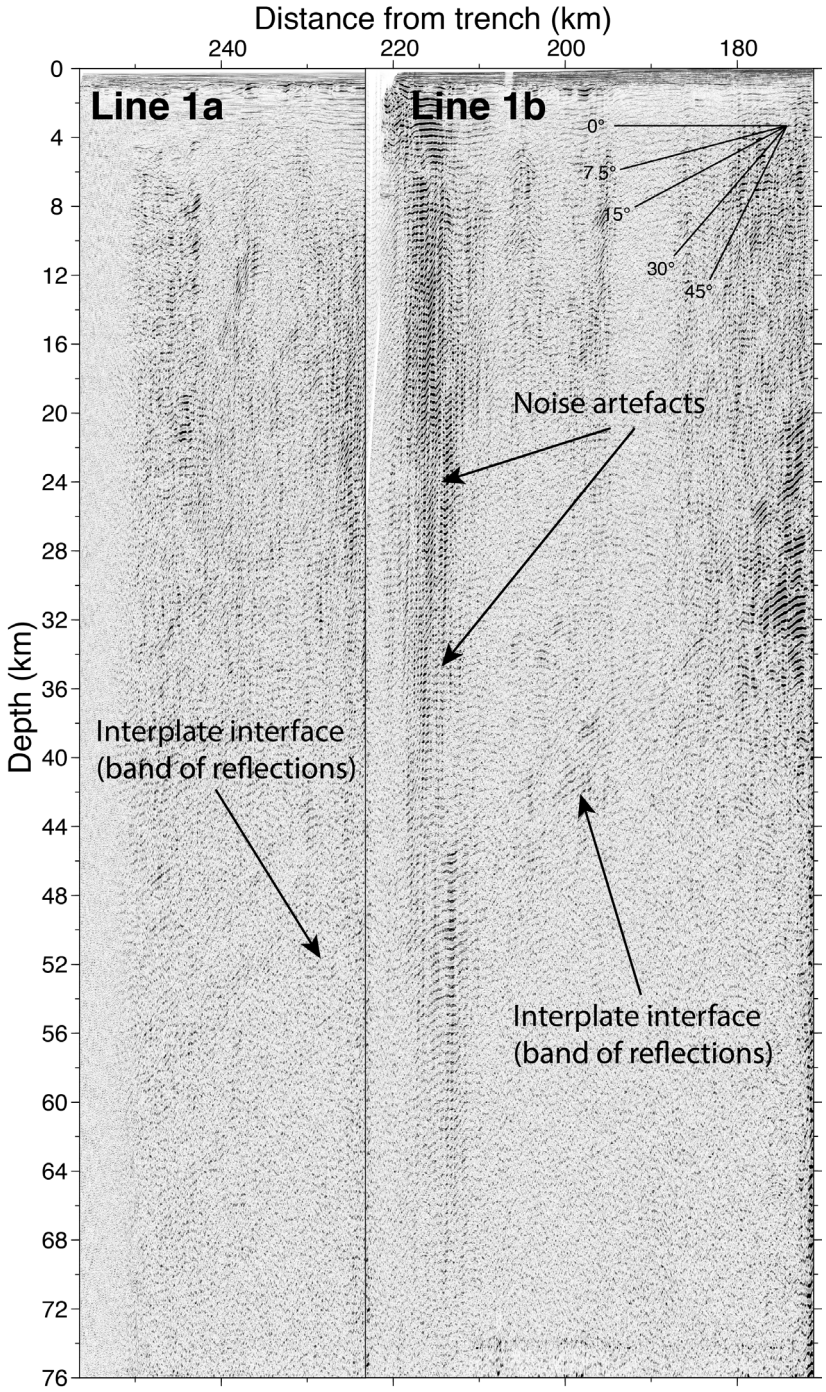

Figure A.15: Same as Figure A.14 but without the velocity model overlay and interplate interface interpretation.

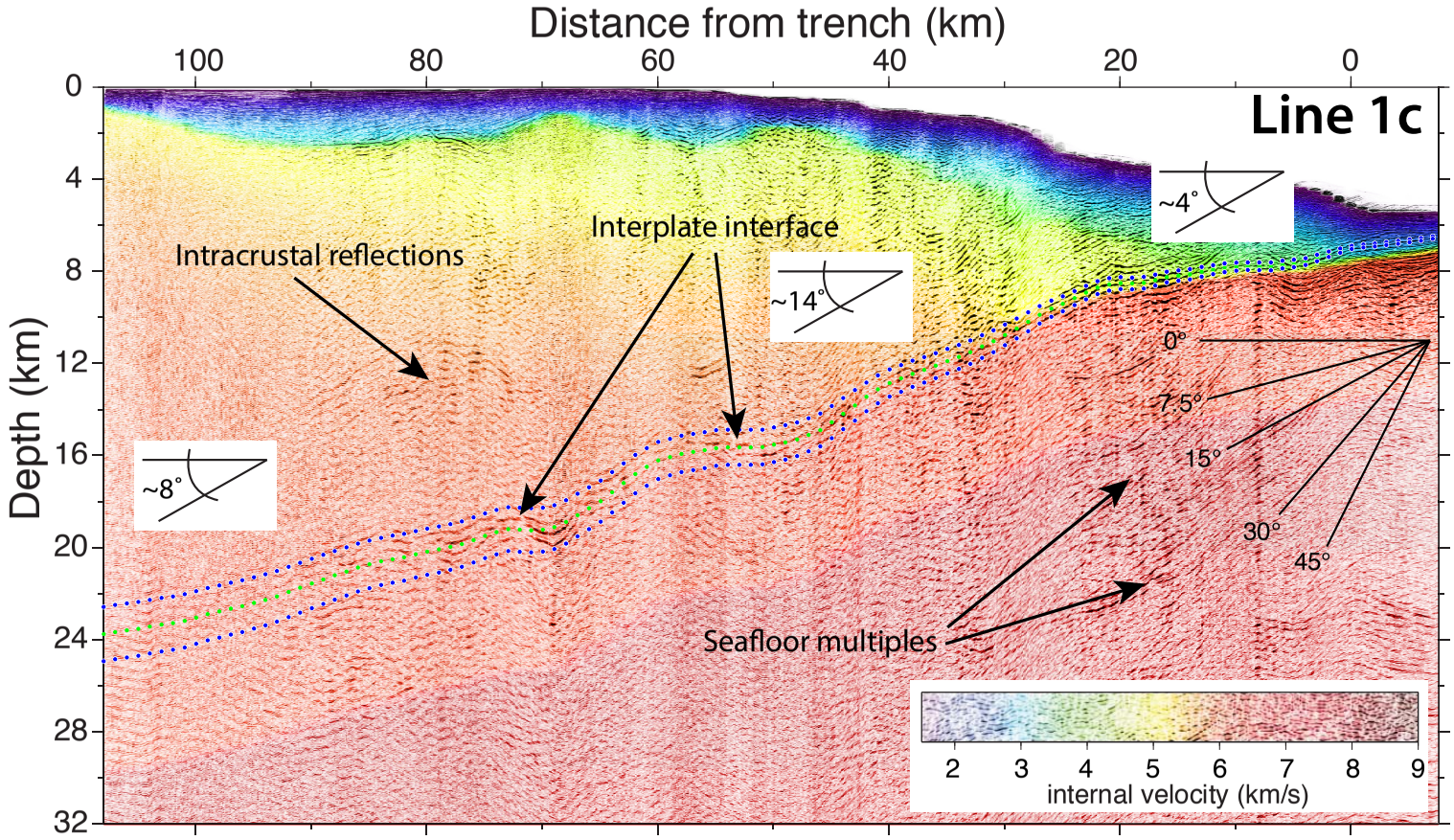

Figure A.16: Migrated and depth converted stack of MCS Line 1c in gray scale with the corresponding color composite velocity model superimposed. See Figure A.2 caption for explanations of additional figure components.

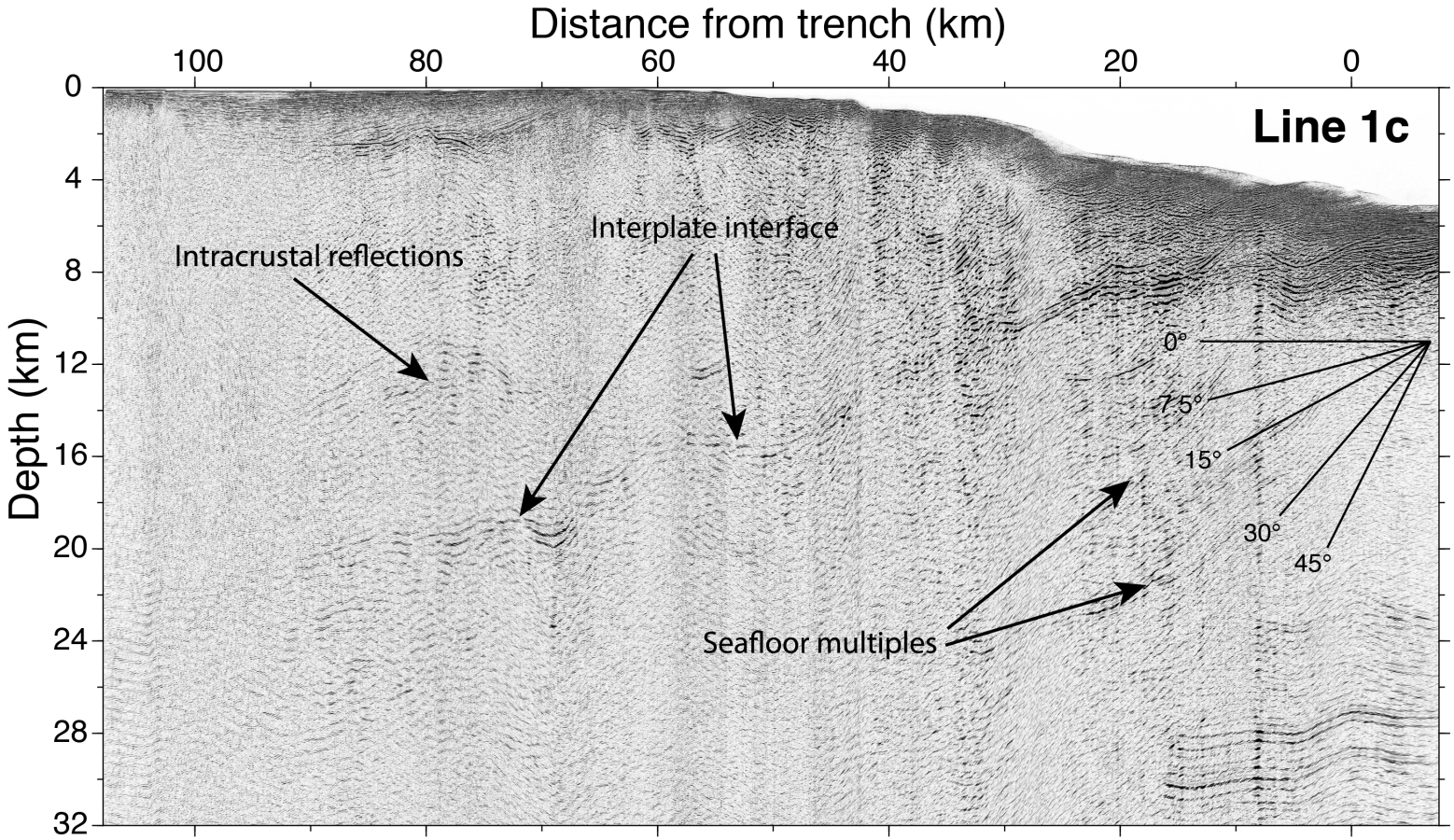

Figure A.17: Same as Figure A.16 but without the velocity model overlay and interplate interface interpretation.

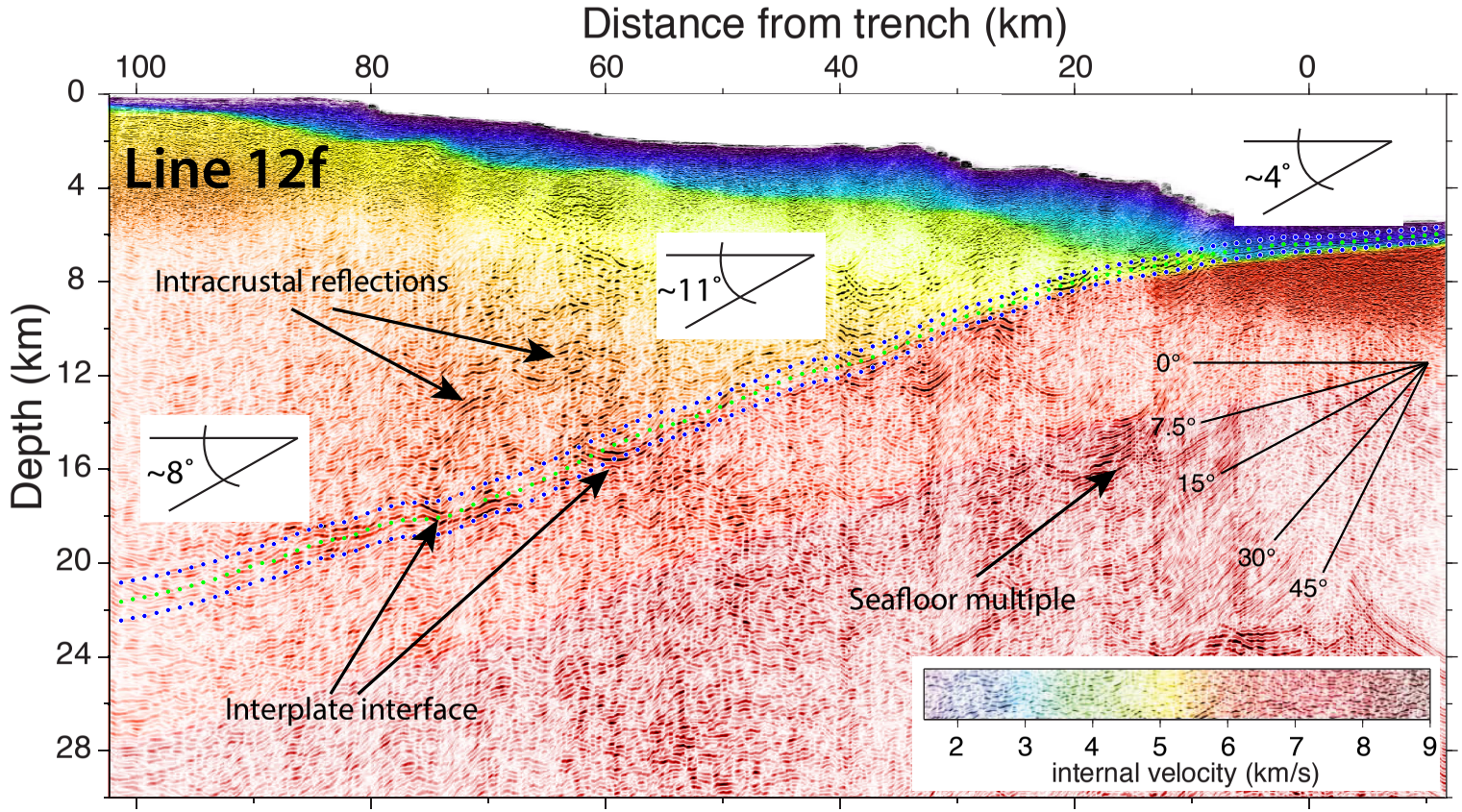

Figure A.18: Migrated and depth converted stack of MCS Line 12f in gray scale with the corresponding color composite velocity model superimposed. See Figure A.2 caption for explanations of additional figure components.

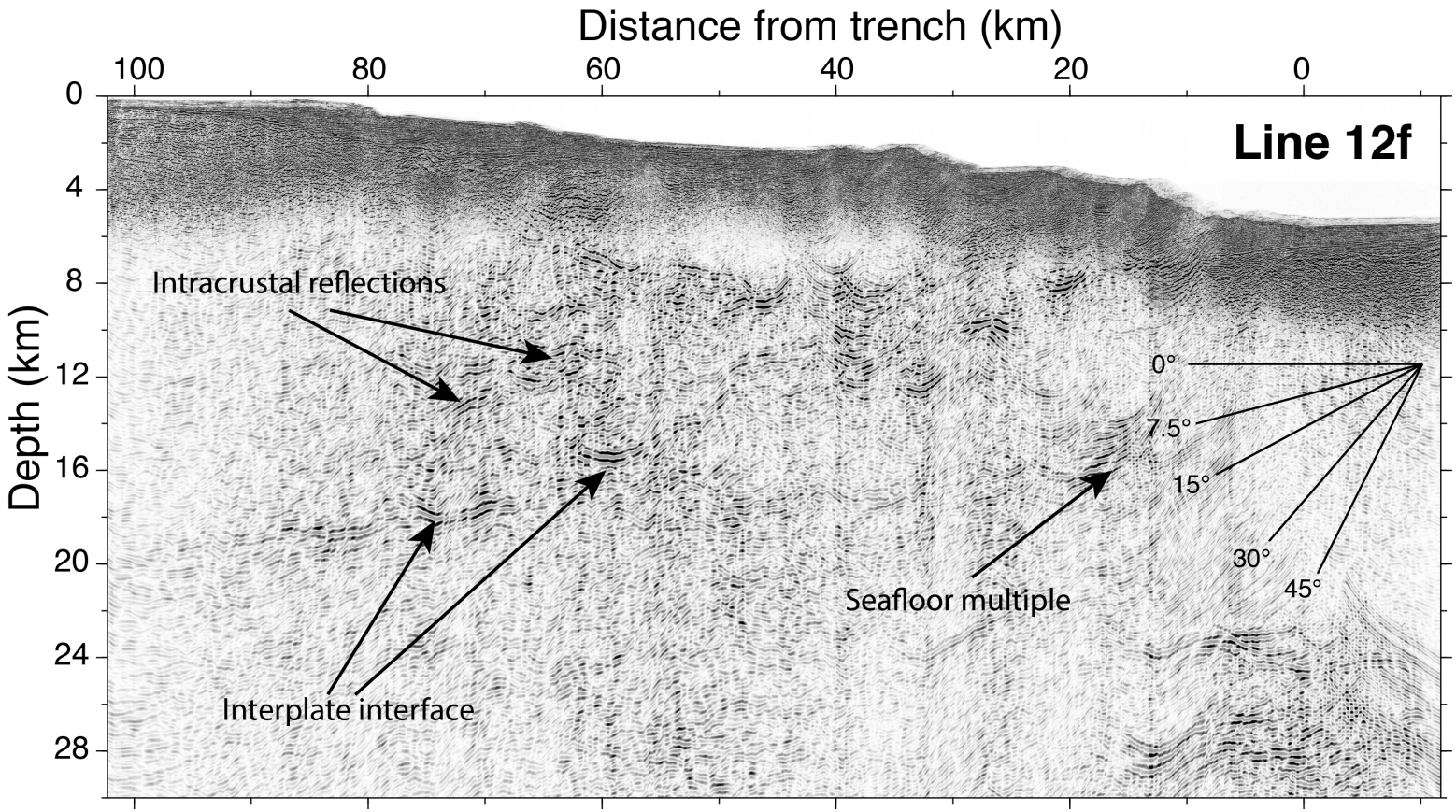

Figure A.19: Same as Figure A.18 but without the velocity model overlay and interplate interface interpretation.

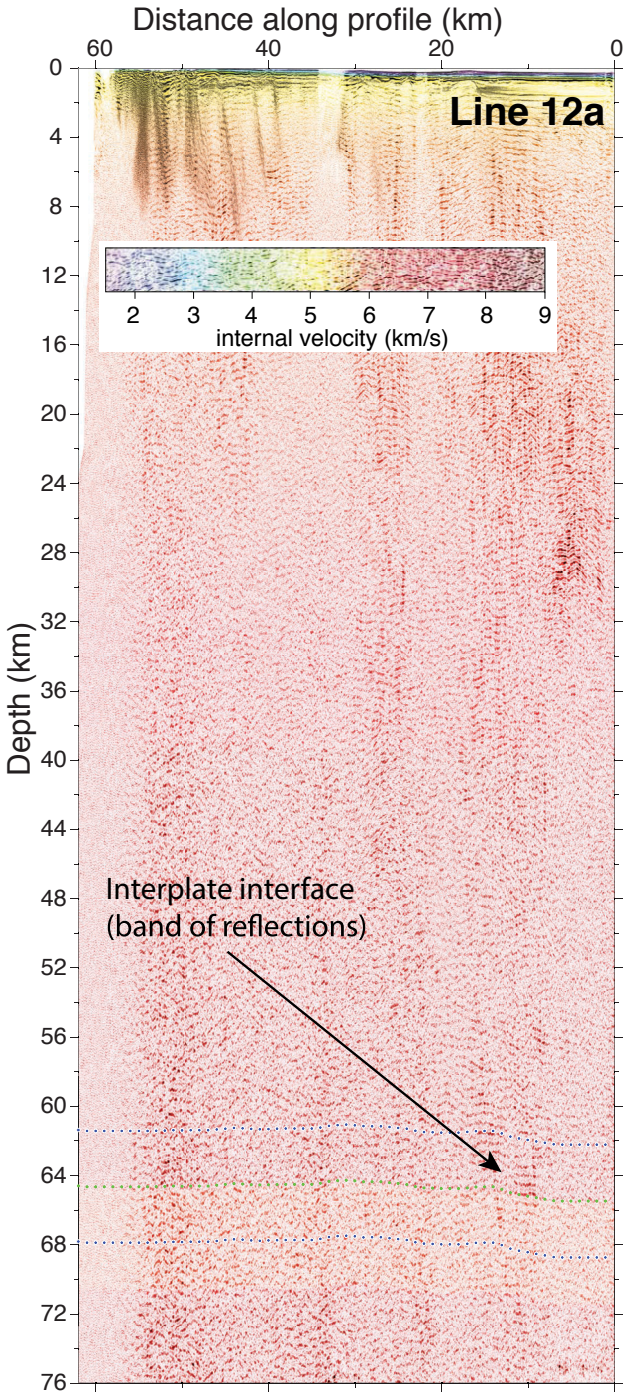

Figure A.20: Migrated and depth converted stack of MCS Line 12a in gray scale with the corresponding color composite velocity model superimposed. See Figure A.2 caption for explanations of additional figure components.

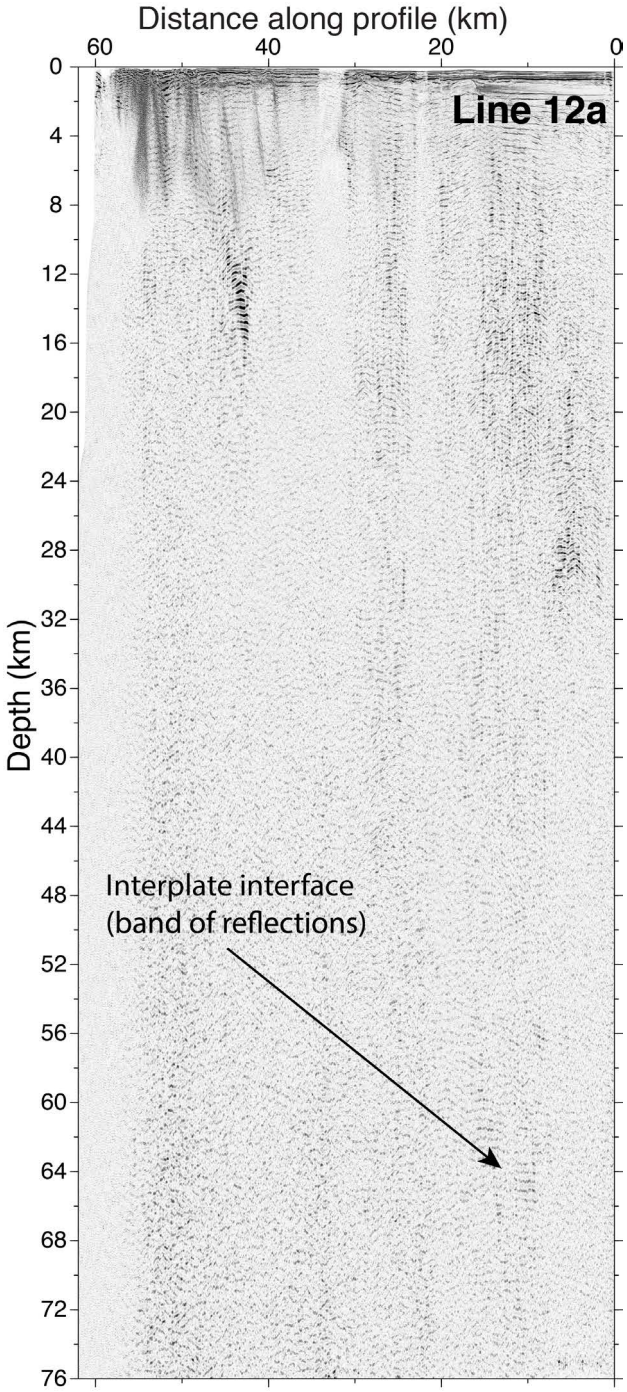

Figure A.21: Same as Figure A.20 but without the velocity model overlay and interplate interface interpretation.

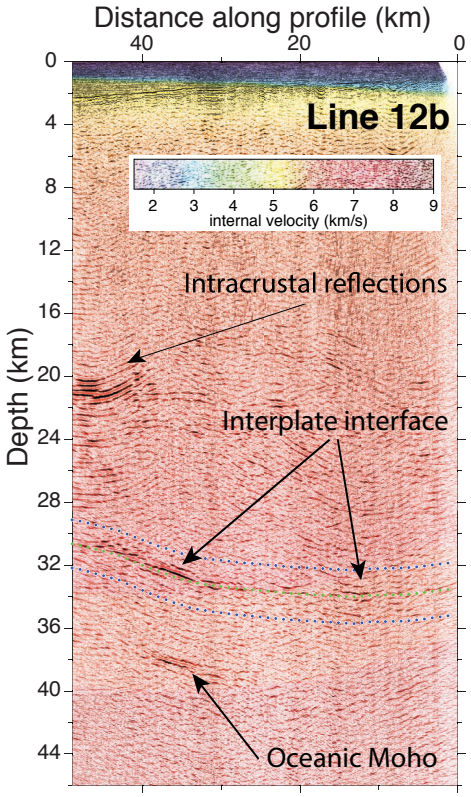

Figure A.22: Migrated and depth converted stack of MCS Line 12b in gray scale with the corresponding color composite velocity model superimposed. See Figure A.2 caption for explanations of additional figure components.

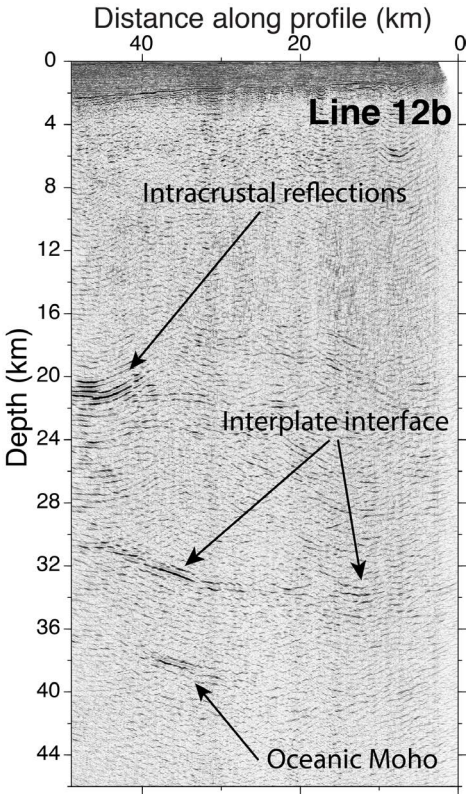

Figure A.23: Same as Figure A.22 but without the velocity model overlay and interplate interface interpretation.

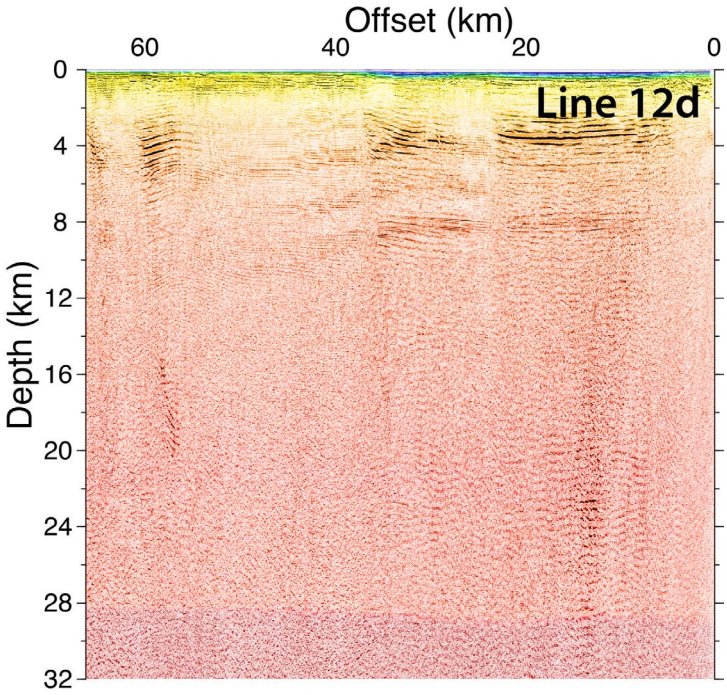

Figure A.24: Migrated and depth converted stack of MCS Line 12d in gray scale with the corresponding color composite velocity model superimposed. See Figure A.2 caption for explanations of additional figure components.

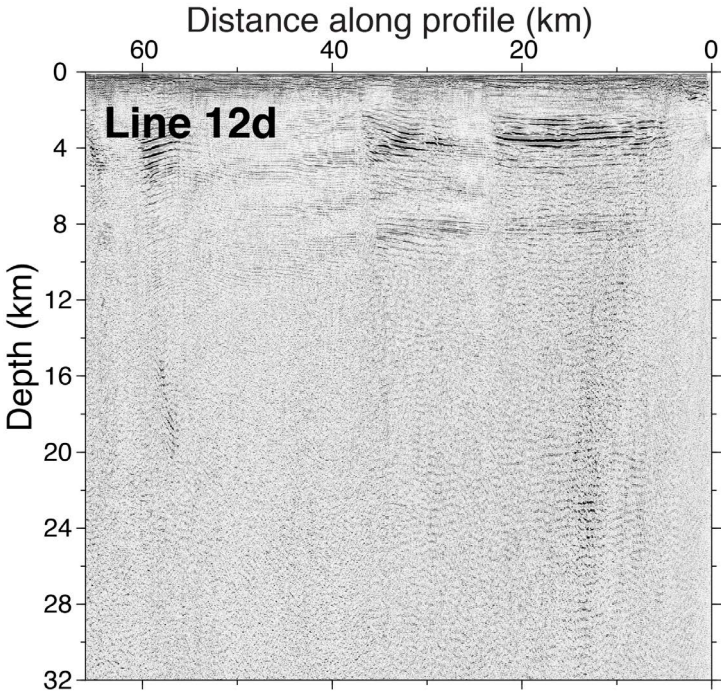

Figure A.25: Same as Figure A.24 but without the velocity model overlay and interplate interface interpretation.

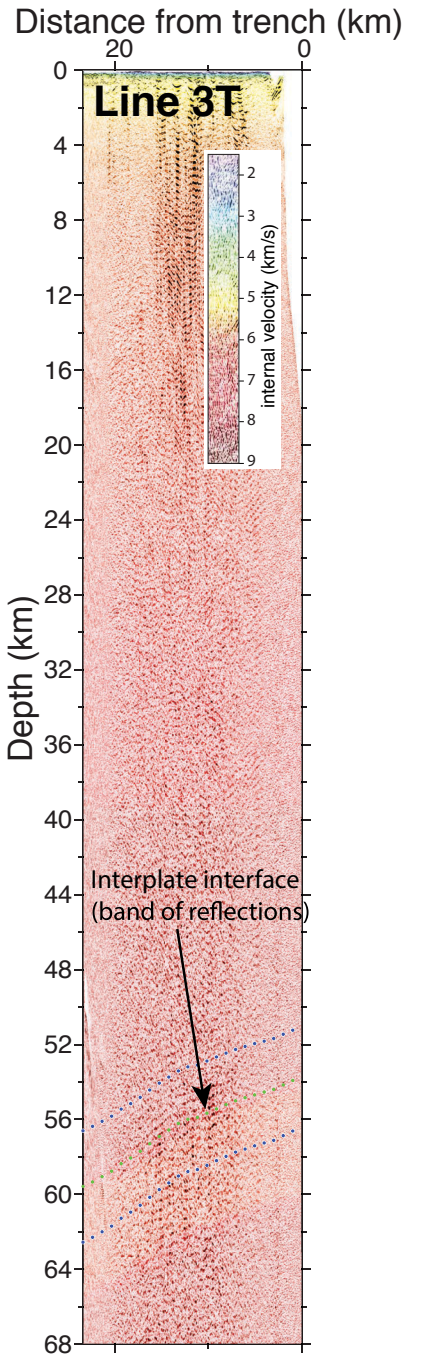

Figure A.26: Migrated and depth converted stack of MCS Line 3T in gray scale with the corresponding color composite velocity model superimposed. See Figure A.2 caption for explanations of additional figure components.

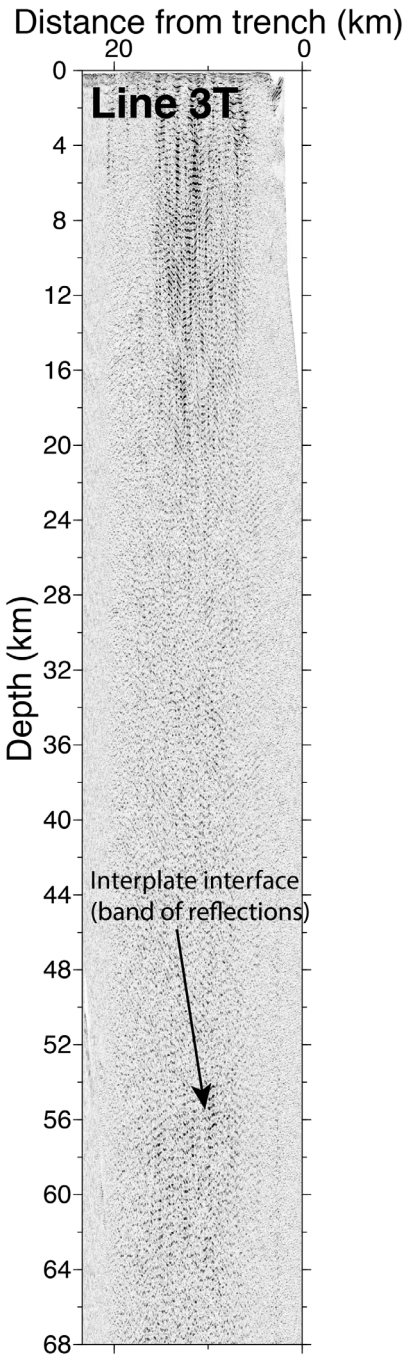

Figure A.27: Same as Figure A.26 but without the velocity model overlay and interplate interface interpretation.

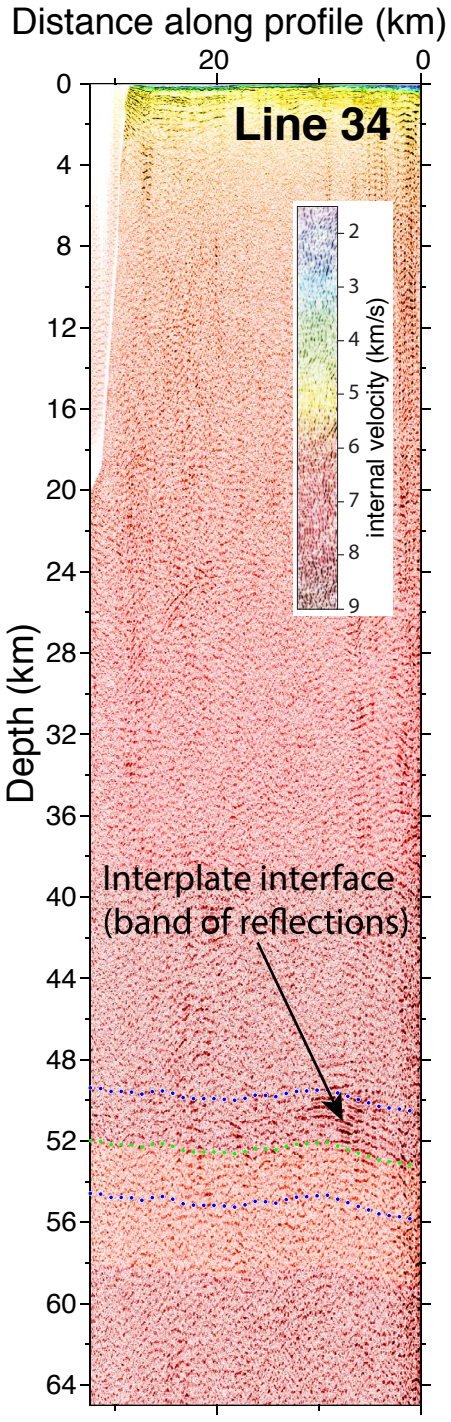

Figure A.28: Migrated and depth converted stack of MCS Line 34 in gray scale with the corresponding color composite velocity model superimposed. See Figure A.2 caption for explanations of additional figure components.

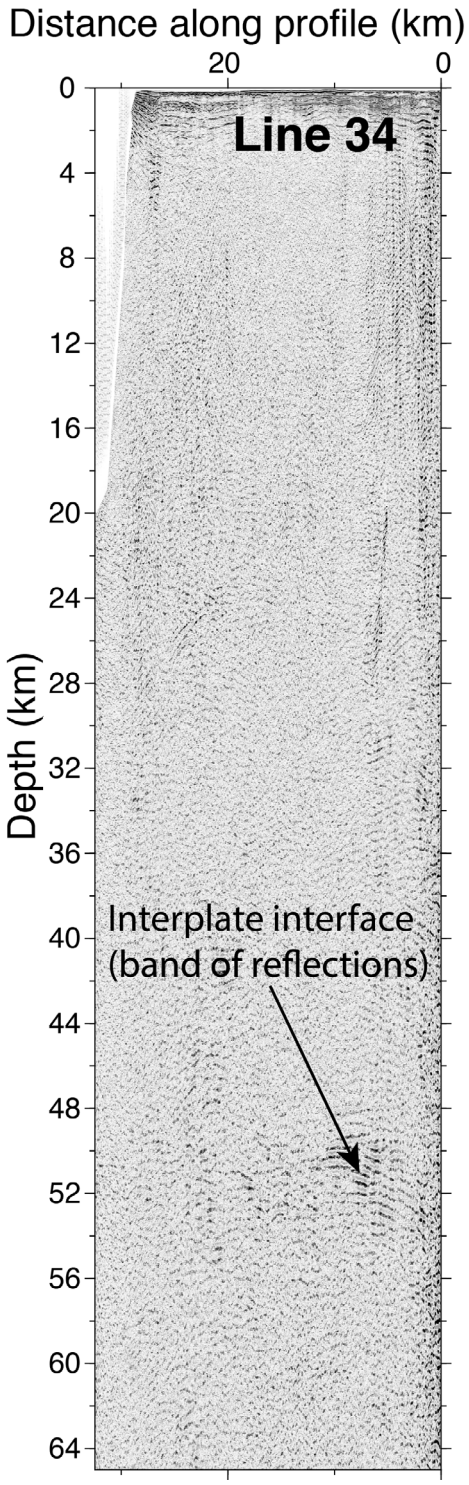

Figure A.29: Same as Figure A.28 but without the velocity model overlay and interplate interface interpretation.

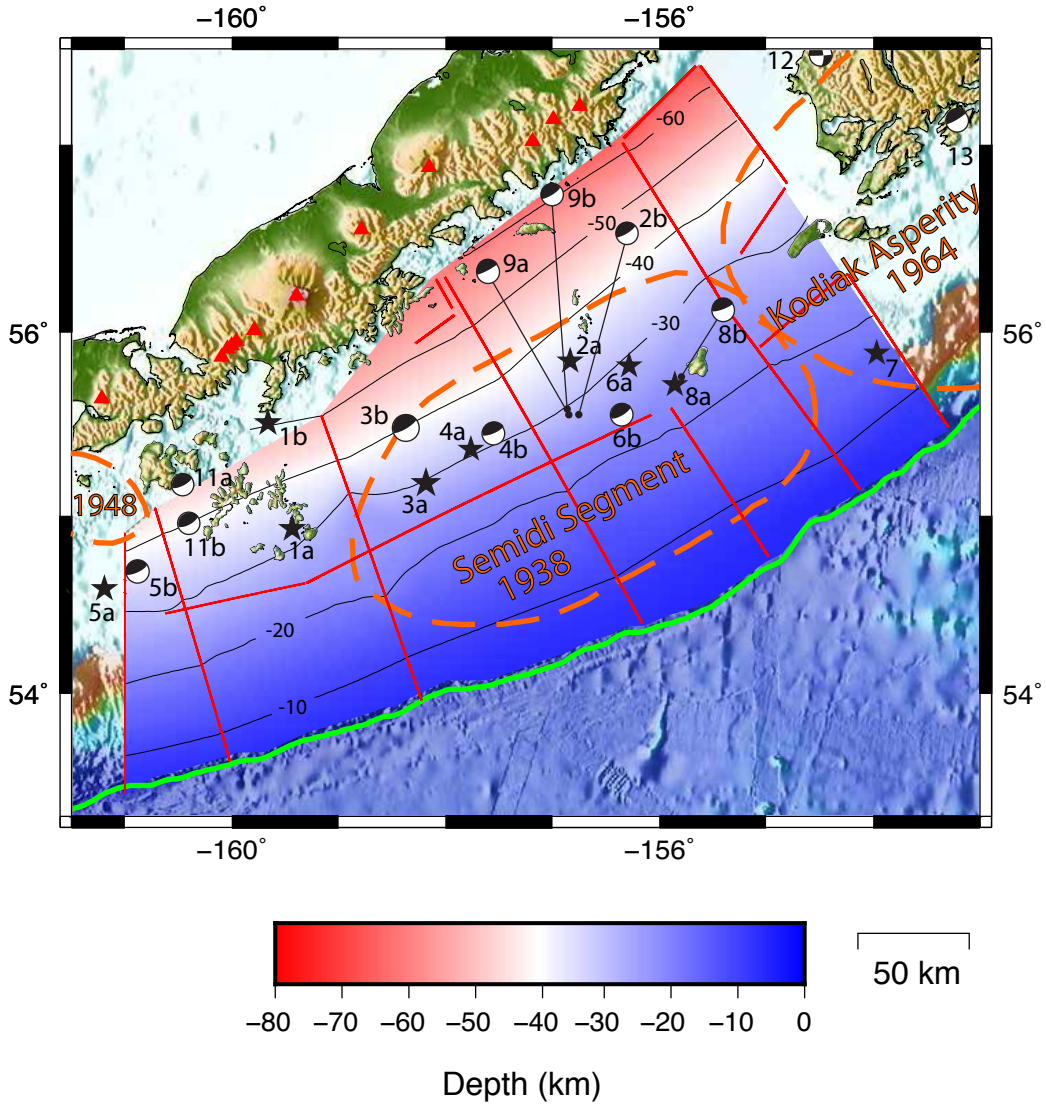

Figure A.30: Map of the depth to the subduction interface for the study area derived from ALEUT data. This map was formed by interpolation of the picked subduction interface on the MCS reflection profiles (minimum curvature function in Kingdom Suite software). Black lines are depth contour lines of the downgoing interface in 10-km intervals. Red lines show position of the ALEUT MCS profiles. Green line is the trench location. Dashed orange line encompasses the rupture areas derived from aftershock locations for the M_W 8.3 1938 Semidi Segment and Mw_W 9.2 1964 Prince William Sound earthquakes and the M_W 7.1 1948 earthquake as defined Estabrook et al., 1994 and McCann et al. (1980). Epicenter locations of earthquakes $\geq M_W$ 6.9 are represented by black stars and, where available, by focal mechanisms (see earthquake details in Table 1). Red triangles show the position of active volcanoes taken from the Alaska Volcano Observatorys web page (https://www.avo.alaska.edu/volcanoes/).

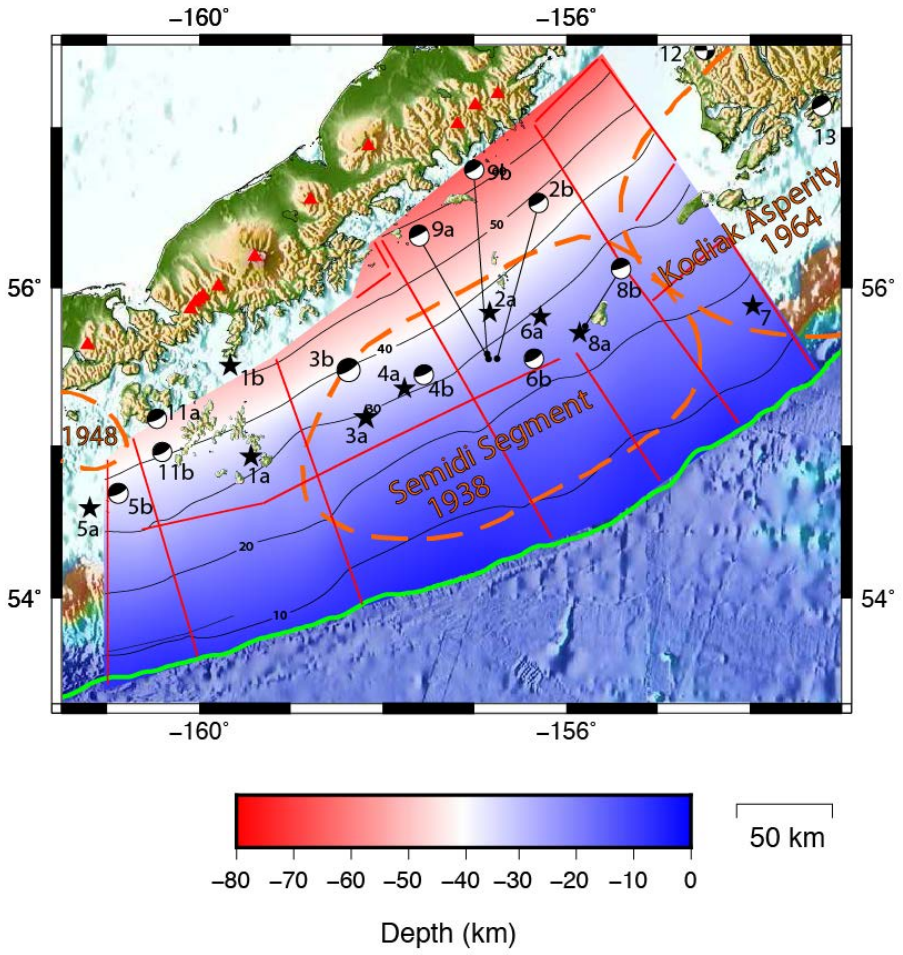

Figure A.31: Map of the depth to the subduction interface for the study area derived from ALEUT data. This map was formed an interpolation algorithms which used continous curvature spline function (surface) from General Mapping Tool (GMT) to calculate the plate interface between the MCS reflection profiles. Black lines are depth contour lines of the downgoing interface in 10-km intervals. Red lines show position of the ALEUT MCS profiles. Green line is the trench location. Dashed orange line encompasses the rupture areas derived from aftershock locations for the M_W 8.3 1938 Semidi Segment and Mw_W 9.2 1964 Prince William Sound earthquakes and the M_W 7.1 1948 earthquake as defined Estabrook et al., 1994 and McCann et al. (1980). Epicenter locations of earthquakes $\geq M_W$ 6.9 are represented by black stars and, where available, by focal mechanisms (see earthquake details in Table 1). Red triangles show the position of active volcanoes taken from the Alaska Volcano Observatorys web page (https://www.avo.alaska.edu/volcanoes/).

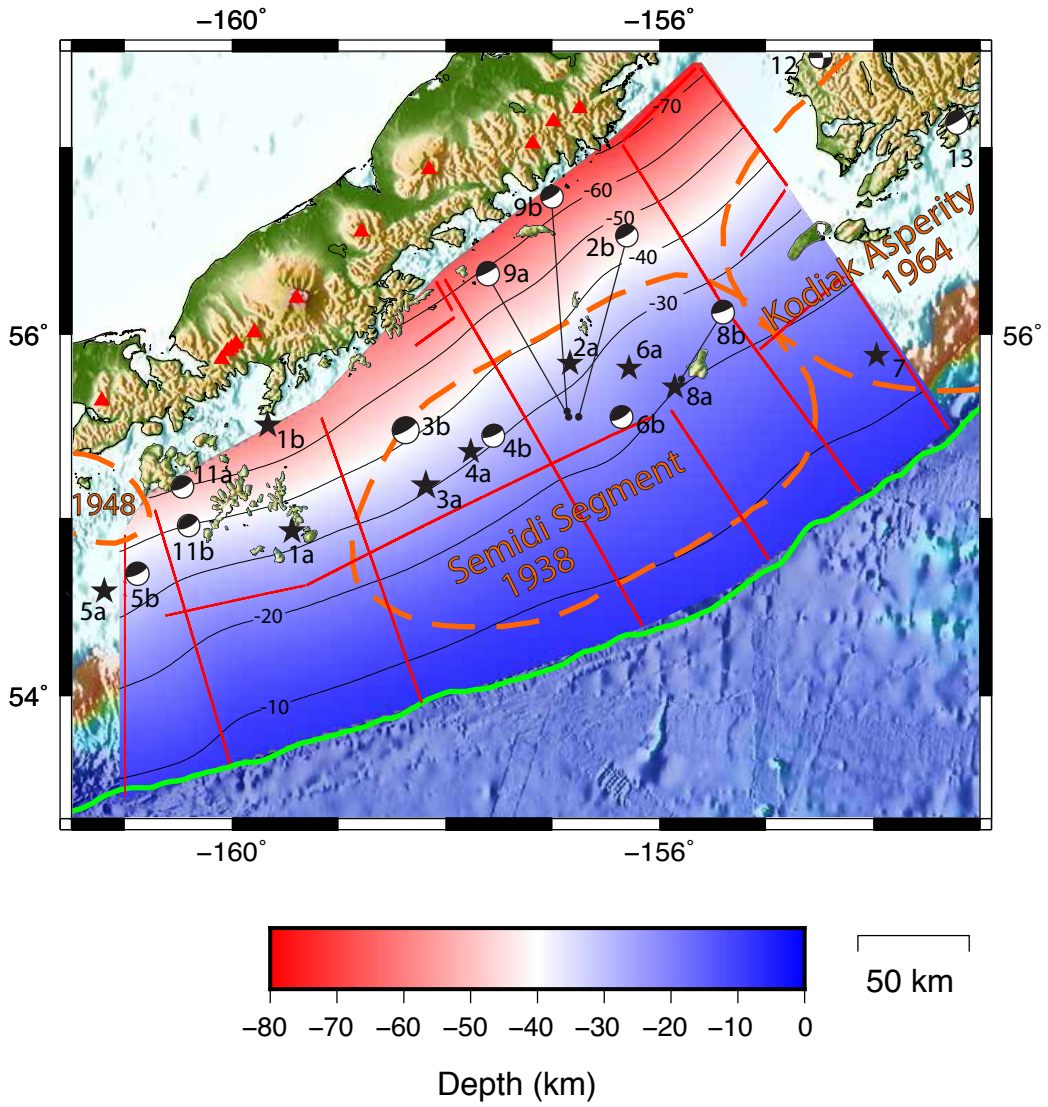

Figure A.32: Map of the depth to the subduction interface for the study area extracted from the slab interface model from Hayes et al. (2012). The depth of the interface is estimated mostly from earthquake catalogues and for the shallow part from seismic profiles, sediment thickness and bathymetry. See Figure A.26 caption for explanations of additional figure components.

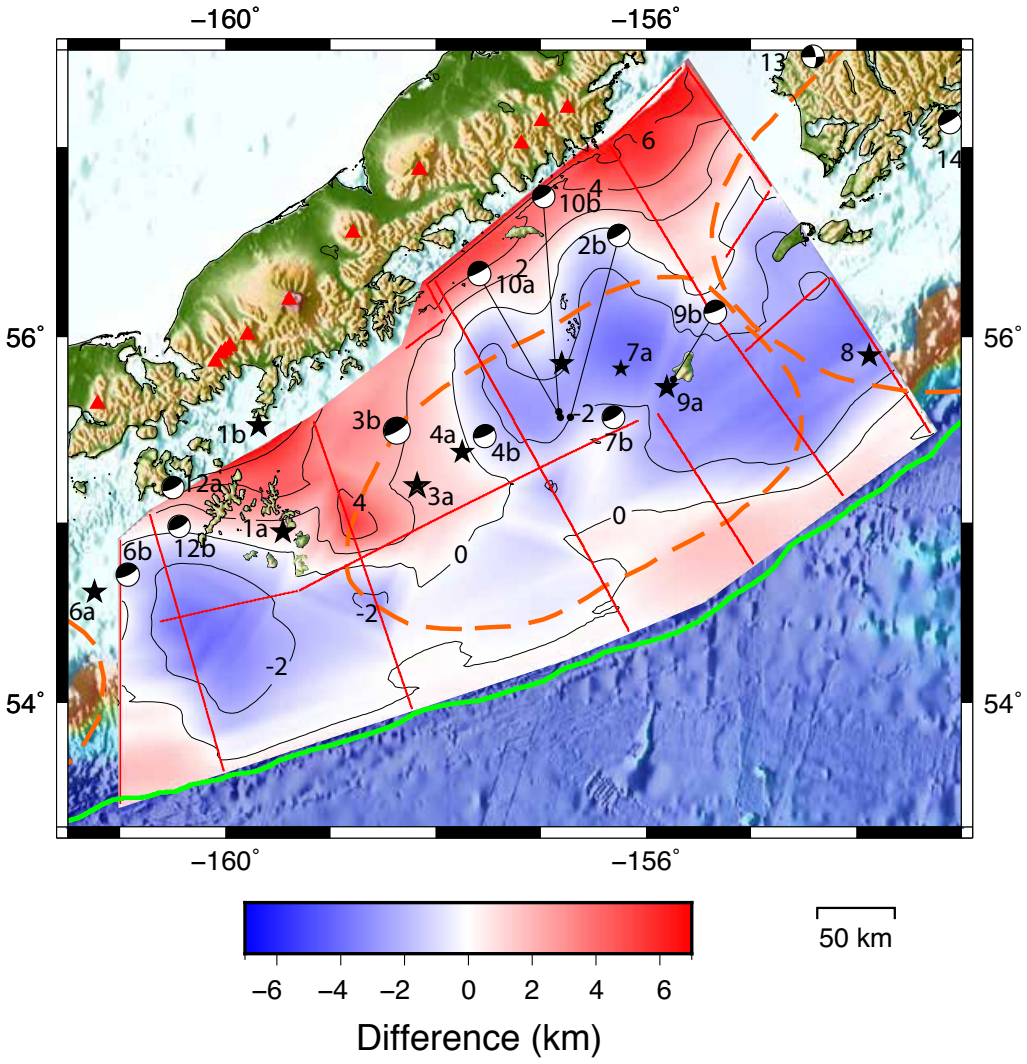

Figure A.33: Map of the difference in the subduction interface depth for the study area between the ALEUT data model (Fig. A.26) and Hayes slab1.0 model (Figure A.27). Positive areas (red) represent regions where the ALEUT model is shallower than the slab1.0 model, while the negative (blue) areas show regions where the ALEUT model is deeper than the slab 1.0 model. Note that two positive anomalies are coincident with lateral extend of the 1938 rupture (Semidi Segment). See Figure A.26 caption for explanations of additional figure components.

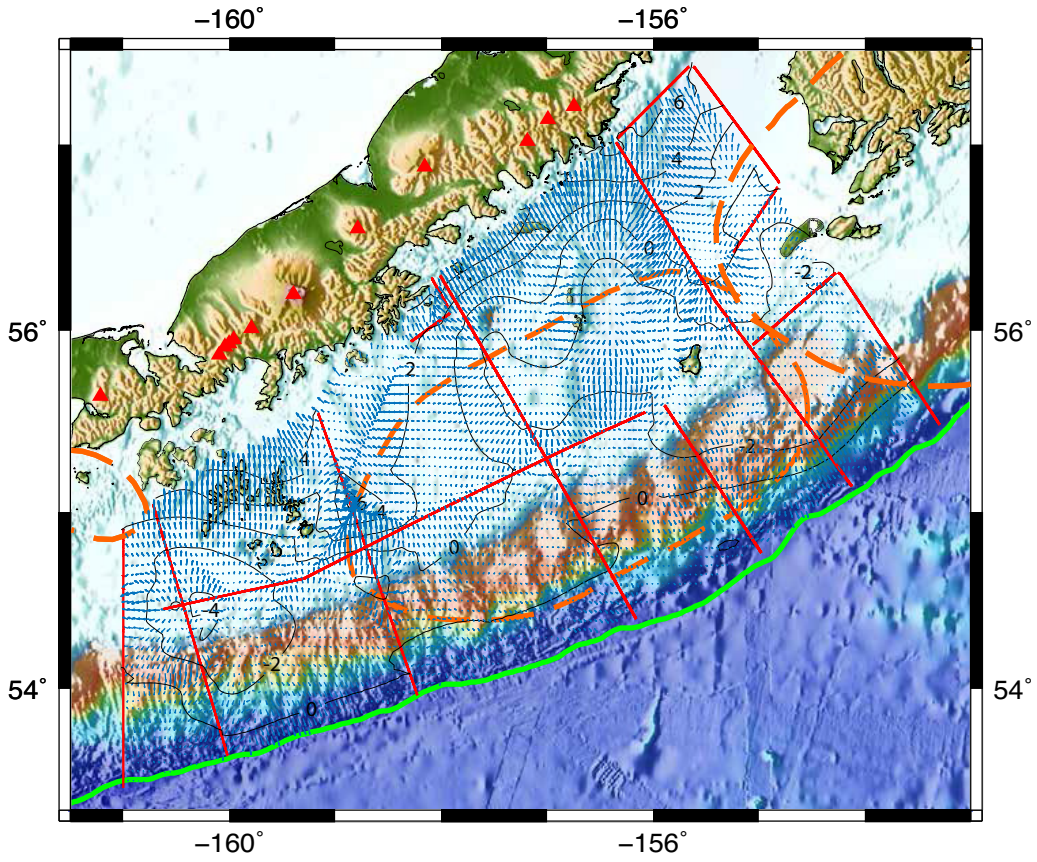

Figure A.34: Map of the 2D gradient of the difference in the subduction interface depth for the study area between the ALEUT data model (Fig. A.26) and Hayes slab1.0 model (Figure A.27). Length of arrows is proportional to the lateral rate of change in difference between the two models. See Figure A.26 caption for explanations of additional figure components

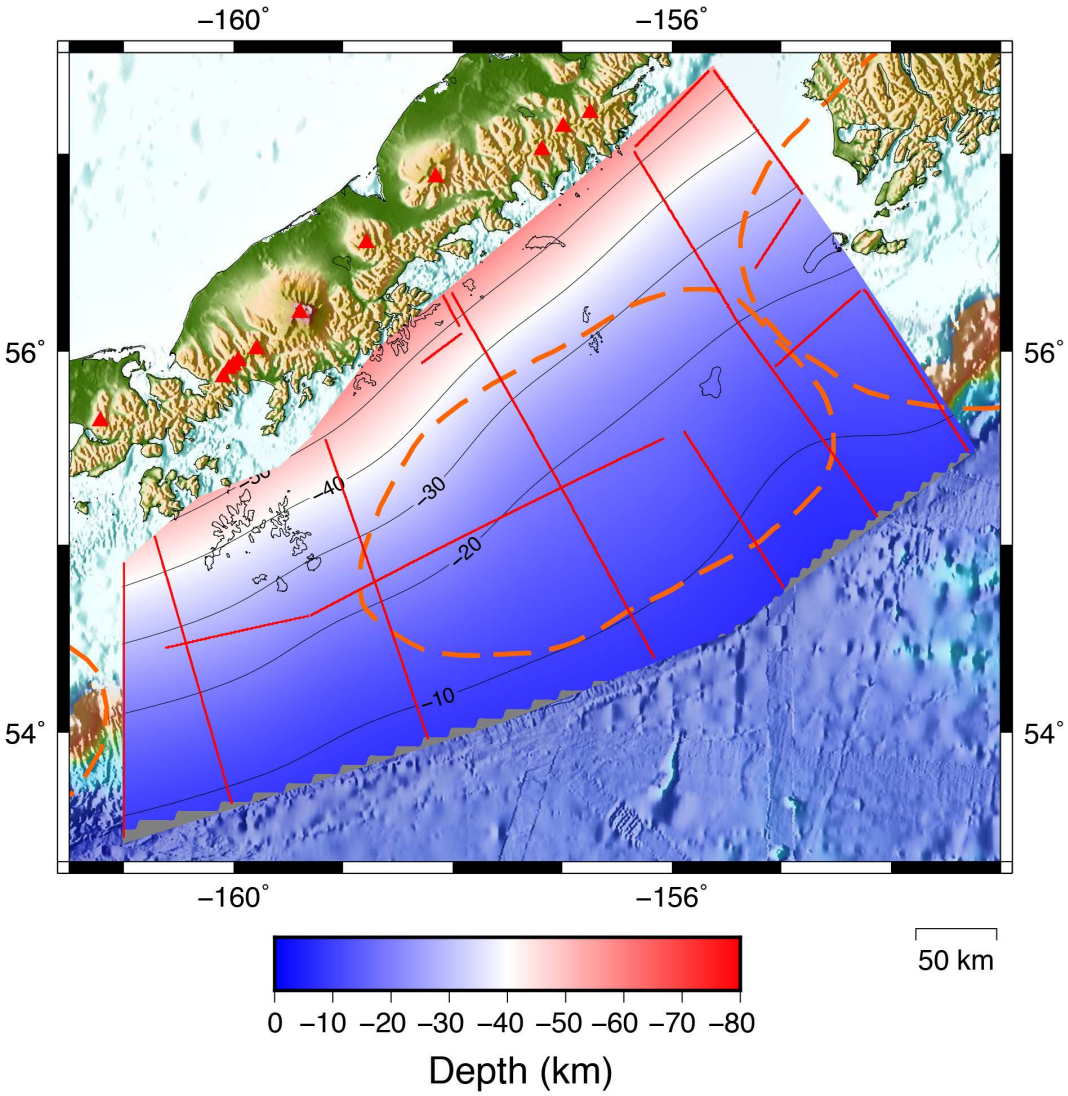

Figure A.35: Map of the depth to the subduction interface for the study area extracted from the slab interface model Slab2 from Hayes et al. (2018). See Figure A.26 caption for explanations of additional figure components.

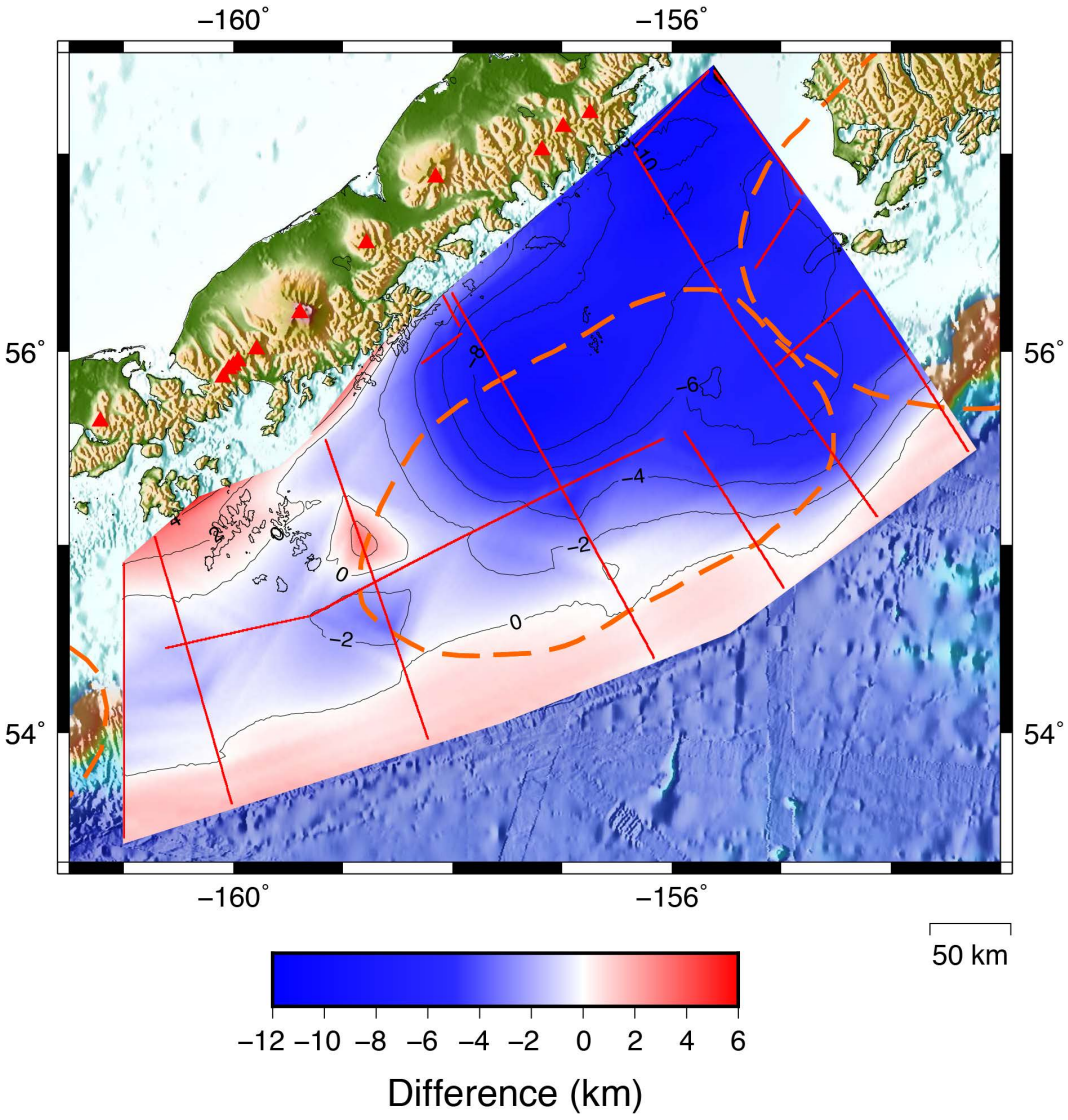

Figure A.36: Map of the 2D gradient of the difference in the subduction interface depth for the study area between the ALEUT data model (Fig. A.26) and Hayes slab2 model [Hayes et al., 2018]. See Figure A.26 caption for explanations of additional figure components.

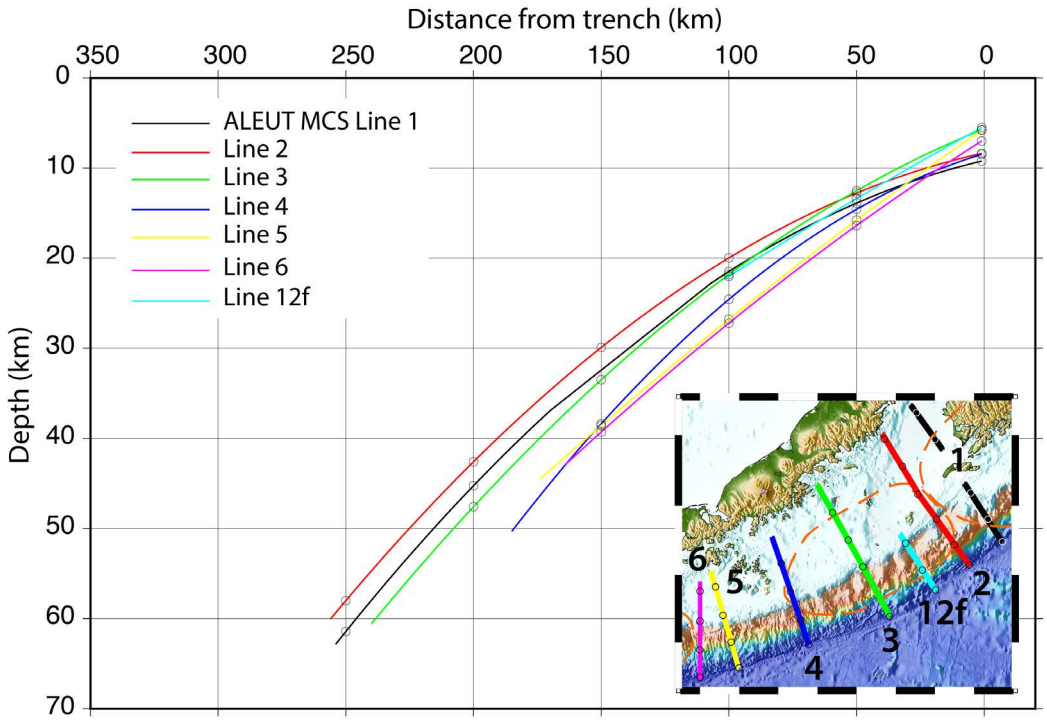

Figure A.37: Plate interface depth versus distance from the trench for quadratic polynomial fits through ALEUT MCS trench-normal profiles (see Figure 3.14). Inlet at the bottom right corner shows position of the displayed profiles (thick multi-colored lines) in the ALEUT survey area. Black circles are positioned in 50-km-intervals along the profiles and are used as depth constraints for a smooth background models as seen as in Figure A.38.

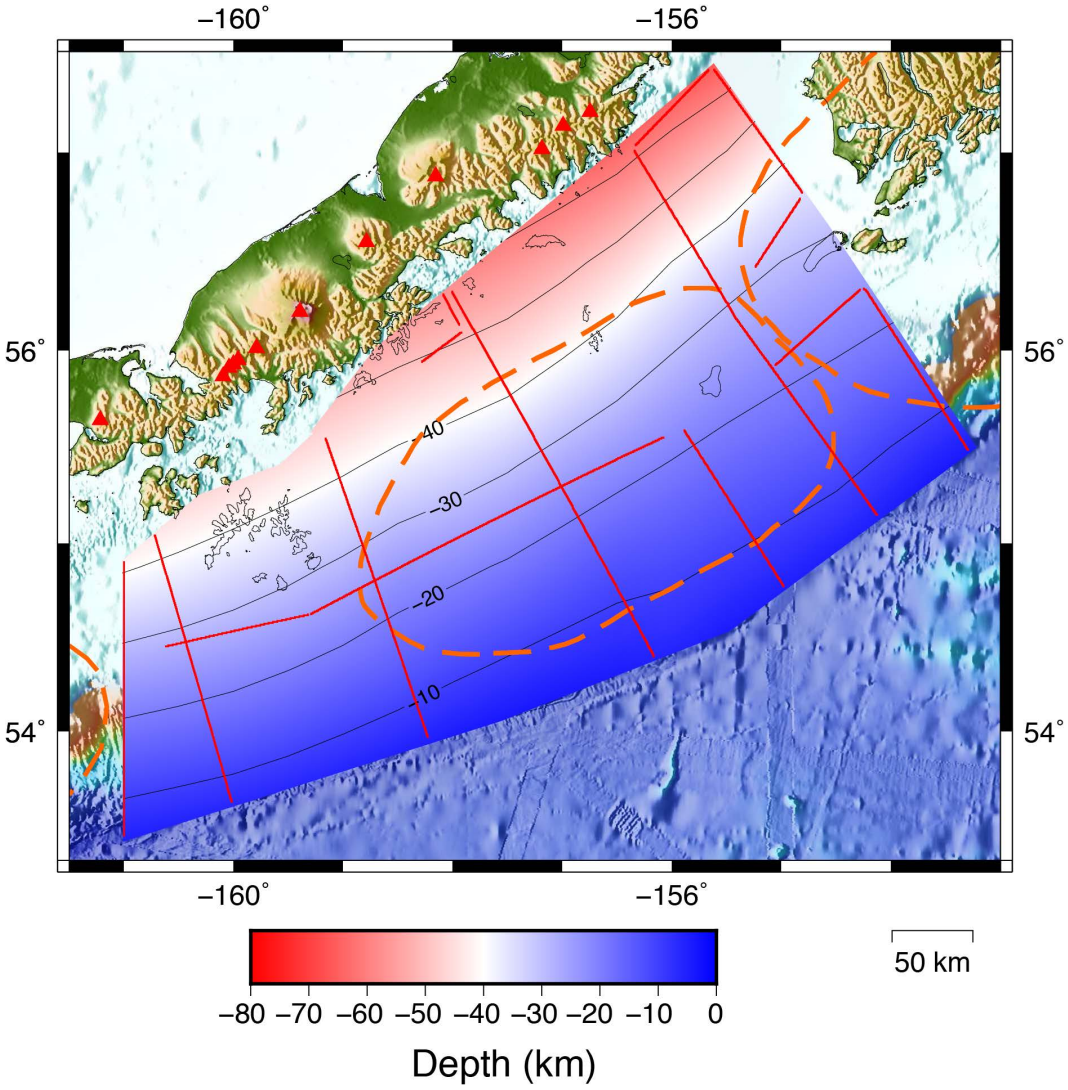

Figure A.38: Smooth background plate interface model constraint by 50-km-interval data points along the polynomial fitted depth function through ALEUT MCS plate interface depth profiles. See Figure A.26 caption for explanations of additional figure components

Earthquakes above M_W 6.9					
#	Date (YYYY-MM-DD)	Magnitude (Mw)	Hypocenter Depth (km)	Focal Mechanism (Y)es (N)o	Located by
1a	1917-05-31	7.4	35.0	N	ISC-GEM*
1b	1917-05-31	M_S 7.9	n/a	N	Boyd and Lanert-Lam, 1988
2a	1923-05-04	7.0	25.0	N	ISC-GEM
2b	1923-05-04	7.0	27.0 ± 4	Y	Sykes et al., 1971
3a	1938a-11-10	8.3	35.0	N	ISC-GEM
3b	1938a-11-10	8.2	26.0	Y	Davies et al., 1981
4a	1938b-11-17	6.9	35.0	N	ISC-GEM
4b	1938b-11-17	7.0	27.0 ± 2	Y	Sykes, 1971
5a	1946a-04-01	8.6	n/a	N	Lopez and Okal, 2006
5b	1946b-04-01	M_S 7.4	n/a	N	Sykes, 1971
6a	1948-05-14	7.1	25.0	N	ISC-GEM
6b	1948-05-14	7.2	31.0 ± 2	Y	Sykes, 1971
7a	1951-02-13	6.9	20.0	N	ISC-GEM
7b	1951-02-13	7.0	25.0 ± 2	Y	Sykes, 1971
8	1957-04-10	7.0	15.0	N	ISC-GEM
9a	1964-02-06	6.9	20.0	N	ISC-GEM
9b	1964-02-06	7.0	24.0 ± 3	Y	Sykes, 1971
10a	1989-09-04	7.1	11.4	Y	ISC-GEM
10b	1989-09-04	6.9	26.0 ± 3	Y	Sykes, 1971
11	1991-05-30	7.0	28.4	Y	ISC-GEM
12a	1993-05-13	6.9	32.3	Y	ISC-GEM
12b	1993-05-13	6.9	36.0 ± 2	Y	Abers et al., 1995
13	1999-12-06	7.0	66.0	Y	ISC-GEM
14	2001-01-10	7.0	33.0	Y	ISC-GEM

Table 1: List of earthquake parameter for $M_W \geq 6.9$ earthqakes in the ALEUT survey area as shown in Figures 2.2 and 2.10. *International Seismological Centre - Global Earthquake Model [*On-line Bulletin, http://www.isc.ac.uk, Internatl. Seismol. Cent., Thatcham, United Kingdom*, 2018].

Appendix B

ALEUT MCS reflection images with interpreted plate interface boundary thickness, reflection maps with alternative definition of thin-/thick reflection packages and continental Moho reflections

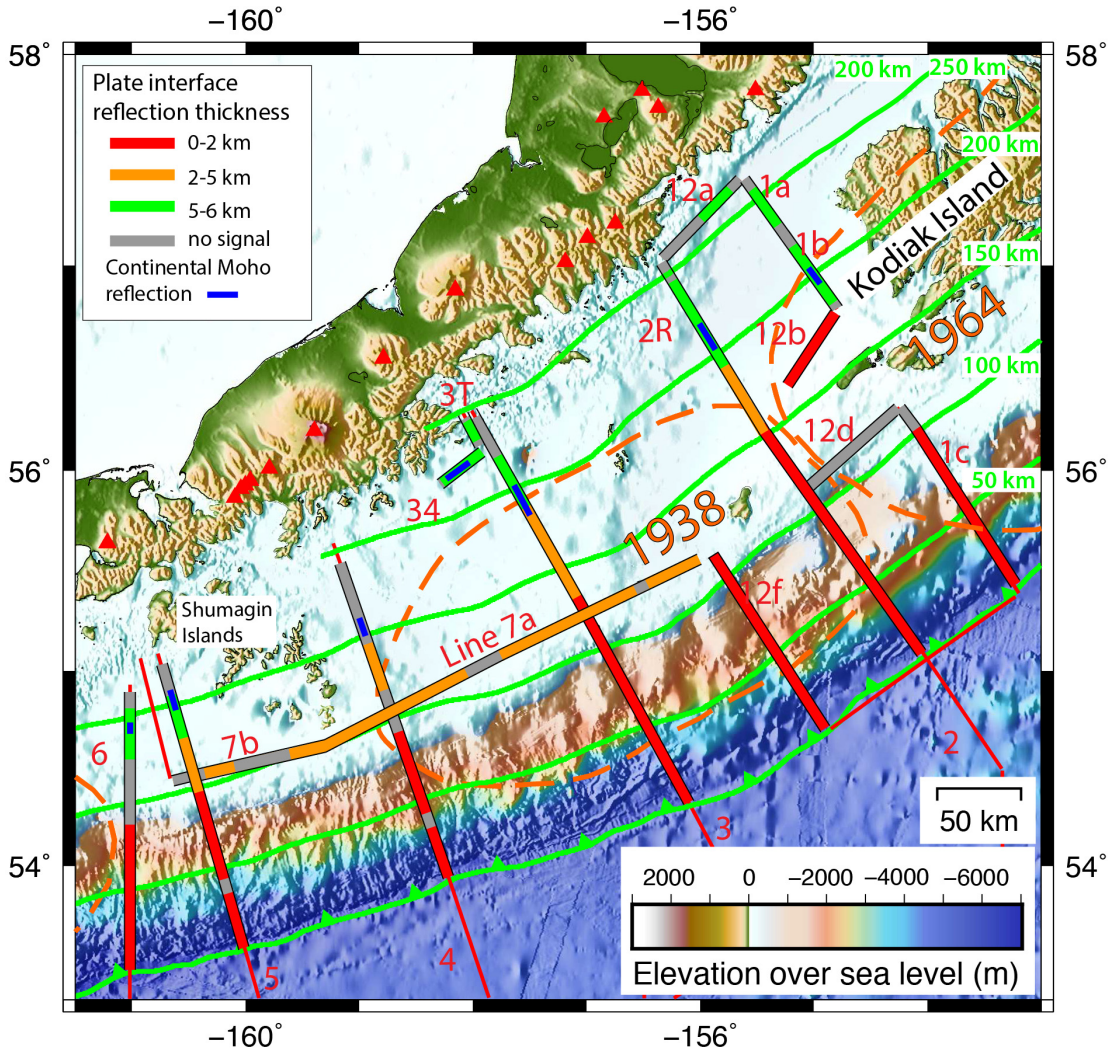

Figure B.1: ALEUT survey area with MCS profile location displaying plate interface reflection thicknesses as interpreted on fully processed and migrated depth profiles (Fig. B.2-B.15). See legend in the top left corner for plate interface thickness categorization. Rupture areas of past megathrust earthquakes are outlined by orange dashed lines with the year of the rupture event attached. Green lines with green triangles represents trench location and the begin of plate subduction. Green parallel lines landward of the trench are positioned in 50-km distance interval from the trench to facilitate length/distance estimations. Red triangles show the position of active volcanoes taken from the Alaska Volcano Observatorys web page (https://www.avo.alaska.edu/volcanoes/).

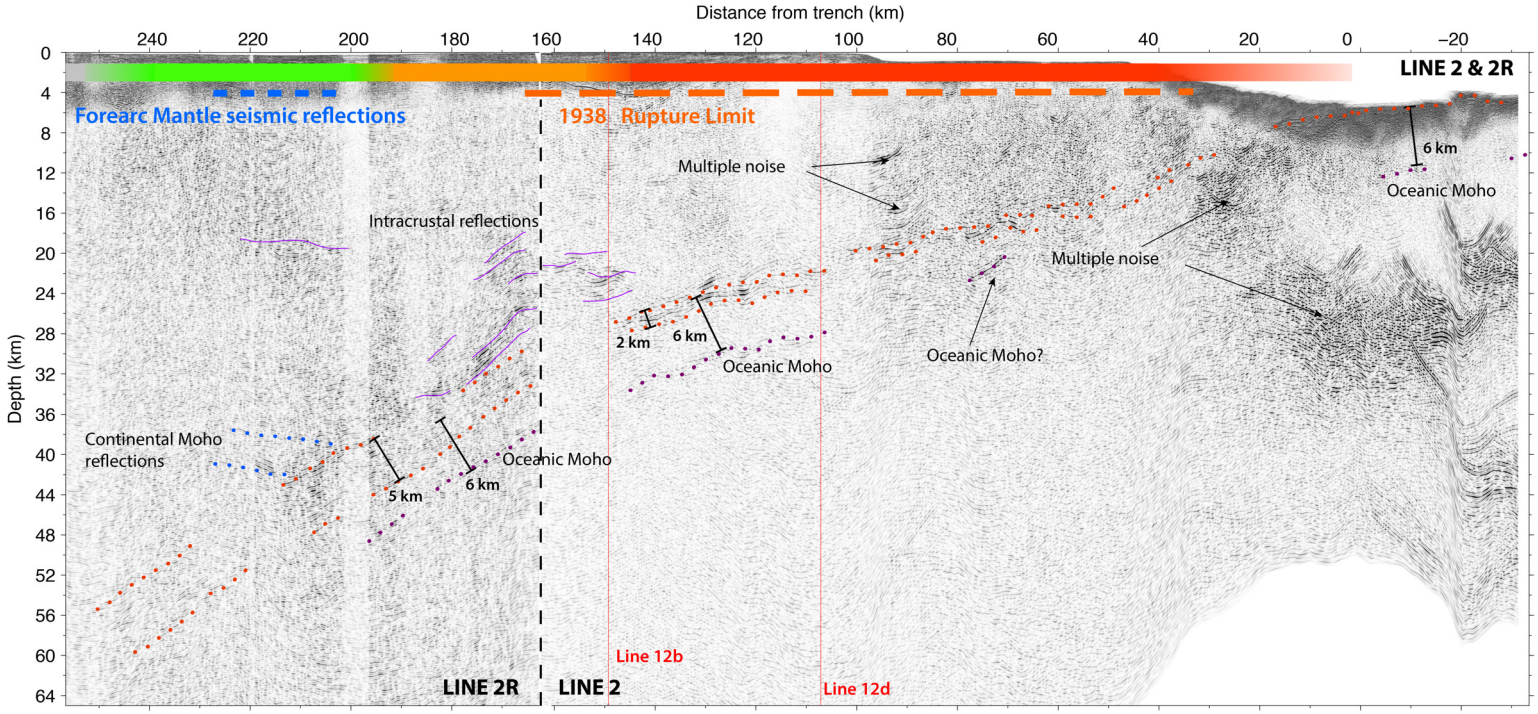

Figure B.2: Migrated and depth converted stack of MCS Lines 2 and 2R in gray scale. Red dotted lines represent the thickness extent of seismic reflection packages associated with the plate interface boundary zone. Purple dotted lines represent reflections interpreted to originate from the oceanic Moho. Thin purple lines show intracrustal reflections. The thick horizontal bar at the top of the seismic sections displays the extent of thin (red, < 2 km thickness), transitional (orange, 2-5 km thickness) and thick (green, > 5 km thickness) plate interface reflections. Areas with no clear plate interface reflections are displayed as grey parts in the horizontal bar. The plate interface thickness distribution is transferred into map view in Figure B.1 for a better overview. The thick dashed blue line shows the extent of continental Moho reflections and the thick dashed orange line shows the rupture extent derived from aftershock locations as seen in map view in Figure B.1. Black dashed vertical line at ca. 160 km distance from the trench mark the transition from ALEUT MCS Line 2 and 2R. Thin vertical red lines show intersections with other ALEUT MCS profiles.

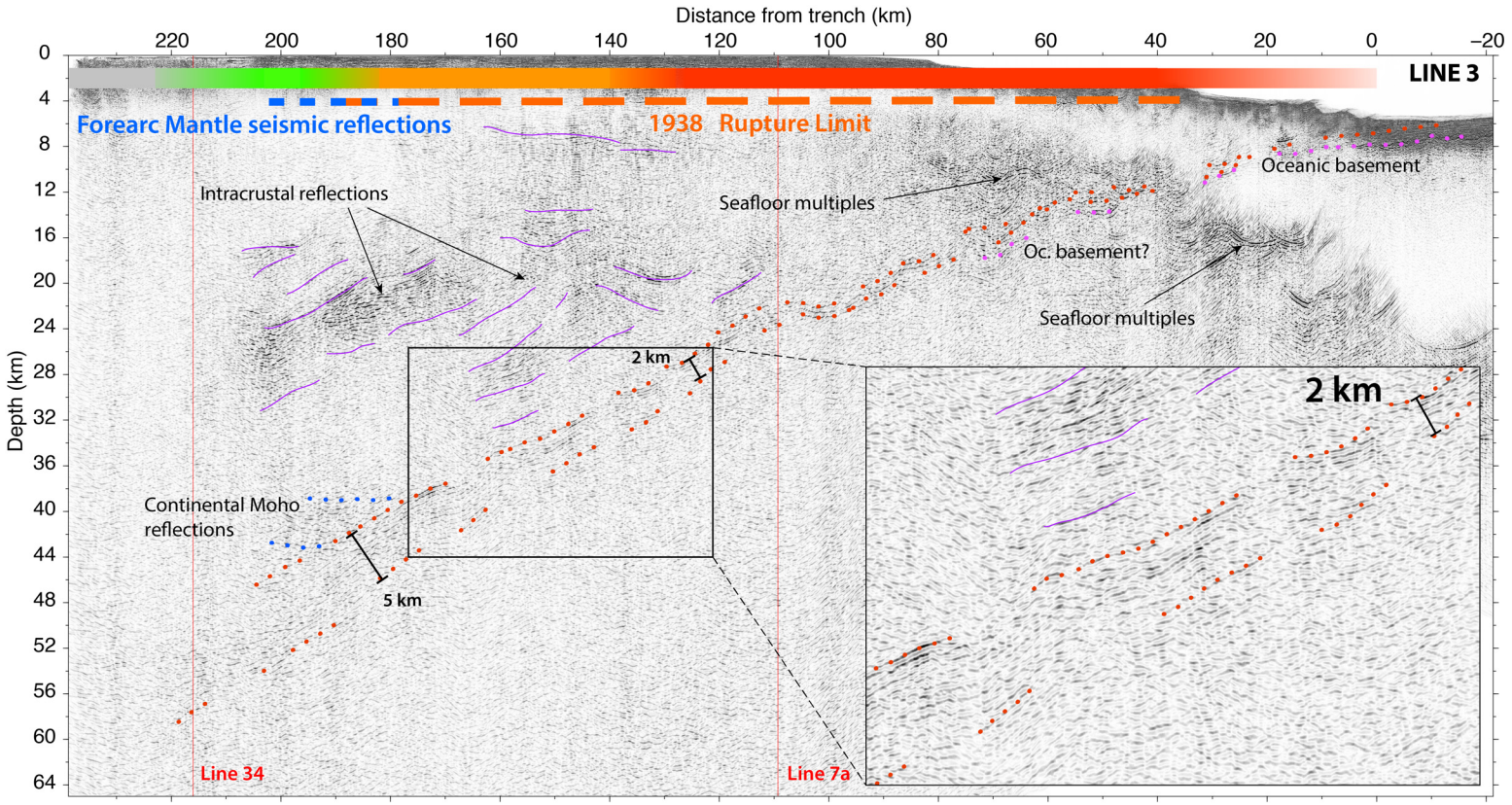

Figure B.3: Migrated and depth converted stack of MCS Line 3 in gray scale. See Figure B.2 caption for explanations of additional figure components.

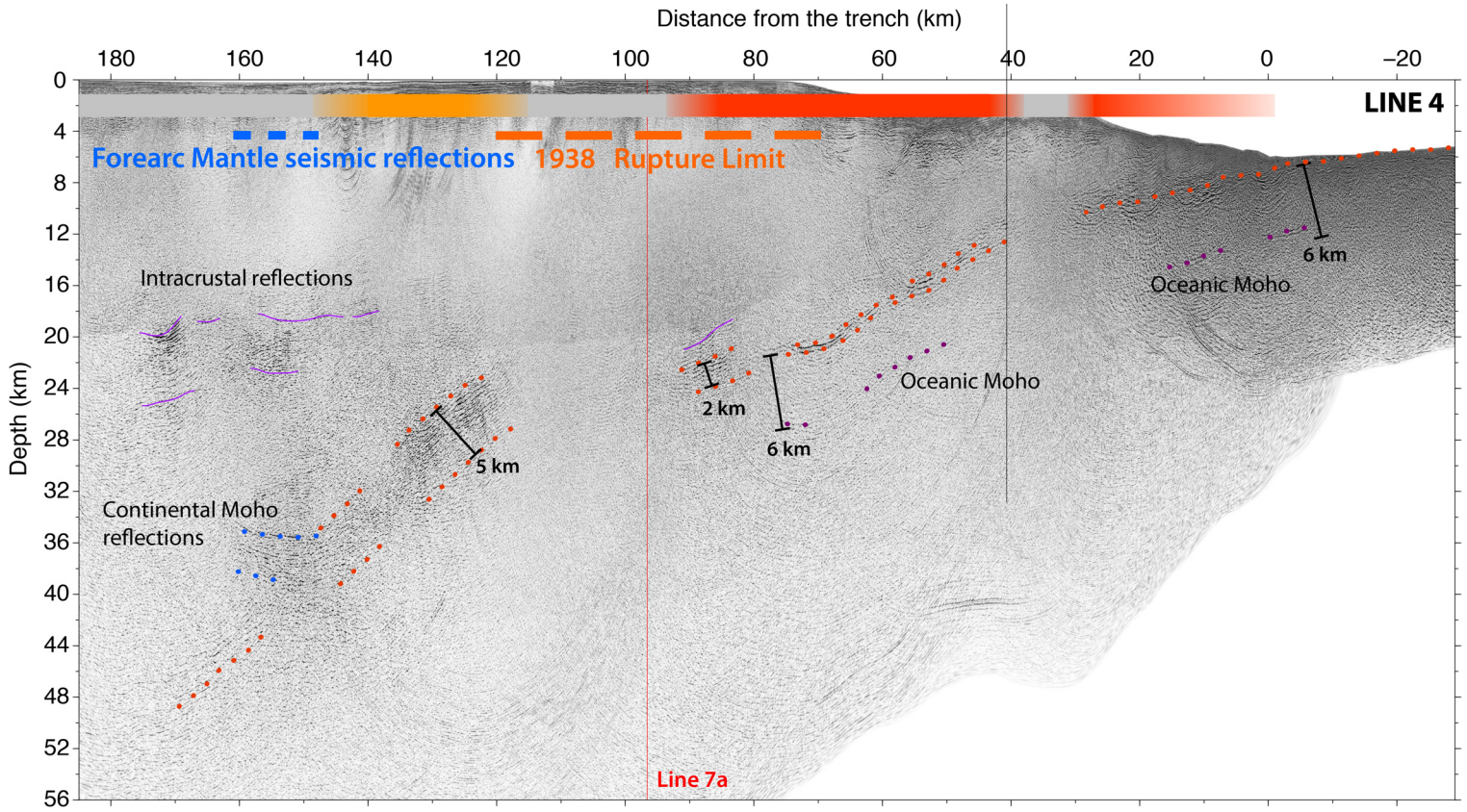

Figure B.4: Migrated and depth converted stack of MCS Line 4 in gray scale. See Figure B.2 caption for explanations of additional figure components.

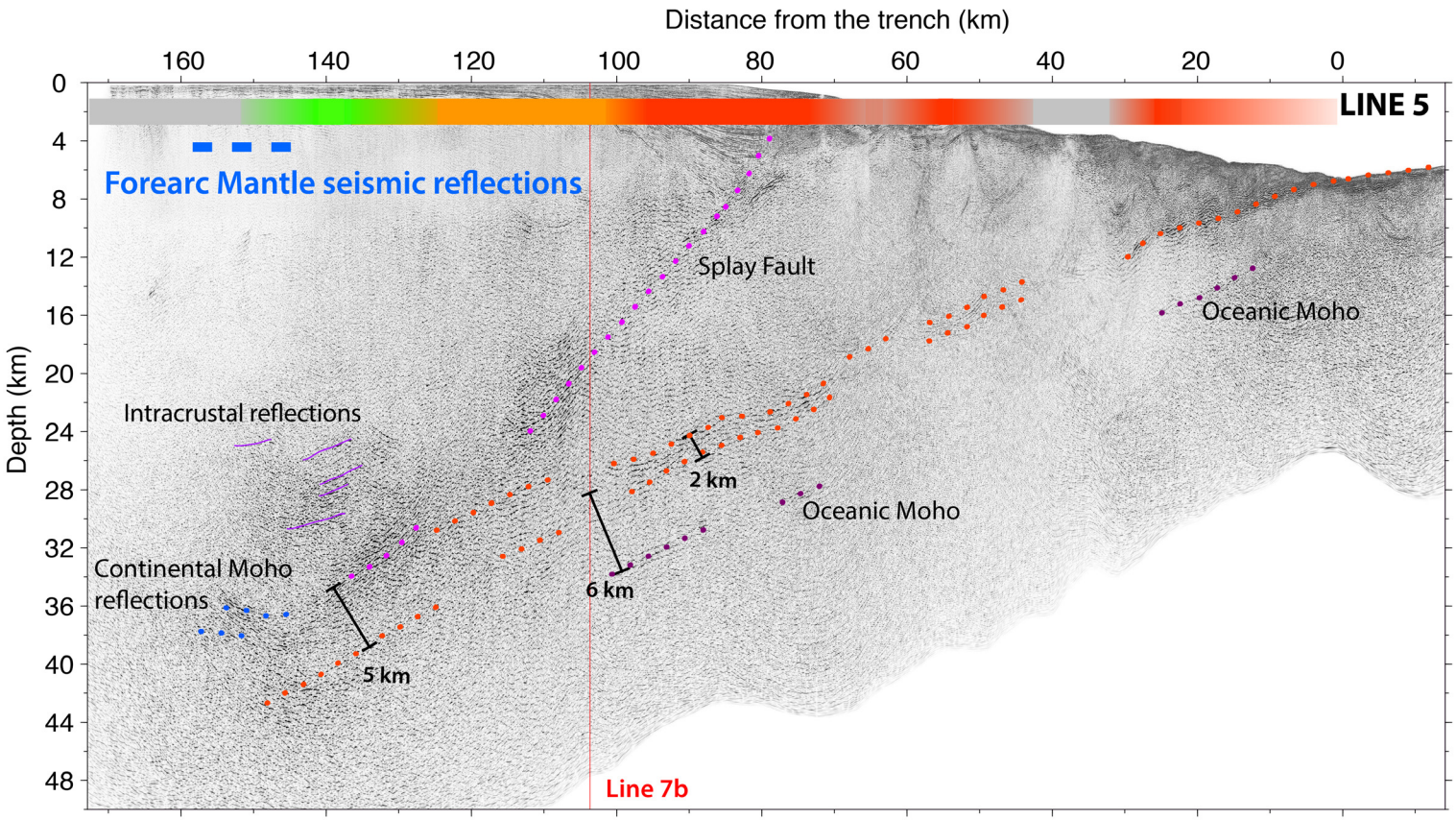

Figure B.5: Migrated and depth converted stack of MCS Line 5 in gray scale. Pink dots represent a splay fault extending from the plate interface at ca. 140 km from the trench to the acoustic basement at ca. 80 km from the trench. See Figure B.2 caption for explanations of additional figure components.

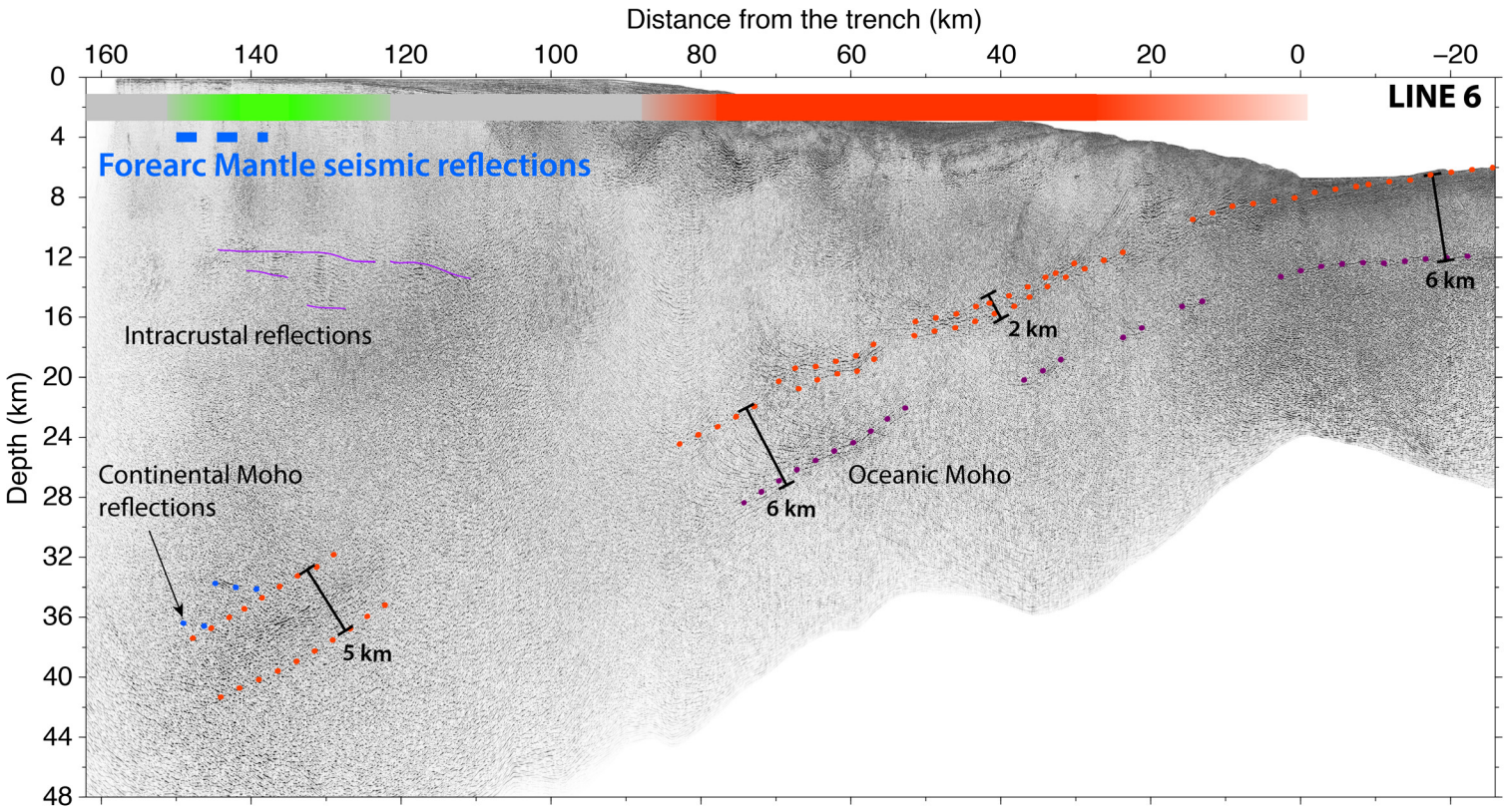

Figure B.6: Migrated and depth converted stack of MCS Line 6 in gray scale. See Figure B.2 caption for explanations of additional figure components.

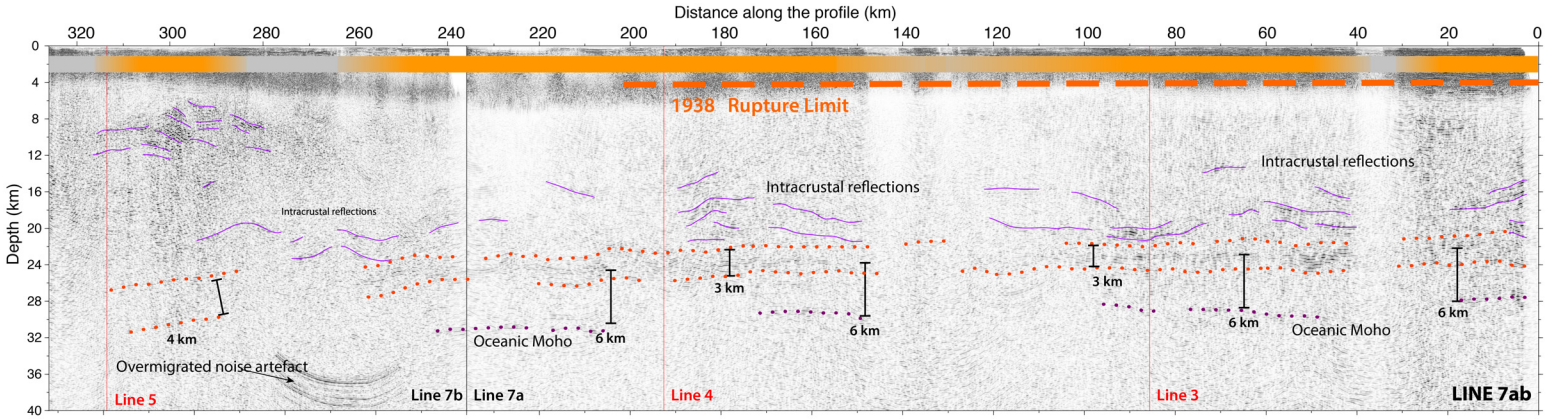

Figure B.7: Migrated and depth converted stack of MCS Line 7a and 7b in gray scale. See Figure B.2 caption for explanations of additional figure components.

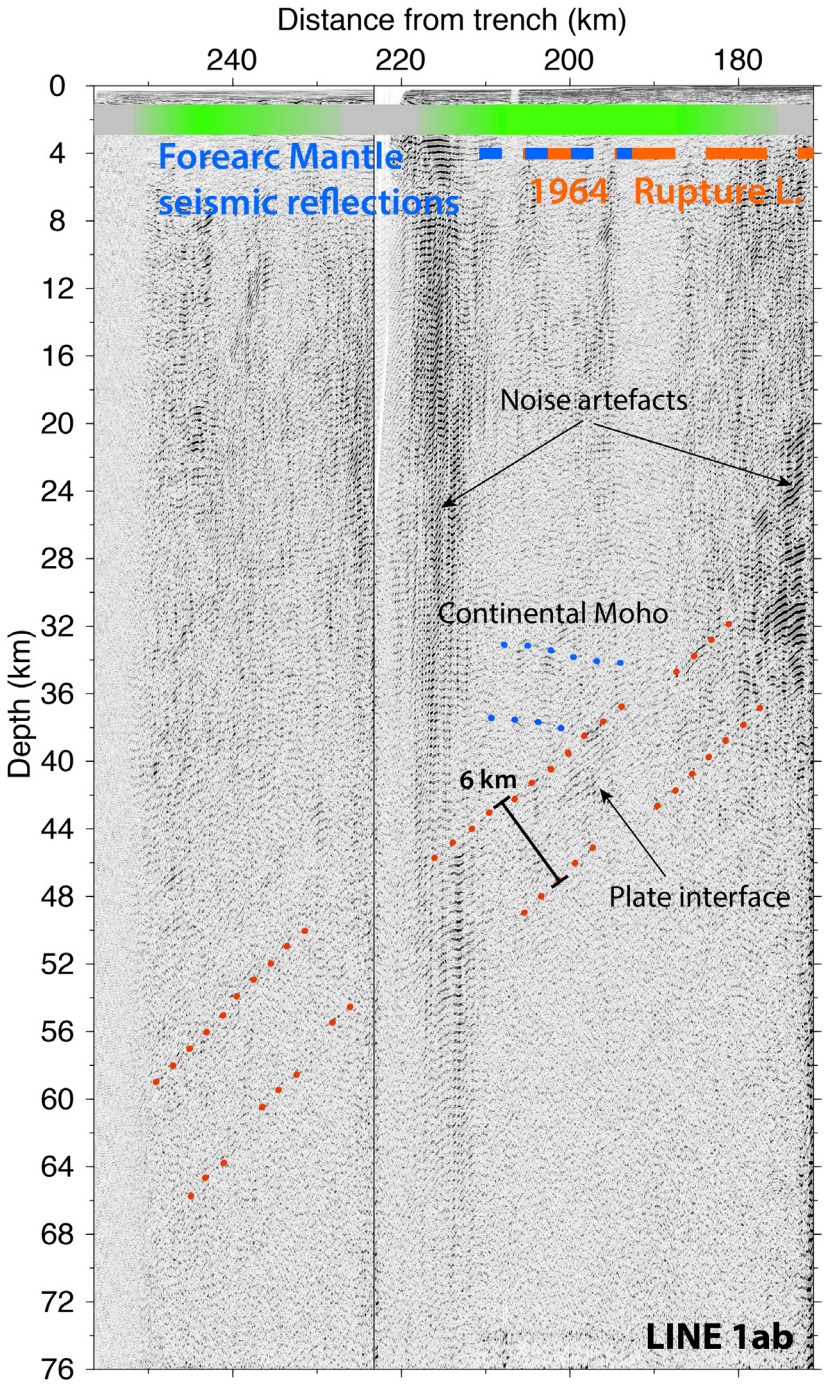

Figure B.8: Migrated and depth converted stack of MCS Line 1a and 1b in gray scale. See Figure B.2 caption for explanations of additional figure components.

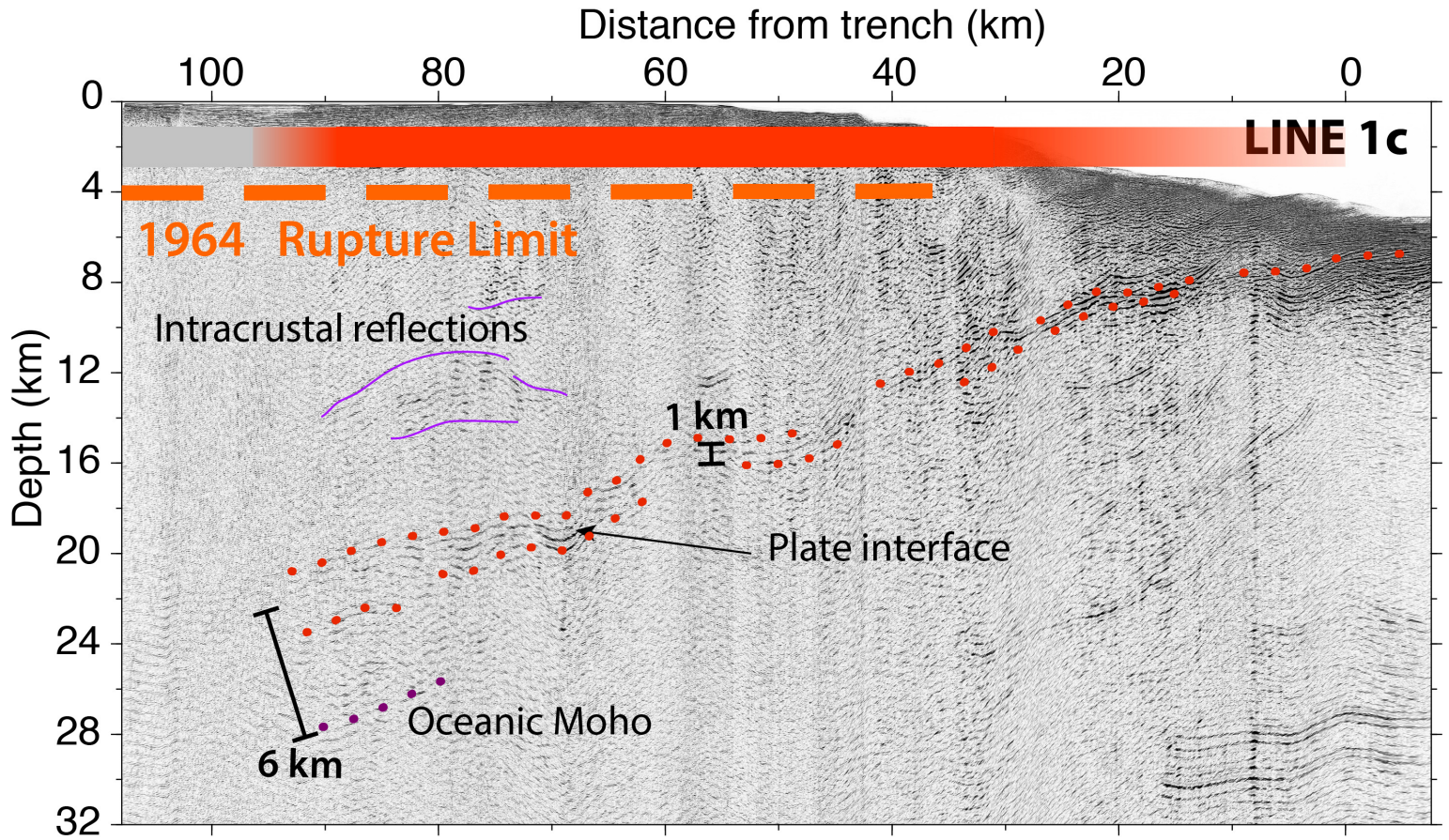

Figure B.9: Migrated and depth converted stack of MCS Line 1c in gray scale. See Figure B.2 caption for explanations of additional figure components.

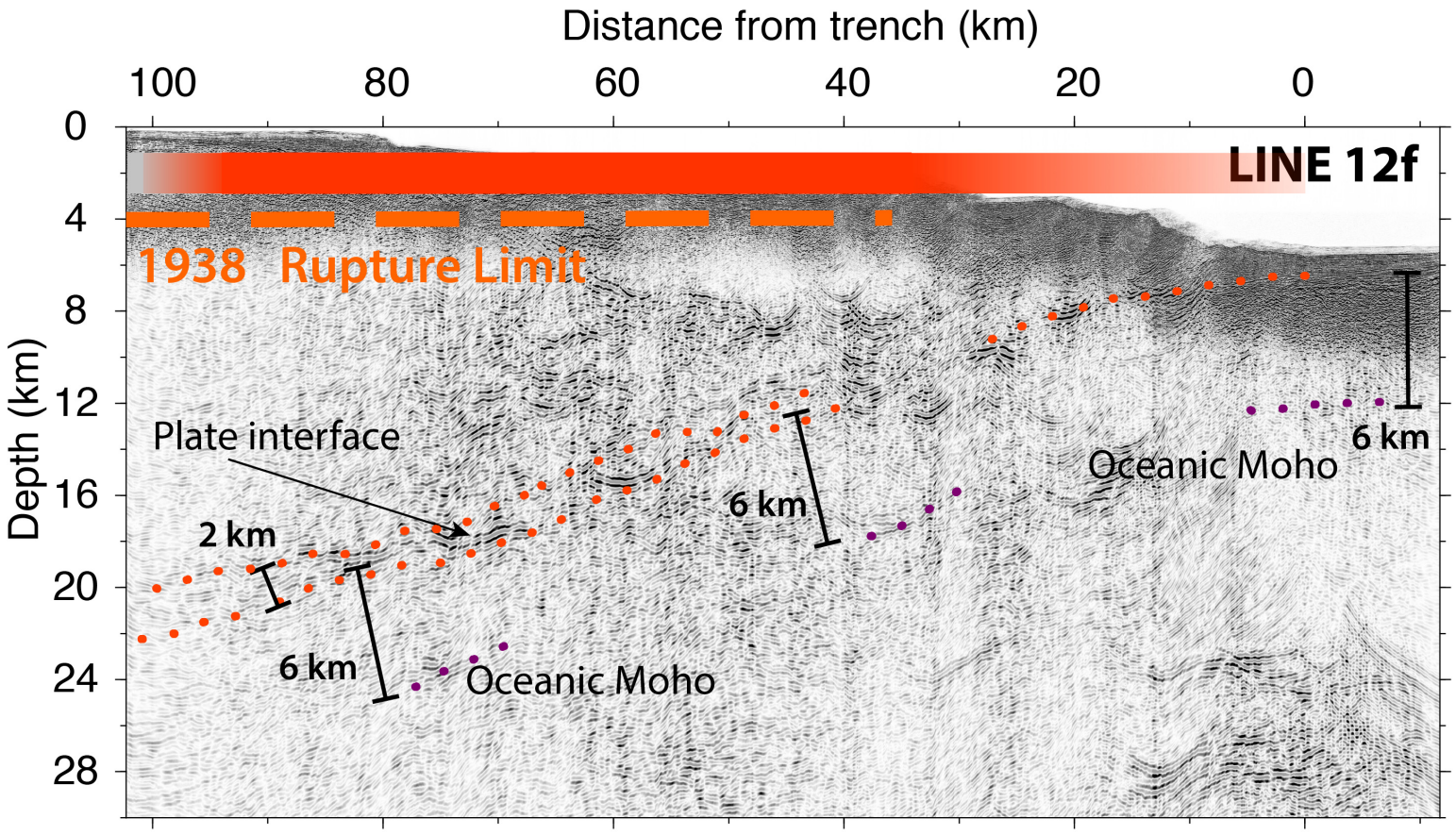

Figure B.10: Migrated and depth converted stack of MCS Line 12f in gray scale. See Figure B.2 caption for explanations of additional figure components.

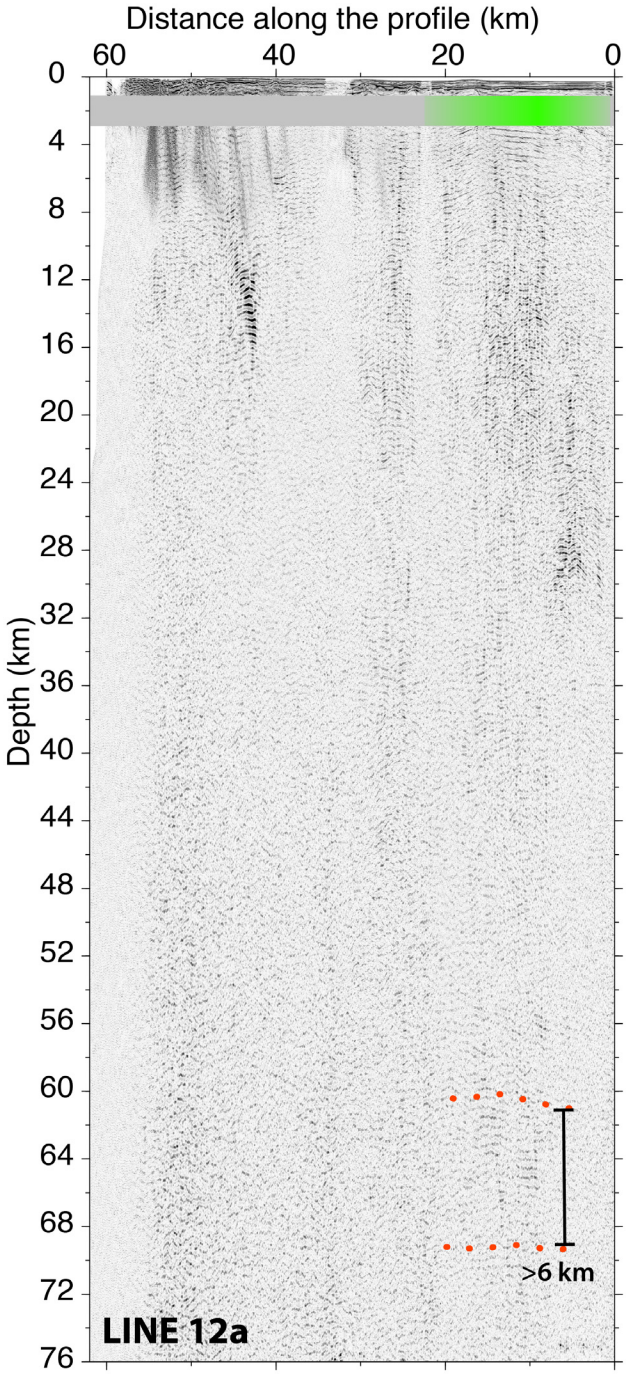

Figure B.11: Migrated and depth converted stack of MCS Line 12a in gray scale. See Figure B.2 caption for explanations of additional figure components.

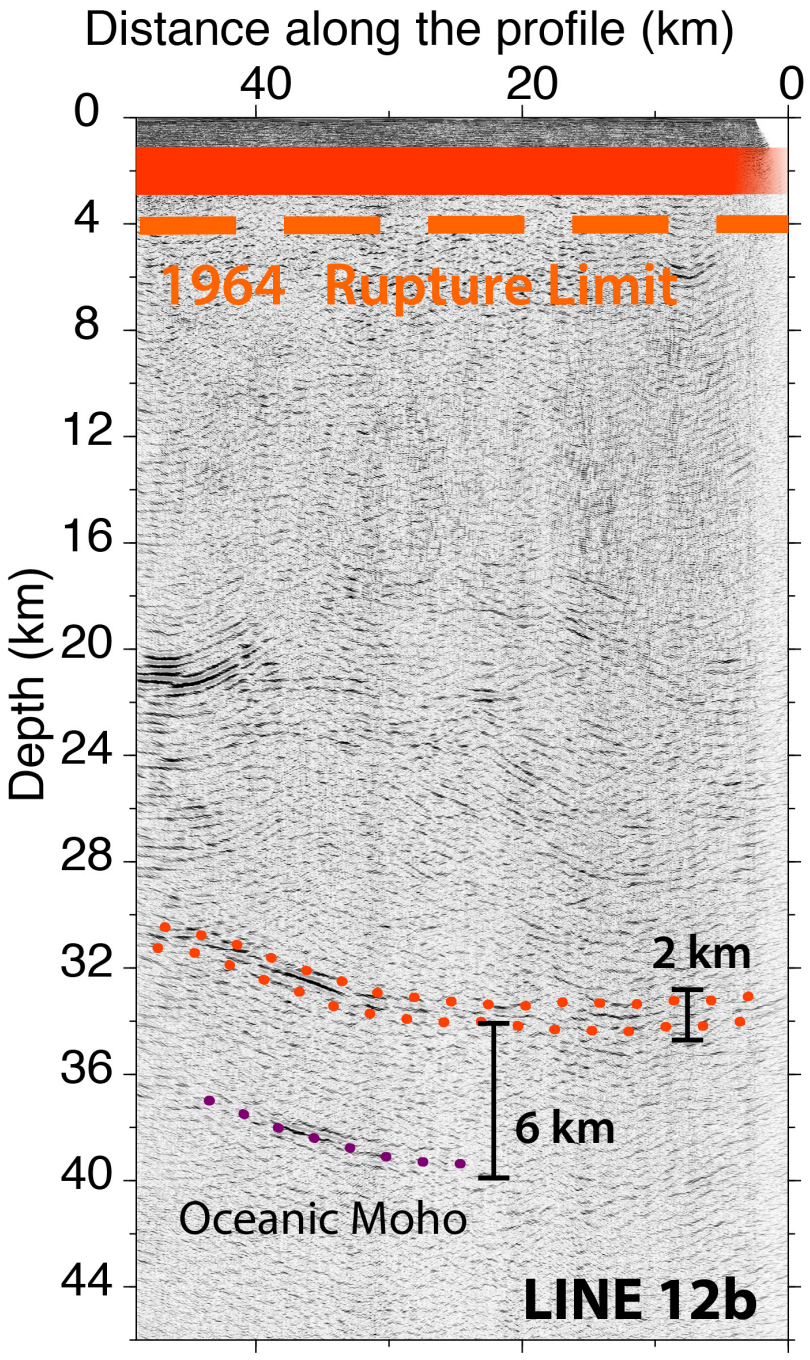

Figure B.12: Migrated and depth converted stack of MCS Line 12b in gray scale. See Figure B.2 caption for explanations of additional figure components.

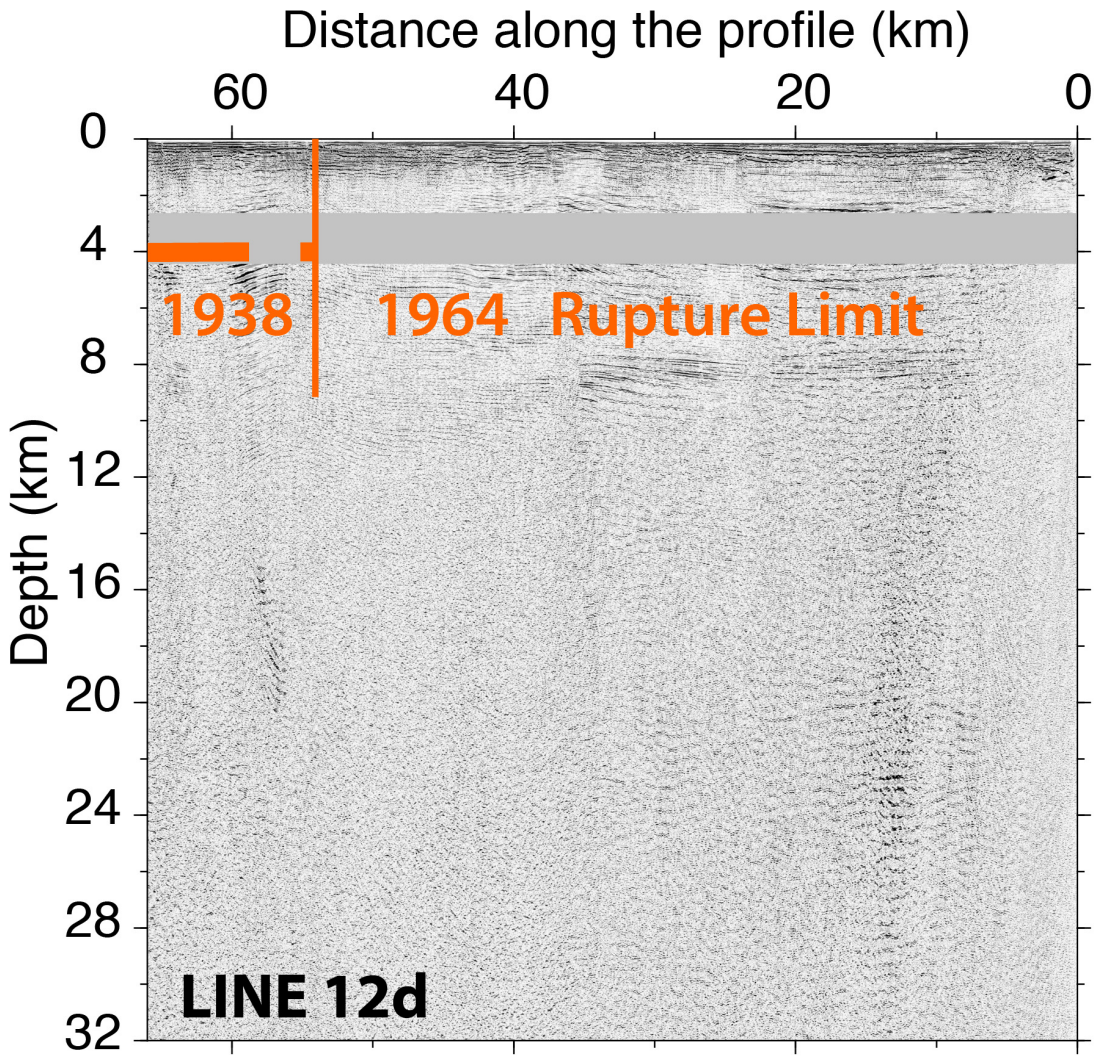

Figure B.13: Migrated and depth converted stack of MCS Line 12d in gray scale. See Figure B.2 caption for explanations of additional figure components.

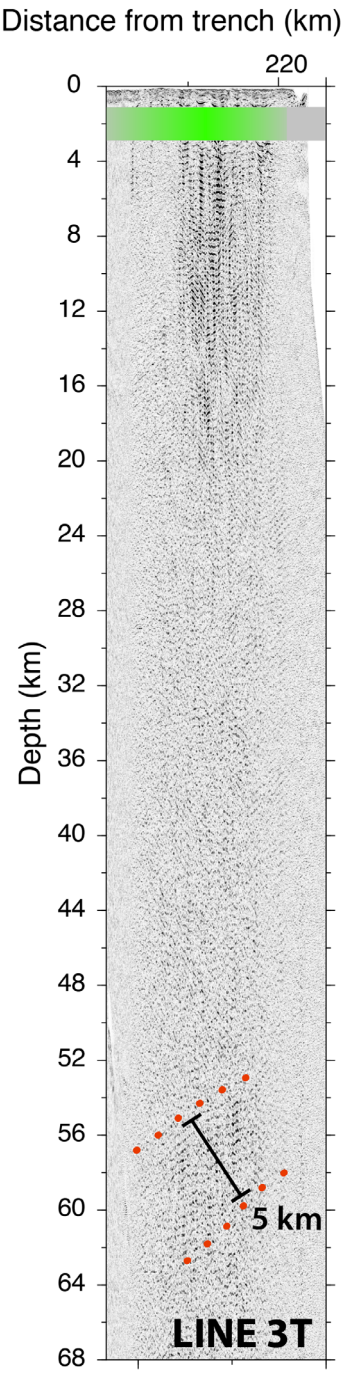

Figure B.14: Migrated and depth converted stack of MCS Line 3T in gray scale. See Figure B.2 caption for explanations of additional figure components.

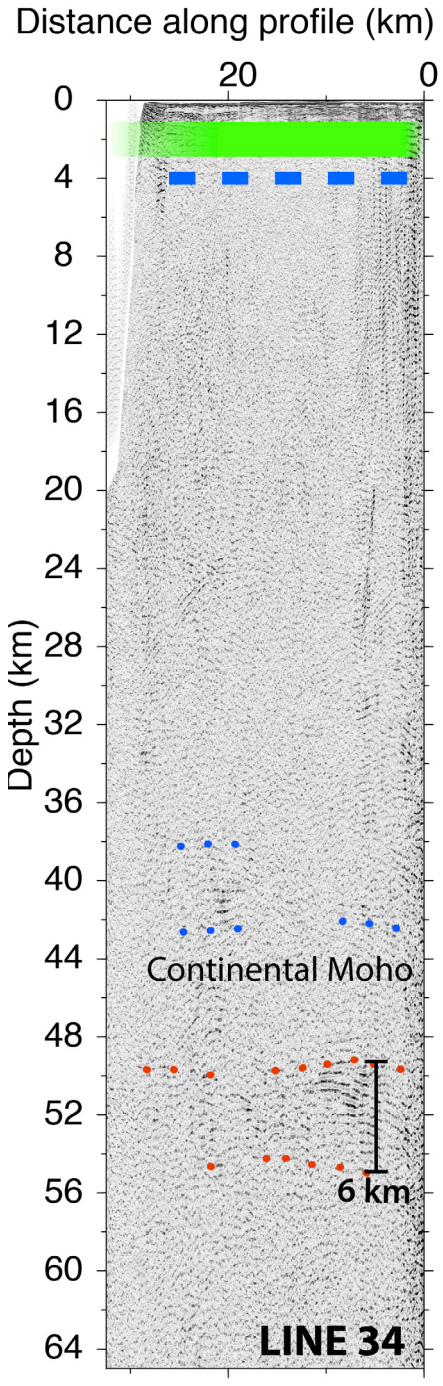

Figure B.15: Migrated and depth converted stack of MCS Line 34 in gray scale. See Figure B.2 caption for explanations of additional figure components.

Line	Distance from trench: Thin reflection band (> 2 km thickness)	Transitional reflection band (> 2 km, < 5 km thickness)	Thick reflection band (> 5 km thickness)
1abc	0 - 93 km	-	178 - 214 km, 227 - 250 km
2,2R	0 - 149 km	149 - 195 km	195 - 249 km
3	0 - 135 km	135 - 184 km	184 - 219 km
3T*	-	-	0 - 32 km
34	-	-	220 - 235 km
4	0 - 30 km, 40 - 92 km	118 - 145 km	-
5	0 - 30 km, 44 - 102 km	102 - 125 km	125 - 149 km
6	0 - 83 km	-	122 - 148 km
7ab*	-	0 - 30 km, 40 - 260 km, 285 - 313 km	-
12a*	-	-	5 - 21 km
12b*	0 - 49 km	-	-
12d*	-	-	-
12f	0-97 km	97 - 102 km	-

Table B.1: Spatial extent of thin, transitional and thick plate interface reflection packages along ALEUT MCS profiles as determined from Fig. A.2 - A.29 (Appendix A). Asterisk (*) denotes trench-parallel oriented profiles and distances along the profile (in east to west direction).

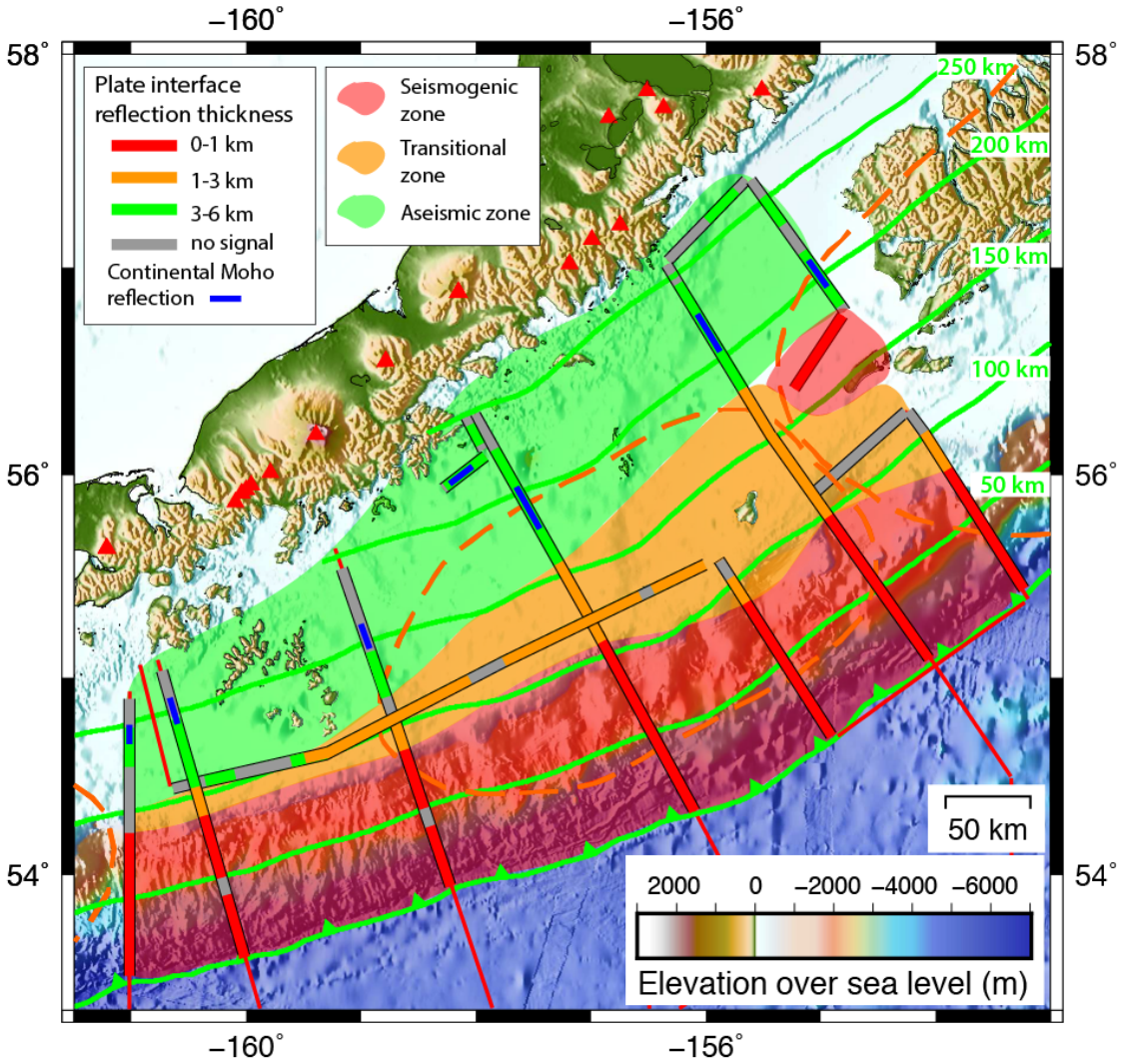

Figure B.16: ALEUT survey area with alternative plate interface reflection thickness presented in colour. Thin plate interface reflections are defined as 1-km-thick and thick plate interface reflections are defined as 3-km-thick packages of reflections. Green line with triangles is the trench location, green trench-parallel lines represent iso-distances to the trench at a 50-km-interval, and red triangles show the location of active volcanoes along the arc.

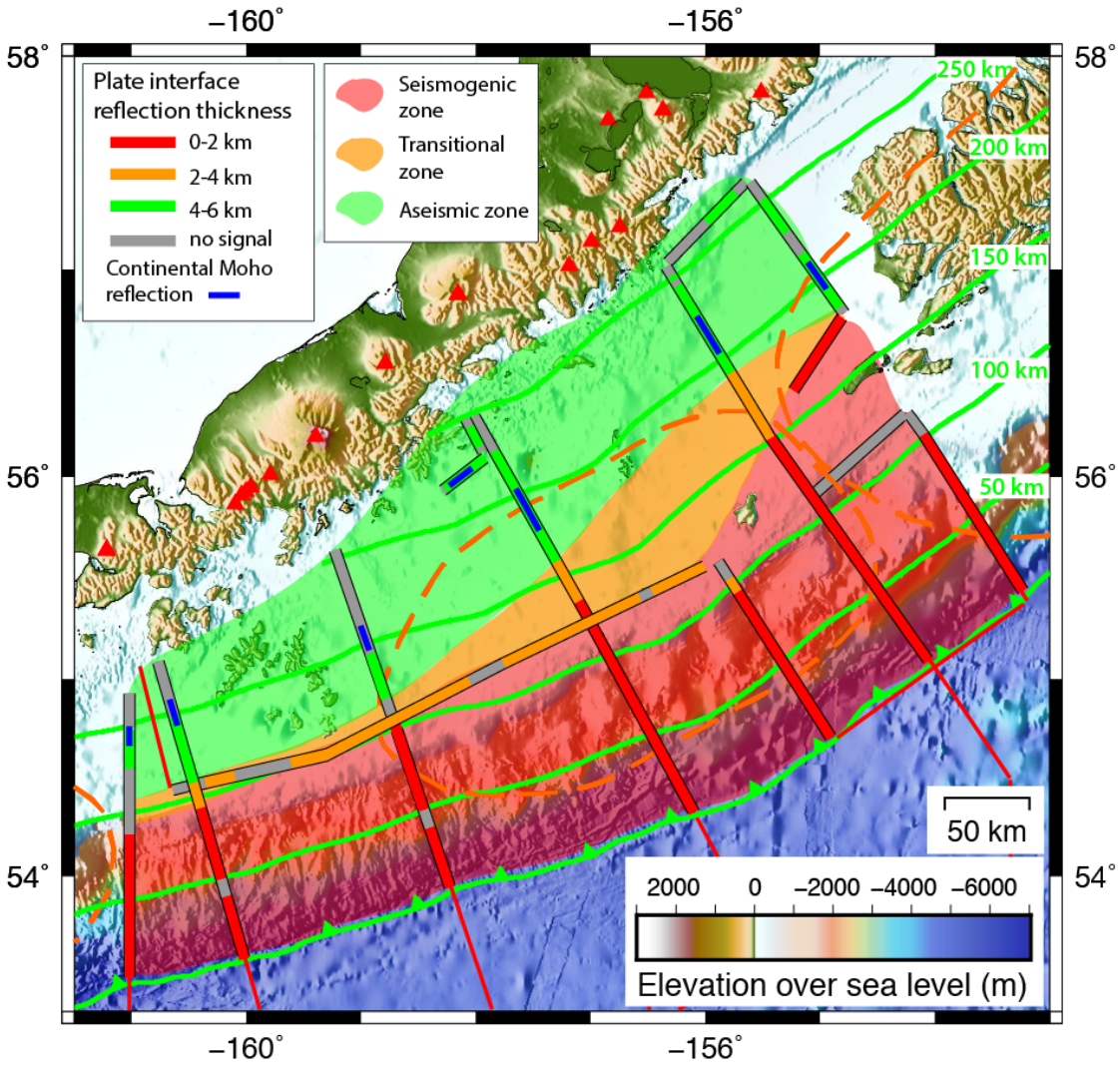

Figure B.17: ALEUT survey area with alternative plate interface reflection thickness presented in colour. Thin plate interface reflections are defined as 2-km-thick and thick plate interface reflections are defined as 3-km-thick packages of reflections. Green line with triangles is the trench location, green trench-parallel lines represent iso-distances to the trench at a 50-km-interval, and red triangles show the location of active volcanoes along the arc

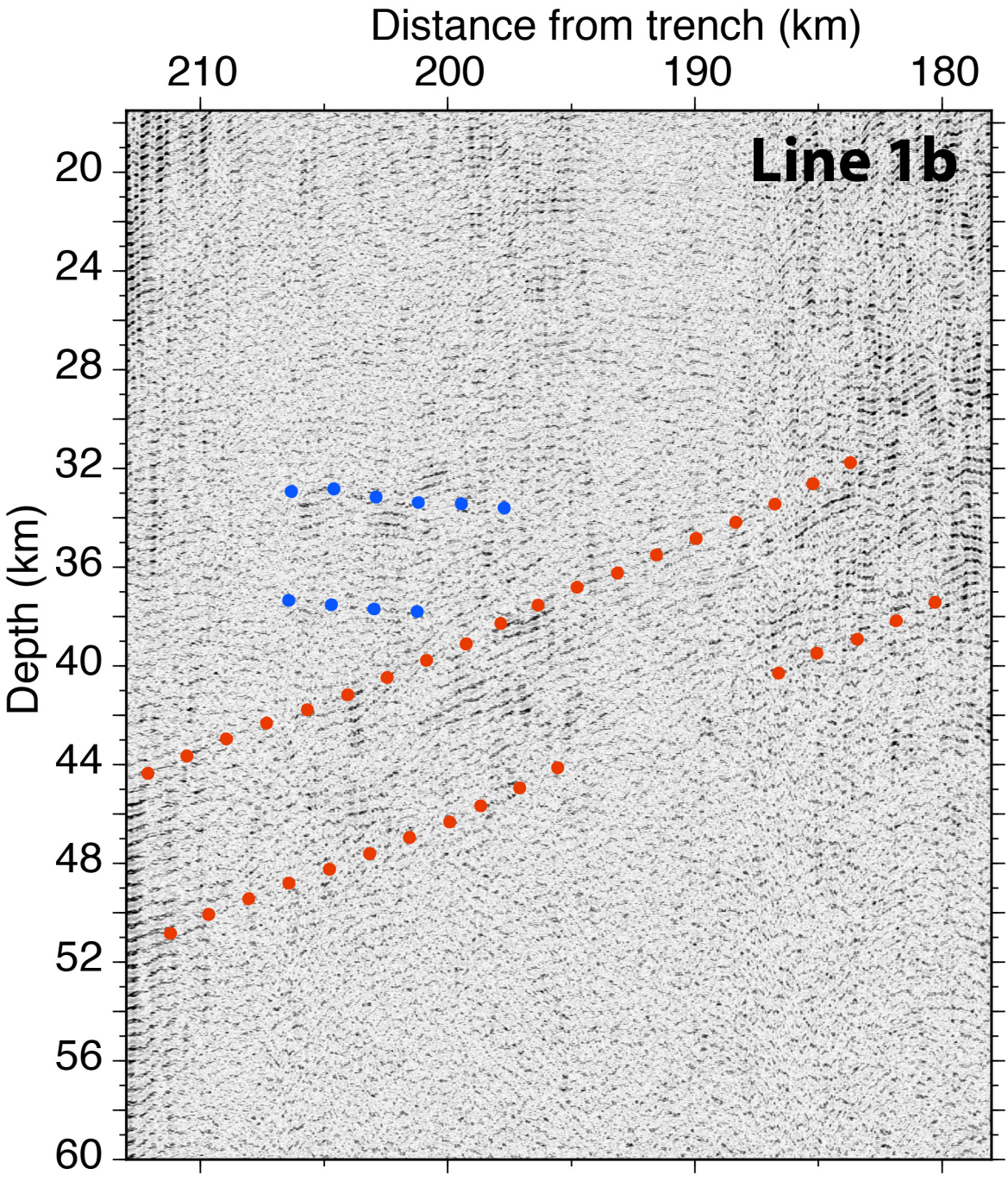

Figure B.18: Deep intracrustal reflection package (encompassed by upper and lower blue dotted line) on ALEUT MCS Line 1b. The top of this reflection package is interpreted to be the continental Moho. Red dotted line represents top and bottom of plate interface reflections.

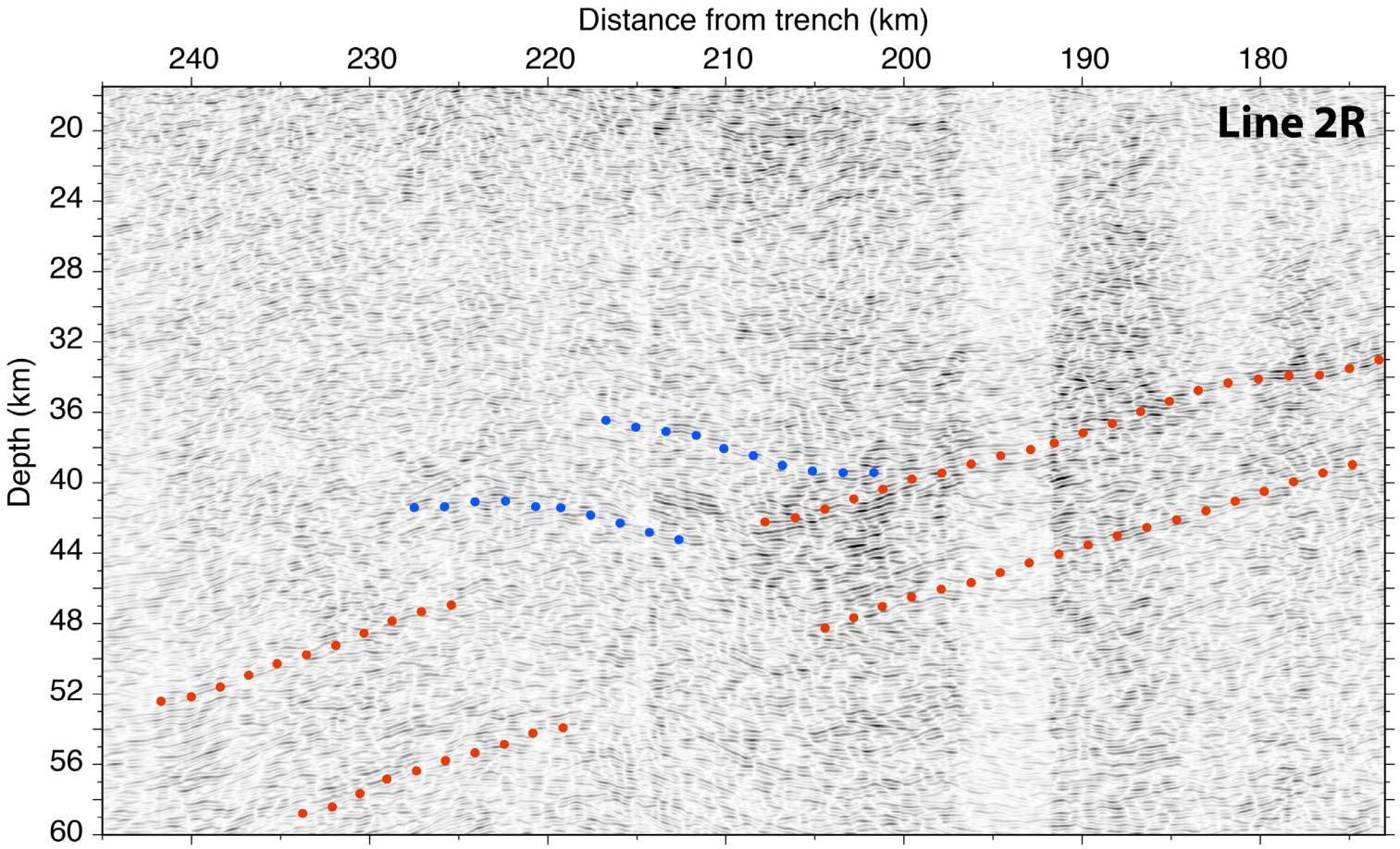

Figure B.19: Deep intracrustal reflection package (encompassed by upper and lower blue dotted line) on ALEUT MCS Line 2R. The top of this reflection package is interpreted to be the continental Moho. Red dotted line represents top and bottom of plate interface reflections.

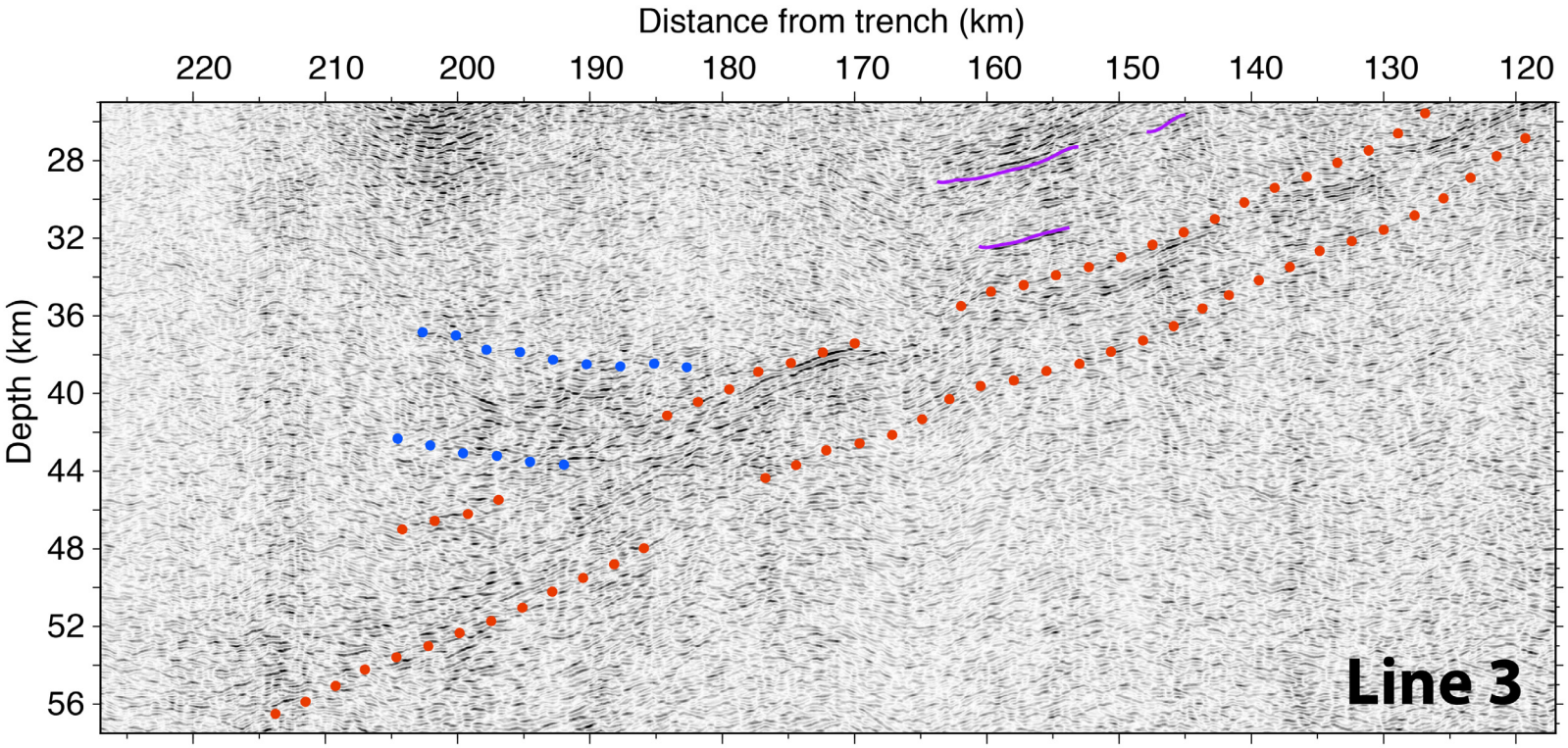

Figure B.20: Deep intracrustal reflection package (encompassed by upper and lower blue dotted line) on ALEUT MCS Line 3. The top of this reflection package is interpreted to be the continental Moho. Red dotted line represents top and bottom of plate interface reflections. Thin purple lines represents non-specified intracrustal reflections.

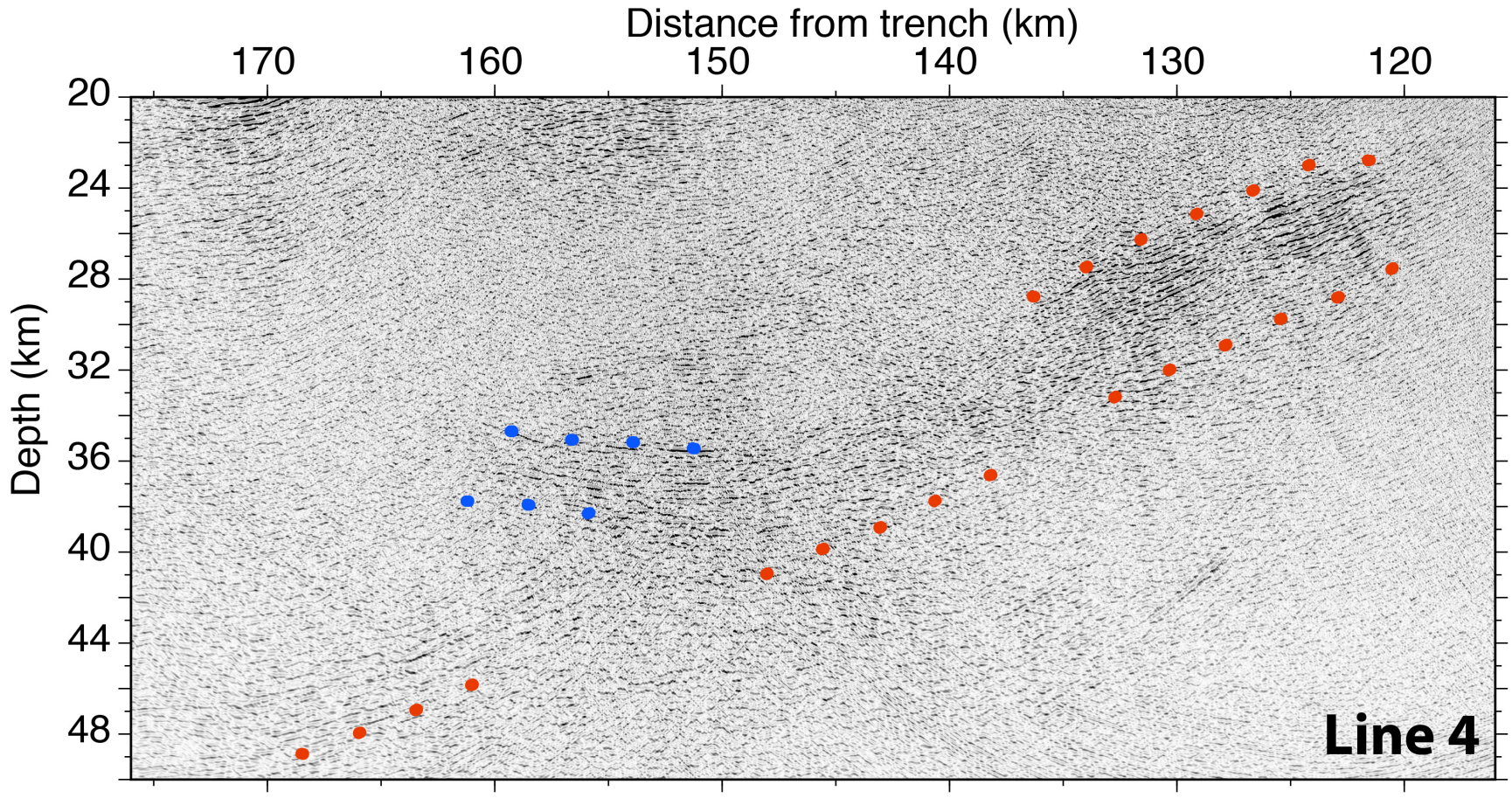

Figure B.21: Deep intracrustal reflection package (encompassed by upper and lower blue dotted line) on ALEUT MCS Line 4. The top of this reflection package is interpreted to be the continental Moho. Red dotted line represents top and bottom of plate interface reflections.

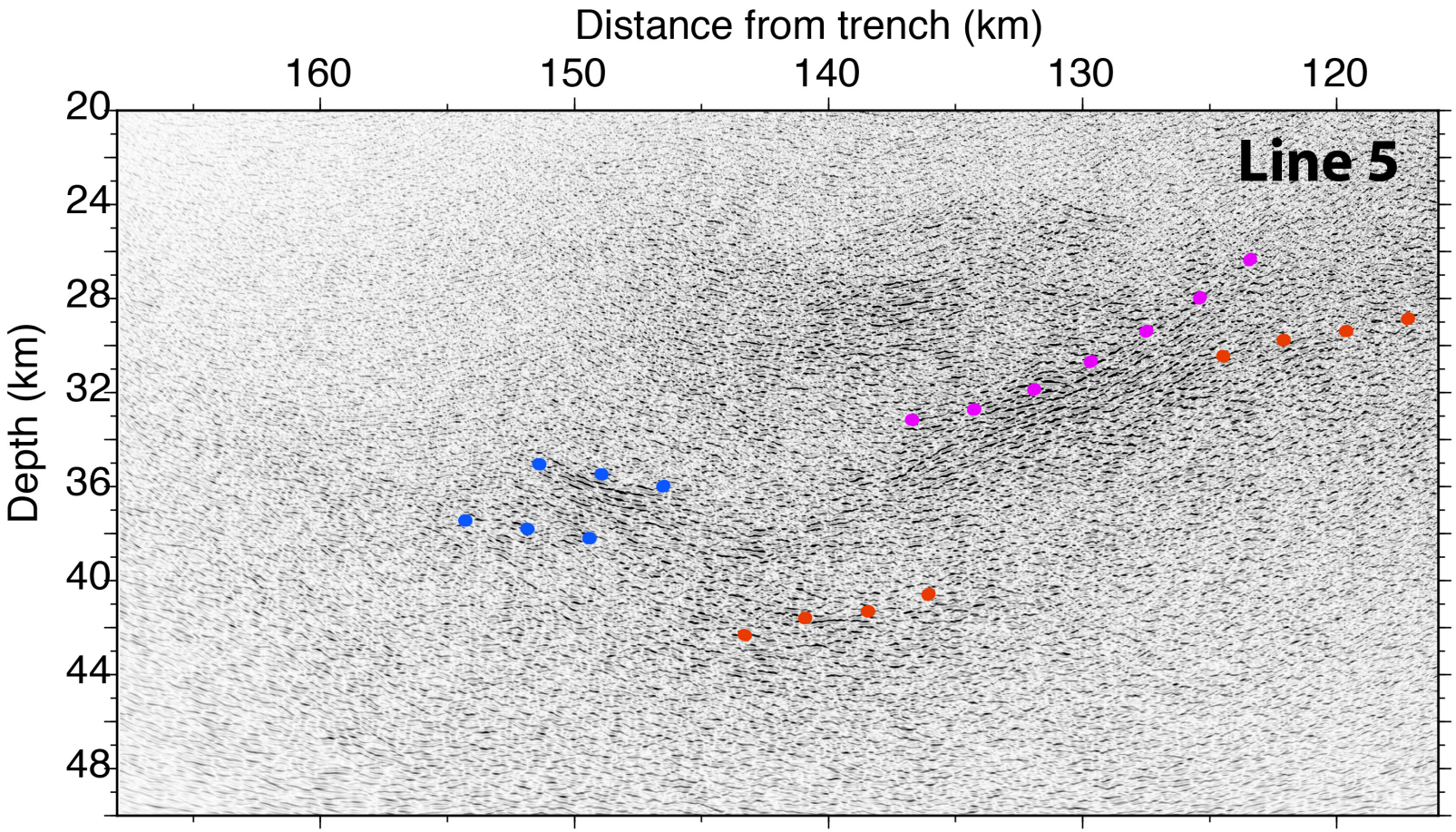

Figure B.22: Deep intracrustal reflection package (encompassed by upper and lower blue dotted line) on ALEUT MCS Line 5. The top of this reflection package is interpreted to be the continental Moho. Red dotted line represents top and bottom of plate interface reflections. Pink dotted line represents a splay fault.

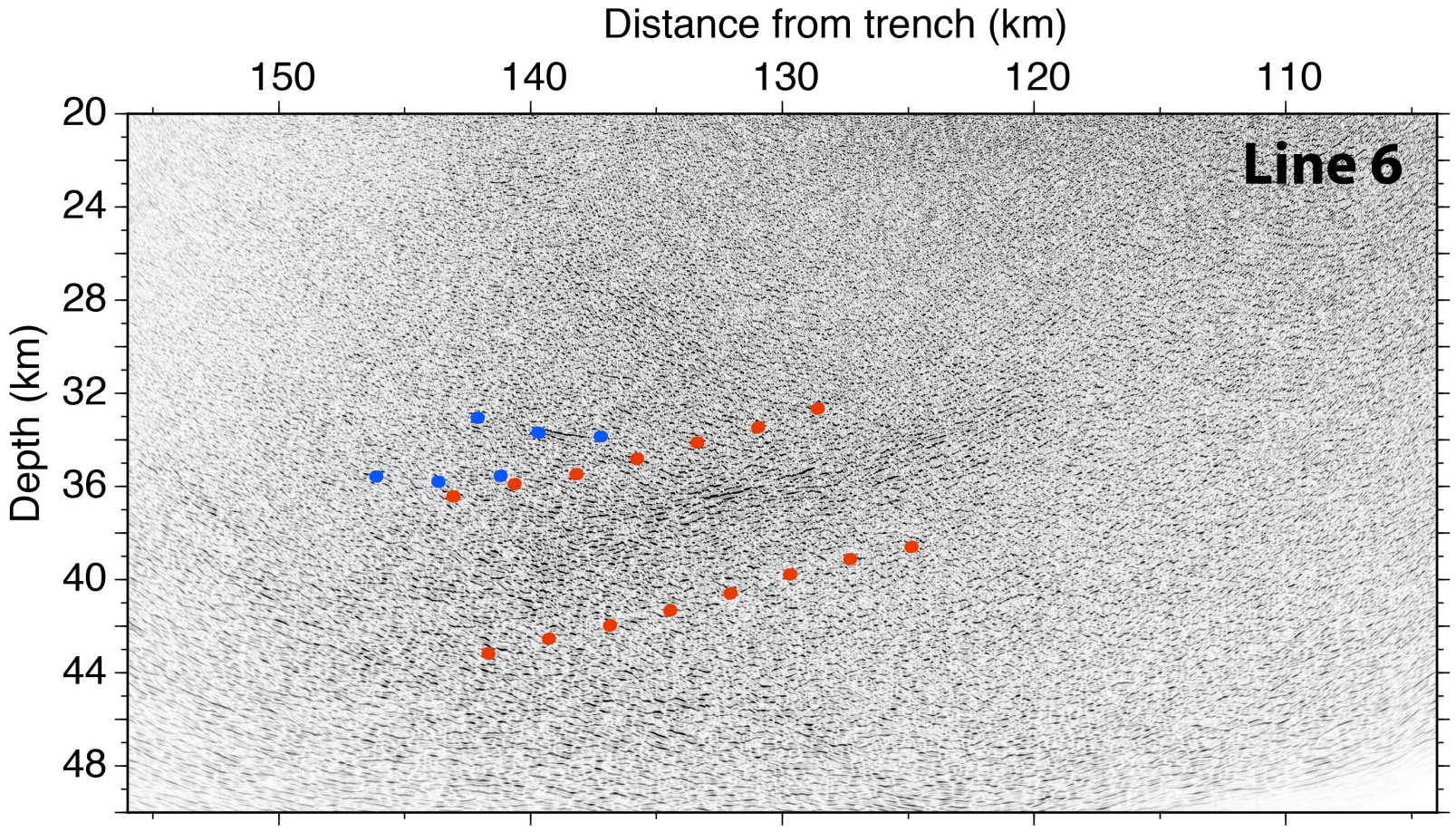

Figure B.23: Deep intracrustal reflection package (encompassed by upper and lower blue dotted line) on ALEUT MCS Line 6. The top of this reflection package is interpreted to be the continental Moho. Red dotted line represents top and bottom of plate interface reflections.

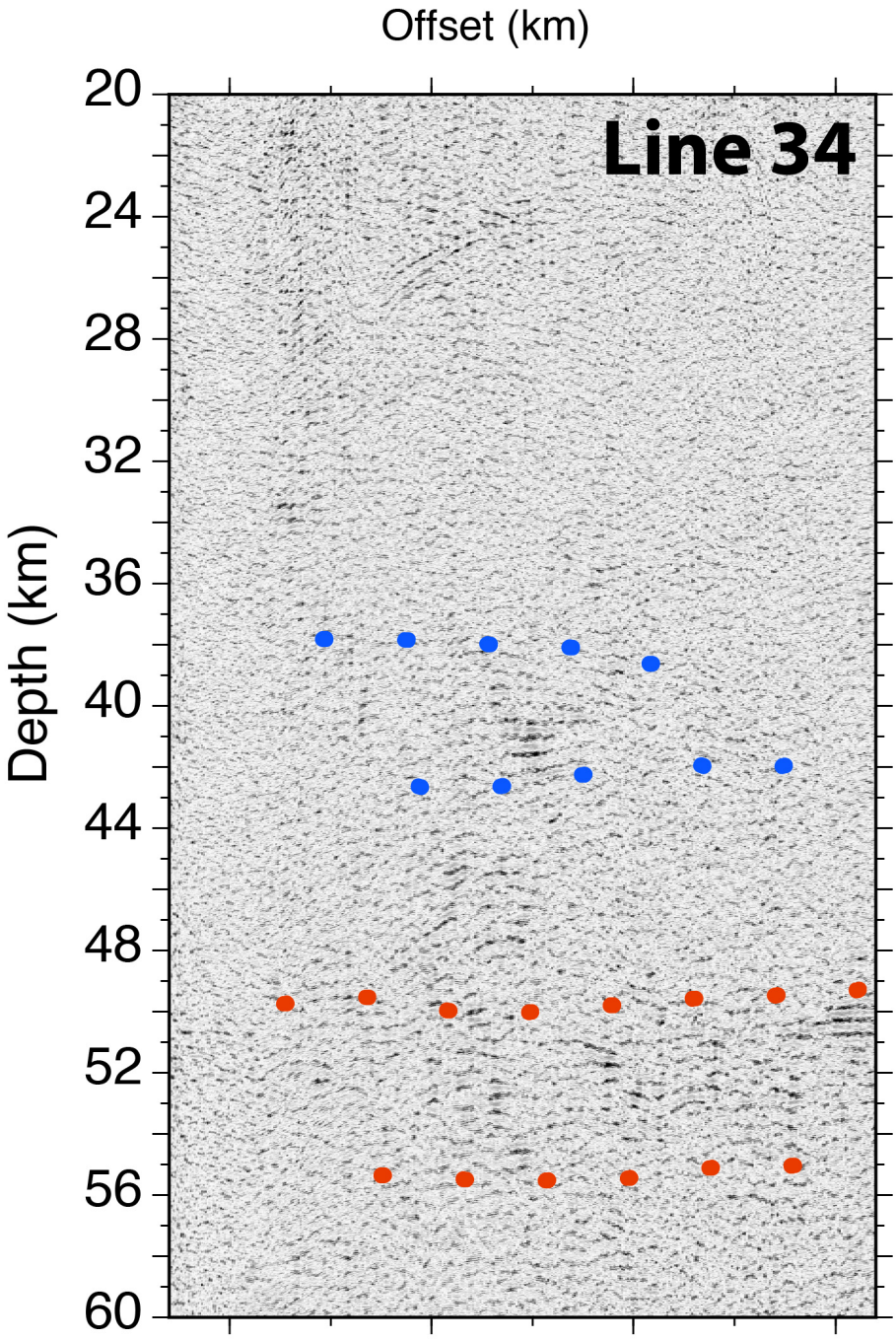

Figure B.24: Deep intracrustal reflection package (encompassed by upper and lower blue dotted line) on ALEUT MCS Line 34. The top of this reflection package is interpreted to be the continental Moho. Red dotted line represents top and bottom of plate interface reflections.

Appendix C

Seismograms of OBS ALEUT Line 3 with and without first arrival interpretation and synthetic travel time arrival and ray coverage of OBS Line 3 and 5.

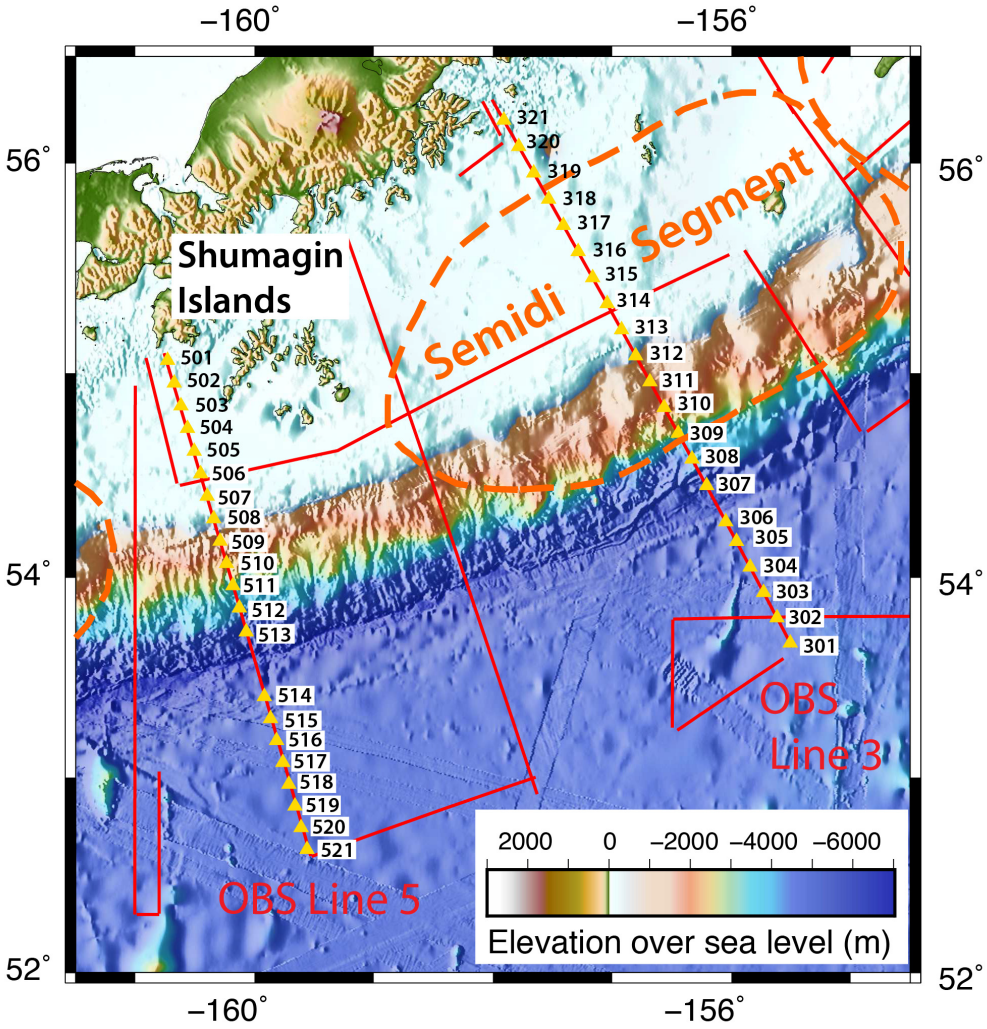

Figure C.1: OBS Line 3 and 5 in the ALEUT survey area. Yellow triangles are deployment position of each OBS instrument used in the ALEUT wide-angle refraction and reflection survey with the name of the instruments next to it. Red lines represent ALEUT MCS narrow incident refelction profiles and thick, orange dashed lines show the extent of past rupture areas constraint by aftershock distribution of great megathrust earthquakes [Sykes 1971, Estabrook et al., 1994].

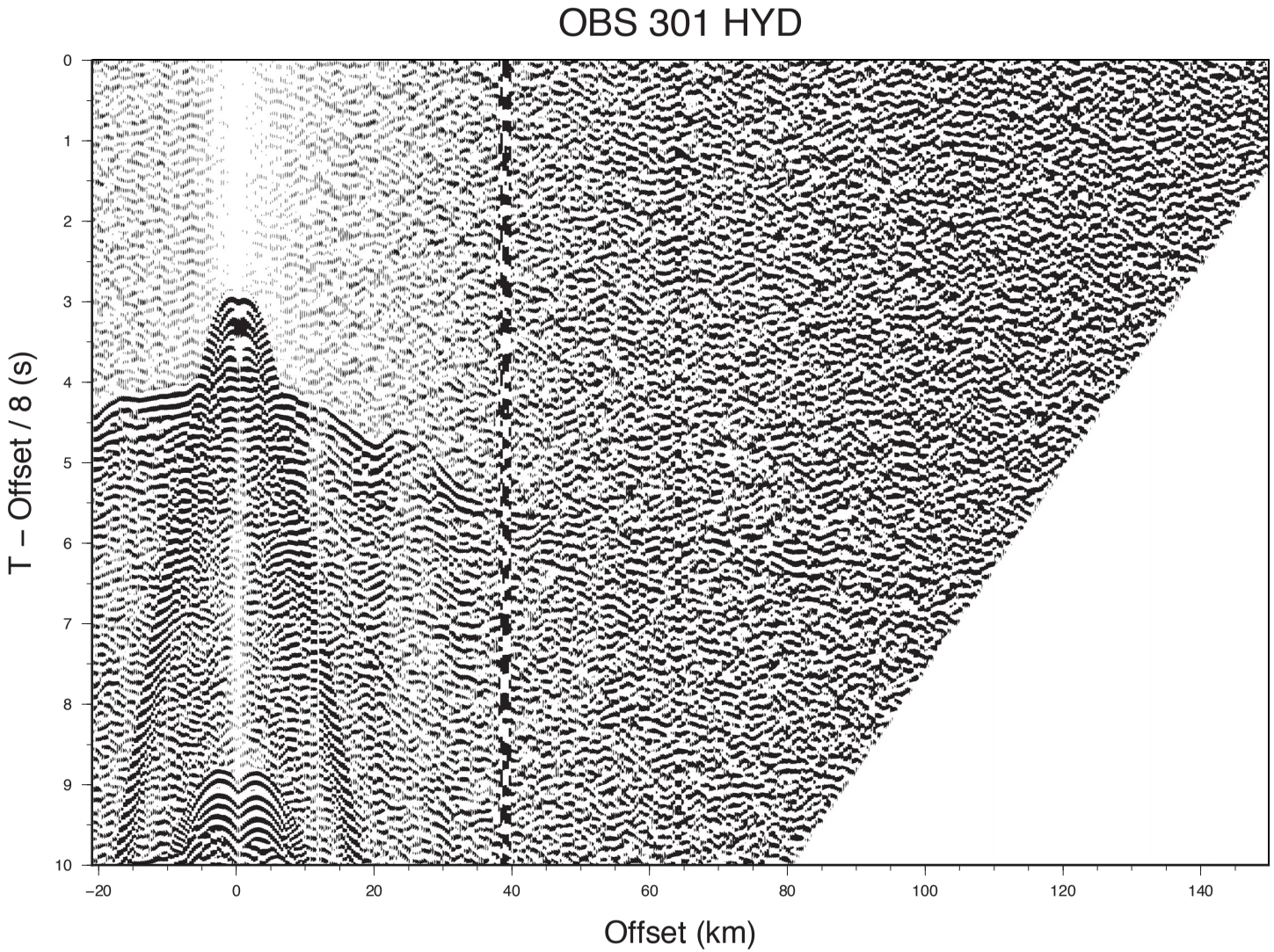

Figure C.2: Fully processed seismogram of OBS 301's hydrophon channel. Processing steps included: 1) Bandpass filtering with corner frequencies 1-3-10-18 Hz, 2) Removal of DC bias, 3) Coherent signals with a cross-dip angle of +- 35 degrees across three traces are enhanced (see chapter 2.2.3). Seismic data is diplayed in reduced travel time domain to facilitate the identification of refraction arrivals at large offsets.

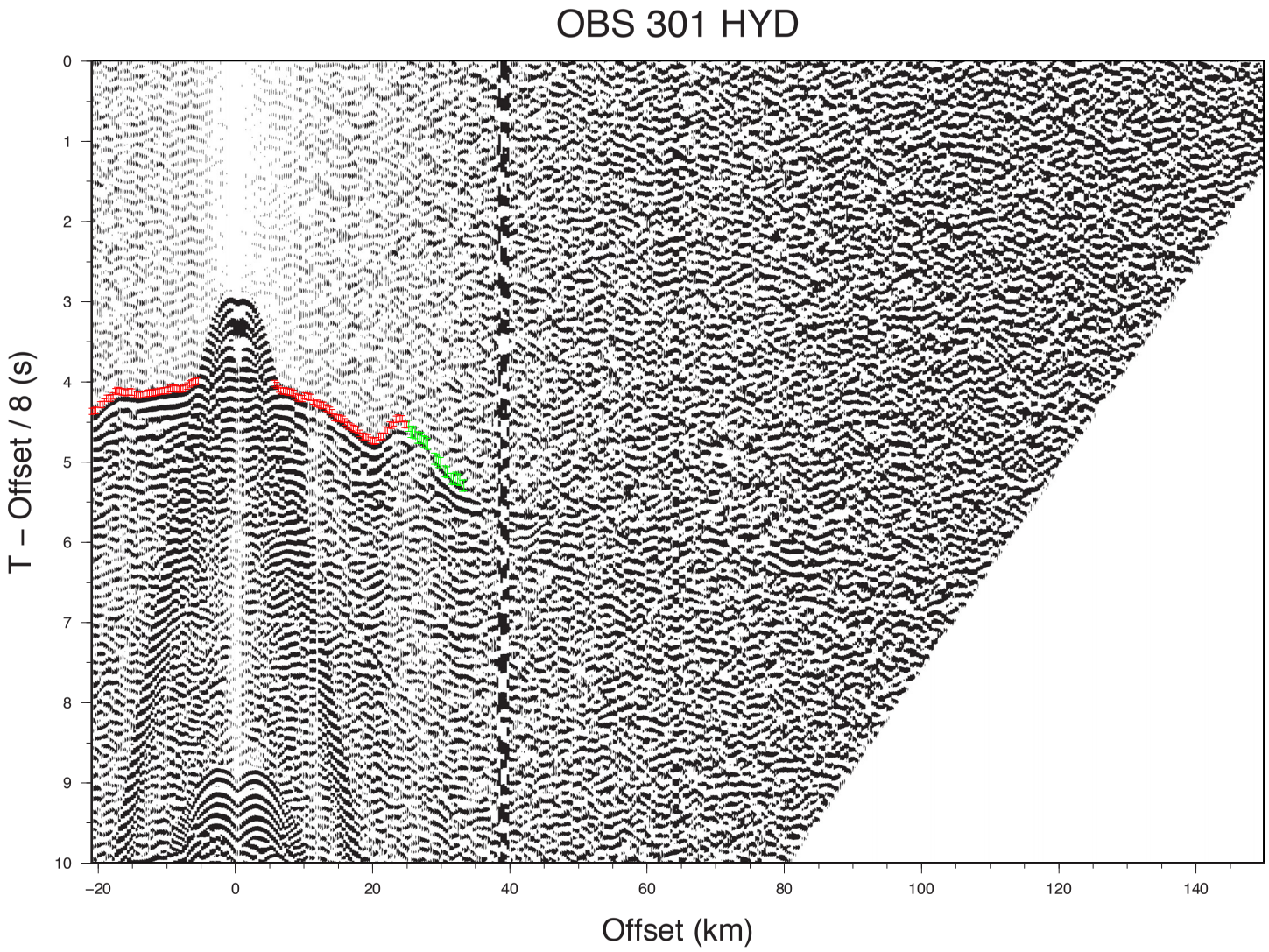

Figure C.3: OBS 301 (hydrophon channel) with first arrival times including picking uncertainties (from very clear to very unclear): 40 ms (red errorbars), 70 ms (green errorbars), 100 ms (blue errorbars), 150 ms (light blue errorbars), 200 ms (pink errorbars), 250 ms (orange errorbars).

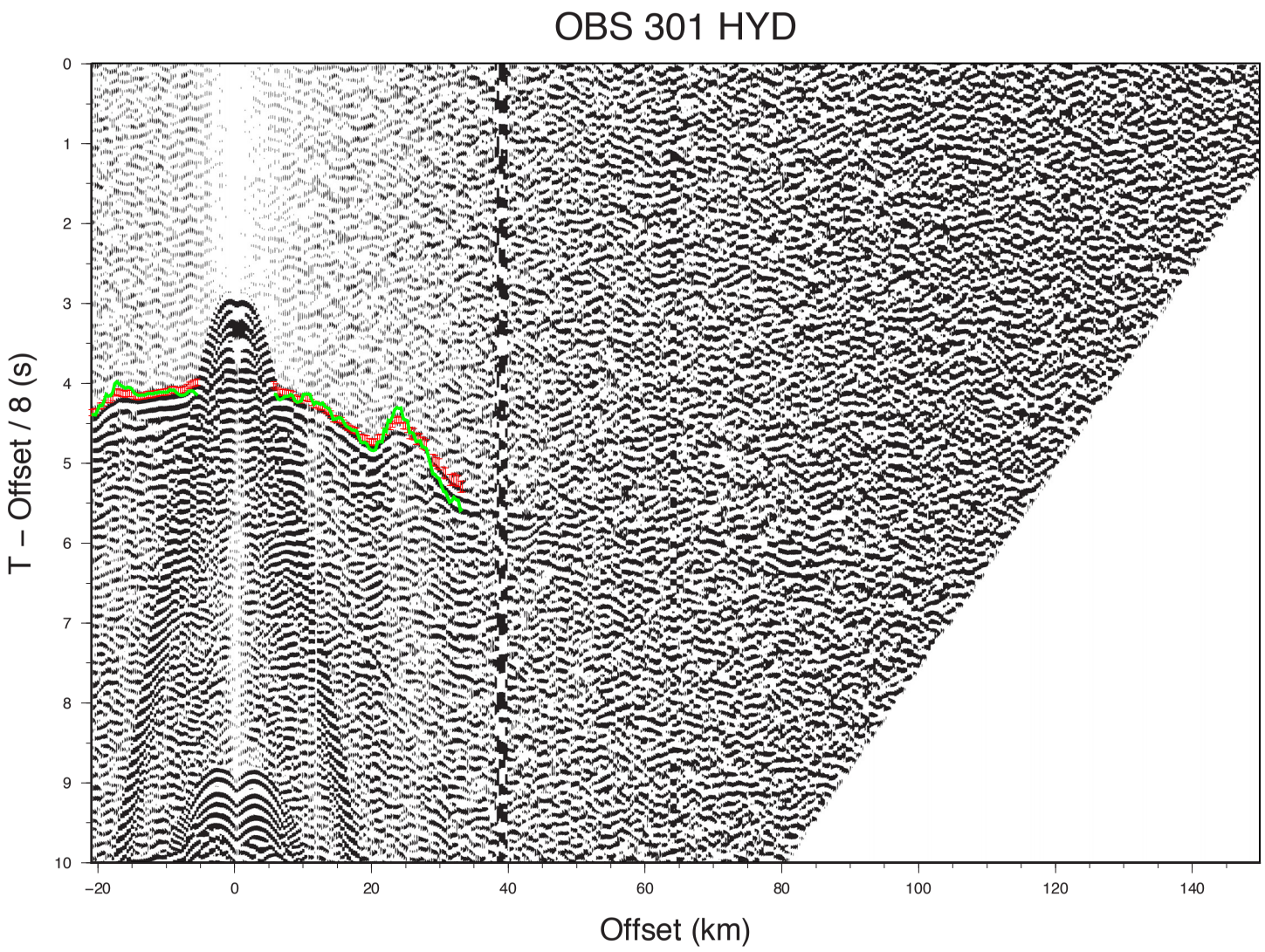

Figure C.4: OBS 301 (hydrophon channel) with observed first arrival times including picking uncertainties (red errorbars: 40 - 250 ms) and calculated (synthetic) arrival times (green line).

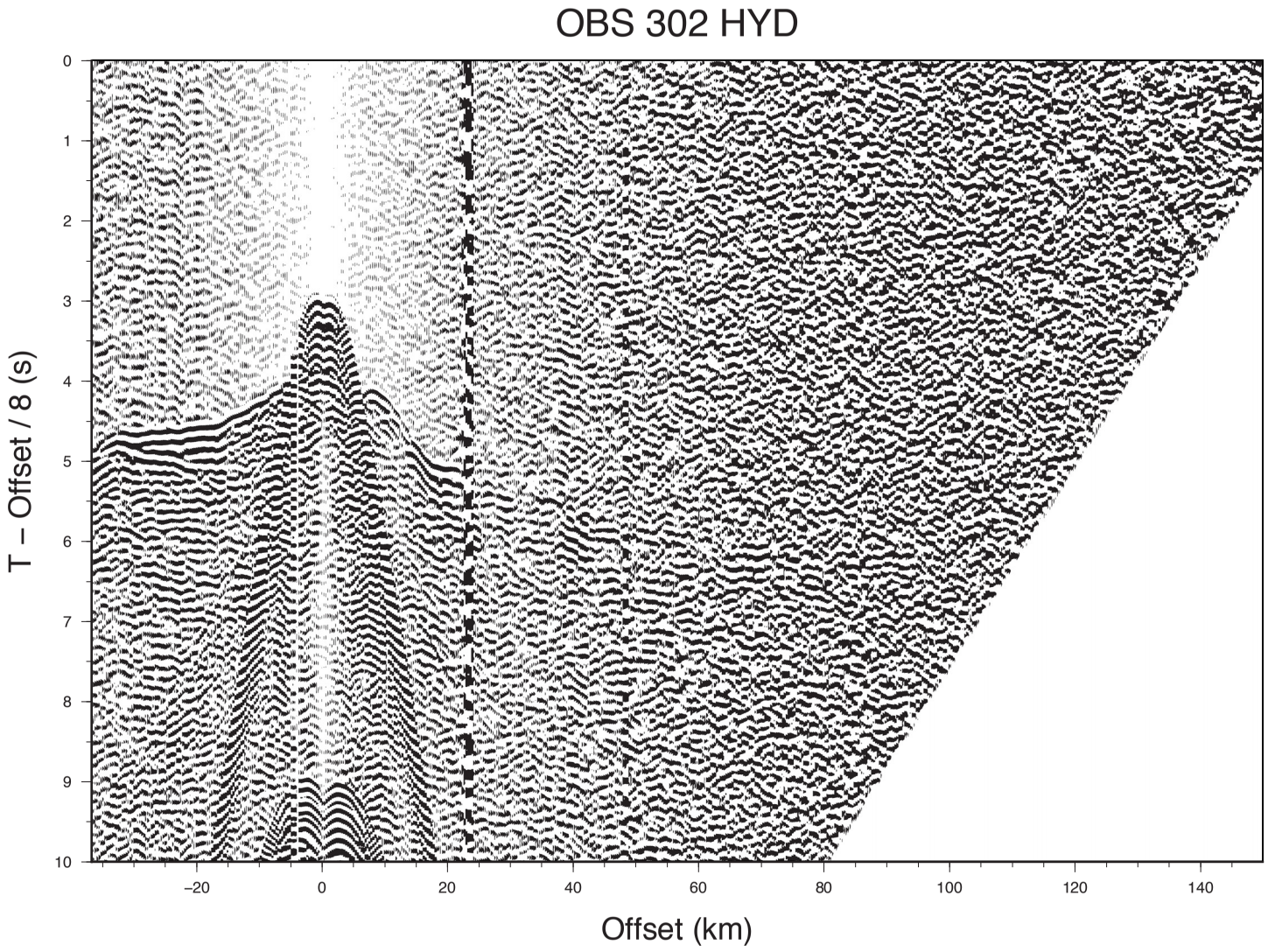

Figure C.5: OBS 302 (hydrophon channel). See Figure C.2 caption for additional description.

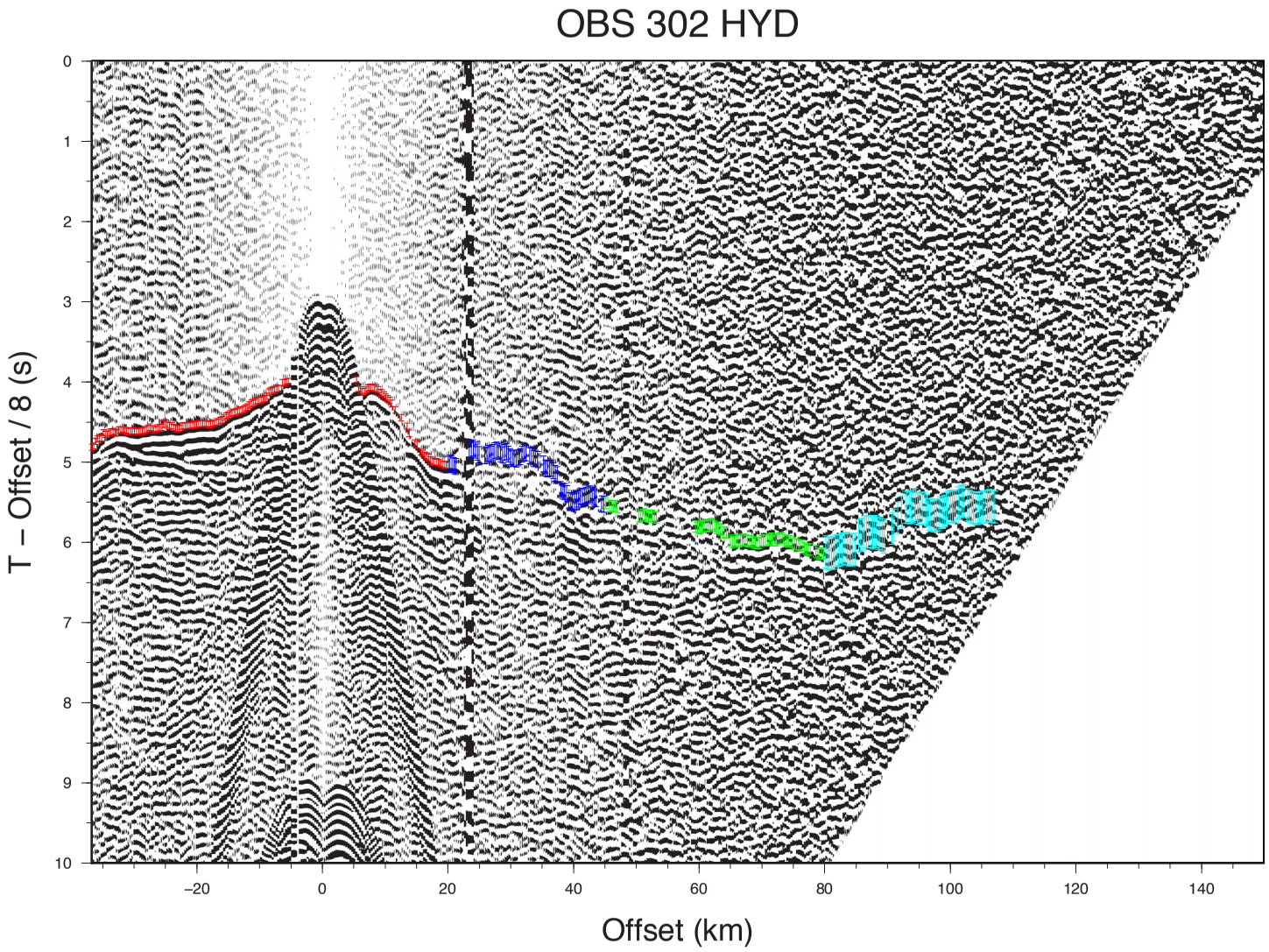

Figure C.6: OBS 302 (hydrophon channel) with first arrival times including picking uncertainties (from very clear to very unclear): 40 ms (red errorbars), 70 ms (green errorbars), 100 ms (blue errorbars), 150 ms (light blue errorbars), 200 ms (pink errorbars), 250 ms (orange errorbars).

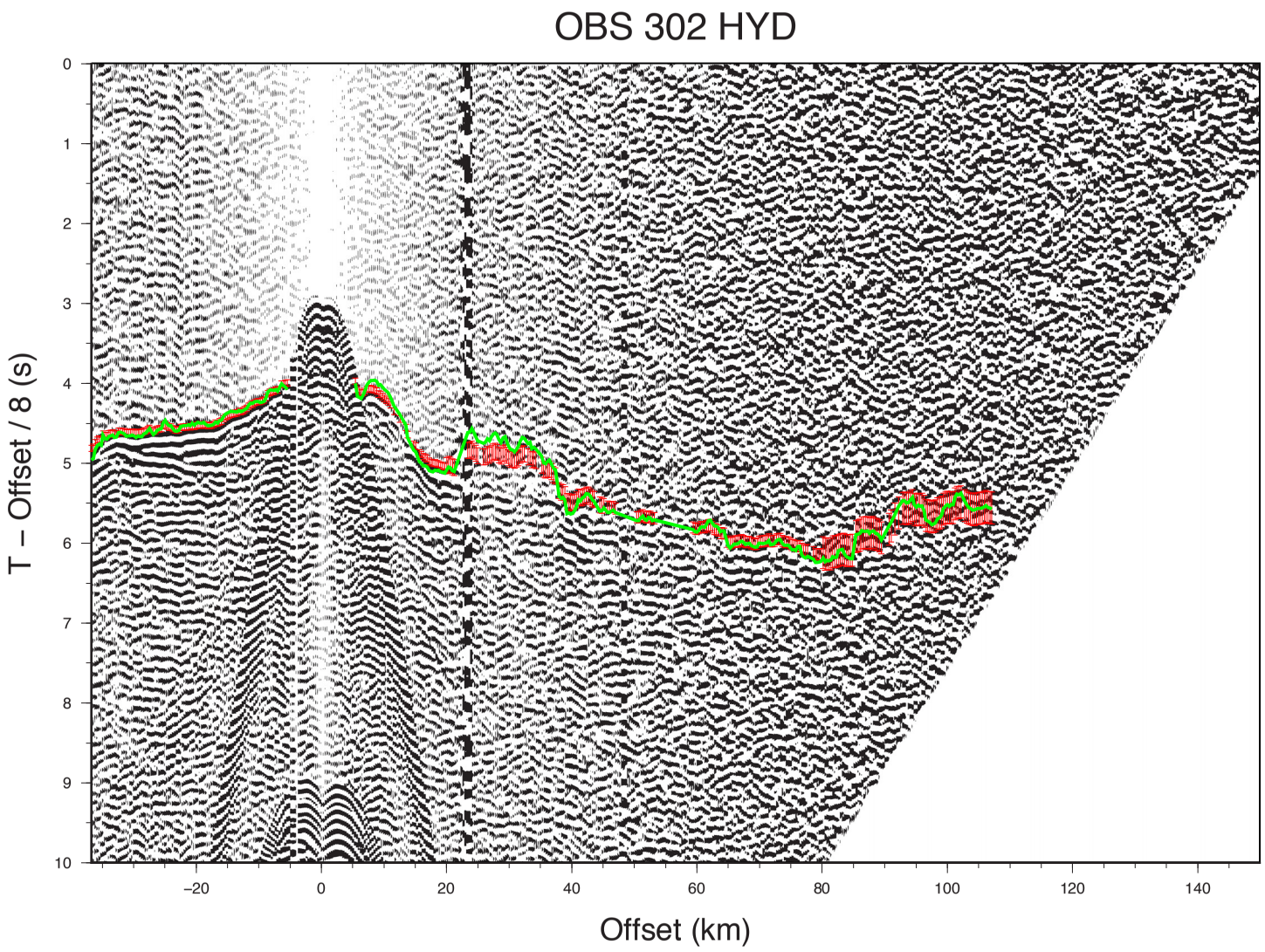

Figure C.7: OBS 302 (hydrophon channel) with observed first arrival times including picking uncertainties (red errorbars: 40 - 250 ms) and calculated (synthetic) arrival times (green line).

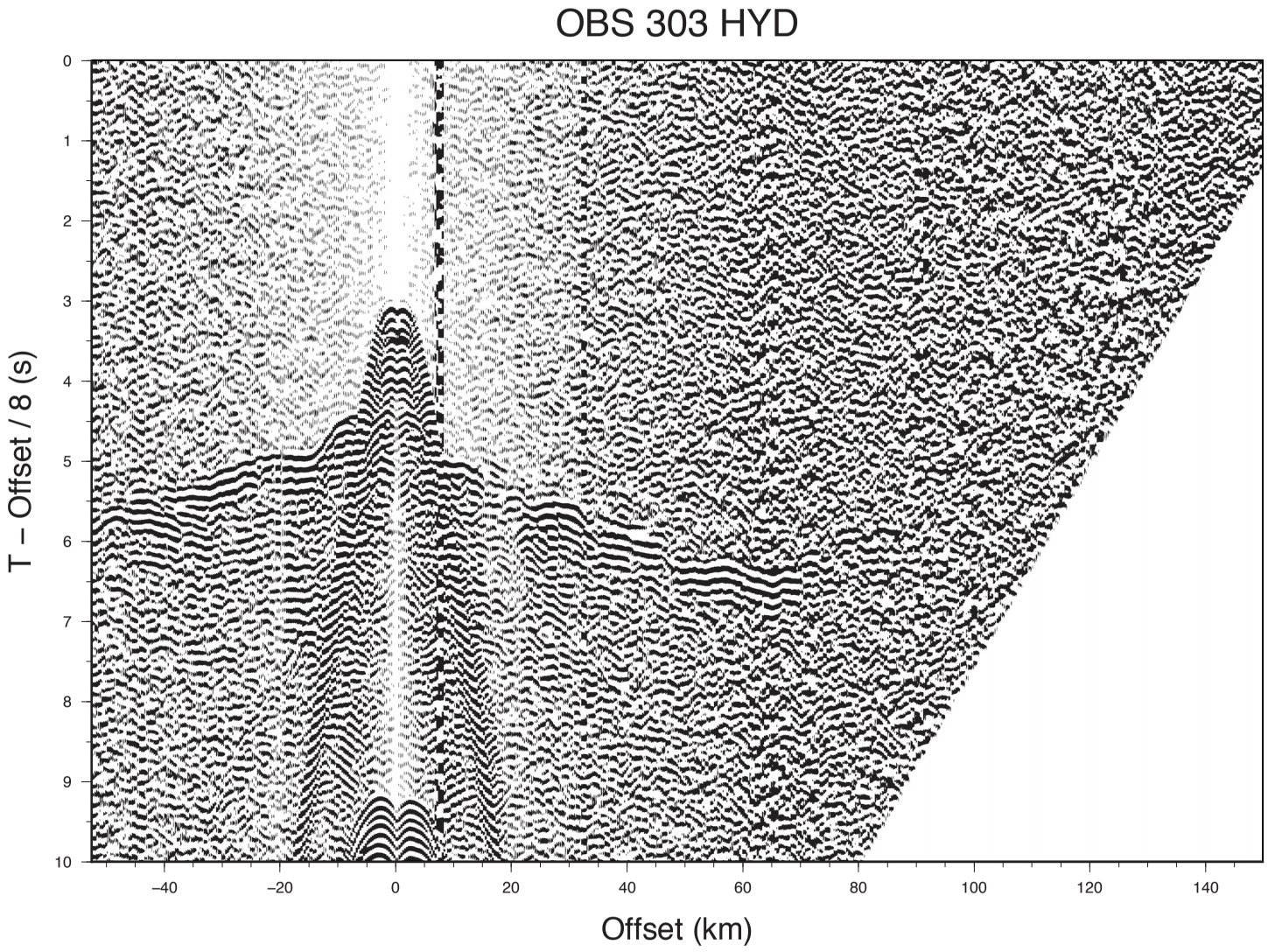

Figure C.8: OBS 303 (hydrophon channel). See Figure C.2 caption for additional description.

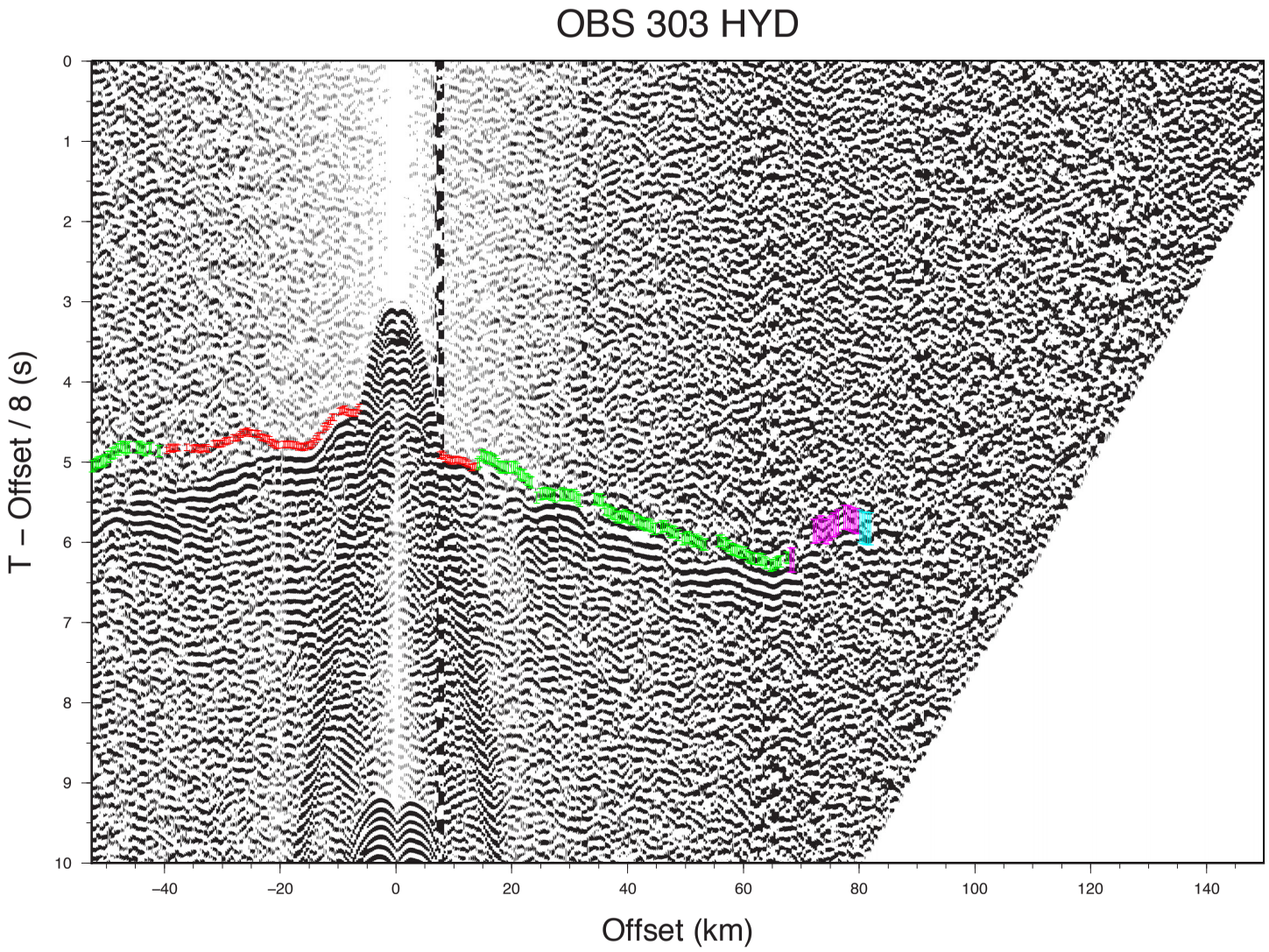

Figure C.9: OBS 303 (hydrophon channel) with first arrival times including picking uncertainties (from very clear to very unclear): 40 ms (red errorbars), 70 ms (green errorbars), 100 ms (blue errorbars), 150 ms (light blue errorbars), 200 ms (pink errorbars), 250 ms (orange errorbars).

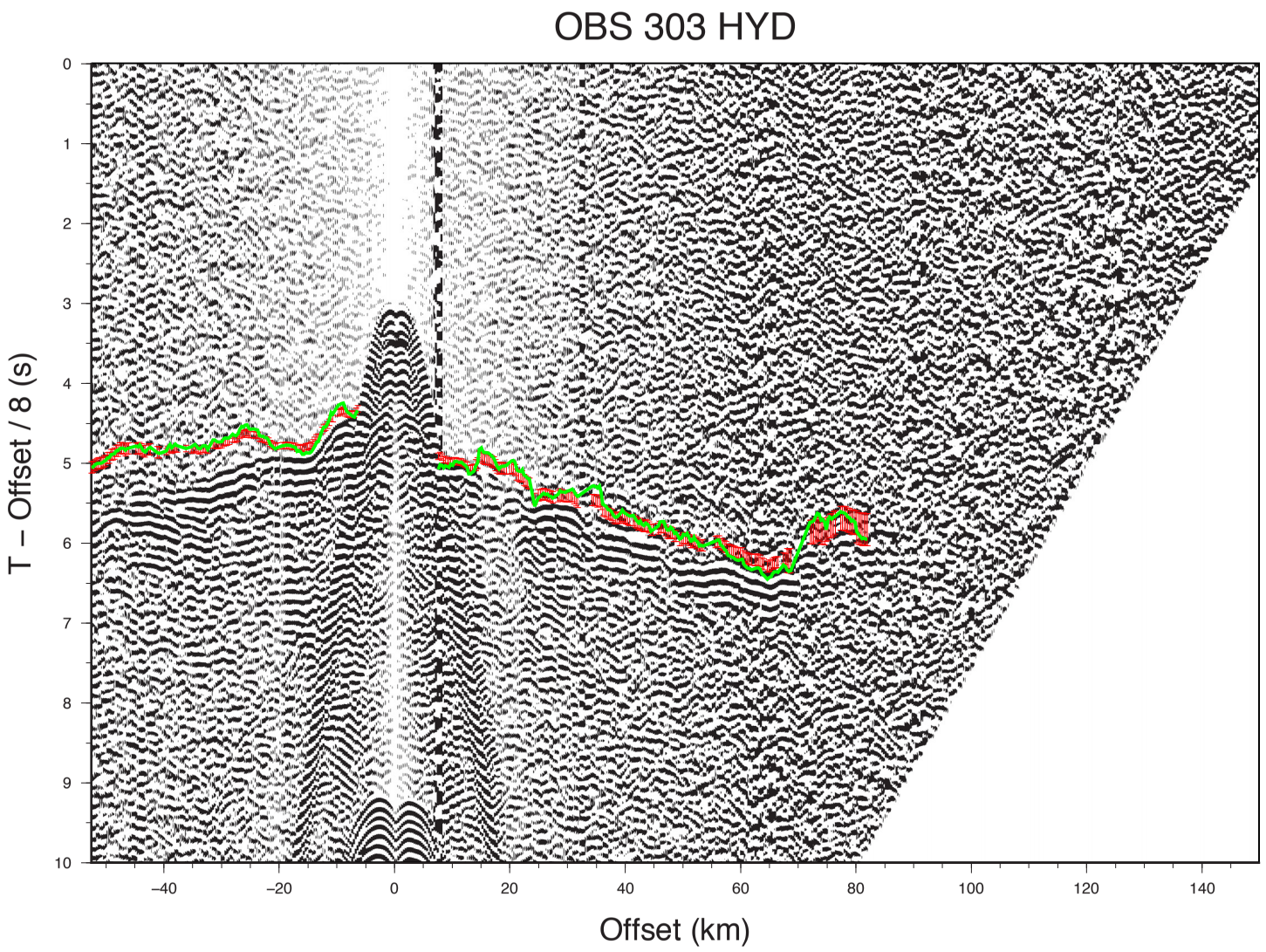

Figure C.10: OBS 303 (hydrophon channel) with observed first arrival times including picking uncertainties (red errorbars: 40 - 250 ms) and calculated (synthetic) arrival times (green line).

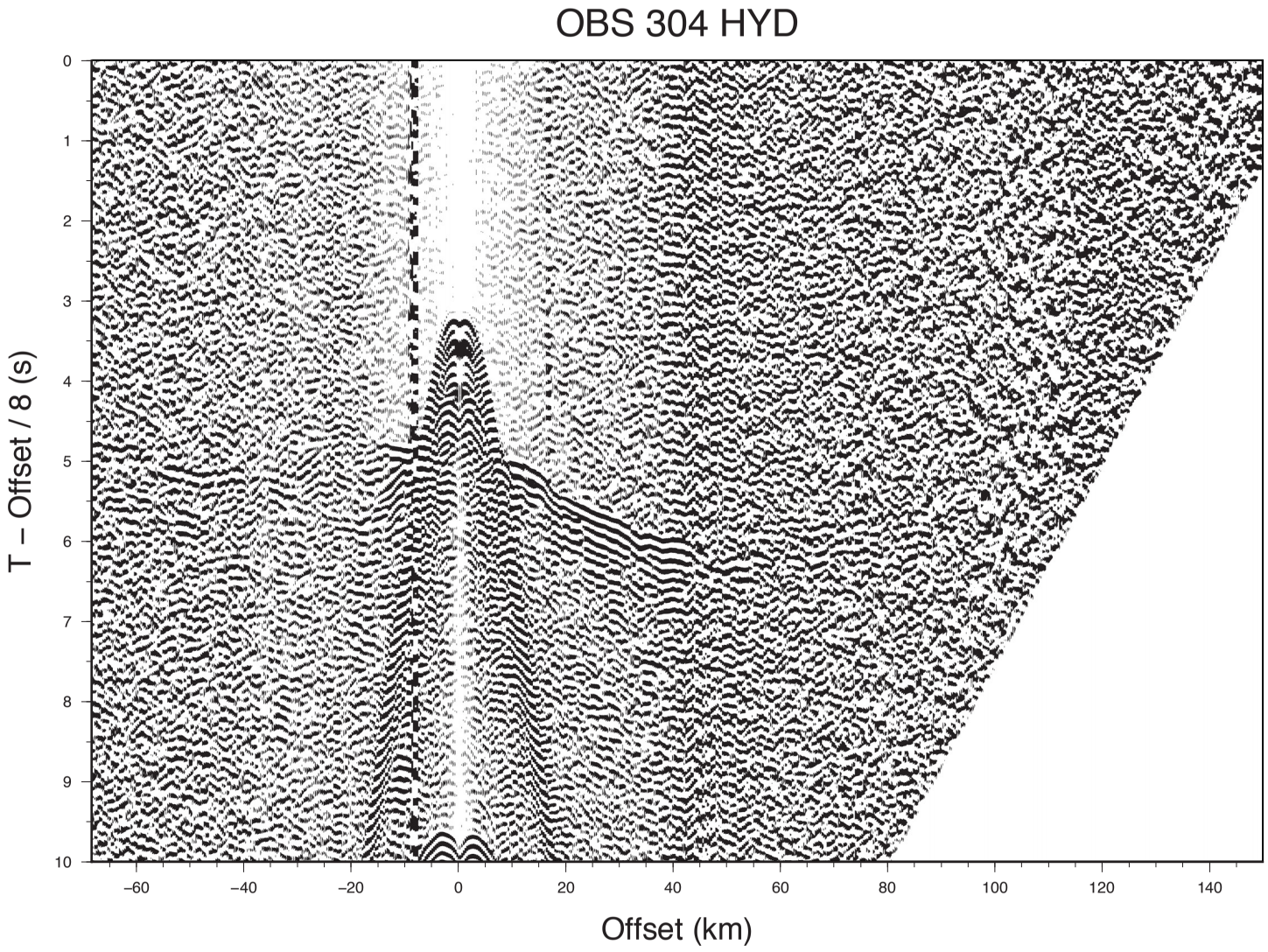

Figure C.11: OBS 304 (hydrophon channel). See Figure C.2 caption for additional description.

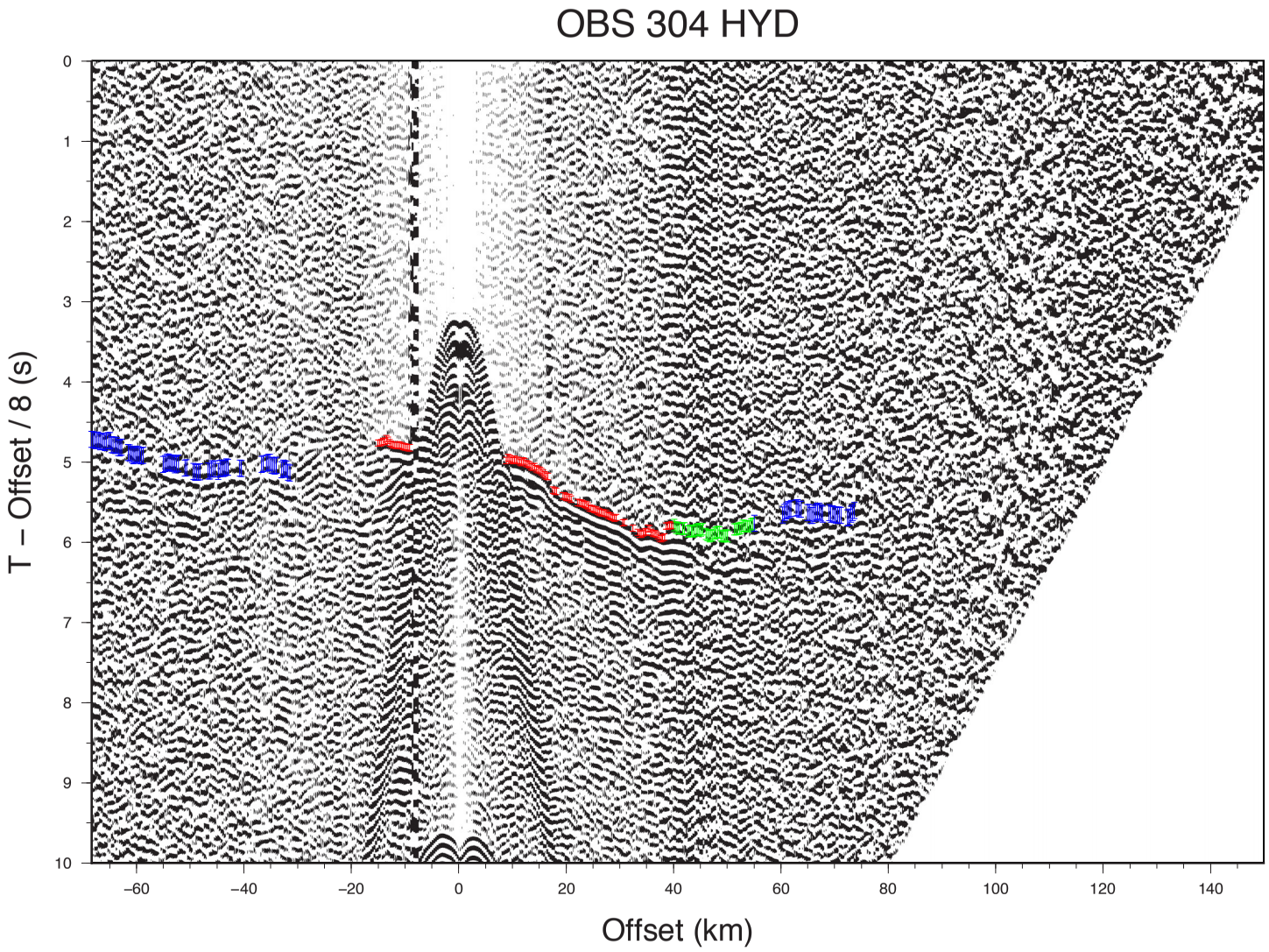

Figure C.12: OBS 304 (hydrophon channel) with first arrival times including picking uncertainties (from very clear to very unclear): 40 ms (red errorbars), 70 ms (green errorbars), 100 ms (blue errorbars), 150 ms (light blue errorbars), 200 ms (pink errorbars), 250 ms (orange errorbars).

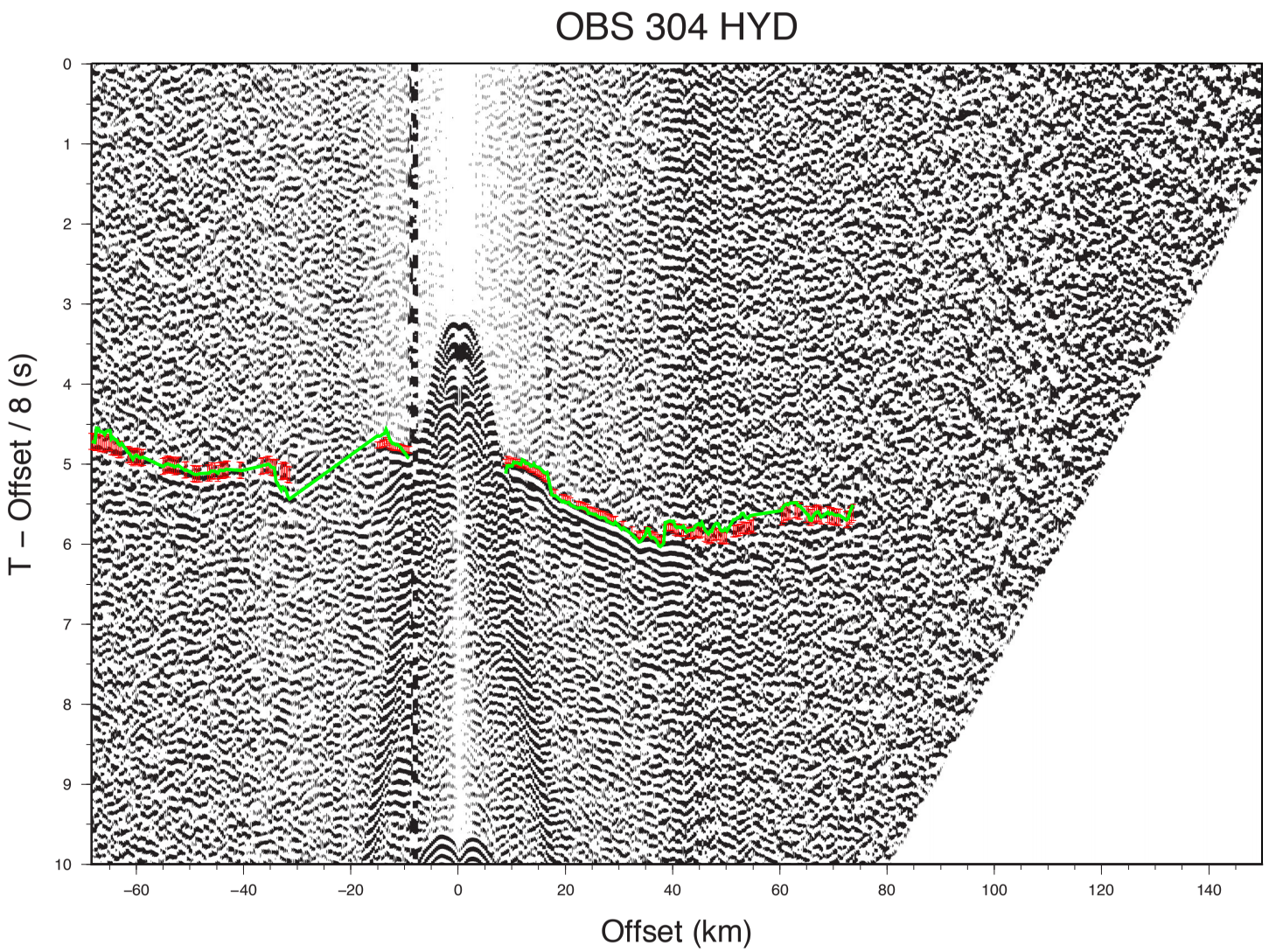

Figure C.13: OBS 304 (hydrophon channel) with observed first arrival times including picking uncertainties (red errorbars: 40 - 250 ms) and calculated (synthetic) arrival times (green line).

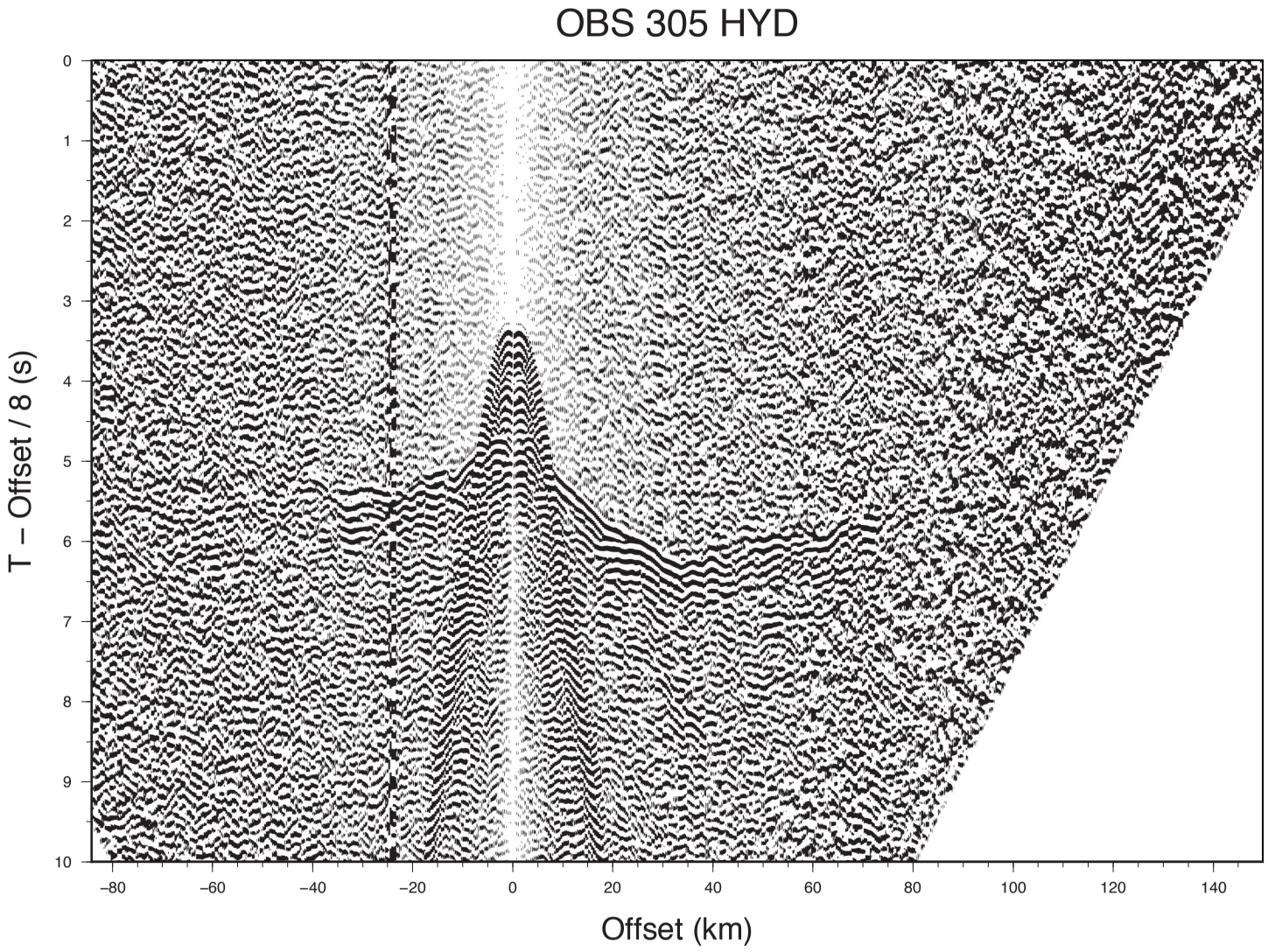

Figure C.14: OBS 305 (hydrophon channel). See Figure C.2 caption for additional description.

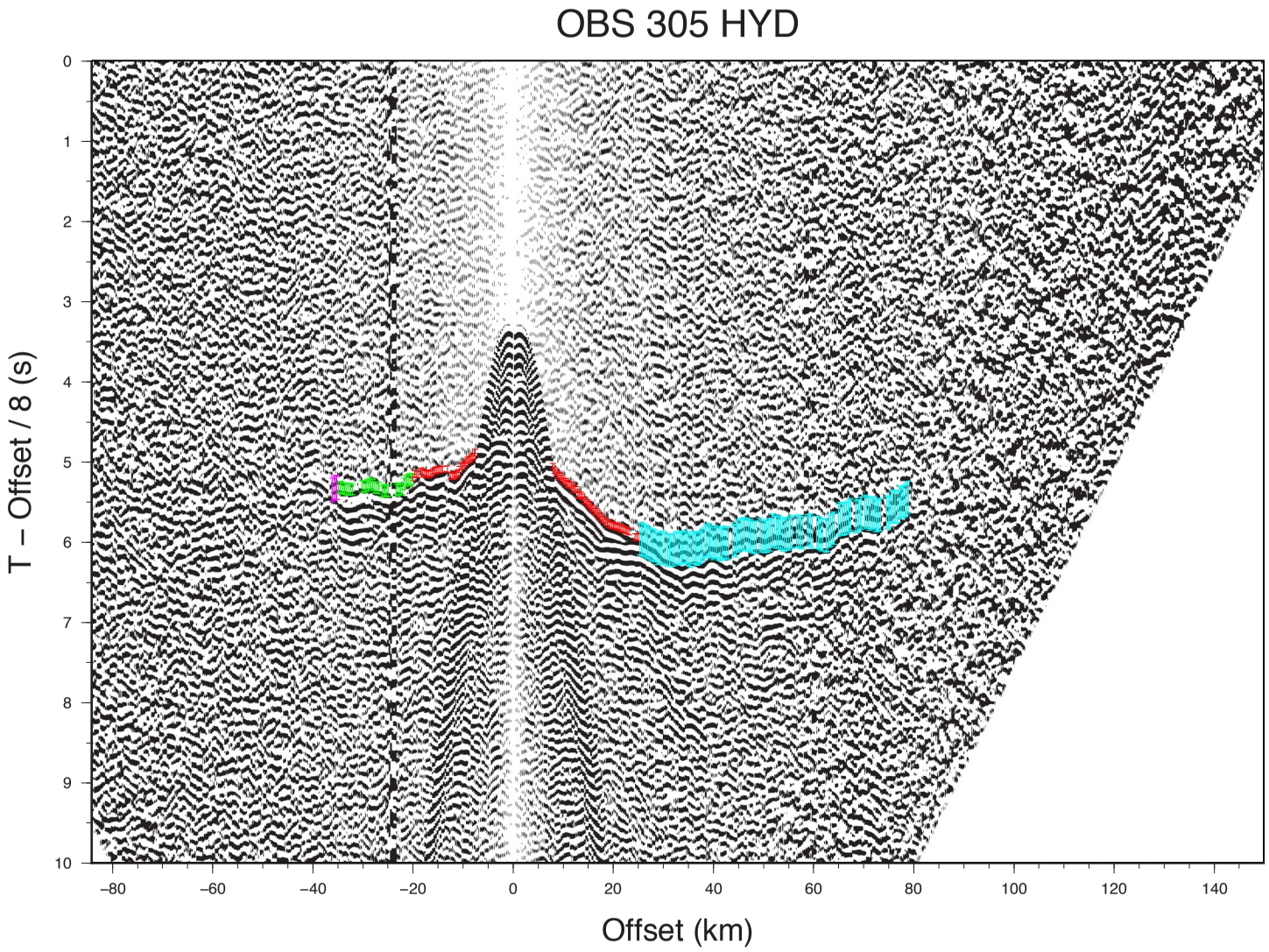

Figure C.15: OBS 305 (hydrophon channel) with first arrival times including picking uncertainties (from very clear to very unclear): 40 ms (red errorbars), 70 ms (green errorbars), 100 ms (blue errorbars), 150 ms (light blue errorbars), 200 ms (pink errorbars), 250 ms (orange errorbars).

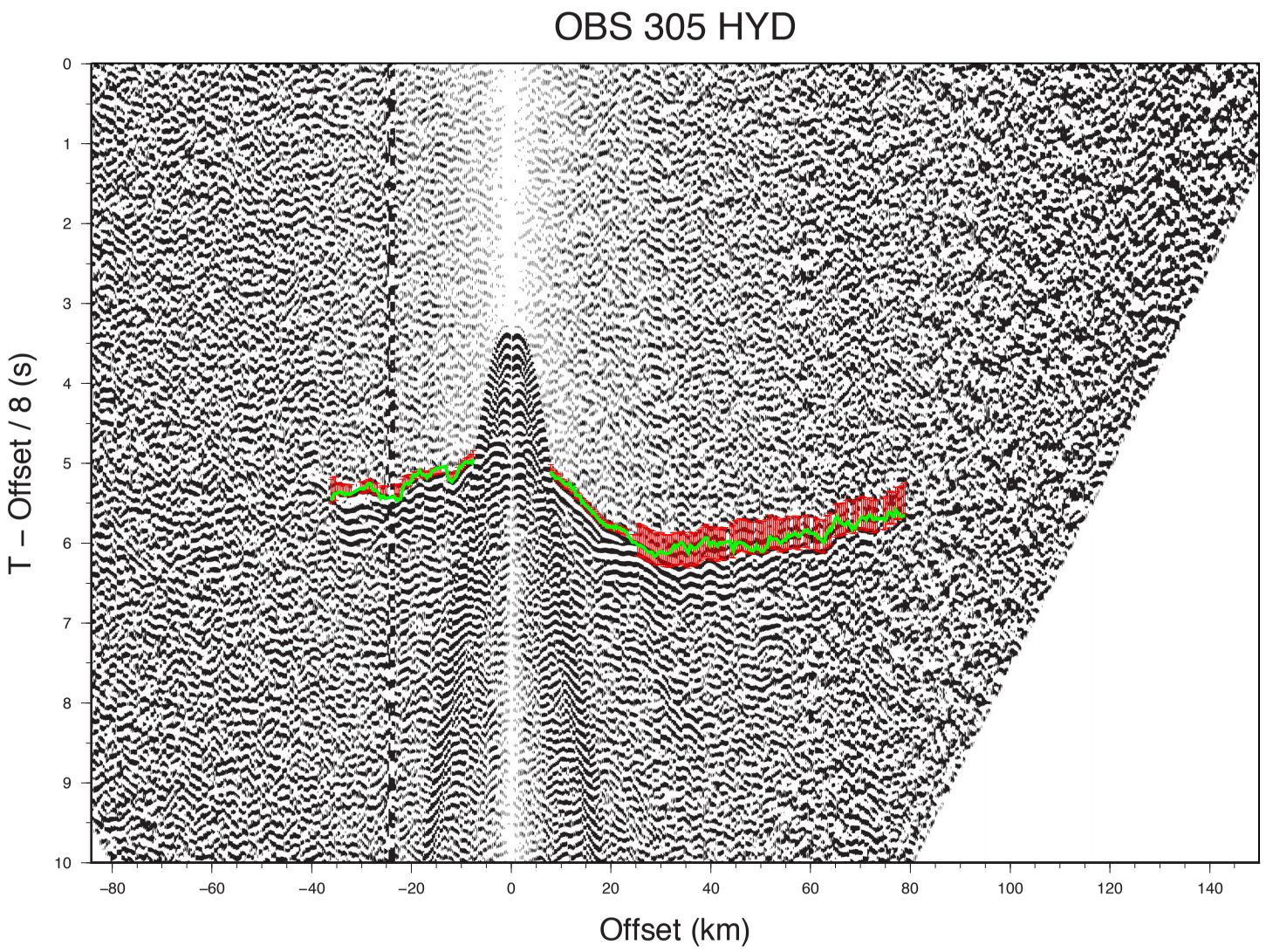

Figure C.16: OBS 305 (hydrophon channel) with observed first arrival times including picking uncertainties (red errorbars: 40 - 250 ms) and calculated (synthetic) arrival times (green line).

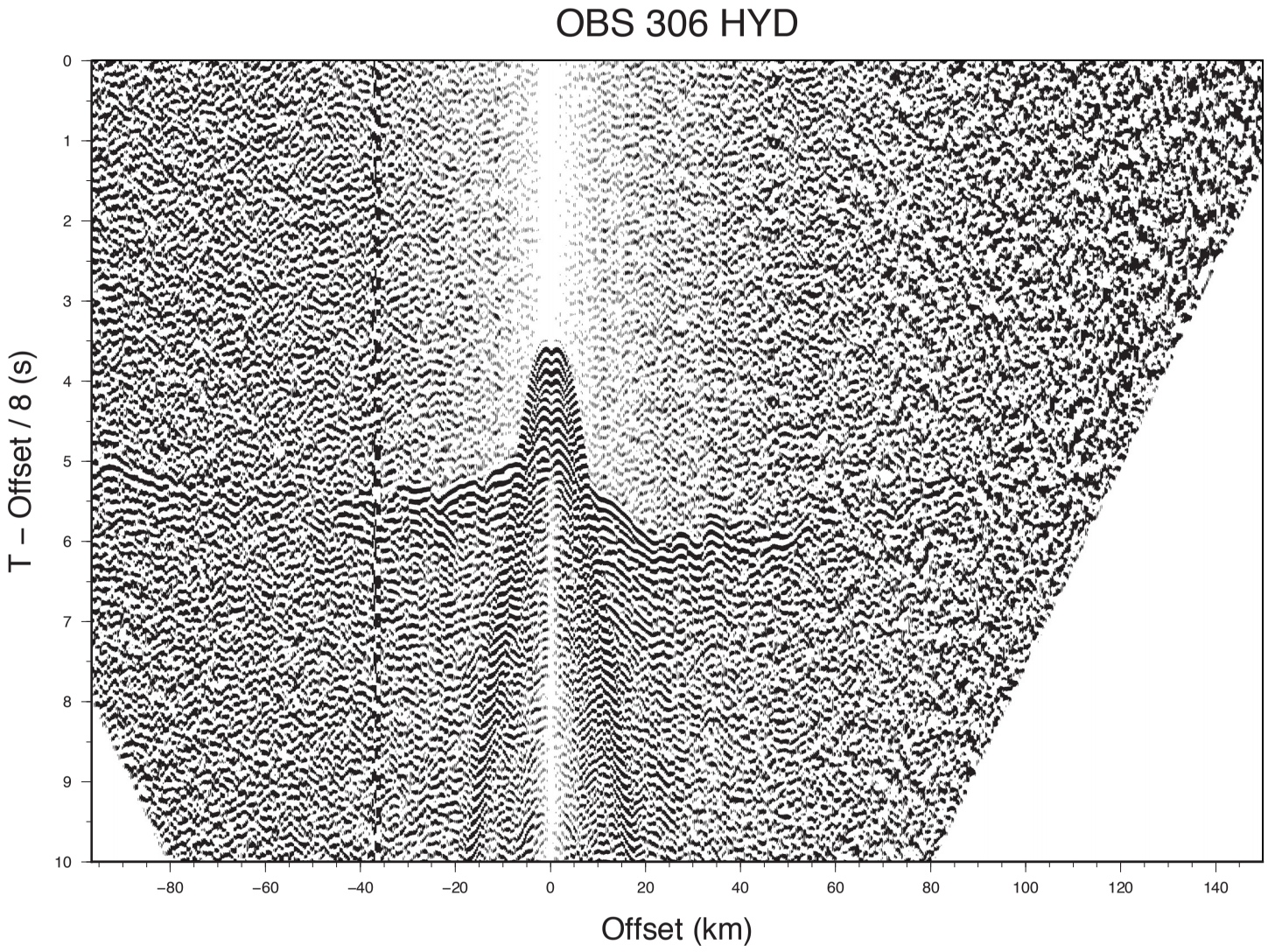

Figure C.17: OBS 306 (hydrophon channel). See Figure C.2 caption for additional description.

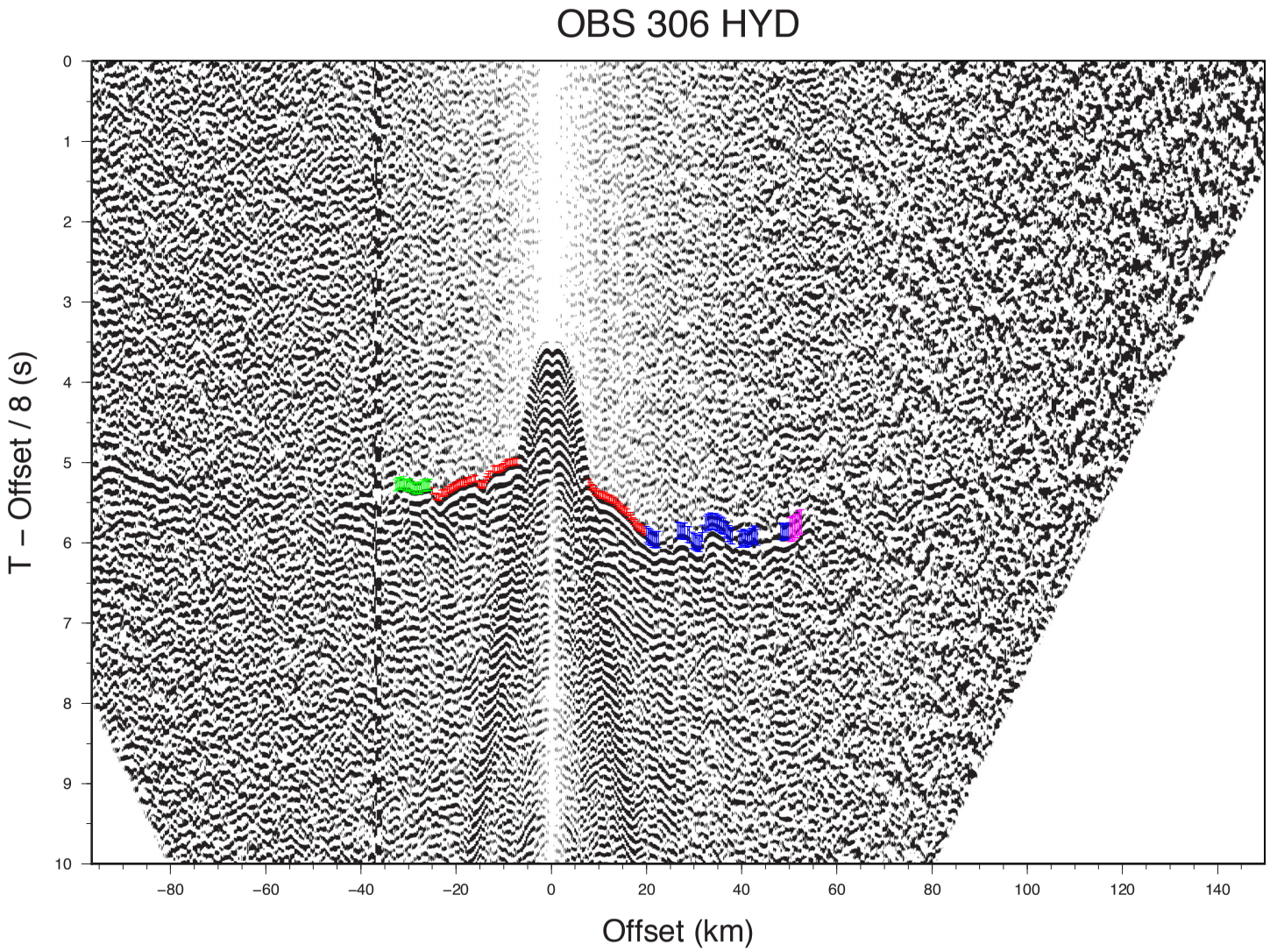

Figure C.18: OBS 306 (hydrophon channel) with first arrival times including picking uncertainties (from very clear to very unclear): 40 ms (red errorbars), 70 ms (green errorbars), 100 ms (blue errorbars), 150 ms (light blue errorbars), 200 ms (pink errorbars), 250 ms (orange errorbars).

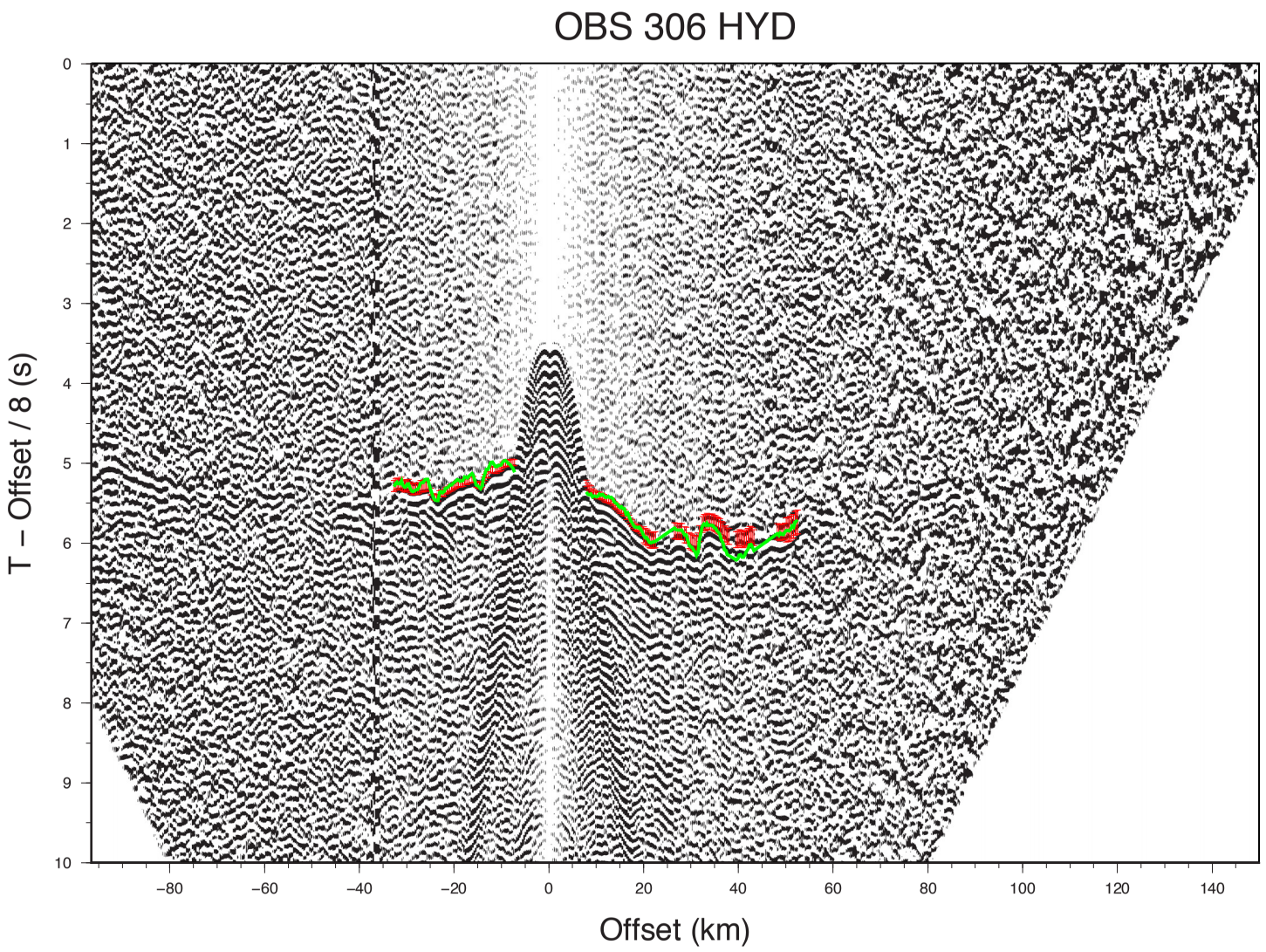

Figure C.19: OBS 306 (hydrophon channel) with observed first arrival times including picking uncertainties (red errorbars: 40 - 250 ms) and calculated (synthetic) arrival times (green line).

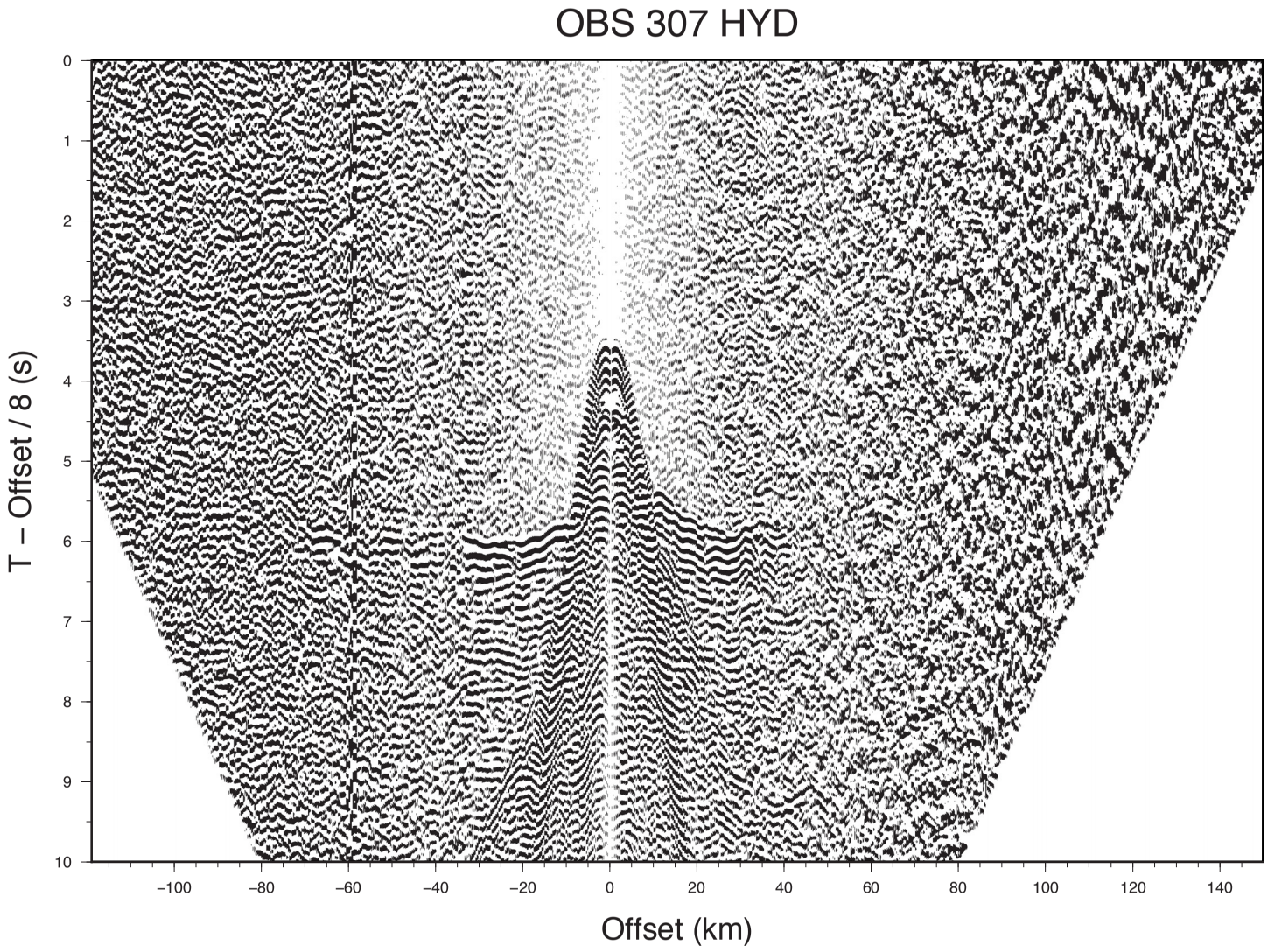

Figure C.20: OBS 307 (hydrophon channel). See Figure C.2 caption for additional description.

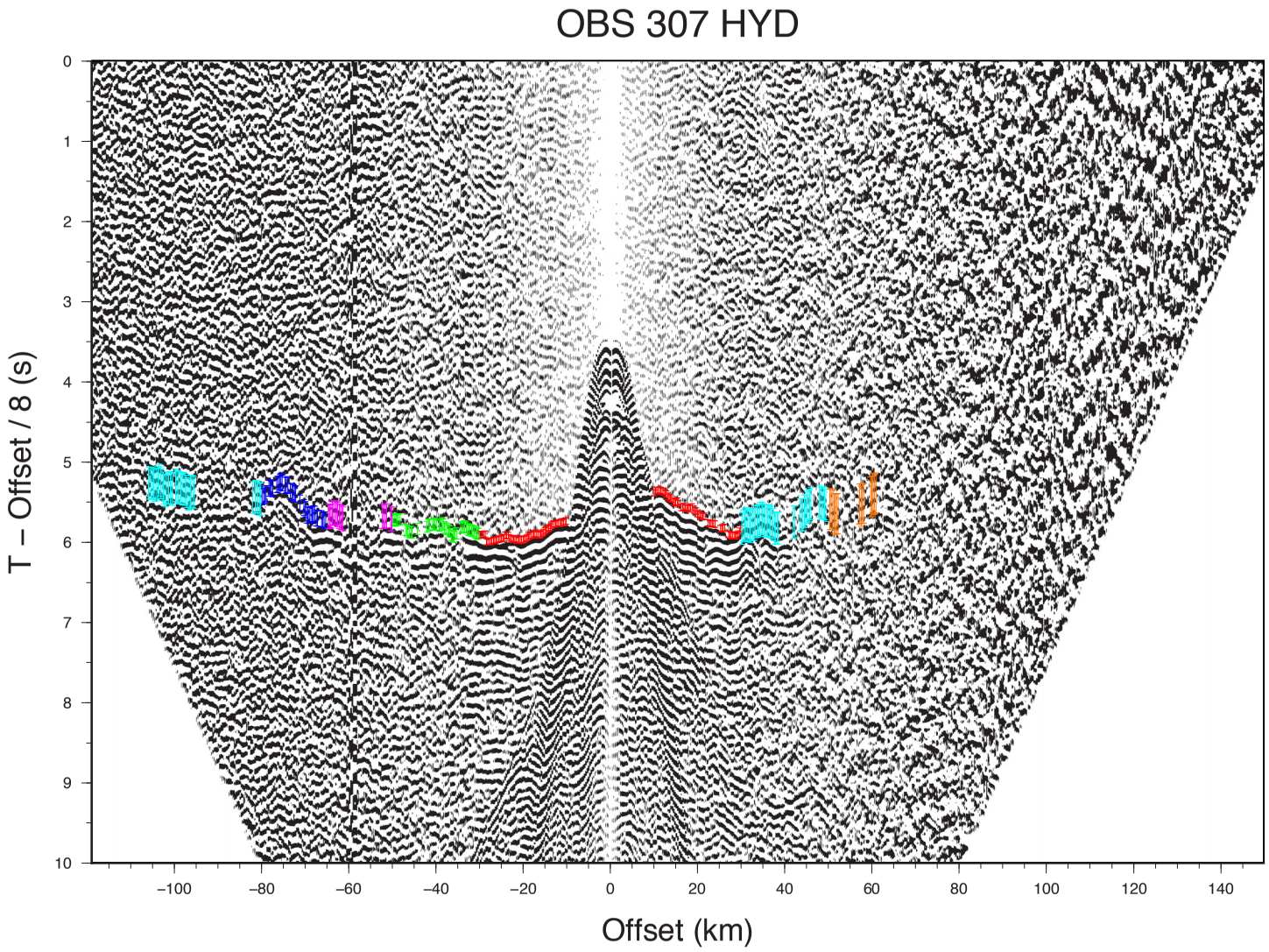

Figure C.21: OBS 307 (hydrophon channel) with first arrival times including picking uncertainties (from very clear to very unclear): 40 ms (red errorbars), 70 ms (green errorbars), 100 ms (blue errorbars), 150 ms (light blue errorbars), 200 ms (pink errorbars), 250 ms (orange errorbars).

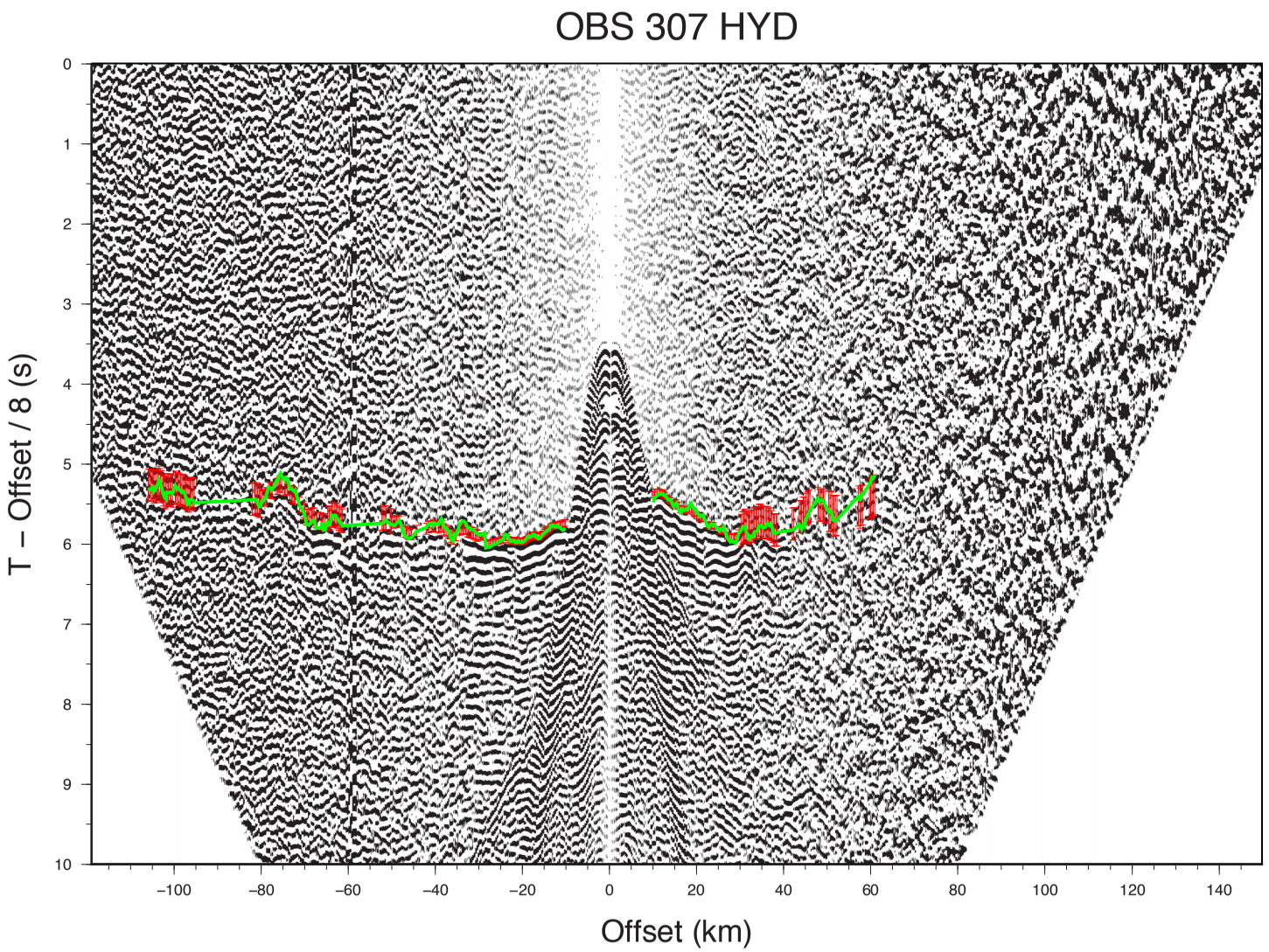

Figure C.22: OBS 307 (hydrophon channel) with observed first arrival times including picking uncertainties (red errorbars: 40 - 250 ms) and calculated (synthetic) arrival times (green line).

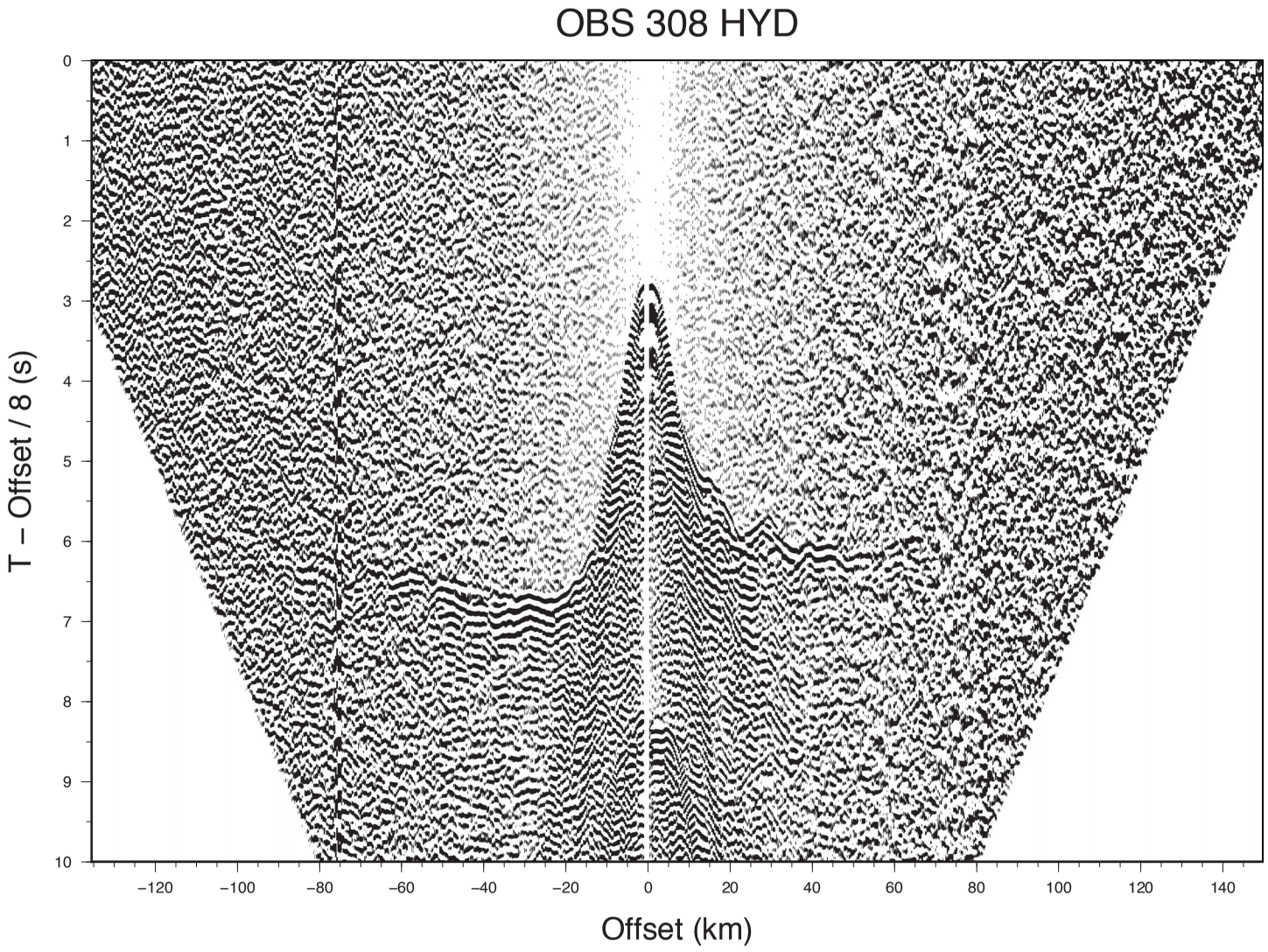

Figure C.23: OBS 308 (hydrophon channel). See Figure C.2 caption for additional description.

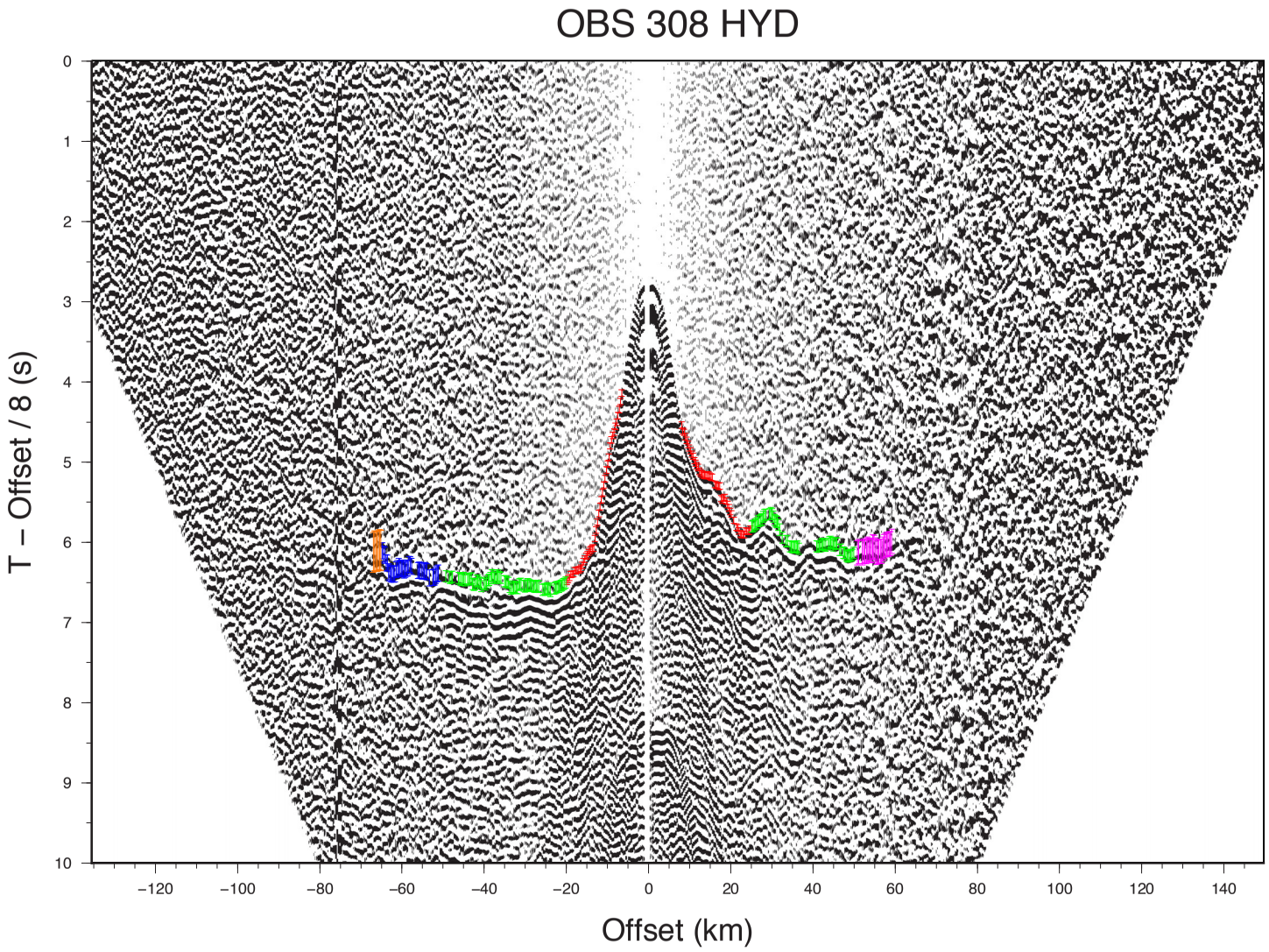

Figure C.24: OBS 308 (hydrophon channel) with first arrival times including picking uncertainties (from very clear to very unclear): 40 ms (red errorbars), 70 ms (green errorbars), 100 ms (blue errorbars), 150 ms (light blue errorbars), 200 ms (pink errorbars), 250 ms (orange errorbars).

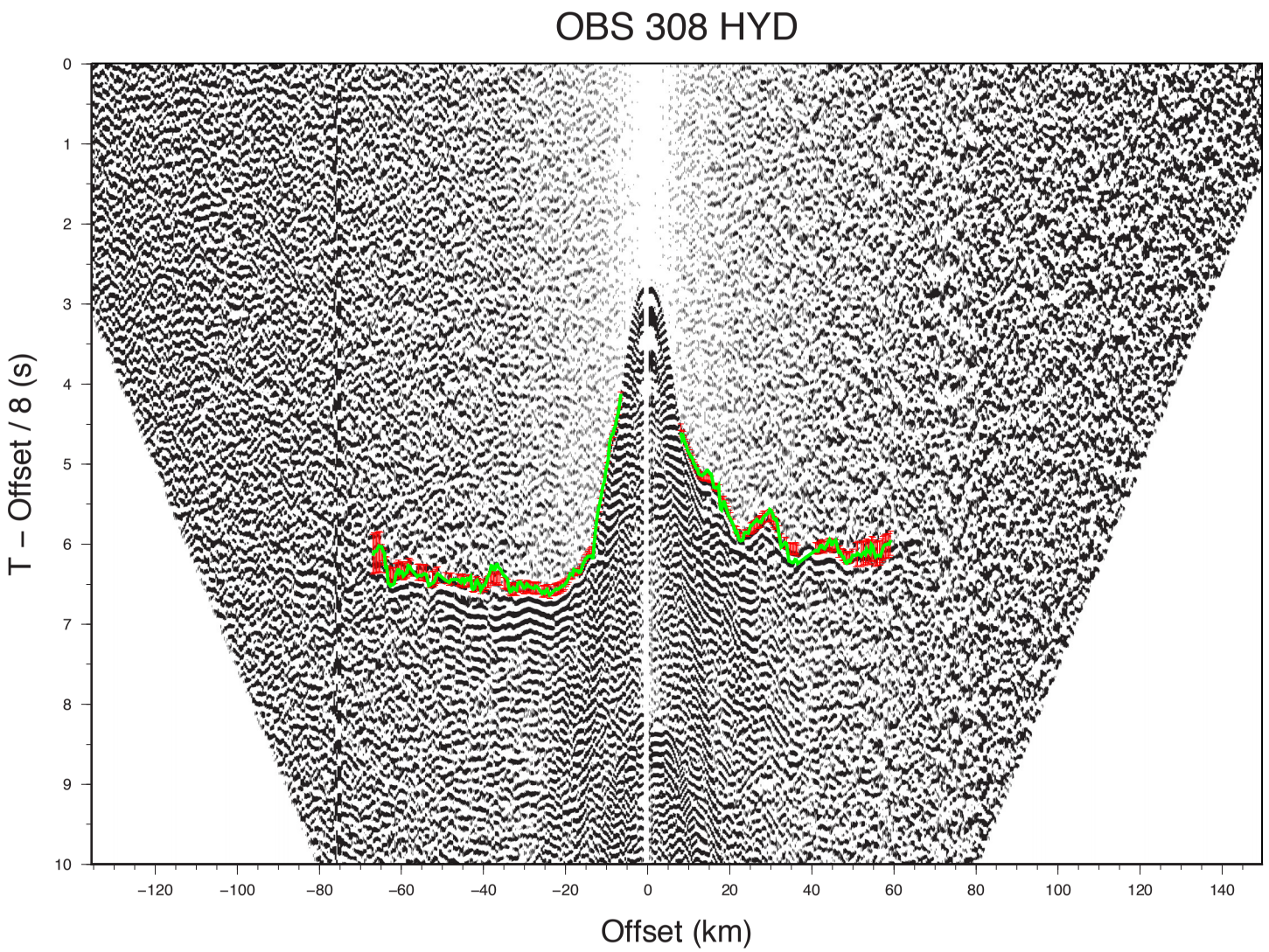

Figure C.25: OBS 308 (hydrophon channel) with observed first arrival times including picking uncertainties (red errorbars: 40 - 250 ms) and calculated (synthetic) arrival times (green line).

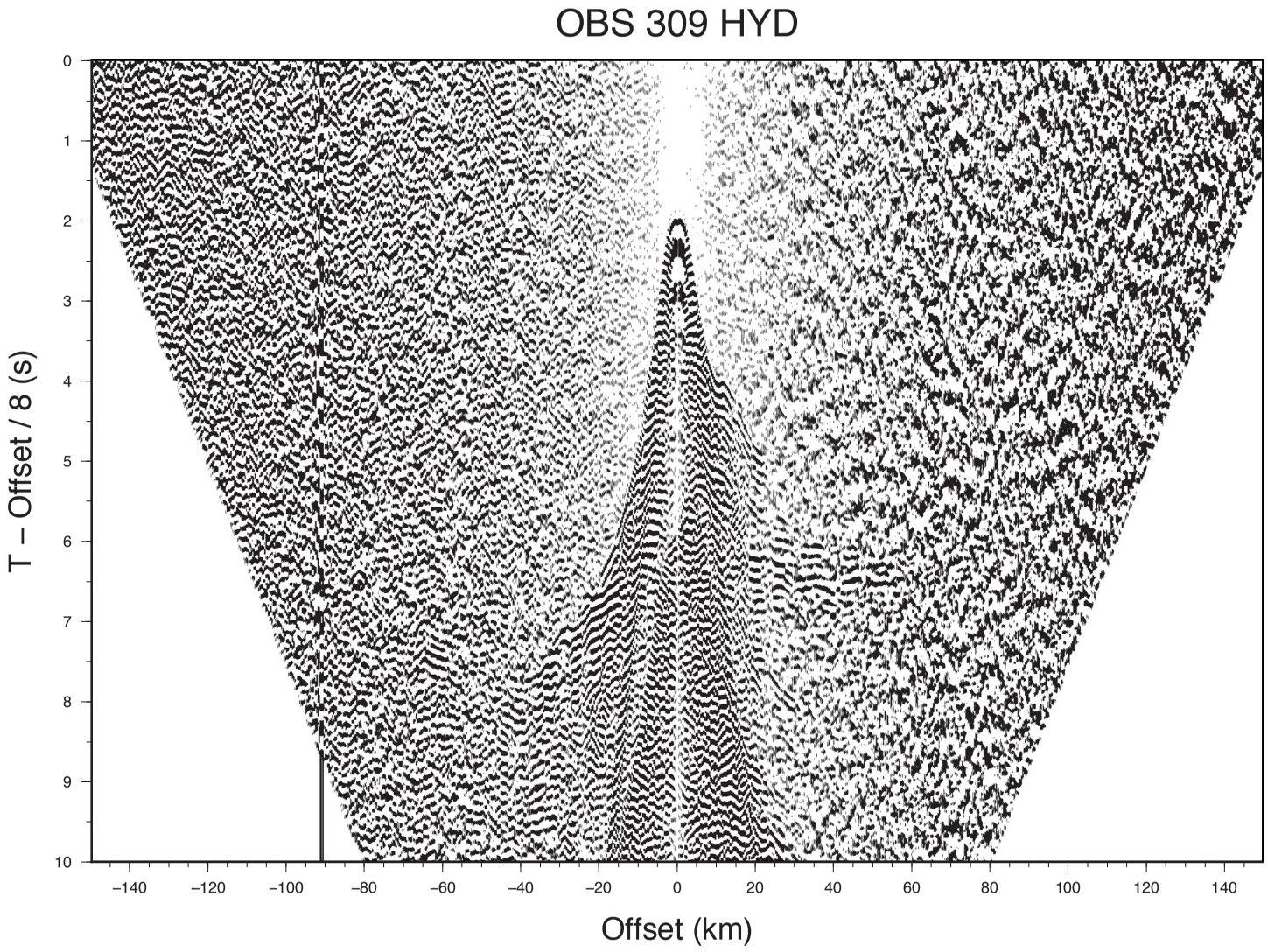

Figure C.26: OBS 309 (hydrophon channel). See Figure C.2 caption for additional description.

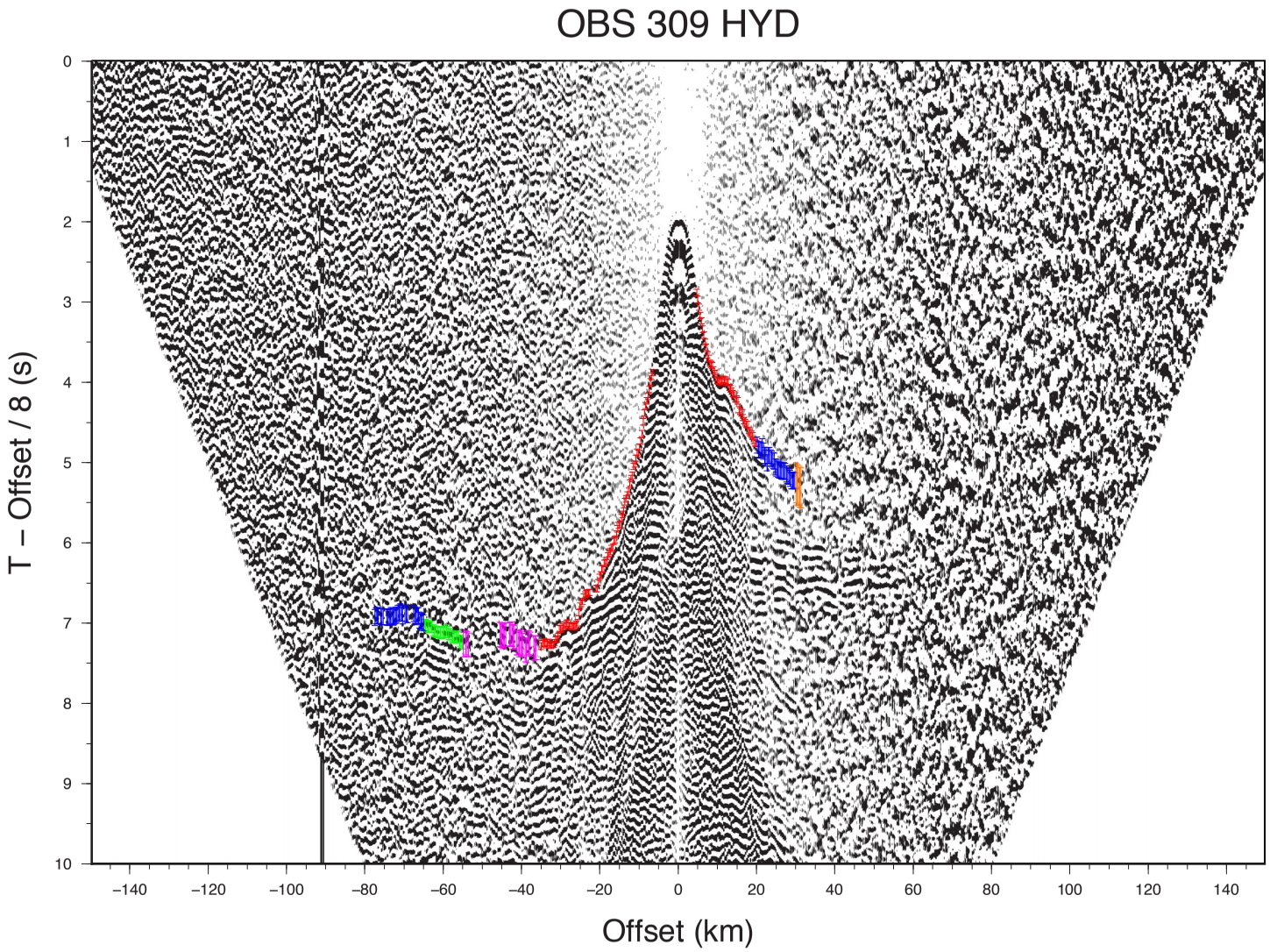

Figure C.27: OBS 309 (hydrophon channel) with first arrival times including picking uncertainties (from very clear to very unclear): 40 ms (red errorbars), 70 ms (green errorbars), 100 ms (blue errorbars), 150 ms (light blue errorbars), 200 ms (pink errorbars), 250 ms (orange errorbars).

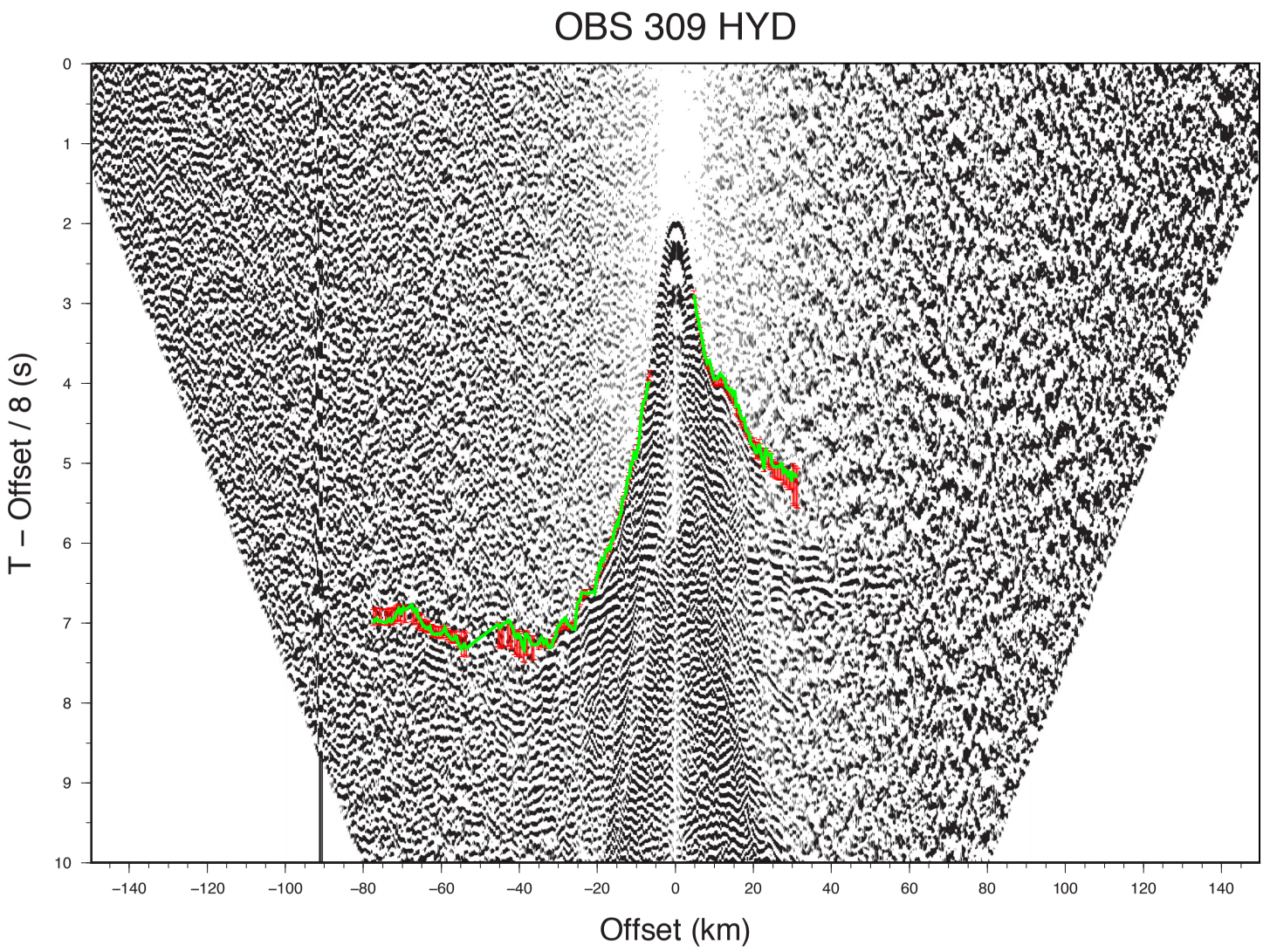

Figure C.28: OBS 309 (hydrophon channel) with observed first arrival times including picking uncertainties (red errorbars: 40 - 250 ms) and calculated (synthetic) arrival times (green line).

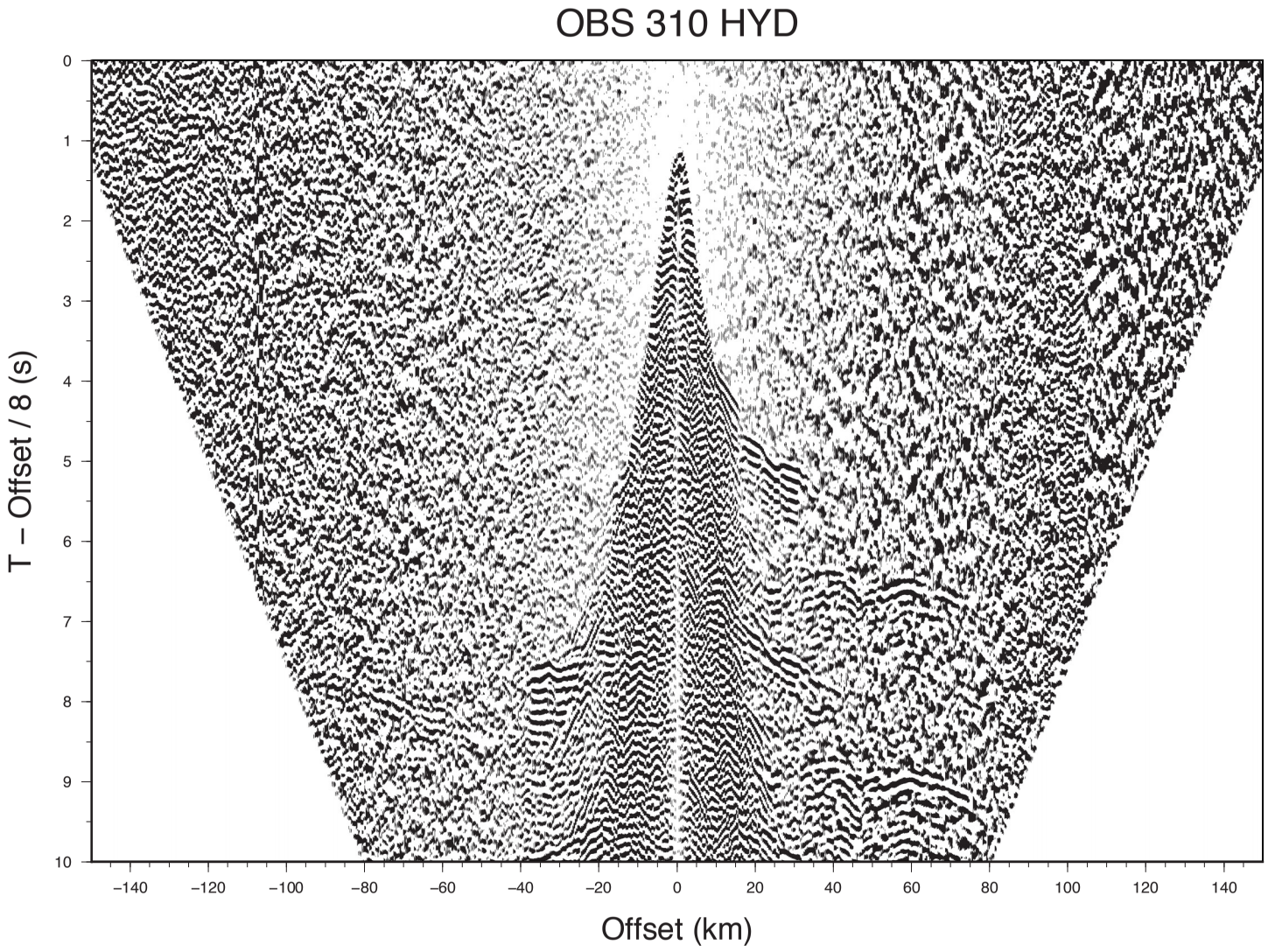

Figure C.29: OBS 310 (hydrophon channel). See Figure C.2 caption for additional description.

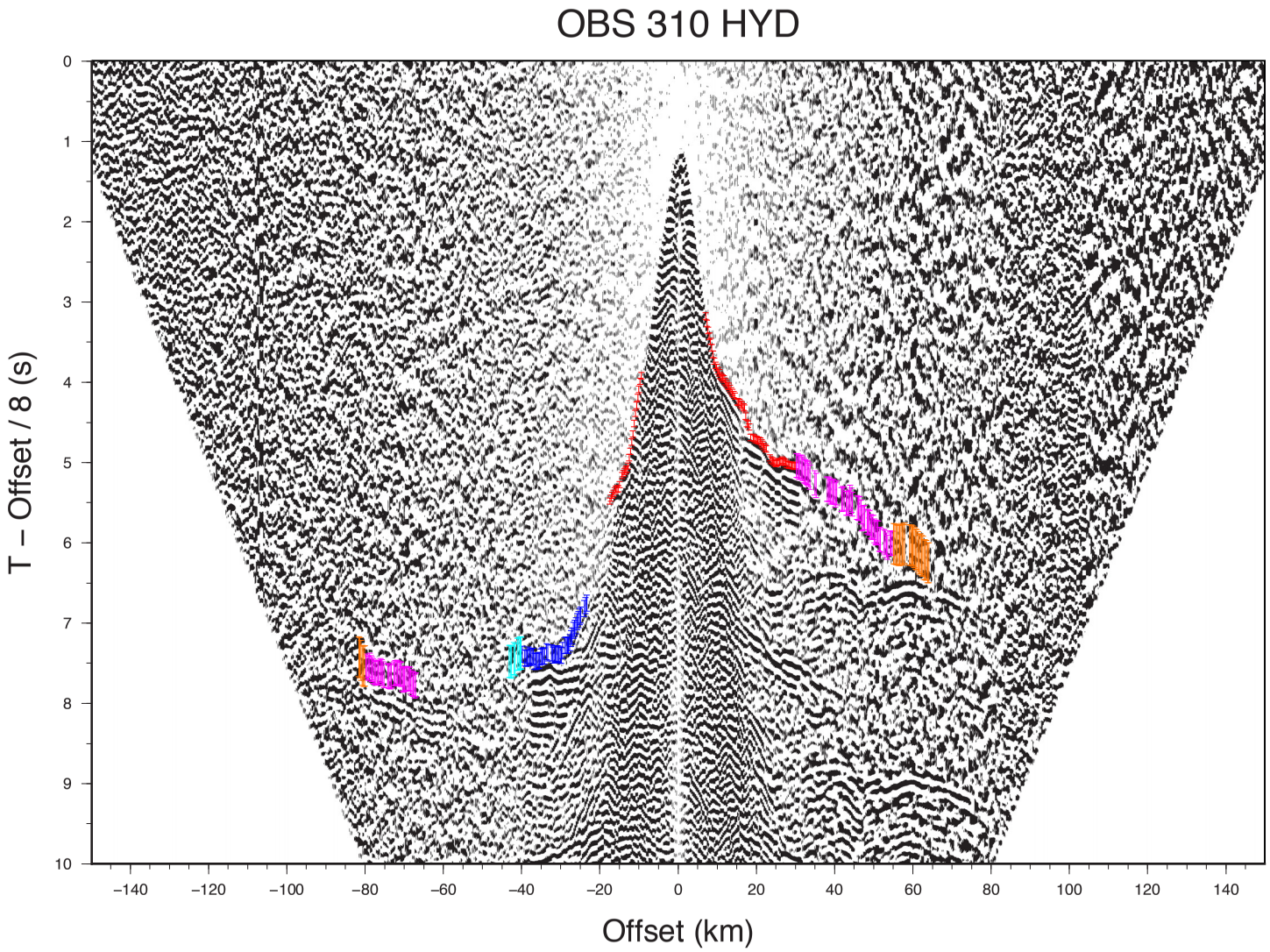

Figure C.30: OBS 310 (hydrophon channel) with first arrival times including picking uncertainties (from very clear to very unclear): 40 ms (red errorbars), 70 ms (green errorbars), 100 ms (blue errorbars), 150 ms (light blue errorbars), 200 ms (pink errorbars), 250 ms (orange errorbars).

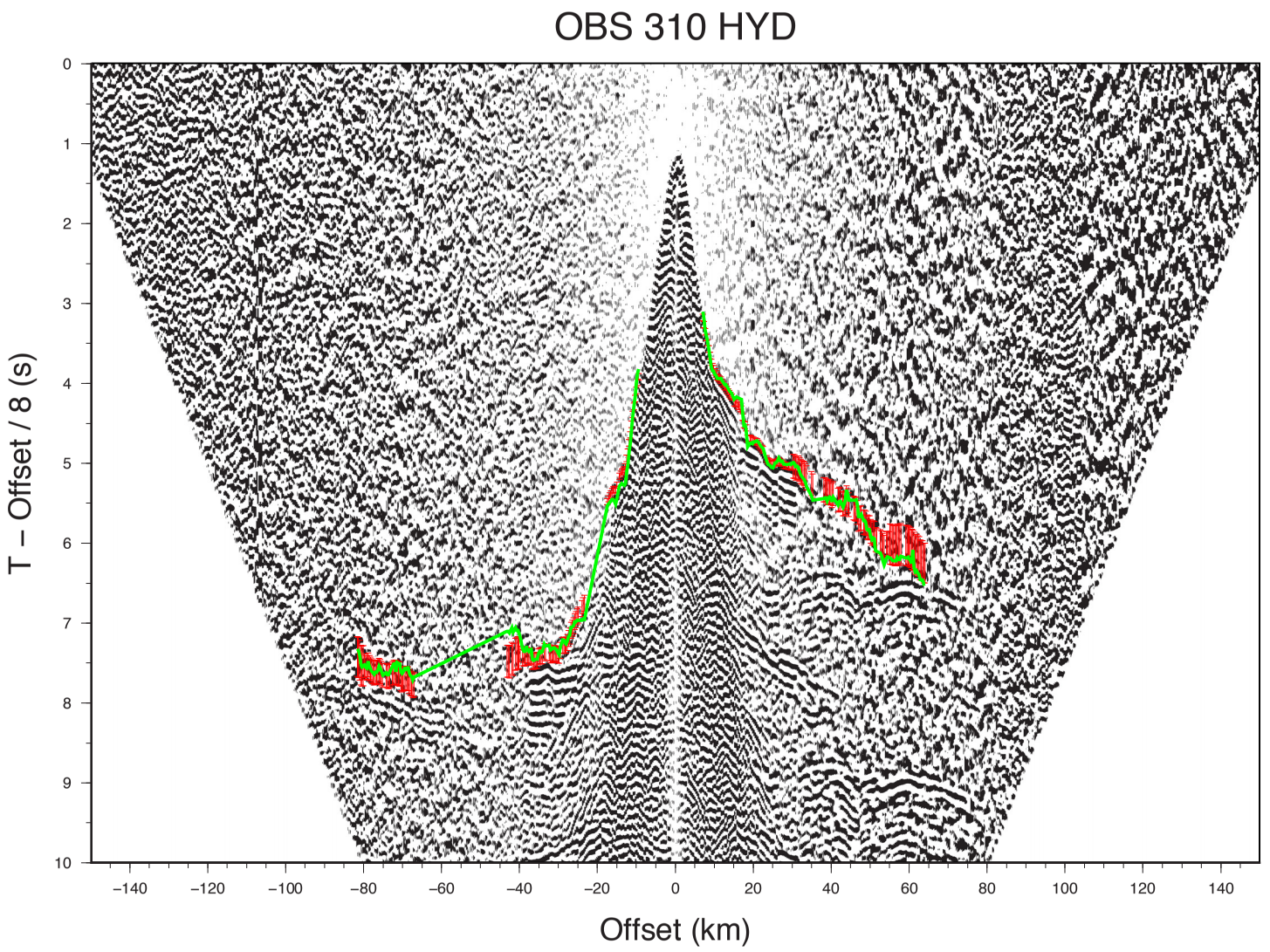

Figure C.31: OBS 310 (hydrophon channel) with observed first arrival times including picking uncertainties (red errorbars: 40 - 250 ms) and calculated (synthetic) arrival times (green line).

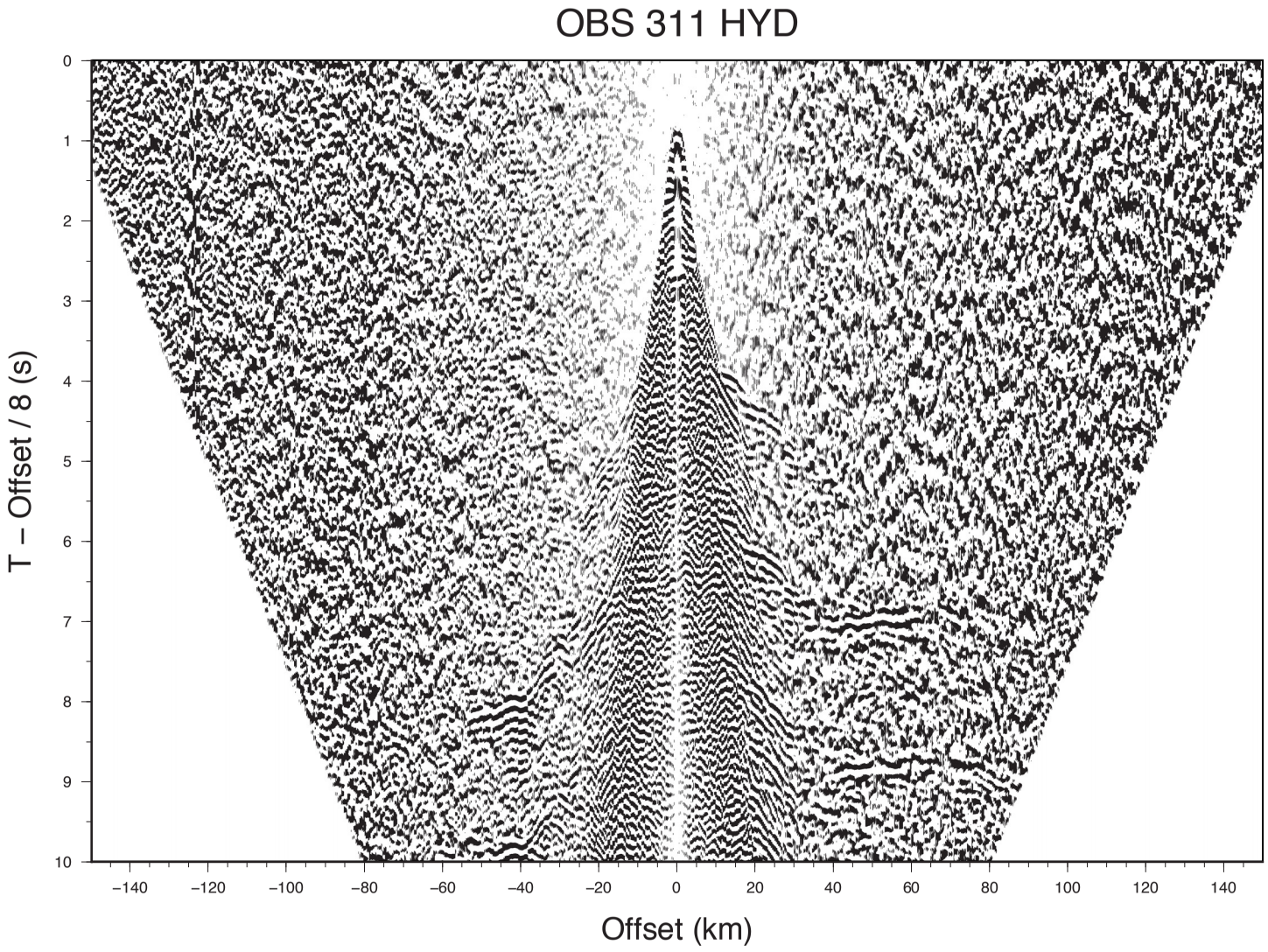

Figure C.32: OBS 311 (hydrophon channel). See Figure C.2 caption for additional description.

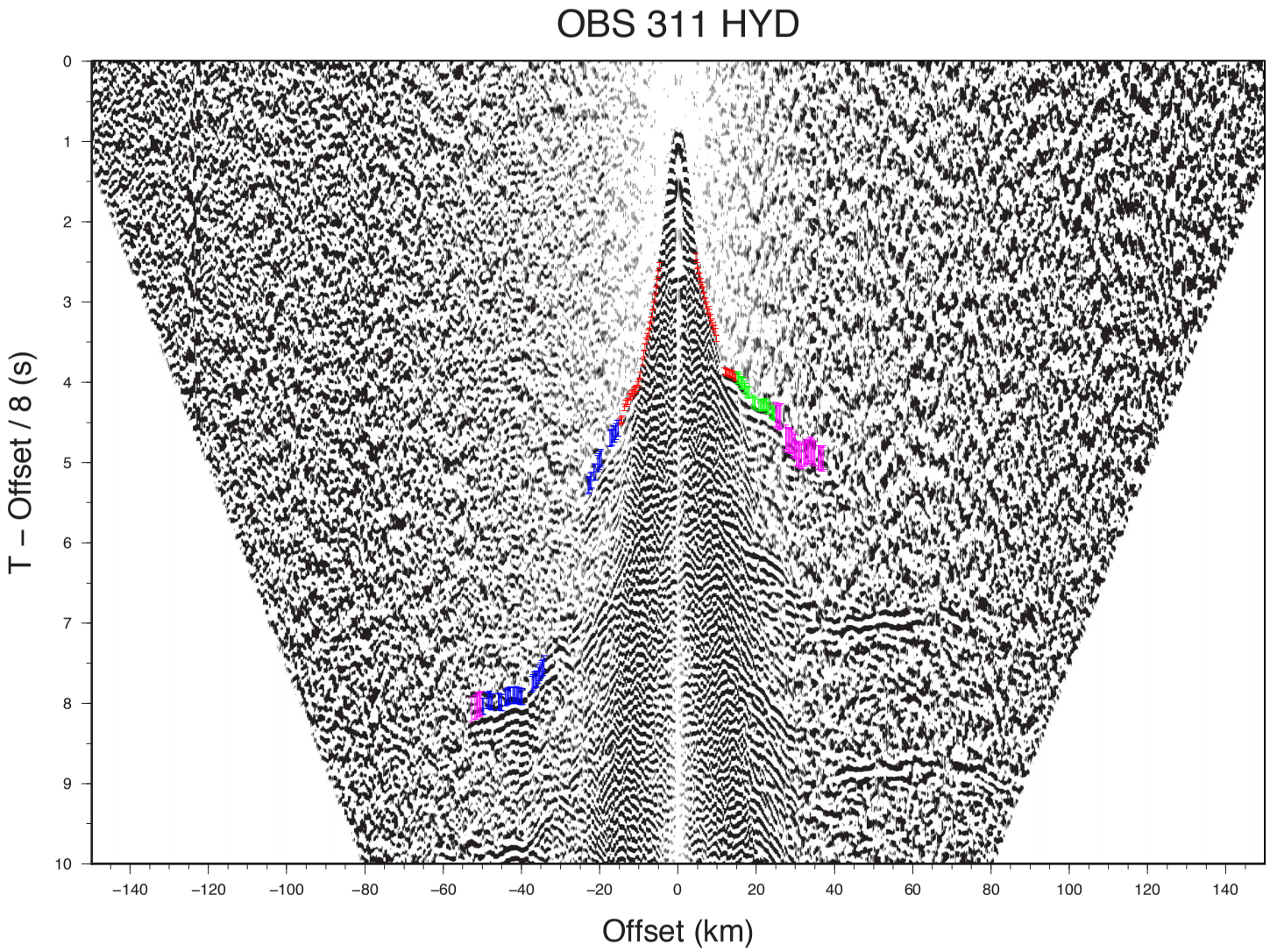

Figure C.33: OBS 311 (hydrophon channel) with first arrival times including picking uncertainties (from very clear to very unclear): 40 ms (red errorbars), 70 ms (green errorbars), 100 ms (blue errorbars), 150 ms (light blue errorbars), 200 ms (pink errorbars), 250 ms (orange errorbars).

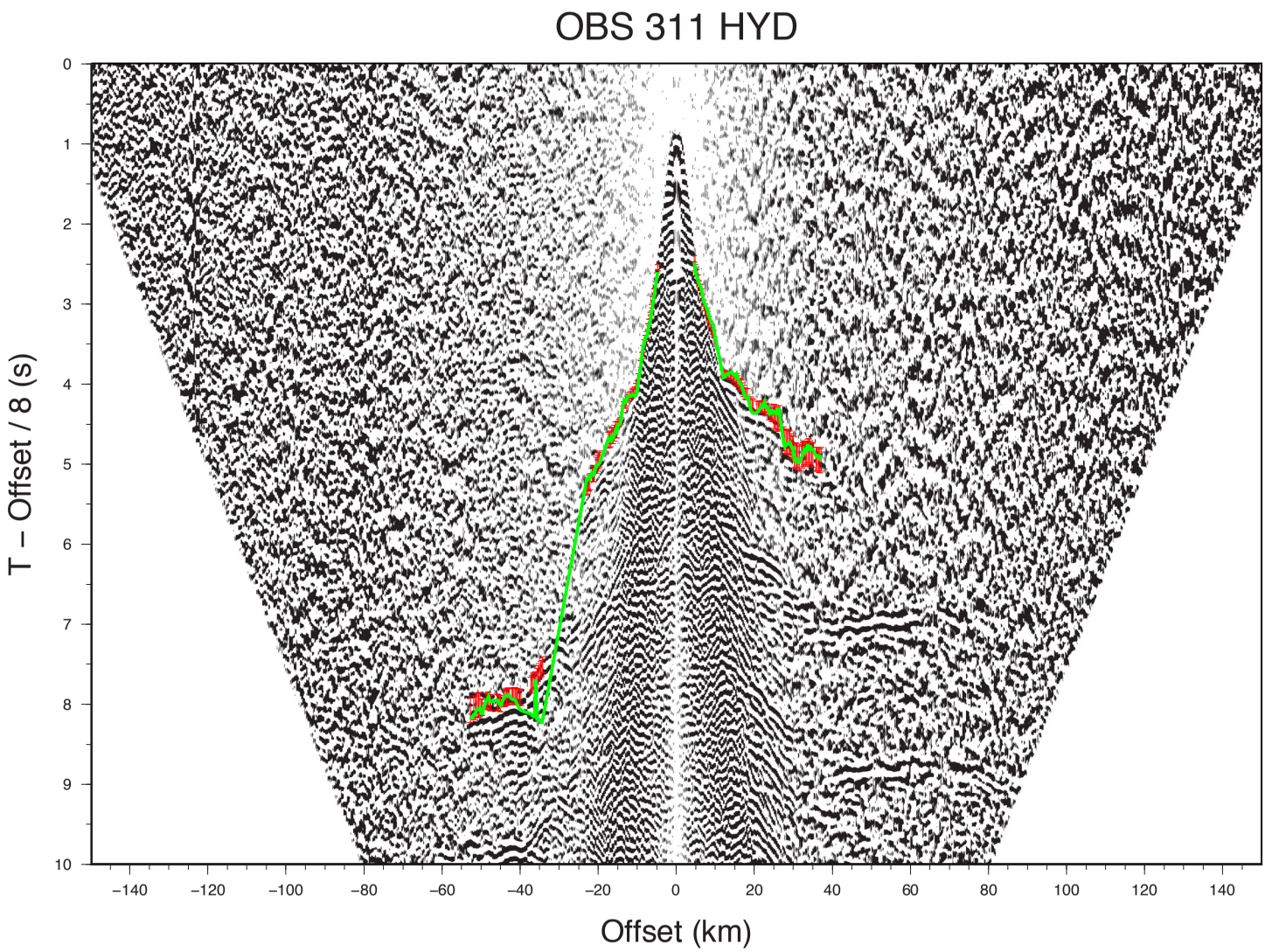

Figure C.34: OBS 311 (hydrophon channel) with observed first arrival times including picking uncertainties (red errorbars: 40 - 250 ms) and calculated (synthetic) arrival times (green line).

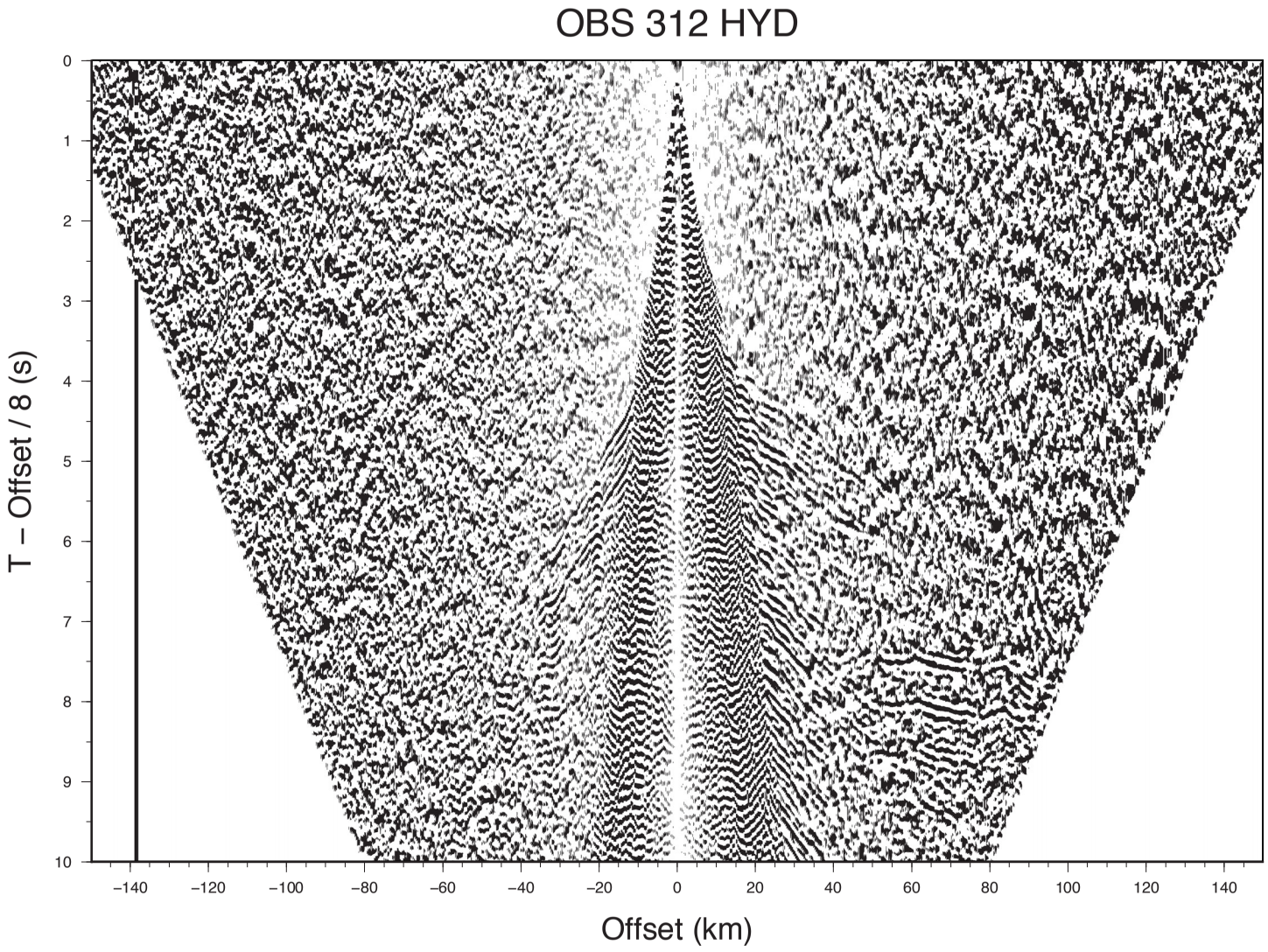

Figure C.35: OBS 312 (hydrophon channel). See Figure C.2 caption for additional description.

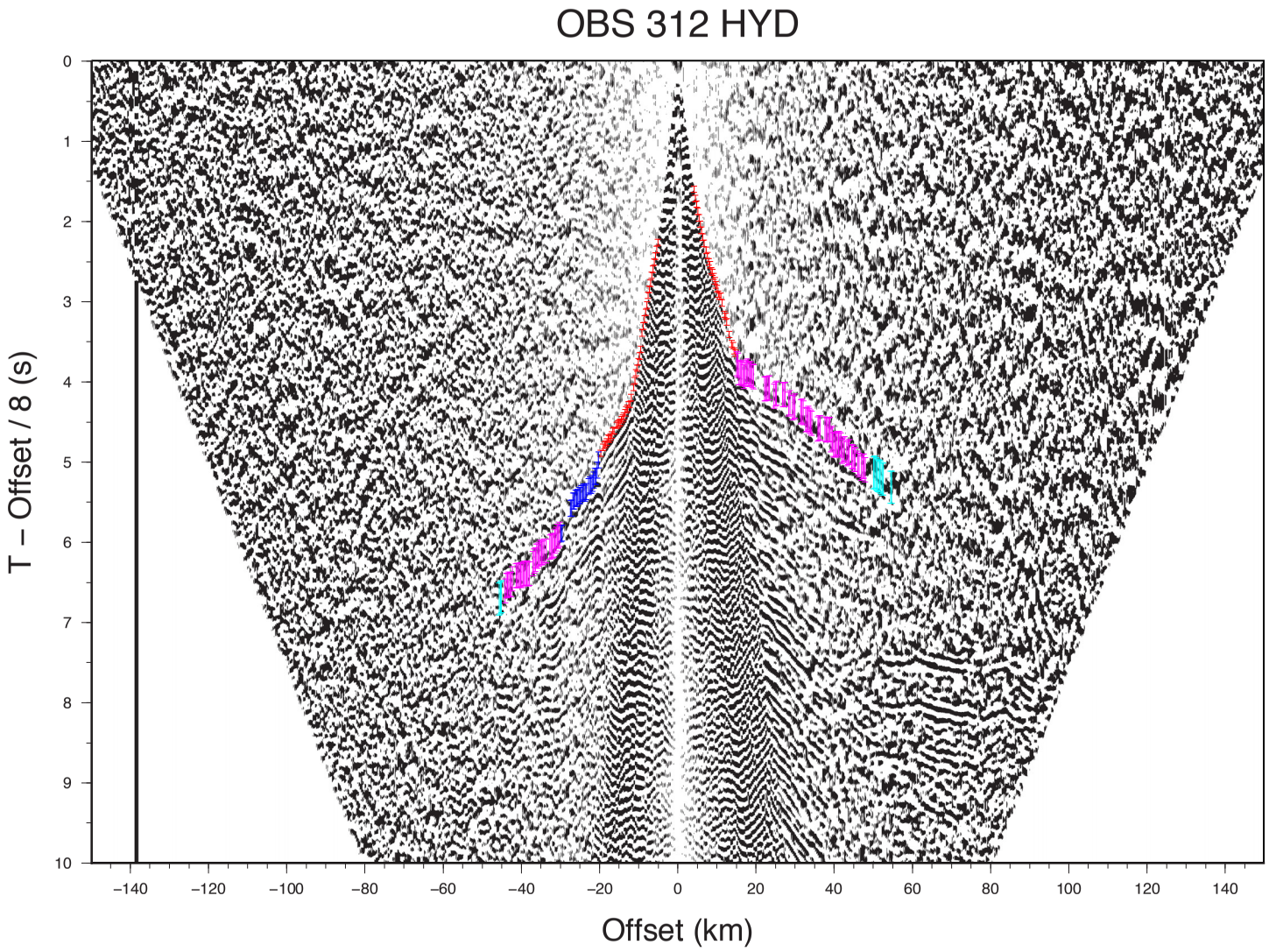

Figure C.36: OBS 312 (hydrophon channel) with first arrival times including picking uncertainties (from very clear to very unclear): 40 ms (red errorbars), 70 ms (green errorbars), 100 ms (blue errorbars), 150 ms (light blue errorbars), 200 ms (pink errorbars), 250 ms (orange errorbars).

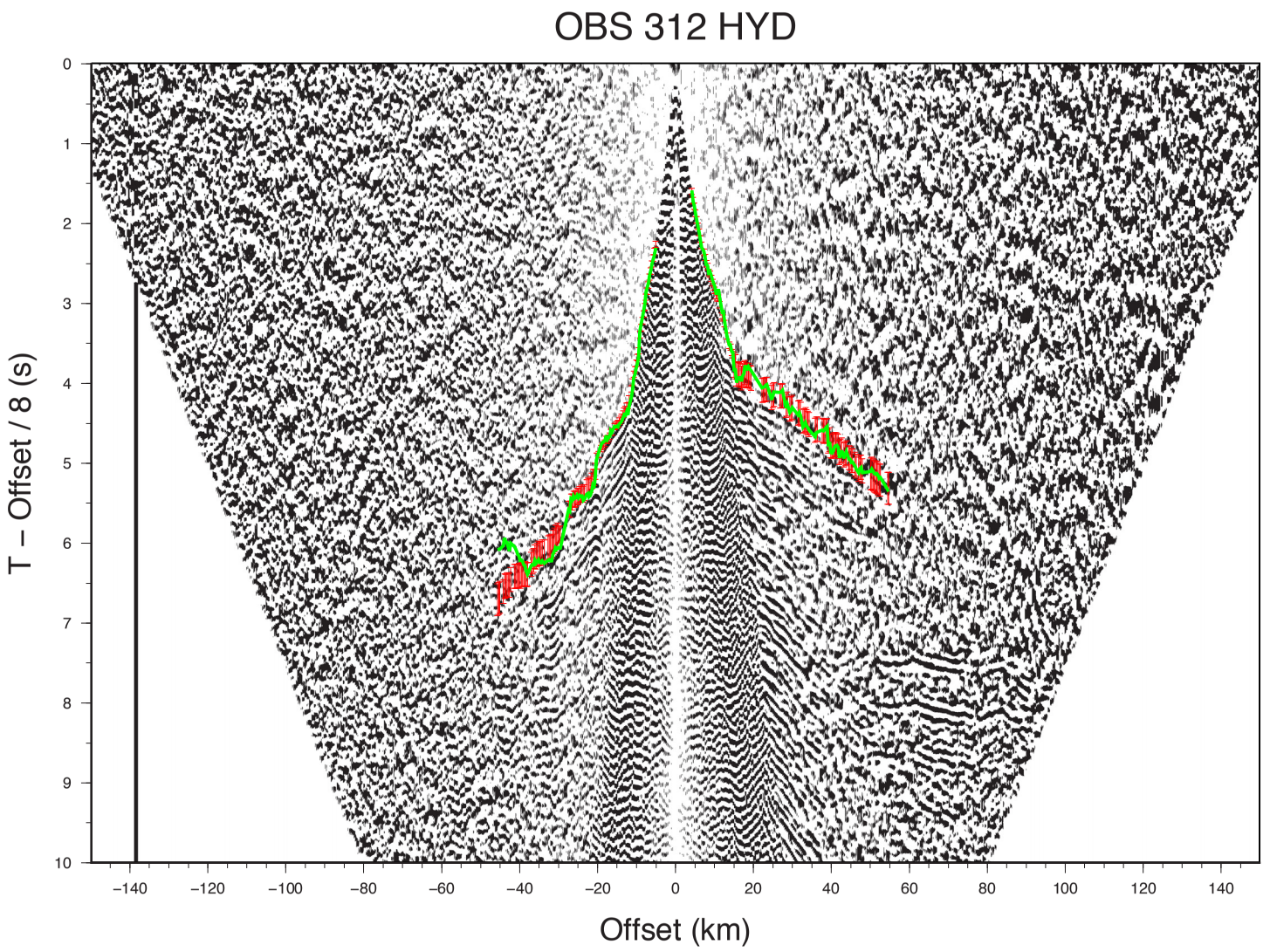

Figure C.37: OBS 312 (hydrophon channel) with observed first arrival times including picking uncertainties (red errorbars: 40 - 250 ms) and calculated (synthetic) arrival times (green line).

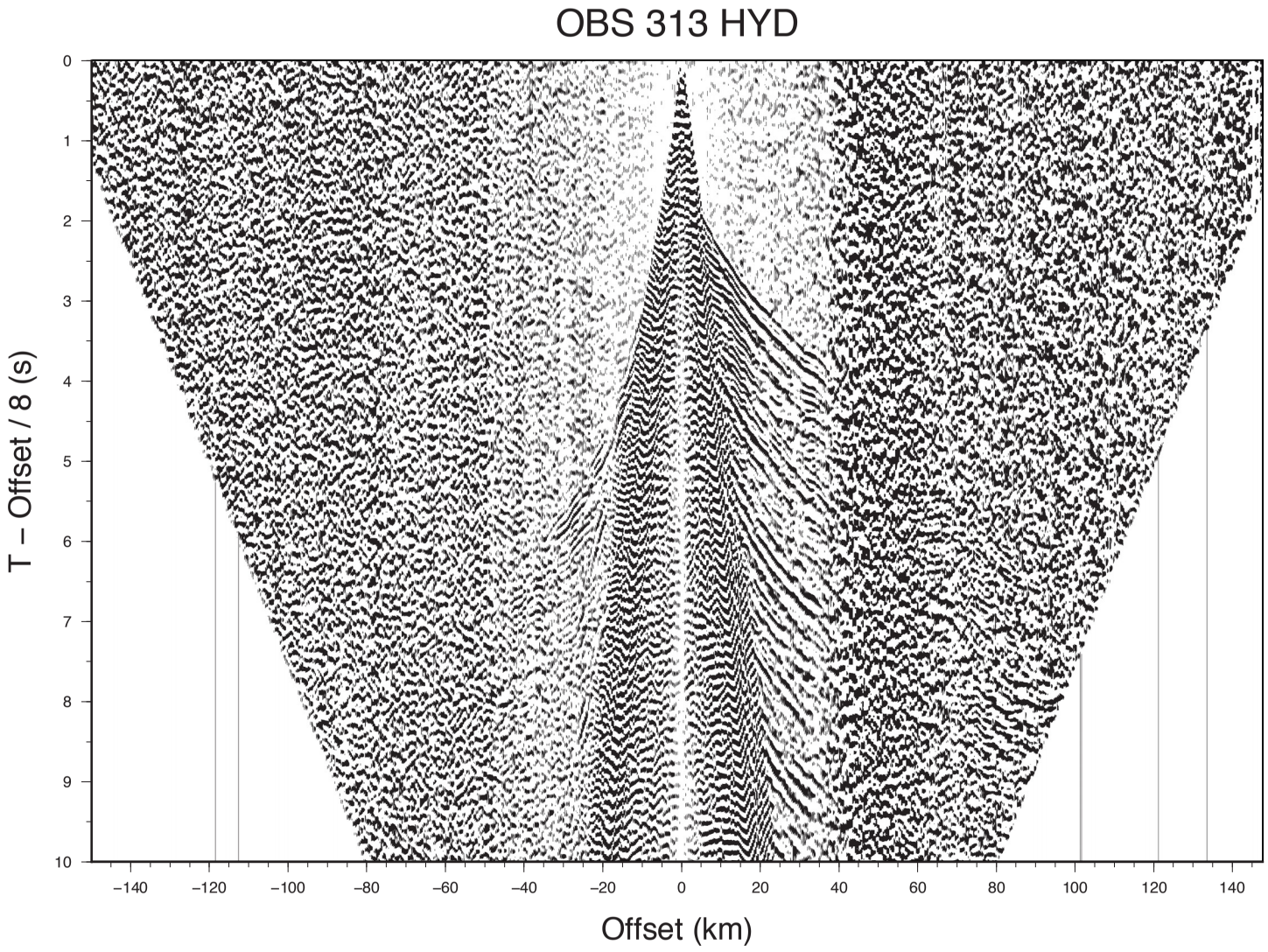

Figure C.38: OBS 313 (hydrophon channel). See Figure C.2 caption for additional description.

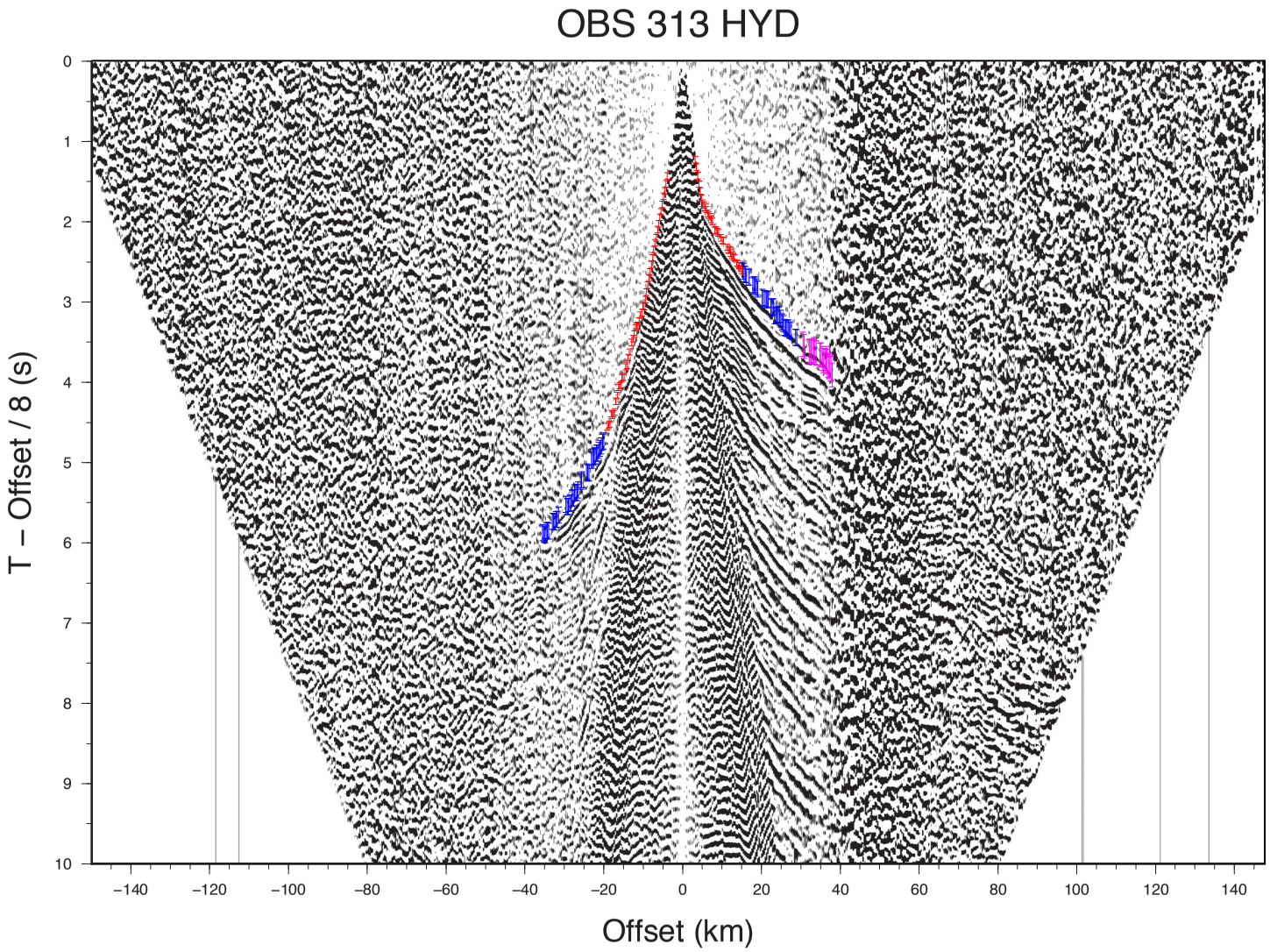

Figure C.39: OBS 313 (hydrophon channel) with first arrival times including picking uncertainties (from very clear to very unclear): 40 ms (red errorbars), 70 ms (green errorbars), 100 ms (blue errorbars), 150 ms (light blue errorbars), 200 ms (pink errorbars), 250 ms (orange errorbars).

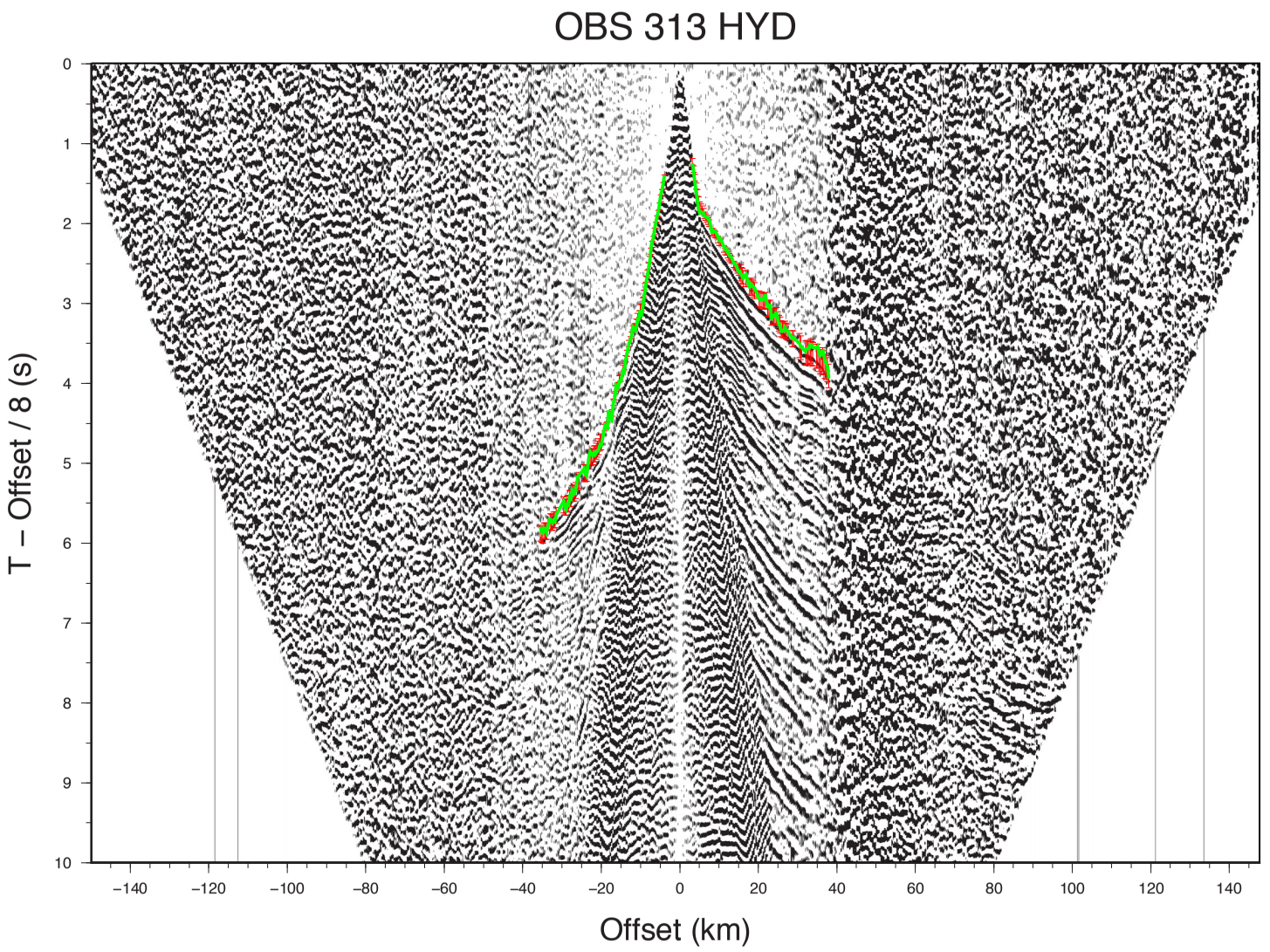

Figure C.40: OBS 313 (hydrophon channel) with observed first arrival times including picking uncertainties (red errorbars: 40 - 250 ms) and calculated (synthetic) arrival times (green line).

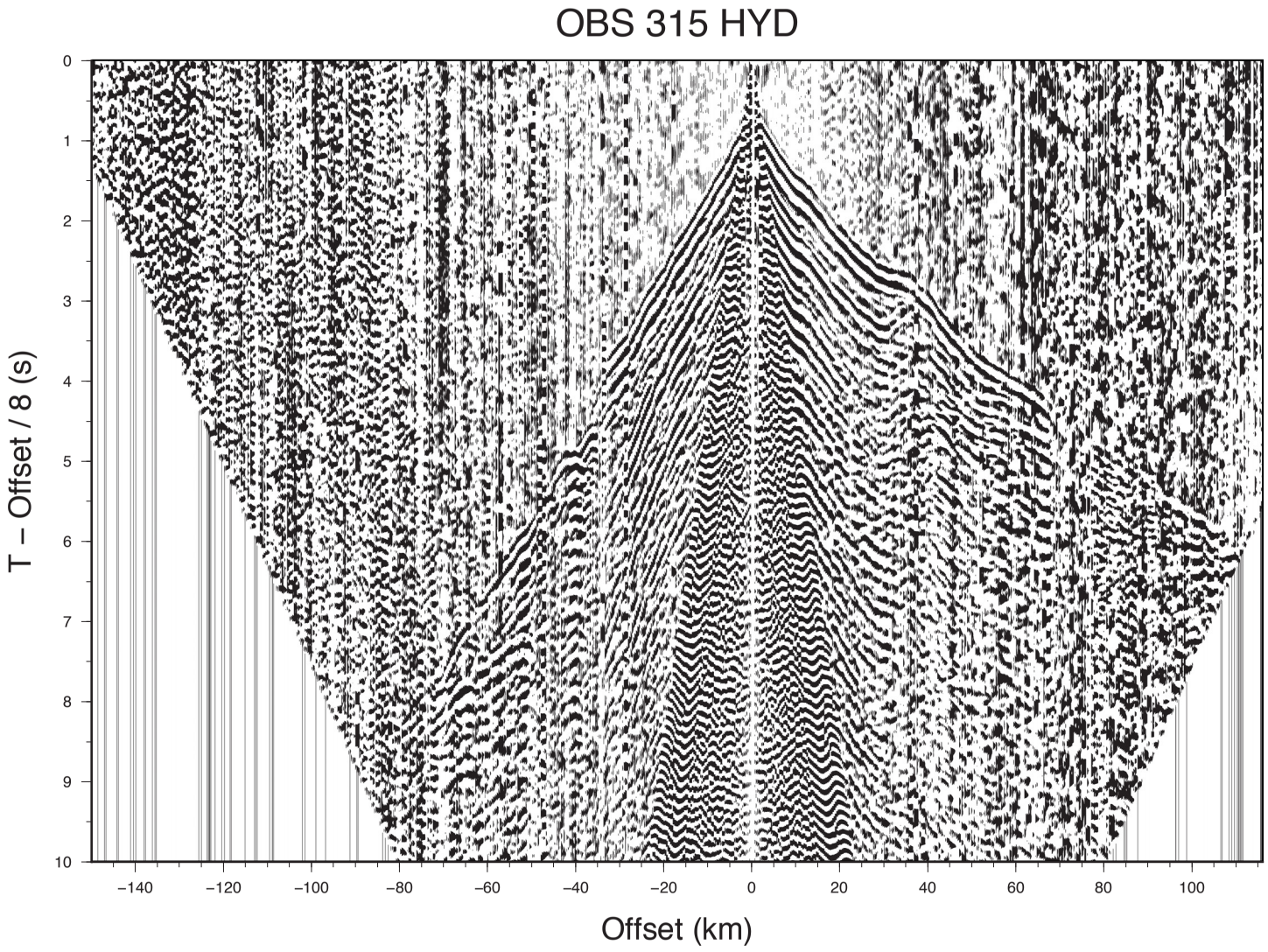

Figure C.41: OBS 315 (hydrophon channel). See Figure C.2 caption for additional description.

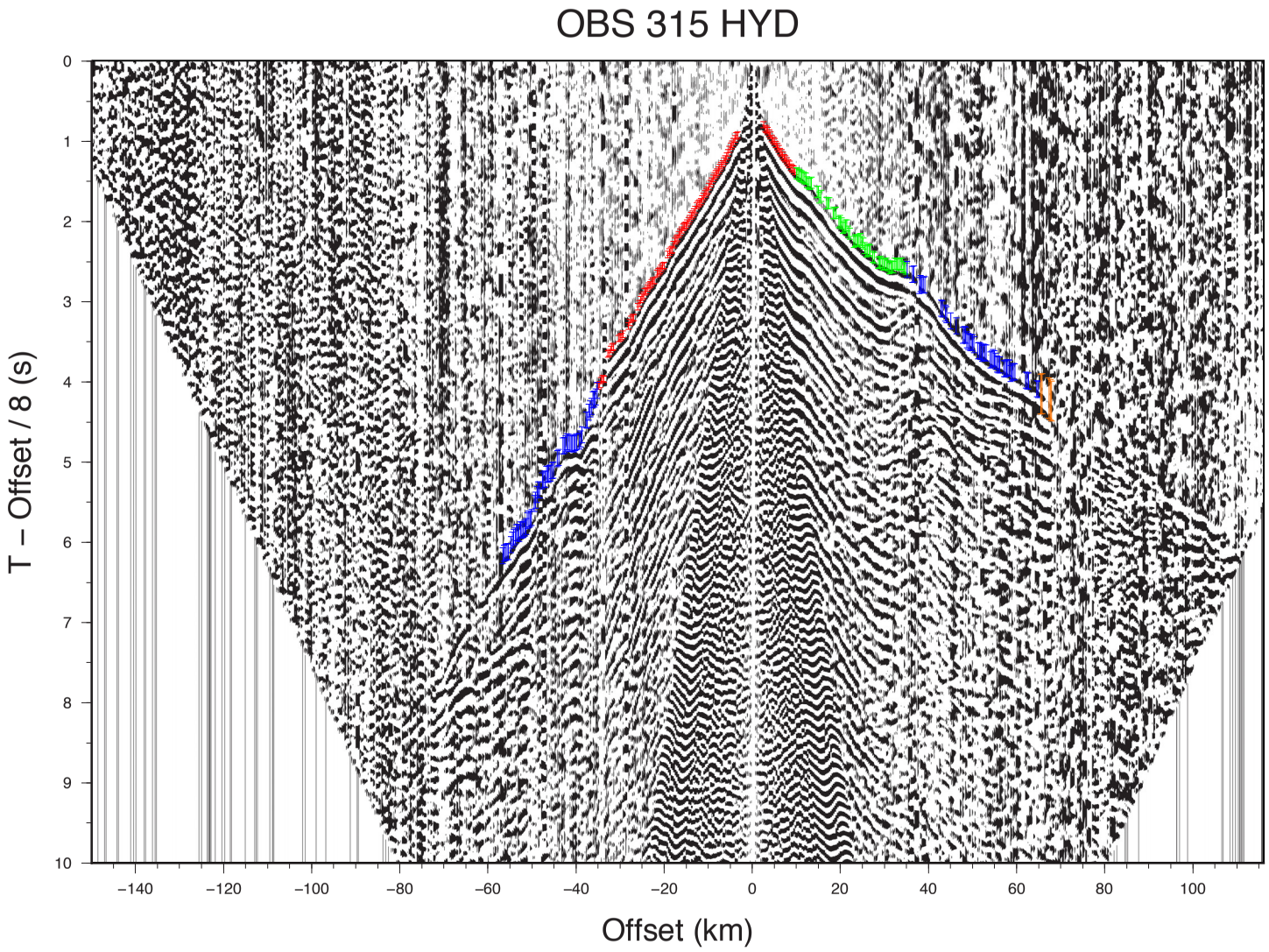

Figure C.42: OBS 315 (hydrophon channel) with first arrival times including picking uncertainties (from very clear to very unclear): 40 ms (red errorbars), 70 ms (green errorbars), 100 ms (blue errorbars), 150 ms (light blue errorbars), 200 ms (pink errorbars), 250 ms (orange errorbars).

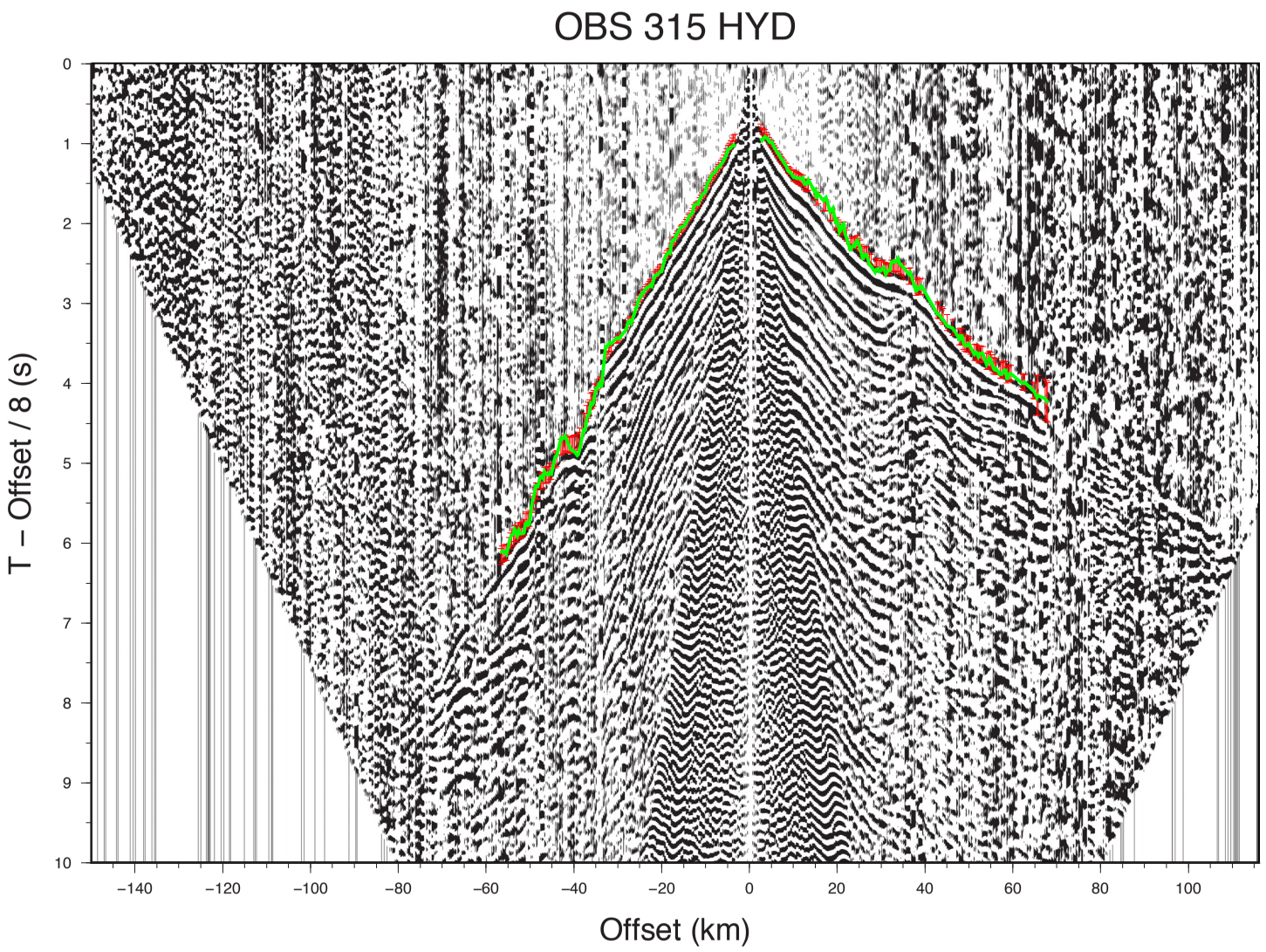

Figure C.43: OBS 315 (hydrophon channel) with observed first arrival times including picking uncertainties (red errorbars: 40 - 250 ms) and calculated (synthetic) arrival times (green line).

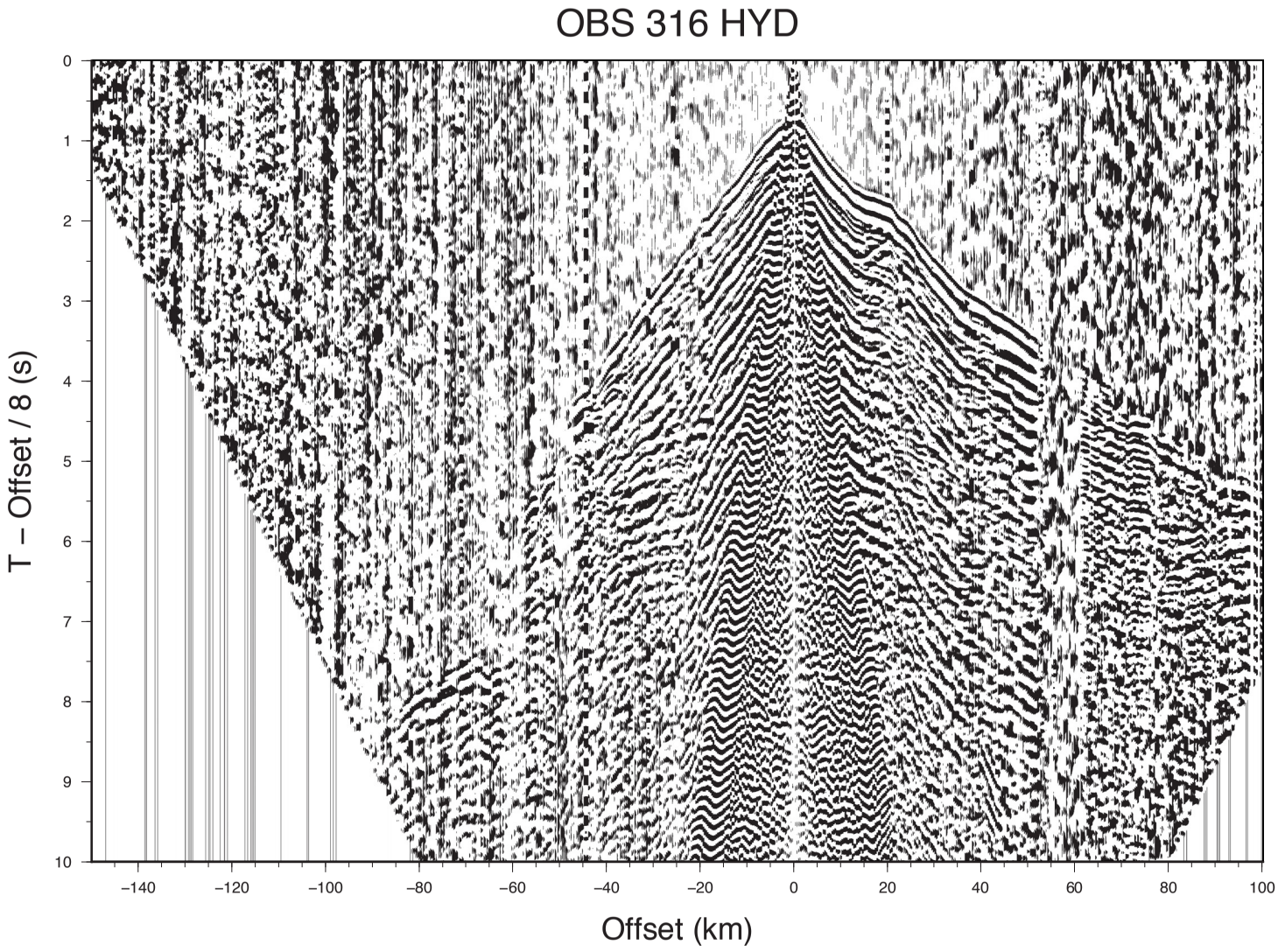

Figure C.44: OBS 316 (hydrophon channel). See Figure C.2 caption for additional description.

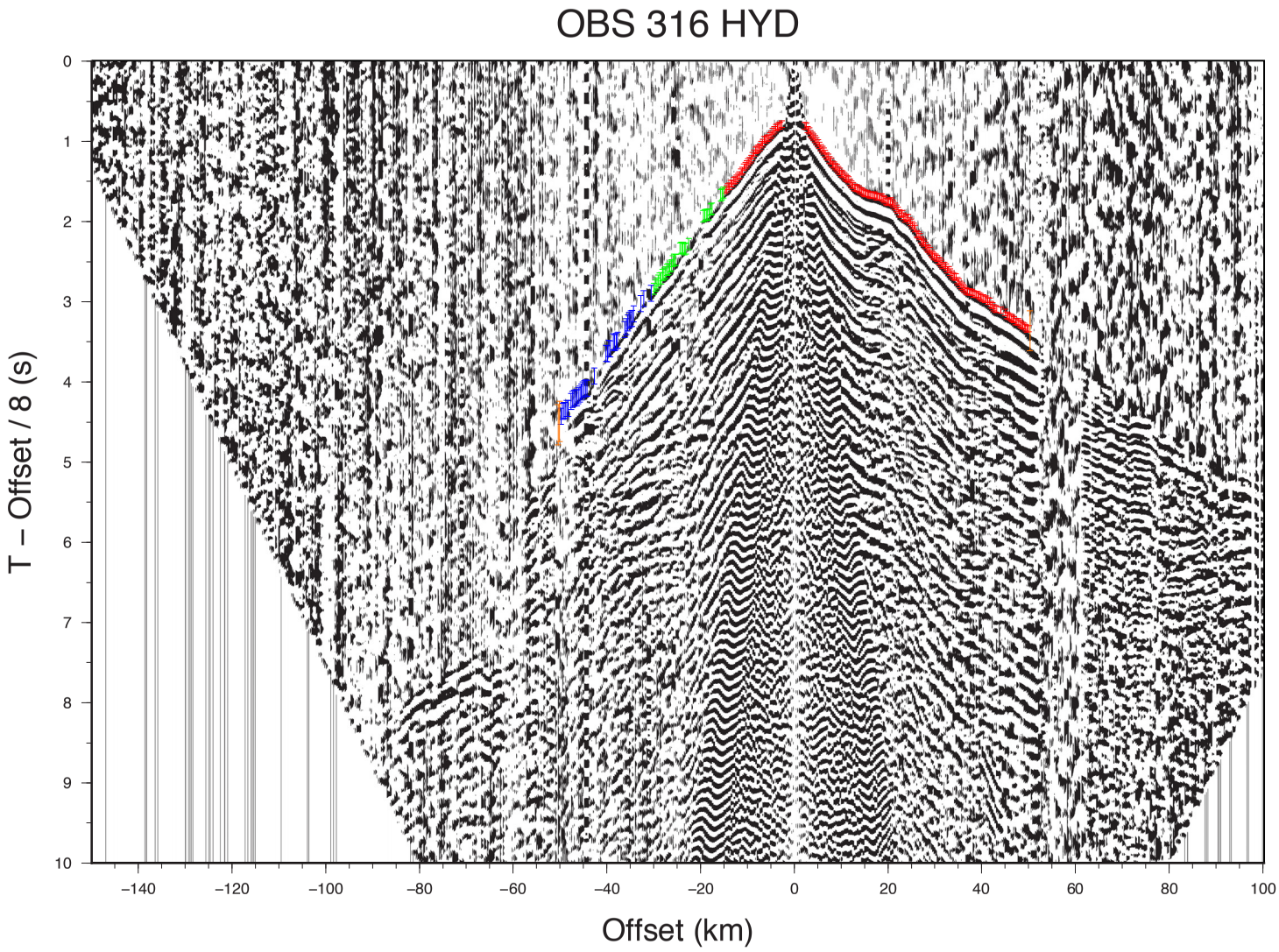

Figure C.45: OBS 316 (hydrophon channel) with first arrival times including picking uncertainties (from very clear to very unclear): 40 ms (red errorbars), 70 ms (green errorbars), 100 ms (blue errorbars), 150 ms (light blue errorbars), 200 ms (pink errorbars), 250 ms (orange errorbars).

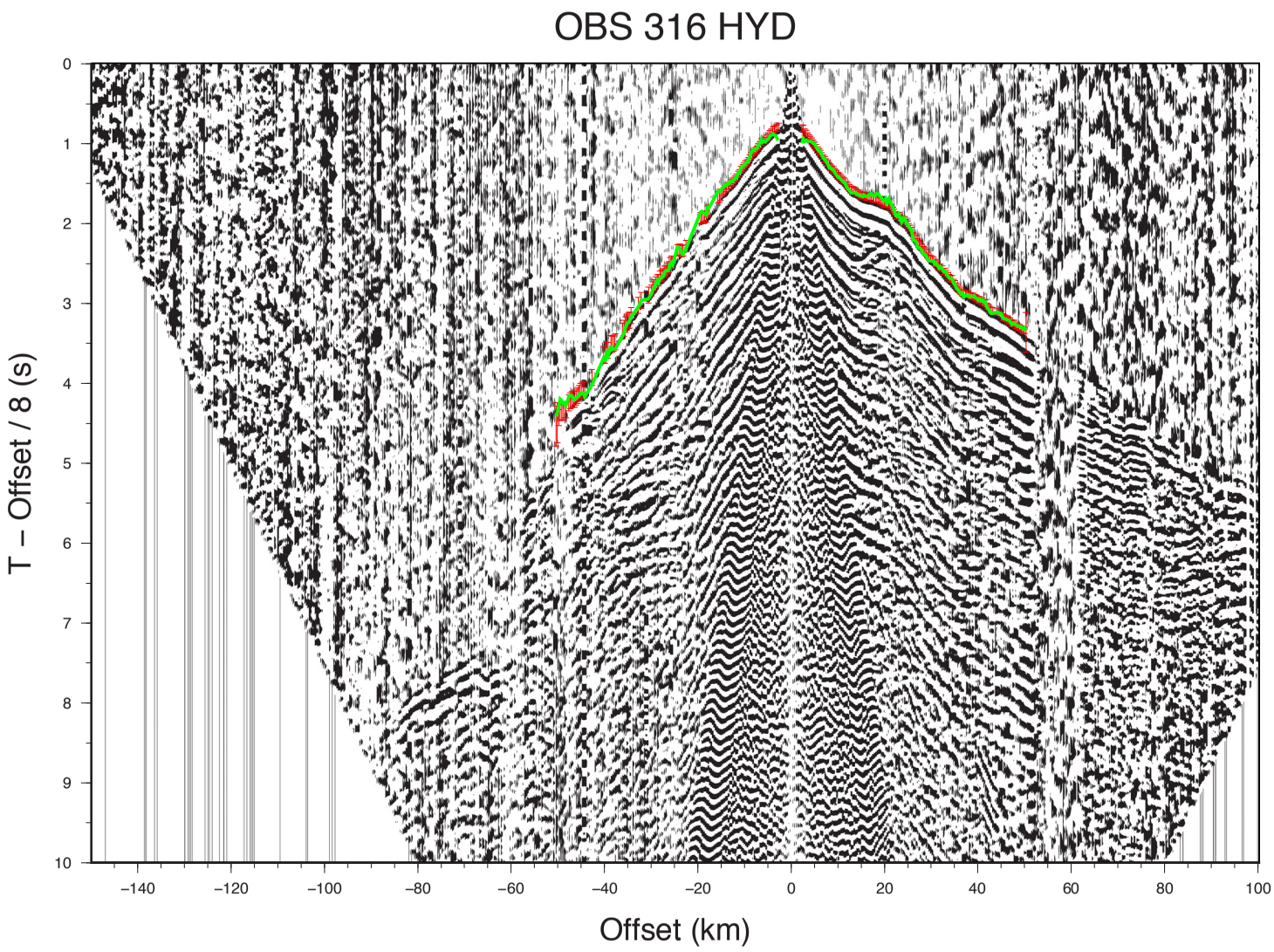

Figure C.46: OBS 316 (hydrophon channel) with observed first arrival times including picking uncertainties (red errorbars: 40 - 250 ms) and calculated (synthetic) arrival times (green line).

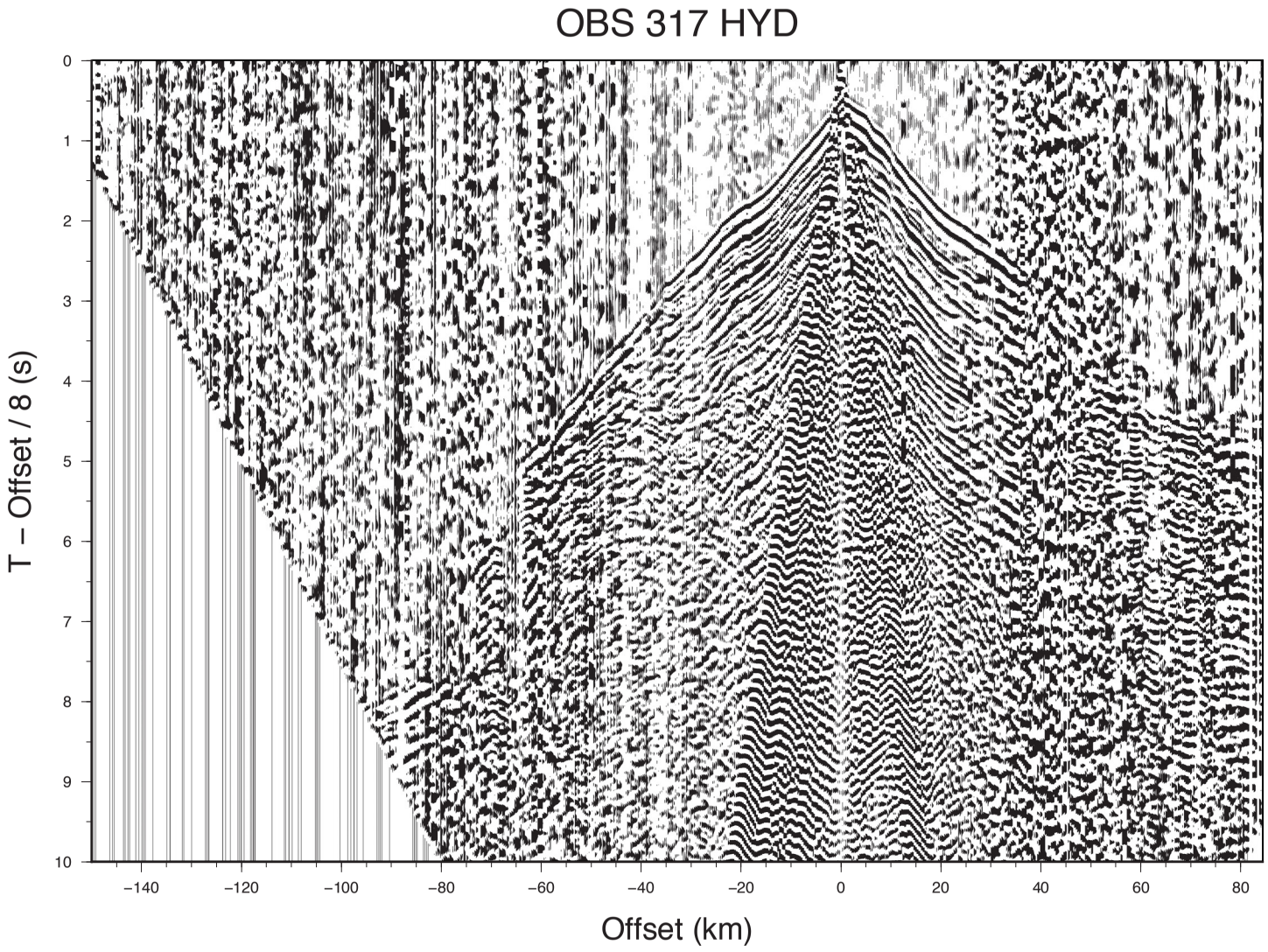

Figure C.47: OBS 317 (hydrophon channel). See Figure C.2 caption for additional description.

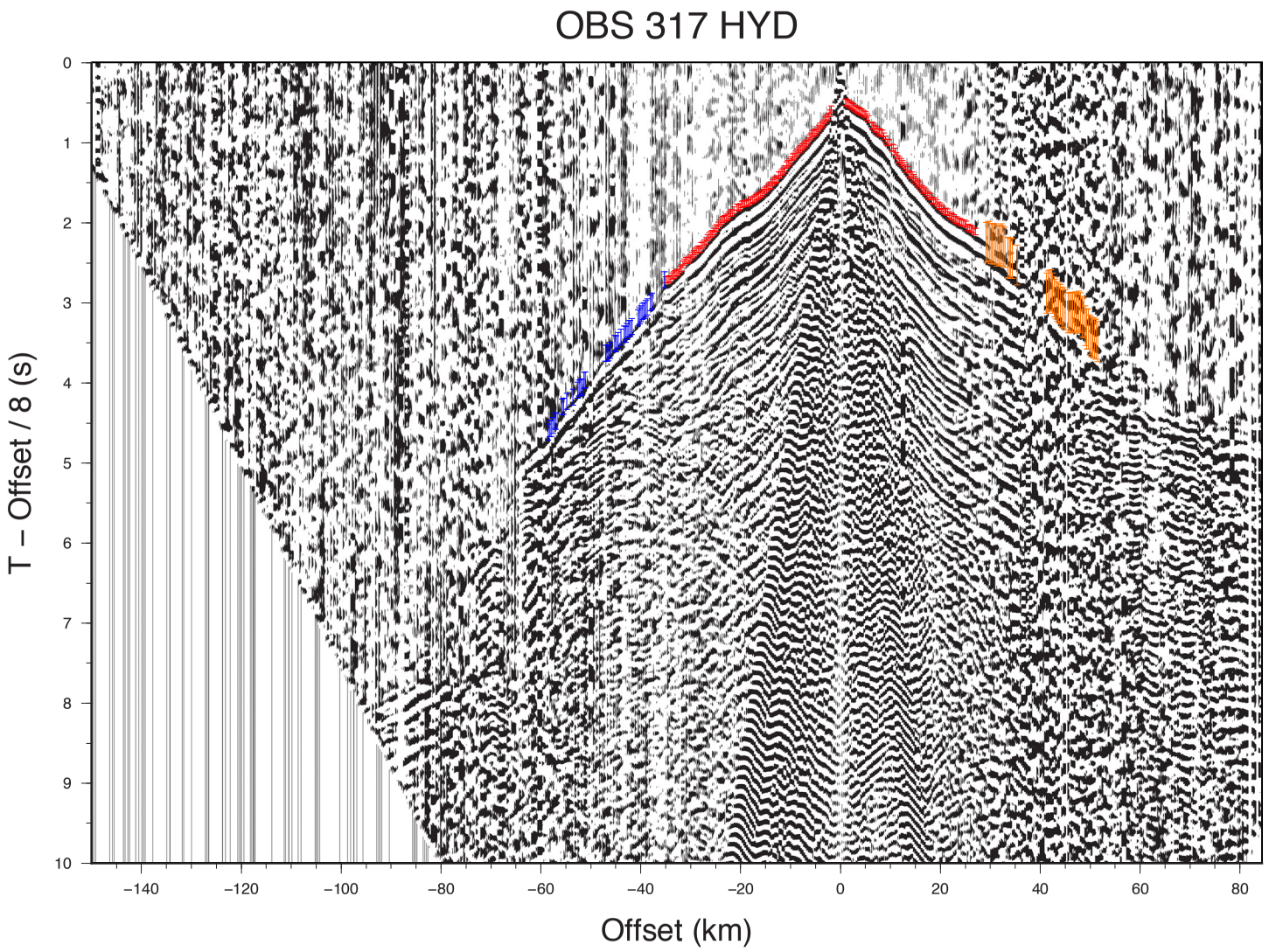

Figure C.48: OBS 317 (hydrophon channel) with first arrival times including picking uncertainties (from very clear to very unclear): 40 ms (red errorbars), 70 ms (green errorbars), 100 ms (blue errorbars), 150 ms (light blue errorbars), 200 ms (pink errorbars), 250 ms (orange errorbars).

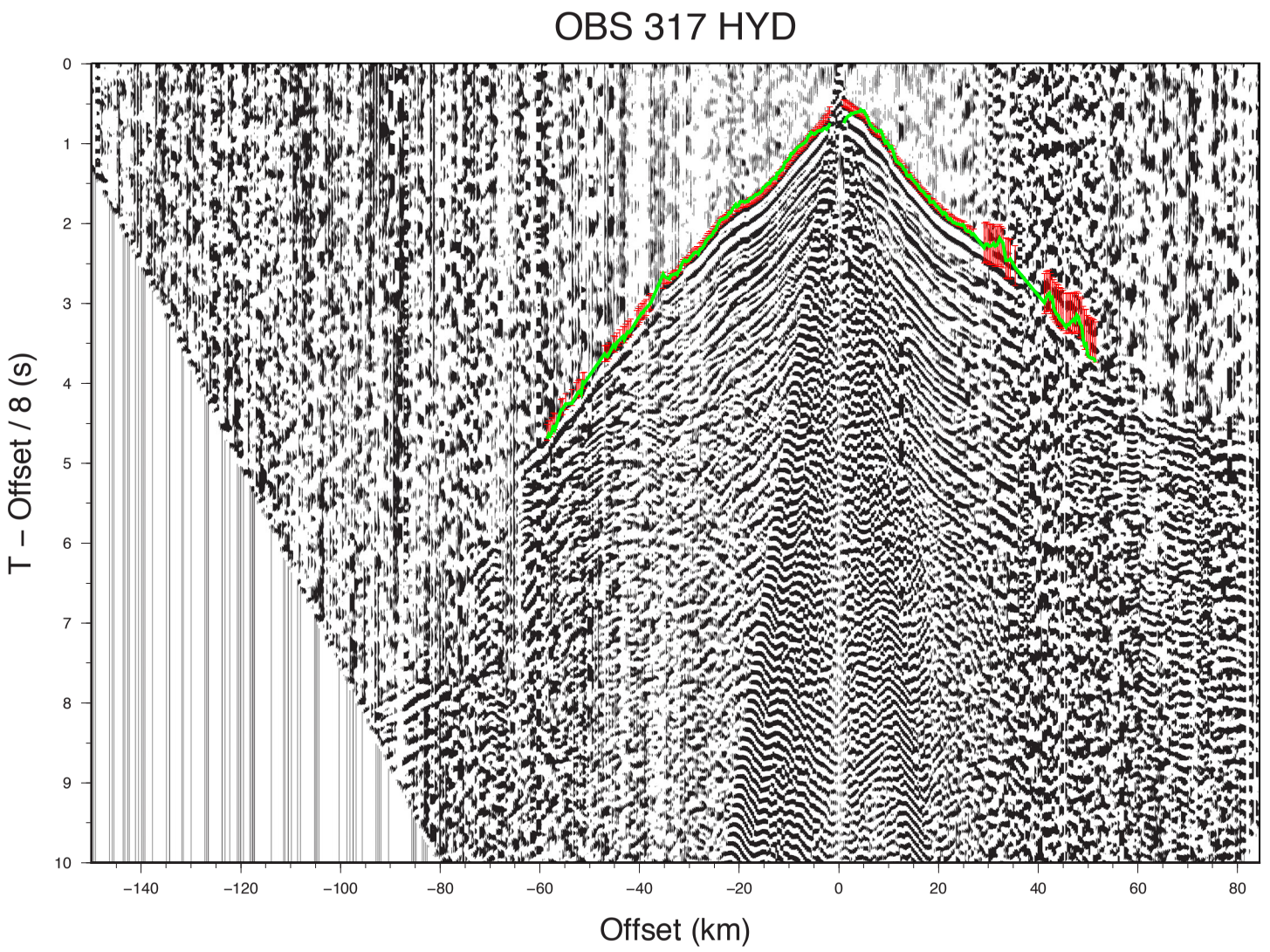

Figure C.49: OBS 317 (hydrophon channel) with observed first arrival times including picking uncertainties (red errorbars: 40 - 250 ms) and calculated (synthetic) arrival times (green line).

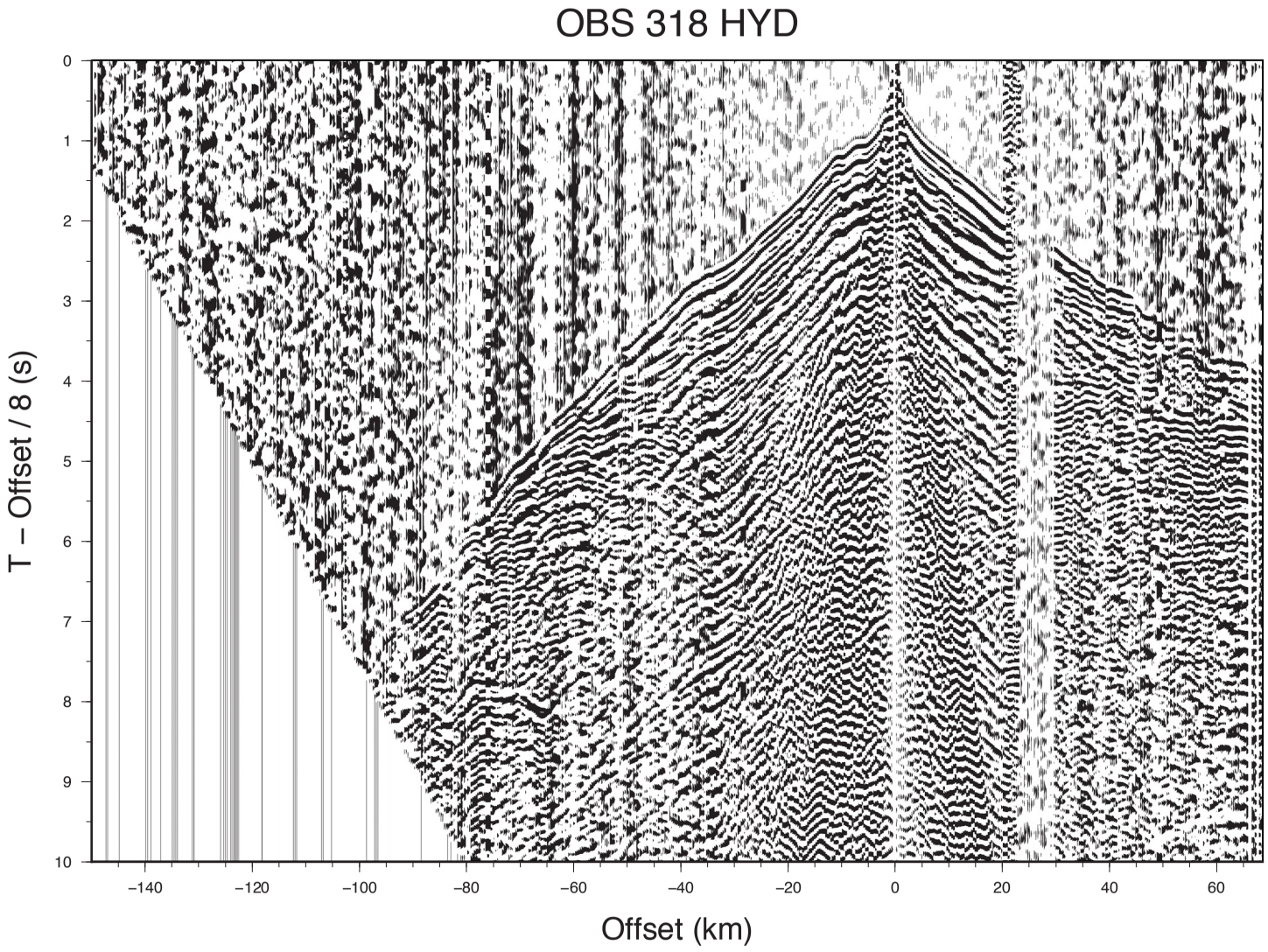

Figure C.50: OBS 318 (hydrophon channel). See Figure C.2 caption for additional description.

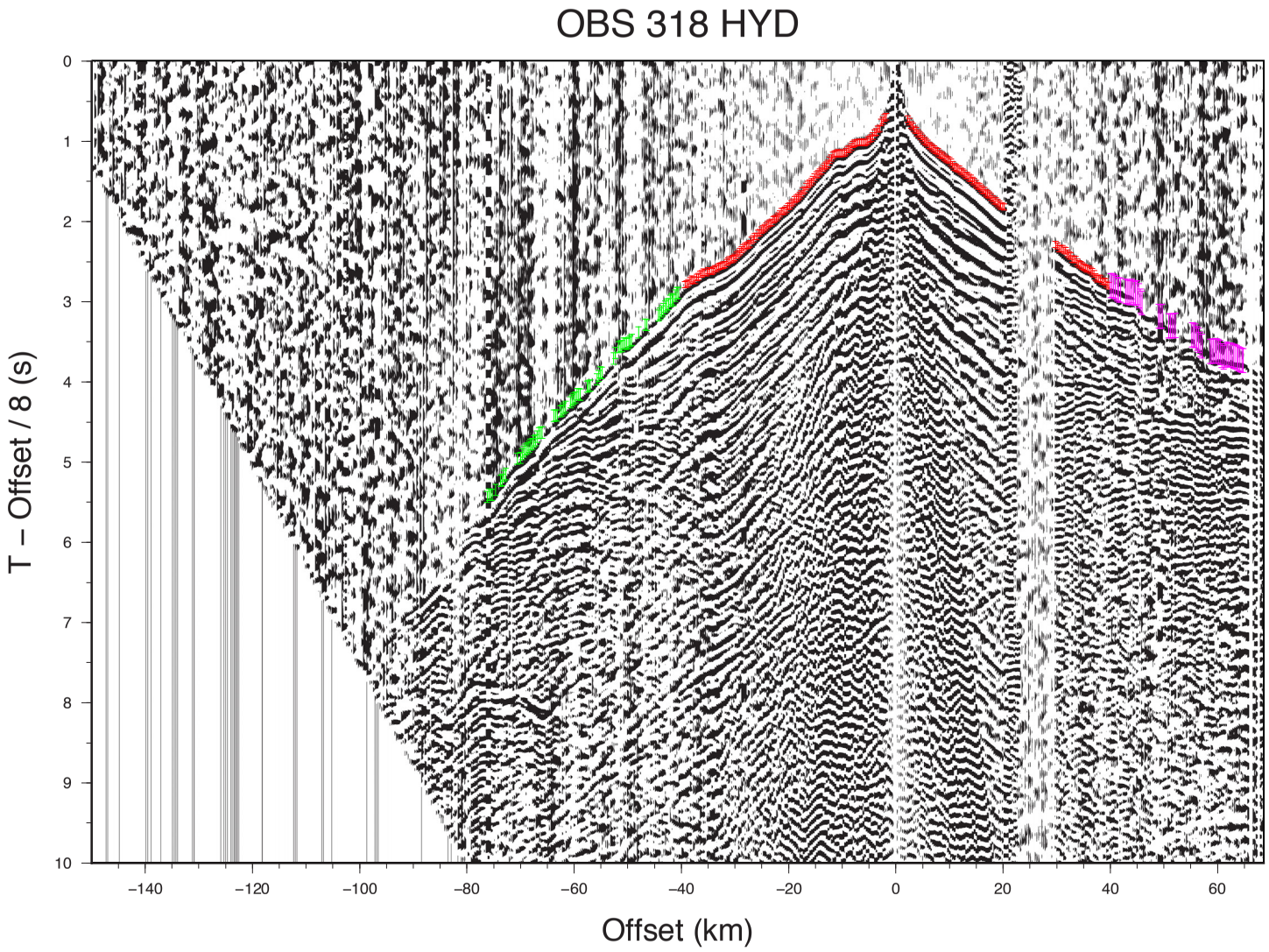

Figure C.51: OBS 318 (hydrophon channel) with first arrival times including picking uncertainties (from very clear to very unclear): 40 ms (red errorbars), 70 ms (green errorbars), 100 ms (blue errorbars), 150 ms (light blue errorbars), 200 ms (pink errorbars), 250 ms (orange errorbars).

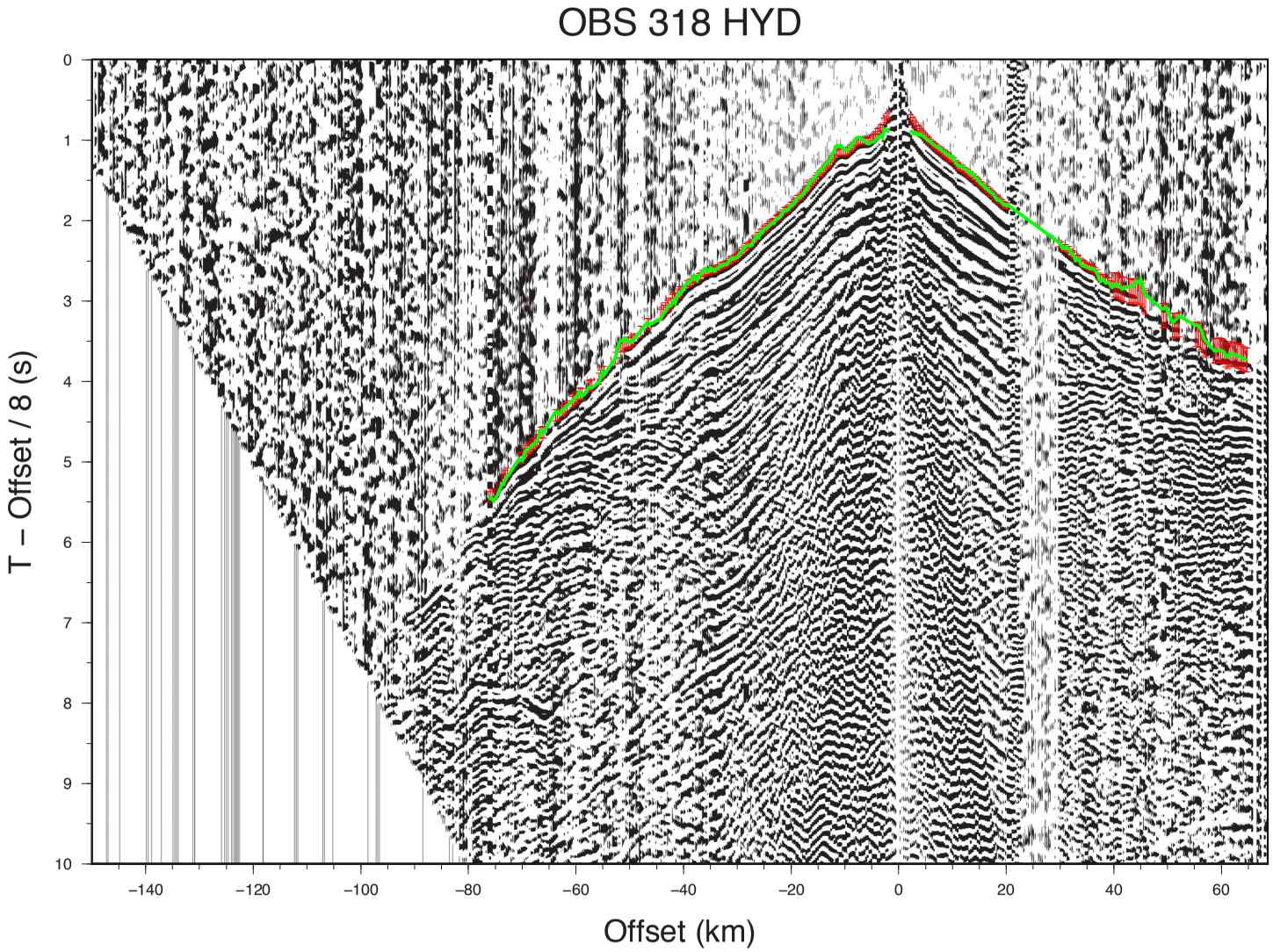

Figure C.52: OBS 318 (hydrophon channel) with observed first arrival times including picking uncertainties (red errorbars: 40 - 250 ms) and calculated (synthetic) arrival times (green line).

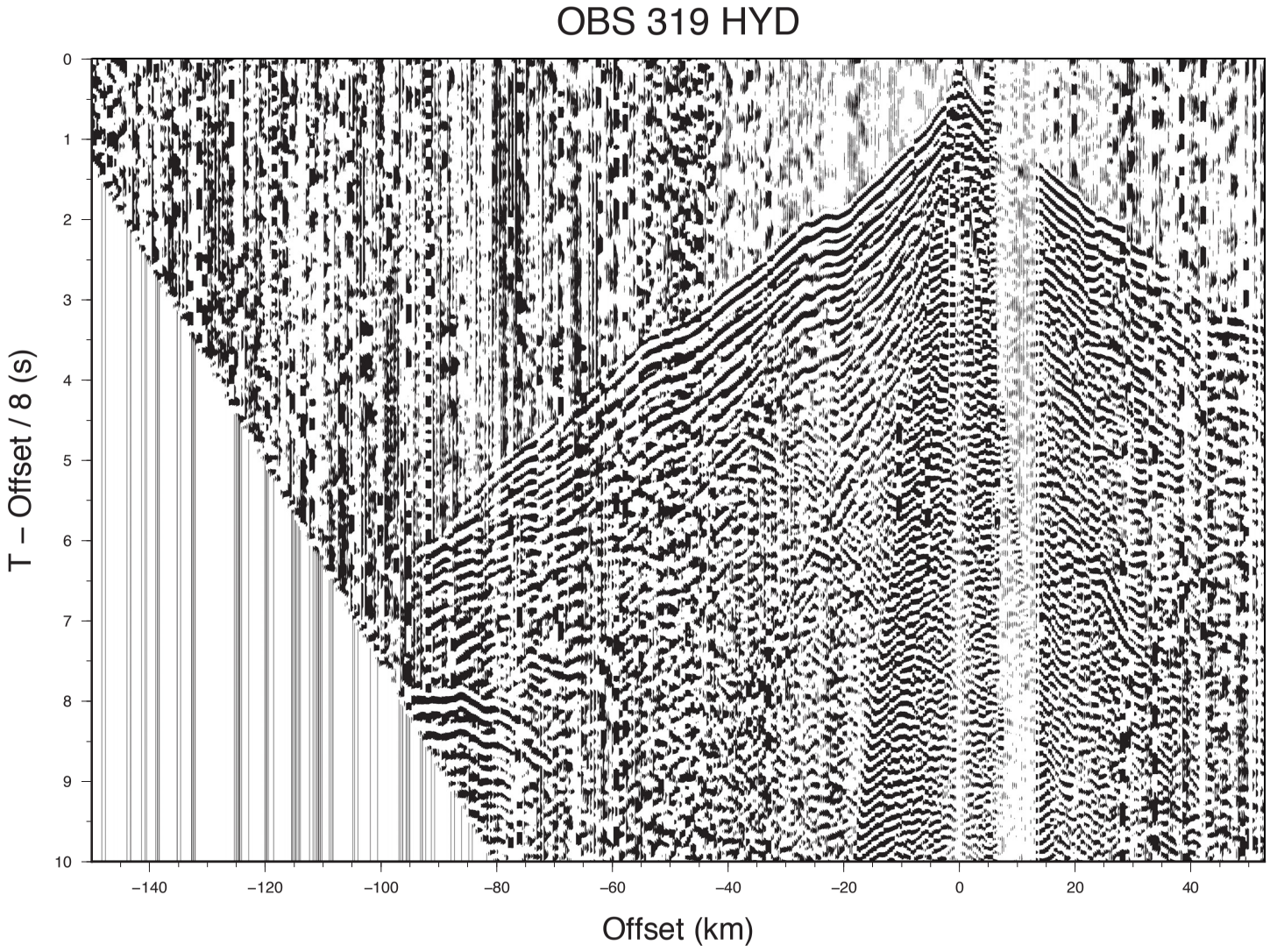

Figure C.53: OBS 319 (hydrophon channel). See Figure C.2 caption for additional description.

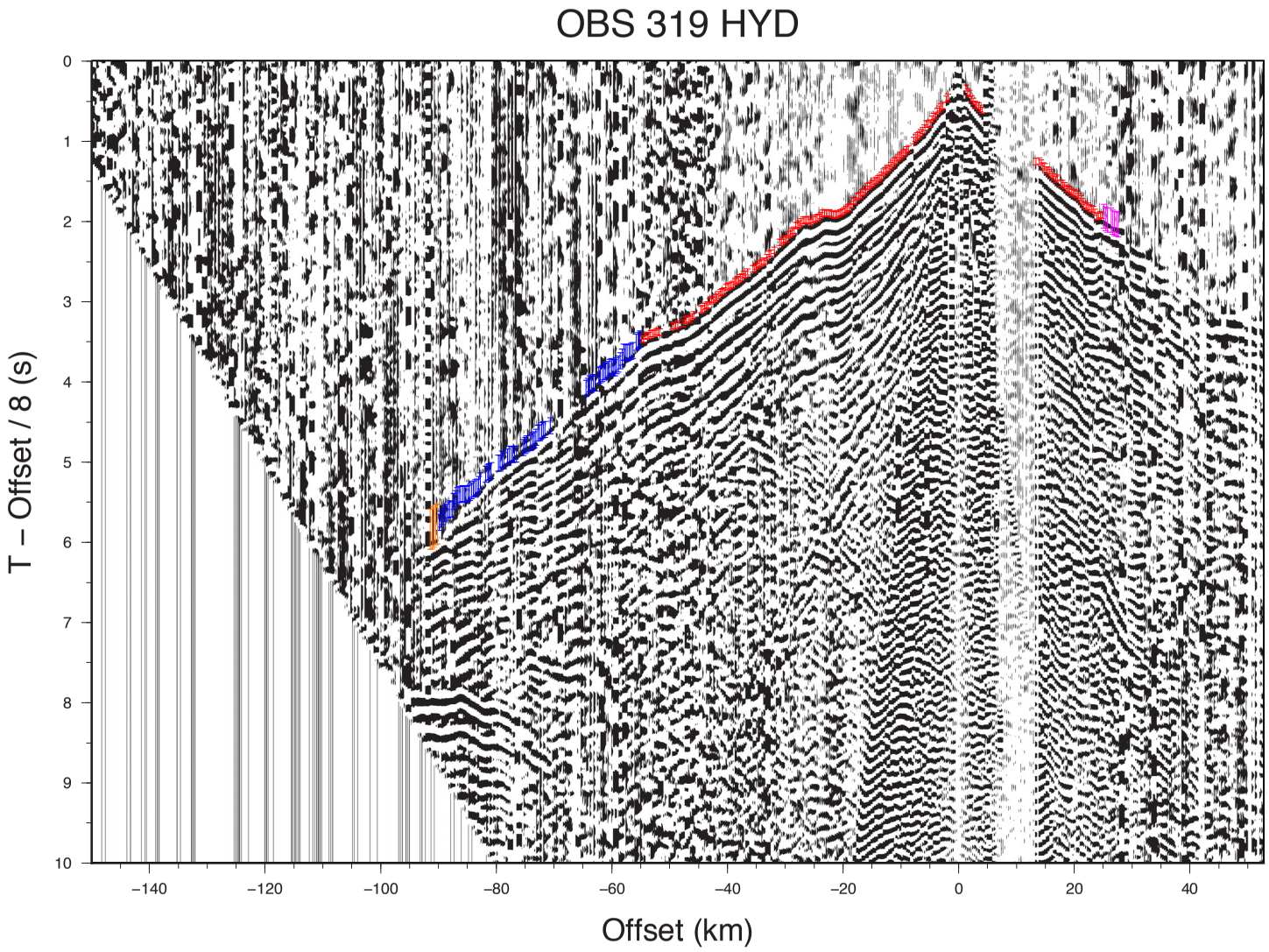

Figure C.54: OBS 319 (hydrophon channel) with first arrival times including picking uncertainties (from very clear to very unclear): 40 ms (red errorbars), 70 ms (green errorbars), 100 ms (blue errorbars), 150 ms (light blue errorbars), 200 ms (pink errorbars), 250 ms (orange errorbars).

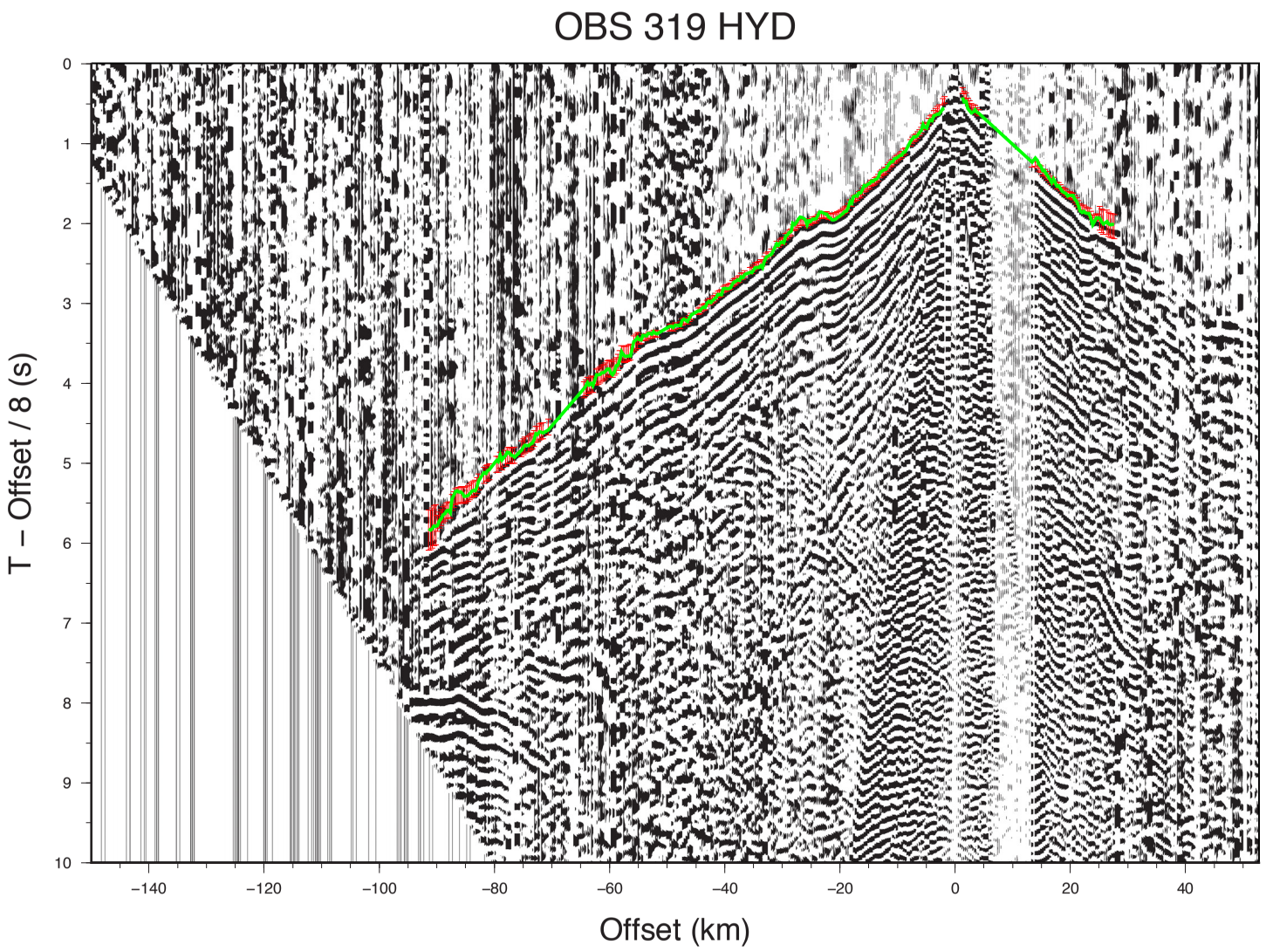

Figure C.55: OBS 319 (hydrophon channel) with observed first arrival times including picking uncertainties (red errorbars: 40 - 250 ms) and calculated (synthetic) arrival times (green line).

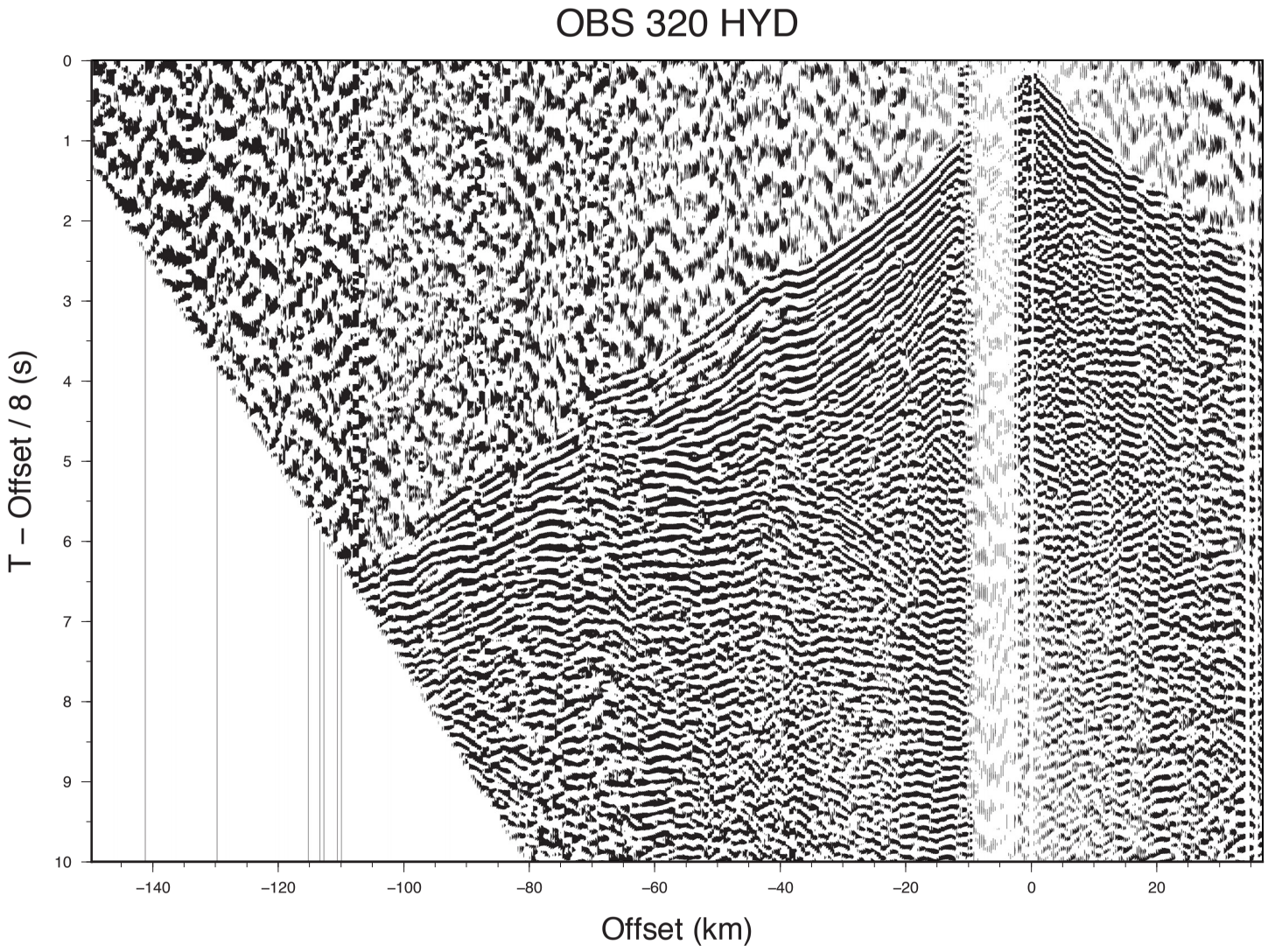

Figure C.56: OBS 320 (hydrophon channel). See Figure C.2 caption for additional description.

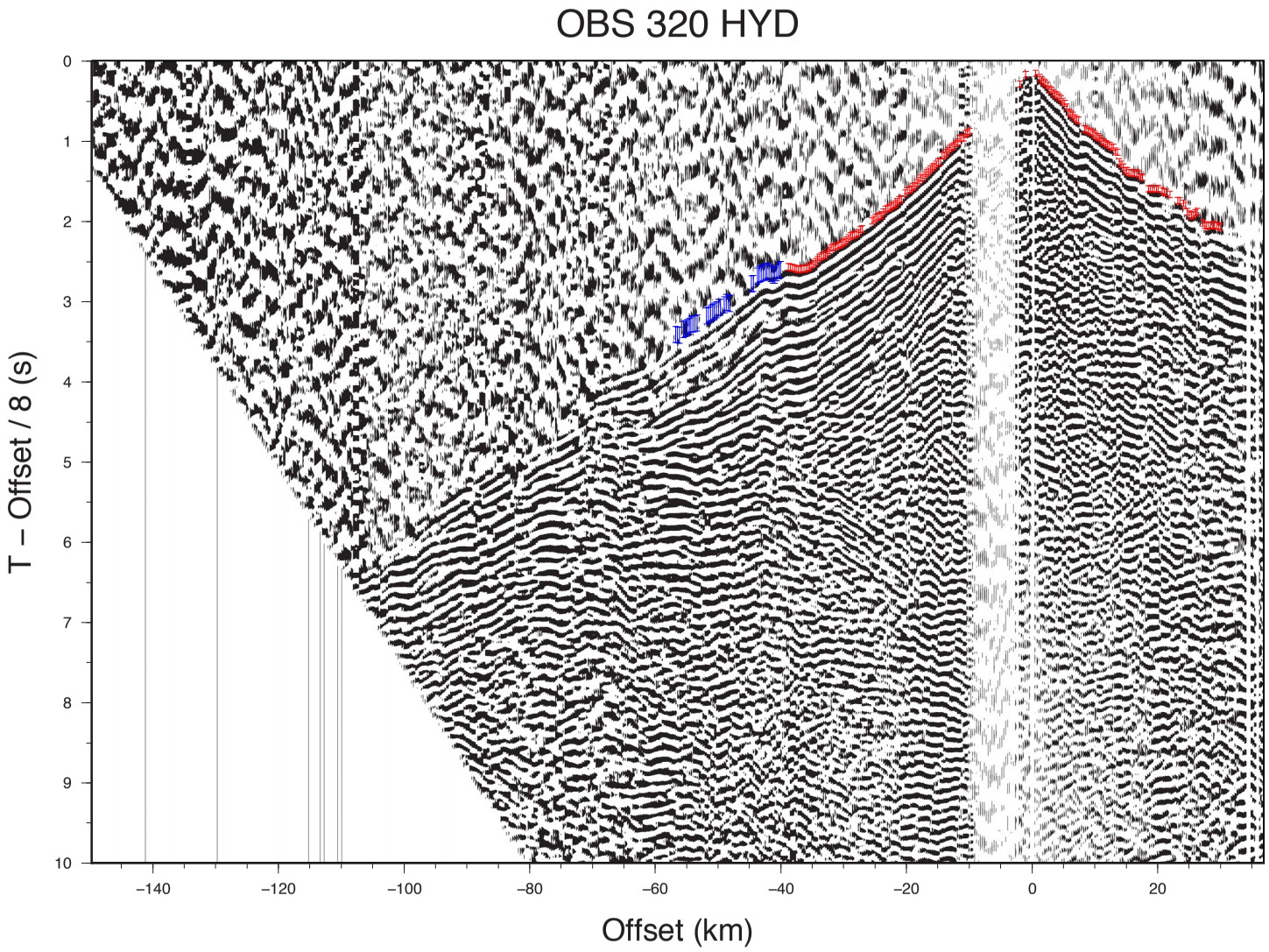

Figure C.57: OBS 320 (hydrophon channel) with first arrival times including picking uncertainties (from very clear to very unclear): 40 ms (red errorbars), 70 ms (green errorbars), 100 ms (blue errorbars), 150 ms (light blue errorbars), 200 ms (pink errorbars), 250 ms (orange errorbars).

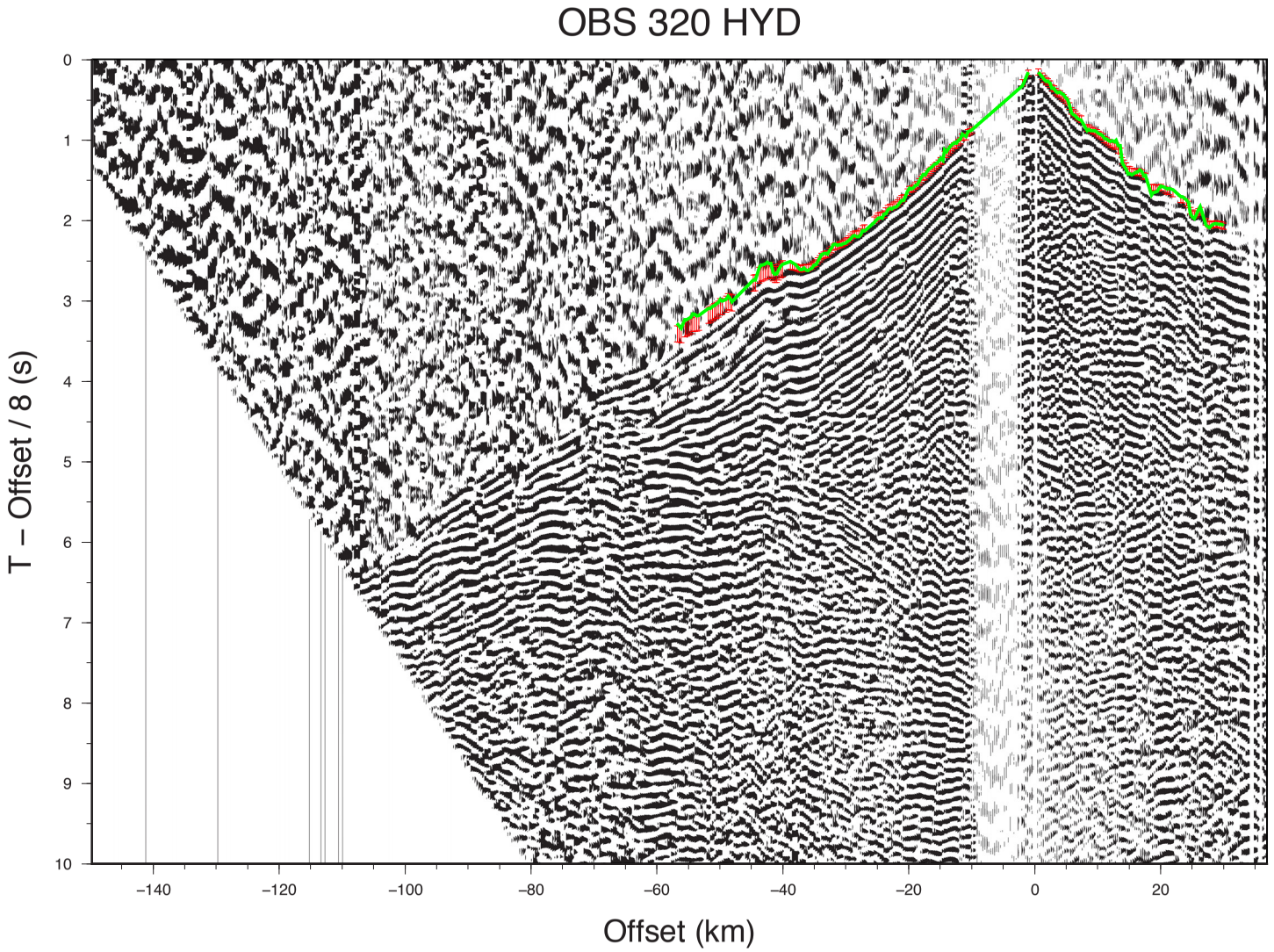

Figure C.58: OBS 320 (hydrophon channel) with observed first arrival times including picking uncertainties (red errorbars: 40 - 250 ms) and calculated (synthetic) arrival times (green line).

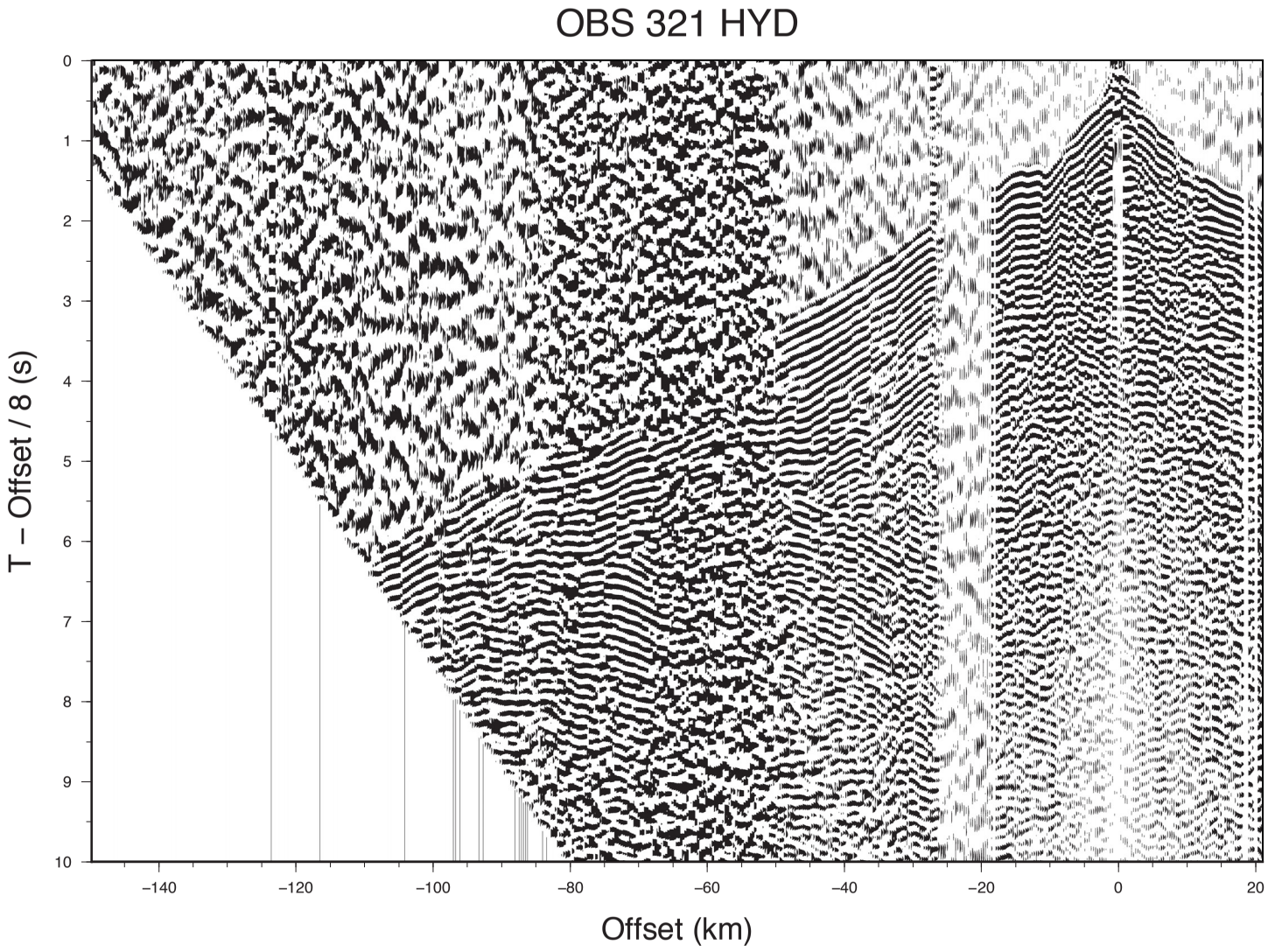

Figure C.59: OBS 321 (hydrophon channel). See Figure C.2 caption for additional description.

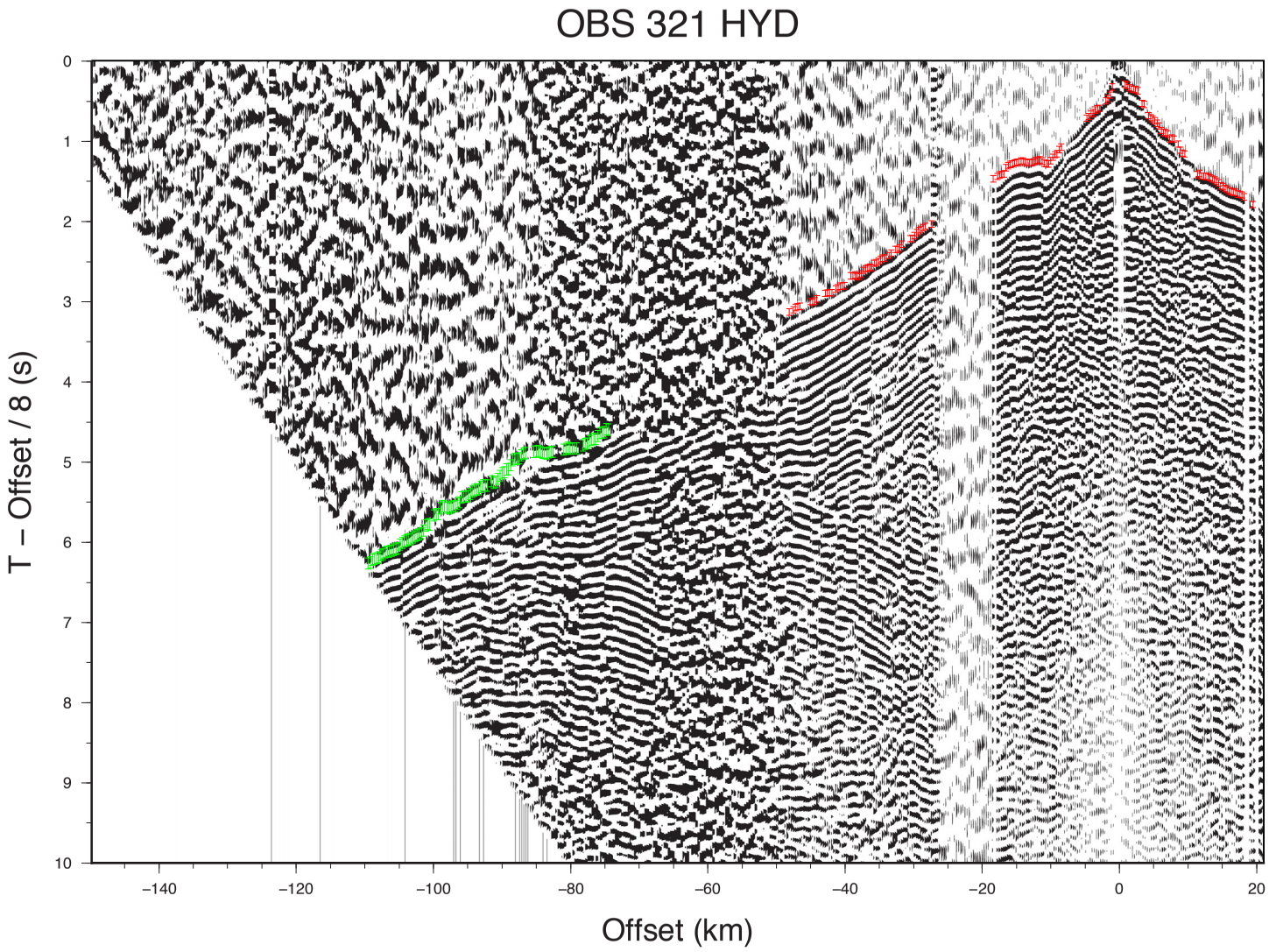

Figure C.60: OBS 321 (hydrophon channel) with first arrival times including picking uncertainties (from very clear to very unclear): 40 ms (red errorbars), 70 ms (green errorbars), 100 ms (blue errorbars), 150 ms (light blue errorbars), 200 ms (pink errorbars), 250 ms (orange errorbars).

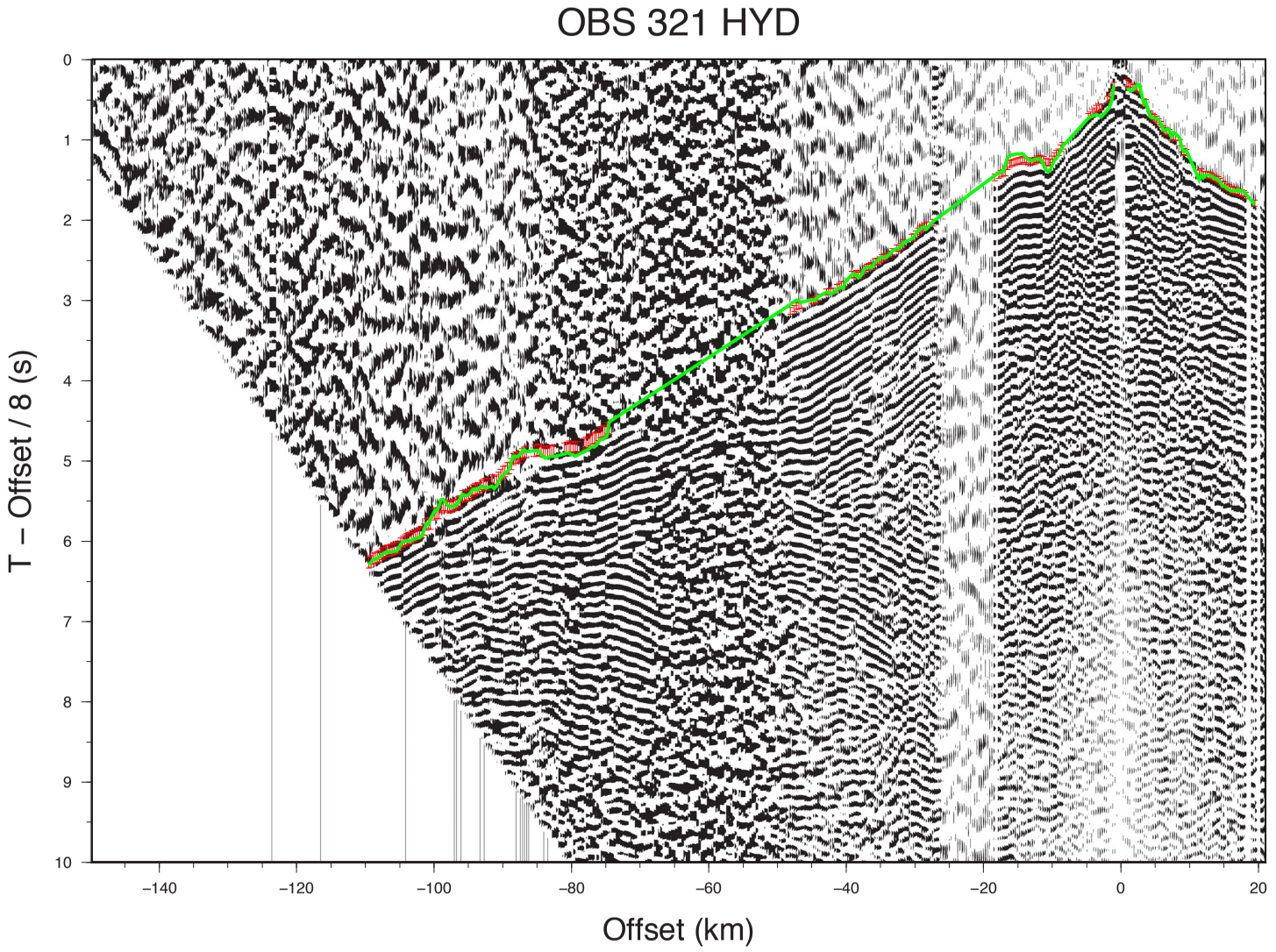

Figure C.61: OBS 321 (hydrophon channel) with observed first arrival times including picking uncertainties (red errorbars: 40 - 250 ms) and calculated (synthetic) arrival times (green line).

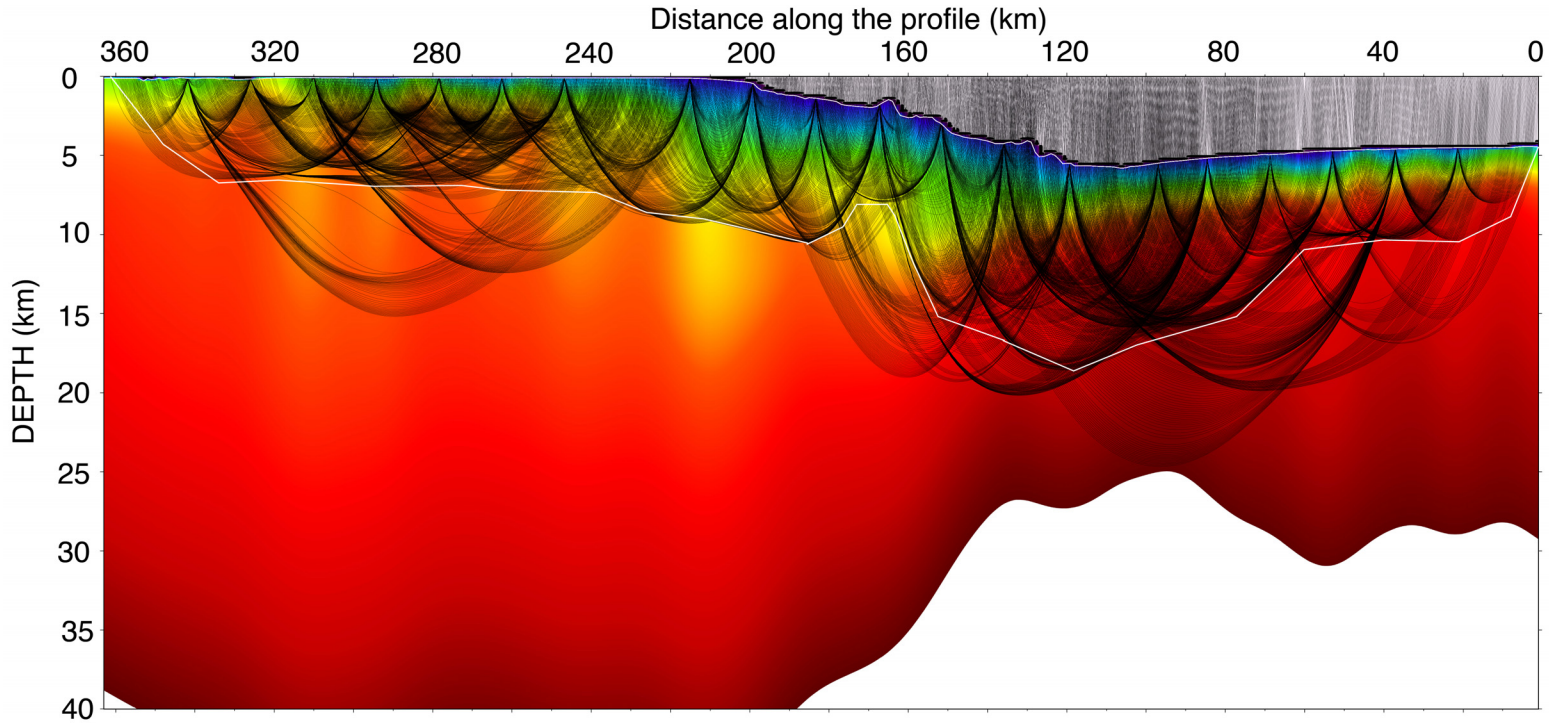

Figure C.62: Jive3d first arrival seismic tomography model of OBS Line 3 including ray coverage (thin black lines). White line marks the area of the velocity model with a sufficient dense ray coverage that were used determine avergae upper crustal velocities.

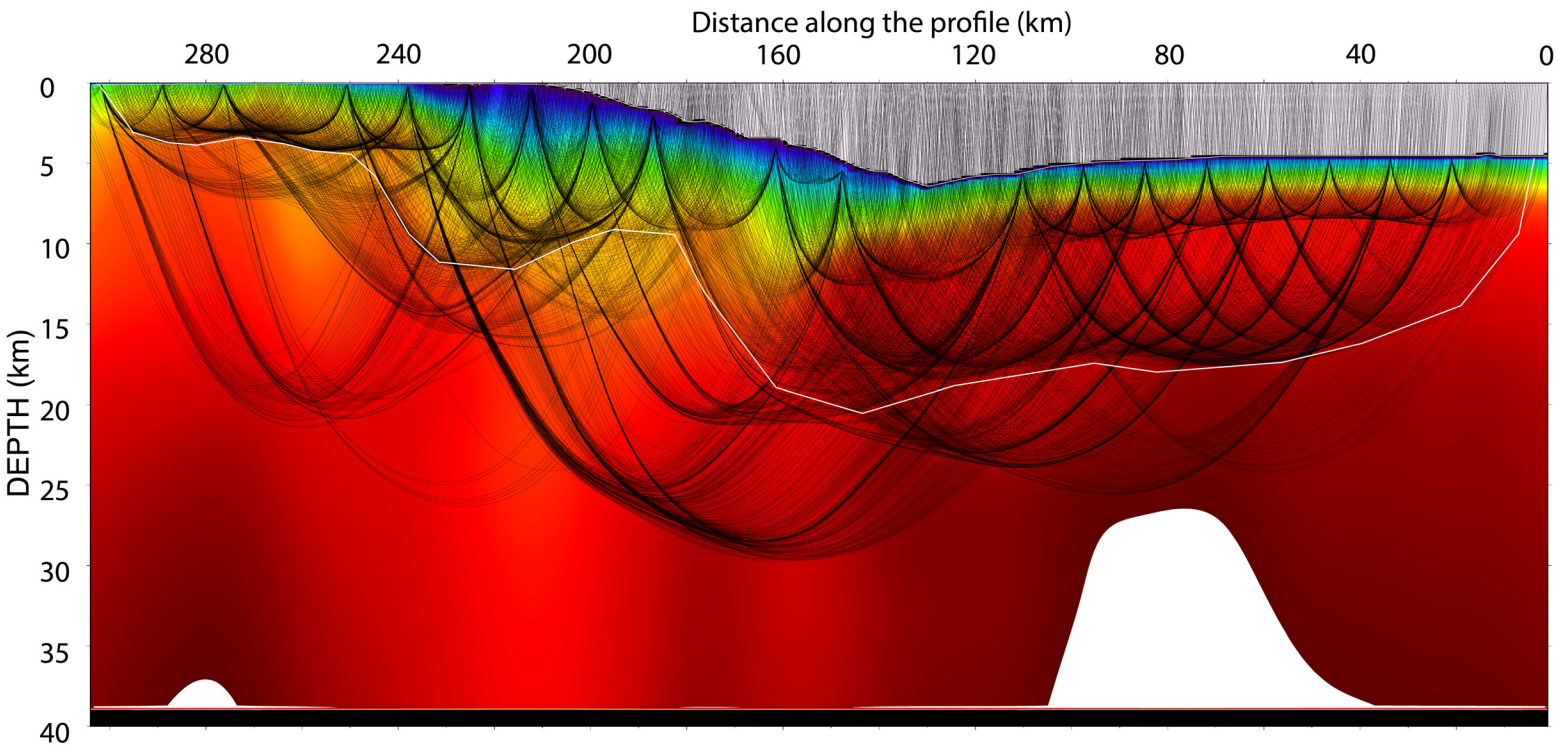

Figure C.63: Jive3d first arrival seismic tomography model of OBS Line 5 including ray coverage (thin black lines). White line marks the area of the velocity model with a sufficient dense ray coverage that were used determine avergae upper crustal velocities.